Alma Mater Studiorum – Università di Bologna

DOTTORATO DI RICERCA IN

Ingegneria Civile, Chimica, Ambientale E Dei Materiali

Ciclo XXXII

Settore Concorsuale: 09/D2 – Sistemi, Metodi e Tecnologie dell'Ingegneria Chimica e di Processo

Settore Scientifico Disciplinare: ING-IND/24 – PRINCIPI DI INGEGNERIA CHIMICA

Thermodynamic and Molecular Simulation of Pure and Mixed Gas Sorption in Polymeric Membranes

Presentata da: **Eleonora Ricci**

Coordinatore Dottorato

Prof. Luca Vittuari

Supervisore

Prof.ssa Maria Grazia De Angelis

Esame finale anno 2020

Abstract

Membrane gas separation has been successfully employed industrially for decades. However, the same few traditional materials still remain prominently in use, despite an ongoing effort in synthesizing and characterizing very promising new structures. One of the reasons of this impasse is that the characterization of membrane performance is often performed with pure-gas tests and modeling only, which are poor predictors of the effective performance of materials at relevant conditions. The permeation rates of the components of a gaseous stream, and consequently the selectivity of the material towards them, depends on the mixture composition. Especially in the case of high free volume glassy polymers, strong nonidealities are observed, due to competitive sorption and penetrant induced swelling, that radically modify the gas transport at multicomponent conditions compared to pure-gas cases. Therefore, for the development of competitive membranes, capable of performing well in a real-life application, a more realistic assessment of materials properties is required.

In this dissertation, dense polymeric membrane materials suitable for CO_2/CH_4 separation are considered. For these systems, gas transport is described by the solution-diffusion mechanism. The focus of this work was laid primarily on the study of the solubility contribution to permeability and on its evaluation at multicomponent conditions, both with experiments and with modeling tools using a minimum number of adjustable parameters, in an effort to reduce the experimental tests required. For the case of high free volume materials, the contribution of diffusivity to the overall separation is found to be lower than the contribution of solubility, therefore, a more fundamental understanding of this property can provide considerable insight on the performance of these materials.

The Non-Equilibrium Lattice Fluid model was applied to study mixed-gas sorption in traditional glassy polymers employed for CO_2/CH_4 separation, such as Cellulose Acetates, and innovative ones, such as polyimides (HAB-6FDA), Thermally Rearranged (TR) Polymers and Polymers of Intrinsic Microporosity (PIMs). The model results were validated against experimental data available and used predictively to gather information on the solubility and solubility-selectivity of systems for which mixed-gas sorption has

not been characterized yet. The different level of reduction in solubility with respect to pure-gas conditions experienced by each gas and the consequent enhancement of solubility-selectivity at mixed-gas conditions were correctly predicted by the model, as well as temperature, pressure and concentration effects. The Dual Mode Sorption model was also tested for the same systems and its strengths and weaknesses identified. A sensitivity analysis of its parameterization procedure revealed great uncertainty associated to its predictions of sorption at multicomponent conditions. A combined analysis of mixed-gas sorption predicted with the NELF model and experimental data on mixed-gas permeation from the literature revealed general trends concerning the predominant role of solubility in the selectivity at multicomponent conditions.

A new measurement protocol was developed for the determination of sorption isotherms at constant composition of the gas phase in equilibrium with the polymer, in the case of gas mixtures with an arbitrary number of components. Mixed-gas sorption of binary C_2H_6/CO_2 and C_2H_6/CH_4 mixtures and of ternary $C_2H_6/CO_2/CH_4$ mixtures in PIM-1 was measured with this new technique, finding strong competitive effects related to the presence of ethane. Predictions of the NELF model for binary and ternary sorption, performed using only pure-gas parameters as input, were in good agreement with the experimental data, even in the case of more complex scenarios.

Predictive Molecular Dynamics simulations have been carried out to investigate the effect of CO_2 up to high concentration on several properties of a polymeric material. A multiscale equilibration strategy was employed to study polymer chains up to high molecular weight. A systematic evaluation of thermodynamic and structural properties, local dynamics, gas solubility and diffusivity yielded good agreement with the experimental data for all properties except local dynamics, and meaningful trends with respect to the variables considered were obtained, thus confirming the possibility to investigate at the molecular level the effects of temperature, gas concentration and polymer molecular weight on the properties of polymeric materials with molecular modelling tools.

Table of Contents

List of Figures

Chapter 3

Chapter 4

Chapter 5

Chapter 6

List of Tables

List of Symbols

Latin letters

A	Helmholtz free energy per unit volume
a_e	Parameter from the linear energy relation, equal to 0.64
b_e	Parameter from the linear energy relation, equal to 9.2 for rubbery polymers and 11.5 for glassy polymers
b_i	Langmuir affinity constant of component i
b_0	Pre-exponential factor in Arrhenius law for b_i
c_i	Penetrant concentration inside the membrane
$C'_{H,i}$	Langmuir capacity constant of component i
C_N	Flory's characteristic ration
D, D_i	Binary diffusion coefficient (of component i)
D_0	Pre-exponential factor in Arrhenius law for diffusivity
$\overline{D}_i$	Average effective diffusion coefficient of component i
$D_{i,self}$	Self-diffusion coefficient of component i
$d_{i,exp}$	Experimental datum
$d_{i,calc}$	Calculated datum
$d_{k,j}$	Kinetic diameter of component i
E	Energy of the system
E_D	Activation energy of diffusion
$E_{\mathcal{P}}$	Activation energy of permeation

f_{ub}	Best fit parameter to calculate the upper bound relation
f_i	Fugacity of component i
$f(q)$	Atomic form factors
G	Gibbs free energy
$g(r)_{i-j}$	Radial distribution function of j around i
H_i	Henry's law constant
$I(q)$	X-ray diffracted intensity
J, J_i	Transmembrane flux (of component i)
k_b	Boltzmann constant
$k_{D,i}$	Henry's law constant of penetrant i in the dual mode sorption models
k_{D0}	Pre-exponential factor in Arrhenius law for $k_{D,i}$
k_{ij}	Binary interaction parameter between i and j in the Sanchez-Lacombe and in the Peng-Robinson equations of state
k_p	Thermal expansion coefficient
k_t	Isothermal compressibility
$k_{sw,i}$	Swelling coefficient associated to penetrant i
l	Membrane thickness
l_{BB}	Length of a backbone bond
L_i	Proportionality coefficient between transmembrane flux and chemical potential gradient of component i
M, M_i	Molar mass (of component i)
M_w	Molecular weight of the polymer
m	Mass of the system
N	Total number of molecules in the system
N_0	Number of empty cells in the lattice
N_{BB}	Number of scheletal bonds in a chain
N_{par}	Number of adjustable parameters
N_r	Number of occupied cells in the lattice
N_{tot}	Total number of experimental data points *n*
N_u	Number of experimental points used in the regression
n_u	Number of units in a chain

n_c	Number of components (gases + polymer)
n^i	Moles of component i
$\mathcal{P}$, $\mathcal{P}_i$	Permeability coefficient (of component i)
$\mathcal{P}_0$	Pre-exponential factor in Arrhenius law for permeability
$P_k(t)$	Legendre polynomial of order k
p	Pressure
p_i	Partial pressure of component i
p_i^{sat}	Vapor pressure of component i
p_i^*	Characteristic pressure of component i
$\tilde{p}_i$	Reduced pressure of component i
p^*	Characteristic pressure of the mixture
$\tilde{p}$	Reduced pressure of the mixture
P_{STP}	Pressure at standard conditions: 101325 Pa
q	Wavevector
q_i	Partial charge of interaction site i
R	Universal gas constant
R^2	Squared distance between chain segments
R_g	Radius of gyration
R_i	Position of particle i
R_{max}	End-end- distance of a fully stretched chain
r	Number of segments in a chain ("*mers*") Radial distance
r_i^0	Number of lattice cells occupied by a molecule of pure component i
r_i	Number of lattice cells occupied by a molecule in mixture
r_{ij}	Distance between two interaction sites
S, S_i	Solubility coefficient (of component i)
S_0	Pre-exponential factor in Arrhenius law for solubility
s_i	Confidence interval associated to datum i
$S(q)$	Static structure factor
T	Temperature

T_g	Glass transition temperature
T_m	Melting temperature
T_i^*	Characteristic temperature of component i
$\tilde{T}_i$	Reduced temperature of component i
T^*	Characteristic temperature of the mixture
$\tilde{T}$	Reduced temperature of the mixture
T_{STP}	Temperature at standard conditions: 273 K.
t	Time
t_0	Initial time
U	Potential energy
V	Volume of the system
V_0	Initial volume of the system
V_{pre}	Volume of the pre-chamber
V_{valve}	Volume of the valve stem
V_{sc}	Volume of the sample chamber
V_{tot}	Total unoccupied volume of the pressure-decay uquipment
v_i^*	Molar volume of a lattice cell of component i
v^*	Average close-packed molar volume in the mixture
w_i	Mass fraction of component i
x	Direction of the flux across the membrane
y_i	Molar fraction of component i
Z	Compressibility factor
z	Coordination number of the lattice

Greek letters

$\alpha_{i,j}$	Permselectivity of the membrane for component i over component j
$\alpha_{i,j}^S$	Solubility selectivity of the membrane for component i over component j
$\alpha_{i,j}^D$	Diffusivity selectivity of the membrane for component i over component j
α_{lib}	Amplitude of the fast exponential decay in mKWW function

$\beta_{i,j}$	Parameter in the upper bound relation
β_{KKW}	Stretching exponent in a mKWW function
β	Inverse of the product between Boltzmann constant and temperature $1/k_BT$
γ_i	Activity coefficient component i
ΔH_c	Enthalpy of condensation
ΔH_f	Heat of fusion
ΔH_f^o	Heat of fusion of a perfect crystal
ΔH_m	Partial molar enthalpy of mixing
ΔH_s	Enthalpy of sorption
ΔH_D	Enthalpy of sorption of Henry's mode
ΔH_b	Enthalpy of sorption of Langmuir's mode
Δu_{inter}	Change to the pairwise energy of the system in Widom's test
ε_{ij}	Non-bonded interaction energy between component i and j
ϵ_0	Vacuum permittivity
ζ	Partition function
$\lambda_{i,j}$	Parameter in the upper bound relation
μ_i	Chemical potential of component i
μ_i^{ex}	Excess chemical potential of component i
ρ	Mass density of the mixture
ρ_i	Mass density of component i
ρ_{mol}	Molar density of the polymer
ρ_{pol}	Polymer mass density in the mixture
ρ_{pol}^0	Dry polymer mass density
ρ_i^*	Characteristic density of component i
$\tilde{\rho}_i$	Reduced density of component i
ρ^*	Characteristic density of the mixture
$\tilde{\rho}$	Reduced density of the mixture
ρ_A	Density of the amorphous phase
ρ_C	Density of the crystalline phase
ρ_{SC}	Density of the semicrystalline material

σ_i	Distance at which the inter-particle Lennard-Jones potential is zero
τ_c	Segmental relaxation time
τ_{lib}	Characteristic times of librations in a mKWW function
τ_{seg}	Characteristic decay time in a mKWW function
ϕ_i	Volume fraction of component i in closed packed conditions
Ψ	Number of microstates
Ω	Vector of mass ratios between the i^{th} penetrant and the polymer
ω_i	Mass fraction of component i

Subscripts, superscripts and abbreviations

com	Center of mass
eq	Equilibrium
gas	Gas phase
loc	Local variable
pol	Polymer phase
ref	Reference state
$post$	Post-equilibration
u	Upstream side of the membrane
δ	Downstream side of the membrane
AAD	Average absolute deviation
DMS	Dual Mode Sorption
EoS	Equation of State
FFV	Fractional Free Volume
MAD	Maximum absolute deviation
$mKWW$	modified Kohlrausch–William–Watts function
NE	Nonequilibrium
$NELF$	Non-Equilibrium Lattice Fluid
PIM	Polymer of Intrinsic Microporosity
RSE	Relative Standard Error
SL	Sanchez-Lacombe
TR	Thermally Rearranged

Chapter 1

Introduction

1.1 Motivations

1.1.1 Anthropogenic CO_2 emissions and Climate Change

Taking urgent action to combat climate change has been identified as one of the Sustainable Development Goals of the United Nations to achieve a better and more sustainable future and be able to meet the needs of people living today without compromising the needs and wellness of future generations [1]. Within this perspective, economic, social and environmental considerations need to be balanced. The Intergovernmental Panel on Climate Change (IPCC) produced a special report in October 2018 [2] on the impacts of global warming of 1.5 °C above pre-industrial levels. Research evidences the acceleration of the pace at which global temperature is rising compared to pre-industrial levels (**Figure 1.1**) and the IPCC warns that if the 1.5-degree ceiling is not avoided, dramatic consequences for life on earth have to be expected, such as more frequent extreme weather conditions, with associated increase in death, injuries and homelessness resulting from natural disasters, the disappearance of the Arctic sea ice and rise of the sea levels, the irreversible mutation of several ecosystems around the world, tightly tied to the risk of extinction of numerous species. The severity of the threat urges "rapid, far-reaching and unprecedented changes in all areas of society".

Despite the increasing awareness around this compelling issue, nowadays the human-induced temperature increase has already reached about 1 °C above pre-industrial levels, and the projections show that the value of 1.5 °C could be reached as soon as 2040, if the current rate of increase continues.

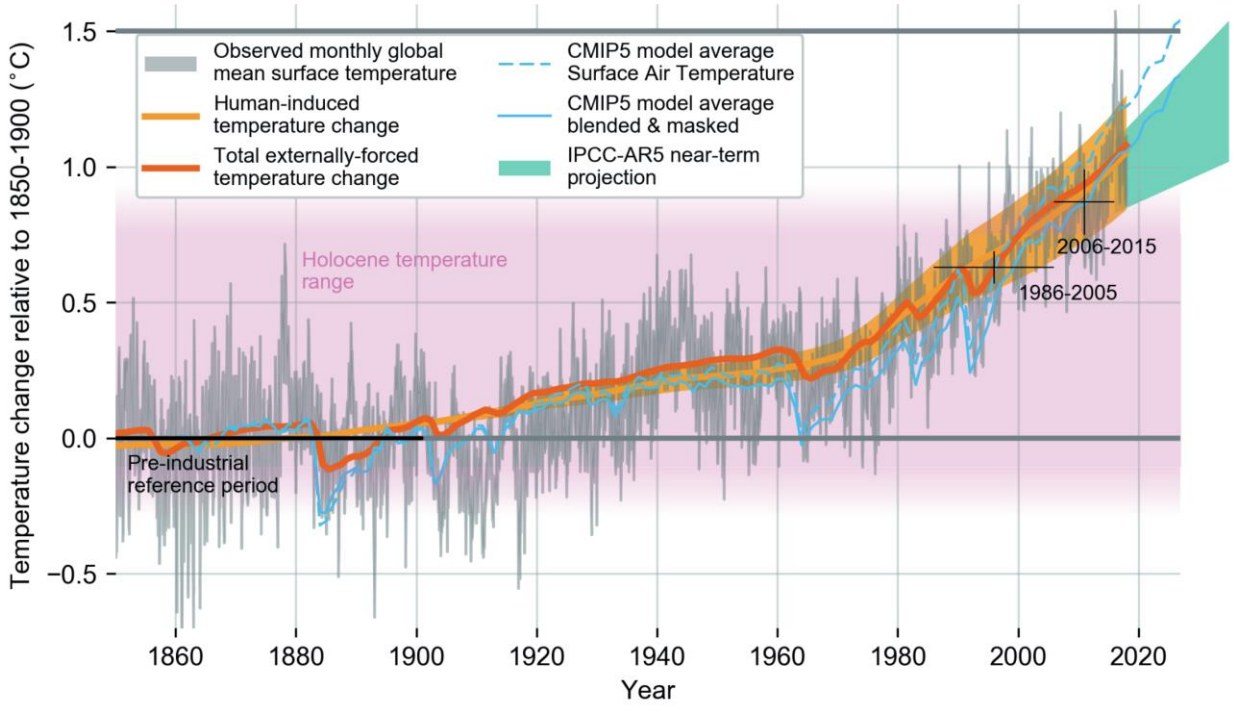

Figure 1.1. Evolution of Global Mean Surface Temperature (GMST) over the period of instrumental observations reported in the IPCC 2018 report [2]. Grey shaded line shows monthly mean GMST, expressed as departures from the 1850–1900 period. The human-induced (yellow) contribution to the total (orange) GMST changes are shown.

Greenhouse gas emissions are recognized as one of the leading causes of the global temperature increase [3], and, among them, CO_2 is the gas released in greatest amount, with current annual emissions estimated at more than 36 billion tons, followed by 8 billion tons of CH_4 and 3 billion tons of N_2O [4]. One of the sectors contributing the most (and to an increasing extent) to the emissions is the energy sector, inclusive of public heat and electricity production, fugitive emissions from solid fuels, oil and gas, manufacturing industries and construction, as shown in **Figure 1.2**. Given the predominant contribution of this sector to the total emissions, cutting energy consumption by increasing energy efficiency is a necessary step towards achieving a greater sustainability of our way of life. The chemical and petrochemical industry is responsible for 30% of the total industrial energy use [5], and it is estimated that a 10-15% of the total world's energy requirement is needed to realize thermal driven separation processes. By adopting the so called best practice commercial technologies, energy efficiency could increase by 18 to 26%, and simultaneously reduce CO_2 produced up to 32% [5].

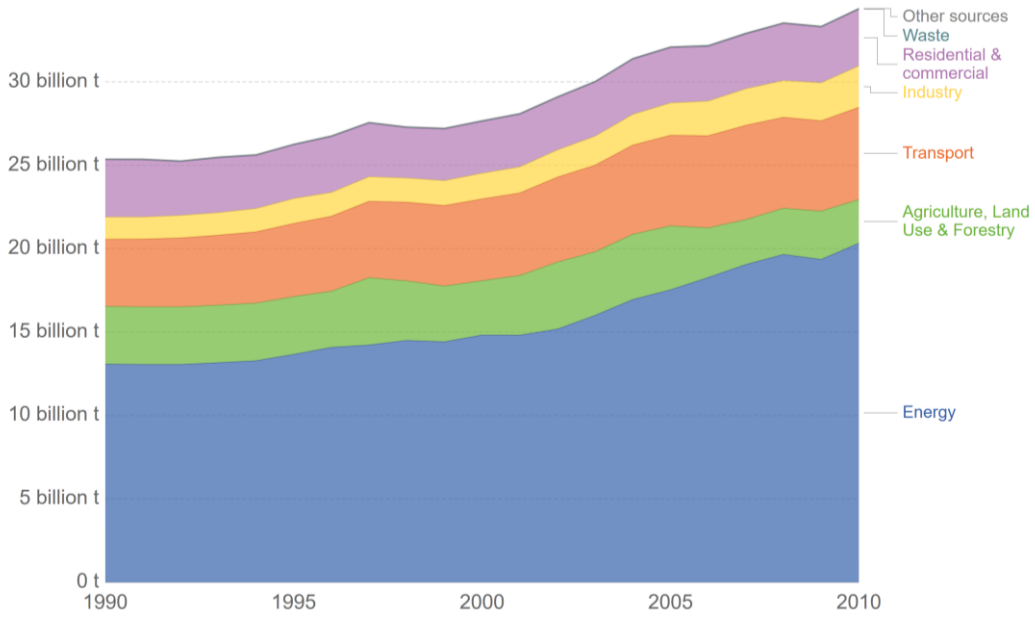

Figure 1.2. Contribution of different economic sectors to CO_2 emissions. Source: Our World in Data [6].

It is meaningful to note that, even though the world energy consumption is increasing, the integration of more energy-efficient technologies has resulted in the decrease of the energy intensity, that is the units of energy consumed per unit of gross domestic product (GDP) produced [7]. This trend is accelerating in recent years: the energy intensity decreased on average 1.3% per year between 1970 and 2010, whereas, since 2010, the intensity has decreased at an average rate of 2.1% per year [7], while, in the same period, economic growth went in the opposite direction [8]. This is an encouraging trend, testifying that economic growth does not need to be the price to pay to combat climate change [8,9]. Moreover, further evidence suggests that decarbonization and economic growth are decoupled. Looking at the relative contributions of different sectors to both GDP increase and CO_2 emissions, it can be seen that, sectors contributing most to economic output typically do not contribute to emissions significantly. In **Figure 1.3**, data for the USA in

2009 is shown, but the same trend is true across different countries [6]. The technology sector, in particular, is one of the largest contributors to economic growth in recent years, and at the same time responsible for a low share of CO_2 emissions, which suggests the possibility that the carbon footprint necessary to sustain economic growth will continue to lower in the future.

Nevertheless, to address the sectors which are responsible for the largest share of CO_2 emissions, increasing energy efficiency alone is not sufficient. In addition to that, deploying technologies for carbon capture to reduce CO_2 emissions from large point sources, such as power plants, is an indispensable strategy to tackle the issue [10]. However, capturing CO_2 will increase the energy requirements of a plant by 25-40% with the use of current available technological solutions [10]. Therefore, the development of technologies with higher energy efficiency is essential for carbon capture applications as well.

There is no definitive way to limit global temperature rise and counteract the effects of climate change. Several complex and interconnected actions will have to take place at all levels. Everyone, from companies, to institutions, to private citizens will have a vital part to play.

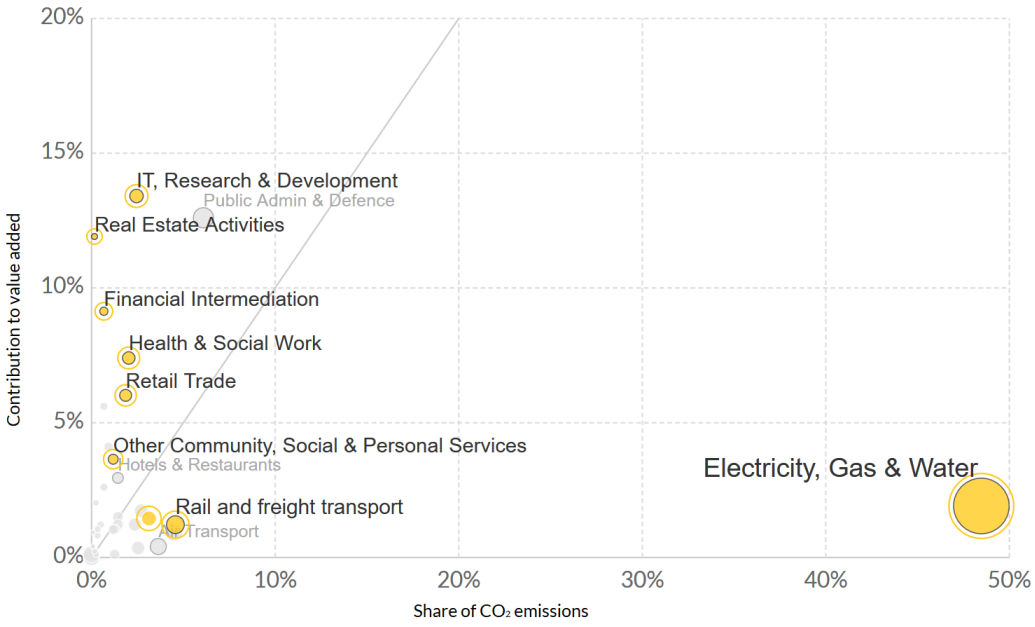

Figure 1.3. Contribution of different economic sectors to CO_2 emissions and GDP in the USA in 2009. Source: Our World in Data [6].

1.1.2 Carbon Capture

Direct CO_2 capture from the atmosphere to progressively bring down its concentration is an appealing idea and several conceptual solutions are being proposed and evaluated from the technical and economical point of view, to meet the challenges posed by the very low concentration of CO_2 in air and the delocalized nature of the problem [11]. As an example, Dittmeyer and co-workers [12] recently presented a preliminary analysis of the potential of retrofitting air conditioning units in offices, commercial and public buildings,

into integrated, scalable, and renewable-powered devices capable of decentralized CO_2 capture and conversion into hydrocarbon fuels. Clearly, also any action taken to enhance the natural processes that remove CO_2 from the atmosphere, such as reforestation, would have a beneficial impact.

The greatest potential for reducing CO_2 emissions in the atmosphere lies in its capture from large point sources in power and chemical plants, where it is found at high concentration. A carbon capture unit can be effectively integrated as a **pre-combustion** operation (CO_2/H_2 separation), characterized by harsh operating conditions (pressure around 40 - 80 bar, temperature in excess of 300 °C), but a rather concentrated stream (20 - 40 mol% CO_2) [13]. Alternatively, it can be implemented as a **post-combustion** operation to treat the flue gases in a power plant (CO_2/N_2 separation), where milder conditions are found (temperature < 200 °C and atmospheric pressure), but also less concentrated streams (5 - 15 mol% CO_2) [14]. Finally, another significant application is in **natural gas sweetening** and **biogas upgrading** (CO_2/CH_4 separation). In these latter applications, the same main separation is performed. In the case of natural gas, the CO_2 concentration in the stream to be treated can vary considerably, depending on the origin and the characteristics of the well (1 - 40 mol% CO_2 [15,16]), but it is already compressed (typically 20 - 70 bar [16]), whereas in biogas treatment typical conditions are atmospheric pressure and 30 - 45 mol% CO_2 [17]. In addition to separating CO_2 from the process stream, the use of membranes for CO_2/hydrocarbon separation, instead of thermal processes, will reduce the energy demand of the plant, thus the carbon footprint of the chemical and petroleum industries implementing this technology.

Once it has been separated, CO_2 must be prevented to enter the atmosphere and several alternatives are at study, such as employing it in performing Enhanced Oil Recovery [18], storing it long-term in underground geological formations [10], or directly consuming it as reactant to produce chemicals, such as ethanol, hydrocarbons, urea or fertilizers [19].

Technologies to perform carbon capture include solvent absorption, adsorption in porous media, cryogenic separation and membrane separation. At present, the most mature technology for CO_2 separation is solvent absorption. **Chemical absorption** is performed for post-combustion capture in various industries, including cement, iron and steel, power plants, and oil refineries, using aqueous ammonia, amine-based solvents such as monoethanolamine (MEA), diethanolamine (DEA), and N-methyldiethanolamine (MDEA) or alkaline solvents such as $Ca(OH)_2$ and NaOH [19]. Examples of **physical absorption** applications to carbon capture are represented by the Selexol® process, which uses a mixture of dimethyl ethers of polyethylene glycol as scrubbing solvent, and the Rectisol® process, using methanol. These solutions are preferable to chemical absorption at high pressure, therefore they are usually applied in pre-combustion capture [20]. The main disadvantage of chemical and physical absorption processes is the high energy required for the regeneration of the solvent [21]. In addition to the high operating costs, other drawbacks are the large footprint of the equipment and the inherent risks associated with the use of chemicals. Recently, ionic liquids (ILs) have been identified as suitable alternatives to conventional physical solvents. Their appeal lies in their low volatility, low vapor pressure, high thermal stability at elevated temperatures, and low regeneration energy requirements. However, their high viscosity, high cost, and potential corrosive nature of their mixture with acid gases, constitute important drawbacks to their application at large scale [22].

Alternatively, **adsorption** in porous media such as activated carbons and zeolites placed in fixed bed columns can be performed. As in the case of amine scrubbing, porous materials need to be periodically regenerated. Since adsorption is favored by high pressure and low temperature, changes in the operating temperature or pressure can be exploited to perform the regeneration, thus adsorption technologies are divided in pressure swing adsorption (PSA) and temperature swing adsorption (TSA) [23,24], which use lower pressure and higher temperature, respectively, to desorb CO_2. The amount of time required for the regeneration step depends on sorption and desorption kinetics of the gases from the solids, controlling the economic efficiency of the process. A high affinity between the gas and the adsorbent facilitates the adsorption step; however, the stronger the affinity, the more difficult it is to desorb the gas, and the higher the energy consumption during the regeneration.

Another possibility is the **cryogenic** removal of carbon dioxide, which does not involve the use of chemical solvents and operates at atmospheric pressure. However, the low temperatures needed to liquefy CO_2 make this technology very energy intensive. Moreover, a "regeneration step" is required also in this case, as CO_2 tends to solidify on the exchanger surface, reducing the heat transfer coefficient [25].

Finally, **membrane separation** is an energy efficient and environmentally friendly technology for CO_2 capture, because it does not utilize a medium requiring regeneration and does not produce waste streams to be treated. However, it is challenging to obtain high purity products and membrane materials performance is sensitive to the presence of trace contaminants, requiring pretreatment of the gaseous streams.

In order to overcome the limitations of different methods and achieve higher energy efficiency and lower cost, the effective design of **hybrid processes**, will be needed, with techno-economic analysis of process flowsheets, optimized design of equipment and pilot scale assessment of each design, using real gas streams, which is an area of research still under-investigated [26].

1.2 Polymeric Membranes for Carbon Capture Applications

Polymeric membrane materials are selective barriers, that are crossed by the different components of a mixture at different rates, and they can be employed to perform a variety of separations of low molecular weight species. Indeed, polymers are used as membrane materials in several industrial, medical and environmental applications dealing with separation and purification of gases and liquids, including water desalination, dialysis, food processing and packaging, sensor development, drug delivery and gas separation. Nowadays, gas separation with membranes is employed industrially for hydrogen recovery, nitrogen production, air dehydration, and natural gas sweetening [27–32].

Compared to other industrial separation technologies, membranes are advantageous owing to their low capital costs, small footprint, thanks to a very compact and modular design, and lower failure rates, due to the absence of moving parts. Moreover, this technology has an inherent higher energy efficiency than thermal separations, because it does not rely on phase changes [31], and in fact it is up to 90% less energy intensive than distillation [33].

Considering carbon capture applications, CO_2 removal from natural gas with membranes, with the aim to meet distribution pipelines specifications [34], has found industrial application since the 1980s [32,34] with the use of anisotropic cellulose acetate membranes [35]. Indeed, in the transition from fossil fuels to renewable energy sources, natural gas is expected to play an important part, due to its lower environmental footprint compared to coal and oil. Nonetheless, nowadays membrane technology for natural gas treatment covers only less than 10% of the market, which is dominated by solvent absorption using amines [27]. At present, the higher convenience of membrane operations is found in small scale applications, with high CO_2 concentration in the feed, and in offshore plants where space constraints are significant. In order to promote a larger market penetration, membrane materials capable of achieving higher selectivity are needed [36]. Natural gas is not the only source of methane: biogas is a renewable energy source produced by anaerobic degradation of organic matter operated by microorganisms [37]. The concentration of CO_2 in this process is generally higher than in natural gas treatment, which favors the use of membranes. In small biorefineries, if the produced biogas is directly consumed as fuel, and not introduced in distribution network, upgrading is not strictly necessary; however, if a carbon capture unit is implemented, it provides an opportunity to realize processes with a negative carbon footprint. Research efforts are devoted also to the development of cost-effective membranes for CO_2/N_2 separation for flue gas treatment, capable of meeting regulatory limits in terms of concentration [38]. While it was demonstrated that there is an opportunity for membranes in this field, it still remains a challenge from the economic point of view [39,40]. Membranes find also application in integrated-gasification combined cycle (IGCC) plants [41], to separate CO_2 from gasified coal syngas, using either CO_2 selective or hydrogen selective materials. With state-of-the-art materials, it was found that, compared to absorption, the capital cost could be reduced by 40% and the energy efficiency by 50%. However, to realize an even more convenient operation, membranes with higher permeance are required [41].

The need for better performing membrane materials has prompted research into the development of new polymer architectures with enhanced gas permeability and gas sieving capability. Hundreds of polymers have been evaluated as membrane materials for gas separations, but fewer than 10 have made it into industrial applications. Several reasons have been identified for this lack of success of new promising polymeric structures to penetrate the market. Physical aging and plasticization effects are detrimental for the long term operation of the membrane and significant effort has been devoted to the fundamental understanding of these phenomena and finding ways to mitigate them in membrane materials [42–46]. Furthermore, a main challenge faced in the development of new membrane materials is represented by the existence of an empirical trade-off between the two key parameters of the operation, i.e. the permeability and the selectivity, which are very seldom simultaneously high. For every gas pair, the logarithm of selectivity versus the logarithm of the permeability of the most permeable gas has been shown to lie at or below a limiting line, customarily referred to as the Robeson upper bound [47,48]. Ultra-permeable materials usually lack in selectivity, whereas highly-selective materials exhibit lower permeability [48]. Therefore, the efficiency that can be achieved by the operation in terms of purity and productivity is limited and it is always necessary to find the right compromise between these factors [49,50] in order to maximize the convenience of the process. The Robeson upper-bound constitutes a benchmark for the comparison of materials performance and its location is progressively shifting as new and improved materials surpass the current threshold. The first definition dates back to 1991 [47], while a major revision was proposed in 2008 [48], to reflect the breakthrough made with the discovery of materials such as Polymers of Intrinsic Microporosity and Thermally Rearranged Polybenzoxazoles. The 2008 upper bound for CO_2/CH_4 separation is reported in **Figure 1.4**.

1.2.1 Materials

In membrane materials design research, countless structural and molecular modifications have been investigated in order to achieve a better separation performance, enhancing both permeability and selectivity, to make membranes more economically competitive, in addition to being more energy-efficient and environmentally friendly [49]. In recent years significant breakthroughs have been witnessed and materials with improved performance, capable of surpassing the Robeson upper bound were reported [43,51–61]. It is striking, however, that despite the ongoing effort and the discovery of polymers with remarkable properties, **cellulose acetate** is still one of the few materials used in real-world applications, together with some perfluoropolymers and polyimides, that found limited commercial application more recently [34]. As it can be seen in **Figure 1.4** for the case of CO_2/CH_4 separation, these materials are located below the upper bound and several better performing structures have been developed. In general**, glassy polymeric materials** display the best combination of properties for the separation of light gases, compared to rubbers, and they dominate the upper bound [62].

Aromatic polyimides exhibit excellent thermal, mechanical and chemical stability [29,63,64], and have already found limited commercial application in CO_2/CH_4 separation with membranes [27]. On average, these materials are characterized by low permeability and high ideal selectivity, owing to their high chain stiffness and low free volume, which enhances differences in the mobility of penetrants inside the polymer. If dianhydrides incorporating a spiro center are used, polyimides of intrinsic microporosity can be obtained (PIM-PI). In these materials, the use of kink units promotes a more inefficient chain packing, resulting in higher free-volume and, consequently, higher gas permeability accompanied by moderate permselectivities [65,66]. Indeed, the best separation performance is found in the case of **high free volume materials**, exhibiting exceptionally high permeability and moderate selectivity. Among those we find the family of **Polymers of Intrinsic Microporosity** (PIMs) [67–70]. These materials have shown very high gas permeation rates, while maintaining acceptable selectivity values, demonstrating at the same time great thermal and chemical stability [70]. The ladder-like backbone of these polymers consists of a series of fused aromatic rings and it is therefore severely rotationally hindered. Moreover, the presence of shape-persistent contortion sites in the repeating unit results in exceptionally high free volume, organized as a network of interconnected micro-cavities, and capable of sieving effects, as shown by experimental and molecular simulation investigations [60,71–76]. **Thermally Rearranged** (TR) **polymers** [71,77–82] constitute another interesting class of materials for gas separation applications. They are polybenzoxazoles or polybenzothiazoles, characterized by excellent thermal and chemical stability, as well as good resistance towards ageing and plasticization. Because of their exceptional chemical resistance, they are insoluble in most solvents and, therefore, unsuitable for membrane fabrication. Nonetheless, Park et al. [77] circumvented this limitation by showing that they could be obtained starting from aromatic polyimide precursors, highly soluble in common solvents, through an irreversible molecular rearrangement process at high temperatures (350 - 450 °C). These materials have received increasing attention for membrane separation applications [58,83–88], owing to higher permeability values with respect to the polyimide precursors. They also maintain good selectivity, especially for CO_2/CH_4 and CO_2/N_2 gas pairs. Positron annihilation lifetime spectroscopy (PALS) measurements and molecular modeling revealed that, during the rearrangement process, a favorable free volume distribution for gas separation is created, which is thought to be shaped as an hourglass. A large average cavity size, favoring high permeability, is coupled with a narrow cavity distribution and small bottlenecks connecting the cavities, which confer higher ideal selectivity compared to other materials with a similar Fractional Free Volume (FFV) [77,78,89,90].

Hybrid and **composite materials** incorporating zeolites, metal organic frameworks, graphene, carbon nanotubes and other kinds of fillers into polymer matrices are being investigated for gas separation applications as well [27,57,61,91–93], especially to provide ways to reduce the detrimental effects of ageing and plasticization shown by amorphous polymer membranes.

1.2.2 Ideal *vs.* Multicomponent Performance

The most commonly used performance metric to evaluate gas separation membranes, the positioning in the Robeson plot, is usually evaluated at ideal conditions, meaning that the pure-gas permeability is measured separately for the two main components of the mixtures and their ratio at a fixed pressure value is taken to be the ideal selectivity of the membrane. If the same evaluation is performed using multicomponent data instead, the position of a point in the Robeson plot can move considerably [70,80,94–96]. Some relevant examples are collected in **Figure 1.4**, which reports the 2008 CO_2/CH_4 upper bound [48]. The source of the data and the corresponding temperature, pressure and composition conditions are summarized in **Table 1.1**. Even though the multicomponent data are not evaluated at the exact same conditions, the absence of systematic trends relating the behavior at ideal and multicomponent conditions emerges: some cases show no significant variation of properties, while in other cases either an increase or a decrease in permeability and/or selectivity is observed. Pure-gas measurements are a necessary first step in the characterization of a new material, however, they are very often a poor predictor of the performance in actual operating conditions [32]. To uncover all the relevant phenomena taking place at multicomponent conditions, a broad experimental campaign, encompassing a wide range of temperatures, pressures and compositions, would be needed. Strikingly, even materials of the same chemical family, such as HAB-6FDA and Matrimid® polyimides, show an opposite behavior with respect to their ideal *vs.* multicomponent selectivity. The picture is complex even considering only a binary mixture, which is still a simplification of the real-life scenario.

Indeed, natural gas for example contains methane, ethane, carbon dioxide, heavier hydrocarbons, hydrogen sulfide, and traces of many other compounds, including toluene, benzene and xylene, with composition varying significantly between different wells [34]. The presence of additional components affects the separation performance as well as the stability of the membrane, since, in realistic conditions, corrosive solutions could be generated by the simultaneous presence of acid gases and water in the gas stream [97]. New materials are potentially able to perform better than current standards, and are likely to reduce the process costs by 5 - 10% [27]. However, since the response of these new materials to the whole set of conditions found in a real-life scenario is rarely documented, they struggle to make it into a commercial application and increase the market share of membrane technology.

The present dissertation is conceived to be part of the ongoing effort to fill this gap, both from the experimental and the modelling point of view. The aim is to develop techniques and modelling strategies that are capable of representing the relevant material properties closer to the actual operating conditions found in natural gas sweetening, and shed light on the nonidealities arising in the multicomponent case.

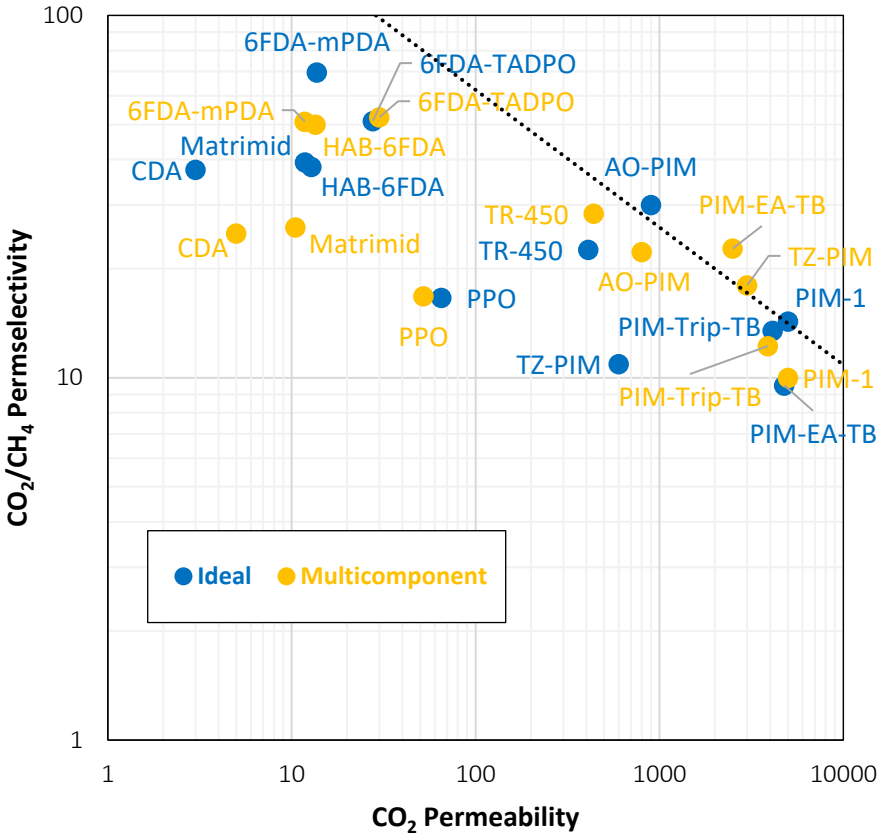

Figure 1.4. CO_2/CH_4 upper bound and positioning of several membrane materials evaluating their properties at ideal (blue) or multicomponent (yellow) conditions. References for the sources of the data are summarized in **Table 1.1**.

Table 1.1. Experimental conditions and sources of the data represented in **Figure 1.4**.

	Ideal case			Multicomponent case			
	Ref.	T (°C)	P (bar)	Ref.	%CO_2	T (°C)	P (bar)
PIM-1	[68,70]	35	10	[70,98],	50	35	10
TZ-PIM	[98,99]	25	10	[98,99]	50/80	25	-
PIM-EA-TB	[100]	35	1-7	[101,102]	30	35	1
AO-PIM	[70]	35	10	[70,103]	50	35	10
PIM-Trip-TB	[104]	35	3	[104]	44	35	3
HAB-6FDA	[81,82,105]	35	10	[80,106]	50	35	10
TR-450	[81,82,105]	35	10	[80,106]	50	35	10
Matrimid	[107–109]	35	2	[109,110]	55	35	2
6FDA-mPDA	[111]	35	24	[111]	44	35	24
6FDA-TADPO	[112]	35	10	[113]	50	35	10
PPO	[114]	35	10	[115]	50	35	10
CDA	[116–119]	35	10	[120,121]	30/50	35	1

1.2.3 Gas Solubility at Multicomponent Conditions

The focus of this work is predominantly laid on the solubility of gases in membrane materials, which, according to the solution-diffusion mechanism that will be described in **Chapter 2**, represents one of the two factors determining gas permeability, together with gas diffusivity. The analysis of this contribution is relevant to investigate multicomponent effects in membrane separation because it was experimentally shown that, in the case of sorption of gas mixtures, strong non-idealities are present [94–96,98,104,111,113,122,123], due to competition between the sorbing gases, which lowers their solubility with respect to the pure-gas case. These effects are stronger when moderately condensable gases such as CO_2 are present in the mixture. Therefore, they are present in carbon capture applications. Furthermore, the data indicate that the pure-gas solubility does not provide a good estimate of the real behaviour of the mixture. In particular, pure-gas data would indicate that the main membrane parameters, like the solubility-selectivity, are a strong function of the gas mixture composition, while in experiments it is observed that the data depend very weakly on such variable. Additionally, for a set of both high and low free volume glassy polymers, it was shown that departure functions, expressing the deviations between the multicomponent properties and the corresponding ideal values, estimated with pure component properties, obey generalized trends which resemble those observed in liquid solutions [110].

Experimental tests to measure mixed-gas sorption are delicate and much more time-consuming than pure-gas tests, so there is a potential advantage in the use of reliable modelling tools capable of predicting the mixed-gas behaviour using pure-gas experimental information only.

In this dissertation, multicomponent sorption measurements with ternary gas mixtures are presented and mixed-gas sorption of binary and ternary mixtures is modelled by means of thermodynamic and empirical models, to assess the accuracy of the predictions and their reliability in the absence of experimental data. Moreover, an assessment of the relative weight of gas solubility in the overall performance of membrane materials at multicomponent conditions is presented, highlighting general trends and the predominant role of the solubility contribution to the permselectivity.

1.3 Dissertation Goals and Outline

A brief introduction to the broader context in which this dissertation is situated was given here, in **Chapter 1**. In **Chapter 2**, the foundations of gas transport in dense polymers are outlined. The solution-diffusion model is presented, followed by models for the calculation of gas solubility and diffusivity in the glassy and in the melt state, using microscopic and macroscopic approaches, suitable also for the study of glassy polymers at nonequilibrium conditions. In **Chapter 3** a modeling approach to evaluate pure- and mixed-gas sorption in cellulose acetates is presented. Experimental data concerning the pure polymer properties of cellulose diacetate and triacetate were obtained and used to parametrize the Nonequilibrium Lattice Fluid model, that was subsequently used to calculate pure- and mixed-gas CO_2/CH_4 sorption.

Chapter 4 presents a systematic comparison of the predictions of the Non-Equilibrium Lattice Fluid model and the Dual Mode Sorption model, validated against experimental data available for six materials at three temperatures and three mixture compositions. The capability of both models to represent the competitive sorption effects on gas sorbed uptake as well as on the selectivity was probed, the sensitivity of the calculations to their input parameters was evaluated and strategies to improve the reliability of the results proposed. In **Chapter 5** a new experimental protocol for the measurement of gas sorption of ternary mixtures is presented and applied to characterize the sorption of CO_2/CH_4/C_2H_6 mixtures in PIM-1. Third component effects on the solubility and solubility-selectivity were assessed and the results were modeled with the Nonequilibrium Lattice Fluid model, finding good agreement with the data. In **Chapter 6**, a predictive molecular modeling approach is applied to investigate the thermodynamic, structural and local dynamics properties of a polymeric material in the presence of CO_2 up to high pressures. The possibility to account in silico for gas concentration, temperature and molecular weight dependencies of the materials properties is assessed by calculating volumetric properties, sorption isotherms, diffusion coefficients, local structural features and local dynamic properties of the system, and comparing the results with experimental measurements or equation of state predictions. Finally, **Chapter 7** reports conclusive remarks and suggestions for future work.

The following references pertain to the results presented in **Chapter 4**:

- E. Ricci, M. G. De Angelis; *Modelling Mixed-Gas Sorption in Glassy Polymers for CO_2 Removal: A Sensitivity Analysis of the Dual Mode Sorption Model*, Membranes (2019), 9, 1 – 26
- E. Ricci, A. E. Gemeda, N. Du, N. Li, M. G. De Angelis, M. D. Guiver, G. C. Sarti; *Sorption of CO_2/CH_4 mixtures in TZ-PIM, PIM-1 and PTMSP: experimental data and NELF-model analysis of competitive sorption and selectivity in mixed gases*, Journal of Membrane Science (2019), 585, 136 – 149
- E. Ricci, F.M. Benedetti, M.E. Dose, M.G. De Angelis, B.D. Freeman, D.R. Paul; *Experimental Characterization and Modelling of Mixed Gas Sorption of CO_2/CH_4 in HAB-6FDA Polyimide and its Thermally Rearranged Derivative*. Submitted to the Journal of Membrane Science.

The following reference pertains to the results presented in **Chapter 6**:

- E. Ricci, N. Vergadou, G.G. Vogiatzis, M.G. De Angelis, D.N. Theodorou; *Molecular Simulations and Mechanistic Analysis of the Effect of CO_2 Sorption on Thermodynamics, Structure, and Local Dynamics of Molten Atactic Polystyrene.* Submitted to Macromolecules.

References

1. https://www.un.org/sustainabledevelopment/climate-change/.
2. Intergovernmental Panel on Climate Change (IPCC) - Global Warming of 1.5 °C. 2018.
3. Höhne, N.; Kuramochi, T.; Warnecke, C.; Röser, F.; Fekete, H.; Hagemann, M.; Day, T.; Tewari, R.; Kurdziel, M.; Sterl, S.; Gonzales, S. The Paris Agreement: resolving the inconsistency between global goals and national contributions. *Clim. Policy* 2017, *17*, 16–32, doi:10.1080/14693062.2016.1218320.
4. https://datacatalog.worldbank.org/dataset/world-development-indicators.
5. International Energy Agency (IEA) Tracking Industrial Energy Efficiency and CO_2 Emissions. *Int. Energy Agency* 2007.
6. https://ourworldindata.org/co2-and-other-greenhouse-gas-emissions.
7. International Energy Agency (IEA) - Energy Efficiency 2017.
8. Obama, B. The irreversible momentum of clean energy. *Science.* 2017, *355*, 126–129, doi:10.1126/science.aam6284.
9. International Energy Agency (IEA) - World energy outlook 2016.
10. IPCC *Special Report on CO_2 Capture and Storage*; 2005; Vol. 49; ISBN 9291691194.
11. Sanz-Pérez, E.S.; Murdock, C.R.; Didas, S.A.; Jones, C.W. Direct Capture of CO_2 from Ambient Air. *Chem. Rev.* 2016, *116*, 11840–11876, doi:10.1021/acs.chemrev.6b00173.
12. Dittmeyer, R.; Klumpp, M.; Kant, P.; Ozin, G. Crowd oil not crude oil. *Nat. Commun.* 2019, *10*, 1818, doi:10.1038/s41467-019-09685-x.
13. Ji, G.; Zhao, M. Membrane Separation Technology in Carbon Capture. In *Recent Advances in Carbon Capture and Storage*; 2016.
14. Olajire, A.A. CO_2 capture and separation technologies for end-of-pipe applications – A review. *Energy* 2010, *35*, 2610–2628, doi:10.1016/J.ENERGY.2010.02.030.
15. Kidnay, A.J.; Kidnay, A.J.; Parrish, W.R.; McCartney, D.G. Fundamentals of Natural Gas Processing. *Fundam. Nat. Gas Process.* 2011, doi:10.1201/b14397.
16. Safari, M.; Ghanizadeh, A.; Montazer-Rahmati, M.M. Optimization of membrane-based CO_2-removal from natural gas using simple models considering both pressure and temperature effects. *Int. J. Greenh. Gas Control* 2009, *3*, 3–10, doi:10.1016/j.ijggc.2008.05.001.
17. Tippayawong, N.; Thanompongchart, P. Biogas quality upgrade by simultaneous removal of CO_2 and H_2S in a packed column reactor. *Energy* 2010, *35*, 4531–4535, doi:10.1016/j.energy.2010.04.014.
18. Green, D.W.; Willhite, G.P. *Enhanced Oil Recovery, SPE textbook series.*; Richardson, Texas, 1998;
19. Al-Mamoori, A.; Krishnamurthy, A.; Rownaghi, A.A.; Rezaei, F. Carbon Capture and Utilization Update. *Energy Technol.* 2017, *5*, 834–849, doi:10.1002/ente.201600747.
20. Kapetaki, Z.; Brandani, P.; Brandani, S.; Ahn, H. Process simulation of a dual-stage Selexol process for 95% carbon capture efficiency at an integrated gasification combined cycle power plant. *Int. J. Greenh. Gas Control* 2015, *39*, 17–26, doi:10.1016/J.IJGGC.2015.04.015.
21. Li, X.; Wang, S.; Chen, C. Experimental Study of Energy Requirement of CO_2 Desorption from Rich Solvent. *Energy Procedia* 2013, *37*, 1836–1843, doi:10.1016/J.EGYPRO.2013.06.063.
22. Aghaie, M.; Rezaei, N.; Zendehboudi, S. A systematic review on CO2 capture with ionic liquids: Current status and future prospects. *Renew. Sustain. Energy Rev.* 2018, *96*, 502–525.
23. Zhu, X.; Li, S.; Shi, Y.; Cai, N. Recent advances in elevated-temperature pressure swing adsorption for carbon capture and hydrogen production. *Prog. Energy Combust. Sci.* 2019, *75*, 100784, doi:10.1016/J.PECS.2019.100784.
24. Zhao, R.; Liu, L.; Zhao, L.; Deng, S.; Li, S.; Zhang, Y. A comprehensive performance evaluation of temperature swing adsorption for post-combustion carbon dioxide capture. *Renew. Sustain. Energy Rev.* 2019, *114*, 109285, doi:10.1016/J.RSER.2019.109285.
25. Hart, A.; Gnanendran, N. Cryogenic CO_2 capture in natural gas. *Energy Procedia* 2009, *1*, 697–706, doi:10.1016/J.EGYPRO.2009.01.092.

26. Kentish, S.E. 110th Anniversary: Process Developments in Carbon Dioxide Capture Using Membrane Technology. *Ind. Eng. Chem. Res.* 2019, *58*, 12868–12875, doi:10.1021/acs.iecr.9b02013.

27. Galizia, M.; Chi, W.S.; Smith, Z.P.; Merkel, T.C.; Baker, R.W.; Freeman, B.D. 50th Anniversary Perspective: Polymers and Mixed Matrix Membranes for Gas and Vapor Separation: A Review and Prospective Opportunities. *Macromolecules* 2017, *50*, 7809–7843, doi:10.1021/acs.macromol.7b01718.

28. Zhang, Y.; Sunarso, J.; Liu, S.; Wang, R. Current status and development of membranes for CO_2/CH_4 separation: A review. *Int. J. Greenh. Gas Control* 2013, *12*, 84–107, doi:10.1016/j.ijggc.2012.10.009.

29. Sanders, D.F.; Smith, Z.P.; Guo, R.; Robeson, L.M.; McGrath, J.E.; Paul, D.R.; Freeman, B.D. Energy-efficient polymeric gas separation membranes for a sustainable future: A review. *Polym. (United Kingdom)* 2013, *54*, 4729–4761, doi:10.1016/j.polymer.2013.05.075.

30. Scholes, C.A.; Stevens, G.W.; Kentish, S.E. Membrane gas separation applications in natural gas processing. *Fuel* 2012, *96*, 15–28, doi:10.1016/j.fuel.2011.12.074.

31. Bernardo, P.; Drioli, E.; Golemme, G. Membrane gas separation: A review/state of the art. *Ind. Eng. Chem. Res.* 2009, *48*, 4638–4663, doi:10.1021/ie8019032.

32. Baker, R.W.; Low, B.T. Gas Separation Membrane Materials: A Perspective. *Macomolecules* 2014, *47*, 6999–7013, doi:10.1021/ma501488s.

33. Sholl, D.S.; Lively, R.P. Seven chemical separations to change the world. *Nature* 2016, *532*, 435–437.

34. Baker, R.W.; Lokhandwala, K. Natural gas processing with membranes: An overview. *Ind. Eng. Chem. Res.* 2008, *47*, 2109–2121, doi:10.1021/ie071083w.

35. Strathmann, H.; Scheible, P.; Baker, R.W. A rationale for the preparation of Loeb-Sourirajan-type cellulose acetate membranes. *J. Appl. Polym. Sci.* 1971, *15*, 811–828, doi:10.1002/app.1971.070150404.

36. George, G.; Bhoria, N.; Alhallaq, S.; Abdala, A.; Mittal, V. Polymer membranes for acid gas removal from natural gas. *Sep. Purif. Technol.* 2016, *158*, 333–356, doi:10.1016/j.seppur.2015.12.033.

37. Awe, O.W.; Zhao, Y.; Nzihou, A.; Minh, D.P.; Lyczko, N. A Review of Biogas Utilisation, Purification and Upgrading Technologies. *Waste and Biomass Valorization* 2017, *8*, 267–283, doi:10.1007/s12649-016-9826-4.

38. Merkel, T.C.; Lin, H.; Wei, X.; Baker, R. Power plant post-combustion carbon dioxide capture: An opportunity for membranes. *J. Memb. Sci.* 2010, *359*, 126–139, doi:10.1016/J.MEMSCI.2009.10.041.

39. Scholes, C.A.; Kentish, S.E.; Stevens, G.W. Carbon Dioxide Separation through Polymeric Membrane Systems for Flue Gas Applications. *Recent Patents Chem. Eng.* 2008, *1*, 52–66, doi:10.2174/2211334710801010052.

40. Khalilpour, R.; Mumford, K.; Zhai, H.; Abbas, A.; Stevens, G.; Rubin, E.S. Membrane-based carbon capture from flue gas: A review. *J. Clean. Prod.* 2015, *103*, 286–300, doi:10.1016/j.jclepro.2014.10.050.

41. Merkel, T.C.; Zhou, M.; Baker, R.W. Carbon dioxide capture with membranes at an IGCC power plant. *J. Memb. Sci.* 2012, *389*, 441–450, doi:10.1016/j.memsci.2011.11.012.

42. Bos, A.; Pünt, I.G.M.; Wessling, M.; Strathmann, H. Plasticization-resistant glassy polyimide membranes for CO_2/CH_4 separations. *Sep. Purif. Technol.* 1998, *14*, 27–39, doi:10.1016/S1383-5866(98)00057-4.

43. He, Y.; Benedetti, F.M.; Lin, S.; Liu, C.; Zhao, Y.; Ye, H.; Van Voorhis, T.; De Angelis, M.G.; Swager, T.M.; Smith, Z.P. Polymers with Side Chain Porosity for Ultrapermeable and Plasticization Resistant Materials for Gas Separations. *Adv. Mater.* 2019, *31*, 1807871, doi:10.1002/adma.201807871.

44. Horn, N.R.; Paul, D.R. Carbon dioxide plasticization and conditioning effects in thick vs. thin glassy polymer films. *Polymer (Guildf).* 2011, *52*, 1619–1627, doi:10.1016/j.polymer.2011.02.007.

45. Zhou, H.; Jin, W. Membranes with intrinsic micro-porosity: Structure, solubility, and applications. *Membranes (Basel).* 2019, *9*, doi:10.3390/membranes9010003.

46. Mason, C.R.; Budd, P.M.; Fritsch, D.; Yampolskii, Y.; Jansen, J.C. Effect of physical aging on the gas transport and sorption in PIM-1 membranes. *Polymer (Guildf).* 2016, doi:10.1016/j.polymer.2016.10.040.

47. Robeson, L.M. Correlation of separation factor versus permeability for polymeric membranes. *J. Memb. Sci.* 1991, *62*, 165–185, doi:10.1016/0376-7388(91)80060-J.

48. Robeson, L.M. The upper bound revisited. *J. Memb. Sci.* 2008, *320*, 390–400, doi:10.1016/j.memsci.2008.04.030.

49. Park, H.B.; Kamcev, J.; Robeson, L.M.; Elimelech, M.; Freeman, B.D. Maximizing the right stuff: The trade-off between membrane permeability and selectivity. *Science.* 2017, *365*, 1138–1148, doi:10.1126/science.aab0530.

50. Lin, H.; Freeman, B.D. Materials selection guidelines for membranes that remove CO_2 from gas mixtures. *J. Mol. Struct.* **2005**, *739*, 57–74, doi:10.1016/j.molstruc.2004.07.045.

51. Swaidan, R.; Ghanem, B.; Pinnau, I. Fine-Tuned Intrinsically Ultramicroporous Polymers Redefine the Permeability/Selectivity Upper Bounds of Membrane-Based Air and Hydrogen Separations. *ACS Macro Lett.* **2015**, *4*, 947–951, doi:10.1021/acsmacrolett.5b00512.

52. Zhang, C.; Cao, B.; Li, P. Thermal oxidative crosslinking of phenolphthalein-based cardo polyimides with enhanced gas permeability and selectivity. *J. Memb. Sci.* **2018**, *546*, 90–99, doi:10.1016/j.memsci.2017.10.015.

53. Zhang, C.; Fu, L.; Tian, Z.; Cao, B.; Li, P. Post-crosslinking of triptycene-based Tröger's base polymers with enhanced natural gas separation performance. *J. Memb. Sci.* **2018**, *556*, 277–284, doi:10.1016/j.memsci.2018.04.013.

54. Ghanem, B.S.; Swaidan, R.; Ma, X.; Litwiller, E.; Pinnau, I. Energy-efficient hydrogen separation by AB-type ladder-polymer molecular sieves. *Adv. Mater.* **2014**, *26*, 6696–6700, doi:10.1002/adma.201401328.

55. Ghanem, B.S.; Swaidan, R.; Litwiller, E.; Pinnau, I. Ultra-microporous triptycene-based polyimide membranes for high-performance gas separation. *Adv. Mater.* **2014**, *26*, 3688–3692, doi:10.1002/adma.201306229.

56. Rose, I.; Bezzu, C.G.; Carta, M.; Comesaña-Gándara, B.; Lasseuguette, E.; Ferrari, M.C.; Bernardo, P.; Clarizia, G.; Fuoco, A.; Jansen, J.C.; Hart, K.E.; Liyana-Arachchi, T.P.; Colina, C.M.; McKeown, N.B. Polymer ultrapermeability from the inefficient packing of 2D chains. *Nat. Mater.* **2017**, *16*, 1–39, doi:10.1038/nmat4939.

57. Li, C.; Meckler, S.M.; Smith, Z.P.; Bachman, J.E.; Maserati, L.; Long, J.R.; Helms, B.A. Engineered Transport in Microporous Materials and Membranes for Clean Energy Technologies. *Adv. Mater.* **2018**, *30*, 1704953, doi:10.1002/adma.201704953.

58. Luo, S.; Zhang, Q.; Zhu, L.; Lin, H.; Kazanowska, B.A.; Doherty, C.M.; Hill, A.J.; Gao, P.; Guo, R. Highly Selective and Permeable Microporous Polymer Membranes for Hydrogen Purification and CO_2 Removal from Natural Gas. *Chem. Mater.* **2018**, *30*, 5322–5332, doi:10.1021/acs.chemmater.8b02102.

59. Low, B.T.; Wang, Y.; Chung, T. Polymeric Membranes for Energy Applications. *Encycl. Polym. Sci. Technol.* 2013, 1–37.

60. Kim, S.; Lee, Y.M. Rigid and microporous polymers for gas separation membranes. *Prog. Polym. Sci.* **2015**, *43*, 1–32, doi:10.1016/j.progpolymsci.2014.10.005.

61. Kim, W.; Nair, S. Membranes from nanoporous 1D and 2D materials: A review of opportunities, developments, and challenges. *Chem. Eng. Sci.* **2013**, *104*, 908–924, doi:10.1016/j.ces.2013.09.047.

62. Robeson, L.M.; Liu, Q.; Freeman, B.D.; Paul, D.R. Comparison of transport properties of rubbery and glassy polymers and the relevance to the upper bound relationship. *J. Memb. Sci.* **2015**, *476*, 421–431, doi:10.1016/j.memsci.2014.11.058.

63. Wind, J.D.; Paul, D.R.; Koros, W.J. Natural gas permeation in polyimide membranes. *J. Memb. Sci.* **2004**, *228*, 227–236, doi:10.1016/j.memsci.2003.10.011.

64. Castro-Muñoz, R.; Martin-Gil, V.; Ahmad, M.Z.; Fíla, V. Matrimid® 5218 in preparation of membranes for gas separation: Current state-of-the-art. *Chem. Eng. Commun.* **2018**, *205*, 161–196, doi:10.1080/00986445.2017.1378647.

65. Ghanem, B.S.; McKeown, N.B.; Budd, P.M.; Selbie, J.D.; Fritsch, D. High-performance membranes from polyimides with intrinsic microporosity. *Adv. Mater.* **2008**, *20*, 2766–2771, doi:10.1002/adma.200702400.

66. Ghanem, B.S.; McKeown, N.B.; Budd, P.M.; Al-Harbi, N.M.; Fritsch, D.; Heinrich, K.; Starannikova, L.; Tokarev, A.; Yampolskii, Y. Synthesis, characterization, and gas permeation properties of a novel group of polymers with intrinsic microporosity: PIM-polyimides. *Macromolecules* **2009**, *42*, 7881–7888, doi:10.1021/ma901430q.

67. Budd, P.M.; Ghanem, B.S.; Makhseed, S.; McKeown, N.B.; Msayib, K.J.; Tattershall, C.E. Polymers of intrinsic microporosity (PIMs): robust, solution-processable, organic nanoporous materials. *Chem. Commun.* **2004**, 230–231, doi:10.1039/b311764b.

68. Budd, P.M.; Msayib, K.J.; Tattershall, C.E.; Ghanem, B.S.; Reynolds, K.J.; McKeown, N.B.; Fritsch, D. Gas separation membranes from polymers of intrinsic microporosity. *J. Memb. Sci.* **2005**, *251*, 263–269, doi:10.1016/j.memsci.2005.01.009.

69. McKeown, N.B.; Budd, P.M. Exploitation of intrinsic microporosity in polymer-based materials. *Macromolecules* **2010**, *43*, 5163–5176, doi:10.1021/ma1006396.

70. Swaidan, R.; Ghanem, B.S.; Litwiller, E.; Pinnau, I. Pure- and mixed-gas CO_2/CH_4 separation properties of PIM-1

and an amidoxime-functionalized PIM-1. *J. Memb. Sci.* **2014**, *457*, 95–102, doi:10.1016/j.memsci.2014.01.055.

71. Han, S.H.; Kwon, H.J.; Kim, K.Y.; Seong, J.G.; Park, C.H.; Kim, S.; Doherty, C.M.; Thornton, A.W.; Hill, A.J.; Lozano, a E.; Berchtold, K. a; Lee, Y.M. Tuning microcavities in thermally rearranged polymer membranes for CO_2 capture. *Phys. Chem. Chem. Phys.* **2012**, *14*, 4365–73, doi:10.1039/c2cp23729f.

72. Chen, Y.-R.; Chen, L.-H.; Chang, K.-S.; Chen, T.-H.; Lin, Y.-F.; Tung, K.-L. Structural characteristics and transport behavior of triptycene-based PIMs membranes: A combination study using ab initio calculation and molecular simulations. *J. Memb. Sci.* **2016**, *514*, 114–124, doi:10.1016/j.memsci.2016.04.063.

73. Chang, K.-S.; Tung, K.-L.; Lin, Y.-F.; Lin, H.-Y. Molecular modelling of polyimides with intrinsic microporosity: from structural characteristics to transport behaviour. *RSC Adv.* **2013**, *3*, 10403–10413, doi:10.1039/c3ra40196k.

74. Tocci, E.; De Lorenzo, L.; Bernardo, P.; Clarizia, G.; Bazzarelli, F.; McKeown, N.B.; Carta, M.; Malpass-Evans, R.; Friess, K.; Pilnáček, K.; Lanč, M.; Yampolskii, Y.P.; Strarannikova, L.; Shantarovich, V.; Mauri, M.; Jansen, J.C. Molecular modeling and gas permeation properties of a polymer of intrinsic microporosity composed of ethanoanthracene and Tröger's base units. *Macromolecules* **2014**, *47*, 7900–7916, doi:10.1021/ma501469m.

75. Larsen, G.S.; Lin, P.; Hart, K.E.; Colina, C.M. Molecular simulations of PIM-1-like polymers of intrinsic microporosity. *Macromolecules* **2011**, *44*, 6944–6951, doi:10.1021/ma200345v.

76. Madkour, T.M.; Mark, J.E. Molecular modeling investigation of the fundamental structural parameters of polymers of intrinsic microporosity for the design of tailor-made ultra-permeable and highly selective gas separation membranes. *J. Memb. Sci.* **2013**, *431*, 37–46, doi:10.1016/j.memsci.2012.12.033.

77. Park, H.B.; Jung, C.H.; Lee, Y.M.; Hill, A.J.; Pas, S.J. Polymers with Cavities Tuned for Fast Selective Transport of Small Molecules and Ions. *Science (80-.).* **2007**, *318*, 254–258, doi:10.1126/science.1146744.

78. Park, H.B.; Han, S.H.; Jung, C.H.; Lee, Y.M.; Hill, A.J. Thermally rearranged (TR) polymer membranes for CO_2 separation. *J. Memb. Sci.* **2010**, *359*, 11–24, doi:10.1016/j.memsci.2009.09.037.

79. Park, H.B.; Jung, C.H.; Lee, Y.M.; Hill, A.J.; Pas, S.J.; Mudie, S.T.; Van Wagner, E.; Freeman, B.D.; Cookson, D.J. Polymers with Cavities Tuned for Fast Selective Transport of Small Molecules and Ions. *Science.* **2007**, *318*, 254–258, doi:10.1126/science.1146744.

80. Gleason, K.L.; Smith, Z.P.; Liu, Q.; Paul, D.R.; Freeman, B.D. Pure- and mixed-gas permeation of CO_2 and CH_4 in thermally rearranged polymers based on 3,3′-dihydroxy-4,4′-diamino-biphenyl (HAB) and 2,2′-bis-(3,4-dicarboxyphenyl) hexafluoropropane dianhydride (6FDA). *J. Memb. Sci.* **2015**, *475*, 204–214, doi:10.1016/j.memsci.2014.10.014.

81. Smith, Z.P.; Sanders, D.F.; Ribeiro, C.P.; Guo, R.; Freeman, B.D.; Paul, D.R.; McGrath, J.E.; Swinnea, S. Gas sorption and characterization of thermally rearranged polyimides based on 3,3'-dihydroxy-4,4'-diamino-biphenyl (HAB) and 2,2'-bis-(3,4-dicarboxyphenyl) hexafluoropropane dianhydride (6FDA). *J. Memb. Sci.* **2012**, *415–416*, 558–567, doi:10.1016/j.memsci.2012.05.050.

82. Sanders, D.F.; Smith, Z.P.; Ribeiro, C.P.; Guo, R.; McGrath, J.E.; Paul, D.R.; Freeman, B.D. Gas permeability, diffusivity, and free volume of thermally rearranged polymers based on 3,3′-dihydroxy-4,4′-diamino-biphenyl (HAB) and 2,2′-bis-(3,4-dicarboxyphenyl) hexafluoropropane dianhydride (6FDA). *J. Memb. Sci.* **2012**, *409*, 232–241, doi:10.1016/j.memsci.2012.03.060.

83. Aguilar-Lugo, C.; Álvarez, C.; Lee, Y.M.; de la Campa, J.G.; Lozano, Á.E. Thermally Rearranged Polybenzoxazoles Containing Bulky Adamantyl Groups from Ortho-Substituted Precursor Copolyimides. *Macromolecules* **2018**, *51*, 1605–1619, doi:10.1021/acs.macromol.7b02460.

84. Scholes, C.A.; Freeman, B.D. Thermal rearranged poly(imide-co-ethylene glycol) membranes for gas separation. *J. Memb. Sci.* **2018**, *563*, 676–683, doi:10.1016/J.MEMSCI.2018.06.027.

85. Luo, S.; Zhang, Q.; Bear, T.K.; Curtis, T.E.; Roeder, R.K.; Doherty, C.M.; Hill, A.J.; Guo, R. Triptycene-containing poly(benzoxazole-co-imide) membranes with enhanced mechanical strength for high-performance gas separation. *J. Memb. Sci.* **2018**, *551*, 305–314, doi:10.1016/J.MEMSCI.2018.01.052.

86. Meckler, S.M.; Bachman, J.E.; Robertson, B.P.; Zhu, C.; Long, J.R.; Helms, B.A. Thermally Rearranged Polymer Membranes Containing Tröger's Base Units Have Exceptional Performance for Air Separations. *Angew. Chemie - Int. Ed.* **2018**, *57*, 4912–4916, doi:10.1002/anie.201800556.

87. Liu, Q.; Paul, D.R.; Freeman, B.D. Gas permeation and mechanical properties of thermally rearranged (TR) copolyimides. *Polym. (United Kingdom)* **2016**, *82*, 378–391, doi:10.1016/j.polymer.2015.11.051.

88. Li, S.; Jo, H.J.; Han, S.H.; Park, C.H.; Kim, S.; Budd, P.M.; Lee, Y.M. Mechanically robust thermally rearranged (TR)

polymer membranes with spirobisindane for gas separation. *J. Memb. Sci.* **2013**, *434*, 137–147, doi:10.1016/j.memsci.2013.01.011.

89. Calle, M.; Lozano, A.E.; Lee, Y.M. Formation of thermally rearranged (TR) polybenzoxazoles: Effect of synthesis routes and polymer form. *Eur. Polym. J.* **2012**, *48*, 1313–1322, doi:10.1016/j.eurpolymj.2012.04.007.

90. Jiang, Y.; Willmore, F.T.; Sanders, D.; Smith, Z.P.; Ribeiro, C.P.; Doherty, C.M.; Thornton, A.; Hill, A.J.; Freeman, B.D.; Sanchez, I.C. Cavity size, sorption and transport characteristics of thermally rearranged (TR) polymers. *Polymer (Guildf).* **2011**, *52*, 2244–2254, doi:10.1016/j.polymer.2011.02.035.

91. Kumar, S.K.; Benicewicz, B.C.; Vaia, R.A.; Winey, K.I. 50th Anniversary Perspective: Are Polymer Nanocomposites Practical for Applications? *Macromolecules* **2017**, *50*, 714–731, doi:10.1021/acs.macromol.6b02330.

92. Du, Y.C.; Huang, L.J.; Wang, Y.X.; Yang, K.; Tang, J.G.; Wang, Y.; Cheng, M.M.; Zhang, Y.; Kipper, M.J.; Belfiore, L.A.; Ranil, W.S. Recent developments in graphene-based polymer composite membranes: Preparation, mass transfer mechanism, and applications. *J. Appl. Polym. Sci.* **2019**, *136*, 1–20, doi:10.1002/app.47761.

93. Vinoba, M.; Bhagiyalakshmi, M.; Alqaheem, Y.; Alomair, A.A.; Pérez, A.; Rana, M.S. Recent progress of fillers in mixed matrix membranes for CO_2 separation: A review. *Sep. Purif. Technol.* **2017**, *188*, 431–450, doi:10.1016/J.SEPPUR.2017.07.051.

94. Vopička, O.; De Angelis, M.G.; Sarti, G.C. Mixed gas sorption in glassy polymeric membranes: I. CO_2/CH_4 and n-C_4/CH_4 mixtures sorption in poly(1-trimethylsilyl-1-propyne) (PTMSP). *J. Memb. Sci.* **2014**, *449*, 97–108, doi:10.1016/j.memsci.2013.06.065.

95. Vopička, O.; De Angelis, M.G.; Du, N.; Li, N.; Guiver, M.D.; Sarti, G.C. Mixed gas sorption in glassy polymeric membranes: II. CO_2/CH_4 mixtures in a polymer of intrinsic microporosity (PIM-1). *J. Memb. Sci.* **2014**, *459*, 264–276, doi:10.1016/j.memsci.2014.02.003.

96. Gemeda, A.E.; De Angelis, M.G.; Du, N.; Li, N.; Guiver, M.D.; Sarti, G.C. Mixed gas sorption in glassy polymeric membranes. III. CO_2/CH_4 mixtures in a polymer of intrinsic microporosity (PIM-1): Effect of temperature. *J. Memb. Sci.* **2017**, *524*, 746–757, doi:10.1016/j.memsci.2016.11.053.

97. Adewole, J.K.; Ahmad, A.L.; Ismail, S.; Leo, C.P. Current challenges in membrane separation of CO_2 from natural gas: A review. *Int. J. Greenh. Gas Control* 2013, *17*, 46–65.

98. Ricci, E.; Gemeda, A.E.; Du, N.; Li, N.; De Angelis, M.G.; Guiver, M.D.; Sarti, G.C. Sorption of CO_2/CH_4 mixtures in TZ-PIM, PIM-1 and PTMSP: Experimental data and NELF-model analysis of competitive sorption and selectivity in mixed gases. *J. Memb. Sci.* **2019**, *585*, 136–149, doi:10.1016/j.memsci.2019.05.026.

99. Du, N.; Park, H.B.; Robertson, G.P.; Dal-Cin, M.M.; Visser, T.; Scoles, L.; Guiver, M.D. Polymer nanosieve membranes for CO_2-capture applications. *Nat. Mater.* **2011**, *10*, 372–375, doi:10.1038/nmat2989.

100. Carta, M.; Malpass-Evans, R.; Croad, M.; Rogan, Y.; Jansen, J.C.; Bernardo, P.; Bazzarelli, F.; McKeown, N.B. An Efficient Polymer Molecular Sieve for Membrane Gas Separations. *Science.* **2013**, *339*, 303–307, doi:10.1126/science.1228032.

101. Fraga, S.C.; Monteleone, M.; Lanč, M.; Esposito, E.; Fuoco, A.; Giorno, L.; Pilnáček, K.; Friess, K.; Carta, M.; McKeown, N.B.; Izák, P.; Petrusová, Z.; Crespo, J.G.; Brazinha, C.; Jansen, J.C. A novel time lag method for the analysis of mixed gas diffusion in polymeric membranes by on-line mass spectrometry: Method development and validation. *J. Memb. Sci.* **2018**, *561*, 39–58, doi:10.1016/j.memsci.2018.04.029.

102. Benedetti, F.M.; Ricci, E.; De Angelis, M.G.; Carta, M.; McKeown, N.B. Sorption of CO_2/CH_4 and their mixtures in PIM-EA-TB. *In preparation.*

103. Gemeda, A.E. *Polymeric Gas Separation Membranes: CO_2/CH_4 Mixed Gas Sorption in Glassy Polymers,* Ph.D. Thesis, University of Bologna, 2015.

104. Genduso, G.; Wang, Y.; Ghanem, B.S.; Pinnau, I. Permeation, sorption, and diffusion of CO_2-CH_4 mixtures in polymers of intrinsic microporosity: The effect of intrachain rigidity on plasticization resistance. *J. Memb. Sci.* **2019**, *584*, 100–109, doi:10.1016/j.memsci.2019.05.014.

105. Stevens, K.A.; Smith, Z.P.; Gleason, K.L.; Galizia, M.; Paul, D.R.; Freeman, B.D. Influence of temperature on gas solubility in thermally rearranged (TR) polymers. *J. Memb. Sci.* **2017**, *533*, 75–83, doi:10.1016/j.memsci.2017.03.005.

106. Ricci, E.; Benedetti, F.M.; Dose, M.E.; De Angelis, M.G.; Freeman, B.D.; Paul, D.R. Experimental Characterization and Modelling of Mixed Gas Sorption of CO_2/CH_4 in HAB-6FDA Polyimide and its Thermally Rearranged Derivative. *Submitted to the Journal of Membrane Science*

107. Ansaloni, L.; Minelli, M.; Giacinti Baschetti, M.; Sarti, G.C. Effects of Thermal Treatment and Physical Aging on the Gas Transport Properties in Matrimid®. *Oil Gas Sci. Technol. – Rev. d'IFP Energies Nouv.* 2015, *70*, 367–379, doi:10.2516/ogst/2013188.

108. Minelli, M.; Cocchi, G.; Ansaloni, L.; Baschetti, M.G.; De Angelis, M.G.; Doghieri, F. Vapor and liquid sorption in matrimid polyimide: Experimental characterization and modeling. *Ind. Eng. Chem. Res.* 2013, *52*, 8936–8945, doi:10.1021/ie3027873.

109. Bos, A. *High Pressure CO_2/CH_4 Separation with Glassy Polymer Membranes: Aspects of CO_2-induced plasticization*; Ph.D. Thes.; University of Twente, Netherlands, 1996; ISBN 903650905X.

110. Ricci, E.; Minelli, M.; De Angelis, M.G. A multiscale approach to predict the mixed gas separation performance of glassy polymeric membranes for CO2 capture: the case of CO_2/CH_4 mixture in Matrimid®. *J. Memb. Sci.* 2017, *539*, 88–100, doi:https://doi.org/10.1016/j.memsci.2017.05.068.

111. Genduso, G.; Ghanem, B.S.; Pinnau, I. Experimental Mixed-Gas Permeability, Sorption and Diffusion of CO_2-CH_4 Mixtures in 6FDA-mPDA Polyimide Membrane: Unveiling the Effect of Competitive Sorption on Permeability Selectivity. *Membranes (Basel).* 2019, *9*, 10, doi:10.3390/membranes9010010.

112. Walker, D.R.B.; Koros, W.J. Transport characterization of a polypyrrolone for gas separations. *J. Memb. Sci.* 1991, *55*, 99–117, doi:10.1016/S0376-7388(00)82329-7.

113. Kamaruddin, H.D.; Koros, W.J. Some observations about the application of Fick's first law for membrane separation of multicomponent mixtures. *J. Memb. Sci.* 1997,*135*,147–159,doi:10.1016/S0376-7388(97)00142-7.

114. Maeda, Y.; Paul, D.R. Selective gas transport in miscible PPO-PS blends. *Polymer (Guildf).* 1985, *26*, 2055–2063, doi:10.1016/0032-3861(85)90187-9.

115. Story, B.J.; Koros, W.J. Comparison of three models for permeation of CO_2/CH_4 mixtures in poly(phenylene oxide). *J. Polym. Sci. Part B Polym. Phys.* 1989, *27*, 1927–1948, doi:10.1002/polb.1989.090270910.

116. Puleo, A.C.; Paul, D.R.; Kelley, S.S. The Effect Of Degree Of Acetylation On Gas Sorption And Transport Behaviour In Cellulose Acetate. *J. Memb. Sci.* 1989, *47*, 301–332.

117. Houde, A.; Krishnakumar, B.; Charati, S.; Stern, S. Permeability of dense (homogeneous) cellulose acetate membranes to methane, carbon dioxide, and their mixtures at elevated pressures. *J. Appl. Polym. Sci.* 1996, *62*, 2181–2192, doi:10.1002/(SICI)1097-4628(19961226)62:13<2181::AID-APP1>3.0.CO;2-F.

118. Stern, S.A.; Kulkarni, S.S. Solubility of Methane in Cellulose Acetate - Conditioning Effect of Carbon Dioxide. *J. Memb. Sci.* 1982, *10*, 235–251.

119. Sada, E.; Kumazawa, H.; Yoshio, Y.; Wang, S. -T; Xu, P. Permeation of carbon dioxide through homogeneous dense and asymmetric cellulose acetate membranes. *J. Polym. Sci. Part B Polym. Phys.* 1988, *26*, 1035–1048, doi:10.1002/polb.1988.090260508.

120. Donohue, M.D.; Minhas, B.S.; Lee, S.Y. Permeation behavior of carbon dioxide-methane mixtures in cellulose acetate membranes. *J. Memb. Sci.* 1989, *42*, 197–214, doi:10.1016/S0376-7388(00)82376-5.

121. Ricci, E.; Di Maio, E.; Degli Esposti, M.; Fabbri, P.; Mensitieri, G.; De Angelis, M.G. A rigorous approach for the description of gas sorption thermodynamics in glassy Cellulose Acetates. *In preparation*

122. Genduso, G.; Litwiller, E.; Ma, X.; Zampini, S.; Pinnau, I. Mixed-gas sorption in polymers via a new barometric test system: sorption and diffusion of CO_2-CH_4 mixtures in polydimethylsiloxane (PDMS). *J. Memb. Sci.* 2019, *577*, 195–204, doi:10.1016/j.memsci.2019.01.046.

123. Story, B.J.; Koros, W.J. Sorption and transport of CO_2 and CH_4 in chemically modified poly (phenylene oxide). *J. Memb. Sci.* 1992, *67*, 191–210.

Chapter 2

Theoretical Background

2.1 Solution-Diffusion Mechanism

The history of research into gas transport in polymers begins with balloons. When, in the 1820s, Dr. J. K. Mitchell witnessed that helium filled balloons made of natural rubber stopped floating at the ceiling of the room after some time, it prompted investigations into how different gases and liquids were able to penetrate through the rubbery membrane with different "power" and "rapidity" [1]. Previously, Dr. Graham [2] had reported the insinuation of carbonic acid through the walls of a bladder, thus giving evidence that mass transfer through dense materials was possible. It was again Dr. Graham to suggest, several years later, a two-stage process interpretation of the permeation phenomenon [3], the so-called "solution-diffusion mechanism", which is currently still accepted to describe the transport of small penetrants in dense polymeric matrices: the fluid comes into contact with the membrane on one side and it is dissolved inside it, the sorbed molecules then diffuse through the material to the other side, where they are desorbed. Von Wroblewski [4] made empirical observations about the dependencies of the steady-state penetrant flux, suggesting the following relation:

$$J = \mathcal{P}\,\frac{\Delta p}{l} \qquad \text{Eq. (2.1)}$$

J is the flux, Δp the pressure difference across the membrane, l is the thickness of the membrane and $\mathcal{P}$ is the permeability coefficient. Over the years the solution-diffusion mechanism has emerged as the most widely accepted for the description of transport in dialysis, reverse osmosis, gas permeation, and pervaporation. The understanding of the permeation process within this framework has been formalized and it is presented here following the derivation by Wijmans and Baker [5,6].

The overall driving force for the motion of a penetrant i is the gradient of its chemical potential [5]:

$$J_i = -L_i \frac{d\mu_i}{dx} \qquad \text{Eq. (2.2)}$$

J_i is the steady-state flux, $\frac{d\mu_i}{dx}$ is the chemical potential gradient along direction x, and L_i is a coefficient of proportionality. Considering an isothermal process and concentration and pressure gradients as driving forces one has:

$$d\mu_i = RT\,dln(\gamma_i y_i) + v_i dp \qquad \text{Eq. (2.3)}$$

T is the temperature, γ_i is the activity coefficient, y_i the molar fraction, v_i is the partial molar volume of species *i* and p the pressure. It is assumed that the fluids on either side of the membrane interface are in equilibrium, therefore the chemical potential is continuous at the interface:

$$\mu_i^{gas} = \mu_i^{pol} \qquad \text{Eq. (2.4)}$$

The rates of absorption and desorption at the interface are assumed to be much higher than the rate of diffusion through the membrane. This hypothesis holds in most membrane processes, but not necessarily in the case of processes involving chemical reactions, such as facilitated transport, or in the case of diffusion of gases through metals, where absorption can be slower than diffusion [5]. **Eq. (2.3)** can be integrated both for the polymer phase, where volume changes associated to pressure are negligible and it

can be considered incompressible, and for the compressible gas phase, introducing the ideal gas law to express volume changes associated to pressure and considering the vapor pressure p_i^{sat} as reference [5]. **Eq. (2.4)** becomes:

$$\mu_i^{ref} + RTln(\gamma_i^{pol} y_i^{pol}) + v_i^{pol}(p - p_i^{sat}) = \mu_i^{ref} + RTln(\gamma_i^{gas} y_i^{gas}) + RTln\left(\frac{p}{p_i^{sat}}\right) \quad \text{Eq. (2.5)}$$

Rearranging this expression to isolate the concentration inside the membrane yields:

$$n_i^{pol} = \frac{\gamma_i^{gas}}{\gamma_i^{pol}} \frac{p_i}{p_i^{sat}} \exp\left[-\frac{v_i^{pol}(p - p_i^{sat})}{RT}\right] \quad \text{Eq. (2.6)}$$

It is convenient to express it as a mass concentration c_i ($c_i = M_i \rho_{mol} y_i$, where M_i is the molecular weight of the penetrant and ρ_{mol} is the molar density of the membrane). Moreover, the following solubility coefficient is introduced:

$$S_i = \frac{\gamma_i^{gas}}{\gamma_i^{pol}} \frac{M_i \rho_{mol}}{p_i^{sat}} \quad \text{Eq. (2.7)}$$

Therefore **Eq. (2.6)** becomes:

$$c_i^{pol} = S_i p_i \exp\left[-\frac{v_i^{pol}(p - p_i^{sat})}{RT}\right] \quad \text{Eq. (2.8)}$$

The same relation applies to both sides of the membrane, with p being either the upstream or the downstream pressure and p_i the corresponding partial pressure of component *i*. The exponential term (Poynting correction) is usually very close to one for gases and therefore it can be neglected:

$$c_i^{pol} = S_i p_i \quad \text{Eq. (2.9)}$$

Contrarily to the pore flow mechanism, in the solution–diffusion mechanism the pressure within a membrane is considered uniformly equal to its upstream value and the chemical potential gradient of a permeant across the membrane stems out of a concentration gradient only:

$$d\mu_i = RT\, dln(\gamma_i y_i) \quad \text{Eq. (2.10)}$$

Under this hypothesis, the flow inside the membrane (**Eq. (2.2)**) can be expressed as a function of the concentration gradient as:

$$J_i = -\frac{RTL_i}{\gamma_i y_i} \frac{d\gamma_i y_i}{dx} \quad \text{Eq. (2.11)}$$

Or more conveniently in a mass-basis, assuming the activity coefficient to be constant:

$$J_i = -\frac{RTL_i}{c_i} \frac{dc_i}{dx} \quad \text{Eq. (2.12)}$$

The quantity RTL_i/c_i, is recognized as the diffusion coefficient in Fick's law:

$$J_i = -D_i \frac{dc_i}{dx} \quad \text{Eq. (2.13)}$$

Integrating this expression across the membrane (subscript u refers to the upstream side, δ to the downstream side) yields:

$$J_i = -D_i \frac{c_{i,\delta} - c_{i,u}}{l} \quad \text{Eq. (2.14)}$$

Introducing **Eq. (2.9)** into **Eq. (2.14)** one obtains finally:

$$J_i = -D_i S_i \frac{p_{i,\delta} - p_{i,u}}{l} \quad \text{Eq. (2.15)}$$

Which correspond to **Eq. (2.1)**, recognizing that $\mathcal{P}_i = D_i S_i$. When there is a high penetrant concentration in the membranes, for example in the case of highly soluble fluids or high upstream pressure, the assumption of constant diffusion coefficient no longer holds, and it is more correctly replaced by average effective diffusion coefficient, $\overline{D}_i$:

$$\overline{D}_i = \frac{1}{c_{i,\delta} - c_{i,u}} \int_{c_{i,u}}^{c_{i,\delta}} \frac{D_i^{loc}}{1 - w_i} dc \quad \text{Eq. (2.16)}$$

Where D_i^{loc} is a local, concentration-dependent, binary mutual diffusion coefficient and w_i is the mass fraction of the gas inside the polymer.

$$\mathcal{P}_i = S_i \cdot \overline{D}_i \quad \text{Eq. (2.17)}$$

Since usually in permeation experiments the downstream side is kept at vacuum, $c_{i,\delta}$ and $p_{i,\delta}$ tend to zero and the solubility coefficient can be simply obtained as the ratio of the concentration of gas dissolved in the polymer and its pressure, partial pressure or fugacity:

$$\mathcal{P}_i = \frac{J_i \, l}{p_{i,\delta} - p_{i,u}} = \frac{c_{i,\delta} - c_{i,u}}{p_{i,\delta} - p_{i,u}} \overline{D}_i \quad \text{Eq. (2.18)}$$

$$\mathcal{P}_i = \frac{c_{i,u}}{p_{i,u}} \overline{D}_i \quad \text{Eq. (2.19)}$$

$$S_i = \frac{c_{i,u}}{p_{i,u}} \quad \text{Eq. (2.20)}$$

According to the solution-diffusion model, and under the hypotheses outlined above, the transport of small molecules in dense polymeric membranes is characterized using a permeability coefficient, which is the product of a thermodynamic factor, the solubility, and a kinetic one, the diffusion coefficient. Gas permeability is defined as the pressure- and thickness-normalized flux of gas across the membrane and expresses how many molecules dissolve into the membrane and how fast they move across the matrix. Therefore, high permeability can result from high solubility, high diffusivity, or a favorable combination of the two. Consequently, the selectivity of the polymer (permselectivity) $\alpha_{i,j}$, which is equal to the ratio between the permeability of the more permeable to the less permeable gas, contains a solubility-selectivity ($\alpha_{i,j}^S$) and a diffusivity-selectivity factor ($\alpha_{i,j}^D$):

$$\alpha_{i,j} = \frac{\mathcal{P}_i}{\mathcal{P}_j} = \frac{S_i}{S_j} \cdot \frac{D_i}{D_j} = \alpha_{i,j}^S \cdot \alpha_{i,j}^D \quad \text{Eq. (2.21)}$$

Analyzing these two properties independently is a useful way to rationalize gas transport in polymers and structure-property relationships, and it can guide a more effective membrane materials design [7]. Solubility-selectivity is expected to provide an important contribution to the overall permselectivity in high free volume glassy polymers, whereas for low and medium free volume polymers, where sieving effects are more important, the diffusivity-selectivity has a higher weight in the overall permselectivity. Whether ultra-high free volume polymers can still be regarded as dense materials to which the solution-diffusion model applies is an open question, however, there have been reports of successful modelling studies relying on this hypothesis [8]. When solubility or diffusivity of pure gases are used in **Eq. (2.21)**, the ideal selectivity is calculated, whereas, if the corresponding properties at mixed-gas conditions are used, the multicomponent selectivity is obtained. One of the main themes of this dissertation revolves around the difference between ideal and multicomponent selectivity, especially concerning the solubility factor, and how to predict the mixed-gas behavior, using at most only pure-gas experimental measurement as input, in order to avoid or reduce the need for the more delicate and time-consuming mixed-gas tests.

It is important to note that all of these properties depend on temperature, pressure differential across the membrane, absolute value of the pressure, gas mixture composition and formation history of the sample [9–11]. Therefore, any permeability or selectivity value should be contextualized with this information and possibly compared with other materials at similar conditions. For instance, the temperature dependence of permeability, solubility and diffusivity is expressed in many cases by an Arrhenius law [12]:

$$S = S_0 \exp(-\Delta H_s/RT) \quad \text{Eq. (2.22)}$$

$$D = D_0 \exp(-E_D/RT) \quad \text{Eq. (2.23)}$$

$$\mathcal{P} = \mathcal{P}_0 \exp(-E_\mathcal{P}/RT) \quad \text{Eq. (2.24)}$$

ΔH_s is the enthalpy of sorption and E_D and $E_\mathcal{P}$ are the activation energies of diffusion and permeation. The enthalpy of sorption, both for gas solubility in liquids and polymers, can be divided in two contributions:

$$\Delta H_s = \Delta H_c + \Delta H_m \quad \text{Eq. (2.25)}$$

ΔH_c is the enthalpy of condensation of the penetrant and ΔH_m is the partial molar enthalpy of mixing the condensed penetrant with the polymer segments.

It must be noted that the use of Fick's law for diffusivity is valid only for a two-component system comprised of a polymer and one diffusing component at low concentration in a non-swollen membrane [13]. When the membrane is highly swollen, a frame of-reference correction to Fick's Law [14,15] needs to be applied. Moreover Kamaruddin and Koros [16] showed that the assumption of negligible bulk flux can lead to significant errors in the case of multicomponent mixtures when the permeability of one component is much higher than the others. An alternative approach is to replace Fick's Law in the solution-diffusion model by the Maxwell-Stefan diffusive transport equation, which is based on the relative velocities of the components of the system to one another, therefore bypassing the frame-of-reference problem. One drawback of this approach is that the concentrations of all permeants in the membrane material are required to calculate the permeant fluxes, which makes it rather impractical. So far, the application of Fick's law has been ubiquitous, even in the cases where caution should be advised.

2.2 Gas Separation Upper Bound

An important issue faced in membrane materials design is the existence of a trade-off between permeability and selectivity: highly-permeable materials usually display very poor selectivity, whereas highly-selective materials exhibit lower permeabilities [17]. This behavior is a general feature evidenced by several gas pairs and polymers of very different chemical makeup. By reporting the logarithm of the selectivity versus the logarithm of the permeability of the most permeable gas, membrane materials have been shown to lie below a limiting line, customarily referred to as the Robeson upper bound [17,18]. **Figure 2.1** shows the Robeson plots for O_2/N_2, H_2/N_2, CO_2/N_2 and CO_2/CH_4 gas couples and how the upper bounds shifted following the discovery of new and better performing polymers.

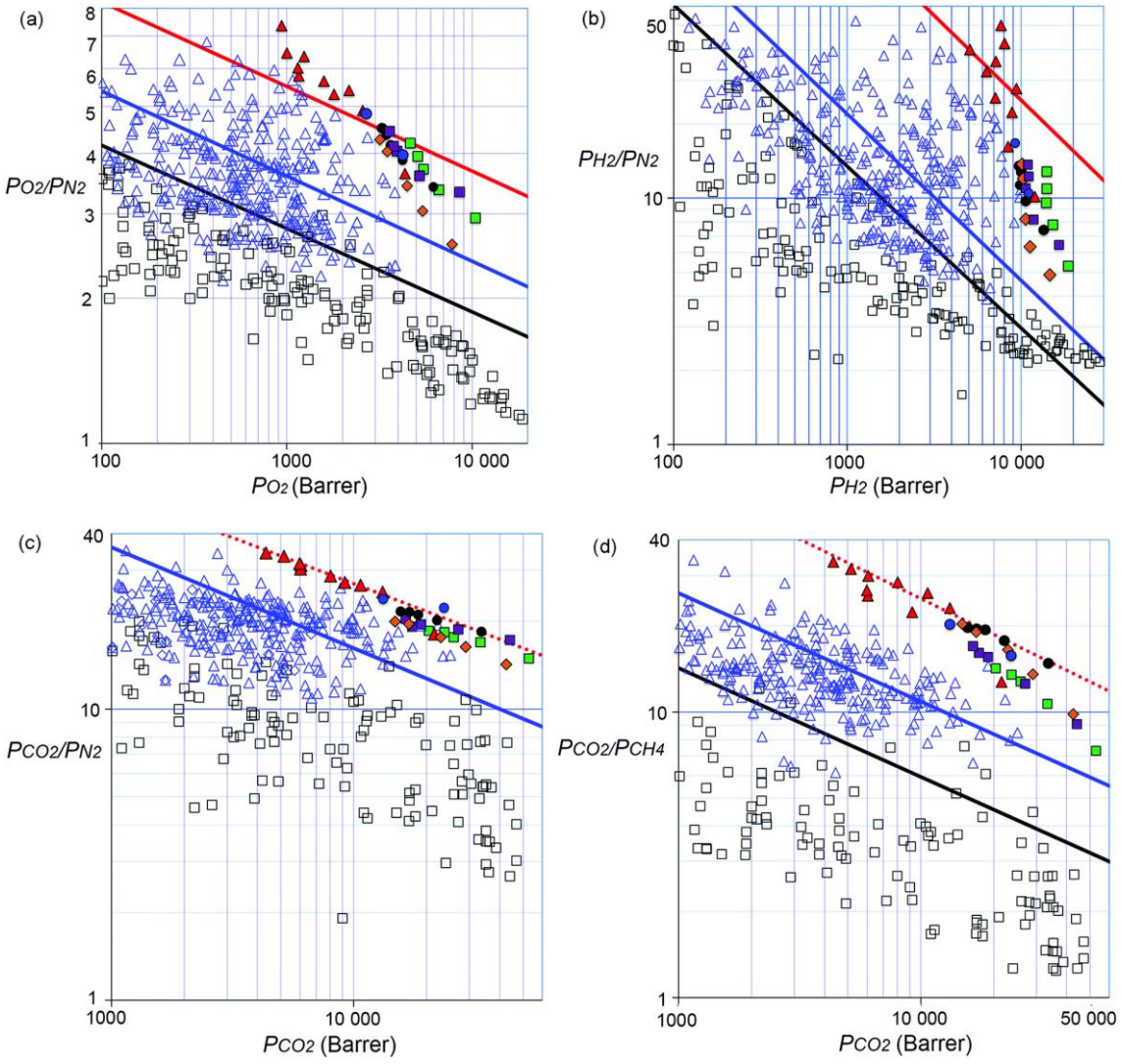

Figure 2.1. Robeson plots for the (a) O_2/N_2, (b) H_2/N_2, (c) CO_2/N_2 and (d) CO_2/CH_4 gas pairs. Upper bounds are represented by black lines (1991) and blue lines (2008). Red lines represent revisions proposed in 2015 (solid) and 2019 (dot). Black squares are non-PIM materials, blue triangles represent PIMs. Filled symbols represent newly synthesized ultrapermeable benzotriptycene-based PIMs. Figure reproduced from [19]. Licensed under CC-BY 3.0 terms.

This trade-off sets an upper limit to the efficiency that can be achieved by the operation [20,21]. The limiting threshold is empirically expressed as:

$$\alpha_{i,j} = \frac{\beta_{i,j}}{P_i^{\lambda_{i,j}}} \qquad \text{Eq. (2.26)}$$

Where P_i is the permeability of the more permeable gas, $\alpha_{i,j}$ is the selectivity of the membrane for the more permeable with respect to the less permeable gas, and $\beta_{i,j}$ and $\lambda_{i,j}$ are parameters, which are different for each gas couple. Similar trends have been highlighted also plotting the solubility of the more soluble gas against solubility-selectivity and diffusivity of the fastest diffusing gas against diffusivity-selectivity [22]. Several theoretical rationalizations of these trends have been proposed, such as Meares's use of cohesion energy density to interpret diffusivity upper bound [23], the use of the Sanchez-Lacombe's lattice fluid theory to interpret the solubility upper bound [24], and free volume theory to interpret the permeability upper bound [25]. Freeman's analysis showed that the slope of the upper bound $\lambda_{i,j}$ is strongly correlated to the kinetic diameters of the gas molecules [26]:

$$\lambda_{i,j} = \left(\frac{d_{k,j}}{d_{k,i}}\right)^2 - 1 \qquad \text{Eq. (2.27)}$$

In this relation $d_{k,j}$ is the kinetic diameter of the larger molecule, and $d_{k,i}$ the kinetic diameter of the smaller molecule. On the other hand, the position of the upper bound line $\beta_{i,j}$ depends both on the size and the solubility of the molecules:

$$\beta_{i,j} = \frac{S_i}{S_j} S_i^{\lambda_{i,j}} \exp\left\{-\lambda_{i,j}\left[b_e - f_{ub}\left(\frac{1-a_e}{RT}\right)\right]\right\} \qquad \text{Eq. (2.28)}$$

S_i is the solubility coefficient of the most permeable gas, S_j the solubility coefficient of the less permeable gas, a and b are parameters from the linear free energy relation between the preexponential factor in Arrhenius equation for diffusivity and the activation energy of diffusion observed by Barrer [27] and Van Amerongen [28]. a_e has a universal value of 0.64, b_e is 9.2 for rubbery polymers and 11.5 for glassy ones, f_{ub} is an adjustable universal parameter, fitted to achieve the best representation of selectivity *vs.* permeability data [26]. Its value was calculated as $f_{ub} = 12600$ cal/mol for polymers in the limiting curves drawn in 1991 and 14154 cal/mol in the 2008 update [29]. The selectivity can be expressed as function of these parameters as:

$$\ln \alpha_{i,j} = -\lambda_{i,j} \ln D_i + \ln \frac{S_i}{S_j} - \lambda_{i,j}\left[b_e - f_{ub}\left(\frac{1-a_e}{RT}\right)\right] \qquad \text{Eq. (2.29)}$$

Under the assumption that the solubility-selectivity changes little from polymer to polymer, and noting that the term $\lambda_{i,j} b_e$ is a constant for a given gas couple and for all glassy or rubbery polymers, the implication of this analysis is that diffusivity plays a more important role than solubility in determining upper bound selectivity values. The typical way to enhance the performance of glassy polymers, which are commonly proposed as gas separation polymers, is to increase the free volume by introducing packing-disrupting units into the polymer backbone, with the effect of increasing the diffusion coefficients and reducing the diffusivity selectivity accordingly.

However, not all separations are dominated by size selectivity: in the case of separations where the species to remove is significantly more soluble than the other, such as in the case of the separation of higher hydrocarbons from natural gas or volatile organic compounds from air, the solubility-selectivity can be higher than the diffusivity-selectivity, especially in the case of rubbery polymers. One example is the propane/methane separation: propane permeation is favored by its higher solubility but penalized by its lower diffusivity. If a glassy size-sieving material is used for the separation, diffusivity-selectivity will be the predominant factor, leading to $\alpha_{C_3H_8/CH_4} < 1$, meaning that the material is methane-selective. On the other hand, if a high free volume glassy polymer or a rubbery one are considered, their weak size-sieving capability allows solubility-selectivity to become the predominant factor and $\alpha_{C_3H_8/CH_4} > 1$. These materials are called "reverse-selective". In such cases, the permeability/selectivity plot does not display an upper bound, but the cloud of different materials points is oriented along the opposite diagonal [30], meaning that permeability and selectivity increase at the same time.

A systematic comparison of gas separation performance of glassy and rubbery polymers for several gases [31] showed that glassy polymers are always found closer to the upper bounds for all gas pairs. This was ascribed both to a higher size-sieving ability compared to rubbery polymers, but also to higher solubility coefficients, owing to their excess free volume. The relative weight of solubility is even more marked in the case of partially fluorinated or perfluorinated glassy polymers [32].

A final remark about the permeability-selectivity performance plots usually used to assess and compare membrane performance is that they are obtained using pure-gas permeability data and in the ambient temperature range. The effect of temperature on the position of the upper bound has been studied [33]. Also the effect of induced T_g depression (related to plasticization) on the position of the upper bound has been analyzed, in the framework of the free volume theory for the gas couple CO_2/CH_4 [34], finding that plasticization induced by CO_2 or other impurities would lower the intercept of the upper bound, $\beta_{i,j}$. However, there are several concomitant phenomena responsible for the change in the performance of membrane materials at mixed-gas conditions. For instance, swelling induced by high concentration of one gas affects the diffusivity of the other species. In glassy polymers competitive sorption limits the solubility of all species present but to a different extent for each one. Owing to these phenomena, mixed-gas performance significantly deviates from the ideal values obtained from pure-gas measurements.

2.3 Macroscopic models for Gas Solubility in Polymers

The calculation of gas sorption equilibria can be performed with Equations of State (EoS) models, such as those based on a Lattice Fluid (LF) representation of substances [35], or on hard sphere chain schemes, like the Statistical Associating Fluid Theory (SAFT) [36]. The general features of the Sanchez-Lacombe EoS are presented in **Section 2.3.1**.

In the case of glassy polymers, due to their nonequilibrium condition, equilibrium models are not applicable. **Figure 2.2** represents the specific volume of polymeric material as a function of temperature. The slope presents a discontinuity, which marks the glass transition of the material. Cooling down the materials from high temperature, the glass transition corresponds to the onset of severe kinetic constraints in the polymer's ability to reorganize itself to attain its equilibrium specific volume. As a result, at temperatures lower than the glass transition temperature T_g, the material exhibits a higher specific volume than expected from the extrapolation of the high temperature trend. The difference between the two is the excess free volume that characterizes the glass states and constitutes a measure of the out-of-equilibrium degree of the material. In these cases the Non-Equilibrium Thermodynamics for Glassy Polymers (NET-GP) approach [37] can be used instead of equilibrium thermodynamic models. This approach gives nonequilibrium expressions for the free energy of the system for any equation of state of choice, by introducing an internal state variable, the polymer density, to describe the out-of-equilibrium degree of the systems. This model has been successfully applied to the prediction of gas and vapor sorption in a variety of polymeric systems [8,38–40], and it will be presented in **Section 2.3.2**.

The calculation of gas solubility in glassy polymers is customarily performed in the literature also using the empirical Dual Mode Sorption (DMS) model [41–51], described in **Section 2.3.3**. Its simplicity of use and its capability to correlate the experimental sorption behavior in glassy polymers well in most of the cases are the main reasons behind its success. However, it suffers from several limitations, that will be addressed in greater detail also in **Chapter 4**.

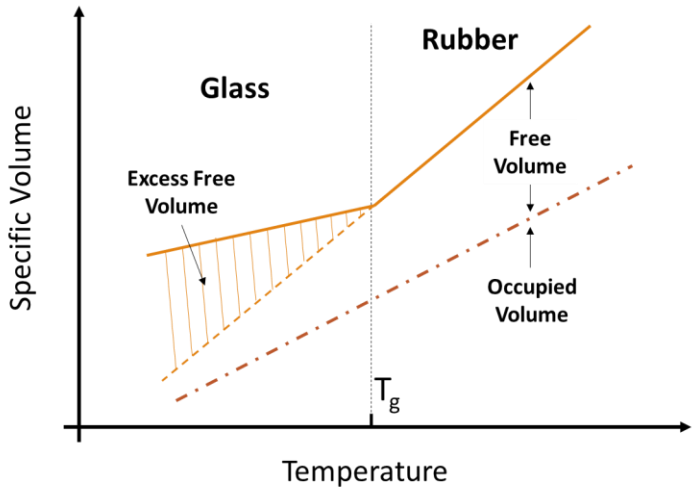

Figure 2.2. Specific volume of a polymeric material as a function of temperature, above and below the glass transition temperature T_g.

2.3.1 Sanchez-Lacombe Equation of State

Lattice fluid theories employ statistical mechanics arguments to define the partition function $\zeta = \zeta(p,T)$, to derive expressions for the free energy G and, in turn, all other properties of the system:

$$\zeta(p,T) = \sum_{V}\sum_{E} \Psi(E,V,N) \exp\left(-\frac{E+pV}{k_b T}\right) \quad \text{Eq. (2.30)}$$

$$\mathrm{G} = -k_b T \, ln\, \zeta(p,T) \quad \text{Eq. (2.31)}$$

k_b is the Boltzmann constant, $\Psi(E,V,N)$ represents the number of accessible configurations (microstates) of a system with N molecules, volume V and energy E. In a lattice fluid representation, each molecule is considered as a flexible chain composed of r segments (*mers*). Different models postulate different expressions for the intermolecular interaction potential and make different assumptions about the geometry of the lattice. The **Flory-Huggins model** [52,53] assumes a repulsive potential and rigid spheres, located in an all-occupied lattice with cubic cells. Compressibility and thermal expansion of the systems are accounted for solely by volume changes of the single cells.

In the evolution proposed by **Sanchez and Lacombe** [35,54], empty cells are possible in the system. In this model, to estimate $\Psi(E,V,N)$, it is considered that molecules are randomly mixed among themselves and empty cells are randomly distributed as well. Moreover, a mean field approximation is considered: when two cells of the lattice are not occupied by the same segment, the probabilities of them being empty or occupied are independent. In this way, the number of possible configurations Ψ depends on the number of empty cells N_0, the number of occupied cells N_r and the coordination number of the lattice z. The energy of the lattice E is obtained by summing all the pairwise energetic contributions of first neighbors and considering null interactions between molecules segments and empty cells. The interaction energy among neighboring segments not covalently bonded is ε. The total volume V is given by the sum of empty volume and occupied volume, and both can be expressed through the definition of the characteristic parameter v^*, which represent the volume of a single cell. The free energy expression in this model is:

$$\mathrm{G} = Nrk_bT^*\left\{-\tilde{\rho} + \frac{\tilde{p}}{\tilde{\rho}} + \tilde{T}\left[\frac{1-\tilde{\rho}}{\tilde{\rho}}\ln(1-\tilde{\rho}) + \frac{1}{r}\ln(\tilde{\rho})\right]\right\} \quad \text{Eq. (2.32)}$$

Here $\tilde{T}$, $\tilde{p}$ and $\tilde{\rho}$ are the reduced temperature, pressure and density, defined as follows:

$$\tilde{T} = \frac{T}{T^*} \quad \text{Eq. (2.33)}$$

$$\tilde{p} = \frac{p}{p^*} \quad \text{Eq. (2.34)}$$

$$\tilde{\rho} = \frac{\rho}{\rho^*} \quad \text{Eq. (2.35)}$$

In the lattice fluid representation, each substance is univocally characterized by three molecular parameters ε, v^*, r or equivalently, by the macroscopic ones T^*, p^*, ρ^*, which can be converted into one another according to the following relations:

$$T^* = \frac{\varepsilon}{k_b} \quad \text{Eq. (2.36)}$$

$$p^* = \frac{\varepsilon}{v^*} \quad \text{Eq. (2.37)}$$

$$\rho^* = \frac{M}{rv^*} \quad \text{Eq. (2.38)}$$

M is the molar mass, ε is associated to the depth of the potential energy well of interaction between "mers" and $r\varepsilon$ represents the total molar energy of interaction, that is the energy necessary to bring one mole of fluid from the close-packed state to that of zero density. The ratio between the molar energy of interaction and the molar volume is a characteristic pressure of the system, and it is a measure of its cohesive energy density. Therefore p^* can be interpreted as a measure of the strength of intermolecular interactions. The characteristic temperature T^* is the ratio of the interaction energy and Boltzman constant, and the characteristic density ρ^* is the ratio of molar mass and closed-pack volume. Among the characteristic parameters of the Lattice fluid model holds a relation analogous to the ideal gas law:

$$p^* v^* = k_b T^* \quad \text{Eq. (2.39)}$$

By minimizing the free energy with respect to the volume at constant temperature and pressure, one obtains the **Sanchez-Lacombe EoS**, which is formally identical for pure components and mixtures, provided that the corresponding definition (*i.e.* that for a pure component or that for the multicomponent case) of the reduced variables $\tilde{T},\ \tilde{p}, \tilde{\rho}$ is used:

$$\tilde{\rho} = 1 - \exp\left[-\frac{\tilde{\rho}^2}{\tilde{T}} - \frac{\tilde{p}}{\tilde{T}} - \tilde{\rho}\left(1 - \sum_i^N \frac{\phi_i}{r_i}\right)\right] \quad \text{Eq. (2.40)}$$

Therefore, the **extension to mixtures** is straightforward. Each species present in the mixture occupies $N_{r,i} r_i$ lattice cells, and the composition of the system ϕ_i is expressed as the fraction of lattice sites occupied by i:

$$N_r r = \sum_i N_{r,i} r_i \quad \text{Eq. (2.41)}$$

$$\phi_i = \frac{N_{r,i} r_i}{N_r r} \quad \text{Eq. (2.42)}$$

It is assumed that the closed-packed volume of each species is conserved at multicomponent conditions and the total number of binary interactions in the mixture is the sum of the corresponding interactions for the pure components. These two hypotheses grant additivity of the closed-packed volumes:

$$r = \frac{1}{N} \sum_i r_j^0 N_j \quad \text{Eq. (2.43)}$$

$$\phi_j^0 = \frac{r_j^0 N_i}{rN} \quad \text{Eq. (2.44)}$$

$$v^* = \sum_i \phi_i^0 v_i^* \quad \text{Eq. (2.45)}$$

Mixing rules for the macroscopic parameters are the following:

$$\frac{1}{\rho^*} = \sum_i^N \frac{\omega_i}{\rho_i^*} \quad \text{Eq. (2.46)}$$

$$p^* = \sum_i^N \phi_i p_i^* - \sum_i^{N-1} \sum_{j>i}^N \phi_i \phi_j \Delta p_{ij}^* \quad \text{Eq. (2.47)}$$

$$T^* = \frac{p^*}{\sum_i^N \frac{p_i^* \phi_i}{T_i^*}} \quad \text{Eq. (2.48)}$$

Δp_{ij}^* expresses the characteristic binary interactions between species i and j and contains an **adjustable binary parameter** k_{ij}, to account for deviations from the geometric mean mixing rule:

$$\Delta p_{ij}^* = p_i^* + p_j^* - 2(1 - k_{ij})\sqrt{p_i^* \cdot p_j^*} \quad \text{Eq. (2.49)}$$

The relationships among the materials parameters along with the relevant expressions and mixing rules of the model are summarized in **Table 2.1**.

Table 2.1. Definition of symbols and parameters used in the SL and NELF models

n_c	Number of components (gases + polymer)	
M_i	Molar mass of component i	
ρ_i	Density of component i	
v_i^*	Molar volume of a lattice cell of component i	
r_i^0	Number of lattice cells occupied by a molecule of pure component i	
ε_i	Non-bonded interaction energy between two lattice cells occupied by component i	
T_i^*	Characteristic temperature of component i	$T_i^* = \frac{\varepsilon_i}{k_b}$
p_i^*	Characteristic pressure of component i	$p_i^* = \frac{\varepsilon_i}{v_i^*}$
ρ_i^*	Characteristic density of component i	$\rho_i^* = \frac{M_i}{r_i v_i^*}$
$\tilde{T}_i$	Reduced temperature of component i	$\tilde{T}_i = \frac{T}{T_i^*}$
$\tilde{p}_i$	Reduced pressure of component i	$\tilde{p}_i = \frac{p}{p_i^*}$
$\tilde{\rho}_i$	Reduced density of component i	$\tilde{\rho}_i = \frac{\rho_i}{\rho_i^*}$
ρ	Density of the mixture	
k_{ij}	Binary interaction parameter between i and j	
ω_i	Mass fraction of component i	
ϕ_i	Volume fraction of component i in closed packed conditions	$\phi_i = \frac{\omega_i/\rho_i^*}{\sum_i^N \omega_i/\rho_i^*}$
ρ^*	Characteristic density of the mixture	$\frac{1}{\rho^*} = \sum_i^{n_c} \frac{\omega_i}{\rho_i^*}$
p^*	Characteristic pressure of the mixture	$p^* = \sum_i^{n_c} \phi_i p_i^* - \sum_i^{n_c-1} \sum_{j>i}^{n_c} \phi_i \phi_j \Delta p_{ij}^*$ $\Delta p_{ij}^* = p_i^* + p_j^* - 2(1-k_{ij})\sqrt{p_i^* \cdot p_j^*}$
T^*	Characteristic temperature of the mixture	$T^* = \frac{p^*}{\sum_i^N \frac{p_i^* \phi_i}{T_i^*}}$
v^*	Average close-packed molar volume in the mixture	$v^* = \frac{T^* R}{p^*}$
r_i	Number of lattice cells occupied by a molecule in mixture	$r_i = \frac{r_i^0 v_i^*}{v^*}$
$\tilde{T}$	Reduced temperature of the mixture	$\tilde{T} = \frac{T}{T^*}$
$\tilde{p}$	Reduced pressure of the mixture	$\tilde{p} = \frac{p}{p^*}$
$\tilde{\rho}$	Reduced density of the mixture	$\tilde{\rho} = \frac{\rho}{\rho^*}$

2.3.2 Non-Equilibrium Thermodynamics for Glassy Polymers (NET-GP)

The Non-Equilibrium Thermodynamics for Glassy Polymers (NET-GP) approach [37,39,55] is a thermodynamics-based framework that provides an extension of Equation of State (EoS) theories to nonequilibrium materials. It is, therefore, suitable for the calculation of the solubility of low molecular weight species in glassy polymers, which could not be described correctly by equilibrium equations of state or activity coefficients models, due to the nonequilibrium nature of such materials. The NET-GP approach applies to homogeneous, isotropic, and amorphous phases, whose state is described by the usual set of state variables, namely temperature, pressure and composition, and, in addition, by the actual nonequilibrium density of the glassy polymer ρ_{pol}, which acts as an internal state variable and accounts for all the effects of thermal history and formation of the polymer, responsible for its departure from equilibrium. The Helmholtz free energy per unit volume A^{NE} of a polymer-penetrant system with an internal state variable is given by **Eq. (2.50)**:

$$A^{NE} = A^{NE}(T, p, \Omega, \rho_{pol}) \qquad \text{Eq. (2.50)}$$

the composition vector, Ω, contains the mass ratios between penetrant i and the polymer. It can be shown [39] that A^{NE} is independent of pressure, which is one of the main results of the NET-GP approach:

$$\left(\frac{\partial A^{NE}}{\partial p}\right)_{T,\rho_i,\rho_{pol}} = 0 \qquad \text{Eq. (2.51)}$$

As a consequence of this, the nonequilibrium Helmholtz free energy of the system can be related to a corresponding equilibrium value A^{Eq}, at the same temperature, density and composition:

$$A^{NE}(T, p, \Omega, \rho_{pol}) = A^{Eq}(T, \Omega, \rho_{pol}) \qquad \text{Eq. (2.52)}$$

For the chemical potential under nonequilibrium conditions the following relation holds [39]:

$$\mu_i^{NE} = \left(\frac{\partial A^{NE}}{\partial \rho_i}\right)_{T,\,\rho_{j\neq i},\rho_{pol}} \qquad \text{Eq. (2.53)}$$

Consequently, the nonequilibrium chemical potential can be obtained from the corresponding equilibrium value at the same temperature, density and composition:

$$\mu_i^{NE}(T, p, \Omega, \rho_{pol}) = \mu_i^{Eq}(T, \Omega, \rho_{pol}) \qquad \text{Eq. (2.54)}$$

Therefore, it is possible to calculate the chemical potential at nonequilibrium conditions using the expression for the free energy provided by an EoS of choice and employ it to solve the phase equilibrium for the composition. Even though the glassy polymer is not in a thermodynamic equilibrium state, because it tends to densify over time, the dynamics of this process is slow compared to the characteristic time of a sorption process, therefore it is possible to assume that a “pseudo” phase equilibrium condition can be reached by the polymer in contact with the gas phase, and therefore calculate the amount of sorbed gas by imposing the equality of the chemical potential of the penetrant in the two phases:

$$\mu_i^{NE(pol)}(T, p, \Omega, \rho_{pol}) = \mu_i^{Eq(gas)}(T, p, y_i) \qquad \text{Eq. (2.55)}$$

The equilibrium chemical potential in the gas phase $\mu_i^{Eq(gas)}$ is obtained by means of a suitable equation of state for the gas phase.

The NET-GP approach requires knowledge of the polymer density at each pressure value used in the computation of a sorption isotherm. For the proper evaluation of how density changes during sorption, experimental dilation measurements would be needed, because the presence of swelling agents can significantly alter it, especially at high pressure. However, with the lack of such data, a linear relation between the polymer specific volume and the partial pressure p_i or the fugacity f_i of the penetrant can be assumed, as it has often been observed experimentally for different light gases [9,56,57]. Under this hypothesis, adjustable **swelling coefficients** $k_{sw,i}$ can be defined as follows:

$$\frac{1}{\rho_{pol}} = \frac{1}{\rho_{pol}^0}\left(1 + \sum_{i=1}^{N_p} k_{sw,i} f_i\right) \qquad \text{Eq. (2.56)}$$

In the case of a single penetrant, k_{sw} can be evaluated by the knowledge of one point of the sorption isotherm in the high-pressure range. When data above T_g are experimentally accessible, k_{sw} values can also be estimated in a predictive way by using the rheology model presented in ref. [38].

2.3.2.1 Non-Equilibrium Lattice Fluid (NELF) model

Sorption equilibria in the glassy polymeric materials considered in this dissertation will be calculated with the NELF model [37,39,55,58], which is the extension of the Sanchez-Lacombe (SL) EoS [35,54,59] to the nonequilibrium glassy state by means of the NET-GP theory. In the nonequilibrium phase, the polymer density value, needed to calculate the parameters, has to be known experimentally, or estimated using **Eq. (2.56)**, whereas for the gas phase, the equilibrium density results from the solution of the SL EoS **Eq. (2.40)**. The expression of the **chemical potential** of the SL model, to be used in **Eq. (2.55)**, is given below. Definitions of the variables used are reported in **Table 2.1**.

$$\frac{\mu_i}{RT} = ln(\tilde{\rho}\phi_i) - ln(1-\tilde{\rho})\left[r_i^0 + \frac{r_i + r_i^0}{\tilde{\rho}}\right] - r_i - \tilde{\rho}\frac{r_i^0 v_i^*}{RT}\left[p_i^* + \sum_{j=1}^{N}\phi_i\left(p_j^* - \Delta p_{i,j}^*\right)\right] + 1 \qquad \text{Eq. (2.57)}$$

2.3.3 Dual Mode Sorption (DMS) model

The first to postulate the existence of a sorption mechanism particular to polymers in the glassy state was Meares [47,48]. From the indication that polymers below the glass transition temperature contain a distribution of microvoids frozen into their structure [47], it was suggested that those regions of reduced density could act as preferential sorption sites. Moreover, it was observed that the sorption isotherms of organic vapors in ethyl cellulose were concave to the pressure axis, whereas sorption isotherms of rubbery materials did not show the same trend. Furthermore, rather high negative values of the heat of solution

were measured for glassy polymers, compared to rubbers. From these observations, Barrer et al. [49] proposed the existence of two concurrent mechanisms of sorption: dissolution and "hole-filling".

The Dual Mode Sorption (DMS) model [41–51] postulates the existence of two different gas populations, inside glassy polymers, at equilibrium with one another. The first is dissolved in the dense portion of the material and it can be described by Henry's law. The second one saturates the nonequilibrium excess free volume of the polymer (**Figure 2.2**) and it is described by a Langmuir curve. The total sorbed gas concentration c_i as a function of gas fugacity f_i can be expressed as a sum of these two contributions:

$$c_i = k_{D,i} f_i + \frac{C'_{H,i} b_i f_i}{1 + b_i f_i} \qquad \text{Eq. (2.58)}$$

The parameter $k_{D,i}$ is Henry's law constant, while b_i is Langmuir affinity constant, which represents the ratio of the rate constants of sorption and desorption of penetrants in the microvoids. $C'_{H,i}$ is the Langmuir capacity constant, which characterizes the sorption capacity of a glassy polymer for a given penetrant in the low-pressure region. This latter parameter is connected to changes in polymer density resulting from differences in formation history or annealing treatments [60,61]. For every gas-polymer pair, the three parameters are retrieved through a nonlinear least-square best fit of pure-gas sorption data. $C'_{H,i}$ decreases as temperature increases and it has been shown to disappear at the glass transition temperature (T_g) of the polymer [62], while the temperature dependence of k_D and b is described by a Arrhenius relation [63]:

$$k_D = k_{D0}\, e^{-\frac{\Delta H_D}{RT}} \qquad \text{Eq. (2.59)}$$

$$b = b_0\, e^{-\frac{\Delta H_b}{RT}} \qquad \text{Eq. (2.60)}$$

In **Eq. (2.59)** and **Eq. (2.60)** ΔH_D and ΔH_b are the enthalpies of sorption for Henry and Langmuir modes of sorption, R is the gas constant and T is the temperature.

The extension to **multicomponent sorption** of this model [64] is based on phenomenological arguments, suggested by the theory of competitive sorption of gases on catalysts, which exhibit a Langmuir behavior. The amount of unrelaxed free volume considered for the polymer is limited and fixed, because the model does not take into account swelling effects. Therefore, the various penetrants will compete to occupy it and, as a consequence, the sorbed concentration is expected to decrease with respect to the pure-gas case. It is assumed that the extent of the competition effect is controlled by the relative values of the product of the affinity constant and partial pressure (or fugacity) of each penetrant. Further hypotheses are that the affinity parameter b, Henry's constant k_D and the molar density of a component sorbed inside the Langmuir sites are independent of the presence of other penetrants. The final expression for the concentration of component i in presence of a second component j is given by:

$$c_i = k_{D,i} f_i + \frac{C'_{H,i} b_i f_i}{1 + b_i f_i + b_j f_j} \qquad \text{Eq. (2.61)}$$

The characteristic gas-polymer parameters found in **Eq. (2.61)** are the same as found in **Eq. (2.58)**, which are retrieved from a least-square fit of pure-gas isotherms. It is also commonplace to write **Eq. (2.58)** and **Eq. (2.61)** using the partial pressure of each gas instead of its fugacity. However, when the approximation

of ideal-gas behavior is not valid, such as when high pressures are considered, the fugacity constitutes a more appropriate measure of the chemical potential, which is the driving force for gas sorption in the polymer. Moreover, when mixtures are concerned, two gases like CH_4 and CO_2 show different departures from ideality and at the same partial pressure they can have rather different fugacity. For this reason, in the context of mixed-gas sorption measurements, results are more often reported using gas fugacity, to account for the different degree of non-ideality of the components in the gas phase. Even though the accuracy of the pure-gas data representation with the DMS model using either partial pressure or fugacity is the essentially the same, the values of the parameters obtained using pressure or fugacity are clearly different [65], therefore it should always be specified which variable was used in the regression, in order to enable a meaningful comparison between different parameter sets. It was verified that using pressure-based parameters or fugacity-based parameters yielded the same results in the mixed-gas sorption calculations. Therefore, the accuracy of the multicomponent calculations with the DMS does not depend on this choice [66]. The same observation was reported also by Sanders et al. [65,67] in their studies on mixed-gas sorption of binary mixtures in PMMA, and by Story et al. [68] in their work on mixed-gas sorption in PPO. The use of pressure-based or fugacity-based DMS parameters in the calculation of mixed-gas sorption yielded very similar results, only slightly more accurate in some of the cases when fugacity was used instead of partial pressure.

The DMS model correlates the pure sorption isotherms of most penetrant in glassy polymers really well, however it does not allow to represent all types of sorption isotherms encountered, such as the sigmoidal shape of the sorption isotherms of alcohols in glassy polymers. There have been studies aimed at overcoming this limitation: for example, by incorporating multilayer sorption theory, a DMS based model capable of representing all the different shapes of sorption isotherms encountered was developed [69]. However, the simpler version is still the most used one. Another known issue with the use of this model is that the adjustable polymer-penetrant parameters of the DMS model depend on polymer history and operating conditions, thus lacking predictive ability outside their range of derivation, as discussed, for example, by Bondar at al. concerning the pressure range [70]. A further limitation of the DMS model is that it does not account for the fact that the polymer matrix, unlike rigid porous materials, can swell when sorbing penetrants. Therefore, possible synergistic effects, due to second-component induced swelling, are not accounted for. However, ultra-high free volume glassy polymers, which are among the best candidates as gas separation materials, have a limited tendency to swell, and the experimental data collected so far on mixed-gas sorption of CO_2/CH_4 mixtures indicate that such effects are not predominant in these materials, at least for pressures of CO_2 below 30 bar [71–74]. The prevailing multicomponent effect observed is the one associated with competition during sorption, which is explicitly included in the multicomponent DMS model. Therefore, as it was found in previous studies [65], the DMS model is expected to provide a reliable estimation of the data also in the cases examined here.

2.4 Molecular Modelling

The use of atomistic simulations for the description of advanced materials and their properties has experienced an impressive outburst in recent years, due to the increase in the computational power of calculators and the development and optimization of new efficient algorithms and methods, capable of addressing larger systems, wider length and time scale phenomena and more complex chemical structures [75–78]. These methods constitute unique means to gain insight into the microscopic structure and dynamics of materials and to perform predictive analyses in conditions that cannot be accessed experimentally. Molecular simulation methods are based on the fundamental principles of statistical mechanics and provide unique means to unravel the microscopic mechanisms that underlie the macroscopic behavior of materials, enabling simultaneously the accurate prediction of materials properties. Theories, such as the Lattice Fluid theory described in **Section 2.3.1**, picture a schematic representation of the polymer-penetrant system and, under suitable approximations, and through statistical mechanical arguments, provide simplified expressions to calculate solubility. Computer simulations, on the other hand, use detailed models for the representation of the molecular structures and interaction potentials of the system and provide numerical solutions based on the statistical mechanics formulation of the problem. Within these limits, in principle, molecular simulations can provide a reliable description of the materials under study. In practice, approximations are introduced also in the case of computer simulations depending on the problem at hand, to overcome computational resources constraints. However, they are generally less strong than those invoked by macroscopic theories. Simulations provide a detailed picture of sorption and diffusion of gases in polymers, allowing the elucidation of the mechanisms behind these phenomena. This can lead to the formulation of more accurate physical models and allows testing the effect of the approximations invoked in theories to validate or dispute their legitimacy. The predictive character of simulations allows to use them in place of longer and more costly experimental screening campaigns in search of the right material. If structure properties correlations are established, then the traditional trial-and-error approach is overcome and a more rational materials design can be achieved [77,79].

Since the 1980s, molecular modelling techniques have been increasingly employed to predict a wide range of properties of dense amorphous polymers, such as the thermodynamic and transport properties relevant for membrane separations. In particular, molecular modelling studies were instrumental in highlighting the microscopic mechanisms that are responsible for penetrant diffusion in dense rubbery and glassy polymers in terms of elementary jumps between neighboring sites of accessible volume. In the calculation of these properties, models with atomistic detail are in the general case necessary, as penetrants diffusional motion in dense amorphous systems is highly influenced by the local environment that the penetrant molecule is surrounded by and, in many cases, especially near or below T_g, by the cooperative motion of the macromolecular matrix. With the development of more accurate molecular models for the description of the energetic interactions of the systems, new algorithms for the generation of amorphous polymeric structures and efficient equilibration protocols, the reliability of the predictions yielded by atomistic techniques has drastically improved over the years. However, despite these progresses, the extremely

broad range of time scales that characterize the various modes of motion of polymeric systems, especially in the glassy state, and in the case of high molecular weight makes their proper equilibration and correct sampling of their dynamics a particularly challenging task.

2.4.1 Generation of Atomistic Models of Amorphous Polymers

In molecular models, the system is depicted as a set of particles, or interaction sites, where the action of the forces is applied and where partial point charges are located. The model may be:

- fully atomistic (or all-atoms, AA), where each interaction site corresponds to an atom of the molecule;
- a united atoms (UA) representation, in which hydrogen atoms are considered in a single interaction site together with the atom they are bonded to;
- a coarse-grained representation (CG), in which multiple atoms are put together to form a single larger interaction site.

The expression of the potential energy U_{TOT} used to compute the forces acting on each interaction site is called a force field. This contains the contributions coming from bonded interactions (U_B), such as deviations of chemical bond lengths ($U(r_{ij})$) and bond angles ($U(\phi_i)$) as well as dihedral angles ($U(\varphi_i)$) and improper torsions ($U(\theta_i)$) from their equilibrium values, and contributions coming from nonbonded interactions (U_{NB}) due to electrostatic forces and van der Waals forces, both attractive and repulsive, resulting from the interactions of electronic clouds. **Eq. (2.62) - Eq. (2.68)** represent the general structure of a force field, in which harmonic or trigonometric functions are used to express the potential energy associated to the various contributions. Van der Waals interactions are often expressed with a 12-6 Lennard Jones potential. All contributions are summed and only pairwise interactions are taken into account. More complex functional forms as well as cross terms expressing coupling between different interactions can be implemented if needed.

$$U_{TOT} = U_B + U_{NB} \quad \text{Eq. (2.62)}$$

$$U_B = \sum_i^{N_{atoms}} \sum_{j>i}^{N_{atoms}} U(r_{ij}) + \sum_i^{N_\phi} U(\phi_i) + \sum_i^{N_\varphi} U(\varphi_i) + \sum_i^{N_\varphi} U(\varphi_i) + \sum_i^{N_\theta} U(\theta_i) \quad \text{Eq. (2.63)}$$

$$U(r_{ij}) = K_l(r_{ij} - r_0)^2 \quad \text{Eq. (2.64)}$$

$$U(\phi_i) = K_\phi(\phi_i - \phi_0)^2 \quad \text{Eq. (2.65)}$$

$$U(\varphi_i) = K_\varphi(1 + \cos(3\varphi_i)^2) \quad \text{Eq. (2.66)}$$

$$U(\theta_i) = K_\theta(\theta_i - \theta_0)^2 \quad \text{Eq. (2.67)}$$

$$U_{NB}(r_{ij}) = 4\varepsilon\left[\left(\frac{\sigma}{r_{ij}}\right)^{12} - \left(\frac{\sigma}{r_{ij}}\right)^{6}\right] + \frac{q_i q_j}{4\pi\epsilon_0 r_{ij}} \quad \text{Eq. (2.68)}$$

The parametrization of the potential energy expression is carried out from quantomechanical calculations of low molecular weight oligomers of the molecule (especially to obtain the parameters for bonded interactions and partial charges) or alternatively from fitting experimental structural and/or thermodynamic properties of the material. For the accurate prediction of sorption and diffusion of penetrants in polymers, local packing is the most important feature, however, this is inextricably interconnected to long range conformational characteristics of the polymer [80], which therefore require accurate representation.

Several strategies have been developed for the generation of dense amorphous polymer models [81–85]. In this work, a three-dimensional model of amorphous polymer chains is constructed to adhere to the random coil hypothesis by Flory [86]. The initial guess configurations were generated through a bond-by-bond growth of the chains under periodic boundary conditions, following the rotational isomeric state model for unperturbed chains as modified by Theodorou and co-workers [87,88] to avoid inter and intramolecular volume overlaps. The initial structure obtained always underwent a molecular mechanics simulation. This consists of a static minimization of the potential energy of the system, at constant volume, without considering thermal motion, whose purpose is to relax close contacts between atoms present in the initial guess configuration, which result in unrealistically high potential energy. Even though without thermal motion the set of information that can be extracted is limited, the energy-minimized configurations obtained constitute a good starting point for subsequent equilibration through Molecular Dynamics or Monte Carlo simulations.

An important difference exists between polymer melts and glasses: **polymer melts** are equilibrium structures and the probability of the system to assume a specific configuration is related to the associated potential energy U, proportionally to the Boltzmann factor: $\exp(-U/k_bT)$. Therefore, the generation of a realistic polymer melt configuration is, in principle, a well-defined problem. Nonetheless, in many cases it demands elaborate hierarchical computational methods, as the molecular weight, stiffness and chemical complexity of the macromolecular system under study increases. **Polymer glasses**, on the other hand, are nonequilibrium structures trapped in local energy minima that depend on their formation history. The energy barriers separating two minima are generally very high and relaxation phenomena, that allow the glass to transition from a minimum energy configuration to another, happen with characteristic times that are usually greater than typical experimental or simulation times. Within a minimum energy well the probability distribution of configurations still follows a Boltzmann distribution. Therefore, the same simulation techniques for the calculation of solubility and diffusivity can in principle be applied both in the case of polymer melts and polymer glasses. However, to obtain realistic results for a glass one should average over configurations that sample different local minima of the potential energy surface. Generating microscopic configurations that incorporate the effects of formation and thermal history of a glass in a well-defined fashion, and being able to assign a probability distribution to the different minimum energy pockets is still an open research area.

2.4.2 Molecular Dynamics (MD) simulations

Molecular Dynamics (MD) simulations [79,89,90] consist of tracking the temporal evolution of the system through the numerical integration of the equations of motion for all the interaction sites present in the system. Materials properties, such as thermodynamic, structural, dynamical, transport properties, are computed as averages over the trajectory of the simulated system. MD is widely used for equilibration and property prediction in computational materials science using atomistic or coarse-grained model systems in several statistical ensembles. The simulations can be carried out at constant number of particles N, constant volume V and constant energy E conditions, in the microcanonical ensemble (NVE simulation). By coupling the system to a thermostat and a barostat, simulations can be performed also at constant number of particles, volume and temperature T, (NVT or canonical ensemble), or at constant temperature, pressure P and number of particles (NPT ensemble). The latter, called isothermal-isobaric ensemble, is the set of constraints that mimics more closely experimental conditions.

The computational cost of this technique is very high and the maximum simulation times that can be achieved are in the order of hundreds of nanoseconds, which allows to obtain direct information only on processes whose dynamics is fast enough to be displayed in such temporal interval. Even though domain decomposition techniques allow splitting the calculations over several processors working in parallel, and even with the implementation of algorithms that allow to speed up the calculation, such as multiple time step integration schemes [91], to use of longer time steps for the interactions that change at a slower rate, such as long range electrostatics, the aforementioned limitations persist. This is particularly relevant in the case of systems (and processes) that are characterized by a wide range of time scales for the relaxation of their various modes of motion. High molecular weight polymeric systems interesting for membrane separation applications, particularly glassy polymers, falls into this category, because their characteristic relaxation times are orders of magnitude greater than simulation times. In these more complex cases, it is paramount that MD simulations are initiated already with realistic structures, because equilibration cannot be achieved in the course of an even very long MD simulation.

2.4.3 Monte Carlo Simulations

In Monte Carlo (MC) simulations [79,89] a series of microscopic configurations of the system is generated, conforming to the probability distribution associated to the statistical ensemble and the thermodynamic conditions in which the simulation is carried out. At each step, starting from the previous configurations, a random perturbation is attempted. This attempted perturbation consists of an elementary move among a set of predefined possibilities, such as atom displacements, rotations, insertions, deletions of particles. Monte Carlo methods can be applied also in ensembles where the number of particles can fluctuate, thus allowing the calculation of phase equilibria and in particular gas sorption.

The attempted perturbation is accepted or rejected according to the energy change that it entails and to an acceptance criterion that ensures that the obtained sequence of microstates asymptotically samples the

probability distribution of the ensemble [92], following the principle of microscopic reversibility in the generation of the Markov chain series of configurations. The properties of interest are then calculated as averages over the collection of microstates generated. MC simulations do not have physical time in them, therefore, they do not yield any dynamical information, such as relaxation times or diffusion constants.

For polymeric systems, sophisticated moves have been devised, which allow to overcome great energy barriers and efficiently equilibrate also high molecular weight polymeric chains up to realistic experimental values, unlike MD. These moves include: reptation, which consists of excising one chain end and appending it on the other side of the chain with a random torsion angle; configurational bias algorithms [93,94] cut the terminal part of a chain and regrow it by avoiding the regions where volumes overlaps would occur, taking this bias into account in the selection criterion; concerted rotations [95] that occur around seven consecutive skeletal bonds to modify chain conformation without affecting bond length and angles. In addition, other connectivity-altering moves [96] have been devised, such as end-bridging [97,98], in which a trimer located in the middle of a chain is excised on one side and rotated to be attached to the end of another chain, and double-bridging [99], where two trimers are simultaneously excised from two chains and used to connect each section of the first chain with one section of the other chain. Equilibrated polymer melt configurations obtained with this method can be used as starting points to generate glassy structures through cooling. A disadvantage of these methods is that crafting the most effective moves is a system-specific process and that their efficiency decreases for macromolecules with complex chemical structure.

2.4.4 Hierarchical Modelling Approaches

In the case of high molecular weight polymers with rigid backbones and complex chemical constitution, simulations at the atomistic level of description are necessary in many cases to extract the relevant properties, but often inadequate to equilibrate the system to obtain a realistic starting configuration. In such cases, systematic hierarchical approaches are required [100–104], in which the system is mapped from an atomistic to a coarse-grained level of representation by substituting a group of atoms with a single interaction site, as shown in **Figure 2.3**.

Carrying out the equilibration at the coarse-grained level is more efficient for several reasons. In a CG representation there are fewer degrees of freedom to be tracked, therefore longer simulations can be run with the same computational effort. The characteristic times in which the coarse-grained features change are higher compared to the atomistic level. For example, a coarse grained bond length will fluctuate more slowly than an atomistic bond length, which is the limiting factor dictating the choice of time step in the integration of the equations of motions: in CG simulations a higher time step can be used and, therefore, longer simulation times can be achieved, allowing the system to explore a greater sample of the configuration space. The CG representation is geometrically simpler, therefore realistic structures can be generated in combination with the powerful connectivity-altering MC algorithms, taking advantage of their superior effectiveness in relaxing high molecular weight polymers, compared to MD.

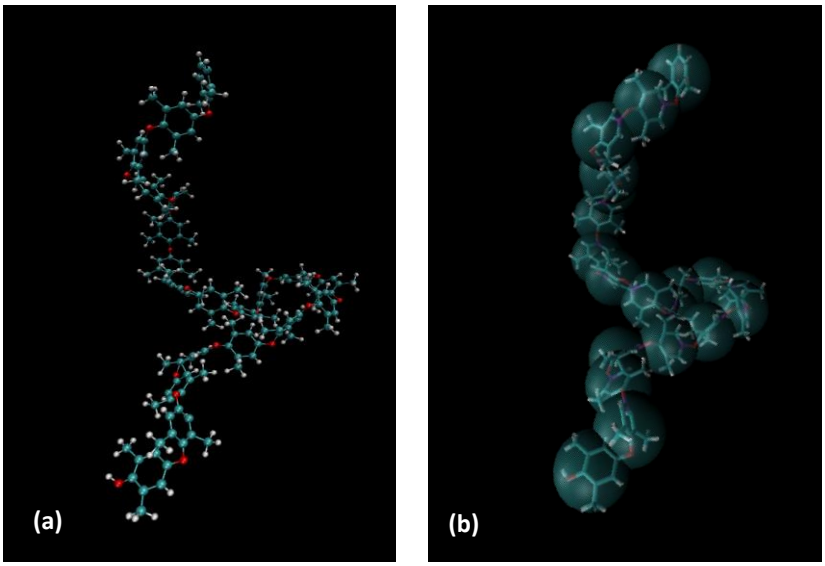

Figure 2.3. (a) All-atom representation of a polymer chain and (b) a corresponding coarse-grained representation, where all atoms of the repeating unit are united into one bead depicted by the transparent spheres.

Depending on the problem under study, once a realistic structure is obtained at the CG level, the system may be back-mapped to its original atomistic representation, reconstructing the underlying geometry and chemistry [105,106]. In adaptive resolution methods [107] two spatial domains, modeled at two different scales, are brought together in a concurrent simulation by defining a hybrid region where particles can switch representation from the coarse-grained representation to the more detailed one and vice versa, depending only on a single parameter that controls the reverse mapping process and it is independent of atomistic and coarse-grained force-fields. There is not a unique way to map to system to a CG representation and the appropriate level of coarse-graining depends on the purpose of the simulation and the properties that are relevant to the specific study. In addition to the migration to a suitable level of coarse-graining, the interaction potential between the CG moieties has to be determined in order to conduct simulations in the CG representation. Effective CG potentials can be parameterized by reproducing macroscopic properties [108] or matching properties of the underlying microscopic representation [109,110], or a combination of these two. Approaches used to this aim include: the Iterative Boltzmann Inversion method [110], in which the fitting procedure targets the reproduction of pair correlation functions of the center-of-mass of groups of atoms corresponding to CG beads, obtained from all-atom simulations; the force matching method [111], based on fitting the potential to ab initio atomic forces of many atomic configurations, can also be used; the reverse Monte Carlo approach [112] consists of the iterative adjustment of the interaction potential to known radial distribution functions using a Monte Carlo simulation technique; relative entropy methods [113,114] also provide a rigorous framework for multiscale simulations and offer numerical techniques for linking models at different scales. CG potentials can be also determined directly from the interactions of groups of atoms that constitute the CG particles based on atomistic potentials [115–117]. Different approaches were also proposed, such as hybrid particle-field methods using Molecular Dynamics simulations employing soft potentials derived from self-consistent field theory [118], that allowed to obtain well relaxed all atom polymer configurations, without the need to back

map the system when changing the resolution of the representation. Ideally, the CG effective potential should be transferable to different thermodynamic points than the ones used in the parametrization [119,120].

Multiscale modelling strategies can also be implemented including continuum models, such as the hybrid atomistic – thermodynamic scheme proposed by Minelli et al. for the calculation of gas solubility in glassy polymers [121,122]. Atomistic simulation results at conditions that are inaccessible experimentally are used to parametrize a nonequilibrium equation of state, which in turn is used to compute gas sorption at pure and mixed-gas conditions with negligible computational effort.

2.4.5 Simulation of Solubility

Solubility depends on the shape and distributions of free volume elements that can accommodate the sorbing molecules, therefore being able to provide a realistic representation of the microstructure of the polymer is a prerequisite. Moreover, it is necessary to have a good model to represent the interactions in the polymer/sorbate mixture. In particular, in the presence of high penetrant concentration, changes occur in the polymer, such as a decrease in its T_g value and plasticization, and these modifications can be interpreted within a molecular picture of the potential energy surface of the system. Indeed, the potential energy of the system is a highly nonlinear function of the coordinates of all the penetrant and polymer atoms present in the system, presenting several local minima. When a melt state is considered, the system can explore different local minimum energy configurations, because the energetic barriers within them can be overcome through thermal fluctuations over the time scale of a simulation. On the contrary, in the case of glassy polymers, thermal fluctuations are insufficient to overcome the energy barrier separating two local minima and the system stays trapped into one local minimum of the potential energy surface. High concentration of penetrant molecules will promote a more pronounced mobility of the polymer chains, allowing the system to overcome the energy barrier separating different potential energy minima. As a consequence of this devitrification and plasticization effect, a polymer glass starts sampling the potential energy surface like a melt.

Calculation of the solubility is a phase equilibrium calculation, with one component present only in one phase, namely the polymer. There are several methods rooted in statistical mechanics principles to predict the phase equilibrium between a polymer and a multicomponent fluid mixture. **Grand Canonical Monte Carlo** simulations [123] are performed at constant chemical potential, volume and temperature. The polymer system is considered to be in contact with a gas reservoir at the specified conditions, with which it can exchange particles and energy, therefore the number of gas particles changes during the simulation, finally fluctuating around an equilibrium value. The **Gibbs Ensemble Monte Carlo** method [124] can also be used for the prediction of phase equilibria. In this method, two simulation boxes at the same temperature are considered simultaneously, each one representing one of the phases in equilibrium. Each box is built under periodic boundary conditions, surrounded by replica of itself, and there are no interfaces. The total number of particles contained in both boxes, the temperature and the total volume of the two boxes is

kept constant, reminiscing of an NVT simulation. Since the two boxes are at equilibrium, the algorithm ensures that the pressure in the two boxes is the same and the chemical potential of each species is the same in each phase. A MC simulation is performed, allowing for atom displacements, redistribution of the volume between the two boxes, and atom exchanges between the boxes. During the course of the simulation the number of atoms in each box and the volume of the box will change until reaching the values corresponding to the two coexisting phases at equilibrium. This method fails close the critical point, as it becomes increasingly difficult to distinguish the liquid and the gas phase densities. In the case of mixtures also MC simulations in the NPT ensemble can be performed. When dealing with dense polymer matrices, or larger penetrant molecules, the acceptance probability of inserting a molecule is drastically lower and the techniques relying on these moves yield unreliable results. Simulations in the **Semigrand Canonical Monte Carlo** [97,125], during which identity exchange trial moves among the various species are considered, are suitable to handle such cases. In **Grand Canonical MD** [126,127] phase equilibrium is computed from two different simulations performed for the liquid phase (NPT) and the gas phase (pseudo grand canonical), without particles exchange between the phases.

One widely used technique to obtain infinite dilution solubility coefficients is the **Widom test particle insertion method** [128]. A ghost penetrant particle is inserted in a fluctuating polymer matrix at random positions and orientations and its interaction energy with the other molecules present in the system is computed. From that, the excess chemical potential of the penetrant inside the polymer and in turn the solubility can be determined. The polymer is not allowed to relax its configuration as a consequence of the insertions. This method can be applied by post-processing a sequence of microstates originated in the course of an MD or MC simulation, by performing several ghost insertions in each configuration. Excluded-volume map sampling [129,130] and grid search methods [131] can be implemented in the case of dense systems, in order to increase the sampling efficiency, by avoiding inserting particles in densely packed regions. However, as the system becomes denser and the solute molecules become bigger, the probability of a successful insertion without overlap with the existing molecules drops dramatically and, therefore, the estimate of solubility through Widom insertions becomes less reliable. Strategies proposed to mitigate the issue include the use of **configurationally biased** [132] bond-by-bond insertions of the penetrant molecules or the use of particle **deletion moves** instead of particle insertions (Staged Particle Deletion [133], Direct Particle Deletion [134]). Alternatively, the **free energy perturbation method** can be applied, where a coupling parameter is introduced between the solute-matrix interactions and the solubility is obtained by thermodynamic integration [135] over a series of simulations conducted at different values of the coupling parameter. The **expanded ensemble scheme** [136] can be implemented to perform calculations of free energy differences between thermodynamic states and can be considered as an application of the free energy perturbation method but within a single simulation. Another technique is **extended ensemble MD** [137] where the coupling of the solute with the rest of the system is dynamically changing, allowing the solute to escape from low-energy pockets and sample the phase space more efficiently. A **minimum-to-minimum mapping** method [138] takes into account local configurational changes to accommodate an inserted molecule to lower superpositions and excluded volume effects. Another approach suitable for sorption of large molecules in dense matrices is the **fast-growth**

thermodynamic integration method [139], which allows the efficient determination of the chemical potential from several independent thermodynamic integrations runs.

Sorption isotherms up to high pressures can be calculated through a series of Monte Carlo simulations performed in the $\boldsymbol{N_{pol}f_{gas}PT}$ **ensemble** [140] (constant number of polymer particles, temperature, pressure and constant fugacity of the penetrant f_{gas} which can be preemptively calculated with an equation of state). This method allows for direct simulation of polymer swelling, since volumes changes are admissible moves. This technique has also the advantage of not simulating explicitly the gas phase. In a similar spirit, an **iterative scheme** can be implemented [141,142] performing $\boldsymbol{N_{pol}N_{gas}PT}$ **MD simulations** of the polymer-penetrant system at fixed composition and at a guess pressure. Subsequently the trajectory is post processed to evaluate the excess chemical potential, for example by performing Widom insertions. The excess chemical potential is then related to penetrant fugacity and to the pressure of the system. This new value of the pressure is used to carry out a new $N_{pol}N_{gas}PT$ MD simulation and the procedure is repeated until a coexistence point with consistent pressure and composition is obtained. The latter method was the strategy adopted in this work.

2.4.6 Simulation of Diffusivity

Computer simulations have revealed that the transition from a pore-flow regime, typical of microporous membrane materials, to a molecular diffusion regime, typical of dense systems, occurs at pore dimensions of 5-10 Å, comparable to polymer chain spacing. Below this value permeation is no longer a pressure driven flow through tiny pores, but a diffusive process controlled by the motion of the polymer chains. Molecular simulations have provided useful insight into the mechanism of diffusion in polymeric materials. Two distinct mechanisms have been identified [143]. In the case of melts [144,145], the thermal motion of the polymer chains randomly and rapidly opens and closes “channels” that enable the passage of the penetrant molecules to neighboring cavities, diffusing with a characteristic time dictated by the frequency of density fluctuations of the order of the penetrant size. On the other hand, in the glassy state the cavities are more permanent over time [146] and a molecule will be trapped moving back and forth into a void until an opening of sufficient size is created by thermal fluctuations of the polymer. Therefore, for a glass, the diffusivity depends on the distribution of cavities located at a distance that can be travelled by the penetrant when a connecting path is opened and on the frequency of this event. In this case, realistic amorphous structures representative of the system at hand and elaborate methods for the study of infrequent events that take into account the cooperative motion of the polymer are necessary to obtain reliable results for diffusion constants. Actually, this infrequent jump process is not limited to diffusion in polymers below T_g. It was shown to occur also in melts and rubbery polymers, when the temperature is sufficiently low for the distribution of accessible volume regions to remain relatively unchanged over the time scale of a penetrant jump [143,145,147].

Self-diffusivity $D_{i,self}$ measures the displacement of a molecule as a result of random thermal motion, and it is proportional to the mean squared displacement (MSD) of the molecule [148], averaged over all molecules.

$$D_{i,self} = \lim_{t\to\infty} \frac{\langle (R_i(t) - R_i(0))^2 \rangle}{6t} \qquad \text{Eq. (2.69)}$$

$(R_i(t) - R_i(0))$ is the distance travelled by a molecule from the initial time to time t. The binary diffusivity coincides with the self-diffusivity in the limit of low concentration (infinite dilution regime). Under the assumption that the velocity correlations between different molecules are negligible, and the self-diffusivity of the polymer is much smaller than that of the penetrant, one obtains the following relation between the self and mutual diffusivity [140]:

$$D_i \simeq \left(\frac{\partial \ln f_i}{\partial \ln c_i}\right)_{T,P} D_{i,self} \qquad \text{Eq. (2.70)}$$

f_i represents gas fugacity and c_i the mass concentration of the gas. $D_{i,self}$ is called the mobility factor and the term in brackets is called the thermodynamic factor. The correction introduced by the thermodynamic factor to the diffusion coefficient is relevant in the case of nonlinear sorption isotherms, such as those typical of sorption of light gases in glassy polymers, whereas for polymers in the melt state effect is less marked.

For small molecular weight penetrants in melt polymers, diffusivities are usually high enough that they can be captured within the time span accessible to a **MD simulation**, by tracking the mean squared displacement of the penetrant molecules. This technique is found to be appropriate for the present study as described in **Chapter 6** and, therefore, it was selected over more complex schemes that are briefly outlined in the following. In some instances [149], it was shown that diffusivity was systematically overestimated, when a united atom representation (implicit hydrogen atoms) for the polymer was used, compared to the corresponding all-atom case. This was attributed to the fact that a united atom representation could originate unrealistically larger interstitial voids, that would accelerate diffusion, therefore, a representation with full detail should yield more reliable results for the estimate of self-diffusion coefficients, especially in the case of larger penetrants. An all-atom representation was adopted in this work.

In industrial processes of interest, the diffusion of gases occurs under the presence of a concentration gradient within the polymer. With **Non-Equilibrium Molecular Dynamics** (NEMD) [79,150], an external driving force is imposed to the system, so that it is kept out-of-equilibrium and the penetrants move inside the matrix under the action of the driving force. For small external forces, the system remains in the linear response regime and the transport properties at steady state can be computed from the ratio of the flux to the acting driving force. In the case of gas transport in polymers, Müller-Plathe et al. [151] compared MD and NEMD results for diffusion of He, H_2, and O_2 in amorphous polyisobutylene, but didn't detect a substantial computational gain. On the other hand, NEMD was found more efficient than equilibrium MD to obtain the diffusivity of penetrants in liquids and microporous sorbents [152].

When the temperature of the system is lower than the glass transition temperature of the polymer, gas diffusivity becomes very often too slow to be predicted by MD. Indeed, this is a consequence of the mechanism of diffusion at these conditions, since the penetrant molecule spends most of its time rattling back and forth inside a specific free volume microvoid, whereas the transition to a neighboring void, which truly contributes to diffusion, occurs very rarely. Therefore, it is impossible to obtain statistically significant information about these jumps by performing brute force MD simulations. In these cases, **transition state theory of infrequent events** (TST) can be adopted [153–155]. Implementing TST for the calculation of penetrant diffusivity in a polymer matrix involves the identification of transition states between neighboring accessible volume regions and the determination of the transition pathways that connect them. In the potential energy surface of the system, the transition state is a saddle-point that can be crossed moving from one state to another, both identified as local minima separated by a high energy barrier. TST enables the calculation of rate constants for the transition between states, based on the probability of the system to be in the transition state in-between two states, compared to the probability of its initial state. This method was first applied by Gusev and Suter [156] in the case of a rigid polymer and subsequently extended to account also for elastic vibrations of the polymer atoms [157], with the amplitude of the elastic motion being dictated by an adjustable parameter (smearing factor) that directly affects the extracted diffusivity results. It was further generalized by Greenfield and Theodorou [158] by including the polymer degrees of freedom into the calculation of transition states and diffusion pathways of a spherical penetrant in generalized coordinates, therefore taking into account the local chain cooperative motion that is crucial in the formation of a passage between neighboring clusters of accessible volume. Further extensions of the methods address complex shapes and chemical constitutions both for the penetrant and the polymer [159] in the multidimensional polymer-penetrant configurational space.

Once the network of possible states and connecting pathways, as well as the rate constants of transitions between states, have been determined, the diffusivity can be obtained considering a Poisson process of successive uncorrelated penetrant jumps between states. A mesoscopic **Kinetic Monte Carlo** (KMC) simulation can be performed to solve the master equation representing the time evolution of the probability that the system is in a particular state [160] and thereby long times can be addressed,à that allow the determination of the diffusion coefficients based on the information obtained from the detailed analysis in the framework of TST at the atomistic level.

2.4.7 Simulation of Gas Separation Membranes

In recent years, atomistic molecular modelling techniques have proven to be very useful for the investigation of the structure and dynamics of dense amorphous membrane polymers and of transport processes in these materials [75–77]. Gas transport in rubbery and glassy polymers has been studied with a variety of approaches, both at pure- and mixed-gas conditions.

The first simulation studies of gas sorption and transport in polymers were performed on materials with a simpler chemical structure than those showing competitive gas separation performance nowadays,

however, they served as benchmarks for the development of methods and algorithms that were subsequently applied also to innovative polymeric materials of interest for these applications.

A detailed molecular analysis of the **solubility and diffusivity** of small gases has been reported in the literature for glassy polyamides [161], poly(amide imide)s [161–163] and polyimides [161,163–167], polysulfones [168,169], polyurethanes [170] high free volume polyacetylenes [171,172] and rubbery materials [161,163,173–175], often using the GCMC method to evaluate solubility and the TST method or analysis of MSD of the gas molecules to evaluate diffusivity, with good agreement with experimental measurements. Thermally Rearranged (TR) polybenzoxazoles are among the best performing materials for gas separation and also for this class of polymers the use of molecular simulations provided useful insight, in particular regarding the free volume size distribution and topology following the thermal rearrangement process, and how this is correlated to the enhanced permeability shown by these materials [167,176–178]. Indeed, analysis of the size distribution of **free volume elements** and comparison with measurements of positron annihilation lifetime allowed to establish correlations between chemical constitution, microstructure and gas transport properties. Differences in gas permeability of materials with similar free volume could be ascribed to variations in the pore-size distribution [179] and important differences in the diffusion mechanism in rubbery and glassy polymers, concerning the lifetime of channels between free volume elements allowing for molecular jumps and the average residence time of gas molecules in each free volume element [161]. Anderson et al. [180] employed NEMD to examine transport of methane and *n*-butane molecules in the bulk and interface region of polyethylene, poly(4-methyl-2-pentyne) and polydimethylsiloxane (PDMS), developing correlations to calculate penetrant diffusivity and permeability from the accessible cavity fraction and the average amplitude of chain oscillations of the polymers. Molecular modelling was also employed to obtain insight on the molecular origin of the structural features of amorphous polymer measured by wide angle **x-ray scattering** measurements [181,182] and of d-spacing [183].

Heuchel et al. were the first to apply TST to the study of gas transport in PIM-1 in the three-dimensional space of a spherical penetrant, simulating He, H_2, Ar, O_2, N_2, CH_4, CO_2 and Xe sorption and diffusion [184]. Solubility tended to be overestimated in the simulations by a factor 2 to 3 (5 for CO_2), with the exception of He and H_2, for which a good agreement with experimental data was found. Simulated diffusivities were overestimated by a factor 2 for the light gases, while they were closer to experimental values for the other gases, with the exception of CO_2, which was one order of magnitude lower than the experimental value. This is ascribed to the fact that the spherical representation used for all gas molecules is unrealistic in the case of CO_2, which is a markedly linear molecule. Different methods and molecular representations allowed to obtain more accurate results for this system. For example, Fang et al. [185,186] applied the Widom Insertion method to predict CO_2 solubility in PIM-1, obtaining close agreement with experimental data. Recently, Kupgan et al. [187], employed a scheme combining Grand Canonical Monte Carlo and Molecular Dynamics simulations devised by Hölck et al. [188], simulated CO_2 sorption in PIM-1 up to 50 bar, while Frentrup et al. [189] performed NEMD simulations for the direct simulation of He and CO_2 permeability through a thin membrane of PIM-1, which was in good qualitative agreement with experimental data. Chen

et al. combined ab initio calculations, molecular dynamics (MD) and Monte Carlo (MC) simulations to investigate the structural characteristics and transport behavior CO_2, CH_4, O_2 and N_2 in PIM-Trip-TB and KAUST-PI-1 membranes [190] showing the capability of atomistic techniques to represent correctly the properties also of rigid polymeric structures of complex chemical constitution [191,192].

Swelling effects were also studied with molecular modelling techniques. Heuchel et al. analyzed glassy polysulfone and poly(ether sulfone), under CO_2 gas pressures up to 50 bar at 308 K [169]. Pre-swollen packing system were prepared based on experimental dilation data and sorption was determined with the GCMC method. Sorption isotherms were determined combining the solubilities obtained for swollen and unswollen systems, with satisfactory accuracy. Gas diffusivity was also determined using the TST method: in this case the results obtained for the preswollen systems were only qualitatively consistent. A similar strategy was employed to study swelling during nitrogen adsorption isotherms at 77 K for five PIM variants [193] by pre-swelling the simulation boxes up to 15%, finding that size of the free volume elements increased with the simulated swelling percentage, while the closely packed polymer chains remained tightly associated. Neyertz et al. [194] performed extensive molecular dynamics simulations of several fluorinated polyimides with CO_2 weight percentages up to 30%. Diffusion coefficients were estimated from a trajectory-extending kinetic Monte Carlo method. Diffusivity values and activation energies were found to be in good agreement with experimental data. Swelling effects were quantified during the simulation together with hysteresis effects related to sorption-desorption cycles, which affected CO_2 diffusivity as well.

In order to obtain plasticization-resistant membranes, **crosslinking** is often employed to tighten the material and prevent significant swelling upon sorption. Strategies to build molecular models of highly crosslinked polymer networks were developed [195–201] and validated against measurements of apparent Brunauer-Emmet-Teller (BET) specific surface areas, cross-linking degrees, porosity and sorption measurements. Moreover, simulations allow to witness the evolution of porosity throughout the crosslinking process [195], or to follow the formation process of membranes prepared through interfacial polymerization [202].

Fewer molecular modelling studies deal with the analysis of **mixed gas sorption** effects. Recently Rizzuto et al. [203] coupled GCMC atomistic simulations and Ideal Adsorbed Solution Theory (IAST) [204] to investigate the mixed-gas permeation properties of CO_2/N_2 mixtures in Thermally Rearranged polymers. Pure-gas sorption of both gases was underestimated by the simulations. However, the competitive effects between the components in the mixture, expected in the case of glassy polymers, were displayed and found to affect greatly the solubility of the less condensable gas of the mixture. Neyertz and Brown [205] performed large-scale MD simulations of air separation with an ultra-thin polyimide membrane surrounded by an explicit gas reservoir. In this work they determined gas solubility, diffusivity and O_2/N_2 selectivity at multicomponent conditions, comparing favorably with experimental results. The multicomponent solubility-selectivity was found to be comparable to the ideal one. Tanis et al. [206] studied CH_4/N_2 separation with several polyimide membranes using atomistic simulations. Solubility coefficients obtained from excluded-volume map sampling test-particle insertions were combined with diffusion coefficients calculated with a variant of the kinetic Monte Carlo approach. Iterative procedures allowed to account for

swelling effects upon sorption, both in the pure- and in the mixed-gas case. Their results highlighted non-ideal behavior in the multicomponent case, affecting both the predicted permeability and selectivity of the membrane material. Liu et al. [207] investigated the separation performance of a thin membrane of a branched PIM-1 architectures for CO_2/CH_4 mixtures. They performed a large-scale direct simulation of permeability incorporating both polymer flexibility and membrane plasticization during gas permeation. Hart et al. studied a hypothetical functionalized polymer of intrinsic microporosity with an ionic backbone (carboxylate) and extra-framework counterions (Na+) for CO_2 gas storage and separation applications [208]. They evaluated CO_2/CH_4 and CO_2/N_2 mixed-gas separation performance with GCMC simulations finding a very appealing performance under several industrially relevant conditions.

Simulations have been employed also to study other candidate systems for gas separation applications, such as nanocomposite materials [209,210] incorporating silica [168,211,212], zeolites [213,214], metal-organic frameworks [215–217], graphene and graphene oxide [218–221], and ionic liquids [222–225]. Molecular simulation strategies are instrumental in identifying how the systems can be tailored towards an optimum selectivity and permeability, investigating a number of crucial factors such as compatibility, interfacial adhesion, the effects of the size and the dispersity of the fillers and nanoparticles.

Molecular modelling is mature enough to go hand-in-hand with the experimentation process to synthesize new materials, making the process more informed and rational [226,227]. Finally, one of the most appealing applications of molecular modelling consists in the preliminary **screening** of different molecular structures for a specific application, even before the hypothetical structures are synthesized, and several studies of this kind were performed in the case of polymeric gas separation materials [228–233] and zeolites and MOFs [214,217,234–238]. Detailed analysis of the changes in structural features associated to a variation in the chemical constitution and calculation of gas transport properties allow to establish structure-properties correlations and provide guidelines for the future design of new chemical structures with controlled macroscopic properties.

References

1. Mitchell, J.K. On the penetrativeness of fluids. *J. Memb. Sci.* **1995**, *100*, 11–16, doi:10.1016/0376-7388(94)00227-P.
2. Graham, T. Notice of the singular inflation of a bladder. *J. Memb. Sci.* **1995**, *100*, 9, doi:10.1016/0376-7388(94)00226-O.
3. Graham, T. On the absorption and dialytic separation of gases by colloid septa. *J. Franklin Inst.* **1867**, *83*, 39–41, doi:10.1080/14786446608644207.
4. v. Wroblewski, S. Ueber die Natur der Absorption der Gase. *Ann. der Phys. und Chemie* **1879**, *244*, 29–52, doi:10.1002/andp.18792440903.
5. Wijmans, J.G.; Baker, R.W. The Solution-Diffusion model: a unified approach to membrane permeation. In *Materials Science of Membranes for Gas and Vapor Separation*; John Wiley & Sons, 2006.
6. Wijmans, J.G.; Baker, R.W. The solution-diffusion model: a review. *J. Memb. Sci.* **1995**, *107*, 1–21, doi:10.1016/S0166-4115(08)60038-2.
7. Robeson, L.M.; Dose, M.E.; Freeman, B.D.; Paul, D.R. Analysis of the transport properties of thermally rearranged (TR) polymers and polymers of intrinsic microporosity (PIM) relative to upper bound performance. *J. Memb. Sci.* **2017**, *525*, 18–24, doi:10.1016/j.memsci.2016.11.085.
8. Minelli, M.; Friess, K.; Vopička, O.; De Angelis, M.G. Modelling gas and vapor sorption in a polymer of intrinsic microporosity (PIM-1). *Fluid Phase Equilib.* **2013**, *347*, 35–44, doi:10.1016/j.fluid.2013.03.003.
9. Pope, D.S.; Fleming, G.K.; Koros, W.J. Effect of various exposure histories on sorption and dilation in a family of polycarbonates. *Macromolecules* **1990**, *23*, 2988–2994, doi:10.1021/ma00213a029.
10. Park, C.H.; Tocci, E.; Lee, Y.M.; Drioli, E. Thermal treatment effect on the structure and property change between hydroxy-containing polyimides (HPIs) and thermally rearranged polybenzoxazole (TR-PBO). *J. Phys. Chem. B* **2012**, *116*, 12864–12877, doi:10.1021/jp307365y.
11. Matteucci, S.; Yampolskii, Y.; Freeman, B.D.; Pinnau, I. Transport of Gases and Vapor in Glassy and Rubbery Polymers. In *Materials Science of Membranes for Gas and Vapor Separation*; Yampolskii, Y., Pinnau, I., Freeman, B.D., Eds.; John Wiley & Sons, Ltd, 2006.
12. Petropoulos, J.H. Mechanisms and theories for sorption and diffusion of gases in polymers. In *Polymeric Gas Separation Membranes*; Paul, D.R., Yampolskii, Y.P., Eds.; CRC Press: Boca Raton, 1994; pp. 17–82.
13. Crank, J.; Park, G.. Diffusion in Polymers 1968.
14. Paul, D.R. Relation between hydraulic permeability and diffusion in homogeneous swollen membranes. *J. Polym. Sci. Part A-2 Polym. Phys.* **1973**, *11*, 289–296, doi:10.1002/pol.1973.180110210.
15. Paul, D.R. Further comments on the relation between hydraulic permeation and diffusion. *J. Polym. Sci. Polym. Phys. Ed.* **1974**, *12*, 1221–1230, doi:10.1002/pol.1974.180120618.
16. Kamaruddin, H.D.; Koros, W.J. Some observations about the application of Fick's first law for membrane separation of multicomponent mixtures. *J. Memb. Sci.* **1997**, *135*, 147–159, doi:10.1016/S0376-7388(97)00142-7.
17. Robeson, L.M. The upper bound revisited. *J. Memb. Sci.* **2008**, *320*, 390–400, doi:10.1016/j.memsci.2008.04.030.
18. Robeson, L.M. Correlation of separation factor versus permeability for polymeric membranes. *J. Memb. Sci.* **1991**, *62*, 165–185, doi:10.1016/0376-7388(91)80060-J.
19. Comesaña-Gándara, B.; Chen, J.; Bezzu, C.G.; Carta, M.; Rose, I.; Ferrari, M.; Esposito, E.; Fuoco, A.; Jansen, J.C.; McKeown, N.B. Redefining the Robeson upper bounds for CO_2/CH_4 and CO_2/N2 separations using a series of ultrapermeable benzotriptycene-based polymers of intrinsic microporosity. *Energy Environ. Sci.* **2019**, *12*, 2733–2740, doi:10.1039/c9ee01384a.
20. Park, H.B.; Kamcev, J.; Robeson, L.M.; Elimelech, M.; Freeman, B.D. Maximizing the right stuff: The trade-off between membrane permeability and selectivity. *Science.* **2017**, *365*, 1138–1148, doi:10.1126/science.aab0530.
21. Lin, H.; Freeman, B.D. Materials selection guidelines for membranes that remove CO_2 from gas mixtures. *J. Mol. Struct.* **2005**, *739*, 57–74, doi:10.1016/j.molstruc.2004.07.045.
22. Robeson, L.M.; Smith, Z.P.; Freeman, B.D.; Paul, D.R. Contributions of diffusion and solubility selectivity to the

upper bound analysis for glassy gas separation membranes. *J. Memb. Sci.* **2014**, *453*, 71–83, doi:10.1016/j.memsci.2013.10.066.

23. Alentiev, A.Y.; Yampolskii, Y.. Meares equation and the role of cohesion energy density in diffusion in polymers. *J. Memb. Sci.* **2002**, *206*, 291–306, doi:10.1016/S0376-7388(01)00777-3.
24. Lou, Y.; Hao, P.; Lipscomb, G. NELF predictions of a solubility – solubility selectivity upper bound. *J. Memb. Sci.* **2014**, *455*, 247–253, doi:10.1016/j.memsci.2013.12.071.
25. Alentiev, A.Y.; Yampolskii, Y.P. Free volume model and tradeoff relations of gas permeability and selectivity in glassy polymers. *J. Memb. Sci.* **2000**, *165*, 201–216, doi:10.1016/S0376-7388(99)00229-X.
26. Freeman, B.D. Basis of permeability/selectivity tradeoff relations in polymeric gas separation membranes. *Macromolecules* **1999**, *32*, 375–380, doi:10.1021/ma9814548.
27. Barrer, R.M. Permeability in relation to viscosity and structure of rubber. *Trans. Faraday Soc.* **1942**, *38*, 322, doi:10.1039/tf9423800322.
28. Van Amerongen, G.J. The Permeability of Different Rubbers to Gases and Its Relation to Diffusivity and Solubility. *J. Appl. Phys.* **1946**, *17*, 972–985, doi:10.1063/1.1707667.
29. Dal-Cin, M.M.; Kumar, A.; Layton, L. Revisiting the experimental and theoretical upper bounds of light pure gas selectivity–permeability for polymeric membranes. *J. Memb. Sci.* **2008**, *323*, 299–308, doi:10.1016/J.MEMSCI.2008.06.027.
30. Freeman, B.D.; Pinnau, I. Separation of gases using solubility-selective polymers. In *Trends in Polymer Science*; 1997; pp. 167–173.
31. Robeson, L.M.; Liu, Q.; Freeman, B.D.; Paul, D.R. Comparison of transport properties of rubbery and glassy polymers and the relevance to the upper bound relationship. *J. Memb. Sci.* **2015**, *476*, 421–431, doi:10.1016/j.memsci.2014.11.058.
32. Wu, A.X.; Drayton, J.A.; Smith, Z.P. The perfluoropolymer upper bound. **2019**, 1–12, doi:10.1002/aic.16700.
33. Alentiev, A.; Yampolskii, Y. Correlation of gas permeability and diffusivity with selectivity: Orientations of the clouds of the data points and the effects of temperature. *Ind. Eng. Chem. Res.* **2013**, *52*, 8864–8874, doi:10.1021/ie302680r.
34. Lin, H.; Yavari, M. Upper bound of polymeric membranes for mixed-gas CO_2/CH_4 separations. *J. Memb. Sci.* **2015**, *475*, 101–109, doi:10.1016/j.memsci.2014.10.007.
35. Lacombe, R.H.; Sanchez, I.C. Statistical Thermodynamics of Fluid Mixtures. *J. Phys. Chem.* **1976**, *80*, 2568–2580, doi:10.1021/j100564a009.
36. W.G. Chapman, K.E. Gubbins, G. Jackson, M.R. SAFT: Equation-of-state solution model for associating fluids. *Fluid Phase Equilib.* **1989**, *52*, 31–38, doi:10.1016/0378-3812(89)80308-5.
37. Doghieri, F.; Sarti, G.C. Nonequilibrium Lattice Fluids: A Predictive Model for the Solubility in Glassy Polymers. *Macromolecules* **1996**, *29*, 7885–7896, doi:10.1021/ma951366c.
38. Minelli, M.; Doghieri, F. Predictive model for gas and vapor solubility and swelling in glassy polymers I: Application to different polymer/penetrant systems. *Fluid Phase Equilib.* **2014**, *381*, 1–11, doi:10.1016/j.fluid.2014.08.010.
39. Doghieri, F.; Quinzi, M.; Rethwisch, D.G.; Sarti, G.C. Predicting Gas Solubility in Glassy Polymers through Nonequilibrium EOS. In *Advanced Materials for Membrane Separations*; American Chemical Society: Washington, DC, USA, 2004; pp. 74–90.
40. Minelli, M.; Campagnoli, S.; De Angelis, M.G.; Doghieri, F.; Sarti, G.C. Predictive model for the solubility of fluid mixtures in glassy polymers. *Macromolecules* **2011**, *44*, 4852–4862, doi:10.1021/ma200602d.
41. Tam, P.M.H.I.M.; Vieth, W.R.; Tam, P.M.H.I.M.; Michaels, A.S. Dual sorption mechanisms in glassy polystyrene. *J. Colloid Interface Sci.* **1966**, *22*, 360–370, doi:10.1016/0021-9797(66)90016-6.
42. Koros, W.J.; Paul, D.R. Design considerations for measurement of gas sorption in polymers by pressure decay. *J. Polym. Sci. Polym. Phys. Ed.* **1976**, *14*, 1903–1907, doi:10.1002/pol.1976.180141014.
43. Michaels, A.S.; Vieth, W.R.; Barrie, J.A. Diffusion of gases in polyethylene terephthalate. *J. Appl. Phys.* **1963**, *34*, 13–20, doi:10.1063/1.1729054.
44. Koros, W.J.; Paul, D.R.; Rocha, A.A. Carbon dioxide sorption and transport in polycarbonate. *J. Polym. Sci. Polym. Phys.* **1976**, *14*, 687–702, doi:10.1002/pol.1976.180140410.

45. Paul, D.R.; Koros, W.J. Effect of partially immobilizing sorption on permeability and the diffusion time lag. *J. Polym. Sci. Polym. Phys. Ed.* **1976**, *14*, 675–685, doi:10.1002/pol.1976.180140409.

46. Fredrickson, G.H.; Helfand, E. Dual-Mode Transport of Penetrants in Glassy Polymers. *Macromolecules* **1985**, *18*, 2201–2207, doi:10.1021/ma00153a024.

47. Meares, P. The Diffusion of Gases Through Polyvinyl Acetate. *J. Am. Chem. Soc.* **1954**, *76*, 3416–3422, doi:10.1021/ja01642a015.

48. Meares, P. The solubilities of gases in polyvinyl acetate. *Trans. Faraday Soc.* **1957**, *54*, 40–46.

49. Barrer, R.M.; Barrie, J.A.; Slater, J. Sorption and Diffusion in Ethyl Cellulose. Part III. Comparison between Ethyl Cellulose and Rubber. *J. Polym. Sci.* **1958**, *XXVII*, 177–197.

50. Vieth, W.R.; Howell, J.M.; Hsieh, J.H.; Engrneerrng, B.; Unrverslty, R.; Brunswzck, N. Dual sorption theory. *J. Memb. Sci.* **1976**, *1*, 177–220, doi:10.1016/S0376-7388(00)82267-X.

51. Vieth, W.R.; Alcalay, H.H.; Frabetti, A.J. Solution of Gases in Oriented Poly(ethylene Terephthalate). *J. Appl. Polym. Sci.* **1964**, *8*, 2125–2138, doi:10.1002/app.1964.070080513.

52. Flory, P.J. Thermodynamics of High Polymer Solutions. *J. Chem. Phys.* **1942**, *10*, 51–61, doi:10.1063/1.1723621.

53. Huggins, M.L. Some Properties of Solutions of Long-chain Compounds. *J. Phys. Chem.* **1942**, *46*, 151–158, doi:10.1021/j150415a018.

54. Sanchez, I.C.; Lacombe, R.H. An elementary molecular theory of classical fluids. Pure fluids. *J. Phys. Chem.* **1976**, *80*, 2352–2362, doi:10.1021/j100562a008.

55. Sarti, G.C.; Doghieri, F. Predictions of the solubility of gases in glassy polymers based on the NELF model. *Chem. Eng. Sci.* **1998**, *53*, 3435–3447, doi:10.1016/S0009-2509(98)00143-2.

56. Jordan, S.S.; Koros, W.J. A Free Volume Distribution Model of Gas Sorption and Dilation in Glassy Polymers. *Macromolecules* **1995**, *28*, 2228–2235, doi:10.1021/ma00111a017.

57. De Angelis, M.G.; Merkel, T.C.; Bondar, V.I.; Freeman, B.D.; Doghieri, F.; Sarti, G.C. Hydrocarbon and fluorocarbon solubility and dilation in poly(dimethylsiloxane): Comparison of experimental data with predictions of the Sanchez-Lacombe equation of state. *J. Polym. Sci. Part B Polym. Phys.* **1999**, *37*, 3011–3026, doi:10.1021/ma0106090.

58. Doghieri, F.; Sarti, G.C. Predicting the low pressure solubility of gases and vapors in glassy polymers by the NELF model. *J. Memb. Sci.* **1998**, *147*, 73–86, doi:10.1016/S0376-7388(98)00123-9.

59. Sanchez, I.C.; Lacombe, R.H. Statistical Thermodynamics of Polymer Solutions. *Macomolecules* **1978**, *11*, 1145–1156.

60. Chan, A.H.; Koros, W.J.; Paul, D.R. Analysis of hydrocarbon gas sorption and transport in ethyl cellulose using the dual sorption/partial immobilization models. *J. Memb. Sci.* **1978**, *3*, 117–130, doi:10.1016/S0376-7388(00)83017-3.

61. Kanehashi, S.; Nagai, K. Analysis of dual-mode model parameters for gas sorption in glassy polymers. *J. Memb. Sci.* **2005**, *253*, 117–138, doi:10.1016/j.memsci.2005.01.003.

62. Koros, W.J.; Paul, D.R. CO2 sorption in poly(ethylene terephthalate) above and below the glass transition. *J. Polym. Sci. Part B Polym. Phys.* **1978**, *16*, 1947–1963, doi:10.1002/pol.1978.180161105.

63. Koros, W.J.; Paul, R.; Huvard, G.S. Energetics of gas sorption in glassy polymers. *Polymer (Guildf).* **1979**, *20*, 956–960, doi:10.1016/0032-3861(79)90192-7.

64. Koros, W.J. Model for sorption of mixed gases in glassy polymers. *J. Polym. Sci. Polym. Phys. Ed.* **1980**, *18*, 981–992, doi:10.1002/pol.1980.180180506.

65. Sanders, E.S.; Koros, W.J. Sorption of CO_2, C_2H_4, N_2O and their Binary Mixtures in Poly(methyl methacrylate). *J. Polym. Sci. B* **1986**, *188*, 175–188, doi:10.1002/polb.1986.180240117.

66. Ricci, E.; De Angelis, M.G. Modelling Mixed Gas Sorption in Glassy Polymers for CO_2 Removal: a Sensitivity Analysis of the Dual Mode Sorption Model. *Membranes (Basel).* **2019**, *9*, *8*.

67. Sanders, E.S.; Koros, W.J.; Hopfenberg, H.B.; Stannett, V.T. Mixed gas sorption in glassy polymers: Equipment design considerations and preliminary results. *J. Memb. Sci.* **1983**, *13*, 161–174, doi:10.1016/S0376-7388(00)80159-3.

68. Story, B.J.; Koros, W.J. Sorption of CO_2/CH_4 mixtures in poly(phenylene oxide) and a carboxylated derivative. *J. Appl. Polym. Sci.* **1991**, *42*, 2613–2626, doi:10.1002/app.1991.070420926.

69. Feng, H. Modelling of vapor sorption in glassy polymers using a new dual mode sorption model based on multilayer sorption theory. *Polymer (Guildf).* 2007, *48*, 2988–3002, doi:10.1016/j.polymer.2006.10.050.

70. Bondar, V.I.; Kamiya, Y.; Yampol'skii, Y.P. On pressure dependence of the parameters of the dual-mode sorption model. *J. Polym. Sci. Part B Polym. Phys.* 1996, *34*, 369–378, doi:10.1002/(SICI)1099-0488(19960130)34:2<369::AID-POLB18>3.0.CO;2-H.

71. Vopička, O.; De Angelis, M.G.; Sarti, G.C. Mixed gas sorption in glassy polymeric membranes: I. CO_2 /CH_4 and n-C4/CH4 mixtures sorption in poly(1-trimethylsilyl-1-propyne) (PTMSP). *J. Memb. Sci.* 2014, *449*, 97–108, doi:10.1016/j.memsci.2013.06.065.

72. Vopička, O.; De Angelis, M.G.; Du, N.; Li, N.; Guiver, M.D.; Sarti, G.C. Mixed gas sorption in glassy polymeric membranes: II. CO_2/CH_4 mixtures in a polymer of intrinsic microporosity (PIM-1). *J. Memb. Sci.* 2014, *459*, 264–276, doi:10.1016/j.memsci.2014.02.003.

73. Gemeda, A.E.; De Angelis, M.G.; Du, N.; Li, N.; Guiver, M.D.; Sarti, G.C. Mixed gas sorption in glassy polymeric membranes. III. CO_2/CH_4 mixtures in a polymer of intrinsic microporosity (PIM-1): Effect of temperature. *J. Memb. Sci.* 2017, *524*, 746–757, doi:10.1016/j.memsci.2016.11.053.

74. Ricci, E.; Gemeda, A.E.; Du, N.; Li, N.; De Angelis, M.G.; Guiver, M.D.; Sarti, G.C. Sorption of CO_2/CH_4 mixtures in TZ-PIM, PIM-1 and PTMSP: Experimental data and NELF-model analysis of competitive sorption and selectivity in mixed gases. *J. Memb. Sci.* 2019, *585*, 136–149, doi:10.1016/j.memsci.2019.05.026.

75. Kupgan, G.; Abbott, L.J.; Hart, K.E.; Colina, C.M. Modelling Amorphous Microporous Polymers for CO_2 Capture and Separations. *Chem. Rev.* 2018, *118*, 5488–5538, doi:10.1021/acs.chemrev.7b00691.

76. Theodorou, D.N. Principles of Molecular Simulation of Gas Transport in Polymers. In *Materials Science of Membranes for Gas and Vapor Separation*; John Wiley & Sons: Hoboken, NJ, USA, 2006 ISBN 047085345X.

77. Vergadou, N.; Theodorou, D.N. Molecular Modelling Investigations of Sorption and Diffusion of Small Molecules in Glassy Polymers. *Membranes (Basel).* 2019, *9*, 98, doi:10.3390/membranes9080098.

78. Fried, J.R. Molecular Simulation of Gas and Vapor Transport in Highly Permeable Polymers. In *Materials Science of Membranes for Gas and Vapor Separation*; Freeman, B.D., Yampolskii, Y., Pinnau, I., Eds.; Wiley, 2006; pp. 95–136.

79. Frenkel, D.; Smit, B. *Understanding Molecular Simulation: From Algorithms to Applications*; Elsevier, Ed.; 2001;

80. Auhl, R.; Everaers, R.; Grest, G.S.; Kremer, K.; Plimpton, S.J. Equilibration of long chain polymer melts in computer simulations. *J. Chem. Phys.* 2003, *119*, 12718–12728, doi:10.1063/1.1628670.

81. Brown, D.; Clarke, J.H.R.; Okuda, M.; Yamazaki, T. The preparation of polymer melt samples for computer simulation studies. *J. Chem. Phys.* 1994, *100*, 6011–6018, doi:10.1063/1.467111.

82. Martínez, L.; Andrade, R.; Birgin, E.G.; Martínez, J.M. PACKMOL: A package for building initial configurations for molecular dynamics simulations. *J. Comput. Chem.* 2009, *30*, 2157–2164, doi:10.1002/jcc.21224.

83. Sliozberg, Y.R.; Kröger, M.; Chantawansri, T.L. Fast equilibration protocol for million atom systems of highly entangled linear polyethylene chains. *J. Chem. Phys.* 2016, *144*, 154901, doi:10.1063/1.4946802.

84. Kröger, M. Efficient hybrid algorithm for the dynamic creation of wormlike chains in solutions, brushes, melts and glasses. *Comput. Phys. Commun.* 2019, *241*, 178–179, doi:10.1016/J.CPC.2019.03.009.

85. Gao, J. An efficient method of generating dense polymer model melts by computer simulation. *J. Chem. Phys.* 1995, *102*, 1074–1077, doi:10.1063/1.469455.

86. Flory, P.J. *Statistical mechanics of chain molecules*; Interscience: New York, 1969;

87. Theodorou, D.N.; Suter, U.W. Detailed Molecular Structure of a Vinyl Polymer Glass. *Macromolecules* 1985, *18*, 1467–1478, doi:10.1021/ma00149a018.

88. Ramos, J.; Peristeras, L.D.; Theodorou, D.N. Monte Carlo simulation of short chain branched polyolefins in the molten state. *Macromolecules* 2007, *40*, 9640–9650, doi:10.1021/ma071615k.

89. Allen, M.P.; Tildesley, D.J. *Computer simulation of liquids*; Clarendon Press: Wotton-under-Edge, UK, 1989; ISBN 9780198556459.

90. Rapaport, D.C. *The Art of Molecular Dynamics Simulation*; Cambridge University Press: New York, 2002;

91. Tuckerman, M.; Berne, B.J.; Martyna, G.J. Reversible multiple time scale molecular dynamics. *J. Chem. Phys.* 1992, *97*, 1990–2001, doi:10.1063/1.463137.

92. Metropolis, N.; Rosenbluth, A.W.; Rosenbluth, M.N.; Teller, A.H.; Teller, E. Equation of State Calculations by Fast

Computing Machines. *J. Chem. Phys.* **1953**, *21*, 1087–1092, doi:10.1063/1.1699114.

93. Siepmann, J.I.; Frenkel, D. Configurational bias Monte Carlo: a new sampling scheme for flexible chains. *Mol. Phys.* **1992**, *75*, 59–70, doi:10.1080/00268979200100061.

94. Rosenbluth, M.N.; Rosenbluth, A.W. Monte Carlo Calculation of the Average Extension of Molecular Chains. *J. Chem. Phys.* **1955**, *23*, 356–359, doi:10.1063/1.1741967.

95. Dodd, L.R.; Boone, T.D.; Theodorou, D.N. A concerted rotation algorithm for atomistic Monte Carlo simulation of polymer melts and glasses. *Mol. Phys.* **1993**, *78*, 961–996, doi:10.1080/00268979300100641.

96. Theodorou, D.N. Variable-Connectivity Monte Carlo Algorithms for the Atomistic Simulation of Long-Chain Polymer Systems. In *Bridging Time Scales: Molecular Simulations for the Next Decade*; Springer: Berlin-Heidelberg, 2002; pp. 67–127.

97. Pant, P.V.K.; Theodorou, D.N. Variable connectivity method for the atomistic Monte Carlo simulation of polydisperse polymer melts. *Macromolecules* **1995**, *28*, 7224–7234.

98. Mavrantzas, V.G.; Boone, T.D.; Zervopoulou, E.; Theodorou, D.N. End-bridging Monte Carlo: a fast algorithm for atomistic simulation of condensed phases of long polymer chains. *Macromolecules* **1999**, *32*, 5072–5096, doi:10.1021/ma981745g.

99. Karayiannis, N.C.; Giannousaki, A.E.; Mavrantzas, V.G.; Theodorou, D.N. Atomistic Monte Carlo simulation of strictly monodisperse long polyethylene melts through a generalized chain bridging algorithm. *J. Chem. Phys.* **2002**, *117*, 5465–5479, doi:10.1063/1.1499480.

100. Theodorou, D.N. Equilibration and Coarse-Graining Methods for Polymers. In *Computer Simulations in Condensed Matter Systems: From Materials to Chemical Biology Volume 2*; Ferrario, M., Ciccotti, G., Binder, K., Eds.; Springer: Berlin-Heidelberg, 2006; pp. 419–448.

101. Gooneie, A.; Schuschnigg, S.; Holzer, C. A review of multiscale computational methods in polymeric materials. *Polymers (Basel).* **2017**, *9*, doi:10.3390/polym9010016.

102. Theodorou, D.N. Hierarchical modelling of polymeric materials. *Chem. Eng. Sci.* **2007**, *62*, 5697–5714, doi:10.1016/j.ces.2007.04.048.

103. Grotendorst, J.; Sutmann, G.; Gompper, G.; Marx, D. *Hierarchical methods for dynamics in complex molecular systems: lecture notes*; 2012; ISBN 9783893367689 3893367683.

104. Florian, M.; Müller-Plathe, F. Coarse-graining in polymer simulation: From the atomistic to the mesoscopic scale and back. *ChemPhysChem* **2002**, *3*, 754–769, doi:10.1002/1439-7641(20020916)3:9<754::AID-CPHC754>3.0.CO;2-U.

105. Krajniak, J.; Zhang, Z.; Pandiyan, S.; Nies, E.; Samaey, G. Reverse mapping method for complex polymer systems. *J. Comput. Chem.* **2018**, *39*, 648–664, doi:10.1002/jcc.25129.

106. Santangelo, G.; Di Matteo, A.; Müller-Plathe, F.; Milano, G. From mesoscale back to atomistic models: A fast reverse-mapping procedure for vinyl polymer chains. *J. Phys. Chem. B* **2007**, *111*, 2765–2773, doi:10.1021/jp0662121.

107. Krajniak, J.; Pandiyan, S.; Nies, E.; Samaey, G. Generic Adaptive Resolution Method for Reverse Mapping of Polymers from Coarse-Grained to Atomistic Descriptions. *J. Chem. Theory Comput.* **2016**, *12*, 5549–5562, doi:10.1021/acs.jctc.6b00595.

108. Marrink, S.J.; Risselada, H.J.; Yefimov, S.; Tieleman, D.P.; Vries, A.H. De The MARTINI Force Field : Coarse Grained Model for Biomolecular Simulations. *J. Phys. Chem. B* **2007**, *111*, 7812–7824, doi:10.1021/jp071097f.

109. Brini, E.; Algaer, E.A.; Ganguly, P.; Li, C.; Rodríguez-Ropero, F.; van der Vegt, N.F.A. Systematic coarse-graining methods for soft matter simulations – a review. *Soft Matter* **2013**, *9*, 2108–2119, doi:10.1039/C2SM27201F.

110. Reith, D.; Puetz, M.; Mueller-Plathe, F. Deriving effective mesoscale potentials from atomistic simulations. *J. Comput. Chem.* **2003**, *24*, 1624–1636.

111. Ercolessi, F.; Adams, J.B. Interatomic Potentials from First-Principles Calculations: The Force-Matching Method. *Europhys. Lett.* **1994**, *26*, 583–588, doi:10.1209/0295-5075/26/8/005.

112. Lyubartsev, A.P.; Laaksonen, A. Calculation of effective interaction potentials from radial distribution functions: A reverse Monte Carlo approach. *Phys. Rev. E* **1995**, *52*, 3730–3737, doi:10.1103/PhysRevE.52.3730.

113. Chaimovich, A.; Shell, M.S. Coarse-graining errors and numerical optimization using a relative entropy framework. *J. Chem. Phys.* **2011**, *134*, 094112, doi:10.1063/1.3557038.

114. Shell, M.S. The relative entropy is fundamental to multiscale and inverse thermodynamic problems. *J. Chem. Phys.* 2008, *129*, 144108, doi:10.1063/1.2992060.

115. Li, C.; Shen, J.; Peter, C.; van der Vegt, N.F.A. A Chemically Accurate Implicit-Solvent Coarse-Grained Model for Polystyrenesulfonate Solutions. *Macromolecules* 2012, *45*, 2551–2561, doi:10.1021/ma202490h.

116. Zacharopoulos, N.; Vergadou, N.; Theodorou, D.N. Coarse graining using pretabulated potentials: Liquid benzene. *J. Chem. Phys.* 2005, *122*, doi:10.1063/1.1948370.

117. Villa, A.; Peter, C.; van der Vegt, N.F.A. Self-assembling dipeptides: conformational sampling in solvent-free coarse-grained simulation. *Phys. Chem. Chem. Phys.* 2009, *11*, 2077, doi:10.1039/b818144f.

118. De Nicola, A.; Kawakatsu, T.; Milano, G. Generation of Well-Relaxed All-Atom Models of Large Molecular Weight Polymer Melts: A Hybrid Particle-Continuum Approach Based on Particle-Field Molecular Dynamics Simulations. *J. Chem. Theory Comput.* 2014, *10*, 5651–5667, doi:10.1021/ct500492h.

119. Huang, H.; Wu, L.; Xiong, H.; Sun, H. A Transferrable Coarse-Grained Force Field for Simulations of Polyethers and Polyether Blends. *Macromolecules* 2019, *52*, 249–261, doi:10.1021/acs.macromol.8b01802.

120. Kuo, A.-T.; Okazaki, S.; Shinoda, W. Transferable coarse-grained model for perfluorosulfonic acid polymer membranes. *J. Chem. Phys.* 2017, *147*, 094904, doi:10.1063/1.4986287.

121. Minelli, M.; De Angelis, M.G.; Hofmann, D. A novel multiscale method for the prediction of the volumetric and gas solubility behavior of high-T_g polyimides. *Fluid Phase Equilib.* 2012, *333*, 87–96, doi:10.1016/j.fluid.2012.07.012.

122. Ricci, E.; Minelli, M.; De Angelis, M.G. A multiscale approach to predict the mixed gas separation performance of glassy polymeric membranes for CO_2 capture: the case of CO_2/CH_4 mixture in Matrimid®. *J. Memb. Sci.* 2017, *539*, doi:10.1016/j.memsci.2017.05.068.

123. Theodorou, D.N. Principles of Molecular Simulations of Gas Transport in Polymers. In *Materials Science of Membranes for Gas and Vapor Separation*; John Wiley & Sons, Ltd., 2006; pp. 49–94.

124. Panagiotopoulos, A.Z. Direct determination of phase coexistence properties of fluids by Monte Carlo simulation in a new ensemble. *Mol. Phys.* 1987, *61*, 813–826, doi:10.1080/00268978700101491.

125. Kofke, D.A.; Glandt, E.D. Monte Carlo simulation of multicomponent equilibria in a semigrand canonical ensemble. *Mol. Phys.* 1988, *64*, 1105–1131, doi:10.1080/00268978800100743.

126. Vrabec, J.; Hasse, H. Grand equilibrium: Vapour-liquid equilibria by a new molecular simulation method. *Mol. Phys.* 2002, *100*, 3375–3383, doi:10.1080/00268970210153772.

127. Eslami, H.; Muller-Plathe, F. Molecular Dynamics Simulation in the Grand Canonical Ensemble. *J. Comput. Chem.* 2007, *28*, 1763–1773, doi:10.1002/jcc.

128. Widom, B. Some Topics in the Theory of Fluids. *J. Chem. Phys.* 1963, *39*, 2808–2812, doi:10.1121/1.418538.

129. Cuthbert, T.; Wagner, N.; Paulaitis, M. Molecular simulation of glassy polystyrene: size effects on gas solubilities. *Macromolecules* 1997, *30*, 3058–3065.

130. Dömötör, G.; Hentschke, R. Efficient molecular simulation of chemical potentials. *J. Chem. Phys.* 1989, *90*, 2370–2385, doi:10.1063/1.455979.

131. and, G.D.; Hentschke*, R. Atomistically Modelling the Chemical Potential of Small Molecules in Dense Systems. 2004, doi:10.1021/JP0367427.

132. Zervopoulou, E.; Mavrantzas, V.G.; Theodorou, D.N. A new Monte Carlo simulation approach for the prediction of sorption equilibria of oligomers in polymer melts: Solubility of long alkanes in linear polyethylene. *J. Chem. Phys.* 2001, *115*, 2860–2875, doi:10.1063/1.1383050.

133. Boulougouris, G.C.; Economou, I.G.; Theodorou, D.N. On the calculation of the chemical potential using the particle deletion scheme. *Mol. Phys.* 1999, *96*, 905–913, doi:10.1080/00268979909483030.

134. Siegert, M.R.; Heuchel, M.; Hofmann, D. A generalized direct-particle-deletion scheme for the calculation of chemical potential and solubilities of small- and medium-sized molecules in amorphous polymers. *J. Comput. Chem.* 2007, *28*, 877–889, doi:10.1002/jcc.20594.

135. Birgitta Knopp; Ulrich W. Suter, * and; Gusev, A.A. Atomistically Modelling the Chemical Potential of Small Molecules in Dense Polymer Microstructures. 1. Method. 1997, doi:10.1021/MA970383U.

136. Lyubartsev, A.P.; Martsinovski, A.A.; Shevkunov, S. V.; Vorontsov-Velyaminov, P.N. New approach to Monte Carlo calculation of the free energy: Method of expanded ensembles. *J. Chem. Phys.* 1992, *96*, 1776–1783,

doi:10.1063/1.462133.

137. van der Vegt, N.F.A.; Briels, W.J. Efficient sampling of solvent free energies in polymers. *J. Chem. Phys.* 1998, *109*, 7578–7582, doi:10.1063/1.477379.

138. Theodorou, D.N. A reversible minimum-to-minimum mapping method for the calculation of free-energy differences. *J. Chem. Phys.* 2006, *124*, 034109, doi:10.1063/1.2138701.

139. Hess, B.; Peter, C.; Ozal, T.; Van Der Vegt, N.F.A. Fast-growth thermodynamic integration: Calculating excess chemical potentials of additive molecules in polymer microstructures. *Macromolecules* 2008, *41*, 2283–2289, doi:10.1021/ma702070n.

140. Theodorou, D.N. Molecular Simulations of Sorption and Diffusion in Amorphous Polymers. In *Diffusion in Polymers*; Neogi, P., Ed.; Marcel Dekker: New York, Basel, Honk Kong, 1996; pp. 67–142.

141. Spyriouni, T.; Boulougouris, G.C.; Theodorou, D.N. Prediction of sorption of CO2 in glassy atactic polystyrene at elevated pressures through a new computational scheme. *Macromolecules* 2009, *42*, 1759–1769, doi:10.1021/ma8015294.

142. Ricci, E.; Vergadou, N.; Vogiatzis, G.G.; De Angelis, M.G.; Theodorou, D.N. Molecular simulation of structure and segmental dynamics of CO2-polystyrene at high pressure. *Prep.* 2019.

143. Pant, P.V.K.; Boyd, R.H. Molecular-dynamics simulation of diffusion of small penetrants in polymers. *Macromolecules* 1993, *26*, 679–686, doi:10.1021/ma00056a019.

144. Muller-Plathe, F. Calculation of the Free Energy for Gas Absorption in Amorphous Polypropylene. *Macromolecules* 1991, *24*, 6475–6479, doi:10.1021/ma00024a017.

145. Sok, R.M.; Berendsen, H.J.C.; van Gunsteren, W.F. Molecular dynamics simulation of the transport of small molecules across a polymer membrane. *J. Chem. Phys.* 1992, *96*, 4699–4704, doi:10.1063/1.462806.

146. Takeuchi, H. A jump motion of small molecules in glassy polymers: A molecular dynamics simulation. *J. Chem. Phys.* 1990, *93*, 2062–2067, doi:10.1063/1.459083.

147. Müller-Plathe, F. Molecular dynamics simulation of gas transport in amorphous polypropylene. *J. Chem. Phys.* 1992, *96*, 3200–3205, doi:10.1063/1.461963.

148. Einstein, A. On the Motion of Small Particles Suspended in a Stationary Liquid, as Required by the Molecular Kinetic Theory of Heat. *Ann. Phys.* 1905, *322*, 549–560, doi:10.1002/andp.19053220806.

149. Muller-plathe, F.; Rogers, S.C.; Gunsterent, W.F. Van Diffusion Coefficients of Penetrant Gases in Polyisobutylene Can Be Calculated Correctly by Molecular Dynamics Simulations Florian. *Macromolecules* 1992, *25*, 6722–6724.

150. Hoover, W.G.; Hoover, C.G. Nonequilibrium molecular dynamics. *Condens. Matter Phys.* 2005, *8*, 247–260.

151. Müller-Plathe, F.; Rogers, S.C.; van Gunsteren, W.F. Gas sorption and transport in polyisobutylene: Equilibrium and nonequilibrium molecular dynamics simulations. *J. Chem. Phys.* 1993, *98*, 9895–9904, doi:10.1063/1.464369.

152. Maginn, E.J.; Bell, A.T.; Theodorou, D.N. Transport diffusivity of methane in silicalite from equilibrium and nonequilibrium simulations. *J. Phys. Chem.* 1993, *97*, 4173–4181, doi:10.1021/j100118a038.

153. Glasstone, S.; Laidler, K.J.; Eyring, H. *The theory of rate processes; the kinetics of chemical reactions, viscosity, diffusion and electrochemical phenomena*; McGraw-Hill, 1941;

154. Voter, A.F.; Doll, J.D. Dynamical corrections to transition state theory for multistate systems: Surface self-diffusion in the rare-event regime. *J. Chem. Phys.* 1985, *82*, 80–92, doi:10.1063/1.448739.

155. Karayiannis, N.C.; Mavrantzas, V.G.; Theodorou, D.N. Detailed Atomistic Simulation of the Segmental Dynamics and Barrier Properties of Amorphous Poly(ethylene terephthalate) and Poly(ethylene isophthalate). *Macromolecules* 2004, *37*, 2978–2995, doi:10.1021/ma0352577.

156. Gusev, A.A.; Suter, U.W. Dynamics of small molecules in dense polymers subject to thermal motion. *J. Chern. Phys.* 1993, *99*, 2228–2234, doi:10.1063/1.466198.

157. Gusev, A.A.; Arizzi, S.; Suter, U.W.; Moll, D.J. Dynamics of light gases in rigid matrices of dense polymers. *J. Chem. Phys.* 1993, *99*, 2221–2227, doi:10.1063/1.465283.

158. Greenfield, M.L.; Theodorou, D.N. Geometric Analysis of Diffusion Pathways in Glassy and Melt Atactic Polypropylene. *Macromolecules* 1993, *26*, 5461–5472, doi:10.1021/ma00072a026.

159. Vergadou, N. Prediction of Gas Permeability of Inflexible Amorphous Polymers via Molecular Simulation,

University of Athens, Athens, Greece, 2006.

160. Fichthorn, K.A.; Weinberg, W.H. Theoretical foundations of dynamical Monte Carlo simulations. *J. Chem. Phys.* 1991, *95*, 1090–1096, doi:10.1063/1.461138.

161. Hofmann, D.; Fritz, L.; Ulbrich, J.; Schepers, C.; Bhning, M. Detailed-atomistic molecular modelling of small molecule diffusion and solution processes in polymeric membrane materials. *Macromol. Theory Simulations* 2000, *9*, 293–327, doi:10.1002/1521-3919(20000701)9:6<293::AID-MATS293>3.0.CO;2-1.

162. Chen, Y.; Liu, Q.L.; Zhu, A.M.; Zhang, Q.G.; Wu, J.Y. Molecular simulation of CO_2/CH_4 permeabilities in polyamide–imide isomers. *J. Memb. Sci.* 2010, *348*, 204–212, doi:10.1016/J.MEMSCI.2009.11.002.

163. Nagel, C.; Schmidtke, E.; Günther-Schade, K.; Hofmann, D.; Fritsch, D.; Strunskus, T.; Faupel, F. Free volume distributions in glassy polymer membranes: comparison between molecular modelling and experiments. *Macromolecules* 2000, *33*, 2242–2248, doi:10.1021/ma990760y.

164. Chang, K.S.; Tung, C.C.; Wang, K.S.; Tung, K.L. Free volume analysis and gas transport mechanisms of aromatic polyimide membranes: A molecular simulation study. *J. Phys. Chem. B* 2009, *113*, 9821–9830, doi:10.1021/jp903551h.

165. Kruse, J.; Kanzow, J.; Rätzke, K.; Faupel, F.; Heuchel, M.; Frahn, J.; Hofmann, D. Free volume in polyimides: Positron annihilation experiments and molecular modelling. *Macromolecules* 2005, *38*, 9638–9643, doi:10.1021/ma0473521.

166. Heuchel, M.; Hofmann, D.; Pullumbi, P. Molecular modelling of small-molecule permeation in polyimides and its correlation to free-volume distributions. *Macromolecules* 2004, *37*, 201–214, doi:10.1021/ma035360w.

167. Park, C.H.; Tocci, E.; Kim, S.; Kumar, A.; Lee, Y.M.; Drioli, E. A simulation study on OH-containing polyimide (HPI) and thermally rearranged polybenzoxazoles (TR-PBO): Relationship between gas transport properties and free volume morphology. *J. Phys. Chem. B* 2014, *118*, 2746–2757, doi:10.1021/jp411612g.

168. Golzar, K.; Amjad-Iranagh, S.; Amani, M.; Modarress, H. Molecular simulation study of penetrant gas transport properties into the pure and nanosized silica particles filled polysulfone membranes. *J. Memb. Sci.* 2014, *451*, 117–134, doi:10.1016/j.memsci.2013.09.056.

169. Heuchel, M.; Boehning, M.; Hoelck, O.; Siegert, M.; Hofmann, D. Atomistic Packing Models for Experimentally Investigated Swelling States Induced by CO_2 in Glassy Polysulfone and Poly(ether sulfone). *J. Polym. Sci. Part B Polym. Phys.* 2006, *44*, 1874–1897.

170. Azizi, M.; Mousavi, S.A. CO_2/H_2 separation using a highly permeable polyurethane membrane: Molecular dynamics simulation. *J. Mol. Struct.* 2015, *1100*, 401–414, doi:10.1016/j.molstruc.2015.07.029.

171. Hofmann, D.; Heuchel, M.; Yampolskii, Y.; Khotimskii, V.; Shantarovich, V. Free Volume Distributions in Ultrahigh and Lower Free Volume Polymers: Comparison between Molecular Modelling and Positron Lifetime Studies. *Macromolecules* 2002, *35*, 2129–2140, doi:10.1021/ma011360p.

172. Wang, X.Y.; Raharjo, R.D.; Lee, H.J.; Lu, Y.; Freeman, B.D.; Sanchez, I.C. Molecular simulation and experimental study of substituted polyacetylenes: Fractional free volume, cavity size distributions and diffusion coefficients. *J. Phys. Chem. B* 2006, *110*, 12666–12672, doi:10.1021/jp060234q.

173. Economou, I.G.; Raptis, V.E.; Melissas, V.S.; Theodorou, D.N.; Petrou, J.; Petropoulos, J.H. Molecular simulation of structure, thermodynamic and transport properties of polymeric membrane materials for hydrocarbon separation. *Fluid Phase Equilib.* 2005, *228–229*, 15–20, doi:10.1016/j.fluid.2004.08.026.

174. De Lorenzo, L.; Tocci, E.; Gugliuzza, A.; Drioli, E. Pure and modified Co-poly(amide-12-b-ethylene oxide) membranes for gas separation studied by molecular investigations. *Membranes (Basel).* 2012, *2*, 346–366, doi:10.3390/membranes2030346.

175. Tocci, E.; Gugliuzza, A.; De Lorenzo, L.; Macchione, M.; De Luca, G.; Drioli, E. Transport properties of a co-poly(amide-12-b-ethylene oxide) membrane: A comparative study between experimental and molecular modelling results. *J. Memb. Sci.* 2008, *323*, 316–327, doi:10.1016/j.memsci.2008.06.031.

176. Jiang, Y.; Willmore, F.T.; Sanders, D.; Smith, Z.P.; Ribeiro, C.P.; Doherty, C.M.; Thornton, A.; Hill, A.J.; Freeman, B.D.; Sanchez, I.C. Cavity size, sorption and transport characteristics of thermally rearranged (TR) polymers. *Polymer (Guildf).* 2011, *52*, 2244–2254, doi:10.1016/j.polymer.2011.02.035.

177. Chang, K.-S.; Wu, Z.-C.; Kim, S.; Tung, K.-L.; Lee, Y.M.; Lin, Y.-F.; Lai, J.-Y. Molecular modelling of poly(benzoxazole-co-imide) membranes: A structure characterization and performance investigation. *J. Memb. Sci.* 2014, *454*, 1–11, doi:10.1016/J.MEMSCI.2013.11.047.

178. Rizzuto, C.; Caravella, A.; Brunetti, A.; Hoon, C.; Moo, Y. Sorption and Di ff usion of CO_2/N_2 in gas mixture in thermally-rearranged polymeric membranes : A molecular investigation. **2017**, *528*, 135–146, doi:10.1016/j.memsci.2017.01.025.

179. Wang, X.Y.; Lee, K.M.; Lu, Y.; Stone, M.T.; Sanchez, I.C.; Freeman, B.D. Cavity size distributions in high free volume glassy polymers by molecular simulation. *Polymer (Guildf).* **2004**, *45*, 3907–3912, doi:10.1016/j.polymer.2004.01.080.

180. Anderson, L.R.; Yang, Q.; Ediger, A.M. Comparing gas transport in three polymers *via* molecular dynamics simulation. *Phys. Chem. Chem. Phys.* **2018**, *20*, 22123–22133, doi:10.1039/C8CP02829J.

181. McDermott, A.G.; Larsen, G.S.; Budd, P.M.; Colina, C.M.; Runt, J. Structural characterization of a polymer of intrinsic microporosity: X-ray scattering with interpretation enhanced by molecular dynamics simulations. *Macromolecules* **2011**, *44*, 14–16, doi:10.1021/ma1024945.

182. Ayyagari, C.; Bedrov, D.; Smith, G.D. Structure of Atactic Polystyrene: A Molecular Dynamics Simulation Study. *Macromolecules* **2000**, *33*, 6194–6199, doi:10.1021/ma0003553.

183. Shimazu, A.; Miyazaki, T.; Ikeda, K. Interpretation of d-spacing determined by wide angle X-ray scattering in 6FDA-based polyimide by molecular modelling. *J. Memb. Sci.* **2000**, *166*, 113–118, doi:10.1016/S0376-7388(99)00254-9.

184. Heuchel, M.; Fritsch, D.; Budd, P.M.; McKeown, N.B.; Hofmann, D. Atomistic packing model and free volume distribution of a polymer with intrinsic microporosity (PIM-1). *J. Memb. Sci.* **2008**, *318*, 84–99, doi:10.1016/j.memsci.2008.02.038.

185. Fang, W.; Zhang, L.; Jiang, J. Polymers of intrinsic microporosity for gas permeation: a molecular simulation study. *Mol. Simul.* **2010**, *36*, 992–1003, doi:10.1080/08927022.2010.498828.

186. Fang, W.; Zhang, L.; Jiang, J. Gas Permeation and Separation in Functionalized Polymers of Intrinsic Microporosity : A Combination of Molecular Simulations and Ab Initio Calculations. *J. Phys. Chem. C* **2011**, *115*, 14123–14130, doi:10.1021/jp204193g.

187. Kupgan, G.; Demidov, A.G.; Colina, C.M. Plasticization behavior in polymers of intrinsic microporosity (PIM-1): A simulation study from combined Monte Carlo and molecular dynamics. *J. Memb. Sci.* **2018**, *565*, 95–103, doi:10.1016/j.memsci.2018.08.004.

188. Hölck, O.; Böhning, M.; Heuchel, M.; Siegert, M.R.; Hofmann, D. Gas sorption isotherms in swelling glassy polymers - Detailed atomistic simulations. *J. Memb. Sci.* **2013**, *428*, 523–532, doi:10.1016/j.memsci.2012.10.023.

189. Frentrup, H.; Hart, K.E.; Colina, C.M.; Müller, E.A. In silico determination of gas permeabilities by non-equilibrium molecular dynamics: CO_2 and He through PIM-1. *Membranes (Basel).* **2015**, *5*, 99–119, doi:10.3390/membranes5010099.

190. Chen, Y.-R.; Chen, L.-H.; Chang, K.-S.; Chen, T.-H.; Lin, Y.-F.; Tung, K.-L. Structural characteristics and transport behavior of triptycene-based PIMs membranes: A combination study using ab initio calculation and molecular simulations. *J. Memb. Sci.* **2016**, *514*, 114–124, doi:10.1016/j.memsci.2016.04.063.

191. Zhou, J.; Zhu, X.; Hu, J.; Liu, H.; Hu, Y.; Jiang, J. Mechanistic insight into highly efficient gas permeation and separation in a shape-persistent ladder polymer membrane. *Phys. Chem. Chem. Phys.* **2014**, *16*, 6075, doi:10.1039/C3CP55498H.

192. Chang, K.-S.; Tung, K.-L.; Lin, Y.-F.; Lin, H.-Y. Molecular modelling of polyimides with intrinsic microporosity: from structural characteristics to transport behaviour. *RSC Adv.* **2013**, *3*, 10403–10413, doi:10.1039/c3ra40196k.

193. Hart, K.E.; Springmeier, J.M.; McKeown, N.B.; Colina, C.M. Simulated swelling during low-temperature N2 adsorption in polymers of intrinsic microporosity. *Phys. Chem. Chem. Phys.* **2013**, *15*, 20161–20169, doi:10.1039/c3cp53402b.

194. Neyertz, S.; Brown, D.; Pandiyan, S.; Van Der Vegt, N.F.A. Carbon dioxide diffusion and plasticization in fluorinated polyimides. *Macromolecules* **2010**, *43*, 7813–7827, doi:10.1021/ma1010205.

195. Abbott, L.J.; Colina, C.M. Formation of microporosity in hyper-cross-linked polymers. *Macromolecules* **2014**, *47*, 5409–5415, doi:10.1021/ma500579x.

196. Kupgan, G.; Liyana-Arachchi, T.P.; Colina, C.M. Pore size tuning of poly(styrene-co-vinylbenzyl chloride-co-divinylbenzene) hypercrosslinked polymers: Insights from molecular simulations. *Polymer (Guildf).* **2016**, *99*, 173–184, doi:10.1016/j.polymer.2016.07.002.

197. Jiang, J.X.; Trewin, A.; Su, F.; Wood, C.D.; Niu, H.; Jones, J.T.A.; Khimyak, Y.Z.; Cooper, A.I. Microporous poly(tri(4-ethynylphenyl)amine) networks: synthesis, properties, and atomistic simulation. *Macromolecules* 2009, *42*, 2658–2666, doi:10.1021/ma802625d.

198. Abbott, L.J.; Colina, C.M. Atomistic structure generation and gas adsorption simulations of microporous polymer networks. *Macromolecules* 2011, *44*, 4511–4519, doi:10.1021/ma200303p.

199. Doherty, D.C. Polymerization molecular dynamics simulations. I.Cross-linked atomistic models for poly(methacrylate) networks. *Comput. Theor. Polym. Sci.* 1998,*8*,169–178,doi:10.1016/S1089-3156(98)00030-0.

200. Yarovsky, I.; Evans, E. Computer simulation of structure and properties of crosslinked polymers: Application to epoxy resins. *Polymer (Guildf).* 2001, *43*, 963–969, doi:10.1016/S0032-3861(01)00634-6.

201. Trewin, A.; Willock, D.J.; Cooper, A.I. Atomistic simulation of micropore structure, surface area, and gas sorption properties for amorphous microporous polymer networks. *J. Phys. Chem. C* 2008, *112*, 20549–20559, doi:10.1021/jp806397f.

202. Muscatello, J.; Müller, E.A.; Mostofi, A.A.; Sutton, A.P. Multiscale molecular simulations of the formation and structure of polyamide membranes created by interfacial polymerization. *J. Memb. Sci.* 2017, *527*, 180–190, doi:10.1016/j.memsci.2016.11.024.

203. Rizzuto, C.; Caravella, A.; Brunetti, A.; Park, C.H.; Lee, Y.M.; Drioli, E.; Barbieri, G.; Tocci, E. Sorption and Diffusion of CO_2/N_2 in gas mixture in thermally-rearranged polymeric membranes: A molecular investigation. *J. Memb. Sci.* 2017, *528*, 135–146, doi:10.1016/j.memsci.2017.01.025.

204. Myers, A.L.; Prausnitz, J.M. Thermodynamics of mixed-gas adsorption. *AIChE J.* 1965, *11*, 121–127.

205. Neyertz, S.; Brown, D. Air Sorption and Separation by Polymer Films at the Molecular Level. *Macromolecules* 2018, *51*, 7077–7092, doi:10.1021/acs.macromol.8b01423.

206. Tanis, I.; Brown, D.; Neyertz, S.; Heck, R.; Mercier, R.; Vaidya, M.; Ballaguet, J.P. A comparison of pure and mixed-gas permeation of nitrogen and methane in 6FDA-based polyimides as studied by molecular dynamics simulations. *Comput. Mater. Sci.* 2018, *141*, 243–253, doi:10.1016/j.commatsci.2017.09.028.

207. Liu, J.; Jiang, J. Molecular Design of Microporous Polymer Membranes for the Upgrading of Natural Gas. *J. Phys. Chem. C* 2019, doi:10.1021/acs.jpcc.8b12422.

208. Hart, K.E.; Colina, C.M. Ionomers of Intrinsic Microporosity: In Silico Development of Ionic-Functionalized Gas-Separation Membranes. *Langmuir* 2014, *30*, 12039–12048, doi:10.1021/la5027202.

209. Vogiatzis, G.G.; Theodorou, D.N. Multiscale Molecular Simulations of Polymer-Matrix Nanocomposites. *Arch. Comput. Methods Eng.* 2017, doi:10.1007/s11831-016-9207-y.

210. Mathioudakis, I.G.; Vogiatzis, G.G.; Tzoumanekas, C.; Theodorou, D.N. Molecular Modelling and Simulation of Polymer Nanocomposites at Multiple Length Scales. *IEEE Trans. Nanotechnol.* 2016, *15*, 416–422, doi:10.1109/TNANO.2016.2538460.

211. Zhou, J.-H.; Zhu, R.-X.; Zhou, J.-M.; Chen, M.-B. Molecular dynamics simulation of diffusion of gases in pure and silica-filled poly(1-trimethylsilyl-1-propyne) [PTMSP]. *Polymer (Guildf).* 2006, *47*, 5206–5212, doi:10.1016/J.POLYMER.2006.05.041.

212. Chang, K.-S.; Yoshioka, T.; Kanezashi, M.; Tsuru, T.; Tung, K.-L. Molecular simulation of micro-structures and gas diffusion behavior of organic–inorganic hybrid amorphous silica membranes. *J. Memb. Sci.* 2011, *381*, 90–101, doi:10.1016/J.MEMSCI.2011.07.020.

213. Dutta, R.C.; Bhatia, S.K. Structure and Gas Transport at the Polymer-Zeolite Interface: Insights from Molecular Dynamics Simulations. *ACS Appl. Mater. Interfaces* 2018, *10*, 5992–6005, doi:10.1021/acsami.7b17470.

214. Krishna, R.; van Baten, J.M. Using molecular simulations for screening of zeolites for separation of CO_2/CH_4 mixtures. *Chem. Eng. J.* 2007, *133*, 121–131, doi:10.1016/J.CEJ.2007.02.011.

215. Zhang, L.; Hu, Z.; Jiang, J. Metal–Organic Framework/Polymer Mixed-Matrix Membranes for H_2/CO_2 Separation: A Fully Atomistic Simulation Study. *J. Phys. Chem. C* 2012, *116*, 19268–19277, doi:10.1021/jp3067124.

216. Semino, R.; Durholt, J.P.; Schmid, R.; Marin, G. Multiscale modelling of the HKUST-1/polyvinyl alcohol) interface: From an atomistic to a coarse graining approach. *J. Phys. Chem. C* 2017, *121*, 21491–21496, doi:10.1021/acs.jpcc.7b07090.

217. Jiang, J. Recent development of in silico molecular modelling for gas and liquid separations in metal–organic frameworks. *Curr. Opin. Chem. Eng.* 2012, *1*, 138–144, doi:10.1016/J.COCHE.2011.11.002.

218. Bonakala, S.; Lalitha, A.; Shin, J.E.; Moghadam, F.; Semino, R.; Park, H.B.; Maurin, G. Understanding of the

Graphene Oxide/Metal-Organic Framework Interface at the Atomistic Scale. *ACS Appl. Mater. Interfaces* **2018**, *10*, 33619–33629, doi:10.1021/acsami.8b09851.

219. Jiao, S.; Xu, Z. Selective gas diffusion in graphene oxides membranes: A molecular dynamics simulations study. *ACS Appl. Mater. Interfaces* **2015**, *7*, 9052–9059, doi:10.1021/am509048k.
220. Wang, P.; Li, W.; Du, C.; Zheng, X.; Sun, X.; Yan, Y.; Zhang, J. CO_2/N_2 separation via multilayer nanoslit graphene oxide membranes: Molecular dynamics simulation study. *Comput. Mater. Sci.* **2017**, *140*, 284–289.
221. Wu, T.; Xue, Q.; Ling, C.; Shan, M.; Liu, Z.; Tao, Y.; Li, X. Fluorine-Modified Porous Graphene as Membrane for CO_2/N_2 Separation: Molecular Dynamic and First-Principles Simulations. *J. Phys. Chem. C* **2014**, *118*, 7369–7376.
222. Maginn, E.J. Molecular simulation of ionic liquids: current status and future opportunities. *J. Phys. Condens. Matter* **2009**, *21*, 373101, doi:10.1088/0953-8984/21/37/373101.
223. Liu, H.; Dai, S.; Jiang, D. Solubility of Gases in a Common Ionic Liquid from Molecular Dynamics Based Free Energy Calculations. *J. Phys. Chem. B* **2014**, *118*, 2719–2725, doi:10.1021/jp500137u.
224. Liu, H.; Dai, S.; Jiang, D. Molecular Dynamics Simulation of Anion Effect on Solubility, Diffusivity, and Permeability of Carbon Dioxide in Ionic Liquids. *Ind. Eng. Chem. Res.* **2014**, *53*, 10485–10490.
225. Vergadou, N.; Androulaki, E.; Hill, J.-R.; Economou, I.G. Molecular simulations of imidazolium-based tricyanomethanide ionic liquids using an optimized classical force field. *Phys. Chem. Chem. Phys.* **2016**, *18*, 6850–6860, doi:10.1039/C5CP05892A.
226. Xiao, Y.; Zhang, L.; Xu, L.; Chung, T.S. Molecular design of Tröger's base-based polymers with intrinsic microporosity for gas separation. *J. Memb. Sci.* **2017**, *521*, 65–72, doi:10.1016/j.memsci.2016.08.052.
227. Rose, I.; Bezzu, C.G.; Carta, M.; Comesaña-Gándara, B.; Lasseuguette, E.; Ferrari, M.C.; Bernardo, P.; Clarizia, G.; Fuoco, A.; Jansen, J.C.; Hart, K.E.; Liyana-Arachchi, T.P.; Colina, C.M.; McKeown, N.B. Polymer ultrapermeability from the inefficient packing of 2D chains. *Nat. Mater.* **2017**, *16*, 1–39, doi:10.1038/nmat4939.
228. Abbott, L.J.; McDermott, A.G.; Del Regno, A.; Taylor, R.G.D.; Bezzu, C.G.; Msayib, K.J.; McKeown, N.B.; Siperstein, F.R.; Runt, J.; Colina, C.M. Characterizing the structure of organic molecules of intrinsic microporosity by molecular simulations and X-ray scattering. *J. Phys. Chem. B* **2013**, *117*, 355–364, doi:10.1021/jp308798u.
229. Larsen, G.S.; Lin, P.; Hart, K.E.; Colina, C.M. Molecular simulations of PIM-1-like polymers of intrinsic microporosity. *Macromolecules* **2011**, *44*, 6944–6951, doi:10.1021/ma200345v.
230. Hart, K.E.; Abbott, L.J.; McKeown, N.B.; Colina, C.M. Toward effective CO_2/CH_4 separations by sulfur-containing PIMs via predictive molecular simulations. *Macromolecules* **2013**, *46*, 5371–5380, doi:10.1021/ma400334b.
231. Abbott, L.J.; McKeown, N.B.; Colina, C.M. Design principles for microporous organic solids from predictive computational screening. *J. Mater. Chem. A* **2013**, *1*, 11950, doi:10.1039/c3ta12442h.
232. Hart, K.E.; Colina, C.M. Estimating gas permeability and permselectivity of microporous polymers. *J. Memb. Sci.* **2014**, *468*, 259–268, doi:10.1016/j.memsci.2014.06.017.
233. Larsen, G.S.; Hart, K.E.; Colina, C.M. Predictive simulations of the structural and adsorptive properties for PIM-1 variations. *Mol. Simul.* **2014**, *40*, 599–609, doi:10.1080/08927022.2013.829222.
234. Yilmaz, G.; Keskin, S. Predicting the Performance of Zeolite Imidazolate Framework/Polymer Mixed Matrix Membranes for CO_2, CH_4, and H_2 Separations Using Molecular Simulations. *Ind. Eng. Chem. Res.* **2012**, *51*, 14218–14228, doi:10.1021/ie302290a.
235. Jiang, J. Computational screening of metal–organic frameworks for CO_2 separation. *Curr. Opin. Green Sustain. Chem.* **2019**, *16*, 57–64, doi:10.1016/j.cogsc.2019.02.002.
236. Yang, W.; Liang, H.; Peng, F.; Liu, Z.; Liu, J.; Qiao, Z. Computational Screening of Meta Organic Framework Membranes for the Separation of 15 Gas Mixtures. *Nanomaterials* **2019**, *9*, doi:10.3390/nano9030467.
237. Wilmer, C.E.; Leaf, M.; Lee, C.Y.; Farha, O.K.; Hauser, B.G.; Hupp, J.T.; Snurr, R.Q. Large-scale screening of hypothetical metal-organic frameworks. *Nat. Chem.* **2012**, *4*, 83–89, doi:10.1038/nchem.1192.
238. Zarabadi-Poor, P.; Marek, R. Metal-Organic Frameworks for Helium Recovery from Natural Gas via N_2/He Separation: A Computational Screening. *J. Phys. Chem. C* **2019**, *123*, 3469–3475, doi:10.1021/acs.jpcc.8b07804.

Chapter 3

Thermodynamic Modelling of Gas Sorption in Glassy Cellulose Acetates

3.1 Introduction

Cellulose esters are materials of great commercial value. Cellulose acetates (CAs), in particular, have held a longstanding presence in the field of gas separation and, therefore, constitute an important benchmark for new materials candidate to enter the market [1,2]. Indeed, Cellulose Triacetate (CTA) was the first material in use for removal of CO_2 and H_2S from natural gas, and cellulose acetates remain among the few polymers commercialized to date for use in industrial CO_2/CH_4 gas separations [3], despite the discovery of new polymer families, such as polymers of intrinsic microporosity and thermally rearranged polymers, that have demonstrated higher gas separation performance [4]. Moreover, cellulose acetates are employed industrially in water desalination with reverse osmosis, because they are less expensive, have a longer life, require less cleaning, and are much more resistant to chlorine than other membrane material. Other advantages of using CAs, also in the case of gas separation, are their ease of procurement and processability, coupled to a good selectivity. However, they are quite prone to plasticization and their performance drop significantly when impurities are present in the gaseous streams to be treated [5,6]. Despite their widespread use and the presence of several experimental studies on the properties of this materials family, very few studies have been specifically devoted to modelling their separation properties. In particular, their transport properties are a function of the degree of substitution (DS) [7], a parameter which indicates the average number of acetyl substituents per glucose unit (3 is the maximum value). The different steric and electronegativity qualities of the -OH and $-COOCH_2$ groups result in different chain packing efficiency and mobility, which, in turn, is reflected on the volumetric, mechanical and transport properties.

The research interest in cellulose acetate as a membrane material is not declining, not only in natural gas and biogas treatment [8], but also in post-combustion CO_2 capture [9]. In fact, cellulose triacetate membranes have potential for CO_2 separation in both pre- and post-combustion capture due to their good CO_2/N_2 and CO_2/H_2 selectivity and commercial readiness. The possibility to improve upon its current performance by the fabrication of polymer blends of nanocomposite Mixed Matrix Membranes (MMM) is currently actively studied. Uddin et al. [10] prepared non-covalently functionalized reduced graphene oxide/cellulose acetate nanocomposite membranes through solution mixing. The resulting material had improved tensile strength, higher temperature resistance and oxygen gas barrier properties. Mubashir et al. [11] studied cellulose acetate in combination with an ionic liquid NH2-MIL-53, successfully modelling its gas permeability with the Maxwell model. Moreover, CAs have been employed in the preparation of Poly(ionic liquid membranes) for CO_2/CH_4 and CO_2/N_2 separation [12]. Ding et al. [13] prepared MMMs with CA and mesoporous silica and investigated the structural and transport properties of the system, while Najafi et al. [14] studied the effect of silica nanoparticles on the permeability of pure CO_2 and N_2 gases in CA, finding an increase in CO_2/N_2 ideal selectivity upon addition of 20 wt% of nanoparticles, due to a simultaneous increase in CO_2 permeability and decrease in N_2 permeability. Alternatively, blends with other polymers are tested, in search for improved separation performance. Sanaeepur et al. [15] blended CA with Pebax®, a block co-polymer (polyether block amide). CO_2 permeability in CA/Pebax® (8 wt.% Pebax®) membrane increases more than 25% and the CO_2 /N_2 ideal selectivity increased by 59%. Sundell et al. [16]

used post-polymerization acid-catalyzed silanation to obtain modified CA membranes exhibiting substantially higher CO_2 and CH_4 permeabilities for both pure- and mixed-gas feeds, as well as higher plasticization resistance and improved permeability.

Concerning modelling studies, Saberi et al. [17,18] proposed a permeation model based on the Dual Mode Sorption model for solubility and on the partial immobilization model for diffusivity. Through fitting of the adjustable parameters on experimental data, they were able to represent multicomponent permeability and selectivity. Magnanelli et al. [19] developed a model to represent CO_2/CH_4 permeation through asymmetric cellulose acetate, representing both the effects of heat and mass transport. For the description of solubility in the dense selective layer they employed the empirical Dual Mode Sorption (DMS) model, and they neglected the presence of other impurities in the stream. Guo et al. [20,21] proposed a modified Dual Mode Sorption model accounting for hole formation to address inconsistencies found in the application of the traditional Dual Mode Sorption model to sorption-desorption hysteresis curves. Perrin et al. modeled water and ethanol sorption in CA using the ENSIC model to account for clustering of the penetrant molecules [22]. A molecular simulation study was also reported [23], in which the different conformations adopted by the material as a function of the decree of substitution were analyzed.

The objective of this study is to broaden the experimental characterization of Cellulose Acetates and develop a more predictive modelling strategy for the study of multicomponent effects, capable of addressing practical problems of industrial interest, such as the drastic loss of performance in presence of small amounts of heavy pollutants. Crystallinity is taken into account in the analysis. In fact, cellulose acetates glasses are not fully amorphous materials, but exhibit a degree of crystallinity that depends on the degree of substitution (DS) as well as on the sample preparation protocol. In the operative conditions of interest, these polymers are in the glassy state, therefore gas solubility can be modelled with the Non-Equilibrium Thermodynamics for Glassy Polymers (NET-GP) approach [24]. In particular, the Non-Equilibrium Lattice Fluid model [24,25], which is an extension of the Sanchez-Lacombe (SL) Equation of State (EoS) [26,27] to the case of nonequilibrium materials, was used in this work. The equilibrium model (SL) and its nonequilibrium counterpart (NELF) share the same pure-component parameters. Therefore, it is possible to model equilibrium properties of the polymer to obtain the parameters and then use them to model nonequilibrium properties below the glass transition. In the case of polymers, volumetric data at different pressures and temperatures (*PVT* data) are usually employed to this aim, but these measurements are not available for cellulose acetates in the literature yet. Therefore, the first part of the study focused on sample preparation, thermal characterization, and *PVT* properties measurement. Combining these data allowed to obtain the parameters of the Sanchez-Lacombe equation of state and employ them to model sorption data using the Non-Equilibrium Lattice Fluid model. From the analysis of pure-gas sorption isotherms, the binary interaction parameter and swelling coefficient of each penetrant were obtained. With this information the NELF model can be used to perform predictive calculations of sorption equilibria with multicomponent gas mixtures.

3.2 Samples Preparation

Materials with two different degrees of acetylation (or degrees of substitution, DS) have been selected, which are the most commonly used in the membrane industry: cellulose diacetate (CDA – DS 2.4) and cellulose triacetate (CTA – DS 2.9). Suppliers specifications for the two materials are given in **Table 3.1**.

Table 3.1. Suppliers specifications for cellulose acetates

Cellulose Diacetate	Eastman (TM) Cellulose Ester (CE-PP200)
Form	powder
Melting Point	230-250°C
Decomposition Temperature (DSC)	304°C
Acetyl content	39.8%
Combined Acetic Acid Content	55.5%
Hydroxyl Content	3.5%wt.
Acidity as Acetic Acid (max.)	1500 pppm
Moisture content (max.)	3%wt.
Specific Gravity	1.31 g/cm^3
Cellulose Triacetate	Acros Organics/Fisher Scientific Cellulose Triacetate
Form	pellets
Acetyl content	43-44%

3.2.1 Slabs for *PVT* Measurements

At first, an attempt to prepare thick samples by **compression molding** was made. The materials in powder and pellet form were dried in the oven overnight and kept in a nitrogen atmosphere prior to the experiment, in order to reduce the content of water as much as possible. Molds of different thickness were tested, and in the end a 1 mm one was selected, in order to guarantee a fast and homogeneous heating. Different combinations of time/temperature of exposure were tried. However, the samples obtained would be either not entirely melted or partially thermally decomposed. The difficulty in obtaining samples in this way arises from the very narrow interval existing between the melting and the decomposition temperatures [28], and the kinetics of the two processes. The press used was equipped with a water cooling system, which prevented the application of high temperature only for a very short period of time, and a partial decomposition was always observed at the conditions necessary to ensure complete melting.

Therefore, samples were prepared via **solution casting**. In the case of cellulose diacetate, a well stirred 8 wt% solution with acetone was casted into a 7.6 cm Teflon Petri dish and covered to allow for a slow evaporation of the solvent, in order to obtain a homogeneous and smooth surface of the sample. For cellulose triacetate, a 5 wt% solution with dichloromethane was prepared, left under magnetic stirring overnight and then casted into a 7.6 cm Teflon Petri dish, which was covered to allow for a slow solvent evaporation. After 12 days at room temperature, the samples, that had detached from the Teflon container

and slightly shrunk in diameter, were placed under vacuum at 100 °C for 72 hours to remove residual solvent. A final thickness of approximately 1 mm was achieved in both cases.

3.2.2 Films for Sorption Measurements

Sorption measurements were performed by Dr. Liang Liu at the University of Melbourne on samples of CDA and CTA of the same batch as the ones used in *PVT* measurements. Films for sorption measurements were obtained using the following protocol. A 1 wt% solution was prepared by dissolving the polymer into dichloromethane (CTA) or acetone (CDA). The solution was filtered and cast into glass petri dishes, which were then kept covered for solvent evaporation. After 24 hours, the membranes were peeled from the petri dishes and annealed in a vacuum oven for 24 hours at 35 °C and another 24 hours at 100 °C. The annealed membranes were kept in a desiccator for 14 days prior to utilization in sorption and permeation studies, to minimize the impact of the initial physical aging of the glassy membranes.

3.3 Thermal Characterization

The samples were characterized through DSC experiments, performing heating at a rate of 10 °C/min and cooling at 20 °C/min, in nitrogen flux. Furthermore, TGA measurements were performed, with a heating rate of 10 °C/min, in nitrogen atmosphere as well. Results of the tests for the slabs used in *PVT* measurements are shown in **Figure 3.1** and **Figure 3.2** and summarized in **Table 3.2**. The thermal measurements for cellulose acetates differ greatly among different samples, depending on the cellulose source and the method of preparation [29,30]. The resulting glass transition and melting temperature values are within the range of those reported in the literature [7,28–31].

CDA shows a more complex melting behavior, which manifests itself over a broad range of temperatures, with two different wells at about 211 °C and 233 °C. A similar behavior was observed also previously [32]. A shift in the baseline associated with the glass transition was detected at about 167 °C. In the case of CTA, after the glass transition was observed around 170 °C, the materials exhibited a crystallization peak at 212 °C, and a melting peak at 290 °C. Torsional braid analysis [33] reported the glass transition happening at a higher temperature (186 °C), while the two subsequent peaks were detected at the same temperatures. The lower melting temperature of cellulose diacetate compared to triacetate has been attributed to the presence of smaller and less perfect CTA crystallites in materials with lower DS, which was confirmed by X-ray analysis [31]. Other studies had shown a decreasing trend of T_g with increasing DS, while in the present case a slightly higher value for CTA was obtained. This discrepancy might be ascribed to differences in the molecular weight of the samples, that is not known in the present samples.

From the integration of the melting wells, the crystalline fraction was estimated with the following relation:

$$\%c = \frac{\Delta H_f}{\Delta H_f^o} \cdot 100 \qquad \text{Eq. (3.1)}$$

Where ΔH_f is the heat of fusion of the sample and ΔH_f^o is the heat of fusion of a perfect crystal, whose value was taken to be 58.8 J/g [34], assuming it applies both to CDA and CTA. The crystalline fraction values obtained were 31 ± 2 wt% for CDA and 51 ± 2 wt% for CTA. In the case of CTA, the crystalline fraction associated to the crystallization peak was subtracted, in order to obtain the crystalline fraction of the pristine sample.

From the analysis of TGA measurements it was verified that the samples, in the absence of oxygen and water, were thermally stable in the whole temperature range of the subsequent *PVT* measurements.

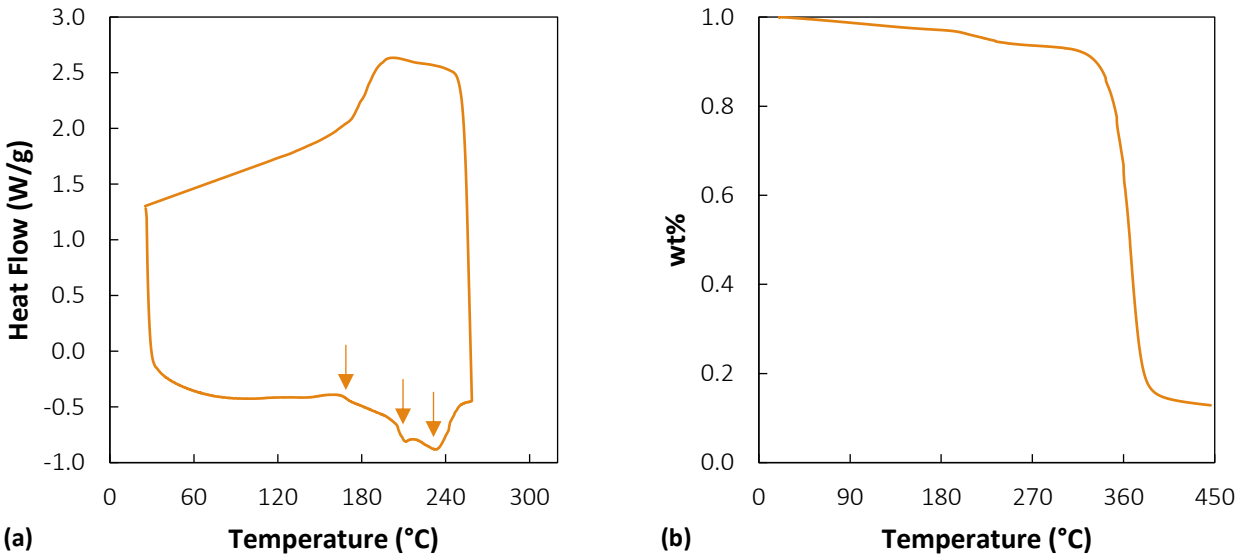

Figure 3.1. (a) DSC and (b) TGA tests on cellulose diacetate (CDA) slabs obtained via solution casting.

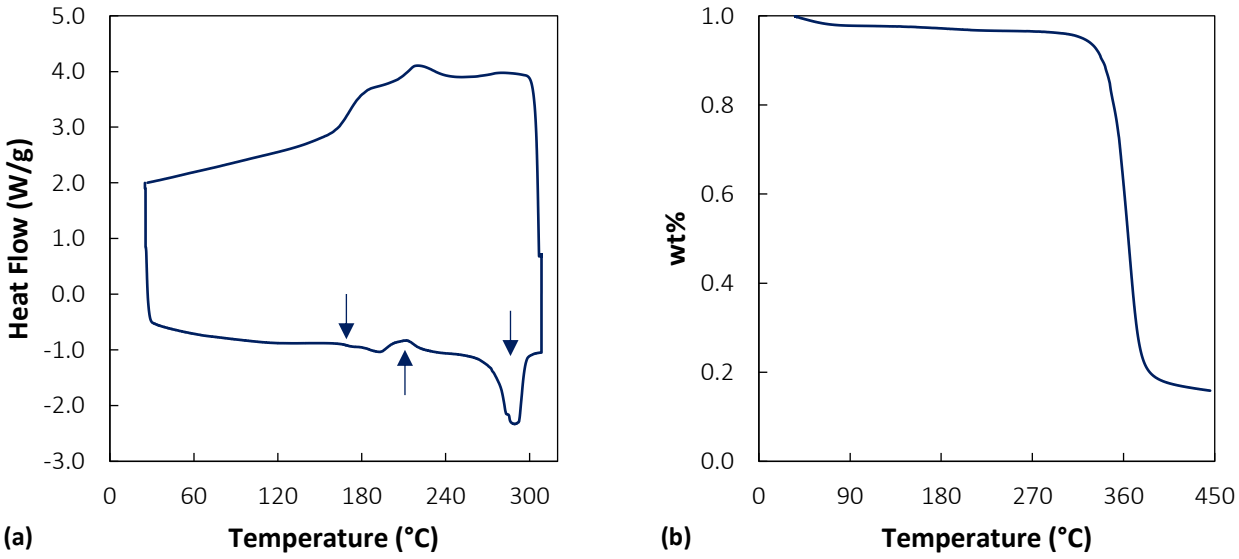

Figure 3.2. (a) DSC and (b) TGA tests on cellulose triacetate (CTA) slabs obtained via solution casting.

Table 3.2. Melting temperature (T_m), glass transition temperature (T_g), crystalline fraction and room temperature density of cellulose diacetate and triacetate slab samples used in *PVT* tests.

	CDA	CTA
T_g (°C)	167	170
T_m (°C)	210-230	285
wt% crystal	31 ± 2%	51 ± 2 wt%
$\rho_{25\,°C}$ (g/cm^3)	1.281 ± 0.002	1.300 ± 0.002

3.4 *PVT* Measurements

At first, an attempt was made to measure *PVT* curves using a Göttfert **capillary rheometer**, in which a cap can be placed on one end the end of the sample holder, while at the other hand a piston applies pressure to the sample. The samples were degassed and dehumidified prior to the test, to avoid the acceleration of degradation phenomena due to the presence of water and oxygen. However, the configuration of the equipment did not allow to have control over the atmosphere during the test, which led to partial degradation of the samples, making the results inconclusive. For these reasons, this technique was abandoned.

Pressure-volume-temperature measurements were performed at DICMaPI of Università di Napoli, using a **GNOMIX** apparatus, which employs the confining fluid technique. In this apparatus, the material studied is surrounded by mercury as the confining fluid, which ensures that the sample is under hydrostatic pressure at all times. The apparatus is able to collect data in the range from 10 to 200 MPa in increments of 10 MPa, and from room temperature up to 400 °C. The tests were carried out in isothermal mode in the range 30 – 220 °C for CTA and 30 – 250 °C for CDA, at 10 °C intervals, and from 0 to 200 MPa, at 10 MPa intervals. The values for atmospheric pressure are obtained by extrapolation of the values from 30 MPa to 10 MPa according to the Tait equation for each temperature, using the internal GNOMIX software. The results are shown in **Figure 3.3**. Only five curves per sample are shown, for clarity. An initial density value at the starting temperature and pressure condition must be provided as input, to evaluate all the subsequent results in relative terms. The densities at room temperature of our samples were evaluated with the buoyancy method using water and n-dodecane as displacement fluids. Weighting in air before and after immersion in liquid yielded the same values, thus confirming that, especially in the case of water, no liquid absorption had occurred during the test. Resulting densities (reported also in **Table 3.2**) were 1.281 ± 0.002 g/cm^3 for cellulose diacetate and 1.300 ± 0.002 g/cm^3 for cellulose triacetate at 25 °C.

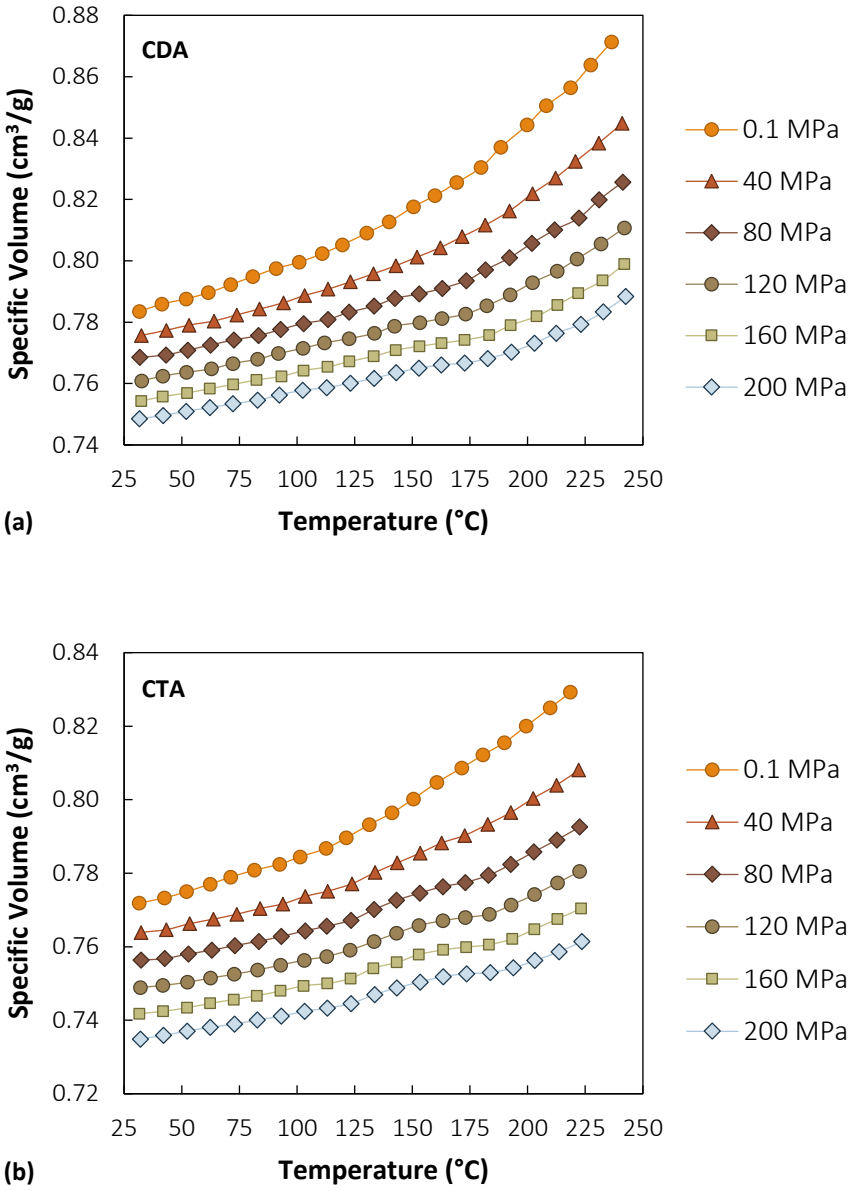

Figure 3.3. *PVT* curves for cellulose diacetate (a) and triacetate (b).

3.4.1 Comparison with Literature Data

The measured behavior is compared in **Figure 3.4** with volumetric curves at atmospheric pressure obtained via dilatometric experiments [35,36]. The deviations between the different samples is significant: among our CDA sample and the one of Mandelkern and Flory [35] there is an average 3.5% difference in specific volume, while the difference with the sample of Russel and Van Kerpel [36] is 6.5%. For CTA the average differences are lower and amount to 1% and 2.3% respectively. It must be noted that in the case of CDA the samples have a slightly different degree of acetylation (2.3 in [35], 2.2 in [36] 2.4 here). It is striking that the diacetate sample is less dense than the triacetate one, contrary to what the literature data show. However, fully substituted cellulose acetate can easily form crystalline structures, whose density has been reported

to be 1.375 g/cm^3 [37] and samples with a higher DS, owing to a more regular structure, usually exhibit a higher crystalline fraction [31]. Indeed, there is a 20 wt% difference in the crystalline content of the CDA and CTA sample, that can account for the fact that the CTA sample is denser than the CDA one. Our samples were obtained through very slow solvent evaporation, in conditions favoring the formation of a high crystalline fraction. The crystalline fraction of the literature samples was not reported, so it cannot be compared to support or dispute this hypothesis. Taking into account the substantial difference displayed by two different literature sources, the results obtained here for the density at atmospheric pressure of CDA and CTA are within the expected range. This is an indication that the thick samples produced were free of defects, such as air bubbles, which could have profoundly affected the *PVT* measurements.

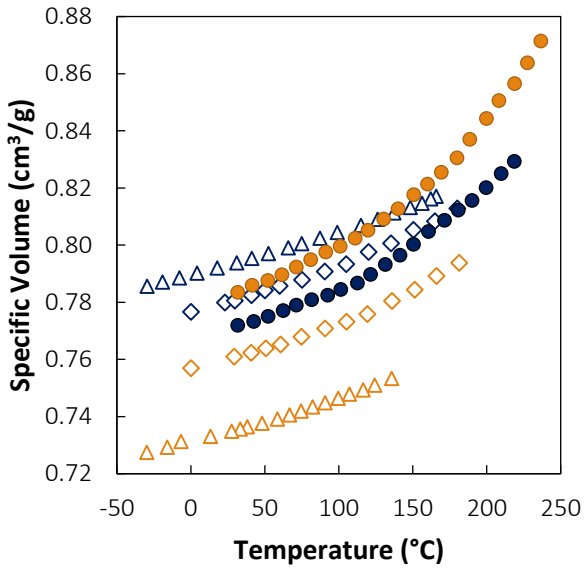

Figure 3.4. Comparison with volumetric curves at atmospheric pressure measured here (circles) for cellulose diacetate (orange) and triacetate (blue) with results taken from ref. [35] (diamonds) and from ref. [36] (triangles).

The thermal expansion coefficients k_p were evaluated using **Eq. (3.2)** and the results are reported in **Table 3.3**:

$$k_p = -\frac{1}{V}\frac{\partial V}{\partial T}\bigg|_p \qquad \text{Eq. (3.2)}$$

For the literature data sets, the values between parenthesis in **Table 3.3** were evaluated above the upper transition reported in the referenced works, which is still below the T_g value determined by the DSC measurements performed in this work.

According to the calorimetric T_g values, the experiments of refs. [35,36] did not reach the rubbery state. Nonetheless, they both report secondary transition temperatures in the range inspected (40/120/155 °C for CTA and 55/115°C for CDA in ref. [36], 30/105 °C for CTA and 60/120 °C for CDA in ref. [35]). By analyzing the trend of the derivative of the volumetric curves measured in this work, it is possible to recognize multiple transitions also in our measurements, at similar temperatures: 65 (weak) – 127 – 187°C for CDA

and 115 – 190 (weak) °C for CTA (**Figure 3.5**). It is not straightforward to recognize the glass transition temperature. During the *PVT* measurement, heat is applied to the sample for considerably longer time than in the DSC measurements, therefore it is reasonable to expect the onset of the glass transition at lower temperatures. If that is the case, the glass transition would be assigned to the temperatures of 127 °C for CDA and 115 °C for CTA.

Table 3.3. Thermal expansion coefficients of semicrystalline CDA and CTA at atmospheric pressure calculated on data from [35,36] and on our volumetric measurements.

	CDA		CTA	
Ref.	**Low T**	**High T**	**Low T**	**High T**
[36]	$2.037 \cdot 10^{-4}$	$(3.753 \cdot 10^{-4})$	$1.999 \cdot 10^{-4}$	$(3.305 \cdot 10^{-4})$
[35]	$1.789 \cdot 10^{-4}$	$(2.575 \cdot 10^{-4})$	$2.040 \cdot 10^{-4}$	$(2.460 \cdot 10^{-4})$
this work	$3.011 \cdot 10^{-4}$	$8.475 \cdot 10^{-4}$	$2.354 \cdot 10^{-4}$	$5.414 \cdot 10^{-4}$

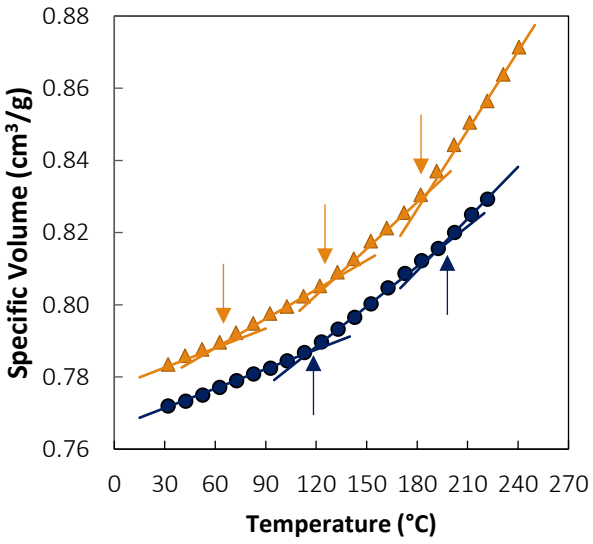

Figure 3.5. Secondary transitions in cellulose acetates, marking discontinuities in the isobaric curves at atmospheric pressure.

3.5 Sanchez-Lacombe Equation of State Parameters Regression

The Sanchez-Lacombe equation of state (SL EoS) [26,27,38] was used to study gas sorption in CDA and CTA with the NET-GP approach. The model was described in **Chapter 2**. EoS parameters are needed for all the pure components and those of the two polymers are retrieved here through a fitting procedure on the volumetric data of the amorphous phase above the glass transition.

In fact, the equation of state describes the behavior of an amorphous, isotropic phase, therefore it cannot be applied directly on the results of the *PVT* experiment, because they refer to a semi-crystalline phase. In order to extract the *PVT* data of the amorphous phase, the following additional information were used: the density of the CTA I crystal (1.375 g/cm^3 [37]), the volumetric thermal expansion coefficient of the CTA I crystal from ref. [39] ($15.6 \cdot 10^{-5}$) and a typical value for isothermal compressibility for polymeric crystals of $1.5 \cdot 10^{-5}$, in the absence of a specific measurement for CTA I. Subsequently, the data in the rubbery region were fitted to the SL EoS. In **Figure 3.6** the results of the fitting procedure are shown, with black arrows in the plots marking the DSC glass transition temperatures. Only some data points are shown for clarity, the full data set used in the regression contains measurements at 10 °C and 10 MPa intervals.

The best fit parameters obtained for each material are summarized in **Table 3.4**. 95% confidence intervals of the parameters resulting from the nonlinear regression were obtained with a Monte Carlo method [40].

Table 3.4. SL parameters for amorphous CDA and CTA. 95% confidence intervals of the parameters were obtained with a Monte Carlo method [40].

	CDA	CTA
T* (K)	608 ± 8	560 ± 6
P* (MPa)	730 ± 15	780 ± 20
ρ* (g/cm^3)	1.400 ± 0.005	1.450 ± 0.005

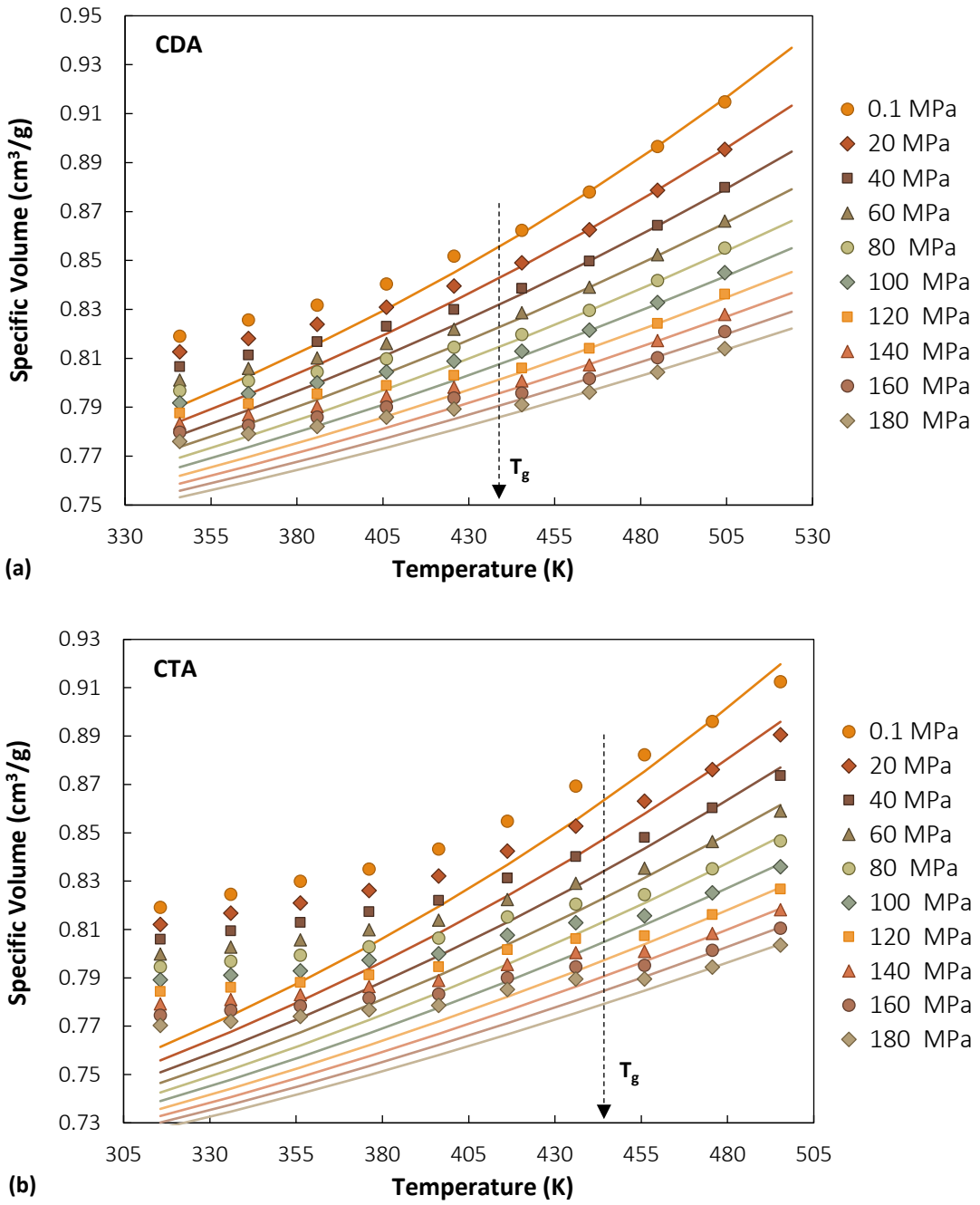

Figure 3.6. *PVT* data of the amorphous fraction of CDA (a) and CTA (b), together with Sanchez Lacombe EoS calculations performed with the parameters reported in **Table 3.4**.

3.6 Pure-gas Sorption Isotherms Modelling

Cellulose acetates are in the glassy state at the temperatures of interest for gas separation. Consequently, they can be properly described by a non-equilibrium model such as the NELF model [24], extension of the Sanchez-Lacombe equation of state to the non-equilibrium state of glassy polymers, within the framework of the NET-GP approach, which was described in detail in **Chapter 2**.

One of the preliminary hypotheses of this model is that the material under consideration is isotropic and amorphous. This assumption does not hold true in general in the case of cellulose acetates samples, which are very often semi-crystalline. Even though it is reasonable to consider the crystalline fraction impermeable to penetrants, and therefore picture the penetrants forming a mixture only with the amorphous fraction, the presence of the crystallites alters the properties of the amorphous phase in a way which is dependent on the crystalline fraction.

Bonavoglia et al. [41] argue that the presence of the crystalline phase hinders the mobility of the amorphous one to the point it causes it to exhibit non-equilibrium behavior even above the glass transition temperature, and that a nonequilibrium model is best suited to evaluate sorption also in semi-crystalline rubbery polymers. Minelli et al. modelled gas sorption in semi-crystalline rubbers [42] accounting for the effect of the crystallites on the amorphous phase with the introduction of an additional "constraining pressure", which has the effect of increasing the density of the amorphous phase, with respect to the unconstrained, totally amorphous material. In this way, they could calculate the density of the amorphous phase of the material by solving the equation of state not at the operative pressure, but at the operative pressure incremented by the constraining pressure resulting from the presence of the crystallites.

Below the glass transition, the density of the amorphous phase cannot be reliably calculated with an equation of state, given the nonequilibrium condition of the system. In fact, this variable constitutes an input to the nonequilibrium model used to calculate the solubility, and, in order to evaluate it from the knowledge of the experimental density of the semi-crystalline material, the density of the crystal and the crystalline fraction are required:

$$\rho_A = \frac{\rho_C(1-\omega_C)}{\frac{\rho_C}{\rho_{SC}} - \omega_C} \qquad \text{Eq. (3.3)}$$

ρ_A indicates the density of the amorphous fraction, ρ_C is the density of the crystalline fraction, ρ_{SC} the density of the semi-crystalline material and ω_C the weight fraction of the crystallites. The value 1.375 g/cm^3 [37] is used for ρ_C.

The ability of the cellulose acetate SL parameter sets reported in **Table 3.4** to represent gas sorption in the glassy state was tested by modelling CO_2 and CH_4 sorption data at 35 °C for CDA and CTA using the NELF model. Sorption tests on CDA and CTA were performed by Dr. Liang Liu at the University of Melbourne. The samples used in these tests were obtained using the preparation protocol described in **Section 3.2.2**. The density was measured with the buoyancy technique, obtaining a value of 1.306 g/cm^3 for CDA and 1.290 g/cm^3 for CTA at 25 °C.

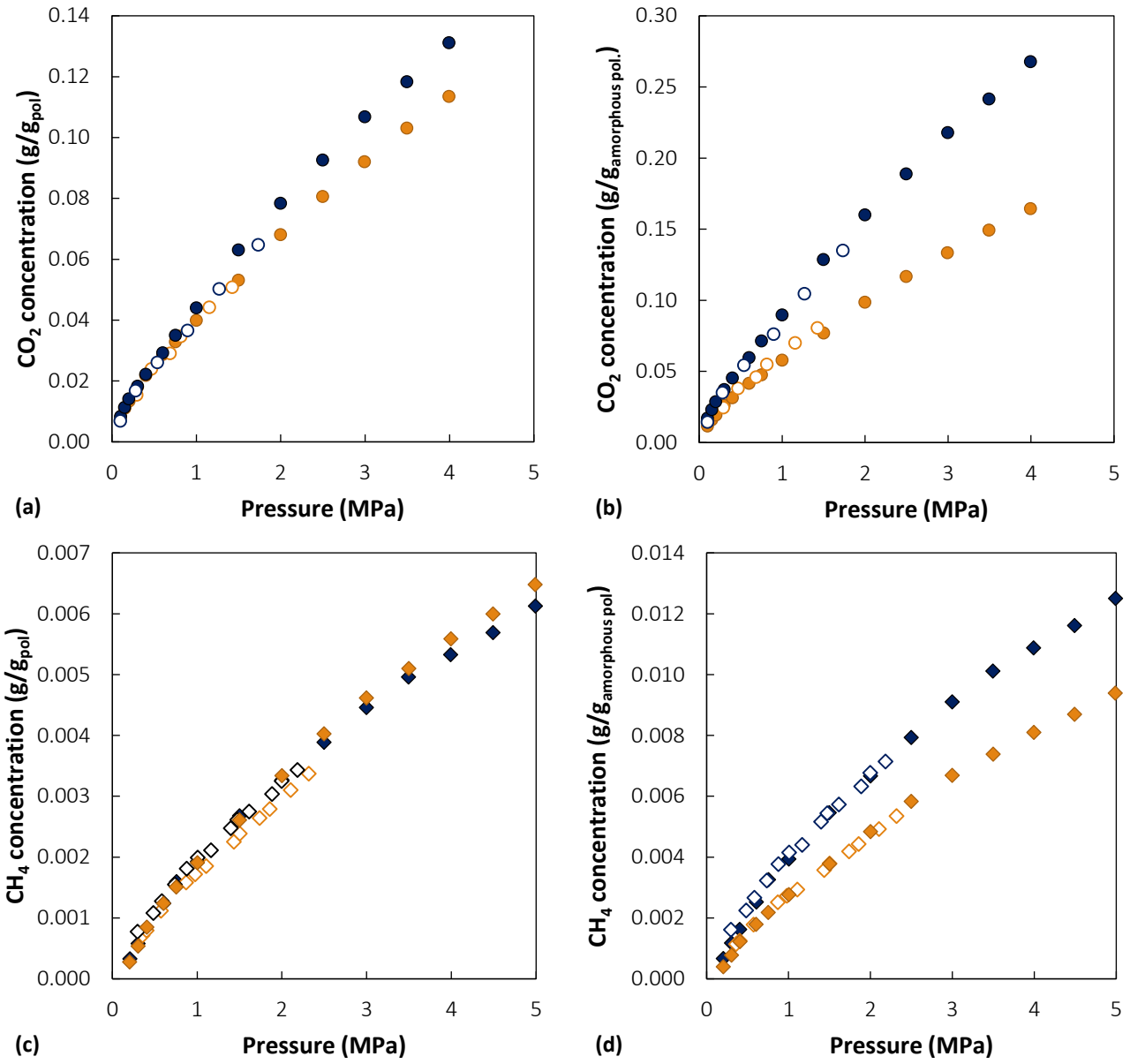

Figure 3.7. Sorption isotherms of CO_2 (circles, figures (a) and (b)) and CH_4 (diamonds, figures (c) and (d)) in CDA (orange) and CTA (blue). Figures (a) and (c) display gas concentration calculated over the total mass of the polymer, while in figures (b) and (d) the gas concentration is evaluated only in the amorphous polymer phase. Filled symbols are data measured in this work, empty symbols literature data from [7].

The results are shown in **Figure 3.7** and compared with the measurements of Puleo et al. [7]. In **Figure 3.7 (a) and (c)** the gas concentrations are calculated over the total mass of the polymer, while in **Figure 3.7 (b) and (d)**, gas concentrations are rescaled by dividing them by the amorphous phase weight fraction (1- ω_C), since it was assumed that the gas is present only in the amorphous phase. The crystalline content of these samples was not measured, therefore it was assumed to be 31 wt% in CDA and 51 wt% in CTA, *i.e.* the same values of the samples used for *PVT* measurements and EoS parameters regression: these value are in the range of those reported in the literature for films obtained through solution casting [7,43].

CO_2 and CH_4 sorption of our samples is in very good agreement with the literature values. By looking at concentrations evaluated over total polymer mass, very similar values are obtained both for CDA and CTA.

In the measurements of Puleo et al., CTA shows higher sorption than CDA both for CO_2 and CH_4, while in our case, CDA has a slightly higher CH_4 sorption than CTA. However, when the crystallinity of the samples is taken into account (0.37 wt% for CDA and 0.52 wt% for CTA in the data from the literature [7]) the differences are eliminated and the curves obtained here overlap with the literature ones.

Subsequently, the sorption isotherms were modelled with the NELF model. In order to use the model, the dry polymer density is required, and it was obtained by applying **Eq. (3.3)**. For CDA a value of 1.277 ± 0.005 g/cm^3 was obtained, while 1.212 ± 0.008 g/cm^3 was calculated for CTA at 25 °C. These data can be compared with the results of atomistic simulations on amorphous cellulose acetate performed by Bocahut et al. [44]. They report a density of 1.22 g/cm^3 and 1.19 g/cm^3 for CDA and CTA respectively. The higher density of amorphous CDA displayed both by experiments and simulations can be explained by the lower number of acetate substituents, which are bulkier than the hydroxyl groups. The difference of 4% in the case of CDA and 2% in the case of CTA of the experimental density values compared to the simulated ones can be a result of the force field used in the simulations, but also a consequence of the aforementioned constraining effect exerted by the crystalline fraction on the amorphous one in the experimental samples, which leads to higher values for ρ_A. Following the previous discussion about the effect of the crystallites on the density of the amorphous phase, the results obtained here for ρ_A should in principle be considered valid only at their corresponding crystalline content.

The corresponding values of the dry amorphous polymer densities at 35 °C (the temperature of the sorption tests) were calculated using the thermal expansion coefficient of the amorphous phase determined for each material from the experimental *PVT* measurements. The values obtained are reported in **Table 3.5**. The values of the binary interaction and swelling coefficients used in the NELF model are also reported in the same table. These were obtained as the best fit parameters to the experimental data. The model was able to give a faithful representation of the experimental data with low values of the binary interaction coefficients. It can be noted that the swelling coefficient obtained for CO_2 sorption in CTA is double than the value obtained for CDA, which is an indication that the latter has a higher plasticization resistance compared to the material with a higher DS. In the case of CH_4 very small values of the swelling coefficients were obtained as best fit parameters. This value is often assumed to be zero, when sorption at lower pressure (around 30 bar) is calculated with the NELF model [45]. However, the present data set extends well beyond 30 bar. The values obtained for both CDA and CTA are similar for this gas.

Table 3.5. Parameters used to calculate CO_2 and CH_4 sorption isotherms in CDA and CTA using the NELF model.

	CDA	CTA
ρ_{am}^0(35 °C) (g/cm^3)	1.273	1.209
$k_{CO_2,pol}$	–0.060	0.023
k_{sw,CO_2} (MPa^{-1})	0.037	0.061
$k_{CH_4,pol}$	–0.089	0.030
k_{sw,CH_4} (MPa^{-1})	0.003	0.003

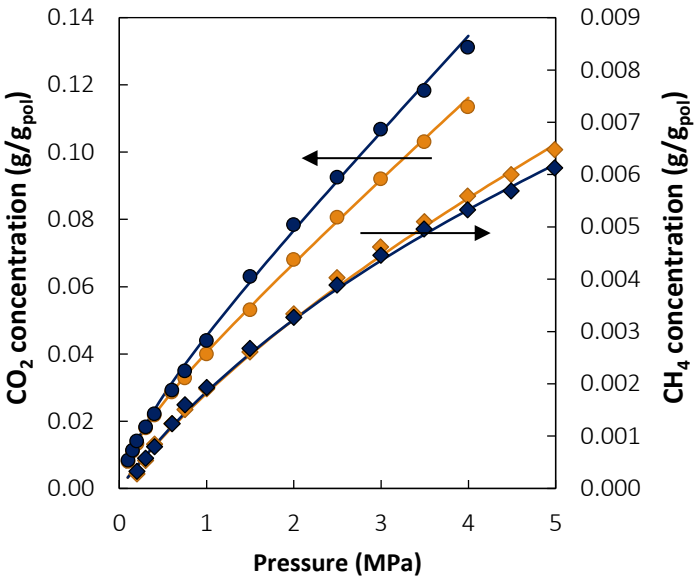

Figure 3.8. Sorption isotherms of CO_2 (circles) and CH_4 (diamonds) in CDA (blue) and CTA (orange) at 35 °C. Lines represent NELF model calculations

3.6.1 Temperature Dependence of Gas Sorption

As a test of consistency and transferability of the SL parameters obtained, two literature data sets were analyzed [46,47], which report the solubility of CH_4 and CO_2 in CDA as a function of temperature. In neither of these works a measurement of the crystalline content of the film is reported, therefore a typical value of ~30 wt% for CDA was employed. The temperature dependence of the density was accounted for using the thermal expansion coefficient at atmospheric pressure retrieved from the *PVT* measurements (**Table 3.3**). The data set was well represented by the NELF model, as it can be seen in **Figure 3.9**. The best fit values of the binary interaction parameters obeyed a linear temperature dependence, whereas a quadratic one was obtained in the case of the swelling coefficients. These relations are reported in **Table 3.6**. In this case, higher values of the binary interaction parameters were obtained compared to those reported in **Table 3.5**. In particular, in the case of CO_2 the value obtained is approximately double, while for CH_4 it is about 40% higher. The binary parameters are much more sensitive to the uncertainty in the calculation, in particular on the crystalline fraction of the sample and, in turn, on the density values used. The swelling coefficients, on the other hand, are much more similar (about 10% difference) between the two data sets, which is a positive indication of their physical meaning and of the assumptions made in the calculation.

This test showed a good transferability of the pure component parameters of CDA in the representation of sorption isotherms of CO_2 and CH_4 at different temperatures.

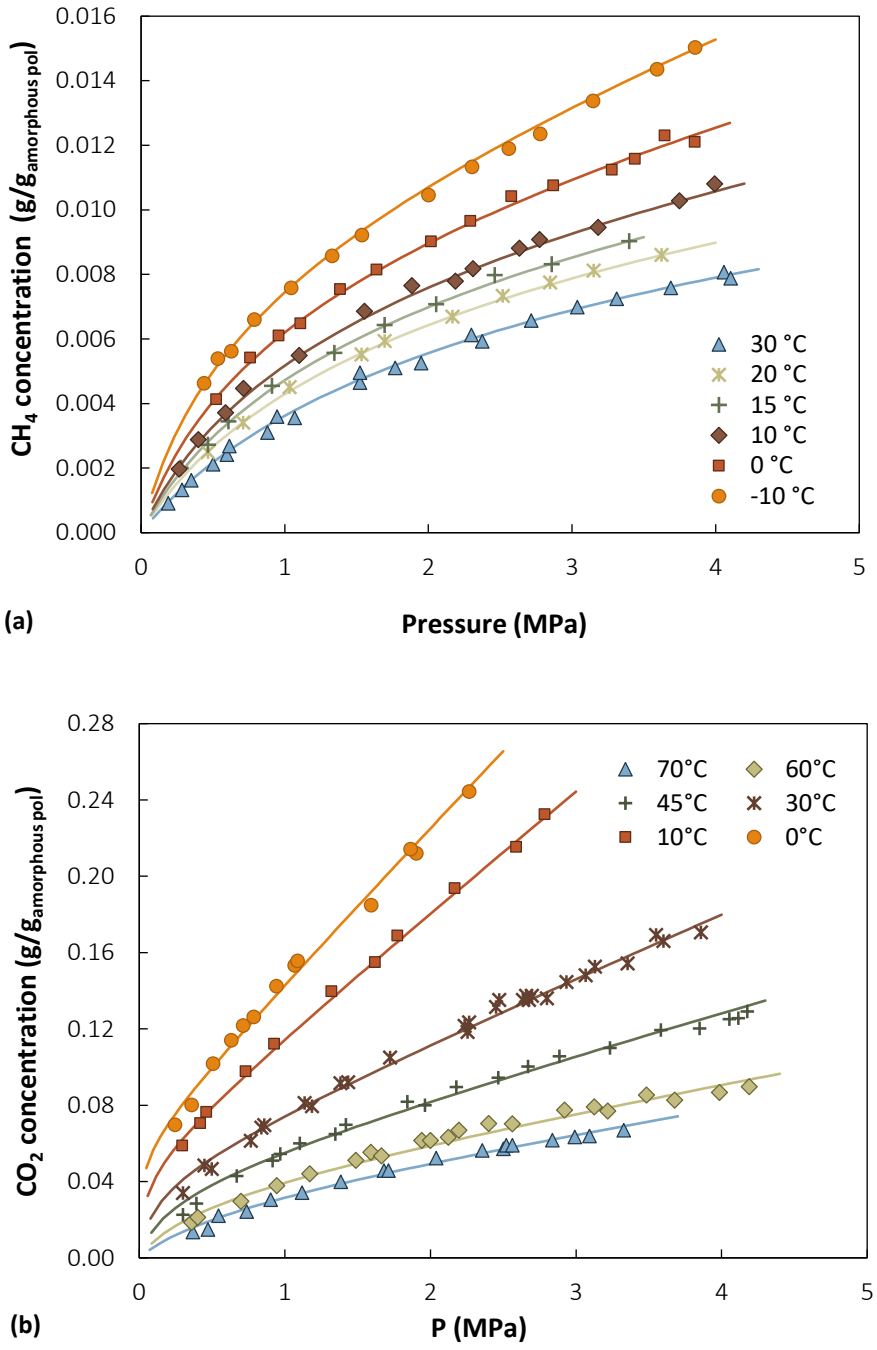

Figure 3.9. Experimental sorption isotherms of (a) CH_4 (ref. [47]) and (b) CO_2 (ref. [46]) in cellulose diacetate at different temperatures, together with NELF model calculations.

Table 3.6. Temperature dependence of the binary interaction and swelling coefficients used to model sorption isotherms of refs. [46,47].

	k_{ij} (T in K)	k_{sw} MPa^{-1} (T in K)
CH_4	$-3.927 \cdot 10^{-4}\,T + 1.233 \cdot 10^{-2}$	$2.208 \cdot 10^{-6}\,T^2 - 1.354 \cdot 10^{-3}\,T + 0.208$
CO_2	$1.060 \cdot 10^{-3}\,T - 4\text{-}653 \cdot 10^{-1}$	$1.308 \cdot 10^{-5}\,T^2 - 8.992 \cdot 10^{-3}\,T + 1.558$

3.7 Mixed-gas Sorption Prediction

The NELF model allows to perform mixed-gas sorption calculations predictively, once the parameters of the pure components and the binary interaction coefficients have been retrieved from the analysis of pure-gas sorption data. In **Figure 3.10**, the results of mixed-gas sorption of CO_2/CH_4 mixtures at three different compositions (10/90 – 30/70 – 50/50) in CDA and CTA are shown. The calculation was performed using the SL parameters reported in **Table 3.4** and the binary interaction coefficients reported in **Table 3.5**. Data are reported in terms of gas fugacity. Fugacity was calculated using the Peng-Robins Equation of State [48], using a value of 0.09 for the binary interaction parameter between CO_2 and CH_4 [49].

The results suggest the existence of strong competitive sorption effects for both materials: CH_4 sorption is markedly lowered in the presence of CO_2, while at multicomponent conditions CO_2 is sorbed to a very similar extent to the pure-gas case. Competitive sorption in the case of the sorption of CO_2/CH_4 mixtures in glassy polymers has been measured experimentally for several high and low free volumes materials, as it will be seen in **Chapter 4**. The predicted effect of the presence of CH_4 on CO_2 sorption is negligible in the case of CAs, compared to the materials analyzed in the next chapter. Indeed, in this case the difference in solubility of CO_2 and CH_4 is markedly higher, which can explain why CO_2 is less affected by competition in this case: previous analysis [50] had shown that the higher the molar concentration of one gas with respect to another inside the membrane, the more favored it would be in the competition for sorption sites.

The calculated sorption isotherms allowed to determine the **solubility-selectivity** of the two materials at multicomponent conditions, using the following relation:

$$\alpha^{S}_{CO2/CH4} = \frac{S_{CO2}}{S_{CH4}} = \frac{c_{CO2}/f_{CO2}}{c_{CH4}/f_{CH4}} \qquad \text{Eq. (3.4)}$$

The results are shown in **Figure 3.11** together with the predicted ideal selectivity, which is simply taken as the ratio of the solubility coefficients of the two gases at a given value of the total pressure. Competitive sorption enhances the solubility-selectivity at multicomponent conditions, up to a factor 2 at higher CO_2 concentration in the mixture. The solubility-selectivity is found to increase at higher CO_2 content in the gas phase, and it shows a non-monotonic trend with pressure, but qualitatively similar for both materials and the three compositions, whereas ideal solubility selectivity shows a minimum around 15 bar. This is an indication of how misleading evaluations based on pure-gas data can be, not only quantitatively, but also qualitatively.

The concentration dependence of the solubility-selectivity predicted by the model is very modest and it was found to be smaller than the error bars associated to the evaluation of the solubility-selectivity at a given concentration. The uncertainty in the solubility-selectivity calculation was assessed as follows: the error bars of the SL parameters reported in **Table 3.4** were subdivided into small intervals and triplets of SL parameters were constructed from all possible combinations of admissible parameters. For each triplet, optimal values of the adjustable coefficients were obtained and used to perform mixed-gas sorption calculations, from which the selectivity was then evaluated. As an example, the range of calculated solubility-selectivity for the 30:70 CO_2/CH_4 mixture in CDA is reported in **Figure 3.12**. The same qualitative

and quantitative behavior was observed also in the other cases. The variability in the evaluation of the selectivity resulting from the uncertainty in the determination of the SL parameters is remarkably limited (about ± 0.5), which is an indication of the robustness of the model.

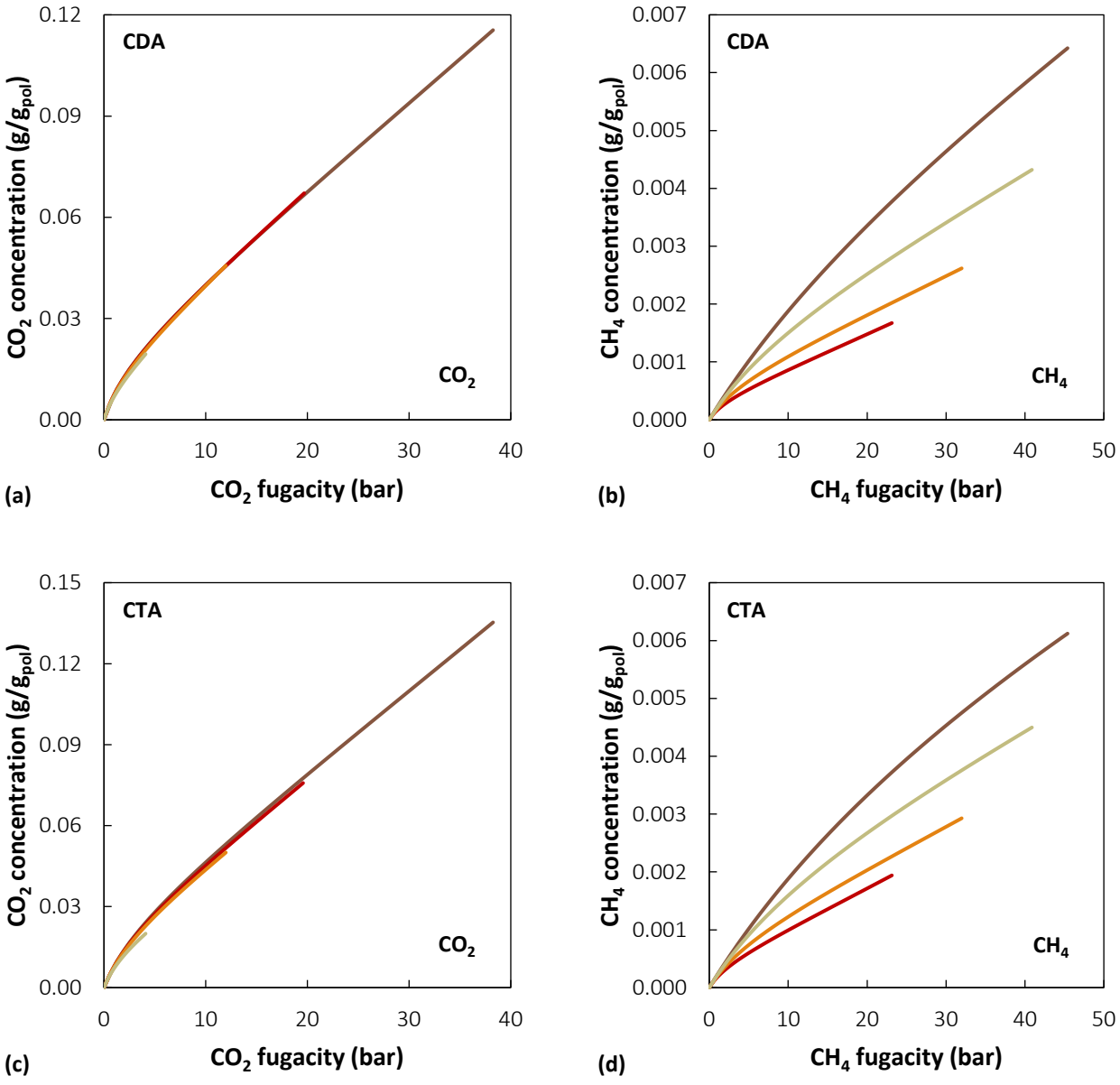

Figure 3.10. Mixed-gas sorption of 10/90 (green), 30/70 (orange) and 50/50 (red) mol% CO_2/CH_4 mixtures in CTA and CDA at 35 °C calculated with the NELF model. The brown lines represent pure-gas sorption.

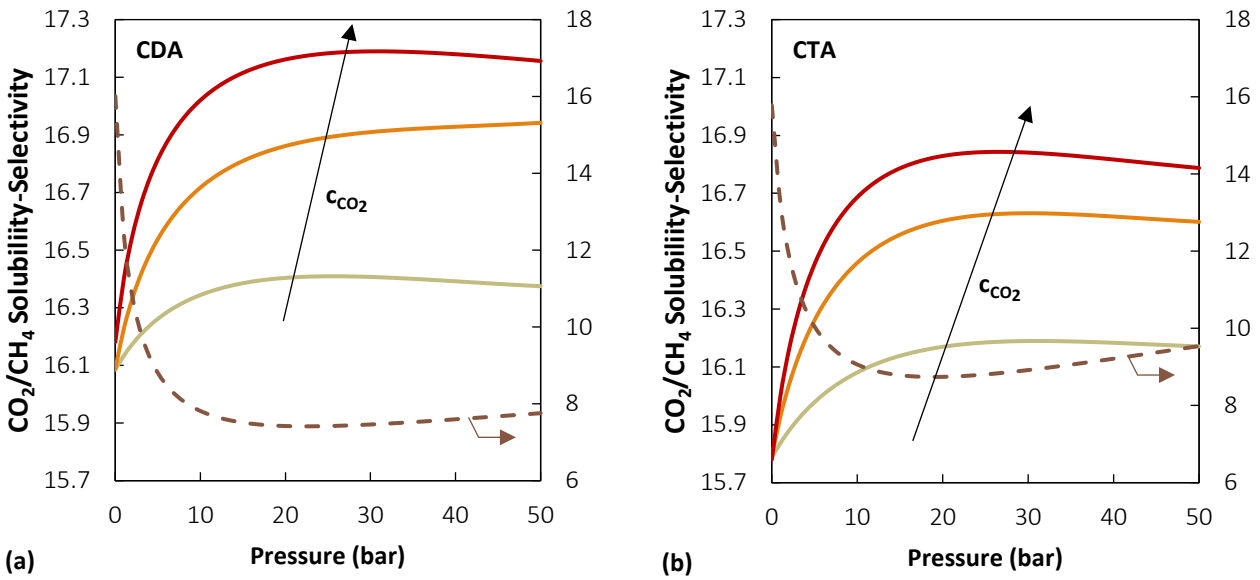

Figure 3.11. CO_2/CH_4 solubility-selectivity in (a) CDA and (b) CTA calculated with the NELF model at 35 °C and at different mixture compositions: 10/90 mol% in green, 30/70 mol% in orange, 50/50 mol% in red. Brown dashed lines represent the ideal solubility-selectivity calculated with pure-gas solubility and it is read on the right y-axis.

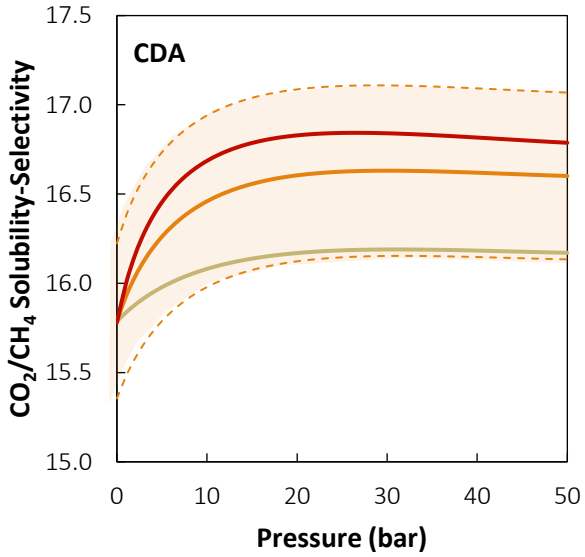

Figure 3.12. The shaded area represents the range of calculated solubility-selectivity for a 30:70 CO_2/CH_4 mixture in CDA at 35 °C as a result of the uncertainty in the estimation of the SL parameters of the polymer.

The enhancement of solubility-selectivity at multicomponent conditions, which is a positive effect for the separation at hand, can be quantified in the following way. For a given value of the total pressure and composition, one has the corresponding values of the sorbed concentration and fugacity of both gases. These values can be compared to the sorbed concentration of the pure gases at the same fugacity. In this way, the ratio of multicomponent to ideal solubility selectivity is calculated. The results of this comparison

is shown in **Figure 3.13** and it can be seen that the enhancement of solubility-selectivity at multicomponent conditions is stronger in CDA. Even though CDA has a lower ideal solubility-selectivity, at multicomponent conditions, CDA displays a higher solubility selectivity compared to CTA. This effect could be ascribed to its higher plasticization resistance, testified by the lower values of the CO_2 swelling coefficients associated to CDA compared to CTA.

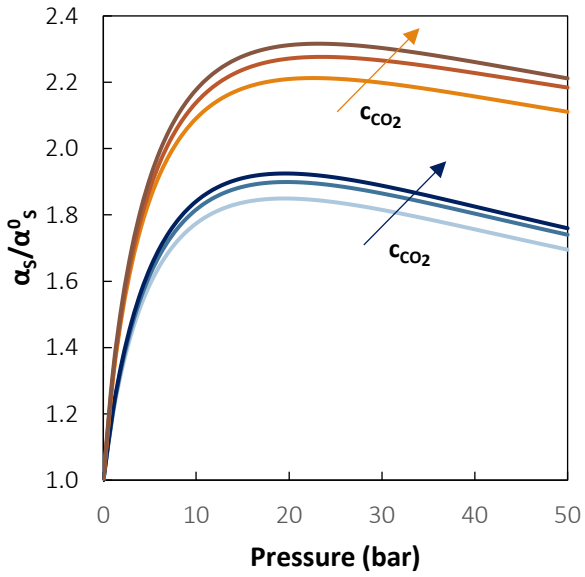

Figure 3.13. Ratio of ideal and multicomponent solubility-selectivity in CDA (orange) and CTA (blue) calculated with the NELF model at 35 °C. The arrows point in the direction of increasing CO_2 content in the gas phase.

3.8 Conclusions

Pressure-Volume-Temperature measurements were performed on thick samples of cellulose diacetate and triacetate obtained via solution casting and characterized via DSC and TGA measurements. There is great variability in the literature concerning the characterization of cellulose acetate materials, due to the complex dependency of their properties on multiple variables, such as crystalline content, degree of substitution and preparation protocol. Nonetheless, the results obtained for the samples in this study were within the expected range.

The volumetric behavior of the materials in their equilibrium region (i.e. above T_g) was used to obtain the parameters of the Sanchez-Lacombe equation of state for both materials. Subsequently, these parameters were used to model sorption isotherms of CO_2 and CH_4, in a wide range of temperatures and pressures with small values of the adjustable parameters. This provided a good indication of the transferability of the pure-polymer parameters obtained. The model allowed also to carry out a predictive simulation of sorption at multicomponent conditions. These results could not be validated, in the absence of the corresponding

experimental measurements. Nonetheless, this analysis provided indications of the strength of competitive sorption effects at different mixture compositions and different degrees of substitution of the material. CDA exhibited a higher enhancement of the solubility-selectivity as a result of competitive sorption compared to CTA, and also higher values of the solubility-selectivity at multicomponent conditions.

In the future, the volumetric data reported here could be used to parametrize also other equations of state, for example of the SAFT family, more suited to the representation of polar and associating components such as water or alcohol vapors. This could benefit the study of the effect of humidity on the solubility in gas separation applications or extend the modelling analysis of cellulose acetates with the NET-GP approach also to other potential applications.

Moreover, the characterization of the properties amorphous CAs reported here could also be useful in assessing the accuracy of different general-purpose force fields used in molecular simulations in the representation of the properties of amorphous cellulose acetates at different DS, since molecular modelling studies on amorphous CAs were not reported to date, with one exception [44]. More studies were performed to investigate the crystalline phase [51–53] to support the experimental analysis [37,39,54–57]. A valuable contribution coming from molecular modelling would be also the analysis of the crystalline phase, as the assumption of its impermeability to penetrant molecules could be tested and insight on the constraining effects of the crystallites on the amorphous phase gained.

3.9 Attribution

Pressure-Volume-Temperature tests with a GNOMIX apparatus were performed by prof. E. Di Maio at the University of Naples, while pure CO_2 and CH_4 sorption measurements were performed by Dr. Liang Liu at the University of Melbourne.

References

1. Scholes, C.A.; Stevens, G.W.; Kentish, S.E. Membrane gas separation applications in natural gas processing. *Fuel* 2012, *96*, 15–28, doi:10.1016/j.fuel.2011.12.074.
2. Adewole, J.K.; Ahmad, A.L.; Ismail, S.; Leo, C.P. Current challenges in membrane separation of CO_2 from natural gas: A review. *Int. J. Greenh. Gas Control* 2013, *17*, 46–65.
3. Baker, R.W.; Lokhandwala, K. Natural gas processing with membranes: An overview. *Ind. Eng. Chem. Res.* 2008, *47*, 2109–2121, doi:10.1021/ie071083w.
4. Robeson, L.M.; Dose, M.E.; Freeman, B.D.; Paul, D.R. Analysis of the transport properties of thermally rearranged (TR) polymers and polymers of intrinsic microporosity (PIM) relative to upper bound performance. *J. Memb. Sci.* 2017, *525*, 18–24, doi:10.1016/j.memsci.2016.11.085.
5. Funk, E.W.; Kulkarni, S.S.; Swamikannu, A.X. Effect of impurities on cellulose acetate membrane performance. *Recent Adv. Sep. Tech. AIChE Symp. Ser.* 1986, *250*.
6. Lu, H.T. The impact of impurities on the performance of cellulose triacetate membranes for CO_2 separation, University of Melbourne, 2018.
7. Puleo, A.C.; Paul, D.R.; Kelley, S.S. The Effect Of Degree Of Acetylation On Gas Sorption And Transport Behaviour In Cellulose Acetate. *J. Memb. Sci.* 1989, *47*, 301–332.
8. Cerveira, G.S.; Borges, C.P.; Kronemberger, F. de A. Gas permeation applied to biogas upgrading using cellulose acetate and polydimethylsiloxane membranes. *J. Clean. Prod.* 2018, *187*, 830–838, doi:10.1016/j.jclepro.2018.03.008.
9. Lu, H.T.; Kanehashi, S.; Scholes, C.A.; Kentish, S.E. The potential for use of cellulose triacetate membranes in post combustion capture. *Int. J. Greenh. Gas Control* 2016.
10. Uddin, M.E.; Layek, R.K.; Kim, H.Y.; Kim, N.H.; Hui, D.; Lee, J.H. Preparation and enhanced mechanical properties of non-covalently-functionalized graphene oxide/cellulose acetate nanocomposites. *Compos. Part B Eng.* 2016, *90*, 223–231, doi:10.1016/j.compositesb.2015.12.008.
11. Mubashir, M.; Fong, Y.Y.; Leng, C.T.; Keong, L.K. Prediction of CO_2 permeability in NH2-MIL-53(Al)/cellulose acetate mixed matrix membranes using theoretical models. *Int. J. Integr. Eng.* 2018, *10*, 176–180, doi:10.30880/ijie.2018.10.05.026.
12. Nikolaeva, D.; Azcune, I.; Tanczyk, M.; Warmuzinski, K.; Jaschik, M.; Sandru, M.; Dahl, P.I.; Genua, A.; Loïs, S.; Sheridan, E.; Fuoco, A.; Vankelecom, I.F.J. The performance of affordable and stable cellulose-based poly-ionic membranes in CO_2/N_2 and CO_2/CH_4 gas separation. *J. Memb. Sci.* 2018, *564*, 552–561, doi:10.1016/j.memsci.2018.07.057.
13. Ding, S.H.; Chew, T.L.; Oh, P.C.; Ahmad, A.L.; Jawad, Z.A. Preparation of mixed matrix membrane using cellulose acetate incorporated with synthesized KIT-6 silica. *J. Mech. Eng. Sci.* 2018, *12*, 3505–3514, doi:10.15282/jmes.12.1.2018.17.0311.
14. Najafi, M.; Sadeghi, M.; Bolverdi, A.; Pourafshari Chenar, M.; Pakizeh, M. Gas permeation properties of cellulose acetate/silica nanocomposite membrane. *Adv. Polym. Technol.* 2018, *37*, 2043–2052, doi:10.1002/adv.21862.
15. Sanaeepur, H.; Ahmadi, R.; Sinaei, M.; Kargari, A. Pebax-Modified Cellulose Acetate Membrane for CO_2/N_2 Separation. *J. Membr. Sci. Res.* 2019, *5*, 25–32, doi:10.22079/JMSR.2018.85813.1190.
16. Sundell, B.J.; Harrigan, D.J.; Hayden, S.C.; Vaughn, J.T.; Guzan, K.A.; Lawrence III, J.A.; Ostraat, M.L. Improved gas transport properties of cellulose acetate via sub-Tg acid-catalyzed silanation. *J. Memb. Sci.* 2018, *573*, 448–454, doi:10.1016/j.memsci.2018.11.077.
17. Saberi, M.; Dadkhah, A.A.; Hashemifard, S.A. Modeling of simultaneous competitive mixed gas permeation and CO_2 induced plasticization in glassy polymers. *J. Memb. Sci.* 2016, *499*, 164–171, doi:10.1016/j.memsci.2015.09.044.
18. Saberi, M.; Hashemifard, S.A.; Dadkhah, A.A. Modeling of CO2/CH4 gas mixture permeation and CO_2 induced plasticization through asymmetric cellulose acetate membrane. *RSC Adv.* 2016, *6*, 16561–16567, doi:10.1039/C5RA23506E.
19. Magnanelli, E.; Wilhelmsen, Ø.; Johannessen, E.; Kjelstrup, S. Enhancing the understanding of heat and mass transport through a cellulose acetate membrane for CO_2 separation. *J. Memb. Sci.* 2016, *513*, 129–139, doi:10.1016/j.memsci.2016.04.021.

20. Guo, J.; Barbari, T.A. Unified dual mode description of small molecule sorption and desorption kinetics in a glassy polymer. *Macromolecules* 2009, *42*, 5700–5708, doi:10.1021/ma9007576.

21. Guo, J.; Barbari, T.A. A dual mode, local equilibrium relaxation model for small molecule diffusion in a glassy polymer. *Macromolecules* 2008, *41*, 238–245, doi:10.1021/ma071662c.

22. Perrin, L.; Nguyen, Q.T.; Sacco, D.; Lochon, P. Experimental studies and modelling of sorption and diffusion of water and alcohols in cellulose acetate. *Polym. Int.* 1997, *42*, 9–16, doi:10.1002/(SICI)1097-0126(199701)42:1<9::AID-PI637>3.0.CO;2-A.

23. Bocahut, A.; Delannoy, J.-Y.; Long, D.R.; Sotta, P. Modeling Molecular Relaxation Mechanisms in Amorphous Polymers: Application to Polyamides. *Macomolecules* 2016, *49*, 1918–1932, doi:10.1021/acs.macromol.5b01963.

24. Doghieri, F.; Sarti, G.C. Nonequilibrium Lattice Fluids: A Predictive Model for the Solubility in Glassy Polymers. *Macromolecules* 1996, *29*, 7885–7896, doi:10.1021/ma951366c.

25. Sarti, G.C.; Doghieri, F. Predictions of the solubility of gases in glassy polymers based on the NELF model. *Chem. Eng. Sci.* 1998, *53*, 3435–3447, doi:10.1016/S0009-2509(98)00143-2.

26. Sanchez, I.C.; Lacombe, R.H. Statistical Thermodynamics of Polymer Solutions. *Macomolecules* 1978, *11*, 1145–1156.

27. Lacombe, R.H.; Sanchez, I.C. Statistical Thermodynamics of Fluid Mixtures. *J. Phys. Chem.* 1976, *80*, 2568–2580, doi:10.1021/j100564a009.

28. Kamide, K.; Saito, M. Thermal analysis of cellulose acetate solids with total degrees of substitution of 0.49, 1.75, 2.46, and 2.92. *Polym. J.* 1985, *17*, 919–928.

29. Spanic, N.; Jambrekovic, V.; Medved, S.; Antonovic, A. Chemical and Thermal properties of Cellulose Acetate Prepared from White Willw (Salix almba) and Black Alder (Alnus glutinosa) as Potential Polymeric Base of Biocomposite Materials. *Chem. Biochem. Eng. Q* 2015, *29*, 357–365, doi:10.15255/CABEQ.2015.2176.

30. Barud, H.S.; De Araújo Júnior, A.M.; De Assunção, R.M.N.; Meireles, C.S.; Cerqueira, D.A.; Filho, G.R.; Messaddeq, Y.; Ribeiro, S.J.L. Thermal Characterization of Cellulose Acetate Produced From Homogeneous Acetylation of Bacterial Cellulose. In *9no Congresso Brasilero de Polymeros*.

31. Zugenmaier, P. Characterization and physical properties of cellulose acetates. *Macromol. Symp.* 2004, *208*, 81–166, doi:10.1002/masy.200450407.

32. Tang, L.-G.; Hon, D.N.-S.; Zhu, Y.-Q. Polymorphic Transformations of Cellulose Acetates Prepared by Solution Acetylation at an Elevated Temperature. *J. Macromol. Sci. Part A* 1996, *33*, 203–208, doi:10.1080/10601329608010863.

33. Gillham, J.K. A semimicro thermomechanical technique for characterizing polymeric materials: Torsional braid analysis. *AIChE J.* 1974, *20*, 1066–1079, doi:10.1002/aic.690200603.

34. Cerqueira, D.A.; Filho, G.R.; Assunção, R.M.N.; Rodrigues Filho, G.; Assunção, R.M.N. A new value for the heat of fusion of a perfect crystal of cellulose acetate. *Polym. Bull.* 2006, *56*, 475–484, doi:10.1007/s00289-006-0511-9.

35. Mandelkern, L.; Flory, P.J. Melting and Glassy State Transitions in Cellulose Esters and their Mixtures with Diluents. 1951, *73*, 3206–3212.

36. Russel, J.; Van Kerpel, R.G. Transitions in Plasticized and Unplasticized Cellulose Acetates. *J. Polym. Sci.* 1957, *25*, 77–96.

37. Sikorski, P.; Wada, M.; Heux, L.; Shintani, H.; Stokke, B.T. Chrystal Structure of Cellulose Triacetate I. *Macromolecules* 2004, *37*, 4547–4553.

38. Sanchez, I.C.; Lacombe, R.H. An elementary molecular theory of classical fluids. Pure fluids. *J. Phys. Chem.* 1976, *80*, 2352–2362, doi:10.1021/j100562a008.

39. Wada, M.; Hori, R. X-Ray Diffraction Study of the Thermal Expansion Behavior of Cellulose Triacetate I. *J. Polym. Sci. B* 2009, *47*, 517–523, doi:10.1002/polb.

40. Hu, W.; Xie, J.; Chau, H.W.; Si, B.C. Evaluation of parameter uncertainties in nonlinear regression using Microsoft Excel Spreadsheet. *Environ. Syst. Res.* 2015, *4*, doi:10.1186/s40068-015-0031-4.

41. Bonavoglia, B.; Storti, G.; Morbidelli, M. Modeling of the sorption and swelling behavior of semicrystalline polymers in supercritical CO_2. *Ind. Eng. Chem. Res.* 2006, *45*, 1183–1200, doi:10.1021/ie050842c.

42. Minelli, M.; De Angelis, M.G. An equation of state (EoS) based model for the fluid solubility in semicrystalline

polymers. *Fluid Phase Equilib.* 2014, *367*, 173–181, doi:10.1016/j.fluid.2014.01.024.

43. Chen, G.Q.; Kanehashi, S.; Doherty, C.M.; Hill, A.J.; Kentish, S.E. Water vapor permeation through cellulose acetate membranes and its impact upon membrane separation performance for natural gas purification. *J. Memb. Sci.* 2015, *487*, 249–255, doi:10.1016/j.memsci.2015.03.074.
44. Bocahut, A.; Delannoy, J.-Y.; Caroll, V.; Mazeau, K. Conformational analysis of cellulose acetate in the dense amorphous state. 2014.
45. Doghieri, F.; Quinzi, M.; Rethwisch, D.G.; Sarti, G.C. Predicting Gas Solubility in Glassy Polymers through Nonequilibrium EOS. In *Advanced Materials for Membrane Separations*; American Chemical Society: Washington, DC, USA, 2004; pp. 74–90.
46. Stern, S.A.; De Meringo, A.H. Solubility of Carbon Dioxide in Cellulose Acetate at Elevated Pressures. *J. Polym. Sci. Part B Polym. Phys.* 1978, *16*, 751.
47. Stern, S.A.; Kulkarni, S.S. Solubility of Methane in Cellulose Acetate - Conditioning Effect of Carbon Dioxide. *J. Memb. Sci.* 1982, *10*, 235–251.
48. Peng, D.; Robinson, D.B. A New Two-Constant Equation of State. *Ind. Eng. Chem. Fundam.* 1976, *15*, 59–64, doi:10.1021/i160057a011.
49. Sandler, S.I. *Chemical, Biochemical, and Engineering Thermodynamics*; 5th Editio.; John Wiley & Sons: Hoboken, NJ, USA, 2017;
50. Ricci, E.; Minelli, M.; De Angelis, M.G. A multiscale approach to predict the mixed gas separation performance of glassy polymeric membranes for CO_2 capture: the case of CO_2/CH_4 mixture in Matrimid ®. *J. Memb. Sci.* 2017, *539*, doi:10.1016/j.memsci.2017.05.068.
51. Hayakawa, D.; Ueda, K.; Yamane, C.; Miyamoto, H.; Horii, F. Molecular dynamics simulation of the dissolution process of a cellulose triacetate-II nano-sized crystal in DMSO. *Carbohydr. Res.* 2011, *346*, 2940–2947, doi:10.1016/j.carres.2011.10.019.
52. Kobayashi, T.; Hayakawa, D.; Khishigjargal, T.; Ueda, K. Ab initio studies of the crystal structure of cellulose triacetate I. *MRS Proc.* 2012, *1470*, mrss12-1470-xx03-05, doi:10.1557/opl.2012.1204.
53. Kobayashi, T.; Hayakawa, D.; Khishigjargal, T.; Ueda, K. Investigation of the structure and interaction of cellulose triacetate I crystal using ab initio calculations. *Carbohydr. Res.* 2014, *388*, 61–66, doi:10.1016/j.carres.2014.02.015.
54. Roche, E.; Chanzy, H.; Boudeulle, M.; Marchessault, R.H.; Sundararajan, P. Three-Dimensional Crystalline Structure of Cellulose Triacetate II. *Macromolecules* 1978, *11*, 86–94, doi:10.1021/ma60061a016.
55. Hiroyuki K.; Tomoki E.; Takai, M. CP/MAS ^{13}C NMR Study of Cellulose and Cellulose Derivatives. 2. Complete Assignment of the ^{13}C Resonance for the Ring Carbons of Cellulose Triacetate Polymorphs. 2002, doi:10.1021/JA010705G.
56. Braun, J.L.; Kadla, J.F. CTA III: A third polymorph of cellulose triacetate. *J. Carbohydr. Chem.* 2013, *32*, 120–138, doi:10.1080/07328303.2012.752493.
57. Stipanovic, A.J.; Sarko, A.; The, I. Molecular and crystal structure of cellulose triacetate I: A parallel chain structure. *Polymer (Guildf).* 1978, *19*, 3–8, doi:10.1016/0032-3861(78)90164-7.

Chapter 4

Modelling Mixed-Gas Sorption in Glassy Polymers

4.1 Introduction

The sorption of gas mixtures in materials suitable for CO_2 separation has been characterized experimentally in previous works, which showed that, in the multicomponent case, these systems exhibit rather marked deviations from the ideal pure-gas behavior. Due to competitive sorption effects, the solubility of both species at mixed-gas conditions is lower than the corresponding pure-gas solubility at the same fugacity.

This behavior has been documented in the following glassy polymers: hexafluorodianhydride–3,3,4,4-tetraaminodiphenyl oxide polypyrrolone (6FDA-TADPO) [1], poly(1-trimethylsilyl-1-propyne) (PTMSP) [2], polybenzodioxane PIM-1 [3,4], tetrazole-modified PIM-1 (TZ-PIM) [5], 4,4'-(hexafluoroisopropylidene) diphthalic dianhydride-m-phenylenediamine (6FDA-mPDA) [6], PIM-Trip-TB, a ladder polymer of intrinsic microporosity [7], PIM-EA-TB, an ethanoanthracene-based (EA) polymer of intrinsic microporosity (PIM), obtained through Tröger's base (TB) polymerization reaction [8], 3,3'-dihydroxy-4,4'-diamino-biphenyl (HAB) 2,2'-bis-(3,4-dicarboxyphenyl) hexafluoropropane dianhydride (6FDA) polyimide and in its thermally rearranged (TR) derivative, TR450 [9]. Moreover, competitive sorption effects have been highlighted also in the case of CO_2/CH_4 sorption in a rubbery polymer, polydimethylsiloxane (PDMS) [10], and in other systems, such as CO_2/C_2H_4 and CO_2/N_2O sorption in PMMA [11–13], CH_4/nC_4H_{10} sorption in PTMSP [14] and PDMS [15], CO_2/C_2H_6 sorption in a cross-linked poly(ethylene oxide) copolymer [16].

In general, competition originating from the presence of other penetrants has a higher effect on CH_4, while CO_2 behavior is hardly altered, therefore competitive sorption effects enhance the solubility-selectivity compared to its ideal value up to a factor 5, especially at high pressure and when the fraction of the second component is increased. Therefore, neglecting these effects in the design of the separation operation can be a nonnegligible source of error. Mixed-gas experiments are very delicate and much more time consuming than pure-gas tests, therefore, in an effort to reduce the experimental tests required to characterize the mixed-gas solubility and solubility-selectivity of materials for membrane separation processes, there is a need for reliable models which involve a minimum number of adjustable parameters.

Here, the Non-Equilibrium Lattice Fluid Model (NELF) [17] and the Dual Mode Sorption (DMS) model are applied to predict mixed-gas CO_2/CH_4 solubility and solubility-selectivity in PTMSP, PIM-1, TZ-PIM, PIM-EA-TB, HAB-6FDA and its thermally rearranged derivative TR450, at three mixture compositions (10, 30, 50 mol.% CO_2) and in the case of PIM-1 and TZ-PIM at three temperatures (25, 35, 50 °C), up to 35 bar. These conditions were chosen because experimental data are available for comparison and validation of the calculations. The repeating units of the materials considered in this study are reported in **Figure 4.1**. They are all glassy polymers, characterized by very high free volume (reported in **Table 4.1**) , with the exception of HAB-6FDA, which is a low free volume glassy polymer.

PTMSP, being the most permeable dense polymer [18], is a natural reference point to assess the separation performance of high free volume materials, as is PIM-1, which was the first material of the PIM class to be reported [19]. It is interesting to compare the behavior of TZ-PIM and PIM-1, since TZ-PIM constitutes an attempt at improving the selectivity of PIM-1 towards CO_2 by incorporating more CO_2-philic groups into its structure. In this case the nitrile groups were substituted by tetrazole groups [20], but Satilmis et al. [21]

showed that it is also possible to reduce them to primary amines, obtaining a material termed amine-PIM-1, with intermediate features between PIM-1 and TZ-PIM. These materials were chosen, among the few glassy polymers for which CO_2/CH_4 mixed-gas sorption has been characterized experimentally, because their NELF model parameters are available in the literature. Equation of State parameters for gases and vapors are usually retrieved fitting Vapor-Liquid Equilibrium (VLE) data, whereas for polymers, the most appropriate choice would be fitting pressure-volume-temperature (*pVT*) data above the glass transition, where the material is in a state of thermodynamic equilibrium, and this was indeed the approach followed to study gas sorption in cellulose acetates presented in **Chapter 3**. However, for high free volume glassy polymer these data are usually unavailable, because of the onset of degradation phenomena before the glass transition is reached. In most calorimetric experiments, PIM-1, for instance, decomposed around 350 °C without an apparent glass transition [22]. Recently, Yin et al. [23] were able to observe a glass transition for PIM-1 at 442 °C without degrading the material, by employing fast scanning calorimetry. In conventional dilatometric experiments performed to measure *pVT* data, however, such heating rates required to avoid degradation would be unattainable. In these cases, an alternative approach can be followed, fitting the EoS parameters on the sorption equilibrium data directly, using a nonequilibrium model [24]. The parameters for PIM-1 used in this work were indeed retrieved using this method [25] by analyzing a large data set comprising solubility at infinite dilution of light gases (CO_2, N_2, CH_4, O_2) and several vapors (n-butane, n-pentane, i-pentane, n-hexane, n-heptane, methanol, ethanol, 1-propanol, 1-butanol, water, chloroform, toluene, 1,4-dioxane, tetrahydrofurane). Pure-gas sorption of several gases in HAB-6FDA and its TR variants was modelled by Galizia et al. [26] using the Non-Equilibrium Lattice Fluid (NELF) model. In their work, pure component parameters of the Sanchez-Lacombe EoS for HAB-6FDA and TR450 were obtained, optimized over solubility at infinite dilution of light gases (He, H_2, N_2, CH_4, CO_2) in the temperature range -10/50 °C. If a large enough characterization of pure-gas sorption has not been performed for a material with a very high T_g, neither parametrization route can be employed to obtain the pure-polymer parameters, therefore, calculations with the NELF model cannot be performed. This is a limitation which is not present in the case of the DMS model: in order to perform mixed-gas sorption calculations at one temperature, for one gas couple, all the DMS parameters needed can be retrieved from pure-gas sorption isotherms of the two gases at the same temperature. However, the parameters of this model are non-transferable to other conditions.

In this work, pure component NELF parameter sets from the literature were used to model pure-gas sorption isotherms, in order to optimize the values of the binary adjustable parameters, k_{ij} and k_{sw}. DMS model parameters sets were obtained for each polymer-gas couple and applied to predict mixed-gas sorption in the conditions listed above. Moreover, sensitivity analyses were carried out, in order to verify the robustness of the calculations to various perturbations and the reliability of the prediction in absence of experimental data for validation. It should be pointed out that neither model requires additional parameters to take into account the mixed-gas effects in the ternary system, and all the system-specific parameters come from the best fit of pure-gas sorption data. This makes these models potentially powerful tools, considering that pure-gas sorption has already been characterized for a wide variety of polymer materials in the past decades, and, for many of them, NELF and DMS parameters can be readily obtained.

(a) **PTMSP**

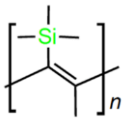

(b) **PIM-1**

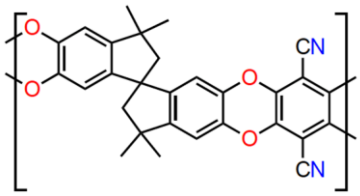

(c) **TZ-PIM**

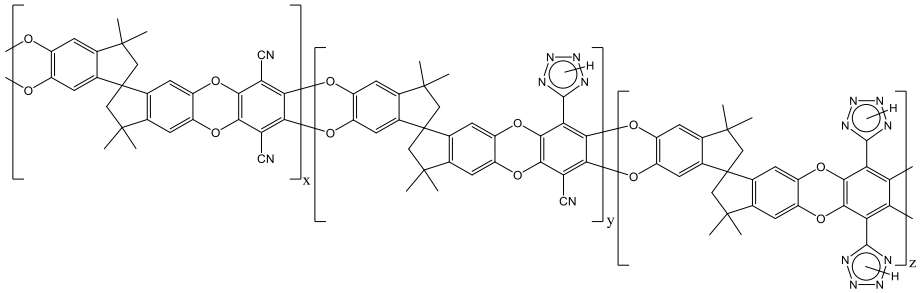

(d) **PIM-EA-TB**

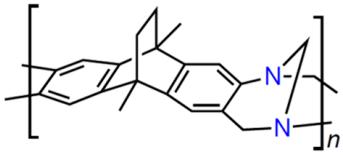

(e) **HAB-6FDA**

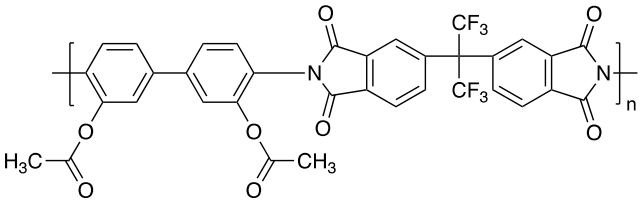

(f) **TR450**

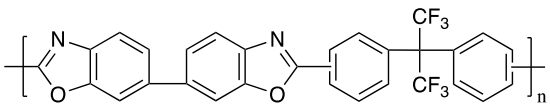

Figure 4.1. Repeating units of the polymers considered in this study: (a) PTMSP (b) PIM-1 (c) TZ-PIM (d) PIM-EA-TB (e) HAB-6FDA (f) TR450.

Table 4.1. Fractional free volumes of the polymers considered in this work.

	FFV %	Ref.		*FFV* %	Ref.
PTMSP	34	[27]	**PIM-EA-TB**	23	*
PIM-1	26	[28]	**HAB-6FDA**	15	[29]
TZ-PIM	25	*	**TR450**	19.6	[29]

* Estimated here with Bondi's group contribution method [30].

4.2 Pure-Gas Sorption Modelling

4.2.1 NELF model parameters

The values of Sanchez-Lacombe EoS pure-component parameters for the materials considered in this study are reported in **Table 4.2**. The extension of this EoS to the non-equilibrium case (NELF) was used to model pure gas sorption isotherms. The first step of the calculation consisted in the analysis of pure-gas sorption isotherms with the model, in order to obtain also the values of the binary interaction parameter k_{ij} and the swelling coefficient k_{sw}, subsequently used in the calculation of mixed-gas sorption. The value of the binary interaction parameter is obtained from the best fit of the low-pressure range of the sorption isotherms, taking advantage of the fact that, in these conditions, penetrant-induced swelling is negligible, and therefore the value of k_{sw} does not influence the result and can be set equal to zero. The value of k_{sw} is subsequently obtained from the best fit of the high-pressure range of the curve, once the appropriate value for k_{ij} has been retrieved. In this way, the effects of coupling of the adjustable parameters are minimized. However, it was verified that such effects would not results in large uncertainty in the model parameters in the case of NELF: a simultaneous optimization of both parameters using the whole experimental data set results in less than 1% difference in the values of k_{sw} and less than 5% in the case of k_{ij}. Each point in the sorption isotherm is calculated by solving the phase equilibrium condition (**Eq. (2.55)**) making use of the expression for the chemical potential of the gas in the non-equilibrium glassy matrix given by **Eq. (2.57)** and assuming a linear relationship between the polymer specific volume and the penetrants partial pressure, expressed with the swelling coefficients (**Eq. (2.56)**). The expression for the chemical potential in the gas phase makes use of the equilibrium density of the gas phase calculated by solving the EoS.

Table 4.3 reports the values of binary interaction parameters and swelling coefficients obtained from the analysis of pure-gas sorption data with the NELF model. In the case where data at multiple temperatures were analyzed, the parameters are found to follow a linear temperature dependence. In all cases, the values of the swelling coefficients obtained for CH_4 are lower than the corresponding ones obtained for CO_2, consistently with the experimental evidence of CO_2 being a stronger swelling agent than CH_4. The pure-components and binary parameters are then used to evaluate sorption at mixed-gas conditions, solving the phase equilibrium equations. Even in the multicomponent case, only binary interactions are considered, according to the mixing rules of the lattice fluid theory.

The dry polymer density values adopted are those reported for the experimental samples in the respective works: 0.770 g/cm^3 for PTMSP at 35 °C [2], 1.143 g/cm^3 for PIM-1 at 25 °C [3] and 1.186 g/cm^3 for TZ-PIM at 25 °C [5], 1.08 g/cm^3 for PIM-EA-TB at 35 °C [31], 1.407 g/cm^3 for HAB-6FDA [9] and 1.34 g/cm^3 for TR450 at 35 °C [9]. The temperature dependence of the PIMs density was accounted for, by using the thermal expansion coefficient reported in ref. [32] for a similar material (PIM-7): $6.4 \cdot 10^{-4}$ K^{-1}. Atomistic simulations of the volumetric properties of PIM-1 as a function of temperature, yielded similar values of the thermal expansion coefficient of this material: $8.3 \cdot 10^{-4}$ K^{-1} [33] and $2.5 \cdot 10^{-4}$ K^{-1} [34].

Table 4.2. Sanchez Lacombe EoS pure component parameters used for NELF calculations

	$T^*(K)$	$p^*\ (MPa)$	$\rho^*\ (g/cm^3)$	Ref.
PTMSP	610	380	1.125	[35]
PIM-1	872	523	1.438	[36]
TZ-PIM	550	800	1.657	[37]
PIM-EA-TB	820	430	1.500	[37]
HAB-6FDA	720	481.1	1.609	[26]
TR450	930	446.9	1.528	[26]
CO_2	300	630	1.515	[38]
CH_4	215	250	0.500	[39]

Table 4.3. Binary interaction and swelling coefficients used in NELF calculations (temperature T is in K), obtained from the analysis of pure-gas sorption data from refs. [2–5,9].

		k_{ij}	$k_{sw}\ (MPa^{-1})$
PTMSP	CO_2	0.0876	0.0212
	CH_4	0.0580	0
PIM-1	CO_2	$1.200 \cdot 10^{-4}\ T - 5.578 \cdot 10^{-2}$	$-1.479 \cdot 10^{-3}\ T + 4.949 \cdot 10^{-1}$
	CH_4	$8.000 \cdot 10^{-4}\ T - 2.685 \cdot 10^{-1}$	$-3.284 \cdot 10^{-4}\ T + 1.062 \cdot 10^{-1}$
TZ-PIM	CO_2	$-6.789 \cdot 10^{-4}\ T + 2.353 \cdot 10^{-1}$	$-1.396 \cdot 10^{-3}\ T + 4.532 \cdot 10^{-1}$
	CH_4	$8.000 \cdot 10^{-4}\ T - 3.085 \cdot 10^{-1}$	0.0131 (25 °C) 0 (35 -50 °C)
PIM-EA-TB	CO_2	0.010	0.020
	CH_4	0.012	0
HAB-6FDA	CO_2	-0.025	0.007
	CH_4	0.052	0
TR450	CO_2	-0.085	0.023
	CH_4	-0.037	0

Mixed-gas sorption calculations require the use of a binary interaction parameter also for the gas couple. The value of CO_2/CH_4 binary interaction parameter was optimized by fitting the CO_2/CH_4 pressure-volume-temperature-composition curves reported by Liu et al. [40] to the Sanchez-Lacombe EoS. The details of the calculation are reported in **Section 4.2.1.1**. A value of –0.03 was obtained, which was used in all mixed-gas sorption calculations with the NELF model. However, the effect of this parameter on mixed-gas sorption results is found to be negligible, as discussed in greater detail in **Section 4.3.1.3**.

4.2.1.1 CO_2/CH_4 Binary interaction parameter for the Sanchez-Lacombe Equation of State

The binary interaction parameter (k_{ij}) of the Sanchez-Lacombe (SL) EoS for the CO_2/CH_4 couple was determined from the analysis of pressure-volume-temperature-composition curves reported by Liu et al. [40] in the range 313 to 353 K, 3 to 18 MPa, 10 mol% to 90 mol% CO_2. The sum of absolute errors was minimized in the optimization, by varying the value of k_{ij}:

$$\mathrm{err} = \sum_{n=1}^{N} \left| \frac{\rho_n^{EoS} - \rho_n}{\rho_n} \right| \qquad \text{Eq. (4.1)}$$

In the formula ρ is the experimental density of the mixture, *N* is the number of experimental data points *n*, and ρ^{EoS} is the density of the mixture calculated with the SL EoS, whose expression is recalled below (all variables are defined in **Table 2.1**):

$$\tilde{\rho} = 1 - \exp\left[-\frac{\tilde{\rho}^2}{\tilde{T}} - \frac{\tilde{p}}{\tilde{T}} - \tilde{\rho}\left(1 - \sum\nolimits_i^N \frac{\phi_i}{r_i}\right)\right] \qquad \text{Eq. (4.2)}$$

As goodness-of-fit indicators, the average absolute deviation (AAD) and the maximum absolute deviation (MAD) between experimental data and model predictions were calculated:

$$\mathrm{AAD} = \frac{1}{N_{tot}} \sum_{n=1}^{N} \left| \frac{\rho_n^{EoS} - \rho_n}{\rho_n} \right| \qquad \text{Eq. (4.3)}$$

$$\mathrm{MAD} = max \left| \frac{\rho_n^{EoS} - \rho_n}{\rho_n} \right| \qquad \text{Eq. (4.4)}$$

Here ρ is the experimental mass density, ρ^{EoS} is the value calculated with SL EoS and N_{tot} is the total number of experimental data points n.

The value of k_{ij} that minimizes the error function is –0.03, and it yields an AAD value of 2.2% and a MAD value of 35%. The best fit of the same data set performed by Liu at al. [40] with the Peng-Robinson EoS [41] yielded an AAD of 2%, while with the PC-SAFT EoS [42] the same authors report and AAD of 1.6%. When k_{ij}= 0 is used instead, the AAD for the SL EoS is 2.5% and the MAD is 27%. In **Table 4.4**, the values of AAD and MAD for each mixture composition are reported. The comparison between EoS results and experimental data is reported in **Figure 4.2**. It can be seen that the higher MAD obtained with the optimal k_{ij} value is due to a less accurate representation of the CO_2 rich mixture data, while data in the composition range 10–60 mol% CO_2, which is the range of interest for the present case, are consistently represented better when the optimal value of k_{ij} is used, both in terms of average and maximum deviations.

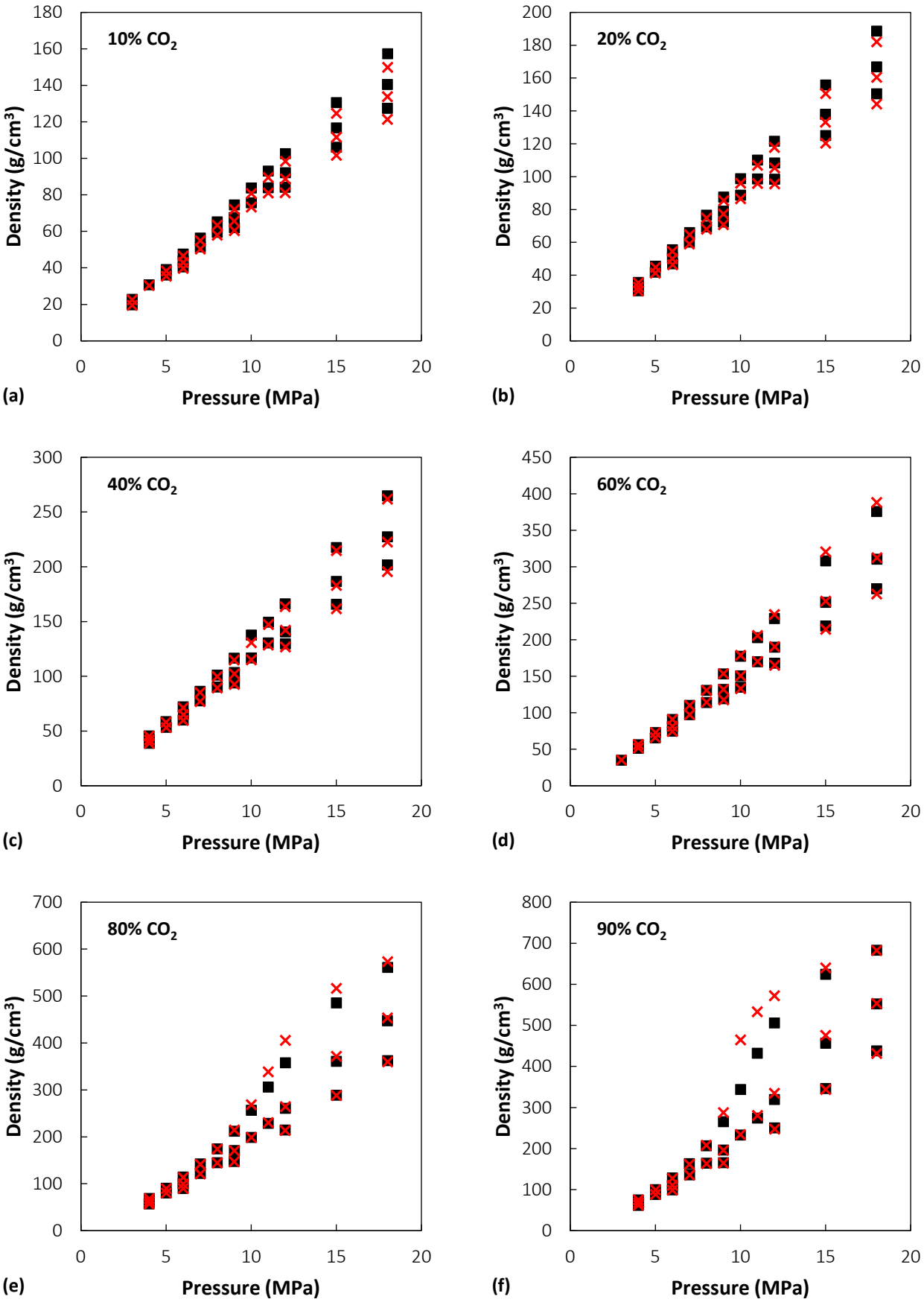

Figure 4.2. Comparison between experimental density of CO_2/CH_4 mixtures in the range 313 to 353 K, 3 to 18 MPa, 10-90 mol% CO_2 reported by Liu et al. [40] (black squares) and values calculated with the Sanchez-Lacombe EoS (red crosses).

Table 4.4. AAD and MAD between experimental CO_2/CH_4 mixtures density [40] and SL EoS predictions obtained with two different values of k_{ij}.

	AAD		MAD	
%CO_2	k_{ij} = 0	k_{ij} = –0.03	k_{ij} = 0	k_{ij} = –0.03
10	3.4%	3.0%	5.4%	4.8%
20	3.0%	2.4%	5.0%	4.2%
40	2.4%	1.4%	6.5%	5.1%
60	1.3%	0.9%	4.5%	4.0%
80	1.5%	1.9%	7.3%	13.4%
90	3.2%	3.8%	26.6%	35.1%
Overall	2.5%	2.2%	26.6%	35.1%

4.2.2 DMS model parameters

DMS parameters for the materials analyzed in this study were obtained from a least-square fitting procedure with the Generalized Reduced Gradient (GRG) method [43], using concentration (c) *vs.* fugacity (f) data, by minimizing χ^2 defined as follows:

$$\chi^2 = \sum_{i=1}^{N_{tot}} \left[c_i - \left(k_{D,i} f_i + \frac{C'_{H,i} b_i f_i}{1 + b_i f_i} \right) \right]^2 \qquad \text{Eq. (4.5)}$$

The parameter $k_{D,i}$ is Henry's law constant, b_i is Langmuir affinity constant, and $C'_{H,i}$ is the Langmuir capacity constant. In most cases, data at only one reference temperature are available, therefor, at first, each data set was treated independently, without additional constraints to impose a temperature dependence to the parameters where sorption isotherms at multiple temperatures were available. The effect of adding a constraint on the temperature dependence during the parameterization procedure is discussed in greater detail in **Section 4.3.2.2**. The resulting parameters are summarized in **Table 4.5** for all materials tested.

Typically, more condensable penetrants, like CO_2 in the present case, exhibit larger affinity constants, and this was indeed observed in the parameters retrieved. It would be expected that the presence of the tetrazole CO_2-philic groups in TZ-PIM would translate into higher affinity constants for CO_2 sorption, compared to PIM-1. However, this correlation of the parameter with the chemistry of the materials was not observed at all three temperatures, but only in the parameter set for the 25 °C case. This issue might be related to the parametrization route adopted, and it will be further discussed in **Section 4.3.2.2**.

Generally, k_D, C'_H and b are expected to decrease as temperature increases [44–46] consistently with their physical meaning. In the case of k_D and b, this trend was verified in all the cases inspected here, while for C'_H the expected trend was observed only in one case (CH_4 in PIM-1), while in the other cases the values fluctuated more. If the regression at each temperature is performed independently, fluctuations of the

parameters have to be expected. This was noted also by Stevens et al. [47] in their analysis of Dual Mode Sorption model parameters for CO_2, CH_4 and N_2 in HAB-6FDA polyimide and its thermally rearranged analogues: when an unconstrained regression was performed independently at each temperature, the expected trends were followed only in some of the cases considered. In order to obtain a consistent parameter set, they imposed temperature dependence during the regression. The effect of these constraints on the mixed-gas sorption prediction will be examined in **Section 4.3.2.2**.

Table 4.5. Dual Mode Sorption model parameters (fugacity-based) for CO_2 and CH_4 sorption in several polymers obtained by a least-square fit on data from refs. [2–5,8,9].

CO_2				
	T (°C)	k_D $\left(\frac{cm^3_{STP}}{cm^3_{pol}bar}\right)$	C'_H $\left(\frac{cm^3_{STP}}{cm^3_{pol}}\right)$	b (bar^{-1})
PTMSP	35	1.973	95.06	0.051
PIM-1	25	4.046	90.04	0.710
	35	2.890	94.83	0.388
	50	1.596	89.30	0.290
TZ-PIM	25	4.127	70.58	1.127
	35	1.982	89.53	0.378
	50	0.903	92.42	0.263
PIM-EA-TB	35	2.694	73.64	0.626
HAB-6FDA	35	1.108	35.85	0.441
TR450	35	1.852	57.95	0.470
CH_4				
	T (°C)	k_D $\left(\frac{cm^3_{STP}}{cm^3_{pol}bar}\right)$	C'_H $\left(\frac{cm^3_{STP}}{cm^3_{pol}}\right)$	b (bar^{-1})
PTMSP	35	0.616	57.77	0.049
PIM-1	25	0.651	78.83	0.136
	35	0.541	75.87	0.106
	50	0.543	57.90	0.105
TZ-PIM	25	1.400	48.09	0.214
	35	0.378	67.12	0.087
	50	0.350	51.41	0.101
PIM-EA-TB	35	0.990	47.43	0.203
HAB-6FDA	35	0.460	9.051	0.224
TR450	35	0.812	26.01	0.215

It has been reported that the DMS parameters are sensitive to the pressure range over which they are regressed [48], in particular b tends to decrease and C'_H to increase, if a broader regression range is considered, and, therefore, extrapolation outside the derivation range should be avoided. In this study, the whole isotherms were used in the regression and the pressure range was the same (0 - 35 bar) in all cases considered.

4.3 Mixed-gas Sorption Modelling

In this section the calculation of mixed-gas sorption isotherms performed for all materials using the NELF and the DMS models is discussed. For most cases, data at 35 °C for a ~30 mol% CO_2 mixture are available. In the case of PTMSP, PIM-1 and TZ-PIM, also data at lower (~10 mol% CO_2) and higher (~50 mol% CO_2) composition are reported. In the case of PTMSP, one mixture composition is different (20 mol% CO_2 instead of ~30%), however, as it can be observed for example in **Figure 4.3**, the experimental data showed little variation between 20 and 50% in that material, therefore the comparison with the other materials is still appropriate. Concerning the temperature range, mixed-gas sorption measurements were performed also at 25 °C and 50 °C in the case of TZ-PIM and PIM-1, therefore calculations were performed also at these temperatures, to evaluate the ability of the models to capture temperature effects.

The Relative Standard Error (RSE) is used as goodness-of-fit indicator, to compare the predictions made by the two models in the various conditions analyzed. RSE was used instead of the correlation coefficient (R^2), because the underlying assumptions in the definition of R^2 are not valid in the case of a nonlinear regression models such as the ones used here [49–51]. The following definition was used in its calculation:

$$RSE \equiv \sqrt{\frac{\sum_i \left(1 - d_{i,calc}/d_{i,exp}\right)^2}{N_u - N_{par}}} \qquad \text{Eq. (4.6)}$$

In the definition, $d_{i,exp}$ are the experimental points, $d_{i,calc}$ are the corresponding values calculated with the model, N_u is the number of experimental points used in the regression and N_{par} is the number of adjustable parameters employed by the model, whose values were optimized using the data series under consideration. In the case of DMS there are 3 adjustable parameters, in the case of NELF they are 2, while in the mixed-gas sorption case no adjustable parameters are employed. For the mixed-gas prediction, when data at more than one composition were modelled, the reported error value is the average deviation from three sorption isotherms at different composition calculated with the same pure-gas parameter sets. The values obtained are summarized in **Table 4.6**. As it can be noticed, the accuracy of the multicomponent predictions is generally higher for CO_2 than for CH_4; for the latter, on average also the experimental accuracy is lower compared to CO_2. Higher uncertainty is correlated to lower sorbed concentration, both in the case of the experiments and the model predictions.

Table 4.6. Relative standard error (RSE) in pure- and mixed-gas sorption calculations with the NELF and DMS model compared to the experimental confidence intervals.

CO_2						
	Pure-gas			**Mixed-gas**		
	$\boldsymbol{RSE}$ **NELF**	$\boldsymbol{RSE}$ **DMS**	**Exp. error bar**	$\overline{\boldsymbol{RSE}}_{mix}$ **NELF**	$\overline{\boldsymbol{RSE}}_{mix}$ **DMS**	**Exp. error bar**
PTMSP	1%	2%	6%	10%	11%	7%
PIM-1 - 25°C	2%	1%	7%	10%	4%	12%
35 °C	2%	1%	7%	6%	11%	9%
50 °C	2%	1%	5%	5%	11%	9%
TZ-PIM - 25 °C	6%	1%	6%	9%	12%	12%
35 °C	2%	2%	9%	8%	12%	12%
50 °C	2%	1%	6%	20%	40%	13%
PI-EA-TB	11%	1%	3%	26%	22%	5%
HAB-6FDA	5%	3%	6%	6%	32%	12%
TR450	2%	1%	6%	14%	23%	5%
CH_4						
	Pure-gas			**Mixed-gas**		
	$\boldsymbol{RSE}$ **NELF**	$\boldsymbol{RSE}$ **DMS**	**Exp. error bar**	$\overline{\boldsymbol{RSE}}_{mix}$ **NELF**	$\overline{\boldsymbol{RSE}}_{mix}$ **DMS**	**Exp. error bar**
PTMSP	4%	2%	10%	10%	14%	12%
PIM-1 - 25°C	1%	1%	13%	35%	21%	16%
35 °C	3%	2%	12%	9%	21%	21%
50 °C	3%	3%	12%	9%	17%	14%
TZ-PIM - 25 °C	3%	1%	8%	17%	10%	18%
35 °C	2%	2%	12%	15%	8%	16%
50 °C	3%	%	14%	12%	54%	16%
PI-EA-TB	14%	2%	7%	43%	53%	15%
HAB-6FDA	9%	2%	25%	8%	67%	63%
TR450	3%	2%	6%	25%	100%	24%

4.3.1 NELF model results

4.3.1.1 PTMSP

In **Figure 4.3** the experimental sorption data of CO_2/CH_4 mixtures (~10/20/50 mol% CO_2) in PTMSP at 35 °C [2], together with the results of mixed-gas sorption calculations with the NELF model are reported. The model is able to capture the fact that, in this material, the competitive effect is less pronounced compared to the polymers of intrinsic microporosity. Average relative deviations (RSE) between the model and the experimental data at 10%, 20% and 50% molar fraction of CO_2 are, respectively, 12%, 8%, 9% in the case of CO_2 and 4%, 9% 16% in the case of CH_4.

Another SL parameter set was reported in the literature for PTMSP (T^*= 416 K, p^* = 405 MPa, ρ^* = 1.250 g/cm^3) [52], which was tested with respect to mixed-gas sorption calculations. With this alternative parameter set, it was possible to represent the pure gas sorption isotherms of CO_2 and CH_4 in PTMSP with indistinguishable results. The binary parameters used in this case are: $k_{CO_2,PTMSP}$ = 0.042, $k_{CH_4,PTMSP}$ = –0.032, k_{sw,CO_2} = 0.015 MPa^{-1}, k_{sw,CH_4} = 0 MPa^{-1}. The results of mixed-gas calculations performed with these parameters are not shown, but were identical to those obtained with the parameters reported in **Table 4.2** and **Table 4.3**. It is noteworthy that, if the same pure-gas sorption representation is obtained with different parameter sets, the same mixed-gas prediction is also obtained. As it will be detailed in **Section 4.4**, this is not the case with the DMS model.

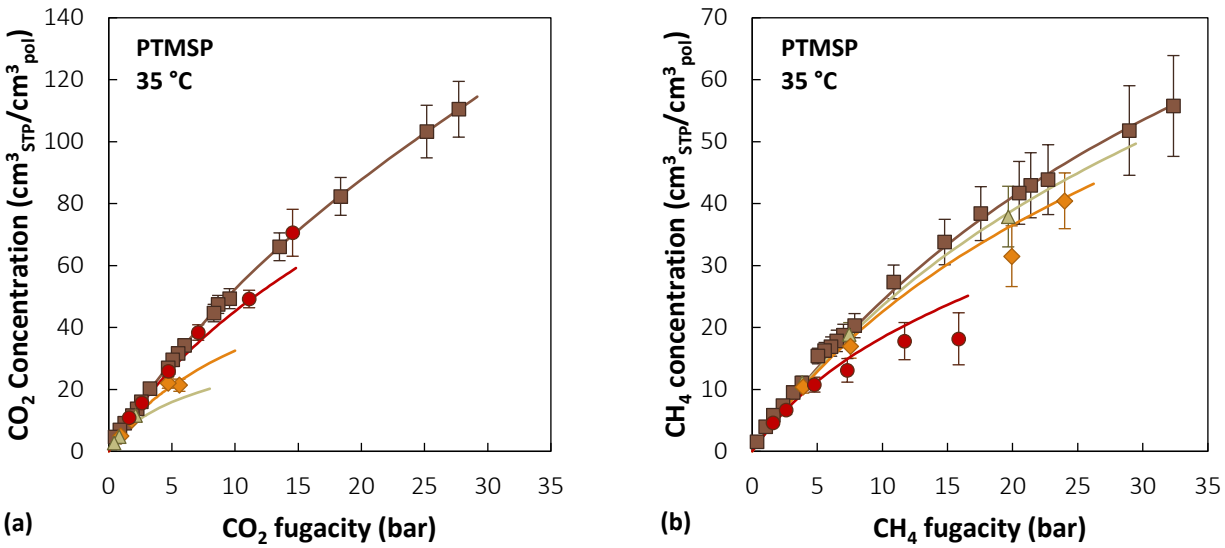

Figure 4.3. Sorption isotherms of (a) CO_2 and (b) CH_4 at 35 °C in PTMSP at pure- and mixed-gas conditions (Brown squares: pure gas – Green triangles: ~10% CO_2 mixture – Orange diamonds: ~20% CO_2 mixture – Red circles: ~50% CO_2 mixture [2]). Solid lines are NELF model predictions.

4.3.1.2 PIMs

In **Figure 4.4** the experimental sorption data of pure CO_2, pure CH_4 and CO_2/CH_4 mixtures (∼10/30/50 mol% CO_2) in **PIM-1** at 25, 35 and 50 °C [3,4], together with the results of mixed-gas sorption calculations with the NELF model are reported. **Figure 4.5** reports the same information for TZ-PIM [5].

In the case of CO_2, the prediction of the model is very satisfactory for PIM-1 and TZ-PIM, with average relative deviations (RSE) below 10%, in all cases except TZ-PIM at 50 °C, where a 20% RSE is obtained. However, this data set shows a peculiar behavior, with higher concentrations in the mixed-gas case compared to the pure-gas case. Mixed-gas sorption tests are indeed significantly longer than pure-gas ones, therefore prolonged contact with a swelling agent such as CO_2 could induce a greater polymer dilation compared to the pure-gas test. Therefore, a possible reason for this discrepancy is that the model parameters retrieved on the pure-gas sorption isotherms measured on the pristine sample could not reproduce the properties of the materials in this swollen state.

In the case of CH_4, the accuracy of the prediction is lower compared to CO_2, as the model tends to underestimate gas concentration at mixed-gas conditions, both in PIM-1 and in TZ-PIM. Average relative deviations (RSE) are found to be 35%, 9% and 9% increasing temperature from 25 to 50 °C in the case of PIM-1 while the corresponding values for TZ-PIM are 17%, 15%, 12%.

In the case of PIM-1, the largest deviations are always obtained in the case of the ∼10 mol% CO_2 mixture for CO_2, while for CH_4 they are obtained in the equimolar mixture case. The same was observed also in the case of TZ-PIM, with the exception of CO_2 at 35 °C and CH_4 at 50°C, where the highest deviations were found in the ∼30 mol% CO_2 mixture case.

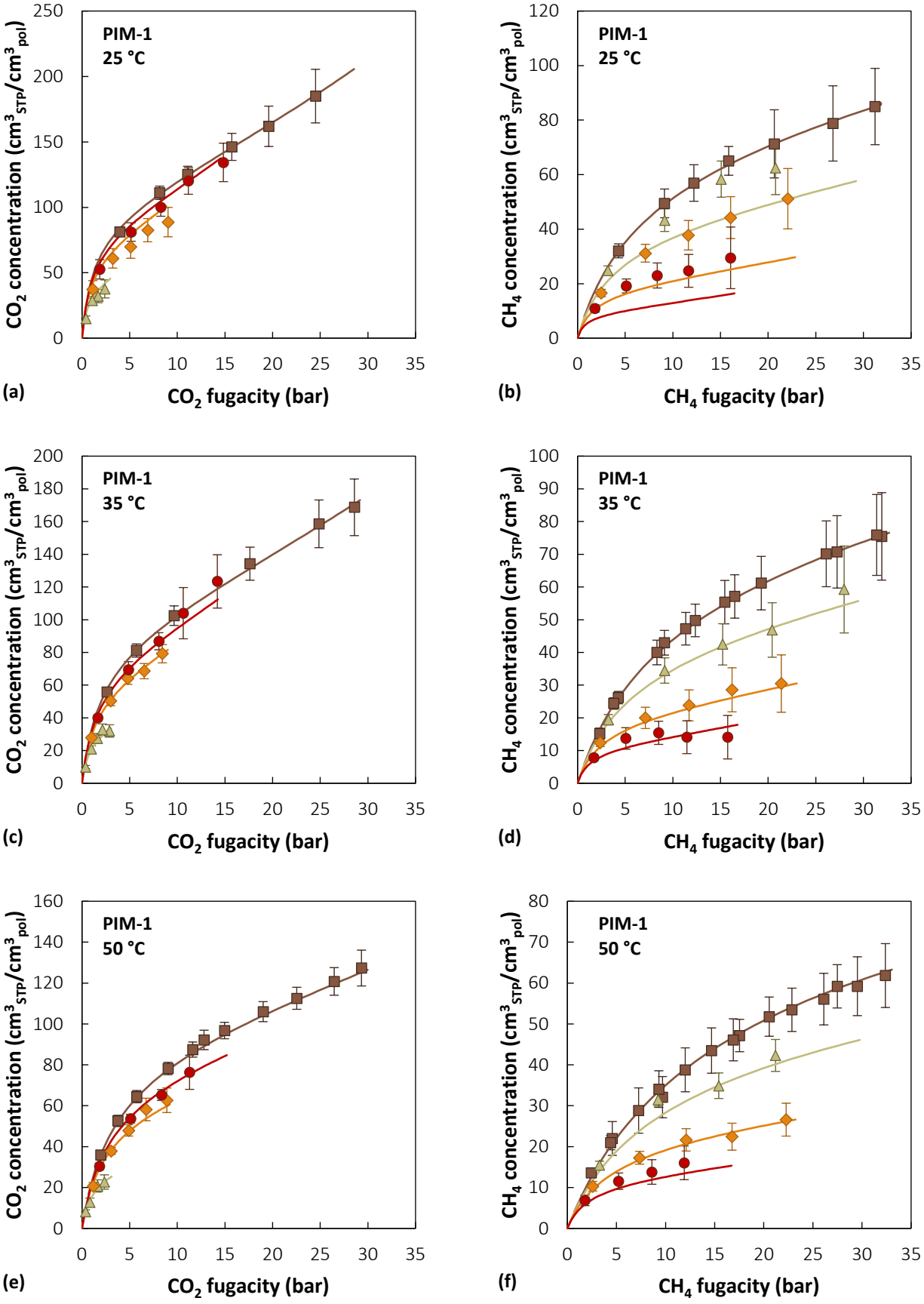

Figure 4.4. Sorption isotherms of (a,c,e) CO_2 and (b,d,f) CH_4 at 25, 35, 50 °C in PIM-1 at pure- and mixed-gas conditions (Brown squares: pure gas – Green triangles: ~10% CO_2 mixture – Orange diamonds: ~30% CO_2 mixture – Red circles: ~50% CO_2 mixture [3,4]). Solid lines are NELF model predictions.

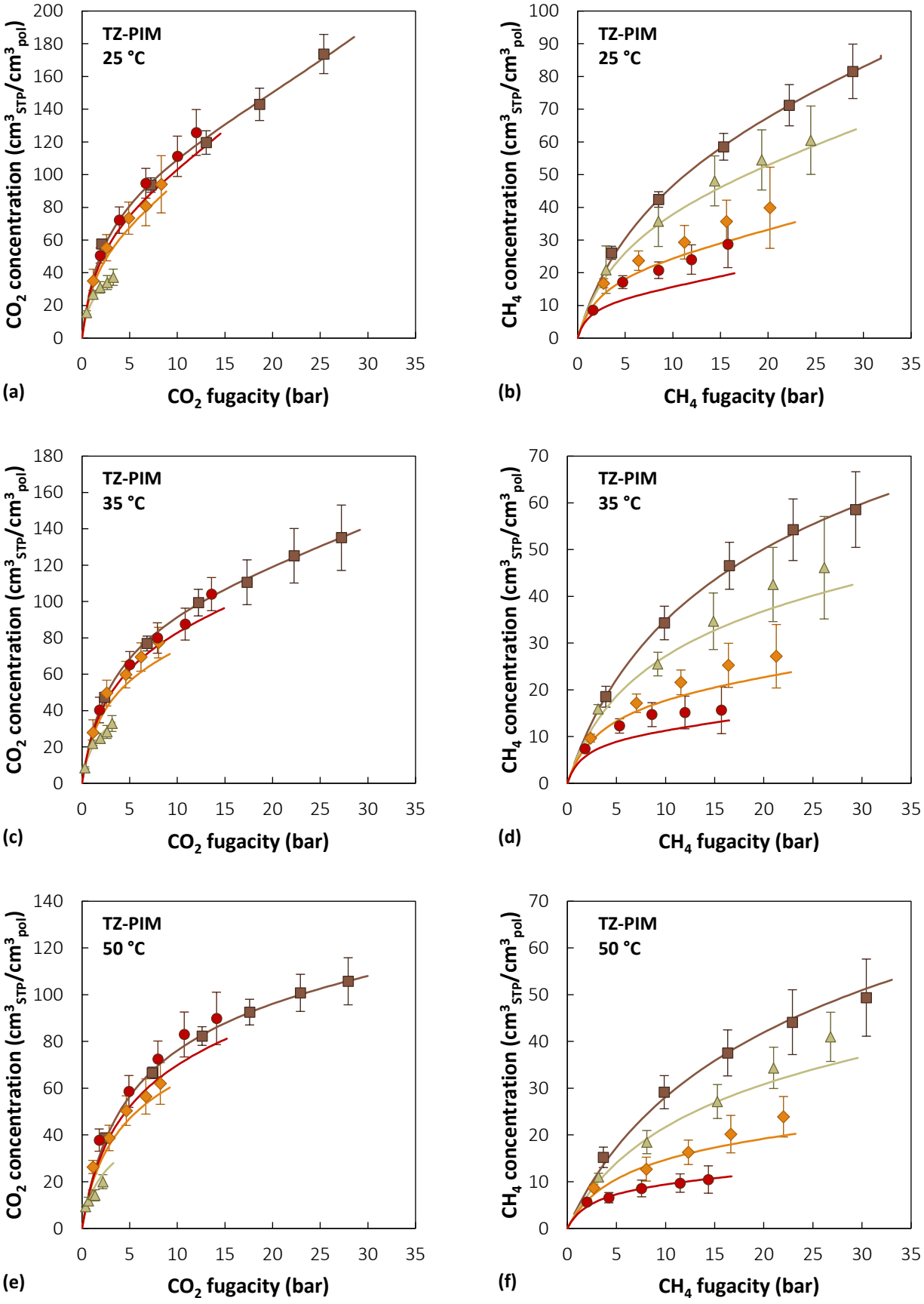

Figure 4.5. Sorption isotherms of (a,c,e) CO_2 and (b,d,f) CH_4 at 25, 35 and 50 °C in TZ-PIM at pure- and mixed-gas conditions (Brown squares: pure gas – Green triangles: ~10% CO_2 mixture – Orange diamonds: ~30% CO_2 mixture – Red circles: ~50% CO_2 mixture [5]). Solid lines are NELF model predictions.

NELF model predictions are sensitive to the **dry polymer density value** that is being considered [53], which affects significantly the values of the adjustable parameters employed to fit the experimental pure-gas sorption data. Taking into account the error bar in the density measurement, the ranges of variation of the adjustable parameters for the representation of pure CO_2 and CH_4 sorption in PIM-1 and TZ-PIM were determined, and they are reported in **Table 4.7** and **Table 4.8**. Moving along the whole error bar, it was always possible to obtain an accurate representation of the pure-gas sorption data by tuning the adjustable coefficients accordingly. It was found that a small deviation (~1%) of the dry polymer density value had a proportionally higher effect on the value of the binary parameter k_{ij}, which, for example, showed variations up to 100% in the case of CO_2 in PIM-1. On the other hand, the swelling coefficient k_{sw} was significantly less affected, with deviations ranging from 2% at 25 °C to 5% at 50 °C in the case of CO_2 in PIM-1. The sensitivity of the mixed-gas predictions, associated with the error in the density measurement and the corresponding variability of the adjustable parameters, was subsequently assessed. It should be noted that the mixed-gas predictions are affected by the adjustable parameters pertaining to both gases. The results are reported in **Figure 4.6** for the case of PIM-1 at all temperatures. The same analysis performed on TZ-PIM yielded very similar results. Remarkably, the results showed a limited variability (below 2%), both for CO_2 and CH_4, at all compositions. Therefore, the mixed-gas calculations with the NELF model are robust with respect to a small perturbation of the initial density value, which is compensated by a variation of the adjustable coefficients, yielding consistent multicomponent results, when the same pure-gas representation is obtained with a different parameter set. This also entails that small errors in the measurement of the density could not be at the origin of the discrepancy observed between NELF model predictions and experimental data, for example of CH_4 in PIM-1 at 25 °C, for which very large deviations are found.

Table 4.7. Range of variation of the NELF model adjustable coefficients for CO_2 and CH_4 sorption in PIM 1 as a result of the polymer density experimental error bar.

T (°C)	$\rho^0\ (g/cm^3)$	$k_{CO_2,PIM-1}$	$k_{CH_4,PIM-1}$	k_{sw,CO_2} (MPa^{-1})	k_{sw,CH_4} (MPa^{-1})
25	1.143 ± 0.008	$-0.023^{+0.008}_{-0.015}$	$-0.018^{+0.007}_{-0.003}$	$0.050^{+0.001}_{-0.001}$	$0.009^{+0.002}_{-0.001}$
35	1.136 ± 0.008	$-0.017^{+0.008}_{-0.012}$	$-0.013^{+0.009}_{-0.007}$	$0.038^{+0.001}_{-0.001}$	$0.006^{+0.001}_{-0.001}$
50	1.125 ± 0.008	$-0.008^{+0.008}_{-0.008}$	$-0.005^{+0.010}_{-0.012}$	$0.018^{+0.001}_{-0.001}$	$0.000^{+0.000}_{-0.000}$

Table 4.8. Range of variation of the NELF model adjustable coefficients for CO_2 and CH_4 sorption in TZ PIM as a result of the polymer density experimental error bar.

T (°C)	$\rho^0\ (g/cm^3)$	$k_{CO_2,TZ-PIM}$	$k_{CH_4,TZ-PIM}$	k_{sw,CO_2} (MPa^{-1})	k_{sw,CH_4} (MPa^{-1})
25	1.186 ± 0.008	$0.033^{+0.009}_{-0.003}$	$-0.072^{+0.012}_{-0.002}$	$0.040^{+0.001}_{-0.003}$	$0.013^{+0.002}_{-0.001}$
35	1.178 ± 0.008	$0.026^{+0.005}_{-0.002}$	$-0.062^{+0.010}_{-0.005}$	$0.018^{+0.004}_{-0.001}$	$0.000^{+0.000}_{-0.000}$
50	1.167 ± 0.008	$0.016^{+0.001}_{-0.001}$	$-0.050^{+0.002}_{-0.010}$	$0.004^{+0.002}_{-0.002}$	$0.000^{+0.000}_{-0.000}$

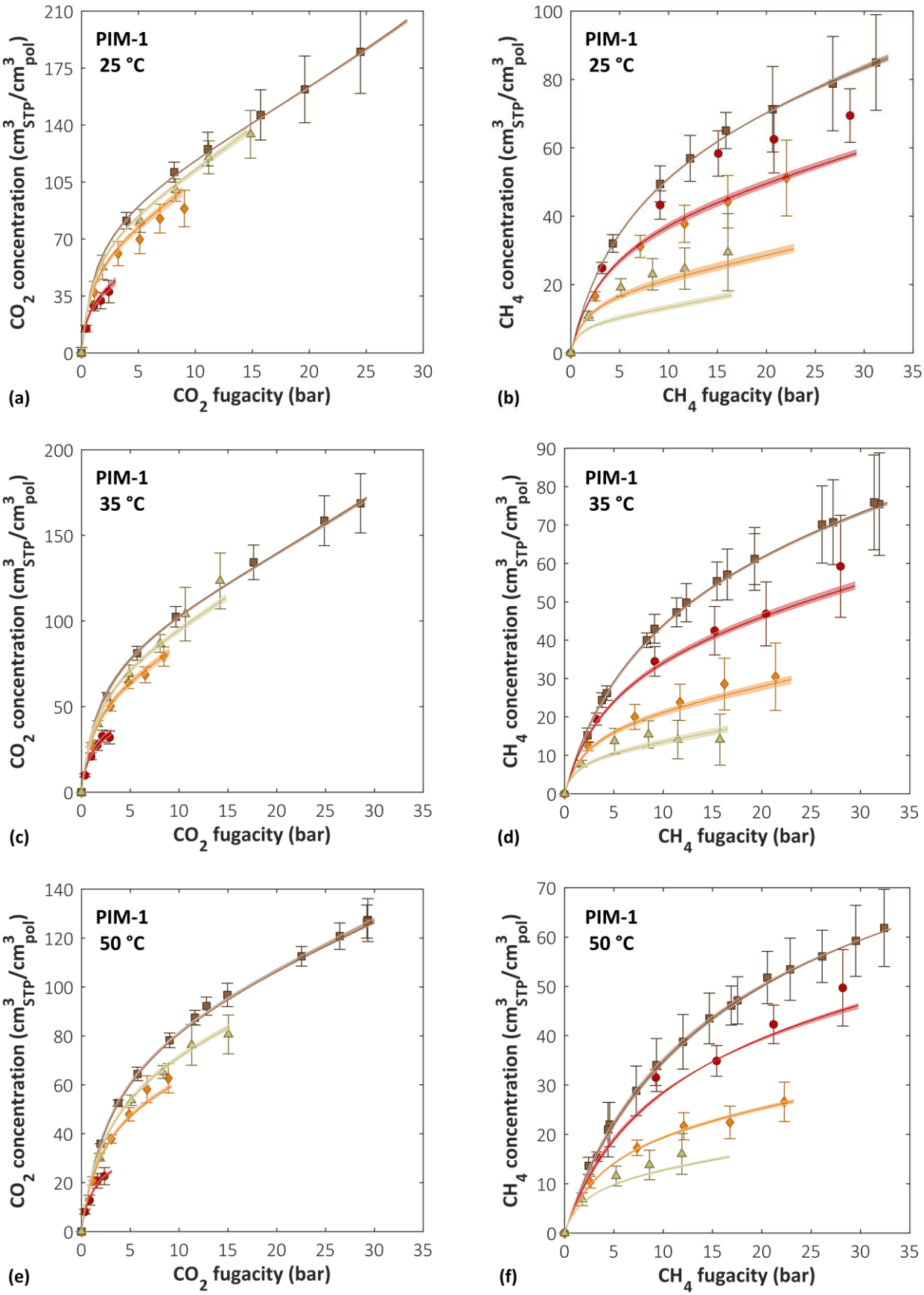

Figure 4.6. Variability in the mixed-gas sorption of CO_2 (a,c,e) and CH_4 (b,d,f) in PIM-1 at 25, 35 and 50 °C predicted by the NELF model, as a result of the dry polymer density error bar. Experimental data from [3,4]. Brown squares: pure gas – Green triangles: ~10% CO_2 mixture – Orange diamonds: ~30% CO_2 mixture – Red circles: ~50% CO_2 mixture.

In **Figure 4.7** the experimental sorption data of pure CO_2, pure CH_4 and of a ~30 mol% CO_2 mixture in **PIM-EA-TB** at 35 °C [8] are reported, together with the results of mixed-gas sorption calculations with the NELF model. In this case, the model was unable to represent faithfully the shape of the pure-gas sorption isotherms, with a RSE of 11% for CO_2 and 14% for CH_4. Consequently, also the predictions for the mixed-gas case are poor, with average relative deviations of 26% for CO_2 and 43% for CH_4.

For this material, the density of the sample could not be reliably measured with the buoyancy technique [8], therefore a literature value was used in the calculations [31]. Preparation protocols can have a significant effect on the final density of the sample, especially in high free volume materials such as PIM-EA-TB, for which also aging affects are pronounced [54,55]. To test whether the discrepancies in the representation of gas sorption of this materials could be reconciled by considering a different density for the sample, the calculation was repeated using the polymer density as an additional adjustable parameter. It resulted that, if a density value of 1.18 g/cm^3 is assumed, the binary parameters yielding the best fit of the experimental data are: $k_{CO_2,PIM-EA-TB}$ = –0.080, $k_{CH_4,PIM-EA-TB}$ = –0.075, k_{sw,CO_2} = 0.029 MPa^{-1}, k_{sw,CH_4} = 0.001 MPa^{-1}. With these parameters, a much more faithful representation of the pure-gas data was obtained (RSE of 2% in the case of CO_2 and 4% in the case of CH_4) and also the mixed-gas result is in much better agreement with the experiments (RSE of 14% in the case of CO_2 and 24% in the case of CH_4). The results obtained considering a different density of the sample are shown in **Figure 4.7 (c)** and **(d)**. It is noteworthy that a better pure-gas representation yielded a better mixed-gas representation, because, as it will be detailed in **Section 4.4**, this is not the case with the DMS model.

The density value adopted is 10% higher than the literature value, and this is approximately one order of magnitude larger than the error bar in density measurements reported for the other two PIMs. Even if the average error in density measurements is of the order of 1%, the variability between the density of different samples can be higher [54,55]. Therefore, even if the model can compensate a small uncertainty in the density value related to the experimental error, caution should be advised if the density of a different sample is adopted in the calculations, because this can lead to large errors.

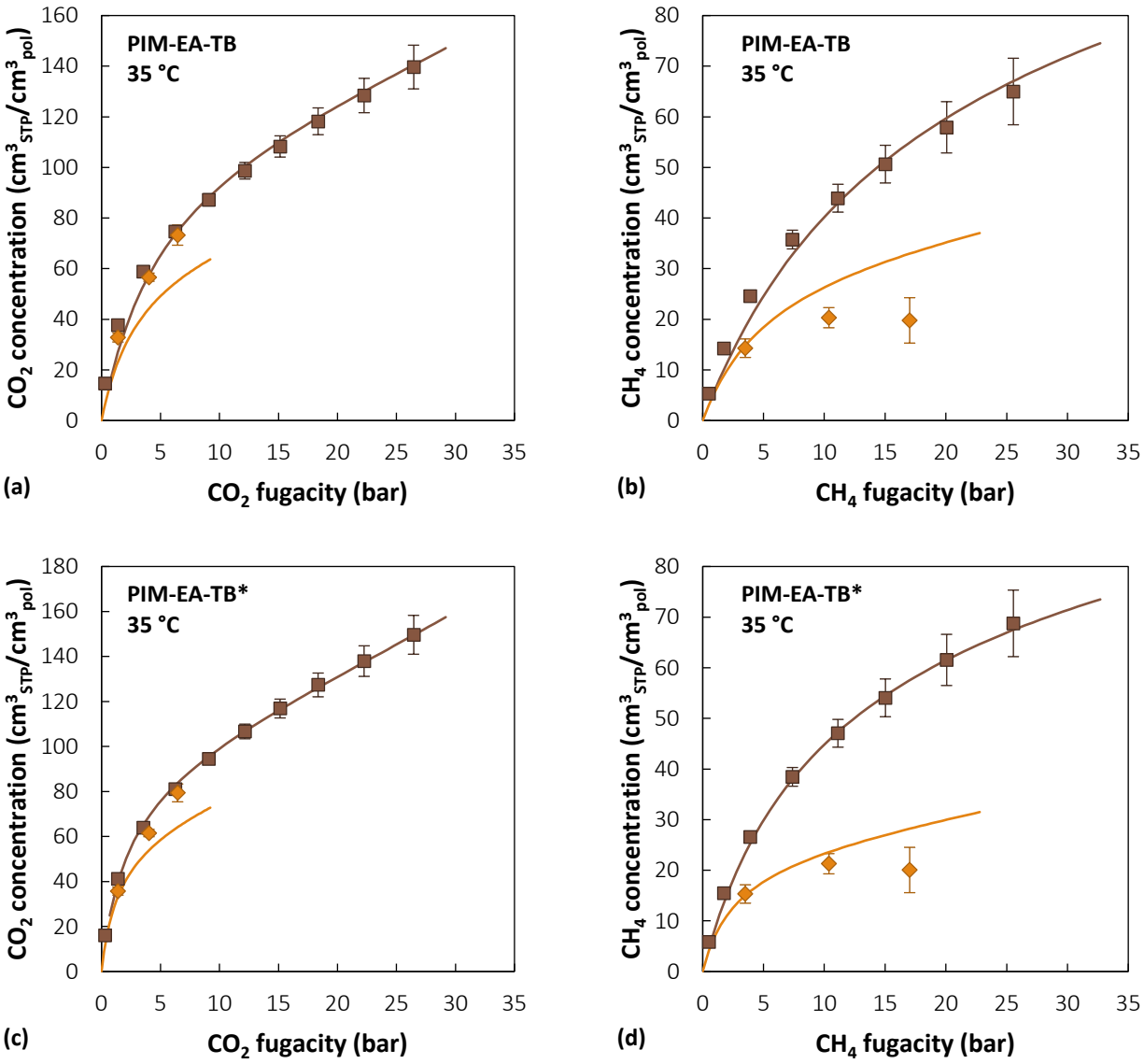

Figure 4.7. Sorption isotherms of (a) CO_2 and (b) CH_4 at 35 °C in PIM-EA-TB at pure- and mixed-gas conditions (Brown squares: pure gas – Orange diamonds: ~30% CO_2 mixture [8]). Solid lines are NELF model predictions. *Figures (c) and (d) show the results obtained by treating the polymer density as an adjustable parameter.

4.3.1.3 HAB-6FDA and TR450

In **Figure 4.8** the experimental sorption data of pure CO_2, pure CH_4 and a ~30 mol% CO_2 mixture in HAB-6FDA and TR450 at 35 °C [9] are reported, together with the results of mixed-gas sorption calculations with the NELF model. As it can be observed, in the case of HAB-6FDA the model yields a very good prediction of multicomponent sorption of both CO_2 and CH_4: RSE values are 6% in the case of CO_2 and 8% in the case of CH_4. In the case of TR450 larger deviations are obtained: 14% relative average deviation for CO_2 and 25% for CH_4. The average experimental standard deviations offer a frame of reference to evaluate the accuracy of the modelling results: 12% and 63% in the case of CO_2 and CH_4 mixed-gas sorption in HAB-6FDA, while in the case of TR450 they are 5% and 24% respectively.

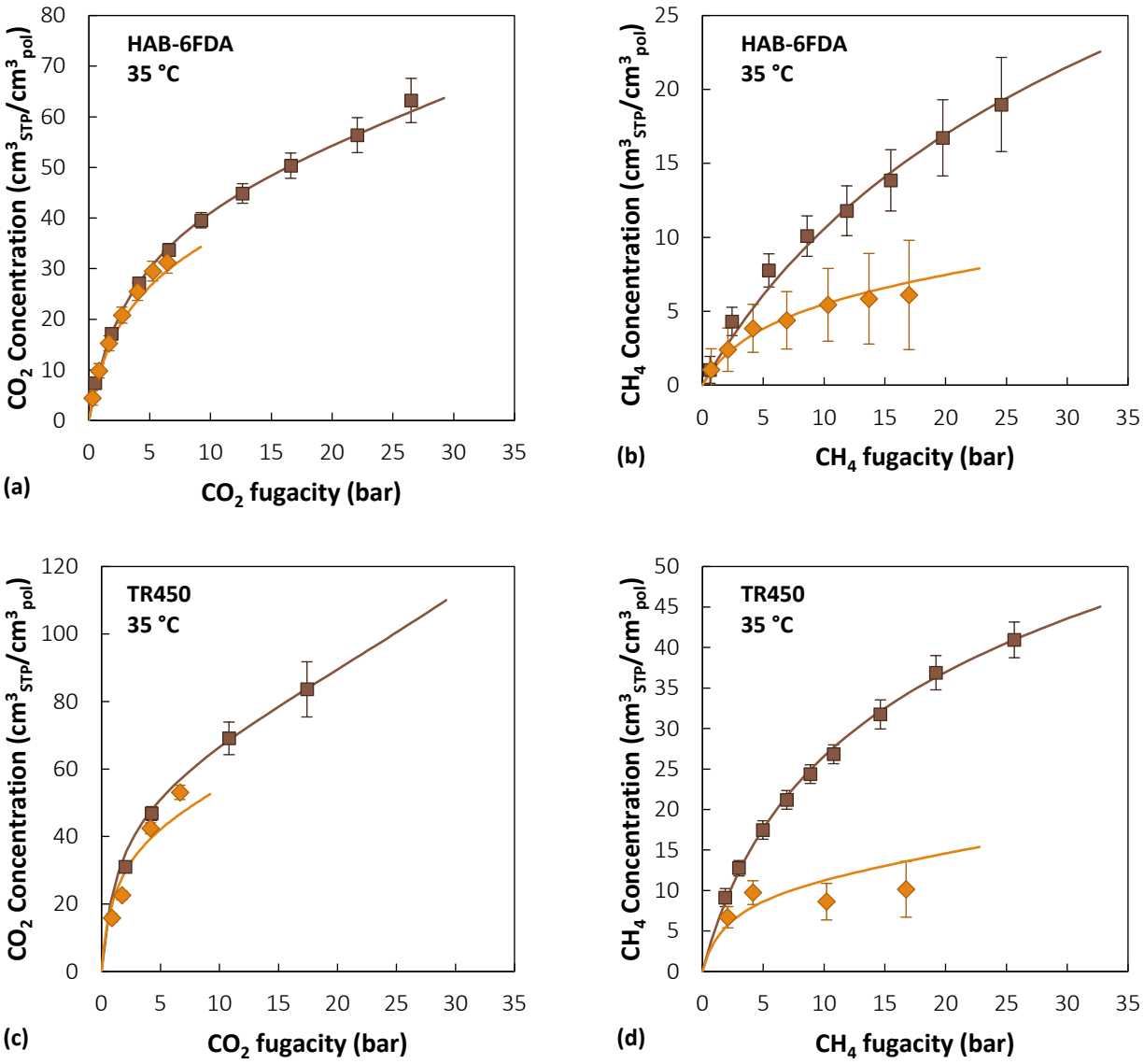

Figure 4.8. Sorption isotherms of CO_2 and CH_4 at 35 °C in HAB-6FDA (a,b) and TR450 (c,d) at pure- and mixed-gas conditions (Brown squares: pure gas – Orange diamonds: ~30% CO_2 mixture [9]). Solid lines are NELF model predictions.

The effect of uncertainty in polymer density measurements was evaluated also in this case, by spanning the whole density error bar, optimizing the adjustable parameters at each density value, and assessing the resulting accuracy in mixed-gas prediction. The effect of a density variation on the values of the adjustable parameters is reported in **Table 4.9** . Remarkably, the mixed-gas sorption results show a limited variability: at the extremes of the density error bar the average relative deviations (with respect to the pressure range covered in the calculation) between for CO_2 and CH_4, mixed-gas sorption (30 mol% CO_2) in HAB-6FDA is 0.7% and 1.6% respectively, while in the case of TR450 it is 0.9% for CO_2 and 3.8% for CH_4. Therefore, also in this case small perturbation of the initial density value is compensated by a variation of the adjustable coefficients, yielding consistent multicomponent results, when the same pure-gas representation is obtained with a different parameter set.

Table 4.9. Range of variation of the NELF model adjustable coefficients for CO_2 and CH_4 sorption in HAb-6FDA and TR450 as a result of the polymer density experimental error bar.

	$\rho^0\ (g/cm^3)$	k_{ij} CO_2	k_{ij} CH_4	k_{sw,CO_2} (MPa^{-1})	k_{sw,CH_4} (MPa^{-1})
HAB-6FDA	1.407 ± 0.009	-0.025 ± 0.012	0.052 ± 0.017	0.007 ± 0.001	$0.000^{+0.000}_{-0.000}$
TR450	1.34 ± 0.01	-0.085 ± 0.013	-0.037 ± 0.014	0.023 ± 0.003	$0.000^{+0.000}_{-0.000}$

The effect of specific penetrant-penetrant interactions in mixed-gas sorption calculations with the NELF model was evaluated by setting the CO_2/CH_4 binary interaction parameter equal to zero. As it can be seen in **Figure 4.9**, this was found to have a negligible effect on the mixed-gas sorption results, with average relative deviations from 0.15% to 1.2% between calculations made with $k_{ij} = -0.03$ or $k_{ij} = 0$. This confirms the assumption made in previous studies dealing with mixed-gas sorption calculation in glassy polymers with the NET-GP theory [56]. For this reason, penetrant-penetrant specific interactions are not believed to be a plausible explanation for the discrepancies emerged in some of the cases studied with the NELF model.

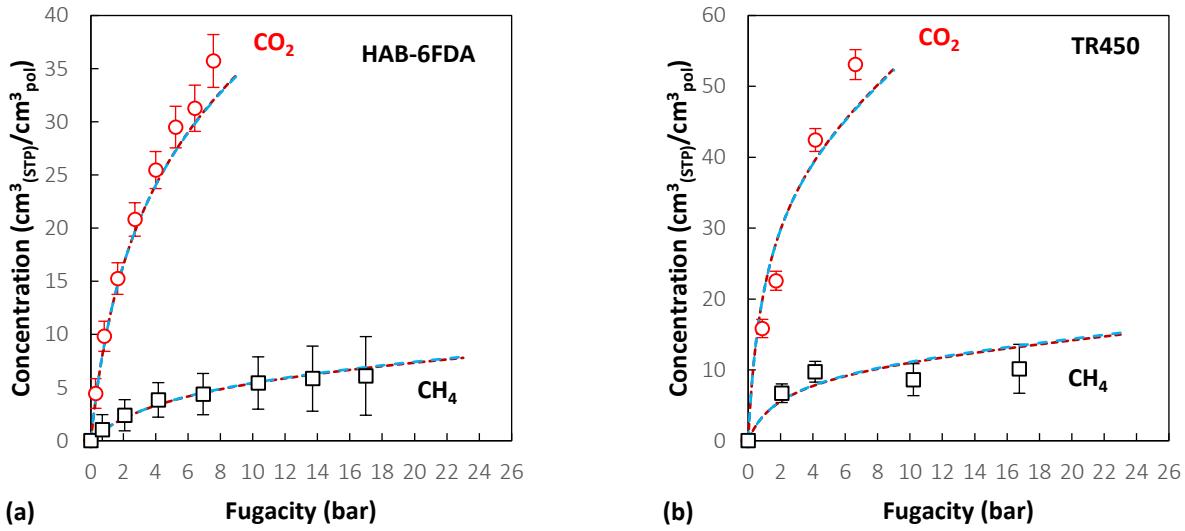

Figure 4.9. Comparison of mixed-gas (30 mol% CO_2) sorption isotherms [9] of CO_2 (red) and CH_4 (black) in (a) HAB-6FDA and (b) TR450 calculated with the NELF model considering specific gas-gas interaction (k_{ij} = - 0.03, dashed blue lines) or neglecting them (k_{ij} = 0, red lines).

In the literature, values of the NELF model binary parameters for these materials are also available [26]. These parameter sets, reported in **Table 4.10** for comparison, were tested with respect to mixed-gas sorption calculations and the results are compared with those obtained with the parameters optimized in this work in **Figure 4.10**. The two sets of parameters were optimized on different pure-gas sorption data, as it is reflected in the two pure-gas sorption isotherms calculated with the model and reported in **Figure 4.10**. For the corresponding mixed-gas predictions, the average relative deviations between the curves are 5.7% in the case of CO_2 sorption in HAB-6FDA, 4.3% for CH_4 sorption in HAB-6FDA, 2.3% for CO_2 sorption in

TR450 and 6.7% for CH_4 sorption in TR450. Therefore, even with a slightly dissimilar pure-gas representation (3.5% deviation for CO_2 and 4.4 % for CH_4) the results of mixed-gas calculations do not change dramatically. This will be shown not to be true for the DMS model in **Section 4.4**.

This can be seen as a test of the robustness of the NELF model mixed-gas calculations with respect to a perturbation of the pure gas sorption data. The positive result is likely to be related to the fact that the two samples considered in this case had the same density. Indeed, in the analysis of mixed-gas sorption predictions in PIM-EA-TB presented in **Section 4.3.1.2**, it was shown that the mixed-gas calculation results are sensitive to a substantial change (5-10%) in the density of the sample. Therefore, provided that two samples have similar density, the use of literature parameter optimized using pure-gas sorption data or the first one could yield a reliable estimate of mixed-gas sorption also for the second sample.

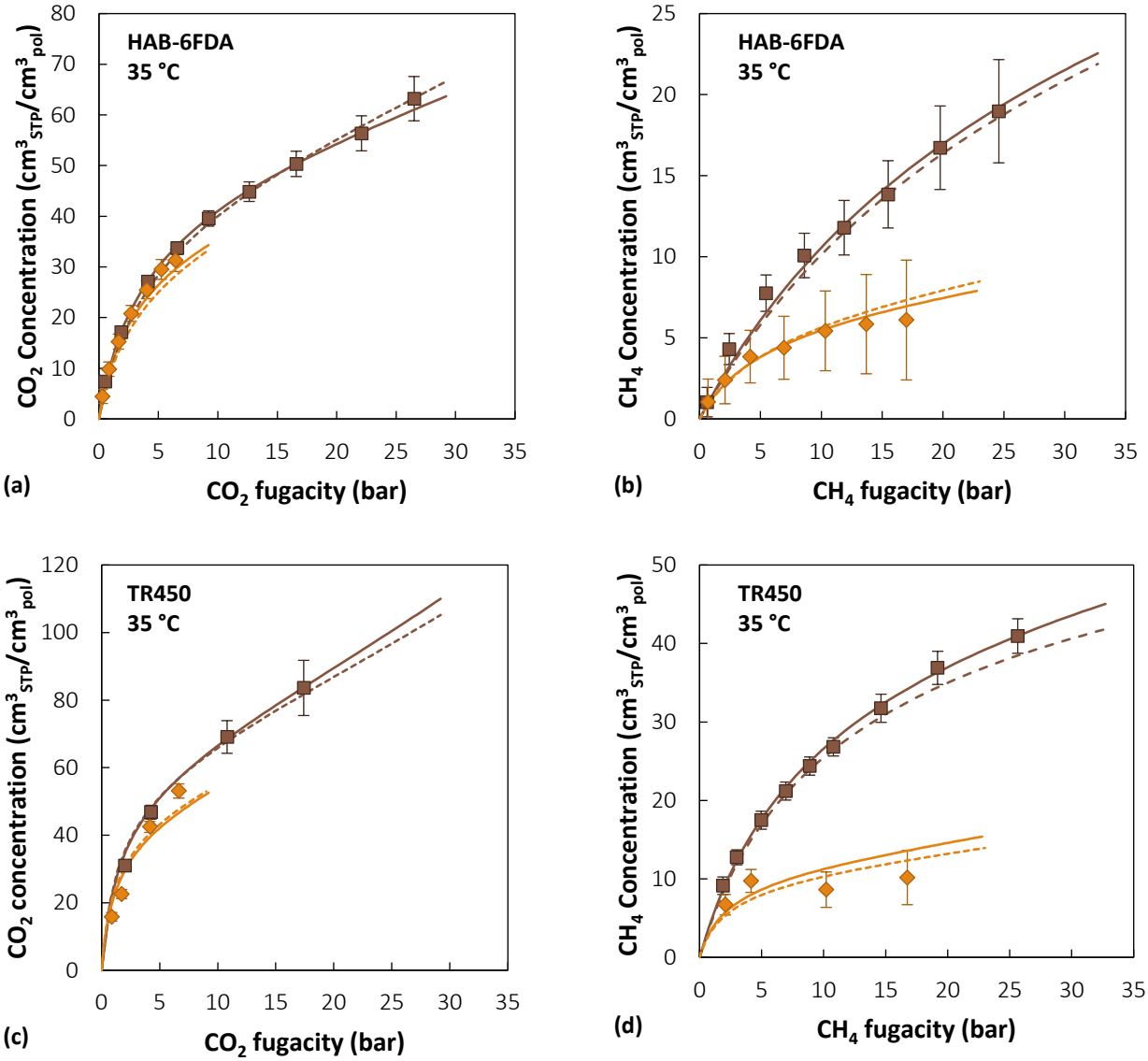

Figure 4.10. Sorption isotherms of CO_2 and CH_4 at 35 °C in HAB-6FDA (a,b) and TR450 (c,d) at pure- and mixed-gas conditions [9] (Brown squares: pure gas – Orange diamonds: ~30% CO_2 mixture). Solid lines are NELF model predictions obtained using the binary parameters reported in **Table 4.3**. Dashed lines were obtained using the binary parameters reported by Galizia et al. [26].

Table 4.10. Binary interaction parameters and swelling coefficients used in mixed gas sorption calculations with the NELF model at 35 °C from ref. [26].

		k_{ij}	k_{sw} (MPa^{-1})	Ref.
HAB-6FDA	CO_2	-0.01	0.01	[26]
	CH_4	0.06	0	
TR450	CO_2	-0.09	0.02	[26]
	CH_4	-0.03	0	

4.3.2 DMS model results

4.3.2.1 PTMSP

Figure 4.11 shows the experimental sorption data of CO_2/CH_4 mixtures (~10/20/50 mol.% CO_2) in PTMSP at 35 °C [2] together with the results of mixed-gas sorption calculations with the DMS parameters reported in **Table 4.5**. The predictions are in very good agreement with the experimental data in the case of CO_2, while in the case of CH_4 at high pressure the model overestimates the concentration for the 30:70 and 50:50 CO_2/CH_4 mixtures, with an RSE of 13% and 27% respectively. Nonetheless, the model captures the fact that there is competition between the gases during sorption, and also that it is less pronounced in this polymer than in the other materials analyzed here, even at high values of the fugacity of the second component.

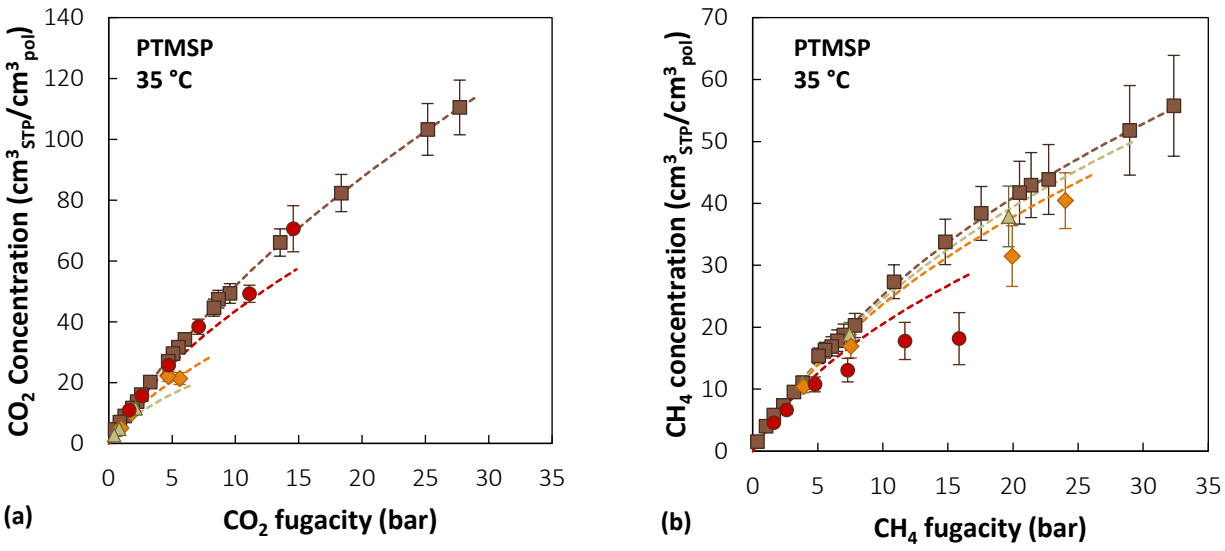

Figure 4.11. Sorption isotherms of (a) CO_2 and (b) CH_4 at 35 °C in PTMSP at pure- and mixed-gas conditions (Brown squares: pure gas – Green triangles: ~10% CO_2 mixture – Orange diamonds: ~30% CO_2 mixture – Red circles: ~50% CO_2 mixture [2]). Dashed lines are DMS model predictions

4.3.2.2 *PIMs*

Figure 4.12 shows the predictions of the Dual Mode Sorption Model together with the experimental data measured at 35°C [8] for the sorption of pure CO_2, pure CH_4 and a 30/70 mol% CO_2/CH_4 mixture in **PIM-EA-TB**. The prediction of the model qualitatively agrees with the observed behavior, but CO_2 sorption in mixed-gas condition tends to be underestimated, and that of CH_4 overestimated. The accuracy of the results is rather low: in the case of CO_2 sorption in mixed-gas conditions the RSE is 22%, and it increases to 53% in the case of CH_4.

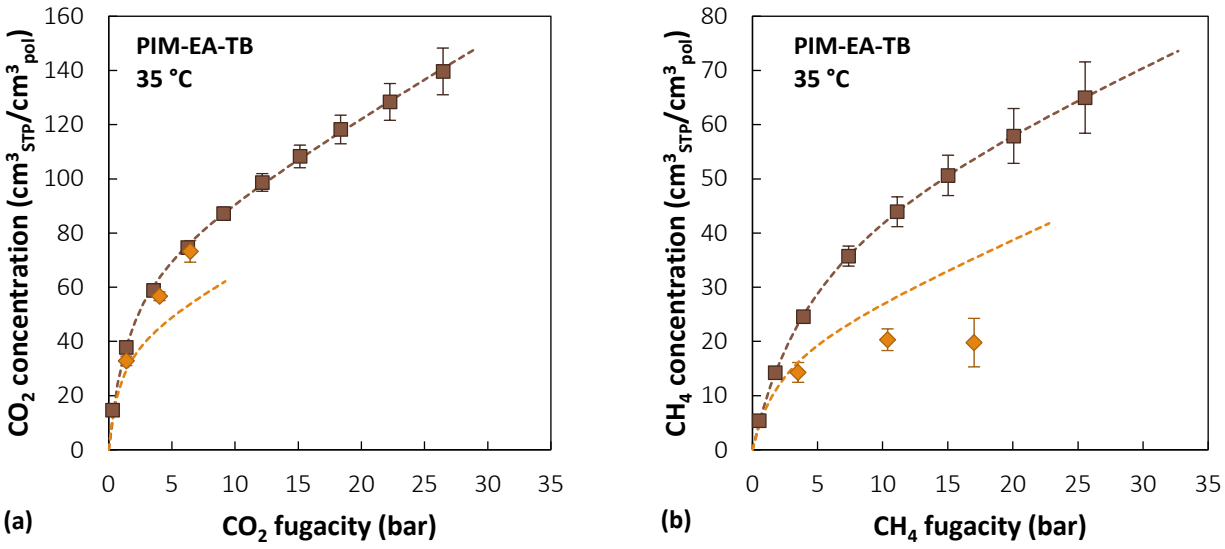

Figure 4.12. Sorption isotherms of (a) CO_2 and (b) CH_4 at 35 °C in PIM-EA-TB at pure- and mixed-gas conditions (Brown squares: pure gas – Orange diamonds: ~30% CO_2 mixture [8]). Dashed lines are DMS model predictions.

Figure 4.13 shows the experimental sorption data of CO_2/CH_4 mixtures (~10/30/50 mol.% CO_2) in **PIM-1** at 25, 35, 50 °C [3], together with the results of mixed-gas sorption calculations with the DMS model. It can be seen that, in the case of CO_2, the prediction is very accurate at the lowest temperature, with average relative deviations (RSE) below 4%. The average relative deviations, however, are increased to 11% at 35 °C and 50 °C.

On the other hand, in the case of CH_4, the accuracy is lower and its trend with temperature is opposite with respect to the case of CO_2: at 25 °C the concentration is significantly underestimated at all compositions (the average relative deviation is 21%), while at 35 °C it is overestimated by a similar extent (the average relative deviation is 20%), while at 50 °C CH_4 sorption is still overestimated by the model, but the prediction is slightly more satisfactory, with average relative deviations of 17%. The deviation between the experimental data and the model predictions is greater than the experimental confidence intervals in several cases, therefore it does not seem to be explained by the uncertainty in the mixed-gas sorption measurements. Generally, for all temperatures analyzed, the lowest deviations are seen for both gases in the mixture case in which they are more abundant (50% CO_2 and 90% CH_4 respectively).

Not much can be done *a priori* to improve the quantitative accuracy of the mixed-gas prediction, because the parametrization at each temperature is independent and relies only on the accuracy of the pure-gas sorption measurements, however the effect of using different parametrization routes will be discussed in following paragraphs.

In **Figure 4.14**, the experimental sorption data of CO_2/CH_4 mixtures (∼10/30/50 mol.% CO_2) in **TZ-PIM** at 25, 35, 50 °C [3], together with the results of mixed-gas sorption calculations with the DMS model are reported. In the case of TZ-PIM, the prediction of CO_2 sorption is more accurate at 25 °C and 35 °C (12% average relative deviations), while it worsens at 50 °C, where the model would seem to underestimate CO_2 concentration both in the 30% CO_2 and in the 50% CO_2 mixtures, with average relative deviations with respect to the experimental data of 42% and 36%, which are greater than the experimental confidence intervals. However, in the case of the 50 mol% CO_2 mixtures, the fact that concentrations higher than the pure-gas value at the same fugacity are obtained might be a signal that significant swelling of the sample took place, thus changing the properties of the material to an extent that would make the original parameterization of the model no longer valid. In the case of CH_4, at 25 °C and 35 °C DMS predictions show very good agreement with the experimental data, with average relative deviations below 10% at all compositions. Conversely, at 50 °C the model significantly overestimates the CH_4 concentration, by as much as 54% on average.

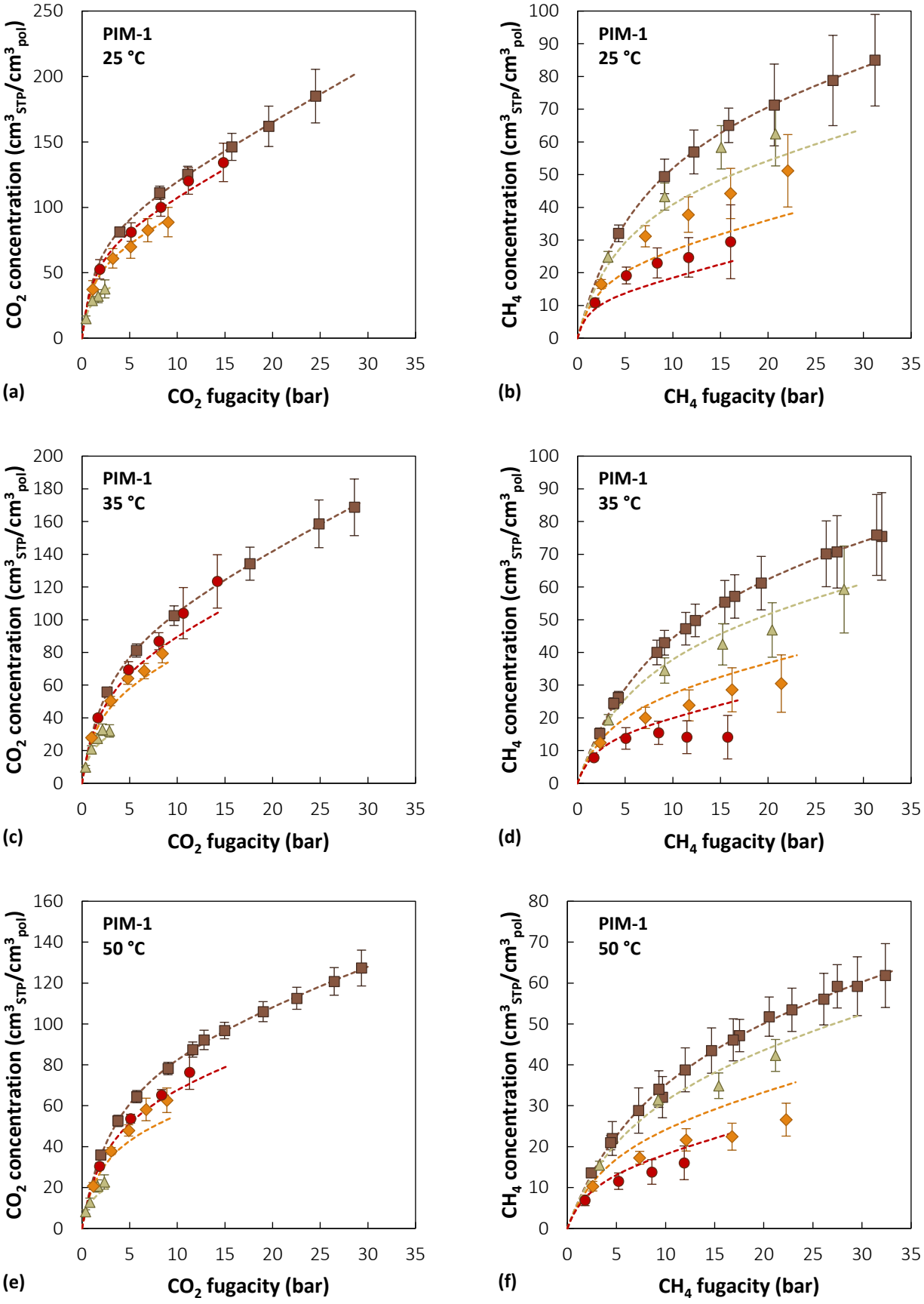

Figure 4.13. Sorption isotherms of (a,c,e) CO_2 and (b,d,f) CH_4 at 25, 35, 50 °C in PIM-1 at pure- and mixed-gas conditions (Brown squares: pure gas – Green triangles: ~10% CO_2 mixture – Orange diamonds: ~30% CO_2 mixture – Red circles: ~50% CO_2 mixture [3,4]). Dashed lines are DMS model predictions.

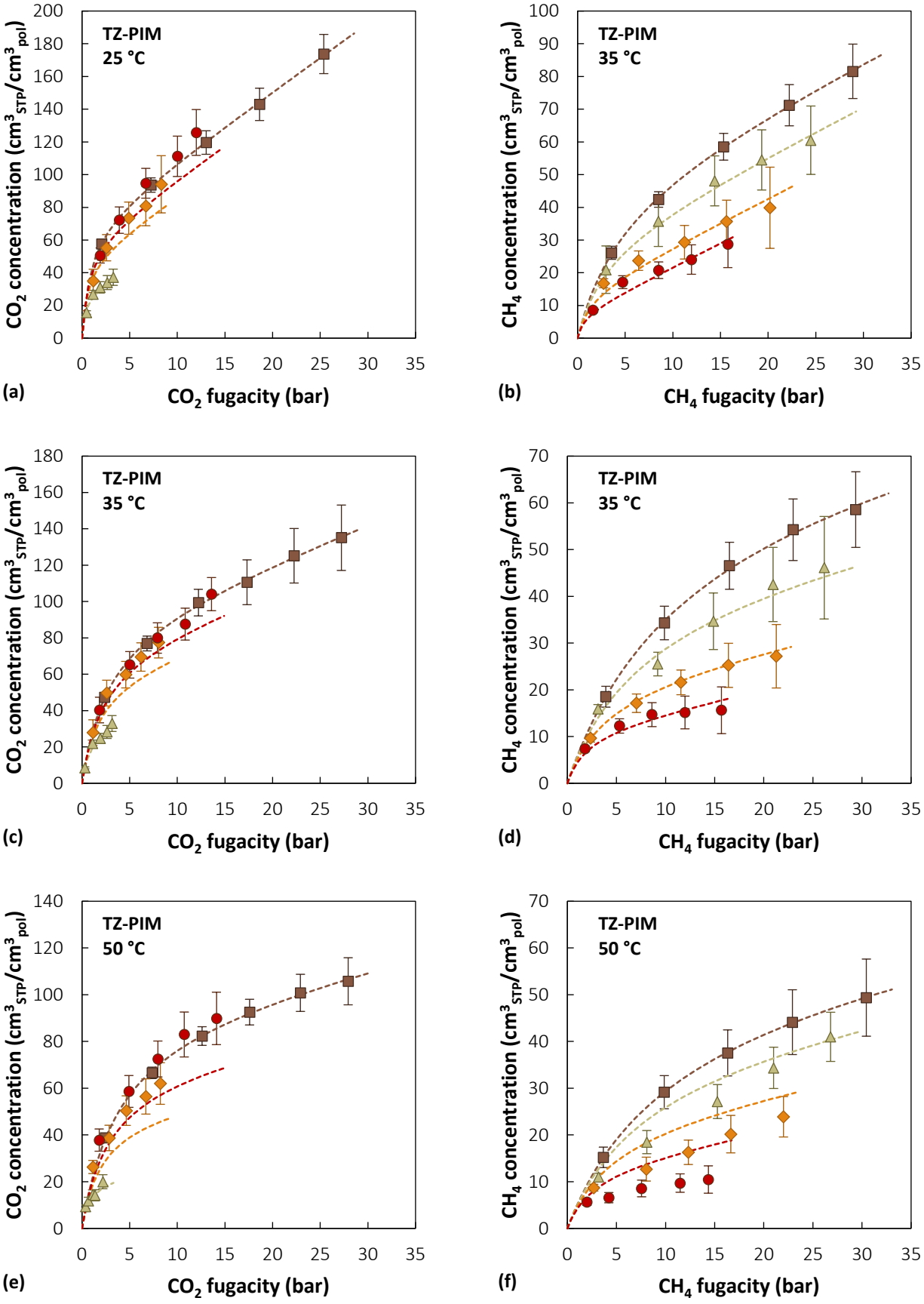

Figure 4.14. Sorption isotherms of (a,c,e) CO_2 and (b,d,f) CH_4 at 25, 35 and 50 °C in TZ-PIM at pure- and mixed-gas conditions (Brown squares: pure gas – Red circles: ~50% CO_2 mixture – Orange diamonds: ~30% CO_2 mixture – Green triangles: ~10% CO_2 mixture [5]). Dashed lines are DMS model predictions.

Effect of an alternative parameterization route

In order to address the inconsistent accuracy of the prediction in several cases, a different parametrization route was tried. A similar analysis was performed also in the case of HAB-6FDA and TR450 and it will be presented in the corresponding section. New parameter sets were obtained (**Table 4.11**) by taking into account the experimental error associated with each experimental point during the nonlinear least-square optimization, by minimizing χ^2 defined as follows [50]:

$$\chi^2 = \sum_{i=1}^{N_{tot}} \frac{1}{s_i^2}\left[c_i - \left(k_{D,i}f_i + \frac{C'_{H,i}b_i f_i}{1+b_i f_i}\right)\right]^2 \qquad \text{Eq. (4.7)}$$

here s_i represents the confidence interval associated with the experimental value of the concentration c_i, N_{tot} is the total number of experimental points, f_i is the gas fugacity and $k_{D,i}$, $C'_{H,i}$, b_i are the DMS parameters for the polymer-i penetrant couple.

Table 4.11. Dual Mode Sorption model parameters (fugacity-based) for CO_2 and CH_4 sorption in PIM-1 and TZ-PIM, obtained by a least-square fit on data from refs. [2–5] to **Eq. (4.7)**. In parenthesis the error in multicomponent prediction obtained by fitting to **Eq. (4.5)** (reference case) is reported. The arrows indicate if the present case performs better ↓ or worse ↑ than the reference case.

			CO_2			
	T (°C)	k_D $\left(\frac{cm^3_{STP}}{cm^3_{pol}bar}\right)$	C'_H $\left(\frac{cm^3_{STP}}{cm^3_{pol}}\right)$	b (bar^{-1})	RSE_{pure}	$\overline{RSE}_{mix}$
PIM-1	25	3.664	100.25	0.506	1%	8% (4%) ↑
	35	3.039	90.42	0.428	1%	7% (11%) ↓
	50	1.666	86.84	0.306	1%	14% (11%) ↑
TZ-PIM	25	4.023	72.88	1.019	1%	12% (12%) =
	35	2.168	84.61	0.420	2%	10% (12%) ↓
	50	1.150	84.84	0.303	1%	36% (40%) ↓
			CH_4			
	T (°C)	k_D $\left(\frac{cm^3_{STP}}{cm^3_{pol}bar}\right)$	C'_H $\left(\frac{cm^3_{STP}}{cm^3_{pol}}\right)$	b (bar^{-1})	RSE_{pure}	$\overline{RSE}_{mix}$
PIM-1	25	0.672	78.56	0.137	1%	11% (21%) ↓
	35	0.401	82.72	0.097	2%	14% (21%) ↓
	50	0.684	50.99	0.124	2%	21% (17%) ↑
TZ-PIM	25	1.526	43.65	0.250	1%	9% (12%) ↓
	35	0.282	73.42	0.079	2%	9% (8%) ↑
	50	0.364	50.63	0.103	1%	48% (54%) ↓

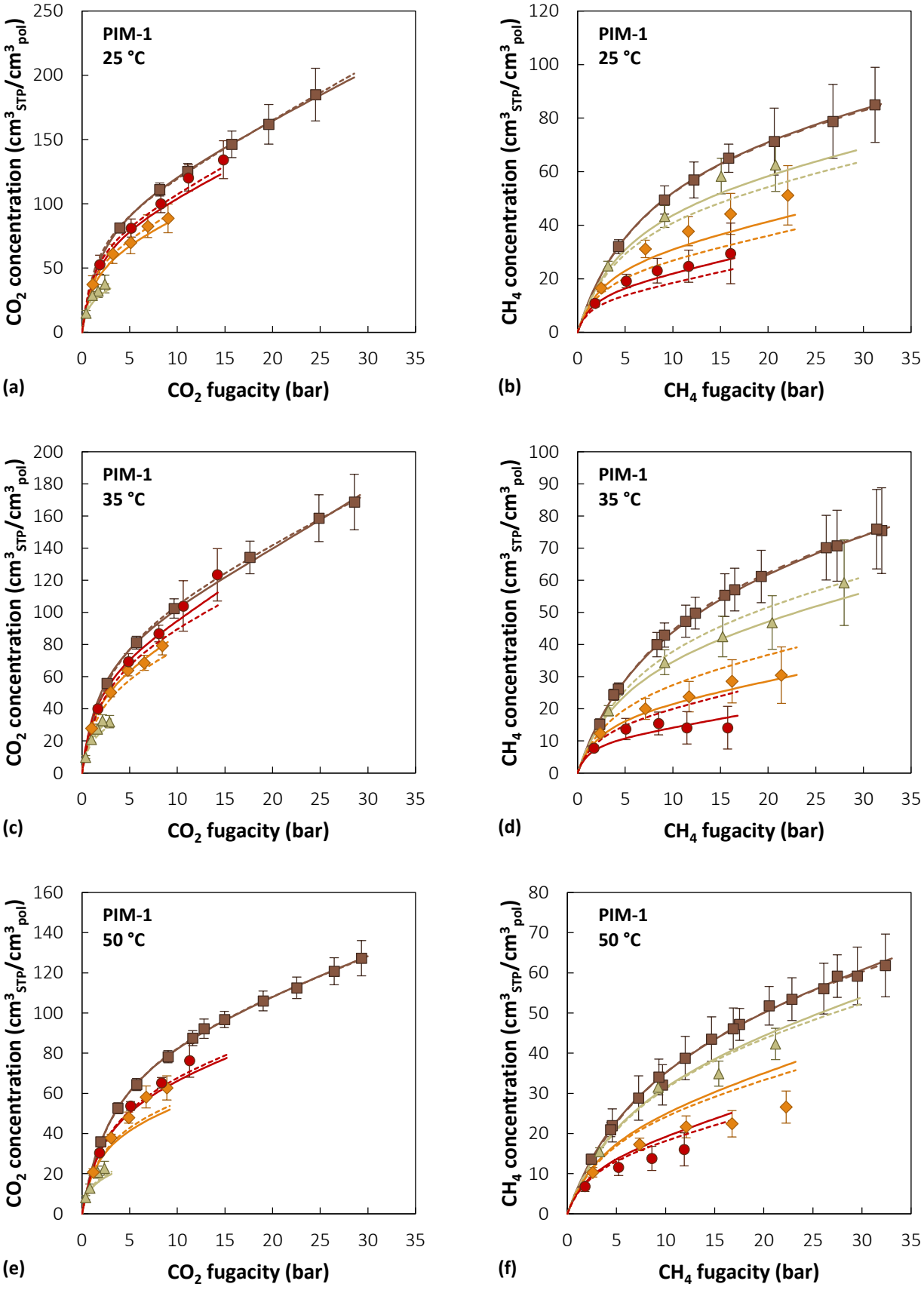

Figure 4.15. Sorption isotherms of CO_2 and CH_4 at 25 °C (a,b), 35 °C (c,d), 50 °C (e,f) in PIM-1, in pure and mixed-gas conditions (Brown squares: pure gas – Red circles: ~50% CO_2 mixture – Orange diamonds: ~30% CO_2 mixture – Green triangles: ~10% CO_2 mixture). Experimental data from [3,4]. Dashed lines represent DMS model predictions obtained using the parameters reported in **Table 4.5**, solid lines are DMS model predictions obtained with parameters reported in **Table 4.11**.

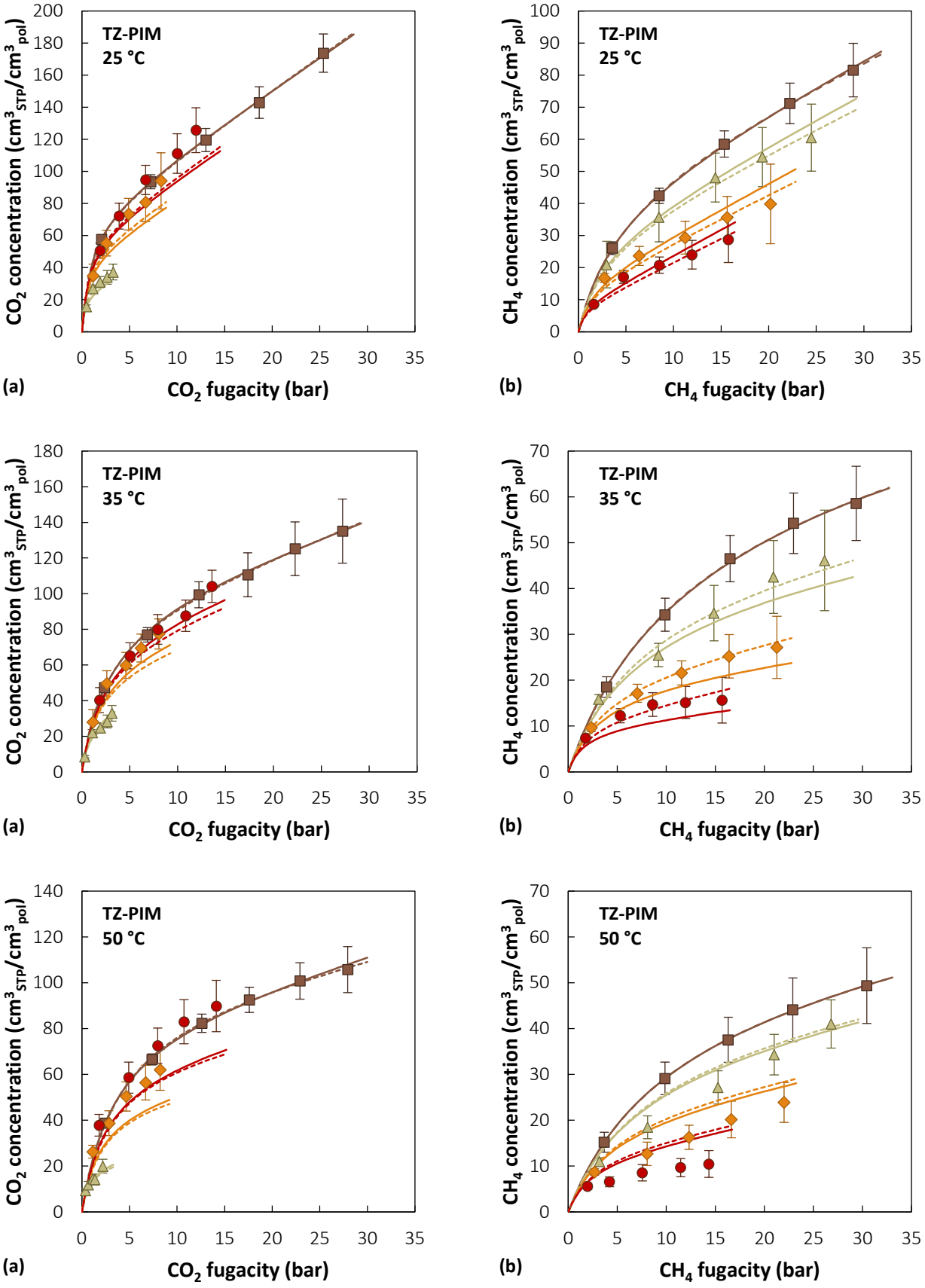

Figure 4.16. Sorption isotherms of CO_2 and CH_4 at 25 °C (a,b), 35 °C (c,d), 50 °C (e,f) in TZ-PIM, in pure and mixed-gas conditions (Brown squares: pure gas – Red circles: ~50% CO_2 mixture – Orange diamonds: ~30% CO_2 mixture – Green triangles: ~10% CO_2 mixture). Experimental data from [5]. Dashed lines represent DMS model predictions obtained using the parameters reported in **Table 4.5**, solid lines are DMS model predictions obtained with parameters reported in **Table 4.11**.

As expected, slightly different parameter sets from the ones reported in **Table 4.5** were obtained. It was observed that an increase in the value of $C'_{H,i}$ was always accompanied by a decrease in the values of $k_{D,i}$ and b_i, and vice versa. The pure- and mixed-gas predictions obtained with each parameter set is compared in **Figure 4.15** and **Figure 4.16**. Solid lines in the figures are obtained with best-fit parameters resulting from the minimization of the sum of squared errors, weighted using the experimental confidence intervals (**Eq. (4.7)**). Dashed lines in the figures are obtained with best-fit parameters resulting from minimizing the sum of squared errors, unweighted (**Eq. (4.5)**). It is remarkable that pure gas representations are almost indistinguishable (as it can be noted also by the very similar values of RSE associated to the two parameter sets), even though some of the parameters used differ by as much as 30%.

The mixed-gas calculations performed with the parameters reported in **Table 4.11** provided a modest improvement in the accuracy of the prediction in some of the cases analyzed (CO_2 in TZ-PIM at 35 °C and 50 °C, CH_4 in TZ-PIM at 50 °C, CO_2 in PIM-1 at 35 °C, CH_4 in PIM-1 at 25 °C and 35 °C, CH_4 in PTMSP at 35 °C), whereas in other cases they produced slightly less accurate results (CO_2 in TZ-PIM at 25 °C, CH_4 in TZ-PIM at 25 °C and 35 °C, CO_2 in PIM-1 at 25 °C and 50 °C, CH_4 in PIM-1 at 50 °C, CO_2 in PTMSP at 35 °C). A systematic trend was not detected, at times the average accuracy was increased for both gases at the same temperature (TZ-PIM at 50 °C case and PIM-1 at 35 °C case), other times only for one of the two gases at the same temperature (TZ-PIM at 35 °C case, PIM-1 25 °C case and PTMSP 35 °C case) and in other cases for none (TZ-PIM 25 °C case and PIM-1 50 °C case). Moreover, in some instances, the results were more accurate at certain compositions but worse at others. On the whole, the discrepancies between the accuracy of the multicomponent calculations in different conditions were not eliminated by taking into account the experimental error during the parametrization.

Effect of a constrained temperature dependence

Since the DMS model parametrization is carried out independently at each temperature, it is striking that the accuracy of the mixed-gas prediction varies so much between different temperatures. To improve the internal consistency of the parameters, a multi-temperature parametrization scheme was tested. For each gas, new parameters were obtained by considering the data at all temperatures simultaneously and constraining the parameters to follow the expected temperature dependence. In particular, the temperature dependence of k_D and b is described by a van't Hoff relation [44]:

$$k_D = k_{D0}\, e^{-\frac{\Delta H_D}{RT}} \qquad \text{Eq. (4.8)}$$

$$b = b_0\, e^{-\frac{\Delta H_b}{RT}} \qquad \text{Eq. (4.9)}$$

In **Eq. (2.59)** and **Eq. (2.60)** ΔH_D and ΔH_b are the enthalpies of sorption for Henry and Langmuir modes, R is the gas constant and T is the temperature. The preexponential factors k_{D0} and b_0 , together with ΔH_D and ΔH_b were treated as adjustable coefficients. For C'_H, no functional temperature dependence was imposed, but the values were constrained to diminish with increasing temperature. In this way, to obtain the

parameters for each gas-polymer couple at three temperatures, only 7 adjustable coefficients were used, instead of 9.

The parameter sets obtained are reported in **Table 4.12**. It is noteworthy that, in this parameter set, the values of Langmuir affinity constant for the couple CO_2-PIM-1 are always lower than the corresponding ones for CO_2-TZ-PIM at each temperature, as it would be expected given the chemical difference between the two materials. The comparison of the mixed-gas predictions obtained with the parameter sets from **Table 4.5** and **Table 4.12** is reported in **Figure 4.17** and **Figure 4.18**. Solid lines in the figures are obtained with best-fit parameters reported in **Table 4.5**, resulting from the simultaneous minimization of the sum of squared errors at three temperatures, imposing a van't Hoff temperature dependence to b and k_D, and constraining C'_H to decrease as temperature increases.

Table 4.12. Dual Mode Sorption model parameters (fugacity-based) for CO_2 and CH_4 sorption in PIM-1 and TZ-PIM, obtained by a least-square fit on data from refs. [3–5], imposing the temperature dependence constraints expressed by **Eq. (2.59)** and **Eq. (2.60)**. In parenthesis the error in multicomponent prediction obtained by fitting to **Eq. (4.5)** (reference case) is reported. The arrows indicate if the present case performs better or worse than the reference case.

			CO_2			
	T (°C)	k_D $\left(\frac{cm^3_{STP}}{cm^3_{pol}bar}\right)$	C'_H $\left(\frac{cm^3_{STP}}{cm^3_{pol}}\right)$	b (bar^{-1})	RSE_{pure}	$\overline{RSE}_{mix}$
PIM-1	25	4.150	90.56	0.638	2%	4% (4%) =
	35	2.883	89.02	0.470	3%	9% (11%) ↓
	50	1.742	85.63	0.308	1%	8% (11%) ↓
TZ-PIM	25	3.625	82.25	0.676	3%	16% (12%) ↑
	35	2.473	77.23	0.511	3%	19% (12%) ↑
	50	1.457	76.94	0.347	3%	41% (40%) ↑
			CH_4			
	T (°C)	k_D $\left(\frac{cm^3_{STP}}{cm^3_{pol}bar}\right)$	C'_H $\left(\frac{cm^3_{STP}}{cm^3_{pol}}\right)$	b (bar^{-1})	RSE_{pure}	$\overline{RSE}_{mix}$
PIM-1	25	0.759	78.51	0.130	2%	17% (21%) ↓
	35	0.561	72.98	0.113	3%	17% (21%) ↓
	50	0.369	66.17	0.093	3%	10% (17%) ↓
TZ-PIM	25	1.275	49.29	0.206	4%	17% (12%) ↑
	35	0.865	42.49	0.171	8%	20% (8%) ↑
	50	0.506	41.58	0.133	3%	52% (54%) ↓

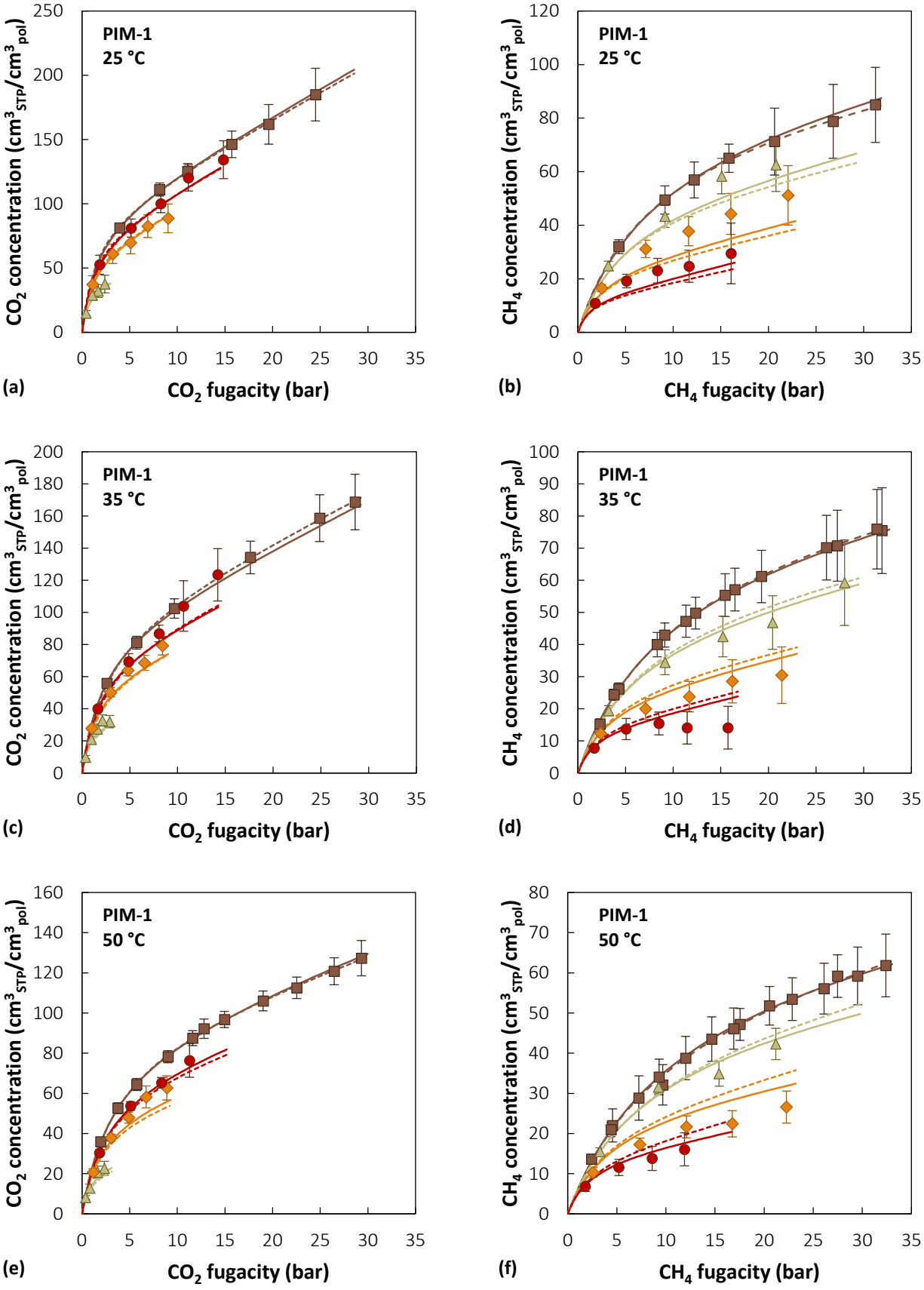

Figure 4.17. Sorption isotherms of CO_2 and CH_4 at 25 °C (a,b), 35 °C (c,d), 50 °C (e,f) in PIM-1, in pure and mixed-gas conditions (Brown squares: pure gas – Red circles: ~50% CO_2 mixture – Orange diamonds: ~30% CO_2 mixture – Green triangles: ~10% CO_2 mixture). Experimental data from [3,4]. Dashed lines represent DMS model predictions obtained using the parameters reported in **Table 4.5**, solid lines are DMS model predictions obtained with parameters reported in **Table 4.12**.

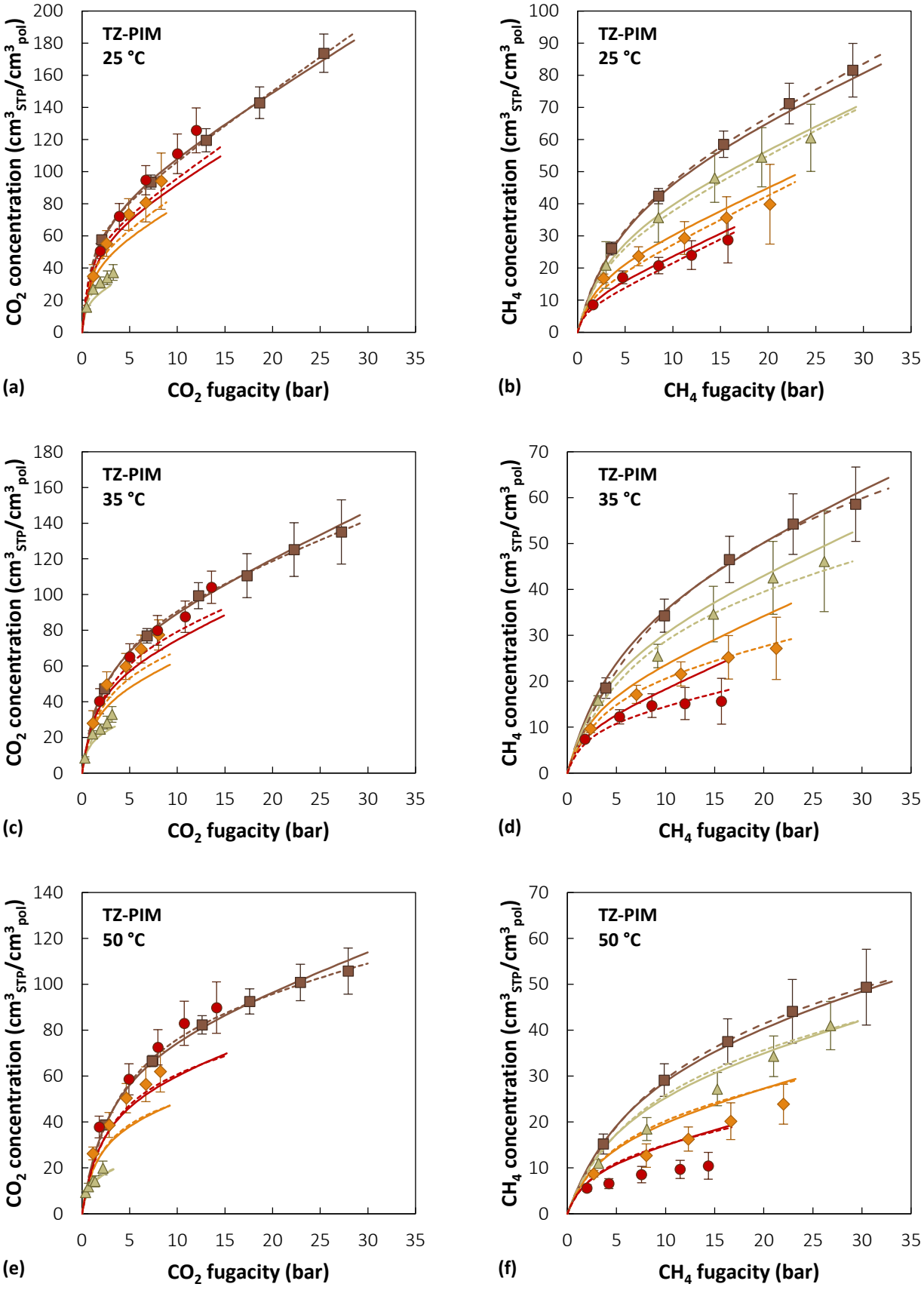

Figure 4.18. Sorption isotherms of CO_2 and CH_4 at 25 °C (a,b), 35 °C (c,d), 50 °C (e,f) in TZ-PIM, in pure and mixed-gas conditions (Brown squares: pure gas – Red circles: ~50% CO_2 mixture – Orange diamonds: ~30% CO_2 mixture – Green triangles: ~10% CO_2 mixture). Experimental data from [5]. Solid lines represent DMS model predictions obtained using the parameters reported in **Table 4.5**, dashed lines are DMS model predictions obtained with parameters reported in **Table 4.12**.

To satisfy the temperature dependence constraint, a slightly less accurate representation of pure-gas sorption is generally observed, especially at higher pressure. The largest deviations are observed in the cases of CO_2 and CH_4 sorption in TZ-PIM at 25 °C and 50 °C, for CO_2 sorption in PIM-1 at 35 °C and for CH_4 sorption in PIM-1 at 25 °C.

The mixed-gas sorption calculations performed with the parameters reported in **Table 4.12** yielded a slight improvement in the accuracy of the prediction of CO_2 and CH_4 sorption in PIM-1 at all temperatures. On the other hand, in the case of TZ-PIM, the mixed-gas calculation yielded comparable results for both gases at 50 °C, but less accurate predictions for both gases in the 35 °C case. At 25 °C, the results for CH_4 sorption in TZ-PIM were slightly better compared to those obtained with parameter set without a consistent temperature dependence, while those for CO_2 were slightly worse. Therefore, on the whole, this parametrization route presented improvements, in terms of internal consistency of the parameter set and their physical interpretation, but it still didn't eliminate the variability in the accuracy of the mixed-gas sorption results. Similar consideration could be made in the case of HAB-6FDA and TR450, addressed in the next section.

4.3.2.3 HAB-6FDA and TR450

In **Figure 4.19** the predictions of the Dual Mode Sorption Model together with the experimental data measured at 35°C [9] for the sorption of pure CO_2, pure CH_4 and a 30/70 mol% CO_2/CH_4 mixture in HAB-6FDA and TR450 are shown. For these two materials the DMS model predictions of mixed-gas sorption were extremely inaccurate. For CO_2 the DMS model prediction has an average 32% relative deviation from the experimental data in the case of HAB-6FDA and 23% in the case of TR450. The corresponding RSE values for CH_4 are 67% and 100%.

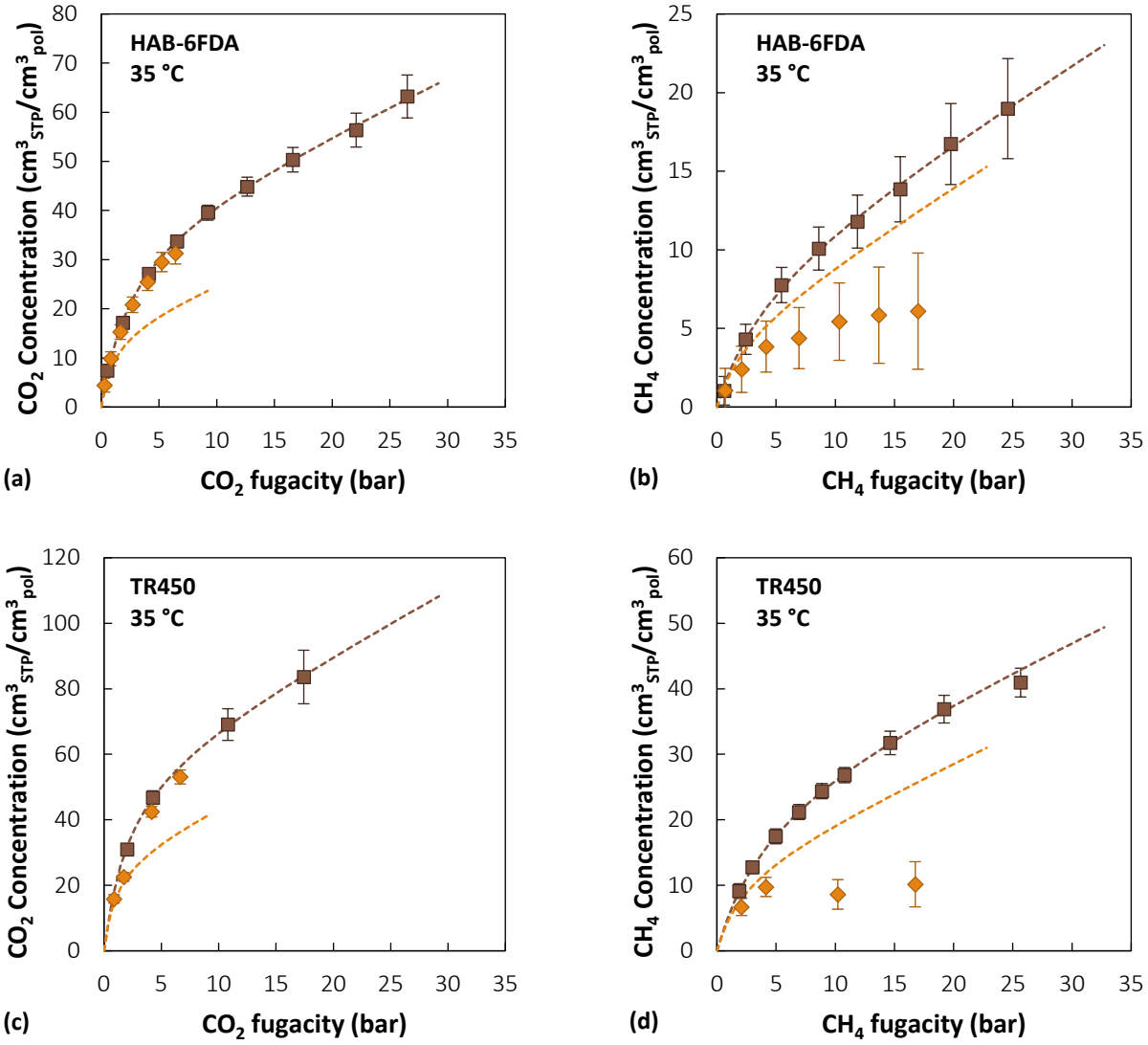

Figure 4.19. Sorption isotherms of CO_2 and CH_4 at 35 °C in HAB-6FDA (a,b) and TR450 (c,d) at pure- and mixed-gas conditions (Brown squares: pure gas – Orange diamonds: ~30% CO_2 mixture [9]). Dashed lines are DMS model predictions.

In an effort to try to determine possible ways to improve the accuracy of the model predictions, different parameter estimation methodology were tested, since the Dual Mode Sorption model parameters are reportedly sensitive, among other factors, to the parametrization route followed [48,57–59].

Four different parameterization routes were examined. Different DMS model parameter sets were obtained as best fits of pure-gas sorption isotherms through a least-square procedure, using either concentration squared differences (**Eq. (4.10)** and **Eq. (4.11)**) or solubility coefficient squared differences (**Eq. (4.12)** and **Eq. (4.13)**). In the case of **Eq. (4.10)** and **Eq. (4.12)**, the squared differences were weighted using the inverse squared experimental confidence intervals [50]. **Eq. (4.11)** was the one employed in all cases to retrieve the DMS parameters reported in **Table 4.5**. The parameters obtained for CO_2 and CH_4 in both materials are summarized for each minimization method in **Table 4.13** and a comparison of the pure- and mixed-gas sorption representation yielded by each parameter set is presented in **Figure 4.20**.

$$\chi^2 = \sum_{i=1}^{N_{tot}} \frac{1}{s_i^2}\left[c_{i,exp} - c_{i,mod}\right]^2 = \sum_{i=1}^{N_{tot}} \frac{1}{s_i^2}\left[c_{i,exp} - \left(k_{D,i}f_i + \frac{C'_{H,i}b_i f_i}{1 + b_i f_i}\right)\right]^2 \quad \text{Eq. (4.10)}$$

$$\chi^2 = \sum_{i=1}^{N_{tot}} \left[c_{i,exp} - c_{i,mod}\right]^2 = \sum_{i=1}^{N_{tot}} \left[c_{i,exp} - \left(k_{D,i}f_i + \frac{C'_{H,i}b_i f_i}{1 + b_i f_i}\right)\right]^2 \quad \text{Eq. (4.11)}$$

$$\chi^2 = \sum_{i=1}^{N_{tot}} \frac{1}{s_i^2}\left[S_{i,exp} - S_{i,mod}\right]^2 = \sum_{i=1}^{N_{tot}} \frac{1}{s_i^2}\left[S_{i,exp} - \left(k_{D,i} + \frac{C'_{H,i}b_i}{1 + b_i f_i}\right)\right]^2 \quad \text{Eq. (4.12)}$$

$$\chi^2 = \sum_{i=1}^{N_{tot}} \left[S_{i,exp} - S_{i,mod}\right]^2 = \sum_{i=1}^{N_{tot}} \left[S_{i,exp} - \left(k_{D,i} + \frac{C'_{H,i}b_i}{1 + b_i f_i}\right)\right]^2 \quad \text{Eq. (4.13)}$$

In the previous formulas, s_i represents the confidence interval associated with the experimental value of the concentration $c_{i,exp}$, N_{tot} is the total number of experimental points, f_i is the gas fugacity, $S_{i,exp}$ the solubility coefficient calculated as $c_{i,exp}/f_i$, and $k_{D,i}$, $C'_{H,i}$, b_i are the DMS parameters for the polymer-i penetrant couple.

Consistently with the fact that more condensable gases tend to have larger affinity constants, the values for the b parameter associated with CO_2 sorption are systematically larger than those estimated for CH_4. In accordance with the difference in free volume between the two materials, which is 19.6% for TR450 and 15.0% for HAB-6FDA, the Langmuir capacity constants C'_H of both gases are found to be higher in TR450 than in HAB-6FDA in all parameter sets except the one obtained by minimizing the error-weighted solubility squared differences in pure CH_4.

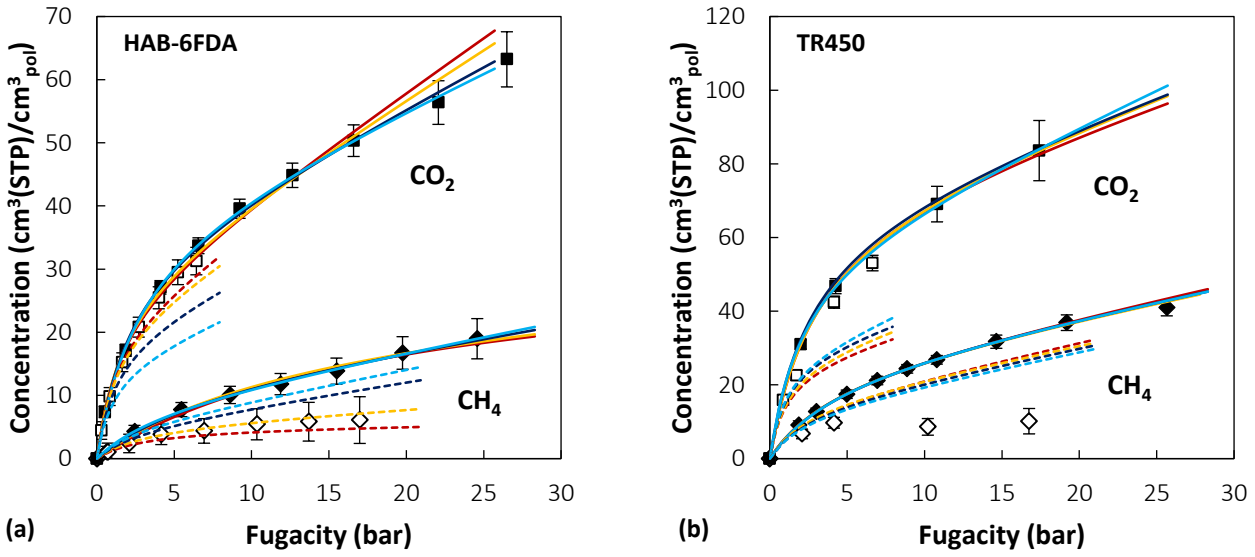

Figure 4.20. Comparison of the Dual Mode Sorption model calculations with different parameter sets of CO_2 (squares) and CH_4 (diamonds) sorption in (a) HAB-6FDA and (b) TR450 at 35 °C, at pure-gas conditions (filled markers and solid lines), and in the case of a 30 mol% CO_2 mixture (empty markers and dashed lines). Blue were obtained with **Eq. (4.10)**, light blue with **Eq. (4.11)**, red with **Eq. (4.12)** and orange with **Eq. (4.13)**.

Table 4.13. Binary DMS model best fit parameter sets obtained by minimizing different squared differences functions.

	Gas	k_D $\left(\frac{cm^3_{STP}}{cm^3_{pol}bar}\right)$	C'_H $\left(\frac{cm^3_{STP}}{cm^3_{pol}}\right)$	b (bar^{-1})	Function minimized
HAB-6FDA	**CO_2**	1.234	33.78	0.462	Eq. (4.10)
		1.081	37.39	0.382	Eq. (4.11)
		1.678	26.07	0.659	Eq. (4.12)
		1.522	28.36	0.595	Eq. (4.13)
	CH_4	0.362	12.75	0.136	Eq. (4.10)
		0.460	9.05	0.224	Eq. (4.11)
		0.015	32.01	0.051	Eq. (4.12)
		0.137	23.31	0.074	Eq. (4.13)
TR450	**CO_2**	1.469	67.11	0.392	Eq. (4.10)
		1.856	57.95	0.469	Eq. (4.11)
		1.323	69.38	0.345	Eq. (4.12)
		1.477	66.96	0.360	Eq. (4.13)
	CH_4	0.812	26.03	0.216	Eq. (4.10)
		0.813	26.01	0.215	Eq. (4.11)
		0.878	24.30	0.237	Eq. (4.12)
		0.799	25.99	0.220	Eq. (4.13)

The different parameter sets obtained in each case yielded predictions of extremely varying accuracy for the mixed-gas case, especially in the case of the polyimide. Indeed, in the case of HAB-6FDA a very good representation of mixed-gas data was given by the parameter set obtained by minimizing the error-weighted solubility squared differences, even though this was accompanied by a less accurate representation of pure CO_2 sorption at high pressure compared to the other cases. On the other hand, in the case of TR450, the parameters obtained by minimizing the unweighted concentration differences yielded the best results. Regrettably, the same method didn't yield improved predictions in both cases.

Stevens et al. [47] reported DMS model parameters for CO_2 and CH_4 sorption in HAB-6FDA and TR450. In their work, the parameters were obtained using data sets for 3 gases (CO_2, CH_4, N_2) and at 5 temperatures simultaneously in the fitting procedure. Moreover, a temperature dependence and a relation with the critical temperature of the penetrants were imposed to further constrain the parameter values. This additional information could not be used to determine the DMS parameters for the samples reported here.

The parameters obtained by Stevens et al. [47] are reported in **Table 4.14** for comparison. They differ from those obtained in this work, as expected, since a different experimental data set and a different parametrization route were employed in their estimation. This DMS parameter set yielded a less faithful

representation of the pure-gas data, but, surprisingly a more accurate prediction in the multicomponent case (as it can be seen in **Figure 4.21**), both in the case of HAB-6FDA and TR450. The values of $\overline{RSE}_{mix}$ of the predictions made with the literature parameter sets are 17% and 31% for CO_2 and CH_4 in HAB-6FDA, and 21% and 41% for CO_2 and CH_4 in TR450, which is an overall significant improvement with respect to the previous parameter set employed.

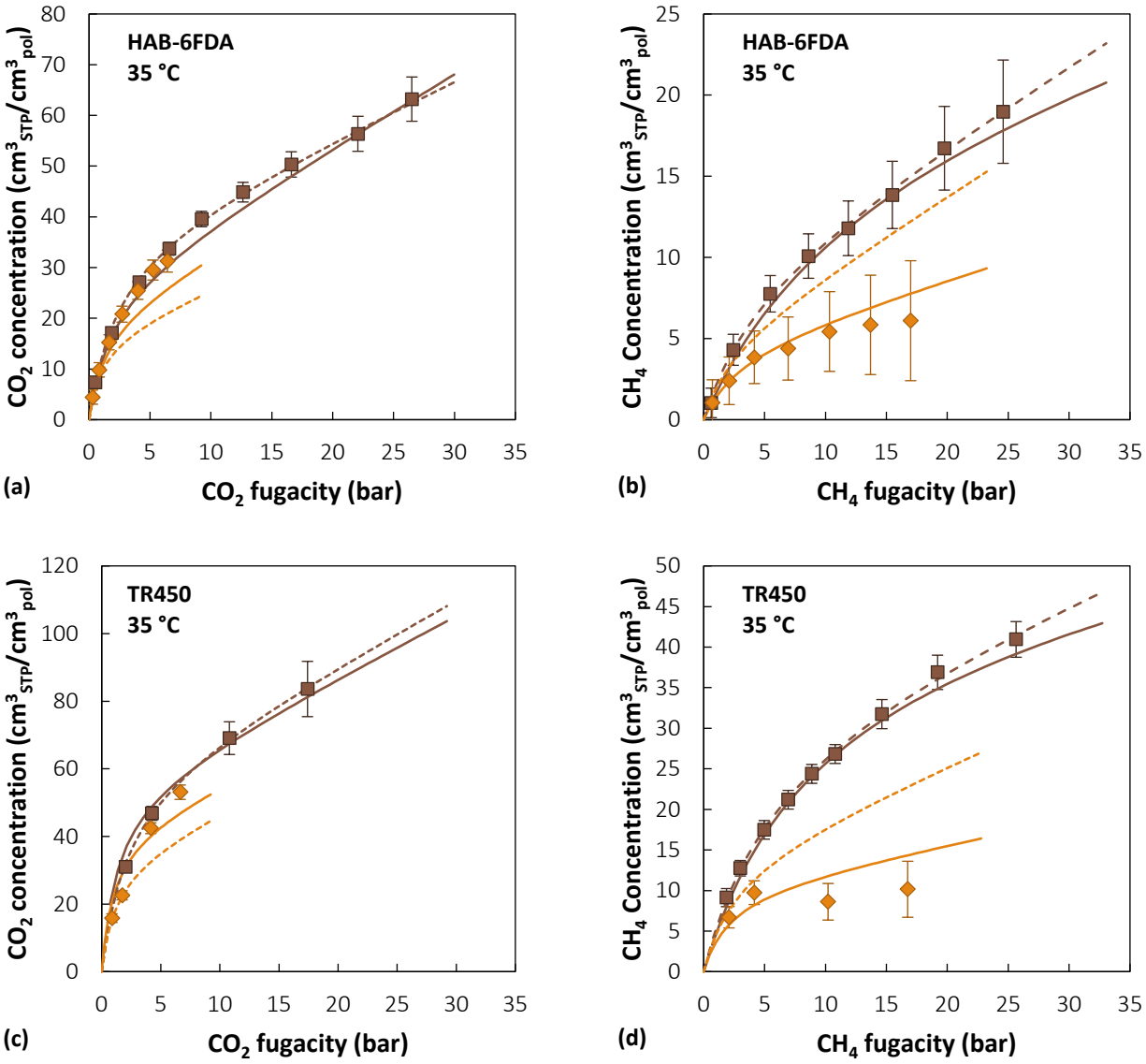

Figure 4.21. Comparison of the Dual Mode Sorption model calculations for CO_2 and CH_4 sorption in HAB-6FDA and TR450 at pure (brown) and mixed-gas (orange, 30 mol% CO_2) conditions at 35 °C. Solid lines are obtained with the parameter set of Stevens et al. [47], while dashed lines with the parameters reported in **Table 4.5**.

Table 4.14. DMS pressure-based parameters for CO_2 and CH_4 sorption in HAB-6FDA and TR-450 at 35 °C obtained by Stevens et al. [47]

	Gas	$k_D \left(\frac{cm^3_{STP}}{cm^3_{pol}atm}\right)$	$C'_H \left(\frac{cm^3_{STP}}{cm^3_{pol}}\right)$	$b\ (atm^{-1})$
HAB-6FDA	CO_2	1.42	27	0.56
	CH_4	0.21	19	0.081
TR450	CO_2	1.78	54	0.76
	CH_4	0.26	44	0.11

4.3.3 Discussion on the DMS and NELF results

In general, the NELF model yielded mixed-gas sorption results of more consistent accuracy. It must be noted that this does not result from the use of a larger number of adjustable parameters. Indeed, calculation with the NELF model requires just 2 adjustable parameters for each gas, k_{ij} and k_{sw}, whereas the DMS model needs 3 adjustable parameters for each gas, k_D, b and C'_H. In the case of HAB-6FDA and TR450, the best DMS parameters, by comparison with the experimental data, were not found by following the same optimization routine for the two materials, therefore, in the absence of experimental data for validation, it would not be possible to anticipate which case would yield the best mixed-gas sorption prediction.

Explanations for the deviation of the multicomponent DMS predictions from the experimental data were identified originally by Koros [45] in the possible presence of non-negligible penetrant-penetrant specific interactions or as a consequence of swelling and plasticization effects, not accounted for in the DMS model, that would make the parameters concentration-dependent. There have been extensions and modifications to the DMS model to include these aspects with the introduction of additional parameters [60–62], but the original version is still the most used one. The effect of specific penetrant-penetrant interactions was tested with the NELF model, and they were found to have a negligible effect on mixed-gas sorption predictions. For this reason, penetrant-penetrant specific interactions are not believed to be a plausible explanation for the discrepancies emerged with the use of the DMS model. On the other hand, swelling is explicitly accounted for in the NELF model, unlike the DMS model.

In order to address the issues uncovered in multicomponent calculations with the DMS model systematically, a sensitivity analysis was carried out: the effect of CO_2 and CH_4 parametrization on the multicomponent calculation was studied separately, analyzing how the mixed-gas sorption results are affected by variations of $C'_{H,i}$, $k_{D,i}$, b_i while b_j is kept fixed, and, subsequently, the effect of changes in the value of b_j were also taken into account.

4.4 Sensitivity analysis of the multicomponent calculations with the DMS model

4.4.1 Confidence intervals of the DMS model parameters

A comprehensive search in the parameters space was conducted, using a grid method, in order to identify a range of DMS model parameter values that allow to obtain equally satisfactory representations of the pure-gas data. Once such a range was estimated, it was tested whether different parameter sets, within those confidence intervals, could lead to better mixed-gas predictions than the ones obtained with the best-fit sets. The results are presented in the following for the case of CH_4 solubility in PIM-1. Results analogous to the ones presented in this section were obtained also for the other cases. The curves presented in the following analysis were fit to **Eq. (4.5)** in order to obtain the various DMS parameter sets.

Figure 4.22 shows a contour plot of the Relative Standard Error (RSE) in the calculation of pure CH_4 sorption in PIM-1 at 25 °C, obtained varying b and C'_H, while holding k_D constant at its best fit value: 0.651 cm^3_{STP}/cm^3_{pol}. Each line represents a locus of constant RSE in the Langmuir parameter space, for a fixed value of Henry's constant. When k_D is allowed to vary as well, surfaces at constant error in the three-dimensional parameter space are obtained. As a criterion to delimit the confidence intervals, a maximum value of 1.5% for the standard error was selected, which represents a small variation from the accuracy of the best fit parameter set for this case, which is 1% at all temperatures (**Table 4.6**).

In **Figure 4.23 (a)** is a 3D plot is presented, in which the three colored regions correspond to domains in the parameter space where $RSE < RSE_{max}$ for CH_4 sorption in PIM-1 at the three different temperatures. Therefore, the coordinates of each point within the colored region correspond to a parameter set that satisfies the accuracy criterion. The sorption isotherms obtained with all the parameter sets included in the colored regions of part (a) of the figure are represented together in **Figure 4.23 (b),** and one can see that there is indeed a small, but detectable, variation in the representation of the experimental data using either of the parameter sets. This variability, however, is always lower than the experimental uncertainty of the data.

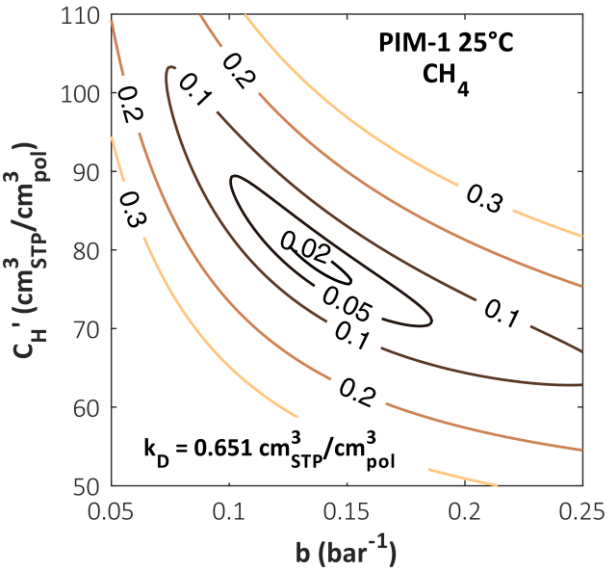

Figure 4.22. Contour plot of the Relative Standard Error (RSE) of CH_4 sorption in PIM-1 at 25 °C, obtained varying the Langmuir sorption parameters, with a fixed value of the Henry's constant.

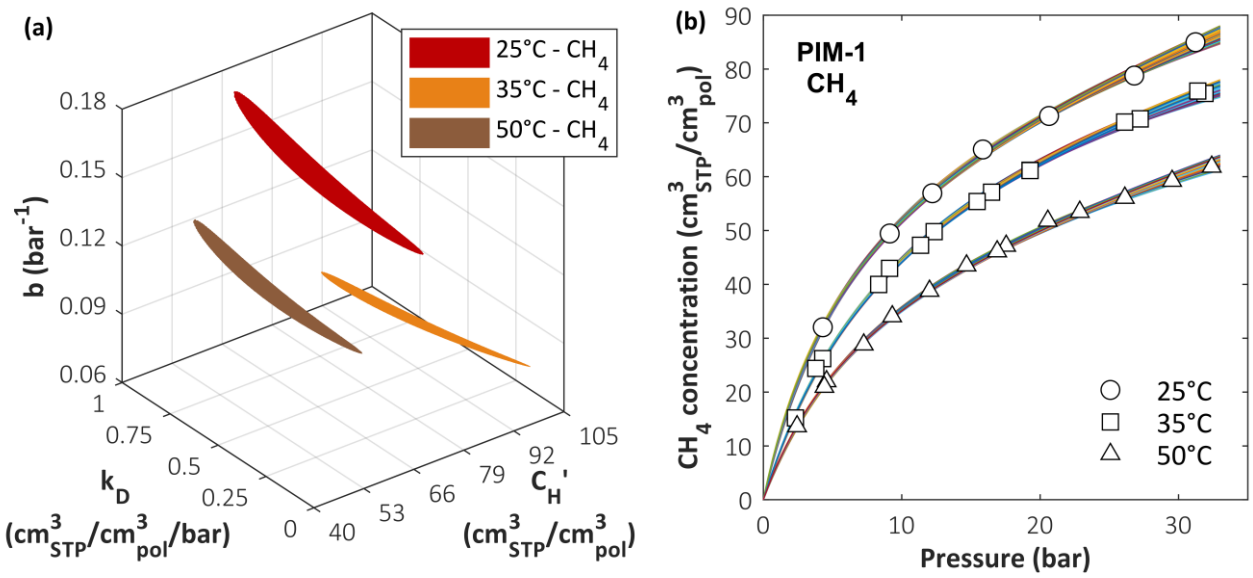

Figure 4.23. (a) Surfaces enclosing the range where DMS parameter sets yield a $RSE < RSE_{max}$ in the prediction of CH_4 sorption in PIM-1 at three different temperatures; (b) CH_4 sorption isotherms in PIM-1 at 25, 35 and 50 °C, calculated with the parameter sets enclosed by the corresponding colored regions in the plot on the left.

The upper and lower limits in each direction of the isosurfaces reported in **Figure 4.23 (a)** can be used to attribute confidence intervals to the DMS parameters. Confidence intervals for nonlinear regression functions are often asymmetrical and this was observed also by other authors for the DMS model parameters [47,57]. Confidence intervals of the DMS parameters for CO_2 and CH_4 sorption in PIM-1 are reported in **Table 4.15**, while those of TZ-PIM are reported in **Table 4.16**. Clearly, not all the combinations of parameters within their respective confidence interval would give a valid set, otherwise the confidence

region in the 3D parameter space would be represented by a parallelepiped. However, for all values included in the confidence interval of one parameter, it would be possible to find values of the other two parameters such that the accuracy criterion is satisfied. As a consequence, when using only one of the parameters, like in the case of b_j in the calculation of mixed-gas sorption for component i, all values belonging to its confidence interval should be considered acceptable.

Table 4.15. Confidence intervals of the fugacity-based DMS parameters (average relative deviation < 1.5%) for CO_2 and CH_4 sorption in PIM-1 at three different temperatures.

T (°C)	k_{D,CO_2} $\left(\frac{cm^3_{STP}}{cm^3_{pol}bar}\right)$	C'_{H,CO_2} $\left(\frac{cm^3_{STP}}{cm^3_{pol}}\right)$	b_{CO_2} (bar^{-1})	k_{D,CH_4} $\left(\frac{cm^3_{STP}}{cm^3_{pol}bar}\right)$	C'_{H,CH_4} $\left(\frac{cm^3_{STP}}{cm^3_{pol}}\right)$	b_{CH_4} (bar^{-1})
25	$4.046^{+0.253}_{-0.552}$	$90.04^{+16.57}_{-6.50}$	$0.710^{+0.272}_{-0.291}$	$0.651^{+0.336}_{-0.290}$	$78.83^{+15.67}_{-15.28}$	$0.136^{+0.059}_{-0.031}$
35	$2.890^{+0.311}_{-0.308}$	$94.83^{+12.53}_{-10.15}$	$0.388^{+0.133}_{-0.083}$	$0.541^{+0.316}_{-0.408}$	$75.87^{+23.78}_{-15.93}$	$0.106^{+0.042}_{-0.029}$
50	$1.596^{+0.325}_{-0.096}$	$89.30^{+6.47}_{-10.88}$	$0.290^{+0.105}_{-0.053}$	$0.543^{+0.237}_{-0.443}$	$57.90^{+25.60}_{-12.74}$	$0.105^{+0.049}_{-0.035}$

Table 4.16. Confidence intervals of the fugacity-based DMS parameters (average relative deviation < 1.5%) for CO_2 and CH_4 sorption in TZ-PIM at three different temperatures.

T (°C)	k_{D,CO_2} $\left(\frac{cm^3_{STP}}{cm^3_{pol}bar}\right)$	C'_{H,CO_2} $\left(\frac{cm^3_{STP}}{cm^3_{pol}}\right)$	b_{CO_2} (bar^{-1})	k_{D,CH_4} $\left(\frac{cm^3_{STP}}{cm^3_{pol}bar}\right)$	C'_{H,CH_4} $\left(\frac{cm^3_{STP}}{cm^3_{pol}}\right)$	b_{CH_4} (bar^{-1})
25	$4.127^{+0.224}_{-0.234}$	$70.58^{+5.75}_{-5.28}$	$1.127^{+0.474}_{-0.278}$	$1.400^{+0.191}_{-0.226}$	$48.09^{+9.50}_{-7.13}$	$0.214^{+0.080}_{-0.055}$
35	$1.982^{+0.226}_{-0.255}$	$89.53^{+8.15}_{-7.18}$	$0.378^{+0.084}_{-0.062}$	$0.378^{+0.066}_{-0.378}$	$67.12^{+27.58}_{-3.99}$	$0.087^{+0.012}_{-0.029}$
50	$0.903^{+0.307}_{-0.346}$	$92.42^{+12.85}_{-10.35}$	$0.263^{+0.070}_{-0.055}$	$0.350^{+0.244}_{-0.292}$	$51.41^{+22.33}_{-13.26}$	$0.101^{+0.047}_{-0.035}$

4.4.2 Evaluation of mixed-gas sorption

All the parameter sets that satisfied the condition $RSE<RSE_{max}$ in the pure-gas sorption representation, were used to calculate mixed-gas sorption isotherms, using the best-fit values reported in **Table 4.5** for b_{CO_2}. To quantify the accuracy of the mixed-gas prediction ($\overline{RSE}_{mix}$), the average RSE of isotherms at three concentrations (10/30/50 mol.% CO_2) for each temperature was used, and then the lowest and the highest results were selected, in order to identify the best and worst predictions, labelled respectively *Set 1* and *Set 2*. The parameter sets that correspond to these two extreme cases and their RSE values are summarized in **Table 4.17**. The calculated sorption isotherms are shown in **Figure 4.24**.

At each temperature, both parameter sets have a remarkably similar accuracy in the representation of pure-gas data, but they yield a significantly different prediction of the mixed-gas behavior. For instance, the solid lines in **Figure 4.24** (obtained with *Set 1*) show a very good agreement with the experimental data, whereas the dashed ones (obtained with *Set 2*) are even less accurate than the initial result obtained with

the best-fit parameter set. Allowing also for the experimental error, the two pure-gas representations (black lines in **Figure 4.24**) at each temperature are deemed to be equivalent and no reason for choosing one over the other could be suggested. Therefore, in absence of mixed-gas experimental data to validate against, the confidence in the accuracy of the calculation would be weakened. The same variability was observed also in the case of CH_4 sorption in TZ-PIM, while for CO_2 sorption in both PIM-1 and TZ-PIM, the uncertainty in the mixed-gas predictions was generally lower within the confidence region of the parameters.

This uncertainty is reflected also in the evaluation of the solubility-selectivity: comparing the results obtained with *Set 1* and *Set 2* (**Figure 4.25**) it is possible to see that not only the results obtained with *Set 1* are in much better agreement with the experimental data, but also that the pressure and concentration dependence predicted by the two sets is significantly different, and in one case it is consistent with the general trend of the experimental point, while in the other case is the opposite.

Table 4.17. DMS model fugacity based parameter sets used in the calculation of mixed gas sorption of CO_2 and CH_4 in PIM-1 reported in **Figure 4.24**.

	T (°C)	k_{D,CH_4} $\left(\frac{cm^3_{STP}}{cm^3_{pol}bar}\right)$	C'_{H,CH_4} $\left(\frac{cm^3_{STP}}{cm^3_{pol}}\right)$	b_{CH_4} (bar^{-1})	RSE_{pure}	$\overline{RSE}_{mix}$
Set 1	25	0.940	66.52	0.174	1.5%	13%
	35	0.084	100.56	0.078	1.5%	7%
	50	0.317	67.15	0.094	1.5%	13%
Set 2	25	0.428	89.57	0.115	1.5%	27%
	35	0.622	73.15	0.108	1.5%	23%
	50	0.763	47.05	0.140	1.5%	21%

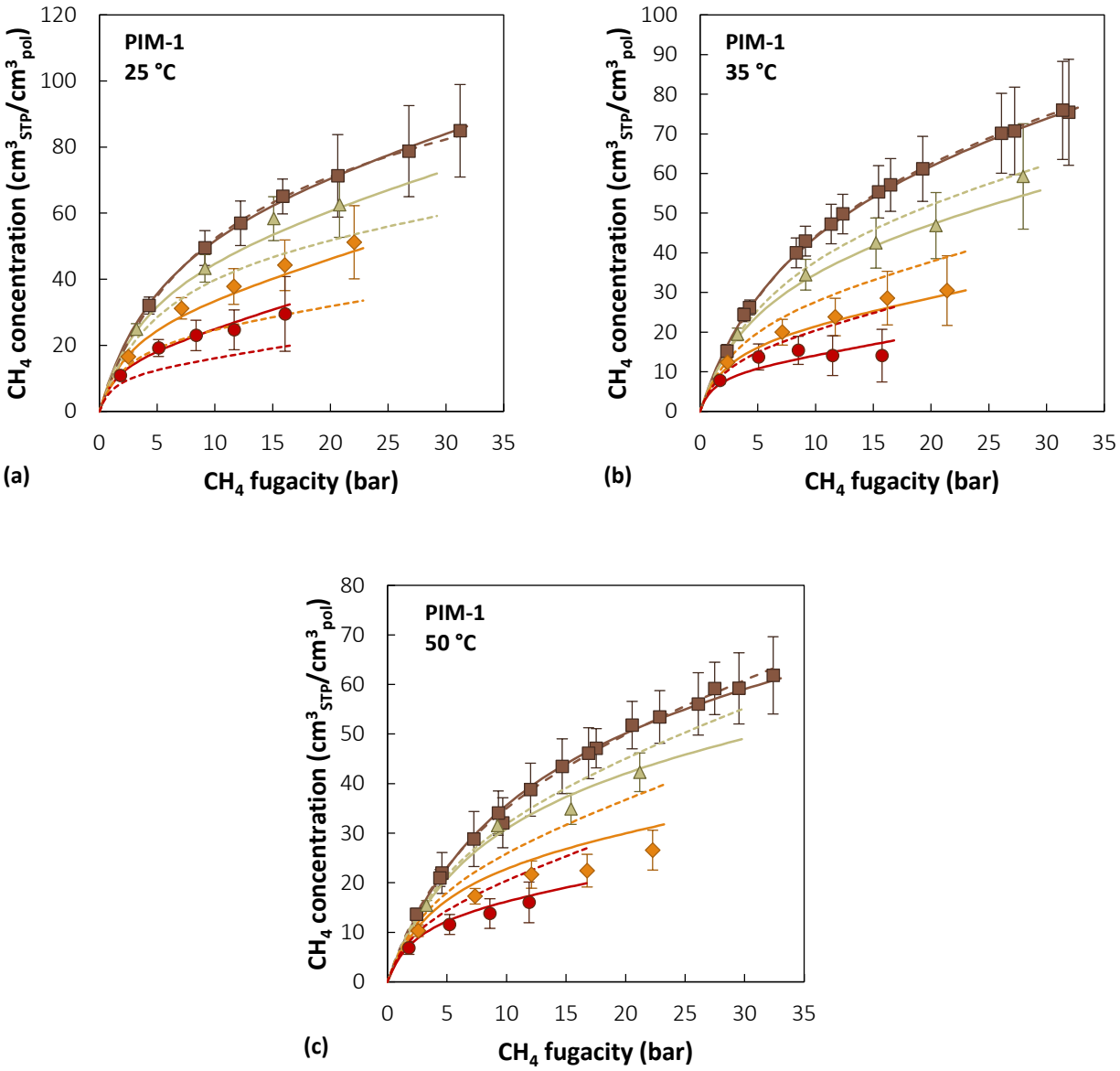

Figure 4.24. Dual Mode Sorption model mixed-gas predictions of CH_4 sorption in PIM-1 at 25 °C (a), 35 °C (b), 50 °C (c) obtained with the two parameter sets reported in **Table 4.17**. (Brown squares: pure gas – Green triangles: ~10% CO_2 mixture – Orange diamonds: ~30% CO_2 mixture – Red circles: ~50% CO_2 mixture [3,4]). Solid lines are predictions of parameter *Set 1*, dashed ones are obtained with parameter *Set 2*.

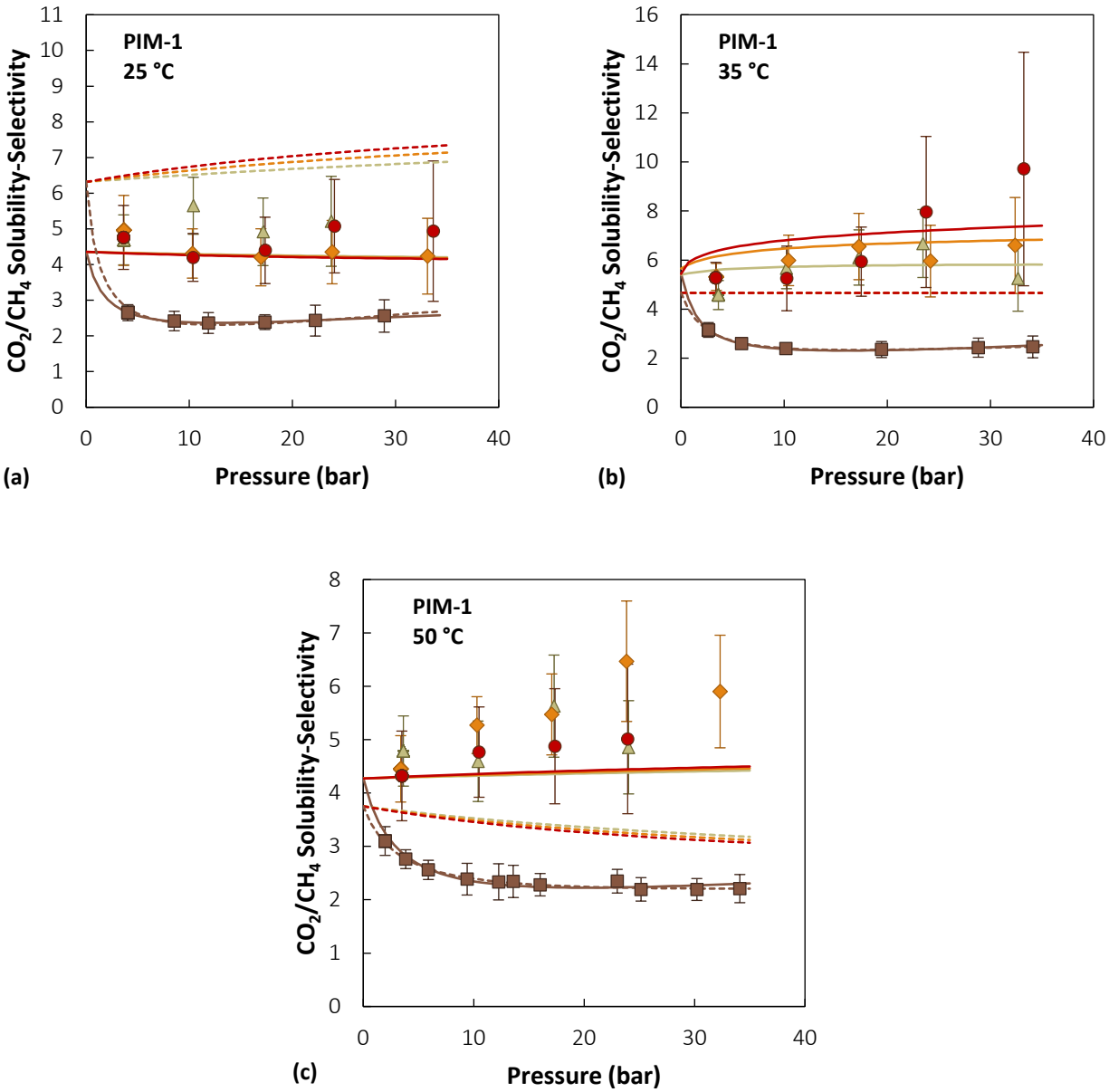

Figure 4.25. CO_2/CH_4 solubility-selectivity at 25, 35 and 50 °C in PIM-1 (Brown squares: pure gas – Red circles: ~50% CO_2 mixture – Orange diamonds: ~30% CO_2 mixture – Green triangles: ~10% CO_2 mixture [3,4]). Solid lines are DMS model predictions performed with Set 1 in **Table 4.17**, dashed lines are obtained with Set 2.

By looking at the relationship between the deviations in the pure-gas data fitting and the mixed-gas prediction, the level of uncertainty that is inherent in the calculation becomes more apparent. In **Figure 4.26** the deviation in the pure-gas data representation (RSE_{pure}) is related to the error in the mixed-gas prediction ($\overline{RSE}_{mix}$). Each point in the plot represents a calculation performed with a different parameter set, among those meeting the accuracy criterion (**Figure 4.23 (a)**).

It can be seen that, when moving to the right, i.e. further away from the best-fit parameter set and therefore towards slightly higher deviations in the pure-gas data correlation, a small variation of RSE_{pure}

results in a much wider range of possible outcomes for $\overline{RSE}_{mix}$, thus the reliability of the calculation becomes less predictable. The interval of the values assumed by $\overline{RSE}_{mix}$ expands both towards higher and lower values, so that better mixed-gas predictions can indeed be found with slightly "less accurate" pure-gas data representations, and not with the best-fit parameter set.

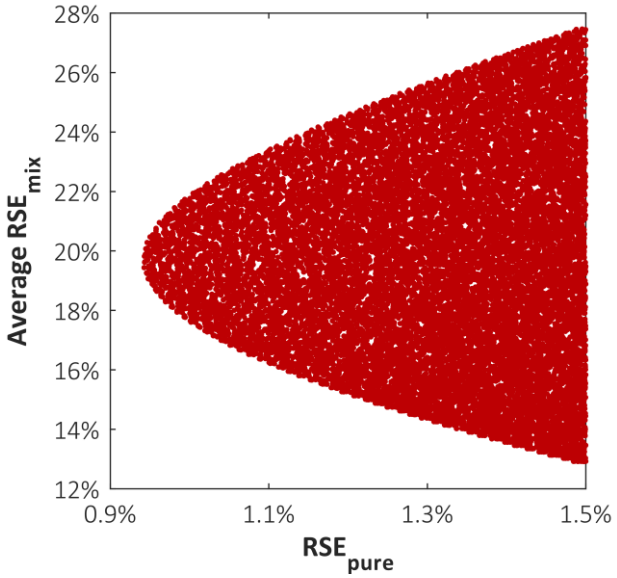

Figure 4.26. Accuracy range of the mixed-gas prediction (y-axis) for CH_4 in PIM-1 at 25 °C corresponding to a given accuracy in the pure-gas data representation (x-axis). Each point represents the result obtained with a different parameter set among those enclosed in the colored region of **Figure 4.23 (a)**.

4.4.3 Effect of the affinity constant of the second gas

The mixed-gas sorption results depend also strongly on the value of the Langmuir affinity constant of the second component, which is found in the Dual Mode Sorption model expression for sorbed concentration in the multicomponent case. The confidence intervals reported in **Table 4.15** and **Table 4.16**, represent the range over which the affinity constant of the second component could vary, and were used to study the its influence on mixed-gas sorption prediction.

In **Figure 4.27**, the same region of acceptable parameter sets for CH_4 sorption in PIM-1 at 25 °C found in **Figure 4.23 (a)** is represented, but, in these plots, a color scale indicates the average accuracy in the mixed-gas prediction corresponding to each point in the plot. The calculation is repeated for different values of b_{CO_2}, chosen to span its entire $RSE < RSE_{max}$ region. It can be seen that a greater accuracy of the mixed-gas predictions is not attained with the best-fit value of b_{CO_2} reported in **Table 4.5** (0.710 bar^{-1}), but with a lower one instead (top-left corner of **Figure 4.27**), whereas with higher values it becomes increasingly difficult to have good predictions at all (bottom-right corner of **Figure 4.27**). Once more, this was not a general trend. For example, in the cases of CH_4 sorption in PIM-1 at 35 and 50 °C, the more accurate mixed-gas predictions could be attained with values of b_{CO_2} higher than the best fit one.

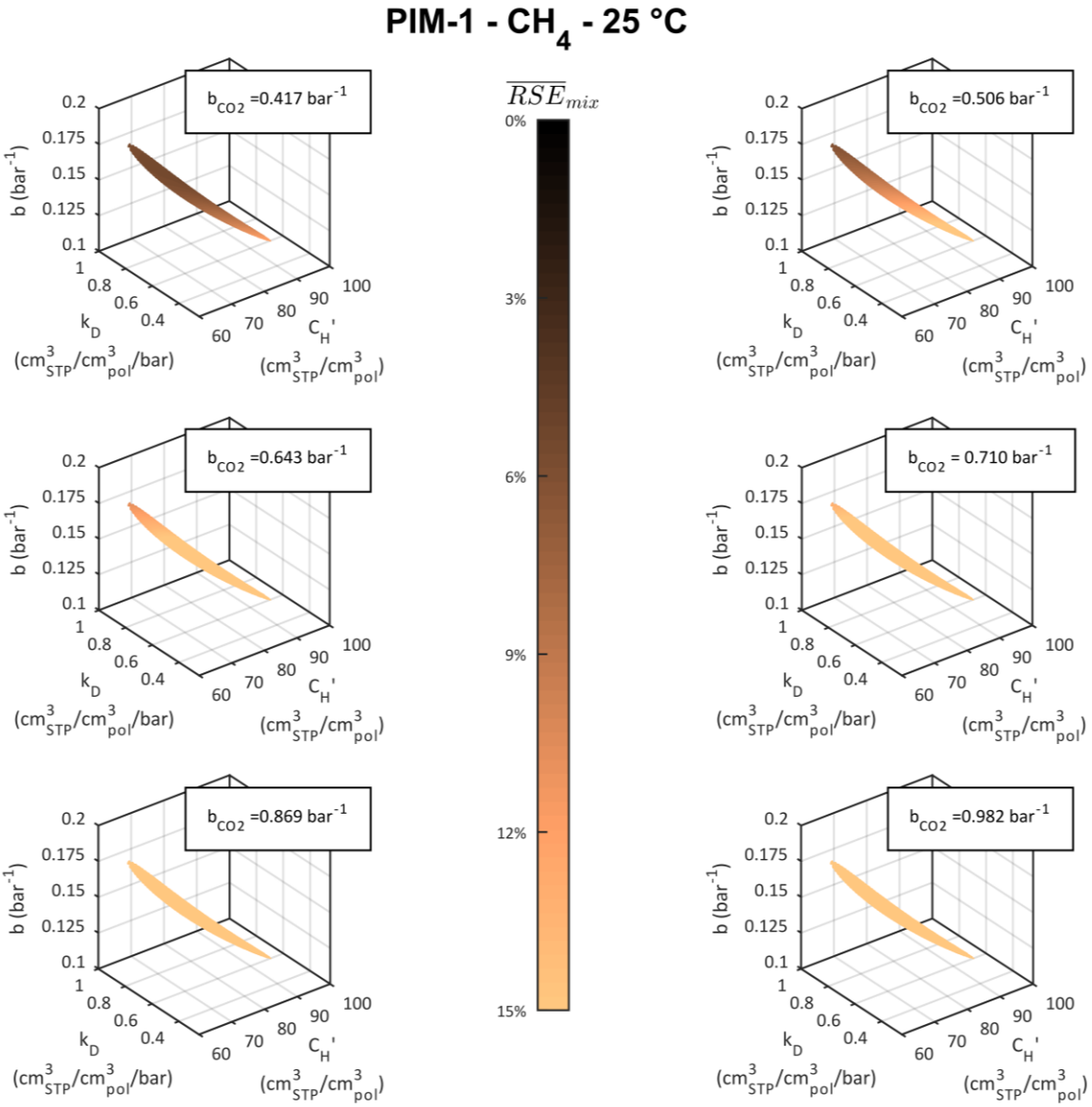

Figure 4.27. Isosurfaces in the DMS parameter space of CH_4 sorption in PIM-1 at 25 °C corresponding to $RSE_{pure} < RSE_{max}$, colored according to the average $\overline{RSE}_{mix}$ obtained with different values within the confidence interval of b_{CO_2}.

4.4.4 Discussion on the sensitivity of the multicomponent DMS model

Due to the form of the DMS model expression for the concentration, the parameters C'_H and b are strongly coupled and, therefore, a deviation of either of them can be compensated by a corresponding variation of the others, yielding a similar overall quality of the fit. The same remark was made also by Gleason et al. [57] in their analysis of Dual Mode parameters for mixed-gas permeation of CO_2/CH_4 in Thermally Rearranged HAB-6FDA. In order to improve the accuracy of the calculation, they chose to incorporate mixed-gas data into the fitting procedure used to retrieve the DM parameters. Raharjo et al. [46] studied sorption of CH_4-nC_4H_{10} mixtures in PTMSP and they noticed a tendency of the DM model to systematically overestimate CH_4 concentration in mixed-gas conditions. They subsequently re-parametrized the model, including the mixture data as well, obtaining different parameter sets from those retrieved considering only pure-gas data. In both cases [46,57] the representation of the mixture behavior was superior when the multicomponent data was included during the parametrization, but the procedure is clearly no longer predictive.

In order to reduce the uncertainty in the regression of the DM parameters, Wang et al. [64] suggested to obtain Henry's constant independently, through the analysis of the temperature dependence of the solubility coefficient above T_g, and then retrieve only C'_H and b from the best-fit of the sorption data. This approach yielded different sets from those obtained in a simultaneous regression of all three parameters and, even though those sets had lower values of the goodness-of-fit indicator, they showed improved self-consistency and the expected temperature dependence. This method, however, was not applicable to the materials studied here, and in general for glassy polymers with very high T_g, for which gas solubility data above T_g are not available.

Comparing the results displayed here for mixed-gas CH_4 sorption in PIM-1 to those of CH_4 sorption in TZ-PIM and also to those of CO_2 sorption in PIM-1 and TZ-PIM, it is not straightforward to identify a general trend and therefore draw guidelines to mitigate the issue. The parameter set obtained by imposing a temperature dependence yielded the most reliable results, therefore, this parametrization route should be followed whenever possible, if the intended use of the parameters is that of performing predictive mixed-gas sorption calculations. If data at only one temperature are available and the quantitative accuracy of the mixed-gas sorption is necessitated, caution in the use of this model is advised.

In general, the prediction was either satisfactory for all compositions or for none: a low average RSE_{mix} was always consequence of a similarly good representation of all three mixed-gas sorption isotherms. Therefore, if one could validate the parameter set adopted at least against experimental data at one composition, it should be possible to calculate the behavior at other compositions with greater confidence.

4.5 Mixed-gas Solubility Selectivity

The results of the calculations performed with parameters from **Table 4.3** and **Table 4.5** are used to evaluate the solubility-selectivity. The solubility-selectivity can be calculated both for pure-gas sorption (ideal case) and for multicomponent sorption (real case) making use of the definition of the solubility coefficient S using the corresponding value of the gas concentrations c, at pure- or mixed-gas conditions.

$$\alpha^{S}_{CO_2,CH_4} = \frac{S_{CO_2}}{S_{CH_4}} = \frac{c_{CO2}/f_{CO2}}{c_{CH4}/f_{CH4}} \qquad \text{Eq. (4.14)}$$

At a fixed value of the total pressure of the mixed-gas feed, the corresponding fugacity of each gas in the mixture and multicomponent concentration were used to obtain the multicomponent solubility-selectivity. The ideal solubility-selectivity was evaluated using the same fugacity values as in the multicomponent case, but with the corresponding concentration values taken from the pure-gas sorption isotherms.

Gas fugacity (f_i) at the various pressures were calculated with the Peng-Robinson equation of state [41], both at pure- and mixed-gas conditions. For the CO_2/CH_4 mixtures in the gas phase, the binary parameter k_{CO_2,CH_4} = 0.09 was used [65] in the mixing rule of the Peng-Robinson EoS. Results are shown in **Figure 4.28** for PTMSP, in **Figure 4.30** for PIM-1 and TZ-PIM, in **Figure 4.29** for PIM-EA-TB and in **Figure 4.31** for HAB-6FDA and TR450. Model results at 10% and 50% CO_2 mixtures are shown also for the materials in which only data at 30% CO_2 were reported. Clearly, a better mixed-gas sorption prediction corresponded to a more reliable estimate of the solubility-selectivity, whereas, discrepancies in the calculated sorption isotherms were amplified when the ratio was calculated to evaluate the selectivity.

The multicomponent values differ significantly from the ideal values: they are up to 6 times higher, It can be observed that, except for some small differences at low pressure, the values of the ideal solubility-selectivity of the various materials are very close, and, in particular, tend to stabilize at high pressure around a constant value of 2 to 3. On the contrary, solubility-selectivity at multicomponent conditions is markedly different from the ideal case for various materials: a threefold increase compared to the ideal one, both for TZ-PIM and PIM-1, is observed, while the average increase for PTMSP is only around 50%. The DMS model seems to underestimate this positive impact of competitive sorption on separation performance, with respect to the NELF model.

In the case of the NELF model, the same concentration dependence is displayed in all cases inspected: the solubility-selectivity is higher in the CO_2-richer mixtures, owing to the stronger exclusion of CH_4 as a result of competitive effects. However, the two PIMs show a somewhat different, though weak, trend with respect to temperature. PIM-1 predicted solubility-selectivity slightly decreases with increasing temperature, while that of TZ-PIM slightly increases, due to the different sorption enthalpies of the two gases in the materials. In all cases the solubility-selectivity is hardly dependent on the total pressure, in agreement with the experimental trends. In the case of DMS model predictions, the results are generally almost independent on concentration, with the only exception being TZ-PIM at 25 °C. The pressure dependence is generally weaker than the results given by the NELF model, however in several cases solubility-selectivity is found to be decreasing with pressure, unlike NELF model results.

Indeed, in the evaluation of the selectivity, the experimental error of both gas concentrations is combined and, therefore, this parameter inevitably has a higher uncertainty. For this reason, it is not straightforward to infer pressure and gas mixture composition dependencies from the experimental data, due to large fluctuations and absence of monotonous trends. Nonetheless, it is clear that the calculations performed with mixed-gas concentrations yield significantly more accurate results than using the corresponding pure-gas values, therefore, even DMS model mixed-gas estimates would seem to be preferable to pure-gas evaluations using experimental data.

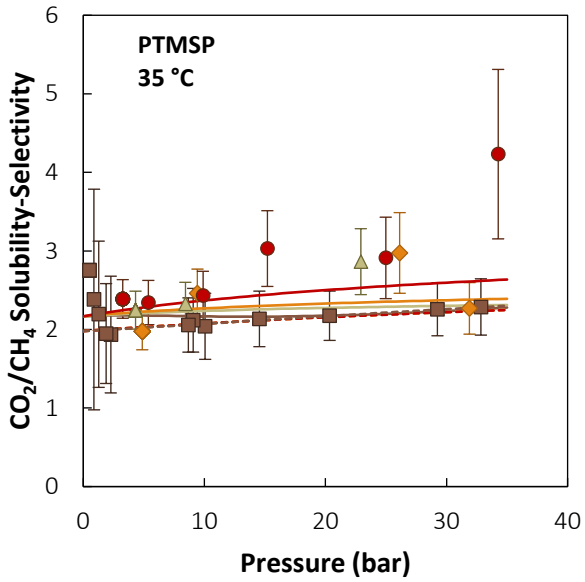

Figure 4.28. CO_2/CH_4 solubility-selectivity at 35 °C in PTMSP (Brown squares: pure gas – Red circles: ~50% CO_2 mixture – Orange diamonds: ~20% CO_2 mixture – Green triangles: ~10% CO_2 mixture [2]). Solid lines are NELF model predictions, Dashed lines are DMS model predictions.

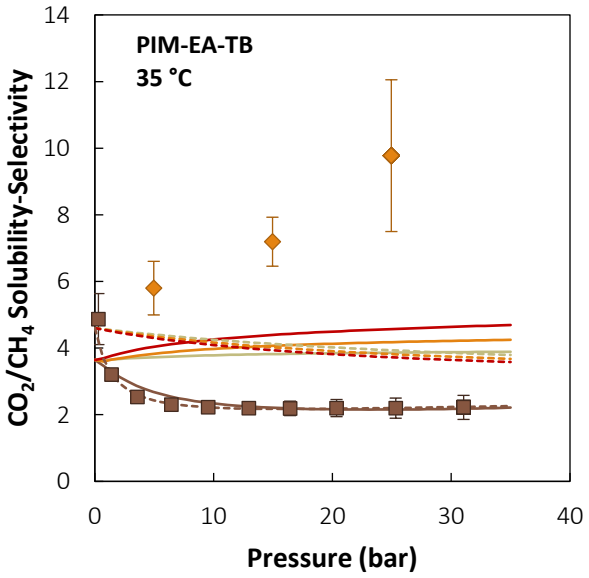

Figure 4.29. CO_2/CH_4 solubility-selectivity at 35 °C in PIM-EA-TB (Brown squares: pure gas – Red: ~50% CO_2 mixture – Orange diamonds: ~30% CO_2 mixture – Green: ~10% CO_2 mixture [8]). Solid lines are NELF model predictions, Dashed lines are DMS model predictions.

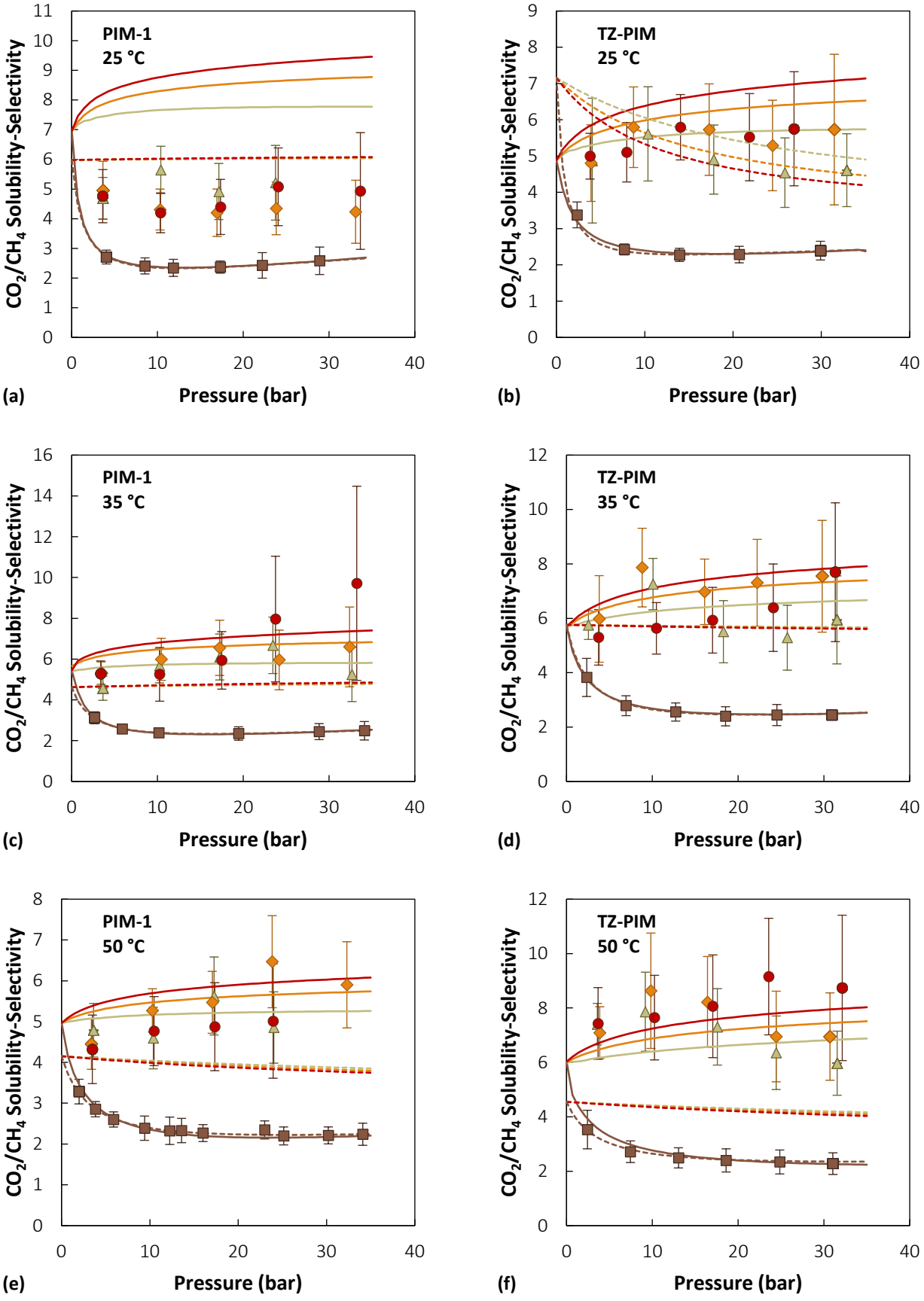

Figure 4.30. CO_2/CH_4 solubility-selectivity at 25, 35 and 50 °C in PIM-1 and TZ-PIM (Brown squares: pure gas – Red circles: ~50% CO_2 mixture – Orange diamonds: ~30% CO_2 mixture – Green triangles: ~10% CO_2 mixture [3–5]). Solid lines are NELF model predictions, Dashed lines are DMS model predictions.

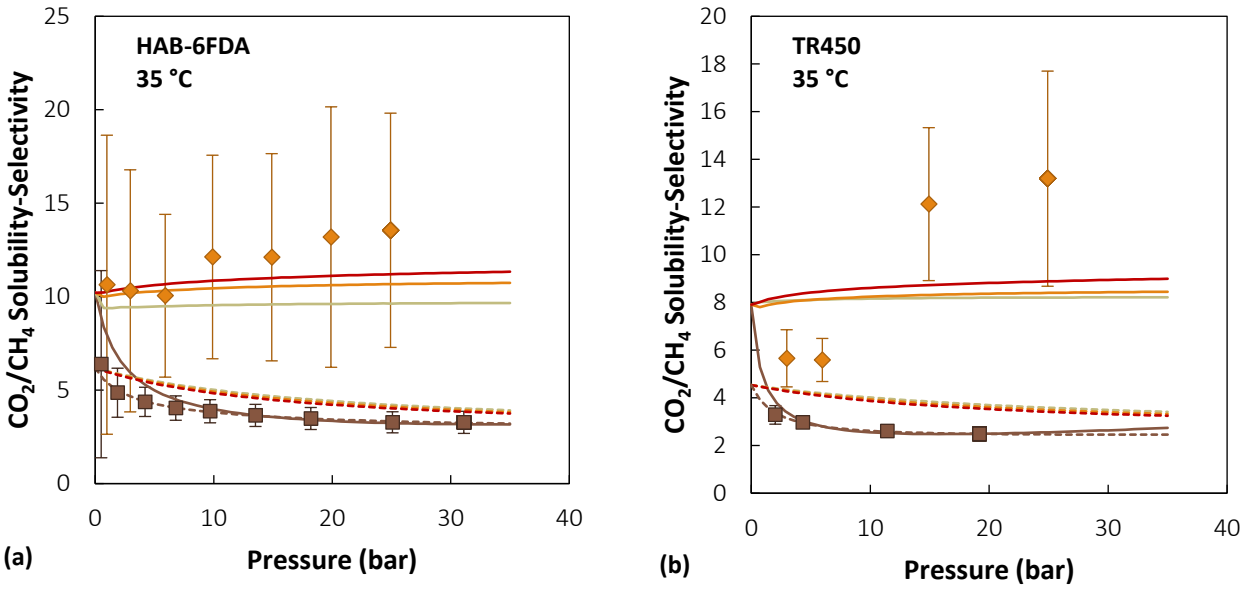

Figure 4.31. CO_2/CH_4 solubility-selectivity at 35 °C in HAB-6FDA and TR450 (Brown squares: pure gas – Red circles: ~50% CO_2 mixture – Orange diamonds: ~30% CO_2 mixture – Green triangles: ~10% CO_2 mixture [9]). Solid lines are NELF model predictions, Dashed lines are DMS model predictions.

4.6 Analysis of multicomponent permeability data

A reliable modelling tool for mixed-gas solubility can prove useful also in decoupling the solubility and diffusivity effects that concur to determine the mixed-gas permselectivity. Indeed, mixed-gas permeation experiments often show a different behavior from what is inferred from pure-gas data (ideal selectivity), and a more detailed understanding of the relative weight of the different phenomena in shaping the performance of a material can provide valuable insight and guide design considerations.

It must be pointed out that the following analysis is performed using permeability and sorption data measured for samples obtained in some cases through different protocols, for example in terms of casting solvent, thermal post-treatment, or ageing period, and this is known to be a source of variability in the transport properties of the membranes [66–69].

For **PTMSP**, CO_2/CH_4 mixed-gas permeation results could not be retrieved in the literature. As expected from the trade-off relationship, in a highly permeable material the ideal selectivity is rather low: 2.10 – 2.15 [70,71] for CO_2/CH_4 at 30 °C and atmospheric pressure. Diffusion coefficients, obtained with the time-lag method at 30 °C are $2.27 \cdot 10^{-5}$ cm^2/s for CH_4, and $2.21 \cdot 10^{-5}$ cm^2/s for CO_2 [71], which yields an ideal diffusivity-selectivity value close to one. The ideal solubility-selectivity at 35 °C is equal to 2.2 and is almost pressure independent, while real solubility-selectivity increases slightly, from 2.2 up to 2.4 (10% CO_2 mixture) - 2.7 (50% CO_2 mixture) at high pressure [2]. Since competitive sorption effects for this gas couple in this material are weak and the diffusivity selectivity is already very low, it is expected that permeability and the selectivity at multicomponent conditions should not differ much from the corresponding values

measured for pure gases. This is not the cases for other gas couples, as shown for example in the case of CH_4/nC_4-H_{10} in PTMSP by Raharjo et al. [46].

Mixed-gas permeation experiments for a 50:50 CO_2/CH_4 mixture in **PIM-1** at 35 °C were performed up to 10 bar of CO_2 [72]. The CO_2 permeability trend was monotonously decreasing with increasing pressure, which is parallel to the observed decrease in the solubility coefficient with increasing pressure, both at pure- and mixed-gas conditions. From the solution-diffusion relation between permeability, solubility and diffusivity coefficients, CO_2 diffusivity could be estimated. An average 4% decrease of CO_2 diffusivity between pure-gas and a 50:50 mixture at 35° C was obtained, which is only a modest effect. CH_4, on the other hand, displayed as much as a 60% increase in permeability at mixed-gas conditions. The permeability trend with pressure is also markedly different: the pure-gas permeability is almost constant with pressure, while the mixed-gas one sharply increases with increasing pressure, which is usually a behavior associated with plasticization effects. Since the CH_4 solubility coefficient at mixed-gas conditions is significantly lower than the pure-gas one, this leads to the conclusion that its diffusivity is increased by a factor 2 to 5 over the pressure range inspected. Multicomponent diffusivity-selectivity is therefore lower than solubility selectivity, as it can be seen in **Figure 4.32 (a)**. This effect was also documented in molecular dynamic simulations of mixtures of CO_2 and N_2 in a Thermally-Rearranged polymer [73] at 35 °C: the diffusivity of N_2 exhibited a threefold increase in the presence of CO_2, while that of CO_2 barely changed. This is a synergistic effect, likely associated with CO_2-induced swelling of the matrix, and outweighs the enhanced solubility-selectivity, leading to an overall 38% decrease in mixed-gas permselectivity, with respect to the ideal value [72].

For **TZ-PIM**, Du et al. [20] reported mixed gas permselectivity data together for 50:50 and 80:20 CO_2/CH_4 mixtures at 25 °C, up to 15 bar of CO_2. The accuracy of the models for mixed-gas selectivity in these conditions (25 °C) was lower, with respect to the analysis of PIM-1 at 35 °C, therefore the estimated diffusivity selectivity trend is expected to be affected correspondingly. However, the qualitative conclusions that can be drawn do not change. The decomposition of the permselectivity in its solubility and diffusivity components is reported in **Figure 4.32 (b)**. For this material, the permselectivity at mixed-gas conditions is fairly close to the ideal one (∼22 at 25 °C and 4.4 bar [20]). TZ-PIM has a more rigid structure compared to PIM-1, owing to the presence of hydrogen bonding [20]. This material shows a better resistance to CO_2-induced swelling, which allows it to maintain part of its sieving capability also at mixed-gas conditions.

Indeed, the CO_2-induced volume dilation can be estimated from the relation used to define the swelling coefficient using **Eq. (4.15)**:

$$\frac{V - V_0}{V_0} = k_{sw} P \qquad \text{Eq. (4.15)}$$

With the values of k_{sw} reported in **Table 4.3**, a volume change of 8% for PIM-1 at 35 °C and 20 bar (CO_2 uptake: 135 cm^3_{STP}/cm^3_{pol}) is calculated. TZ-PIM displays a volume change of 5% in the same conditions. Comparing the behavior at constant CO_2 uptake (135 cm^3_{STP}/cm^3_{pol}), it is found that this sorption level is attained for TZ-PIM at 31 bar, and that this conditions correspond to a volume change of 7%, which is consistent with the hypothesized higher resistance of TZ-PIM to CO_2 induced swelling.

This effect, coupled to the enhancement of solubility-selectivity resulting from to competitive sorption, leads to CO_2/CH_4 permselectivity values very similar for the pure and mixed gas case. Moreover, the combination and relative weight of those effects can sometimes even lead to a higher permselectivity in mixed-gas conditions: the permselectivity for the CO_2/N_2 pair in this material, in the pressure range 0–17 bar, increased from ∼30 – 25 in pure-gas conditions up to ∼40 – 35 for a 50:50 CO_2/N_2 mixture [20] at 25 °C. This behavior is even more pronounced in methyl tetrazole PIM (MTZ-PIM), a derivative of TZ-PIM, for which a twofold increase in permselectivity is witnessed at mixed-gas conditions for the CO_2/N_2 couple [74].

Concerning **HAB-6FDA** and its **TR derivative**, pure-gas measurements revealed that the main factor behind the higher permeability of TR polymers compared to their precursors is an order of magnitude increase in gas diffusivity, consistently with the higher free volume that is created during the thermal rearrangement process [29]. Solubility increased too after the rearrangement, but only by a factor of approximately 2, providing a more modest contribution to the overall increase in permeability. The variations of gas solubility and diffusivity between the two materials are proportionally higher for CH_4 than CO_2, therefore TR450 therefore exhibits a lower permselectivity than that of HAB-6FDA [29,75]. In the ideal case, the diffusivity-selectivity is the most relevant factor for both materials, and it is approximately 2 to 4 times higher than the ideal solubility-selectivity. Ideal values of α^D were calculated using the solution-diffusion relation obtaining values of 8.0 to 13.3 for the polyimide and 8.0 to 8.8 in the pressure range 0 – 50 bar.

Permeability at mixed gas conditions was measured (50:50 CO_2/CH_4 mixture at 35 °C) for both materials [57]. In contrast to the results obtained for PIMs, HAB-6FDA and TR450 show a slightly higher permselectivity in the mixed-gas test [57]. The loss in diffusivity-selectivity at multicomponent conditions was found to be higher for the TR-polymer (-58% at around 4 bar), whereas the polyimide is able of retain a greater size sieving capability, especially at low pressures (-42% at around 4 bar). Contrary to the pure-gas case, in the multicomponent case, the biggest contribution to selectivity comes from the solubility factor. Moreover, the increase in solubility-selectivity outweighs the decrease in diffusivity-selectivity (**Figure 4.32 (c)** and **(d)**) and is indeed responsible for the higher permselectivity observed during mixed-gas permeation experiments, confirming the hypothesis of Gleason et al. [57].

Typically, in CO_2/CH_4 separation, CO_2 acts as a swelling agent, dilating the polymer matrix. When the CO_2 content of the mixture is increased, there is often a substantial concomitant decrease in permselectivity, as found in several materials such as cellulose acetate and various polyimides [76–81]. In fact, based on the experimental observation of CO_2 solubility at mixed-gas conditions, the amount of CO_2 sorbed by the membrane during permeation of a mixture is expected to be close to that of the pure-gas case. Therefore, the polymer matrix will be dilated to a very similar extent and the CO_2 diffusivity is not expected to be significantly altered between the pure-gas and the mixed-gas cases. On the contrary, CH_4 in not capable of inducing the same dilation as CO_2. However, in the mixed gas case, due to the swelling induced by the presence of a high concentration of CO_2 inside the membrane, CH_4 will be exposed to a significantly more dilated polymer matrix, and, therefore, it will diffuse faster with respect to the pure-gas case.

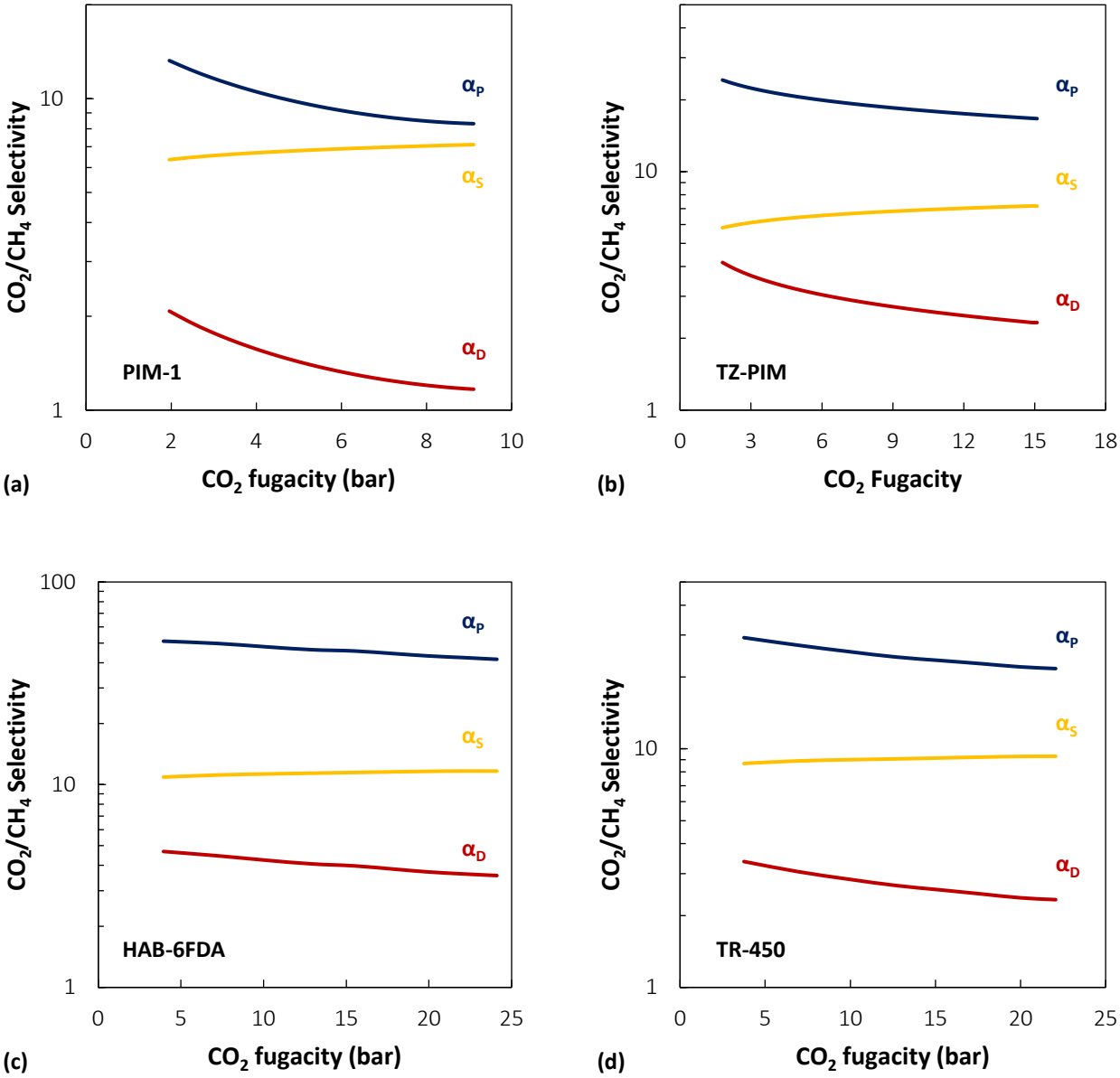

Figure 4.32. Blue lines: permselectivity of 50:50 CO_2/CH_4 mixtures in (a) PIM-1, 35 °C [72], (b) TZ-PIM, 25 °C [20], (c) HAB-6FDA, 35 °C [57] and (d) TR-450, 35 °C [57]. **Yellow** lines are NELF model calculations of solubility-selectivity for these systems, **red** lines are diffusivity selectivity trends estimated through the solution-diffusion relation.

Recently, CO_2/CH_4 diffusivity-selectivity at multicomponent conditions was measured experimentally for other materials [82,83]. Garrido et al. [83], using a combination of ^{13}C NMR spectroscopy and pulsed-field gradient NMR, determined that, for a 50:50 CO_2/CH_4 mixture in 6FDA-TMPDA polyimide, at 30 °C and a partial pressure of CO_2 of ~2.2 bar, the diffusivity-selectivity decreased from an ideal value of about 4 to approximately 2 at mixed-gas conditions. Similarly, Fraga et al. [82] measured for PIM-EA-TB a CO_2/CH_4 multicomponent diffusivity-selectivity value of ~2 on a wide range of compositions (10-50 mol.% CO_2), which is lower than the value of approximately 4 determined by Carta et al. [84] from pure-gas experiments. Recently, a significant increase in CH_4 diffusivity at mixed-gas conditions (estimated through

the solution-diffusion relation, like in the present work) was reported in the case of an equimolar CO_2/CH_4 mixture in PIM-Trip-TB [7] and 6FDA-mPDA [6]. In both cases, CO_2 diffusivity didn't show a significant variation. In the case of the higher free volume PIM-Trip-TB, the estimated diffusivity-selectivity in multicomponent conditions ranged from ∼1.5, much lower than the value of ∼5 obtained for the polyimide 6FDA-mPDA, which is in quantitative agreement with the trend obtained in the analysis carried out here.

The joint analysis of mixed-gas sorption and permeation data suggests that with ultrahigh free volume materials, like PIMs, but also in the case of lower free volume glassy polymers, such as polyimides, the separation in multicomponent conditions is mainly driven by solubility, due to a simultaneous drop in the diffusivity-selectivity and in increase in the solubility-selectivity.

4.6.1 Comparison among glassy polymers

The solubility-selectivity and diffusivity-selectivity at pure-gas and mixed-gas conditions are compared for several polymeric membrane materials in **Figure 4.33**. For most materials experimental data of pure and mixed gas permeability together with pure and mixed-gas solubility were used to estimate diffusivity, both at pure and mixed-gas conditions. In case the mixed-gas solubility data were not available, or they were available at a different composition than the one used to obtain mixed-gas permeability, they were calculated using the NELF model. It should be noted that in some of the cases, data from different literature sources were employed. However, despite some quantitative uncertainty due to combining data from different sources, the qualitative trends emerging from the present analysis are consistent and meaningful. A summary of the sources of the experimental data and the conditions under which they were obtained is given in **Table 1.1**.

It can be observed in **Figure 4.33** that in the case of ultrahigh free volume glassy polymers, such as PIMs, the sorption factor plays a more significant role already in ideal selectivity, so they are located closer to the parity-line than are materials like polyimides. CO_2/CH_4 mixed-gas permselectivity can either be higher, lower or equal to the ideal value, whereas in the case of solubility-selectivity and diffusivity-selectivity a general trend is displayed and α_S always increases at multicomponent conditions while α_D decreases. This behavior is displayed by polymers belonging to very different families, and in particular, it is common also to materials that, based on pure-gas data, would be considered predominantly diffusivity-selective, like HAB-6FDA and TR450.

Concerning the positioning with respect to the Robeson upper-bound at mixed-gas conditions, reported in **Figure 4.34**, the same considerations can be drawn for all materials considered in this analysis. Solubility-selectivity plays a decisive role in multicomponent permeability selectivity, moving the materials point up, while higher diffusivity is responsible for superior permeability, moving points to the right. For instance, in the case of PIMs, their solubility-selectivity alone brings them very close to the upper bound.

The interpretation of the upper-bound trade-off provided by Freeman et al. [85] attributes to the diffusivity-selectivity a predominant role. It is considered that, as the permeability of the faster gas decreases, the gain in permselectivity is associated with an increase in diffusivity-selectivity, due to

enhanced sieving effects, while solubility-selectivity remains nearly invariant with permeability and free volume. Subsequent analysis recognized a correlation of the solubility-selectivity factor with free volume [86]; however these analysis were performed using pure-gas data. Robeson et al. [87] analyzed the transport properties of TR polymers and PIMs relative to the upper bound and identified the importance of high solubility (compared to other materials) rather than high solubility-selectivity in shaping the exceptional performance of these families of materials. Although the current database for mixed-gas sorption is quite limited, the available evidence tends to support their conclusion that competitive sorption affects different families of polymers in a similar way.

The combined analysis of mixed-gas permeation and sorption data revealed that, when multicomponent effects are taken into account, the balance between the diffusivity and solubility factors is reversed, and the selectivity of the materials is solubility-driven. The presence of a swelling agent, such as CO_2, has a detrimental effect on the diffusivity-selectivity of the material, due to enhanced diffusion of CH_4 in the swollen polymer, and the separation becomes controlled by solubility-selectivity. Nonetheless, high diffusivity values are key to achieving high permeability coefficients. Therefore, high free volume materials, that allow for fast diffusion, but at the same time are capable of achieving a more favorable sorption for the faster components in a mixture are expected to exhibit higher permselectivity at multicomponent conditions.

Table 4.18. Experimental conditions and source for the data represented in **Figure 4.33** and **Figure 4.34**.

	Ideal case			Multicomponent case			
	Ref.	T (°C)	P (bar)	Ref.	%CO_2	T (°C)	P (bar)
PIM-1	[72,88]	35	10	[5,72]	50	35	10
TZ-PIM	[5,20]	25	10	[5,20]	50/80	25	-
PIM-EA-TB	[84]	35	1-7	[8,82]	30	35	1
AO-PIM	[72]	35	10	[72,89]	50	35	10
PIM-Trip-TB	[7]	35	3	[7]	44	35	3
HAB-6FDA	[29,47,75]	35	10	[9,57]	50	35	10
TR-450	[29,47,75]	35	10	[9,57]	50	35	10
Matrimid	[25,90,91]	35	2	[91,92]	55	35	2
6FDA-mPDA	[6]	35	24	[6]	44	35	24
6FDA-TADPO	[93]	35	10	[1]	50	35	10
PPO	[94]	35	10	[95]	50	35	10
CDA	[96–99]	35	10	[76,100]	30/50	35	1

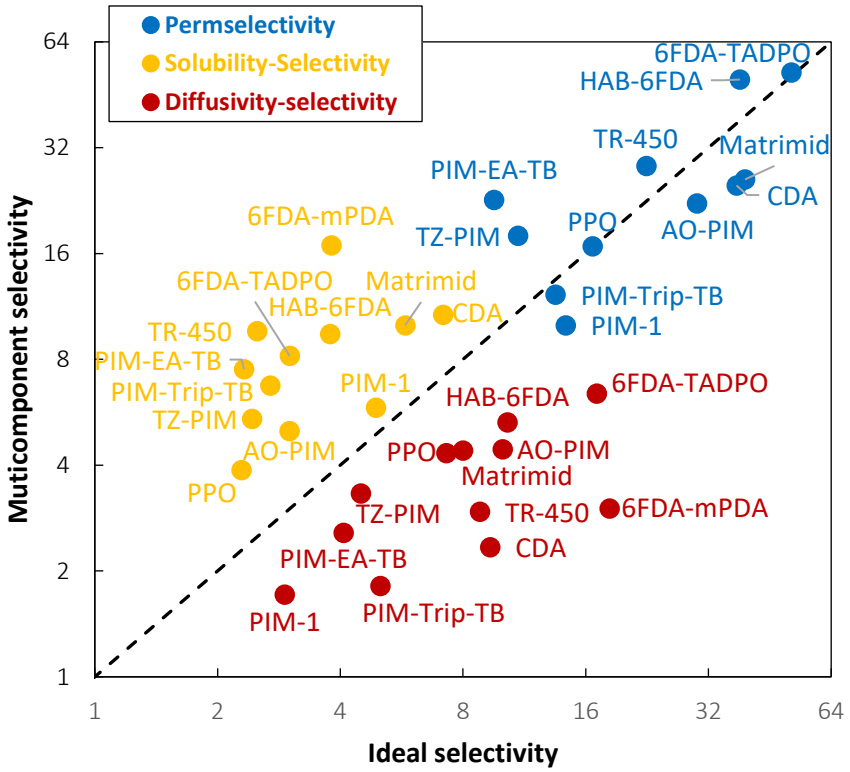

Figure 4.33. Comparison of ideal and multicomponent CO_2/CH_4 permselectivity, diffusivity- and solubility-selectivity for several polymeric materials. Sources of the experimental data and conditions of the tests are reported in **Table 1.1**.

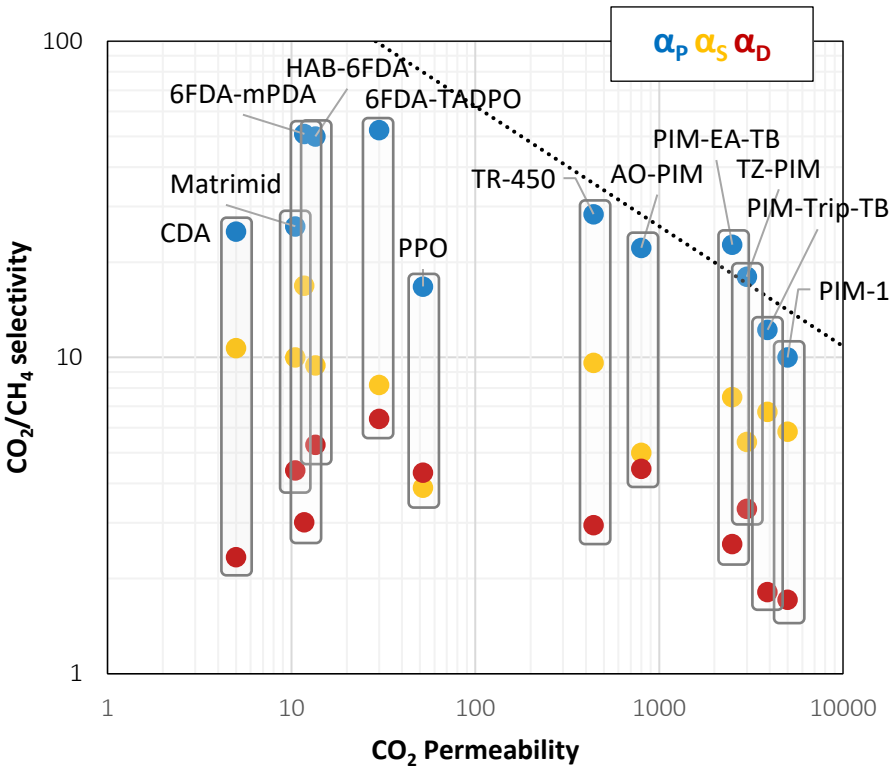

Figure 4.34. 2008 CO_2/CH_4 Robeson upper bound and relative positioning of several materials at multicomponent conditions (see **Table 1.1** for sources and conditions). In the shaded column, solubility- and diffusivity-selectivity contributions are shown.

4.7 Conclusions

In this chapter, modelling of mixed-gas sorption in glassy polymers was presented. Two models were tested: the Non-Equilibrium Lattice Fluid (NELF) model and the Dual Mode Sorption (DMS) model. The accuracy of the models in representing the non-idealities that arise during mixed-gas sorption was assessed by comparing against experimental data available for solubility and solubility-selectivity of CO_2/CH_4 mixtures in six polymers at three different temperatures and at three different mixture compositions. The multicomponent solubility data were modelled using only pure component parameters and binary interaction parameters retrieved from pure-gas sorption data, in the case of NELF, and polymer-gas parameters retrieved from pure-gas sorption, in the case of DMS. No parameters determined from the mixed-gas sorption data were used by either model. The strengths and weaknesses of each model were highlighted and several attempts at improving the predictive ability of the tools were presented. The reduction in solubility due to competition when a second gas is present in the mixture was correctly captured by both models, as well as the temperature and concentration trends expected.

In general, the NELF model was found capable of representing the competitive effects in solubility and solubility selectivity, in a wide range of temperatures and pressures, with a better quantitative accuracy attained at higher temperatures. Moreover, the model is robust with respect to a small perturbation of the polymer density and of the sorbed concentration, and the adjustable parameters are transferable between samples of similar density.

Although it is more easily utilized, the multicomponent DMS model yielded less accurate predictions of mixed-gas sorption and is affected by a severe lack of robustness with respect to a small perturbation of the pure-gas concentration data used in its parametrization. Using the parameters obtained from the best fit of pure-gas sorption isotherms, the agreement between the mixed-gas calculations and the experimental data varied greatly in the different cases inspected, especially in the case of CH_4 absorbed at mixed-gas conditions. A sensitivity analysis revealed that pure-gas data can be represented with the same accuracy by several different parameter sets, which, however, yield markedly different mixed-gas predictions, that, in some cases, agree with the experimental data only qualitatively. However, the multicomponent calculations with the DMS model yield more reliable results than the use of pure-gas data in the estimation of the solubility-selectivity of the material.

Solubility-selectivity was also calculated at multicomponent conditions and the results compared with the experimental findings for the materials considered, with higher accuracy displayed by NELF model predictions.

A combined analysis of multicomponent permeation and sorption data revealed that performance and materials design considerations based on pure-gas permeability/selectivity can be misleading in case of mixtures containing a highly sorbing component, like CO_2. In these conditions, penetrant-induced swelling has a detrimental effect on the diffusivity-selectivity of the material and the separation becomes controlled by solubility differences. Therefore, materials capable of amplifying the competition effects, in order to

achieve a more favorable sorption for one of the components in the mixture are expected to maintain a higher mixed-gas permselectivity.

Future analysis could use the modelling tools available for the calculation of mixed-gas sorption to expand the current database of mixed-gas sorption results, to assess the strength of the competitive effect for different families of polymers, such as perfluorinated materials for example, for which the solubility has a higher importance already in ideal conditions [101], and evaluate correlations between the strength of the competition between materials properties such as free volume, permeability, cohesive energy density… in search of structure-properties correlations. Moreover, systematic investigations of temperature and compositions effects could be carried out, also evaluating the effect of small concentration of contaminants on the separation performance. Finally, it would be interesting to assess the presence and the importance of these effects also in the case of other gas couples.

References

1. Kamaruddin, H.D.; Koros, W.J. Some observations about the application of Fick's first law for membrane separation of multicomponent mixtures. *J. Memb. Sci.* **1997**, *135*, 147–159, doi:10.1016/S0376-7388(97)00142-7.
2. Vopička, O.; De Angelis, M.G.; Sarti, G.C. Mixed gas sorption in glassy polymeric membranes: I. CO_2 /CH_4 and n-C_4/CH_4 mixtures sorption in poly(1-trimethylsilyl-1-propyne) (PTMSP). *J. Memb. Sci.* **2014**, *449*, 97–108, doi:10.1016/j.memsci.2013.06.065.
3. Vopička, O.; De Angelis, M.G.; Du, N.; Li, N.; Guiver, M.D.; Sarti, G.C. Mixed gas sorption in glassy polymeric membranes: II. CO_2/CH_4 mixtures in a polymer of intrinsic microporosity (PIM-1). *J. Memb. Sci.* **2014**, *459*, 264–276, doi:10.1016/j.memsci.2014.02.003.
4. Gemeda, A.E.; De Angelis, M.G.; Du, N.; Li, N.; Guiver, M.D.; Sarti, G.C. Mixed gas sorption in glassy polymeric membranes. III. CO2/CH4 mixtures in a polymer of intrinsic microporosity (PIM-1): Effect of temperature. *J. Memb. Sci.* **2017**, *524*, 746–757, doi:10.1016/j.memsci.2016.11.053.
5. Ricci, E.; Gemeda, A.E.; Du, N.; Li, N.; De Angelis, M.G.; Guiver, M.D.; Sarti, G.C. Sorption of CO_2/CH_4 mixtures in TZ-PIM, PIM-1 and PTMSP: Experimental data and NELF-model analysis of competitive sorption and selectivity in mixed gases. *J. Memb. Sci.* **2019**, *585*, 136–149, doi:10.1016/j.memsci.2019.05.026.
6. Genduso, G.; Ghanem, B.S.; Pinnau, I. Experimental Mixed-Gas Permeability, Sorption and Diffusion of CO_2-CH_4 Mixtures in 6FDA-mPDA Polyimide Membrane: Unveiling the Effect of Competitive Sorption on Permeability Selectivity. *Membranes (Basel).* **2019**, *9*, 10, doi:10.3390/membranes9010010.
7. Genduso, G.; Wang, Y.; Ghanem, B.S.; Pinnau, I. Permeation, sorption, and diffusion of CO_2-CH_4 mixtures in polymers of intrinsic microporosity: The effect of intrachain rigidity on plasticization resistance. *J. Memb. Sci.* **2019**, *584*, 100–109, doi:10.1016/j.memsci.2019.05.014.
8. Benedetti, F.M.; Ricci, E.; De Angelis, M.G.; Carta, M.; McKeown, N.B. Sorption of CO_2/CH_4 and their mixtures in PIM-EA-TB. *In preparation*
9. Ricci, E.; Benedetti, F.M.; Dose, M.E.; De Angelis, M.G.; Freeman, B.D.; Paul, D.R. Experimental Characterization and Modelling of Mixed Gas Sorption of CO_2/CH_4 in HAB-6FDA Polyimide and its Thermally Rearranged Derivative. *Submitted to the Journal of Membrane Science*
10. Genduso, G.; Litwiller, E.; Ma, X.; Zampini, S.; Pinnau, I. Mixed-gas sorption in polymers via a new barometric test system: sorption and diffusion of CO_2-CH_4 mixtures in polydimethylsiloxane (PDMS). *J. Memb. Sci.* **2019**, *577*, 195–204, doi:10.1016/j.memsci.2019.01.046.
11. Sanders, E.S.; Koros, W.J.; Hopfenberg, H.B.; Stannett, V.T. Mixed gas sorption in glassy polymers: Equipment design considerations and preliminary results. *J. Memb. Sci.* **1983**, *13*, 161–174, doi:10.1016/S0376-7388(00)80159-3.
12. Sanders, E.S.; Koros, W.J.; Hopfenberg, H.B.; Stannett Pure and Mixed Gas Sorption of Carbon Dioxide and Ethylene in Poly(Methyl Methacrylate). *J. Memb. Sci.* **1984**, *18*, 53–74.
13. Sanders, E.S.; Koros, W.J. Sorption of CO_2, C_2H_4, N_2O and their Binary Mixtures in Poly(methyl methacrylate). *J. Polym. Sci. B* **1986**, *188*, 175–188, doi:10.1002/polb.1986.180240117.
14. Raharjo, R.D.; Freeman, B.D.; Paul, D.R.; Sarti, G.C.; Sanders, E.S. Pure and mixed gas CH_4 and n-C_4H_{10} permeability and diffusivity in poly(dimethylsiloxane). *Polymer (Guildf).* **2007**, *306*, 75–92, doi:10.1016/j.memsci.2007.08.014.
15. Raharjo, R.D.; Freeman, B.D.; Sanders, E.S. Pure and mixed gas CH_4 and n-C_4H_{10} sorption and dilation in poly (dimethylsiloxane). *J. Memb. Sci.* **2007**, *292*, 45–61, doi:10.1016/j.memsci.2007.01.012.
16. Ribeiro, C.P.; Freeman, B.D. Carbon dioxide/ethane mixed-gas sorption and dilation in a cross-linked poly(ethylene oxide) copolymer. *Polymer (Guildf).* **2010**, *51*, 1156–1168, doi:10.1016/j.polymer.2010.01.012.
17. Sarti, G.C.; Doghieri, F. Predictions of the solubility of gases in glassy polymers based on the NELF model. *Chem. Eng. Sci.* **1998**, *53*, 3435–3447, doi:10.1016/S0009-2509(98)00143-2.
18. George, G.; Bhoria, N.; Alhallaq, S.; Abdala, A.; Mittal, V. Polymer membranes for acid gas removal from natural gas. *Sep. Purif. Technol.* **2016**, *158*, 333–356, doi:10.1016/j.seppur.2015.12.033.
19. Budd, P.M.; Ghanem, B.S.; Makhseed, S.; McKeown, N.B.; Msayib, K.J.; Tattershall, C.E. Polymers of intrinsic microporosity (PIMs): robust, solution-processable, organic nanoporous materials. *Chem. Commun.* **2004**, 230–

231, doi:10.1039/b311764b.

20. Du, N.; Park, H.B.; Robertson, G.P.; Dal-Cin, M.M.; Visser, T.; Scoles, L.; Guiver, M.D. Polymer nanosieve membranes for CO_2-capture applications. *Nat. Mater.* **2011**, *10*, 372–375, doi:10.1038/nmat2989.

21. Satilmis, B.; Lan, M.; Fuoco, A.; Rizzuto, C.; Tocci, E.; Bernardo, P.; Clarizia, G.; Esposito, E.; Monteleone, M.; Dendisová, M.; Friess, K.; Budd, P.M.; Jansen, J.C. Temperature and pressure dependence of gas permeation in amine-modified PIM-1. *J. Memb. Sci.* **2018**, *555*, 483–496, doi:10.1016/j.memsci.2018.03.039.

22. Du, N.; Robertson, G.P.; Song, J.; Pinnau, I.; Guiver, M.D.; Park, M. High-performance carboxylated polymers of intrinsic microporosity (PIMs) with tunable gas transport properties. *Macromolecules* **2009**, *42*, 6038–6043, doi:10.1021/ma9009017.

23. Yin, H.; Chua, Y.Z.; Yang, B.; Schick, C.; Harrison, W.J.; Budd, P.M.; Böhning, M.; Schönhals, A. First Clear-Cut Experimental Evidence of a Glass Transition in a Polymer with Intrinsic Microporosity: PIM-1. *J. Phys. Chem. Lett.* **2018**, *9*, 2003–2008, doi:10.1021/acs.jpclett.8b00422.

24. De Angelis, M.G.; Sarti, G.C. Solubility of Gases and Liquids in Glassy Polymers. *Annu. Rev. Chem. Biomol. Eng.* **2011**, *2*, 97–120, doi:10.1146/annurev-chembioeng-061010-114247.

25. Minelli, M.; Cocchi, G.; Ansaloni, L.; Baschetti, M.G.; De Angelis, M.G.; Doghieri, F. Vapor and liquid sorption in matrimid polyimide: Experimental characterization and modeling. *Ind. Eng. Chem. Res.* **2013**, *52*, 8936–8945, doi:10.1021/ie3027873.

26. Galizia, M.; Stevens, K.A.; Smith, Z.P.; Paul, D.R.; Freeman, B.D. Nonequilibrium lattice fluid modeling of gas solubility in HAB-6FDA polyimide and its thermally rearranged analogues. *Macromolecules* **2016**, *49*, 8768–8779, doi:10.1021/acs.macromol.6b01479.

27. Staiger, C.L.; Pas, S.J.; Hill, A.J.; Cornelius, C.J. Gas separation, free volume distribution, and physical aging of a highly microporous spirobisindane polymer. *Chem. Mater.* **2008**, *20*, 2606–2608, doi:10.1021/cm071722t.

28. Low, Z.X.; Budd, P.M.; McKeown, N.B.; Patterson, D.A. Gas Permeation Properties, Physical Aging, and Its Mitigation in High Free Volume Glassy Polymers. *Chem. Rev.* **2018**, *118*, 5871–5911, doi:10.1021/acs.chemrev.7b00629.

29. Sanders, D.F.; Smith, Z.P.; Ribeiro, C.P.; Guo, R.; McGrath, J.E.; Paul, D.R.; Freeman, B.D. Gas permeability, diffusivity, and free volume of thermally rearranged polymers based on 3,3′-dihydroxy-4,4′-diamino-biphenyl (HAB) and 2,2′-bis-(3,4-dicarboxyphenyl) hexafluoropropane dianhydride (6FDA). *J. Memb. Sci.* **2012**, *409*, 232–241, doi:10.1016/j.memsci.2012.03.060.

30. Bondi, A. Van der waals volumes and radii. *J. Phys. Chem.* **1964**, *68*, 441–451, doi:10.1021/j100785a001.

31. Tocci, E.; De Lorenzo, L.; Bernardo, P.; Clarizia, G.; Bazzarelli, F.; McKeown, N.B.; Carta, M.; Malpass-Evans, R.; Friess, K.; Pilnáček, K.; Lanč, M.; Yampolskii, Y.P.; Strarannikova, L.; Shantarovich, V.; Mauri, M.; Jansen, J.C. Molecular modeling and gas permeation properties of a polymer of intrinsic microporosity composed of ethanoanthracene and Tröger's base units. *Macromolecules* **2014**, *47*, 7900–7916, doi:10.1021/ma501469m.

32. De Miranda, R.L.; Kruse, J.; Rätzke, K.; Faupel, F.; Fritsch, D.; Abetz, V.; Budd, P.M.; Selbie, J.D.; McKeown, N.B.; Ghanem, B.S. Unusual temperature dependence of the positron lifetime in a polymer of intrinsic microporosity. *Phys. Status Solidi - Rapid Res. Lett.* **2007**, *1*, 190–192, doi:10.1002/pssr.200701116.

33. Golzar, K.; Modarress, H.; Amjad-Iranagh, S. Separation of gases by using pristine, composite and nanocomposite polymeric membranes: A molecular dynamics simulation study. *J. Memb. Sci.* **2017**, *539*, 238–256, doi:10.1016/j.memsci.2017.06.010.

34. Abbott, L.J.; Hart, K.E.; Colina, C.M. Polymatic: A generalized simulated polymerization algorithm for amorphous polymers. *Theor. Chem. Acc.* **2013**, *132*, 1–19, doi:10.1007/s00214-013-1334-z.

35. Baschetti, M.G.; Ghisellini, M.; Quinzi, M.; Doghieri, F.; Stagnaro, P.; Costa, G.; Sarti, G.C. Effects on sorption and diffusion in PTMSP and TMSP/TMSE copolymers of free volume changes due to polymer ageing. *J. Mol. Struct.* **2005**, *739*, 75–86, doi:10.1016/j.molstruc.2004.08.027.

36. Minelli, M.; Friess, K.; Vopička, O.; De Angelis, M.G. Modeling gas and vapor sorption in a polymer of intrinsic microporosity (PIM-1). *Fluid Phase Equilib.* **2013**, *347*, 35–44, doi:10.1016/j.fluid.2013.03.003.

37. Minelli, M.; Sarti, G.C. Elementary prediction of gas permeability in glassy polymers. *J. Memb. Sci.* **2017**, *521*, 73–83, doi:10.1016/j.memsci.2016.09.001.

38. Doghieri, F.; Sarti, G.C. Nonequilibrium Lattice Fluids: A Predictive Model for the Solubility in Glassy Polymers. *Macromolecules* **1996**, *29*, 7885–7896, doi:10.1021/ma951366c.

39. Doghieri, F.; Sarti, G.C. Predicting the low pressure solubility of gases and vapors in glassy polymers by the NELF model. *J. Memb. Sci.* **1998**, *147*, 73–86, doi:10.1016/S0376-7388(98)00123-9.

40. Liu, S.; Zhao, C.; Lv, J.; Lv, P.; Zhang, Y. Density Characteristics of the CO_2 -CH_4 Binary System: Experimental Data at 313-353 K and 3-18 MPa and Modeling from the PC-SAFT EoS. *J. Chem. Eng. Data* **2018**, *63*, 4368–4380, doi:10.1021/acs.jced.8b00433.

41. Peng, D.; Robinson, D.B. A New Two-Constant Equation of State. *Ind. Eng. Chem. Fundam.* **1976**, *15*, 59–64, doi:10.1021/i160057a011.

42. Gross, J.; Sadowski, G. Perturbed-Chain SAFT: An Equation of State Based on a Perturbation Theory for Chain Molecules. *Ind. Eng. Chem. Res.* **2001**, *40*, 1244–1260, doi:10.1021/ie0003887.

43. Abadie, J.; Carpentier, J. Generalization of the Wolfe reduced gradient method to the case of nonlinear constraints. In *Optimization Proceedings of a Symposium of the Insitute of Mathematics and its Applications, held at University of Keele, England, 1968*; Fletcher, R., Ed.; Academic Press: London, UK, 1969; pp. 37–49.

44. Koros, W.J.; Paul, R.; Huvard, G.S. Energetics of gas sorption in glassy polymers. *Polymer (Guildf).* **1979**, *20*, 956–960, doi:10.1016/0032-3861(79)90192-7.

45. Koros, W.J. Model for sorption of mixed gases in glassy polymers. *J. Polym. Sci. Polym. Phys. Ed.* **1980**, *18*, 981–992, doi:10.1002/pol.1980.180180506.

46. Raharjo, R.D.; Freeman, B.D.; Sanders, E.S. Pure and mixed gas CH_4 and n-C_4H_{10} sorption and dilation in poly(1-trimethylsilyl-1-propyne). *Polymer (Guildf).* **2007**, *48*, 6097–6114, doi:10.1016/j.polymer.2007.07.057.

47. Stevens, K.A.; Smith, Z.P.; Gleason, K.L.; Galizia, M.; Paul, D.R.; Freeman, B.D. Influence of temperature on gas solubility in thermally rearranged (TR) polymers. *J. Memb. Sci.* **2017**, *533*, 75–83, doi:10.1016/j.memsci.2017.03.005.

48. Bondar, V.I.; Kamiya, Y.; Yampol'skii, Y.P. On pressure dependence of the parameters of the dual-mode sorption model. *J. Polym. Sci. Part B Polym. Phys.* **1996**, *34*, 369–378, doi:10.1002/(SICI)1099-0488(19960130)34:2<369::AID-POLB18>3.0.CO;2-H.

49. Yamane, T. *Statistics: An Introductory Analysis*; Harper & Row, John Weatherhill: New York, Evanston, London, Tokio, 1973; ISBN 0060473134.

50. Bevington, P.R.; Robinson, D.K. *Data Reduction and Error Analysis for the Physical Sciences, 3rd edn.*; McGraw-Hill: Boston, MA, USA, 2003; ISBN 0072472278.

51. Myers, R.H. *Classical and Modern Regression with Applications*; Duxbury press: Belmon, CA, USA, 1990;

52. De Angelis, M.G.; Sarti, G.C. Solubility and diffusivity of gases in mixed matrix membranes containing hydrophobic fumed silica: Correlations and predictions based on the NELF model. *Ind. Eng. Chem. Res.* **2008**, *47*, 5214–5226, doi:10.1021/ie0714910.

53. Galizia, M.; De Angelis, M.G.; Sarti, G.C. Sorption of hydrocarbons and alcohols in addition-type poly(trimethyl silyl norbornene) and other high free volume glassy polymers. II: NELF model predictions. *J. Memb. Sci.* **2012**, *405*, 201–211, doi:10.1016/j.memsci.2012.03.009.

54. Budd, P.M.; McKeown, N.B.; Ghanem, B.S.; Msayib, K.J.; Fritsch, D.; Starannikova, L.; Belov, N.; Sanfirova, O.; Yampolskii, Y.; Shantarovich, V. Gas permeation parameters and other physicochemical properties of a polymer of intrinsic microporosity: Polybenzodioxane PIM-1. *J. Memb. Sci.* **2008**, *325*, 851–860, doi:10.1016/j.memsci.2008.09.010.

55. Tiwari, R.R.; Jin, J.; Freeman, B.D.; Paul, D.R. Physical aging , CO_2 sorption and plasticization in thin films of polymer with intrinsic microporosity (PIM-1). *J. Memb. Sci.* **2017**, *537*, 362–371, doi:10.1016/j.memsci.2017.04.069.

56. Minelli, M.; Campagnoli, S.; De Angelis, M.G.; Doghieri, F.; Sarti, G.C. Predictive model for the solubility of fluid mixtures in glassy polymers. *Macromolecules* **2011**, *44*, 4852–4862, doi:10.1021/ma200602d.

57. Gleason, K.L.; Smith, Z.P.; Liu, Q.; Paul, D.R.; Freeman, B.D. Pure- and mixed-gas permeation of CO_2 and CH_4 in thermally rearranged polymers based on 3,3′-dihydroxy-4,4′-diamino-biphenyl (HAB) and 2,2′-bis-(3,4-dicarboxyphenyl) hexafluoropropane dianhydride (6FDA). *J. Memb. Sci.* **2015**, *475*, 204–214, doi:10.1016/j.memsci.2014.10.014.

58. Sanders, E.S. High-pressure sorption of pure and mixed gases in glassy polymers, North Carolina State University, Raleigh, 1983.

59. Koros, W.J.; Paul, D.R. Sorption and transport of various gases in polycarbonate. *J. Memb. Sci.* **1977**, *2*, 165–190.

60. Kamiya, Y.; Hirose, T.; Mizoguchi, K.; Naito, Y. Gravimetric study of high-pressure sorption of gases in polymers. *J. Polym. Sci. Part B Polym. Phys.* 1986, *24*, 1525–1539, doi:10.1002/polb.1986.090240711.

61. Chiou, J.S.; Maeda, Y.; Paul, D.R. Gas and vapor sorption in polymers just below Tg. *J. Appl. Polym. Sci.* 1985, *30*, 4019–4029, doi:10.1002/app.1985.070301006.

62. Feng, H. Modeling of vapor sorption in glassy polymers using a new dual mode sorption model based on multilayer sorption theory. *Polymer (Guildf).* 2007, *48*, 2988–3002, doi:10.1016/j.polymer.2006.10.050.

63. Ricci, E.; De Angelis, M.G. Modelling Mixed Gas Sorption in Glassy Polymers for CO_2 Removal: a Sensitivity Analysis of the Dual Mode Sorption Model. *Membranes (Basel).* 2019, *9*, *8*.

64. Wang, J.S.; Kamiya, Y. A method of validation and parameter evaluation for dual-mode sorption model. *J. Memb. Sci.* 1999, *154*, 25–32, doi:10.1016/S0376-7388(98)00279-8.

65. Sandler, S.I. *Chemical, Biochemical, and Engineering Thermodynamics*; 5th Editio.; John Wiley & Sons: Hoboken, NJ, USA, 2017;

66. Pope, D.S.; Fleming, G.K.; Koros, W.J. Effect of various exposure histories on sorption and dilation in a family of polycarbonates. *Macromolecules* 1990, *23*, 2988–2994, doi:10.1021/ma00213a029.

67. Guan, R.; Dai, H.; Li, C.; Liu, J.; Xu, J. Effect of casting solvent on the morphology and performance of sulfonated polyethersulfone membranes. *J. Memb. Sci.* 2006, *277*, 148–156, doi:10.1016/j.memsci.2005.10.025.

68. Shao, L.; Chung, T.S.; Wensley, G.; Goh, S.H.; Pramoda, K.P. Casting solvent effects on morphologies, gas transport properties of a novel 6FDA/PMDA-TMMDA copolyimide membrane and its derived carbon membranes. *J. Memb. Sci.* 2004, *244*, 77–87, doi:10.1016/j.memsci.2004.07.005.

69. Park, C.H.; Tocci, E.; Lee, Y.M.; Drioli, E. Thermal treatment effect on the structure and property change between hydroxy-containing polyimides (HPIs) and thermally rearranged polybenzoxazole (TR-PBO). *J. Phys. Chem. B* 2012, *116*, 12864–12877, doi:10.1021/jp307365y.

70. Nagai, K.; Masuda, T.; Nakagawa, T.; Freeman, B.D.; Pinnau, I. Poly[1-(trimethylsilyl)-1-propyne] and related polymers: synthesis, properties and functions. *Prog. Polym. Sci.* 2001, *26*, 721–798.

71. Ichiraku, Y.; Stern, S.A.; Nakagawa, T. An investigation of the high gas permeability of poly(1-trimethylsilyl-1-propyne). *J. Memb. Sci.* 1987, *34*, 5–18, doi:10.1016/S0376-7388(00)80017-4.

72. Swaidan, R.; Ghanem, B.S.; Litwiller, E.; Pinnau, I. Pure- and mixed-gas CO_2/CH_4 separation properties of PIM-1 and an amidoxime-functionalized PIM-1. *J. Memb. Sci.* 2014, *457*, 95–102, doi:10.1016/j.memsci.2014.01.055.

73. Rizzuto, C.; Caravella, A.; Brunetti, A.; Park, C.H.; Lee, Y.M.; Drioli, E.; Barbieri, G.; Tocci, E. Sorption and Diffusion of CO_2/N_2 in gas mixture in thermally-rearranged polymeric membranes: A molecular investigation. *J. Memb. Sci.* 2017, *528*, 135–146, doi:10.1016/j.memsci.2017.01.025.

74. Du, N.; Robertson, G.P.; Dal-Cin, M.M.; Scoles, L.; Guiver, M.D. Polymers of intrinsic microporosity (PIMs) substituted with methyl tetrazole. *Polymer (Guildf).* 2012, *53*, 4367–4372, doi:10.1016/j.polymer.2012.07.055.

75. Smith, Z.P.; Sanders, D.F.; Ribeiro, C.P.; Guo, R.; Freeman, B.D.; Paul, D.R.; McGrath, J.E.; Swinnea, S. Gas sorption and characterization of thermally rearranged polyimides based on 3,3'-dihydroxy-4,4'-diamino-biphenyl (HAB) and 2,2'-bis-(3,4-dicarboxyphenyl) hexafluoropropane dianhydride (6FDA). *J. Memb. Sci.* 2012, *415–416*, 558–567, doi:10.1016/j.memsci.2012.05.050.

76. Donohue, M.D.; Minhas, B.S.; Lee, S.Y. Permeation behavior of carbon dioxide-methane mixtures in cellulose acetate membranes. *J. Memb. Sci.* 1989, *42*, 197–214, doi:10.1016/S0376-7388(00)82376-5.

77. Wind, J.D.; Staudt-Bickel, C.; Paul, D.R.; Koros, W.J. The Effects of Crosslinking Chemistry on CO_2 Plasticization of Polyimide Gas Separation Membranes. *Ind. Eng. Chem. Res.* 2002, *41*, 6139–6148, doi:10.1021/ie0204639.

78. Bos, A.; Pünt, I.G.M.; Wessling, M.; Strathmann, H. Plasticization-resistant glassy polyimide membranes for CO_2/CH_4 separations. *Sep. Purif. Technol.* 1998, *14*, 27–39, doi:10.1016/S1383-5866(98)00057-4.

79. Story, B.J.; Koros, W.J. Sorption of CO_2/CH_4 mixtures in poly(phenylene oxide) and a carboxylated derivative. *J. Appl. Polym. Sci.* 1991, *42*, 2613–2626, doi:10.1002/app.1991.070420926.

80. Barbari, T.A.; Koros, W.J.; Paul, D.R. Polymeric membranes based on bisphenol-A for gas separations. *J. Memb. Sci.* 1989, *42*, 69–86, doi:10.1016/S0376-7388(00)82366-2.

81. Jordan, S.M.; Koros, W.J.; Fleming, G.K. The effects of CO_2 exposure on pure and mixed gas permeation behavior: comparison of glassy polycarbonate and silicone rubber. *J. Memb. Sci.* 1987, *30*, 191–212.

82. Fraga, S.C.; Monteleone, M.; Lanč, M.; Esposito, E.; Fuoco, A.; Giorno, L.; Pilnáček, K.; Friess, K.; Carta, M.;

McKeown, N.B.; Izák, P.; Petrusová, Z.; Crespo, J.G.; Brazinha, C.; Jansen, J.C. A novel time lag method for the analysis of mixed gas diffusion in polymeric membranes by on-line mass spectrometry: Method development and validation. *J. Memb. Sci.* 2018, *561*, 39–58, doi:10.1016/j.memsci.2018.04.029.

83. Garrido, L.; García, C.; López-González, M.; Comesaña-Gándara, B.; Lozano, Á.E.; Guzmán, J. Determination of Gas Transport Coefficients of Mixed Gases in 6FDA-TMPDA Polyimide by NMR Spectroscopy. *Macromolecules* 2017, *50*, 3590–3597, doi:10.1021/acs.macromol.7b00384.

84. Carta, M.; Malpass-Evans, R.; Croad, M.; Rogan, Y.; Jansen, J.C.; Bernardo, P.; Bazzarelli, F.; McKeown, N.B. An Efficient Polymer Molecular Sieve for Membrane Gas Separations. *Science.* 2013, *339*, 303–307, doi:10.1126/science.1228032.

85. Freeman, B.D. Basis of permeability/selectivity tradeoff relations in polymeric gas separation membranes. *Macromolecules* 1999, *32*, 375–380, doi:10.1021/ma9814548.

86. Robeson, L.M.; Smith, Z.P.; Freeman, B.D.; Paul, D.R. Contributions of diffusion and solubility selectivity to the upper bound analysis for glassy gas separation membranes. *J. Memb. Sci.* 2014, *453*, 71–83, doi:10.1016/j.memsci.2013.10.066.

87. Robeson, L.M.; Dose, M.E.; Freeman, B.D.; Paul, D.R. Analysis of the transport properties of thermally rearranged (TR) polymers and polymers of intrinsic microporosity (PIM) relative to upper bound performance. *J. Memb. Sci.* 2017, *525*, 18–24, doi:10.1016/j.memsci.2016.11.085.

88. Budd, P.M.; Msayib, K.J.; Tattershall, C.E.; Ghanem, B.S.; Reynolds, K.J.; McKeown, N.B.; Fritsch, D. Gas separation membranes from polymers of intrinsic microporosity. *J. Memb. Sci.* 2005, *251*, 263–269, doi:10.1016/j.memsci.2005.01.009.

89. Gemeda, A.E. Polymeric Gas Separation Membranes: CO_2/CH_4 Mixed Gas Sorption in Glassy Polymers, University of Bologna, 2015.

90. Ansaloni, L.; Minelli, M.; Giacinti Baschetti, M.; Sarti, G.C. Effects of Thermal Treatment and Physical Aging on the Gas Transport Properties in Matrimid®. *Oil Gas Sci. Technol. – Rev. d'IFP Energies Nouv.* 2015, *70*, 367–379, doi:10.2516/ogst/2013188.

91. Bos, A. *High Pressure CO2/CH4 Separation with Glassy Polymer Membranes (Aspects of CO_2-induced plasticization)*; Ph.D. Thesis; University of Twente, Netherlands, 1996; ISBN 903650905X.

92. Ricci, E.; Minelli, M.; De Angelis, M.G. A multiscale approach to predict the mixed gas separation performance of glassy polymeric membranes for CO_2 capture: the case of CO_2/CH_4 mixture in Matrimid®. *J. Memb. Sci.* 2017, *539*, 88–100, doi:https://doi.org/10.1016/j.memsci.2017.05.068.

93. Walker, D.R.B.; Koros, W.J. Transport characterization of a polypyrrolone for gas separations. *J. Memb. Sci.* 1991, *55*, 99–117, doi:10.1016/S0376-7388(00)82329-7.

94. Maeda, Y.; Paul, D.R. Selective gas transport in miscible PPO-PS blends. *Polymer (Guildf).* 1985, *26*, 2055–2063, doi:10.1016/0032-3861(85)90187-9.

95. Story, B.J.; Koros, W.J. Comparison of three models for permeation of CO_2/CH_4 mixtures in poly(phenylene oxide). *J. Polym. Sci. Part B Polym. Phys.* 1989, *27*, 1927–1948, doi:10.1002/polb.1989.090270910.

96. Puleo, A.C.; Paul, D.R.; Kelley, S.S. The Effect Of Degree Of Acetylation On Gas Sorption And Transport Behaviour In Cellulose Acetate. *J. Memb. Sci.* 1989, *47*, 301–332.

97. Houde, A.; Krishnakumar, B.; Charati, S.; Stern, S. Permeability of dense (homogeneous) cellulose acetate membranes to methane, carbon dioxide, and their mixtures at elevated pressures. *J. Appl. Polym. Sci.* 1996, *62*, 2181–2192, doi:10.1002/(SICI)1097-4628(19961226)62:13<2181::AID-APP1>3.0.CO;2-F.

98. Stern, S.A.; Kulkarni, S.S. Solubility of Methane in Cellulose Acetate - Conditioning Effect of Carbon Dioxide. *J. Memb. Sci.* 1982, *10*, 235–251.

99. Sada, E.; Kumazawa, H.; Yoshio, Y.; Wang, S. -T; Xu, P. Permeation of carbon dioxide through homogeneous dense and asymmetric cellulose acetate membranes. *J. Polym. Sci. Part B Polym. Phys.* 1988, *26*, 1035–1048, doi:10.1002/polb.1988.090260508.

100. Ricci, E.; Di Maio, E.; Degli Esposti, M.; Fabbri, P.; Mensitieri, G.; De Angelis, M.G. A rigorous approach for the description of gas sorption thermodynamics in glassy Cellulose Acetates. *In preparation.*

101. Wu, A.X.; Drayton, J.A.; Smith, Z.P. The perfluoropolymer upper bound. *AIChE Journal* 2019, 65, 12, 1–12, doi:10.1002/aic.16700.

Chapter 5

Experimental Measurement and Modelling of Ternary Mixed-Gas Sorption in PIM-1

5.1 Introduction

Mixed-gas sorption of CO_2/CH_4 mixtures in polymeric materials for gas separation generally displays strong nonidealities, which lead to a more pronounced exclusion of the less soluble gas (CH_4) and result in an increased solubility-selectivity. This behavior has been characterized for a number of materials, as discussed in **Chapter 4** [1–13]. However, in real applications such as natural gas upgrading, the gas mixture contains also additional components. Hydrocarbons, like C_2H_6, are highly soluble in the membrane even when they are present in small amounts, and they can be responsible for significant swelling and strong competitive exclusion of the co-permeants. Therefore, they have a profound impact on the separation performance. Until now, only binary mixtures have been tested with respect to sorption, both in the case of glassy and rubbery polymers, whereas permeation experiments with ternary or even quaternary mixtures have been reported [14–17].

In order to characterize the materials performance as close as possible to actual operating conditions, it is necessary to perform multicomponent tests able to capture the effects of third components as well as impurities. Being able to isolate the contributions coming from solubility can help shed light into the mechanisms shaping the separation performance at the fundamental level. Very few reports of the investigation of these phenomena in membrane materials are found in the literature. Ogieglo et al. [18] studied the mixed-penetrant sorption of water, n-hexane and ethanol mixtures in PIM-1 using an interference-enhanced in situ spectroscopic ellipsometry, registering swelling and the simultaneous changes in refractive index of the film when exposed to pure and mixed penetrants. Interestingly, they found that for penetrants with a low mutual affinity (hexane/water and hexane/ethanol) there was a clear competitive effect for sorption, whereas, for penetrant with higher chemical affinity, a pronounced sorption enhancement of the more weakly sorbing species (water) was found in the presence of the higher sorbing one (ethanol).

In this chapter, a new measurement protocol is presented, which generalizes the procedure to perform mixed-gas sorption tests with a pressure decay apparatus for gas mixtures containing an arbitrary number of components, in order to obtain sorption isotherms at constant composition of the gas phase in equilibrium with the polymer. As a test case, $C_2H_6/CO_2/CH_4$ mixed-gas sorption tests in PIM-1 were performed. The sorption of ternary mixtures at two different compositions was measured, as well as the sorption of binary mixtures of C_2H_6/CO_2 and C_2H_6/CH_4, not reported previously for this material, and interesting for comparison with the ternary case. Pure gas sorption isotherms were preliminarily measured as well and used to parameterize the Non-Equilibrium Lattice Fluid (NELF) model and the Dual Mode Sorption model, which were described in detail in **Chapter 2**. The NELF model is not only tested to assess its predictive ability in the case of more complex mixtures, but it plays an important part in the measurement protocol itself, as it will be explained in **Section 5.2.2**.

5.2 Equipment Design and Measurement Protocol

Sorption experiments were performed using a pressure decay apparatus, whose design is an evolution of the one used by Sanders et al. [19], inspired to the set-up for mixed-gas sorption experiments devised by Vopička et al. previously in use at our laboratory, which was described in detail in previous works [1,2]. The schematic of the new equipment is reported in **Figure 5.1**. The pressure transducers employed (PT01 and PT02) are *Honeywell – Super TJE*, with a full scale of 500 psia and 0.05% accuracy and zero temperature error of less than 0.0015% FS/°F. A known mass of polymer sample is placed into a dead-end sample cell and gas sorption is determined by recording the decrease of pressure in a closed and calibrated volume due to the penetrant leaving the gas phase and dissolving into the polymer. To perform mixed-gas sorption tests, the apparatus is equipped with a gas chromatograph (GC) *Varian CP4900* Micro-GC with a capillary column *PoraPLOT U* and thermal conductivity detector for the determination of gas phase composition. The apparatus is submerged in a thermostatted recirculated water bath. To further stabilize the pressure reading with respect to temperature fluctuations, the part of the manometer which emerges from the water bath is insulated using a heating coil in which the fluid of the bath is continuously recirculated. The apparatus can work in a wide range of pressures (0 – 35 bar), temperatures (25 – 65 °C) and compositions (any gas mixture in the composition range for which the CG was calibrated).

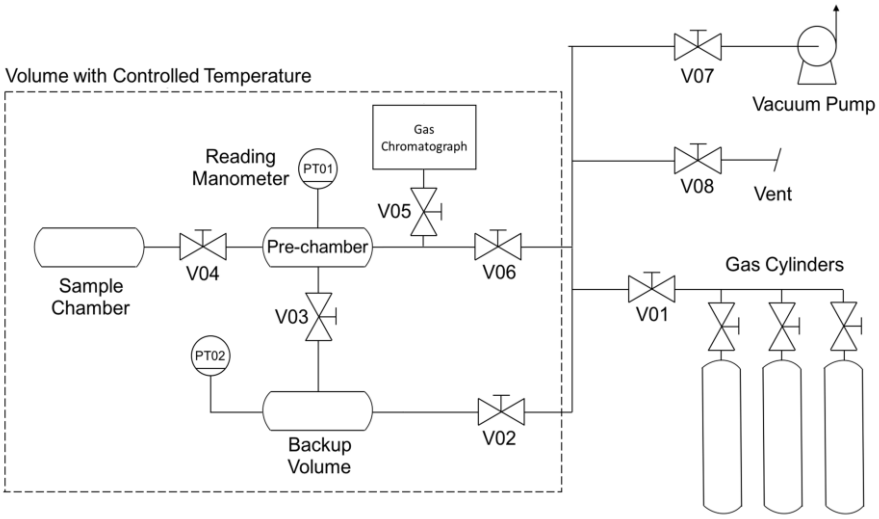

Figure 5.1. Schematic representation of the apparatus used to perform pure- and mixed-gas sorption tests.

5.2.1 Pure-Gas Sorption Measurements

In the case of a pure-gas sorption test, the vacuum is pulled overnight prior to the experiment. Afterwards, the sample chamber is isolated, by closing V04, and the pre-chamber is filled with the desired amount of gas. The pressure is stabilized and then the gas is expanded into the sample chamber. After a sudden pressure drop due to the expansion, a slower pressure decay begins, until the amount of gas sorbed by the polymer sample reaches its equilibrium value, condition identified by the stabilization of the pressure

around a constant value. From the knowledge of (1) the amount of gas already present inside the sample and in the gas phase in equilibrium with it in the sample chamber (which is zero in the first step of the experiment just described), (2) the amount of gas loaded into the pre-chamber and (3) the residual amount of penetrant in the gas phase at the end of the equilibration step, it is possible to calculate the amount of gas sorbed inside the polymer through a simple mass balance:

$$n_i^{A,pol} = n_{i-1}^{A,pol} + n_i^{A,sc} + n_i^{A,pre} - n_i^{A,tot} \qquad \text{Eq. (5.1)}$$

The superscript "A" identifies the penetrant, while the subscript indicates either the current sorption step ("i") or the previous step ("$i-1$"). The superscript "pol" indicates gas sorbed in the polymer sample, "sc" identifies the volume unoccupied by the polymer in the sample chamber, "pre" identifies the volume of the pre-chamber, "tot" designates the total unoccupied volume of the sample chamber and the pre-chamber together, when the connecting valve V04 is open.

To obtain a whole sorption isotherm up to high pressure, it is possible either to pull the vacuum on the system after each equilibration step and repeat the aforementioned steps with a progressively higher loading pressure (integral experiment) or proceed with incremental steps without pulling the vacuum (differential steps). In this latter condition, after the equilibration step V04 is closed and a higher amount of gas is loaded in the pre-chamber, stabilized and then expanded into the sample chamber. At each step, the amount of gas sorbed is obtained recursively from the knowledge of the gas already present in the system plus the one added during the current step, using **Eq. (5.1)**.

5.2.2 Multicomponent Sorption Measurements

Multicomponent sorption tests begin in the same way as a pure-gas sorption test. The system is kept under vacuum overnight, then a known amount of the first gas is loaded in the pre-chamber, and, when the pressure has stabilized, it is expanded into the sample chamber. Measuring pure gas uptake at the beginning of each mixed-gas sorption test serves also as a check of the stability of the sample, to verify that no irreversible swelling has occurred.

When the pressure in the connected pre-chamber and sample chamber stabilizes, V04 is closed, the pre-chamber is evacuated, and the second gas is loaded inside it. After thermal fluctuations of the newly loaded gas are stabilized and the pressure in the pre-chamber becomes constant, V04 is opened and the two gases are allowed to mix. During this stage, either a pressure increase or decrease over time can be recorded, as part of the first gas sorbed inside the polymer reenters into the gas phase and part of the second gas is dissolved. When a constant pressure is reached, V04 is closed and the sample is isolated from the system. The gas mixture in equilibrium with the polymer contained in the pre-chamber is analyzed with the GC to determine its composition. Multiple bleeds are performed, with the aid of a backup volume: the analyte gas is stored in the backup volume and for each composition measurement a dilute mixture with carrier gas (helium) is prepared in the pre-chamber and analyzed. The test is repeated at least 10 times, showing high

reproducibility: the standard deviation in composition measurements performed on the same batch was always lower than 0.5%.

At this stage, all the information necessary to determine a point of a binary gas sorption isotherm have been recorded. Therefore, as a byproduct of a ternary mixed-gas sorption test, one has also a binary sorption isotherm. For example, in the case of the 15% C_2H_6 - 15% CO_2 - 70% CH_4 test performed here loading gases in this order, also a 50% C_2H_6 - 50% CO_2 sorption isotherm was measured. In the binary sorption isotherm, the gases are present approximately in the same relative proportion they have in the final ternary mixture.

To proceed with the ternary test, the backup volume and the pre-chamber are evacuated, and the pre-chamber is loaded with the required amount of the third gas. After the pressure is stabilized, V04 is opened and the third gas is allowed to mix with the mixture of the other two already present in the sample chamber. When equilibrium is reached, V04 is closed once again, the analyte gas in the pre-chamber, which is in equilibrium with the polymer sample, is stored in the backup volume and the composition analysis proceeds as in the previous step. In this way all the information necessary to close the mass balances and calculate the sorbed compositions are obtained. After this final equilibration and composition measurement, the vacuum is pulled on the system and a new test is initiated with a different target final pressure. Therefore, multicomponent sorption tests are performed in the "integral" fashion.

In the case of 3 gases, the experiment can be conceptually divided in 3 phases, each linked to the introduction of a new gas into the system. Molar balances for each component present at each step of the experiment are considered in order to calculate the final sorbed concentration at multicomponent conditions. The set of equations to be solved to calculate the amount of gas sorbed in the polymer is reported below. The superscript "0" identifies the loading pressure, subscript "$post$" indicates values assumed by the variables after closing V04 at the end of an equilibration step, which is indicated with "eq".

Step I : loading gas A and equilibration

A) $$\frac{V_{pre}P_A^0}{R\,T\,Z_A|_{T,P_A^0}} = \frac{V_{tot}P_{eq,\mathrm{I}}}{R\,T\,Z_A|_{T,P_{eq,\mathrm{I}}}} + n_{eq,\mathrm{I}}^{A,pol} \qquad \text{Eq. (5.2)}$$

Closing V04 after equilibration

A) $$\frac{V_{pre}P_A^0}{R\,T\,Z_A|_{T,P_A^0}} = \frac{(V_{tot}-V_{valve})P_{post,\mathrm{I}}}{R\,T\,Z_A|_{T,P_{post,\mathrm{I}}}} + n_{post,\mathrm{I}}^{A,pol} \qquad \text{Eq. (5.3)}$$

Step II : Loading gas B and equilibration

B) $$\frac{V_{pre}P_B^0}{R\,T\,Z_B|_{T,P_B^0}} = \frac{V_{tot}P_{eq,\mathrm{II}}\,y_{eq,\mathrm{II}}^B}{R\,T\,Z_{A,B}\big|_{T,P_{eq,\mathrm{II}},(y_{eq,\mathrm{II}}^A,\,y_{eq,\mathrm{II}}^B)}} + n_{eq,\mathrm{II}}^{B,pol} \qquad \text{Eq. (5.4)}$$

A) $$\frac{(V_{sc}-V_{pol})P_{post,\mathrm{I}}}{R\,T\,Z_A|_{T,P_{post,\mathrm{I}}}} + n_{post,\mathrm{I}}^{A,pol} = \frac{V_{tot}P_{eq,\mathrm{II}}\,y_{eq,\mathrm{II}}^A}{R\,T\,Z_{A,B}\big|_{T,P_{eq,\mathrm{II}},(y_{eq,\mathrm{II}}^A,\,y_{eq,\mathrm{II}}^B)}} + n_{eq,\mathrm{II}}^{A,pol} \qquad \text{Eq. (5.5)}$$

Closing V04 after equilibration

B) $$\frac{V_{pre}P_B^0}{R\,T\,Z_B|_{T,P_B^0}} = \frac{(V_{tot}-V_{valve})P_{post,\mathrm{II}}\,y^B_{post,\mathrm{II}}}{R\,T\,Z_{A,B}\big|_{T,P_{post,\mathrm{II}},(y^A_{post,\mathrm{II}},\,y^B_{post,\mathrm{II}})}} + n^{B,pol}_{post,\mathrm{II}} \qquad \text{Eq. (5.6)}$$

A) $$\frac{(V_{sc}-V_{pol})P_{post,\mathrm{I}}}{R\,T\,Z_A|_{T,P_{post,\mathrm{I}}}} + n^{A,pol}_{post,\mathrm{I}} = \frac{(V_{tot}-V_{valve})P_{post,\mathrm{II}}\,y^A_{post,\mathrm{II}}}{R\,T\,Z_{A,B}\big|_{T,P_{post,\mathrm{II}},(y^A_{post,\mathrm{II}},\,y^B_{post,\mathrm{II}})}} + n^{A,pol}_{post,\mathrm{II}} \qquad \text{Eq. (5.7)}$$

Step III : loading gas C and equilibration

C) $$\frac{V_{pre}P_C^0}{R\,T\,Z_C|_{T,P_C^0}} = \frac{V_{tot}P_{eq,\mathrm{III}}\,y^C_{eq,\mathrm{III}}}{R\,T\,Z_{A,B,C}\big|_{T,P_{eq,\mathrm{III}},(y^A_{eq,\mathrm{III}},\,y^B_{eq,\mathrm{III}},\,y^C_{eq,\mathrm{III}})}} + n^{C,pol}_{eq,\mathrm{III}} \qquad \text{Eq. (5.8)}$$

B) $$\frac{(V_{sc}-V_{pol})P_{post,\mathrm{II}}\,y^B_{post,\mathrm{II}}}{R\,T\,Z_{A,B}\big|_{T,P_{post,\mathrm{II}},(y^A_{post,\mathrm{II}},\,y^B_{post,\mathrm{II}})}} + n^{B,pol}_{post,\mathrm{II}} = \frac{V_{tot}P_{eq,\mathrm{III}}\,y^B_{eq,\mathrm{III}}}{RTZ_{A,B,C}\big|_{T,P_{eq,\mathrm{III}},(y^A_{eq,\mathrm{III}},\,y^B_{eq,\mathrm{III}},\,y^C_{eq,\mathrm{III}})}} + n^{B,pol}_{eq,\mathrm{III}} \qquad \text{Eq. (5.9)}$$

A) $$\frac{(V_{sc}-V_{pol})P_{post,\mathrm{II}}\,y^A_{post,\mathrm{II}}}{R\,T\,Z_{A,B}\big|_{T,P_{post,\mathrm{II}},(y^A_{post,\mathrm{II}},\,y^B_{post,\mathrm{II}})}} + n^{A,pol}_{post,\mathrm{II}} = \frac{V_{tot}P_{eq,\mathrm{III}}\,y^A_{eq,\mathrm{III}}}{RTZ_{A,B,C}\big|_{T,P_{eq,\mathrm{III}},(y^A_{eq,\mathrm{III}},\,y^B_{eq,\mathrm{III}},\,y^C_{eq,\mathrm{III}})}} + n^{A,pol}_{eq,\mathrm{III}} \qquad \text{Eq. (5.10)}$$

In the previous set of equations, R is the universal gas constant and T the temperature of the experiment. V_{sc} represents the volume of the sample chamber, V_{pre} the volume of the pre-chamber, V_{pol} the volume occupied by the polymer sample, taken as the ratio of its mass to its density, and V_{valve} is the volume of the stem of V04, which separates the sample chamber and the pre-chamber when the valve is closed. The value of the polymer volume was considered constant throughout the calculation, neglecting penetrant-induced swelling, since this simplification was found to have little effect on the final result. Finally:

$$V_{tot} = V_{sc} + V_{pre} + V_{valve} - V_{pol} \qquad \text{Eq. (5.11)}$$

The volumes of the chambers were calibrated by means of expansions of known amounts of gas at constant temperature (helium was employed) and the values obtained are reported in **Table 5.1**. The following calibration protocol was adopted. Helium was loaded in the pre-chamber and the pressure was measured. The gas was then expanded into the sample chamber by opening V04 and the pressure was measured again. The sample chamber would either be empty or containing a metal cylinder of known volume. V04 was then closed and the pressure measured again. From these pressure readings, mass balances were solved for the values of the volumes, repeating the test at several loading pressures of gas. The standard deviation associated to the measurement of the larger volumes (pre-chamber and sample chamber) is 0.1%, whereas in the case of the valve, the uncertainty is proportionally higher, with a standard deviation of 18%.

All the pressure values indicated in the previous set of equations (**Eq. (2) – (10)**) are measured during the experiment, as well as the compositions in the gas phase. It must be noted that, after V04 is closed, the pressure in the sample chamber increases from P_{eq} to P_{post}, therefore, in principle, a slight change in the phase equilibrium also takes place. This means that, after V04 is closed, the composition in the

pre-chamber remains constant, because the gas phase has been isolated from the polymer sample, while in the sample chamber a redistribution of the components between the polymer and the gas phase due to increased pressure could lead to a variation of the composition. However, it is assumed that the difference between y_{eq}^{i}, which is measured via GC analysis from the gas sample isolated in the pre-chamber, and the true value y_{post}^{i} found in the sample chamber (which cannot be measured in the present configuration) is negligible and the value y_{eq}^{i} is used in place of y_{post}^{i}. The validity of this assumption was confirmed by calculations performed with the NELF model, as it will be noted later. The compressibility factors Z of pure gases and mixtures were calculated using the Peng-Robinson equation of state [20]. For mixture calculations the following binary interaction parameters were used [21]: k_{CO_2/CH_4}= 0.09, k_{CO_2/C_2H_6}= 0.13, $k_{C_2H_6/CH_4}$ = – 0.003.

The 9 unknowns of the set of equations are, therefore, the sorbed concentrations of each gas at each step of the experiment: $n_{eq,\mathrm{III}}^{A,pol}$, $n_{eq,\mathrm{III}}^{B,pol}$, $n_{eq,\mathrm{III}}^{C,pol}$, $n_{eq,\mathrm{II}}^{A,pol}$, $n_{eq,\mathrm{II}}^{B,pol}$, $n_{eq,\mathrm{I}}^{A,pol}$, $n_{post,\mathrm{II}}^{A,pol}$, $n_{post,\mathrm{II}}^{B,pol}$, $n_{post,\mathrm{II}}^{A,pol}$.

The aim of these tests is to obtain a sorption isotherm in which all the points are characterized by the same composition of the gas phase in the final equilibration step. This is different from the procedure adopted by Genduso et al. [9–11] in which the feed composition is kept constant in all points of an isotherm, while the final composition varies. In order to obtain the same composition of the gas phase in equilibrium with the polymer at the end of each mixed-gas sorption test, the loading pressures of each gas need to be estimated by solving the same set of mass balances reported above. In this case, the target values of the final equilibrium pressure $P_{eq,\mathrm{III}}$ and of the final composition of the gas phase ($y_{eq,\mathrm{III}}^{A}$, $y_{eq,\mathrm{III}}^{B}$, $y_{eq,\mathrm{III}}^{C}$) are fixed and the sorbed concentrations of each gas at each step of the experiment are calculated using the NELF model. In this way, the unknowns become: P_A^0, P_B^0, P_C^0, $P_{eq,\mathrm{I}}$, $P_{eq,\mathrm{II}}$, $P_{post,\mathrm{I}}$, $P_{post,\mathrm{II}}$, $y_{eq,\mathrm{II}}^{A}$, $y_{post,\mathrm{II}}^{A}$. The remainder values of gas phase compositions ($y_{eq,\mathrm{II}}^{B}$, $y_{post,\mathrm{II}}^{B}$) are just obtained as the complement to one of the molar fractions of the first gas. It must be noted that the NELF expressions to calculate the sorbed concentrations depend on the unknown pressure values and gas phase compositions, therefore the system of 9 equations must be solved simultaneously to the 9 phase equilibrium conditions. It can be recognized that it is possible to split the calculation into smaller sets that can be solved sequentially, therefore simplifying the numerical solution considerably. The procedure can be straightforwardly generalized to the case of N gases, and it was implemented as such into a Matlab program.

Table 5.1. Volumes of the mixed-gas sorption equipment section relevant for the measurement.

$\boldsymbol{V_{sc}}$	7.801 ± 0.008 cm^3
$\boldsymbol{V_{pre}}$	15.936 ± 0.016 cm^3
$\boldsymbol{V_{valve}}$	0.170 ± 0.031 cm^3

Several considerations concur in the determination of the order in which the gases are loaded in the system, because each gas has a different conditioning effect on the membrane structure. (1) The more condensable gases (CO_2 or C_2H_6) are responsible for significant swelling effects. If they are loaded and equilibrated first, once the less condensable gas (in this case CH_4) is introduced, the density of the sample is already closer to the one the sample would have if it were constantly exposed to a mixture containing CO_2 or C_2H_6 at the equilibrium composition. Actually, the dilation in this case could be overestimated, because in the initial equilibration steps the sample is in contact with a higher partial pressure of the dilating agents compared to their final partial pressure in the mixture. However, operating the other way around and loading the least condensable gas first, CH_4 would not be able to swell the polymer to the same extent, and the overall amount of CH_4 absorbed would be underestimated. (2) Every gas loaded in the system needs to cross from the pre-chamber to the sample chamber in order to reach the polymer sample. If the sample chamber is at a higher pressure than the pre-chamber because of the gases previously introduced in the system, mixing would be favored in the pre-chamber instead of in the sample chamber, therefore, in order to facilitate mixing in the sample chamber, the gases are loaded preferentially in the order of increasing loading pressure. (3) Some combinations of final equilibrium pressure, final equilibrium composition in the gas phase and loading order could yield for one or more of the gases loading pressure greater than 500 psia, which is the upper limit of the pressure transducer in use. In some cases, this can be resolved by switching the loading order of the gases, whereas in other cases this is not sufficient. If this happens, different loading protocols must be used, as it was described by Vopička et al. [1] for the case of binary mixed-gas sorption tests. They devised four different measurement protocols to be able to span the whole pressure and composition range of interest. In all the cases considered here, the loading pressures of each gas were always lower than 500 psia, therefore the same measurement protocol was applied in all tests.

It must be mentioned that, in the equilibration steps involving mixtures, the characteristic times of diffusion in the gas phase play a nonnegligible role in the total equilibration time required by the system. In particular, the pressure could appear to be equilibrated but the composition of the gas phase might be still varying, and the results are strongly sensitive to the values of the composition in the gas phase. In the current setup, however, it is not possible to track composition during the equilibration. In order to identify the correct equilibration times, preliminary tests were performed by progressively increasing the equilibration time until both pressure and composition were found to be constant and these equilibration times were subsequently adopted in all tests (2 days for binary mixtures, 3 days for ternary mixtures). This quite long equilibration times are one of the main reasons why mixed-gas sorption tests are impractical and the use of reliable models to calculate these properties can yield great benefits timewise.

5.3 Membrane Casting and Density Measurement

PIM-1 was selected for this study because it is one of the few materials for which CO_2/CH_4 mixed-gas sorption was characterized experimentally, therefore direct comparison could be made between binary and ternary tests. Moreover, pure-component NELF model parameters are available for PIM-1. C_2H_6 was chosen as the third component in the gas mixtures because it is, on average, the third most abundant species in natural gas [22], with molar fractions ranging between 0.25% and 14%. The critical temperature of C_2H_6 is 305.3 K [23], therefore it is at supercritical conditions at the temperature of the sorption experiments (308.15 K), and so it does not pose issues related to condensation in the pipes.

PIM-1 powder was supplied by Dr. Tim Merkel (Membrane Technology and Research) and prof. Jianyong Jin (The University of Auckland). A film was prepared via solvent casting, pouring a well-stirred 1.5 wt% solution with chloroform into a petri dish and allowing a slow 4-day evaporation at ambient temperature. This was followed by a methanol soaking treatment overnight and a thermal treatment in the oven at 100 °C under vacuum for 4 days. The thermal treatment was performed to accelerate the physical aging rate of the polymer, which is known to be significant for methanol-treated PIMs [24–27], and stabilize the sample prior to the sorption tests. The density of the film was measured with the buoyancy technique, using water as a displacement fluid, and a value of **1.09 ± 0.01 g/cm^3** was obtained. A mass of **0.395 g** was loaded into the pressure-decay apparatus.

All tests were performed on the same sample, in the following order:

- pure CH_4, pure CO_2 and pure C_2H_6;
- mixed-gas sorption of $C_2H_6/CO_2/CH_4$ at 15/15/70 mol% composition (which includes simultaneously also a 50:50 C_2H_6/CO_2 mixed-gas sorption test);
- mixed-gas sorption of C_2H_6/CH_4 at 17/83 mol% composition;
- mixed-gas sorption of $C_2H_6/CO_2/CH_4$ at 5/25/70 mol% composition (which includes simultaneously also a 15:85 C_2H_6/CO_2 mixed-gas sorption test).

In each mixed-gas sorption test, values of pure-gas sorption of the first gas loaded into the system were compared to the values measured in the corresponding pure-gas test at the beginning of the campaign, to monitor conditioning and physical aging effects.

5.4 Pure-Gas Sorption Isotherms and NELF Model Parametrization

Pure-gas sorption isotherms were measured at 35 °C for CH_4, CO_2 and C_2H_6, in this order. The results are shown in **Figure 5.2** and they have been compared to previous measurements from the literature (CO_2 and CH_4 from ref. [2] and C_2H_6 from ref. [28]), finding good agreement. Pure gas sorption isotherms were fitted with the NELF model [29] to retrieve the values of the binary interaction parameters and of the swelling coefficients for each gas, using the relations and procedure described in detail in **Chapter 2**. The parameters of the Sanchez-Lacombe equation of state adopted for the pure components are reported in **Table 4.2**, while the adjustable parameters obtained for each gas are reported in **Table 4.3**. Moreover, the parameters of the DMS model were retrieved for each gas and they are reported in **Table 5.4**.

Pure-gas uptake of CO_2 and C_2H_6 on a volumetric basis are overall very similar. This was expected since the two gases have fairly close values of the critical temperature (304.2 K in the case of CO_2 and 305.3 K for C_2H_6 [23]), which is a measure of gas condensability, known to scale linearly with the logarithm of solubility [30]. Ethane shows a higher solubility in the lower pressure range, but the two isotherms cross at about 5 bar. Above this pressure value CO_2 concentration remains higher than the one of C_2H_6, both increasing with pressure with a similar slope (this can be seen directly in **Figure 5.4**, where the two curves are plotted together). This is reflected in the values of the DMS model parameters retrieved. The affinity constant b, which is related to the initial slope of the sorption isotherm, in the case of C_2H_6 it is found to be more than double the value obtained for CO_2, whereas k_D values, which express the high pressure asymptotic slope of the sorption isotherm, are similar for the two gases, only a little higher in the case of CO_2. It is interesting to note that the two gases have a slightly different kinetic diameter, with C_2H_6 (3.8 Å [31,32]) being larger than CO_2 (3.3 Å [31,32]) and comparable to CH_4 (3.8 Å [31,32]). Concerning the values of the adjustable parameters of the NELF model, it is observed that the swelling coefficient retrieved for C_2H_6 is 55% higher than the value obtained for CO_2, implying a stronger tendency to induce dilation of the polymer sample. The swelling coefficient for CH_4 is zero, as expected for this gas, whose tendency to induce dilation of the sample is usually found to be very weak. The binary parameters of the NELF model can be compared to the corresponding values obtained by fitting the sorption isotherms by Vopička et al. [2]. For this dataset, the values of the binary interaction parameters k_{ij} obtained are –0.019 for CO_2 and –0.022 for CH_4. It is not uncommon that slightly different values are found for the same material when sorption isotherms of two different samples are considered, as this mirrors the difference both in gas uptake and in the sample density that is observed experimentally. In both cases the values obtained are reasonably small, as expected. The swelling coefficients k_{sw} obtained for the literature sorption isotherms were in better agreement with those of the sample used in this work, which is a positive indication of the physical meaning of k_{sw}: 0.039 MPa^{-1} for CO_2 and 0.005 for CH_4.

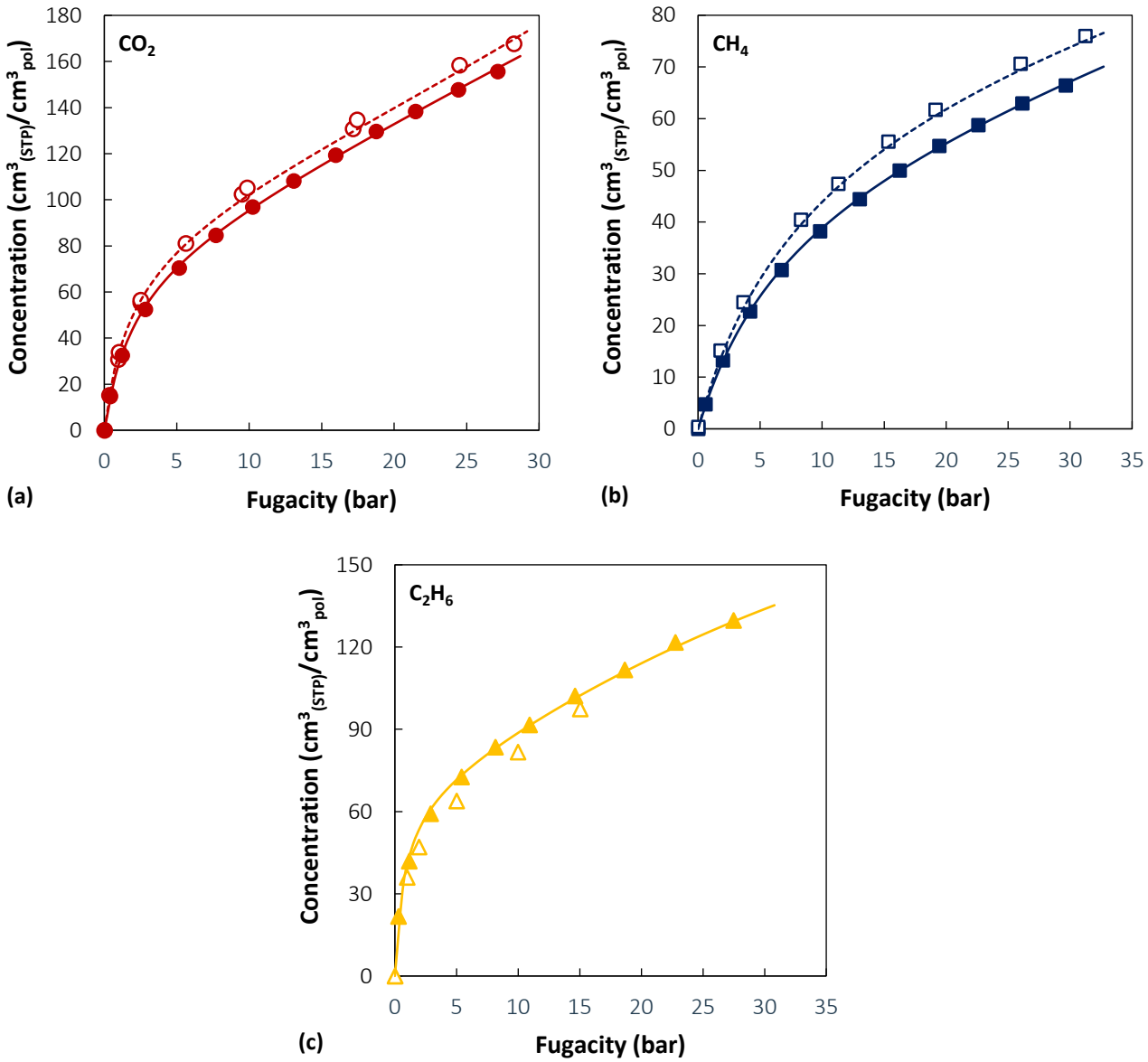

Figure 5.2. Pure-gas sorption of (a) CO_2, (b) CH_4 and (c) C_2H_6 in PIM-1 at 35 °C. Filled symbols refer to the sample used in this work, empty symbols are literature values from ref. [2] for CO_2 and CH_4 and from ref. [28] for C_2H_6. Lines represent NELF model calculations.

Table 5.2. Sanchez Lacombe EoS pure component parameters used for NELF calculations

	$T^*(K)$	$p^*\ (MPa)$	$\rho^*\ (g/cm^3)$	Ref.
PIM-1	872	523	1.438	[33]
C_2H_6	320	330	0.640	[34]
CO_2	300	630	1.515	[29]
CH_4	215	250	0.500	[35]

Table 5.3. Binary interaction and swelling coefficients used in NELF calculations obtained from the best-fit of pure-gas sorption data.

		k_{ij}	k_{sw} (MPa^{-1})
	CO_2	0.044	0.033
PIM-1	**CH_4**	0.053	0
	C_2H_6	0.050	0.051

Table 5.4. DMS model parameters obtained from the best-fit of pure-gas sorption data.

		k_D $\left(\frac{cm^3_{STP}}{cm^3_{pol}bar}\right)$	C'_H $\left(\frac{cm^3_{STP}}{cm^3_{pol}}\right)$	b (bar^{-1})
	CO_2	3.161	76.630	0.496
PIM-1	**CH_4**	0.816	53.094	0.137
	C_2H_6	2.951	66.446	1.324

5.5 Measurement and Modelling of Sorption of Binary Mixtures

One of the aims of this work is to identify the effect of a third component in the equilibrium established between the other two gases. Therefore, in the case of a $C_2H_6/CO_2/CH_4$ ternary mixture, the characterization of the corresponding CO_2/CH_4, C_2H_6/CH_4 and C_2H_6/CO_2 binary mixtures is also required for comparison. Since mixture composition strongly affects the gas uptake, the comparison between the binary and ternary case was made with a binary mixture in which the two gases have the same proportion they have in the ternary mixture, i.e., in the case of a 15% C_2H_6 - 15% CO_2 - 70% CH_4 ternary mixture, the corresponding binary mixture compositions of interest are: 50% C_2H_6 - 50% CO_2, 18% C_2H_6 - 82% CH_4, 18% CO_2 - 82% CH_4. In the case of a 5% C_2H_6 - 25% CO_2 - 70% CH_4 ternary mixture, the corresponding binary mixture compositions of interest are: 15% C_2H_6 - 85% CO_2, 7% C_2H_6 - 93% CH_4, 26% CO_2 - 74% CH_4.

CO_2/CH_4 mixed gas sorption measurements were previously reported for PIM-1 at 35 °C in a wide range of compositions [2], including ~20% CO_2 - 80% CH_4 and ~30% CO_2 - 70% CH_4. In consideration of the similar values of pure-gas uptake obtained with the sample used in the present study, CO_2/CH_4 mixed gas sorption tests were not repeated here. The NELF model showed remarkable accuracy in the prediction of mixed-gas sorption of CO_2/CH_4 mixtures in PIM-1 at 35 °C, as seen in **Chapter 4**, therefore it was used to take into account the different compositions required for comparison.

5.5.1 Ethane/Methane Sorption in PIM-1

C_2H_6/CH_4 mixed gas sorption in PIM-1 was measured at 35 °C. The average final equilibrium composition obtained was 16.9 ± 0.3 mol% C_2H_6 and 83.1 ± 0.3 mol% CH_4, therefore only 1% apart from the target composition of **18% C_2H_6 - 82% CH_4**. By comparing the mixed-gas sorption isotherms to the corresponding pure-gas ones, it is possible to observe the typical behavior displayed also in the case of CO_2/CH_4 sorption in glassy polymers: similarly to CO_2, the presence of C_2H_6 has a strong impact on the solubility of CH_4, leading to a maximum 56% decrease of CH_4 sorbed concentration with respect to the pure gas case, at 20 bar fugacity. Interestingly, calculations performed with the NELF model indicate that the same amount of CO_2 in the gas phase (17 mol%), in place of C_2H_6, would lead only to a 33% decrease of CH_4 concentration at the same fugacity, which indicates that C_2H_6 has a stronger exclusion power over CH_4 compared to CO_2. Even though it is the most abundant component in the gas phase, CH_4 effect on C_2H_6 sorption is minimal: the maximum deviation induced with respect to pure-gas uptake is 16% at 5 bar C_2H_6 fugacity (corresponding to a total equilibrium pressure of 25 bar in the mixed-gas test). NELF model predictions of multicomponent sorption are in very good agreement with the experimental data, with average relative errors of 2.3% in the case of C_2H_6 and 6.2% in the case of CH_4.

The solubility-selectivity was calculated using the following relation and it is reported in **Figure 5.3 (b)**.

$$\alpha^{S}_{CO2/CH4} = \frac{S_{CO2}}{S_{CH4}} = \frac{c_{CO2}/f_{CO2}}{c_{CH4}/f_{CH4}} \qquad \text{Eq. (5.12)}$$

In **Figure 5.3 (b)**, symbols represent the experimental data at multicomponent conditions, solid lines are NELF model predictions, and dashed lines are the values of ideal solubility-selectivity. These are estimated with concentrations measured at pure-gas conditions, but at the same fugacity that the gas has in the mixed-gas test at the same total equilibrium pressure value. Competitive sorption enhances the solubility selectivity on average by 68% over the pressure range inspected, with respect to ideal values. By comparing the results calculated with the NELF model for a 17% CO_2 - 83% CH_4 mixture, it is possible to highlight clearly the higher exclusion power of C_2H_6 over CH_4, as the solubility-selectivity is more than doubled when CO_2 is substituted with an equal amount of C_2H_6 in the mixture. For the C_2H_6/CH_4 mixture at this composition solubility-selectivity at multicomponent conditions displays a decreasing trend with increasing pressure, which is correctly captured by NELF model predictions. On the contrary, CO_2/CH_4 at the same composition displays a weakly increasing trend with increasing pressure.

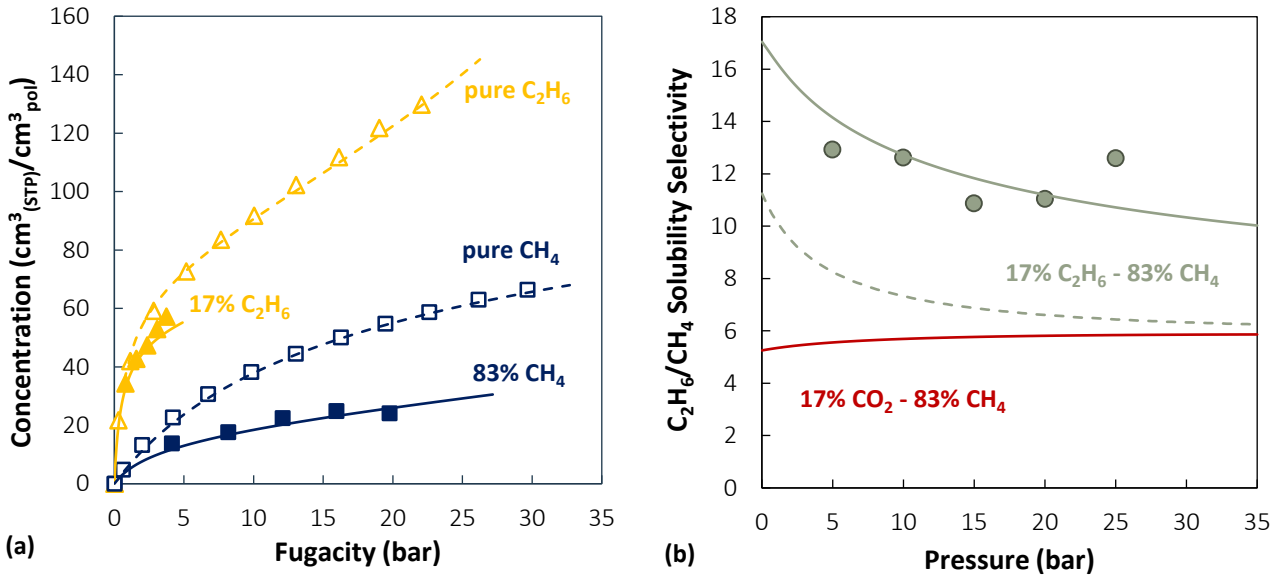

Figure 5.3. Pure and mixed-gas sorption isotherms of C_2H_6 and CH_4 in PIM-1 and solubility selectivity at 35 °C (composition 17% C_2H_6 - 83% CH_4). Empty symbols: pure-gas sorption. Filled symbols: mixed-gas sorption and multicomponent solubility-selectivity. Solid lines: NELF model calculations at multicomponent conditions. Dashed lines: NELF model calculations for pure gases. In subfigure (b) the solubility-selectivity of a 17% CO_2 - 83% CH_4 mixture calculated with the NELF model is shown in red for comparison.

5.5.2 Ethane/Carbon Dioxide Sorption in PIM-1

Sorption of C_2H_6/CO_2 mixtures in PIM-1 was measured at 35 °C at two mixture compositions. Each test was carried out simultaneously to that of a ternary gas mixture as explained in **Section 5.2.2**. In all cases C_2H_6 was loaded to the system first.

In the first test, whose target composition values were **50% C_2H_6 - 50% CO_2**, the average final equilibrium composition obtained was 46.9 ± 1.4 mol% C_2H_6 and 53.1 ± 1.4 mol% CO_2. The target compositions vary slightly along the sorption isotherm in this case, because they are not set independently from that of the ternary mixed-gas sorption test to which they are associated. In fact, once the final composition of the ternary gas sorption test is fixed, the corresponding expected values at the intermediate binary sorption stage are automatically fixed as well and are an output of the calculation. Since it was observed that these values do not differ more than 3% in the pressure range 0 – 30 bar, the results of the intermediate stage of a ternary sorption test can be collected together into a single binary sorption isotherm. For instance, at low pressure the expected mixture composition was 47% C_2H_6 and 53% CO_2, while experimentally 46% C_2H_6 - 54% CO_2 was obtained. At higher pressure the expected composition was 50% C_2H_6 - 50% CO_2, while experimentally 48% C_2H_6 - 52% CO_2 was obtained. This slightly higher deviation at higher pressure is correlated to a less accurate representation of mixed-gas sorption of C_2H_6 at high pressure yielded by the NELF model, as discussed later.

Surprisingly, strong competitive effects were displayed in this case as well, with CO_2 experiencing a marked exclusion from the membrane in the presence of C_2H_6 while the latter is almost unaffected by the presence

of CO_2. The decrease in CO_2 solubility induced by C_2H_6 reaches 54% at 9 bar fugacity of CO_2. The NELF model yielded an accurate representation only in the case of CO_2 at mixed-gas conditions, while C_2H_6 sorption was significantly underestimated, especially at higher pressure. A more detailed discussion of this inconsistency is given **in Section 5.6.1.**

A second test was carried out at a mixture composition of **15% C_2H_6 - 85% CO_2** (average final equilibrium composition: 14.6 ± 0.5 mol% C_2H_6 and 85.4 ± 0.5 mol% CO_2.). In this case, CO_2 is more than 5 times more abundant than C_2H_6 in the gas phase and a more pronounced exclusion from the membrane is observed also for C_2H_6, whereas CO_2 uptake remains closer to its pure-gas values compared to the previous test at an almost equimolar composition. In particular, C_2H_6 uptake at 2 bar fugacity is 39% lower than the corresponding pure-gas uptake at the same fugacity, while for CO_2 the decrease at 13 bar fugacity is 23%. Both values correspond to an equilibrium pressure of the mixture of 16 bar.

The solubility of C_2H_6/CO_2 mixtures in cross-linked Poly(ethylene oxide) was measured and modeled [36] using the Sanchez-Lacombe equation of state [37,38]. In this case, a very limited effect of the presence of C_2H_6 on CO_2 sorption was obtained, both from the experiments and the modelling results. On the other hand, the solubility of C_2H_6 was influenced by the presence of the other component. Unlike the present case, in cross-linked Poly(ethylene oxide), pure CO_2 uptake is approximately 4 times higher than C_2H_6 and the dilation induced by CO_2 in the polymer is such that it enhances solubility of C_2H_6 at multicomponent conditions. This comparison gives an indication of how different phenomena are at play in the case of multicomponent sorption in rubbery and in glassy materials.

The solubility-selectivity is reported for both compositions in **Figure 5.5**. If one neglected to take into account multicomponent effects, almost no solubility-selectivity would be considered for this gas couple in the 47% C_2H_6 - 53% CO_2 case, as expressed by the green dashed line representing ideal solubility-selectivity asymptotically leaning towards unity. The experiment shows instead that the solubility-selectivity is increased by a factor 2 at mixed-gas conditions, at both compositions considered. It was noted also in the case of CO_2/CH_4 solubility selectivity at multicomponent conditions that mixture composition had little effect on the solubility-selectivity.

The ideal selectivity is evaluated at the same fugacity that the gases have at mixed-gas conditions at a given total mixture pressure value, but using the concentration of the pure-gas sorption isotherm at that fugacity value. If one were to simply take the ratio of pure-gas concentration to fugacity at the same pure-gas pressure value, C_2H_6/CO_2 solubility-selectivity in this case would be less than one. By looking also at the ideal solubility-selectivity calculated for the 15% C_2H_6 - 85% CO_2 case, it is apparent how misleading this kind of evaluation can be, not only in term of quantitative accuracy – which was not high in the case of the multicomponent NELF model calculations as well for this case – but in particular in the predicted concentration dependence of the result. Concerning the NELF model, the inaccuracy in the prediction of the C_2H_6 sorption is reflected in an underestimate of the multicomponent solubility selectivity at high pressure. However, a consistent weak dependence of the solubility-selectivity on mixture concentration is correctly predicted.

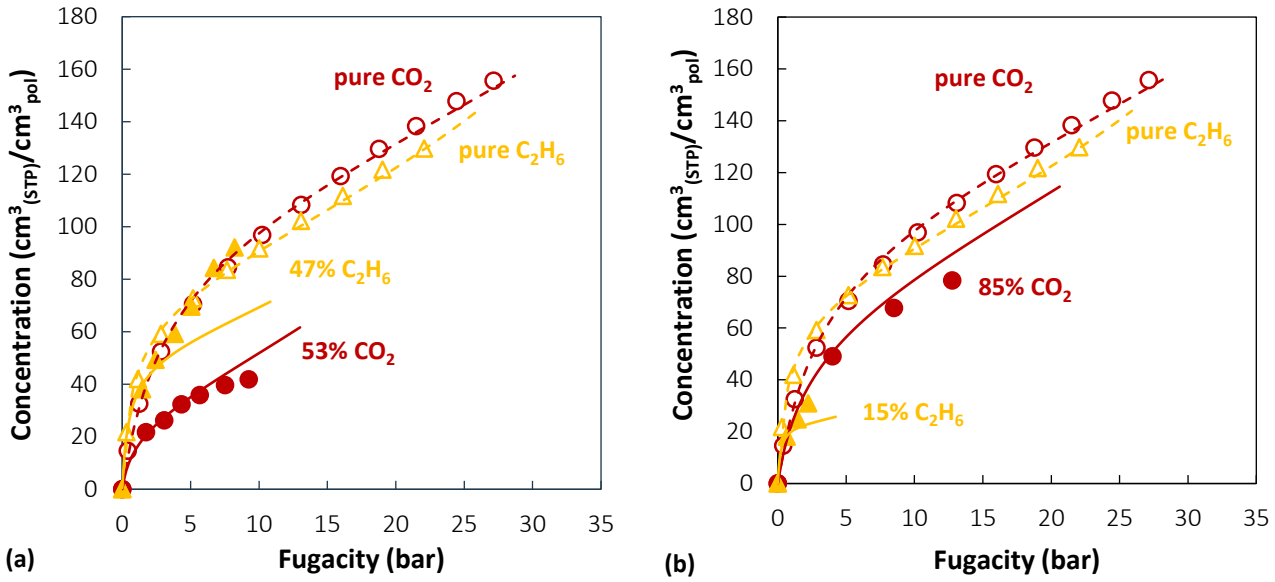

Figure 5.4. Pure and mixed-gas sorption isotherms of C_2H_6 and CO_2 in PIM-1 at 35 °C (mixture composition (a) 47% C_2H_6 - 53% CO_2 (b) 15% C_2H_6 - 85% CO_2). Empty symbols: pure-gas sorption. Filled symbols: mixed-gas sorption. Solid lines: NELF model calculations at multicomponent conditions. Dashed lines: NELF model calculations for pure gases.

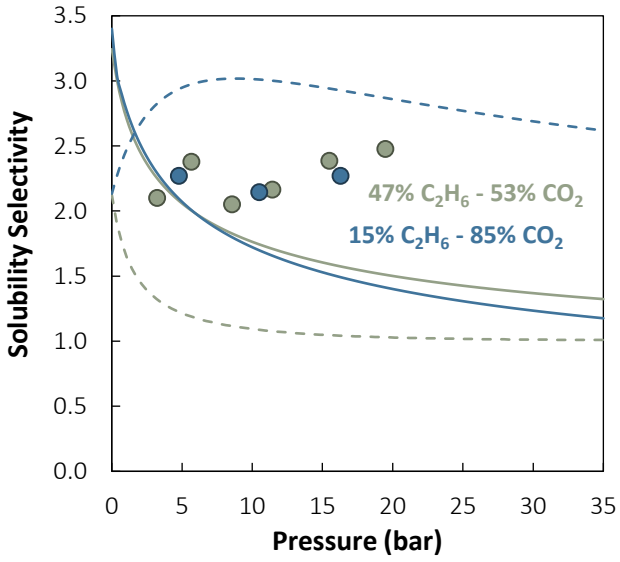

Figure 5.5. C_2H_6 / CO_2 solubility -selectivity in PIM-1 at 35 °C (mixture compositions: 47% C_2H_6 / 53% CO_2 represented in green and 15% C_2H_6 / 85% CO_2 represented in blue). Filled symbols: experimental data. Solid lines: NELF model calculations at multicomponent conditions. Dashed lines: NELF model calculations for pure gases.

5.6 Measurement and Modelling of Sorption of Ternary Mixtures: $C_2H_6/CO_2/CH_4$ sorption in PIM-1

5.6.1 Sorption Isotherms

Ternary gas sorption tests were performed at a target mixture composition of **15% C_2H_6 - 15% CO_2 - 70% CH_4.** The average final equilibrium composition was 14.6 ± 0.7 mol% C_2H_6, 14.3 ± 0.7 mol% CO_2, and 71.2 ± 0.7 mol% CH_4. In this test, the superposition of the competitive effects displayed in the corresponding binary tests was observed, in fact CO_2 and CH_4 solubilities are lower with respect to the pure-gas case, while C_2H_6 is barely altered.

A second test was performed at a target composition of **5% C_2H_6 - 25% CO_2 - 70% CH_4**. This second test had the aim of probing the sensitivity of the equipment when a component is present only in small amounts. The average final equilibrium composition obtained was 4.5 ± 0.1 mol% C_2H_6, 24.5 ± 0.7 mol% CO_2, and 71.0 ± 0.2 mol% CH_4. In this case, the exclusion effect of C_2H_6 over CO_2 is mitigated, while C_2H_6 solubility is slightly decreased with respect to the pure-gas case. CH_4 had the same molar fraction in the mixture in both tests, and its uptake is found to be very similar.

Results for these two cases are reported in **Figure 5.6** and **Figure 5.7**. In subfigure **(a)** all gases are shown together, to provide an overview of the effects on all the components present in the system. Subfigures **(b-d)** show each gas separately for clarity. The NELF model predictions are added to each figure. They were found to be were very accurate in the case of CH_4 and CO_2, whereas, in the case of C_2H_6 in the presence of CO_2 at higher fugacity, the model tends to underestimate C_2H_6 sorption.

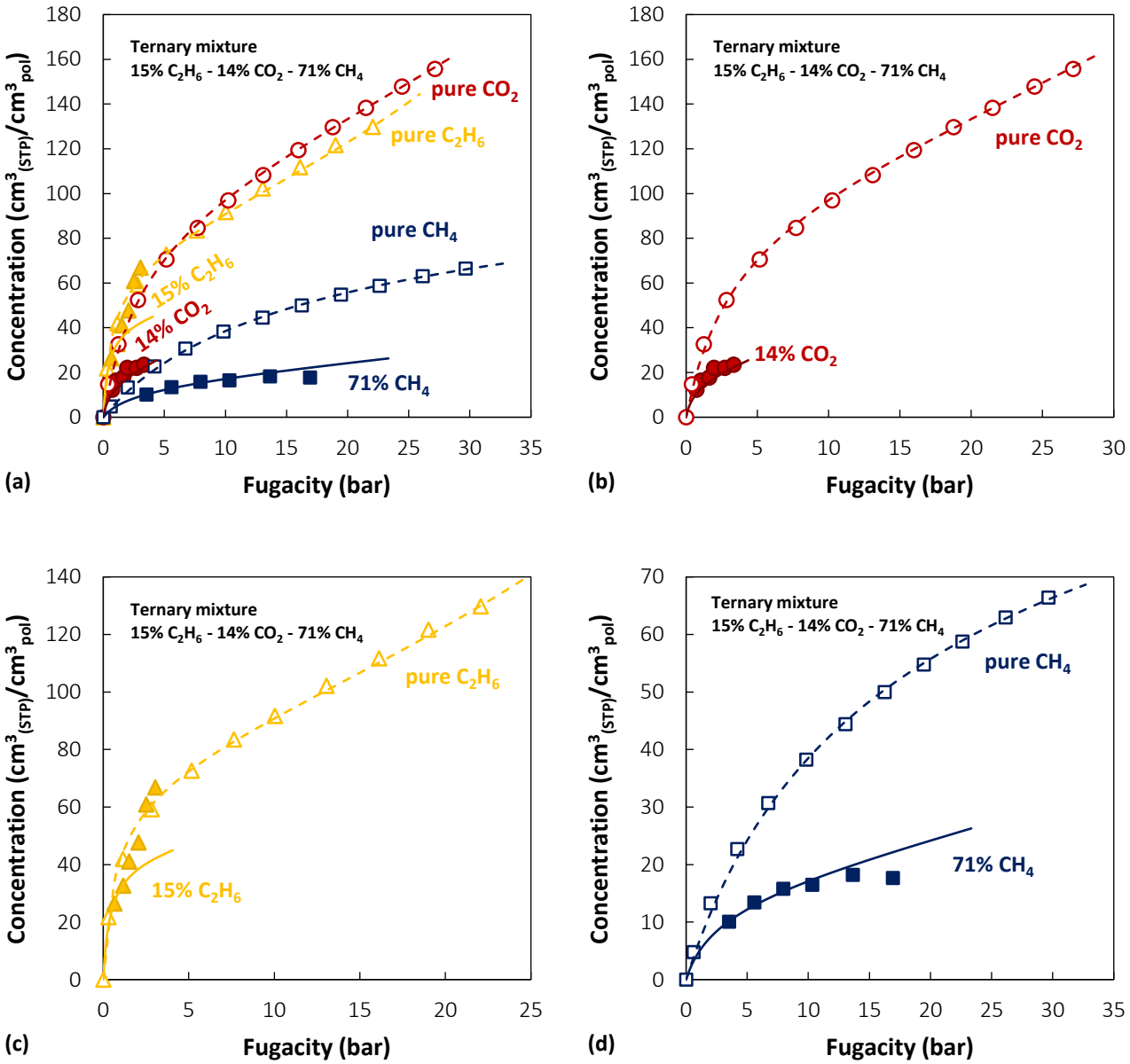

Figure 5.6. Pure- and mixed-gas sorption isotherms of C_2H_6, CO_2 and CH_4 in PIM-1 at 35 °C (mixture composition 15% C_2H_6 - 14% CO_2 - 71% CH_4). Empty symbols: pure-gas sorption. Filled symbols: mixed-gas sorption. Solid lines: NELF model calculations at multicomponent conditions. Dashed lines: NELF model calculations for pure gases.

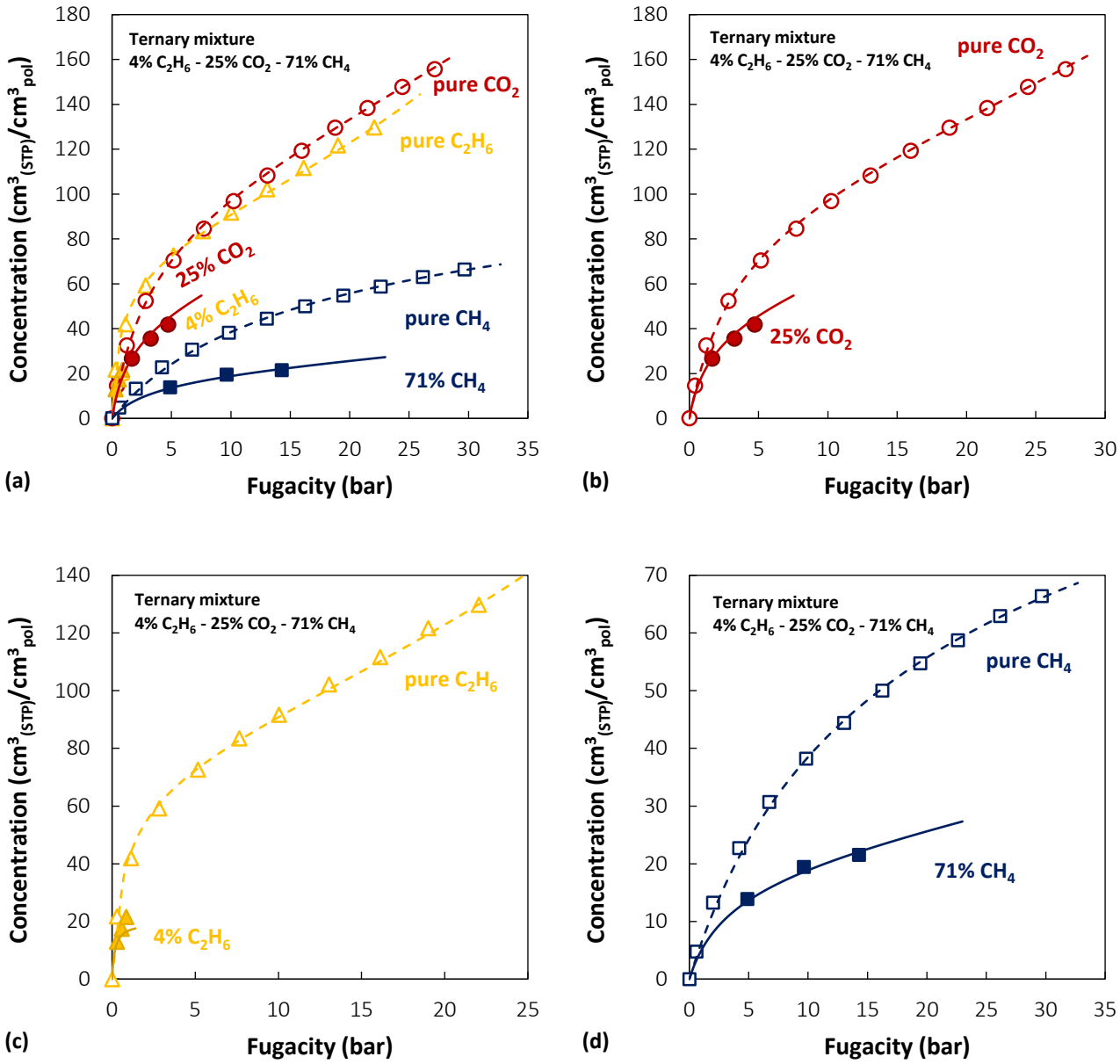

Figure 5.7. Pure- and mixed-gas sorption isotherms of C_2H_6, CO_2 and CH_4 in PIM-1 at 35 °C (mixture composition 4% C_2H_6 - 25% CO_2 - 71% CH_4). Empty symbols: pure-gas sorption. Filled symbols: mixed-gas sorption. Solid lines: NELF model calculations at multicomponent conditions. Dashed lines: NELF model calculations for pure gases.

In **Figure 5.8** the effect of the presence of C_2H_6 on the solubility of CO_2 and CH_4 at multicomponent conditions is shown. The comparison is made by keeping constant the amount of CO_2 relative to CH_4. For this reason, the case at a higher concentration of ethane in the ternary mixture (15%) is compared to a binary mixture containing 19% CO_2 and 81% CH_4. Actually, keeping the same relative composition of CO_2 and CH_4 would require a 17% CO_2 - 83% CH_4 mixture. However, the experimental data available at the slightly different composition (19% CO_2 and 81% CH_4) were used, since a 2% difference in composition has little effect on the final sorbed concentration and direct comparison with experimental measurements provides a more conclusive validation of the results. It is possible to calculate that, in the binary case, methane is responsible for an average 34% decrease in CO_2 sorbed concentration compared to the pure-gas case at the same fugacity. However, when C_2H_6 is present, the average drop in CO_2 concentration is 58%, therefore, in the presence of ethane, an additional 24% decrease is obtained compared to the pure-gas case at the same fugacity. On the other hand, competition with CO_2 alone causes a 27% drop in CH_4 sorbed concentration, that becomes 53% when C_2H_6 is added in the mixture. Therefore, in the presence of C_2H_6, an additional 26% decrease is obtained, which is comparable to the effect on CO_2 sorbed concentration, leading to little variation in the solubility-selectivity between the binary and ternary case, as it will be shown in **Section 5.6.2**. Similarly, the case at a lower concentration of ethane in the ternary mixture (5%) can be compared to a binary mixture containing 26% CO_2 and 74% CH_4. In the binary case methane is responsible for an average 24% decrease in CO_2 sorbed concentration compared to the pure-gas case at the same fugacity. However, when C_2H_6 is present, the average drop in CO_2 concentration is 33%. Therefore, the difference when ethane is added amounts to an additional 9% decrease compared to the pure-gas case at the same fugacity. On the other hand, competition with CO_2 alone causes a 37% drop in CH_4 sorbed concentration, that becomes 49% when C_2H_6 is added in the mixture. In this case the average additional decrease in the presence of C_2H_6 amounts to 12%, which is again comparable to the effect on CO_2 sorbed concentration, leading to little variation in the solubility-selectivity between the binary and ternary case also at this composition.

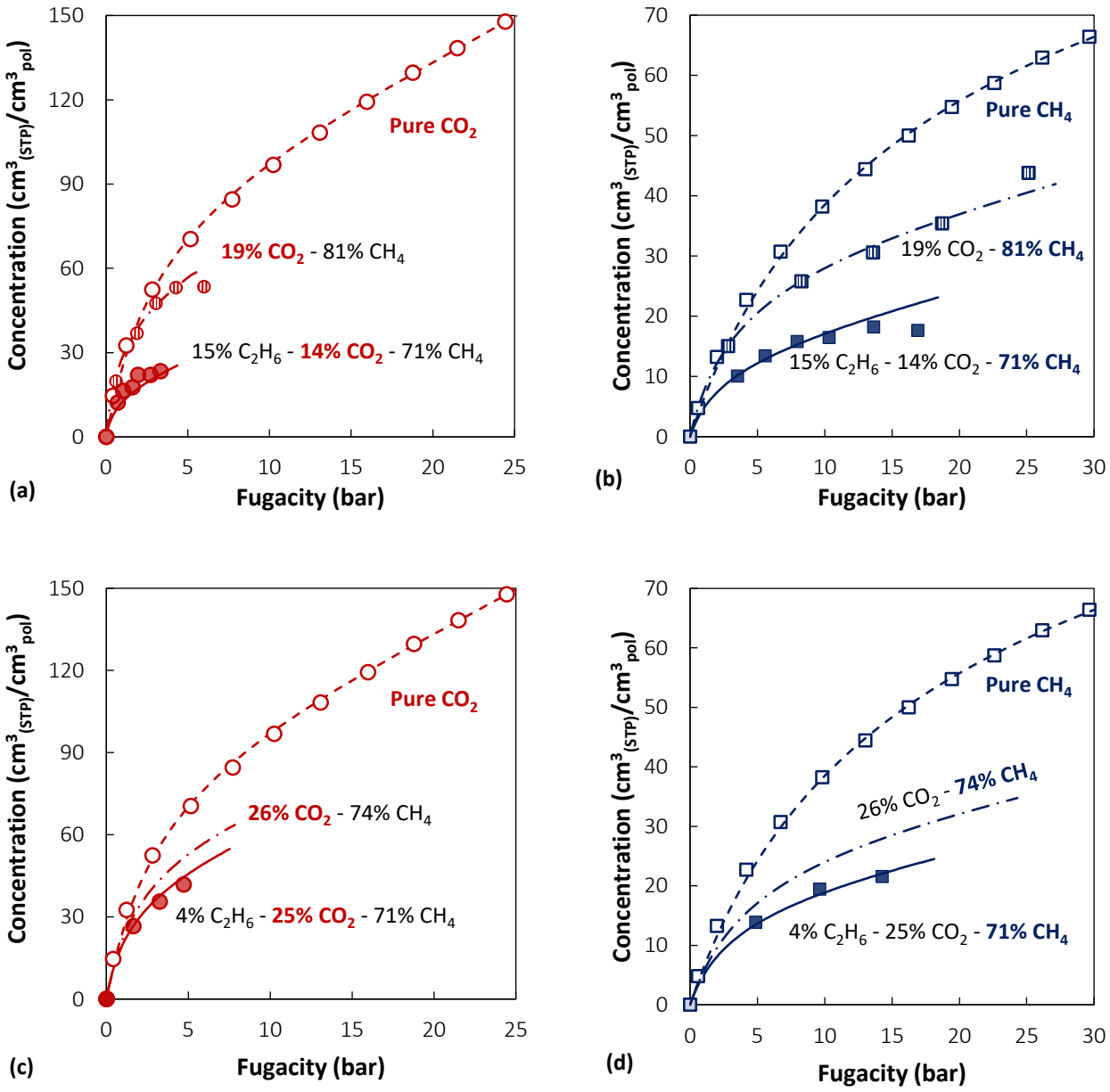

Figure 5.8. Third component (C_2H_6) effects on CO_2 and CH_4 solubility. Empty symbols: pure-gas sorption. Textured symbols: binary mixed-gas sorption tests (CO_2/CH_4) [2]. Filled symbols: ternary mixed-gas sorption tests gas ($C_2H_6/CO_2/CH_4$). Lines are NELF model calculations. Dashed: pure gases. Dot-dash: binary mixtures. Solid: ternary mixtures.

In **Figure 5.9** all the measurements performed including C_2H_6 are grouped together. In subfigure **(a)** the results obtained for C_2H_6 sorption in ternary mixtures are reported, while subfigure **(b)** shows the binary mixtures cases. In both plots, stars represent pure C_2H_6 sorption obtained in the first step of a multicomponent experiment, as described in **Section 5.2.2**. As it was noted previously, this gas is affected more weakly by the competition with the other two gases. Especially in the cases when CO_2 is present in the mixture, the NELF model is unable to capture this effect. A possible explanation was provided by the fact that the pure ethane uptake measured in the first step of a multicomponent sorption experiment tends

to be higher than the corresponding pure-gas value measured preliminarily, at the beginning of the experimental campaign, as it can be seen by comparing yellow triangles and red stars in **Figure 5.9**. Indeed, the fact that mixed-gas sorption of C_2H_6 at high pressure both in the binary and the ternary case is slightly higher than the corresponding pure-gas uptake at the same fugacity can be a result of unrecovered swelling of the sample. The NELF model, parametrized on the initial data set, underestimates the pure C_2H_6 uptake obtained from integral expansions at the beginning of a multicomponent test and, therefore, it consistently underestimates also mixed-gas uptake. However, if this was the case, unrecovered swelling should affect similarly also CO_2 and CH_4 sorption, but these are in line with the model prediction. Moreover, this discrepancy in the prediction of mixed-gas C_2H_6 uptake at high pressure is found also in the case of the test at 4% C_2H_6 - 25% CO_2 - 71% CH_4. In this case, however, at the maximum pressure reached, pure C_2H_6 sorption (blue stars) is still in line with the initial test (yellow triangles), which is a sign that the sample is dilated to a similar extent. On the contrary, in the case of C_2H_6/CH_4 mixed-gas sorption, the NELF model provides an accurate prediction in the whole pressure range (light blue line in **Figure 5.9 (b)**). The calculations had been performed neglecting specific gas-gas interactions, since their effect had been shown to be negligible in the evaluation of mixed-gas sorption in glassy polymers for the CO_2/CH_4 gas couple (**Chapter 4**). However, the validity of this assumption was checked also for this gas couple, by repeating the calculation using a value of $k_{ij} = 0.08$ for CO_2/C_2H_6 interactions [36]. The result differed on average only 0.6% from the previous one for C_2H_6 sorption, therefore it cannot explain the observed discrepancy. On the whole, a satisfactory explanation for this inconsistency in the model predictions has not been found.

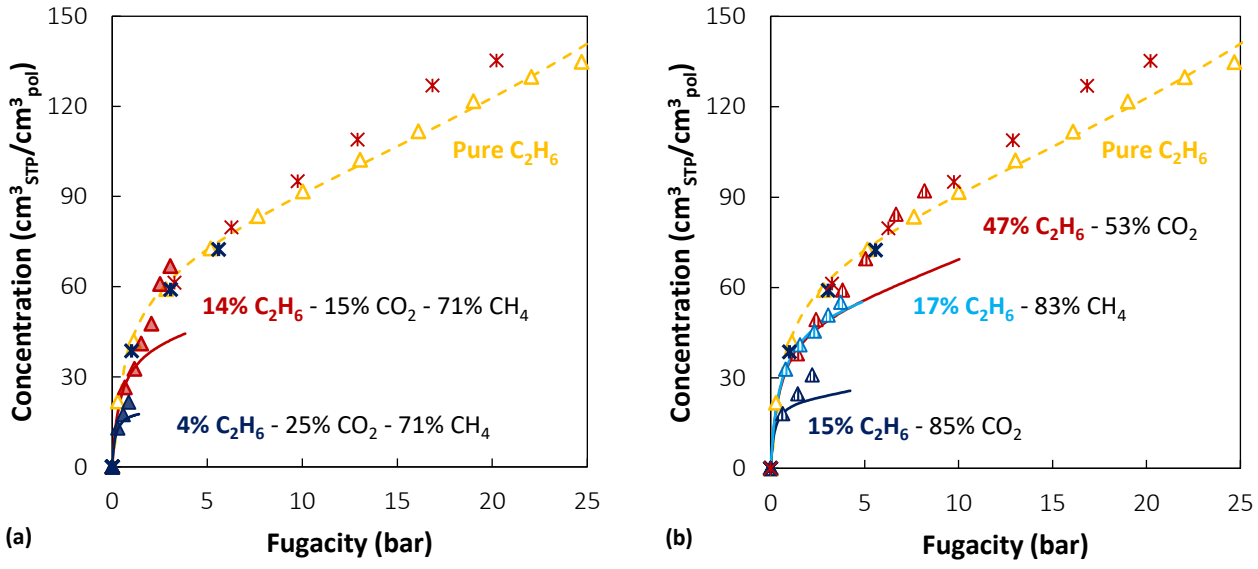

Figure 5.9. C_2H_6 sorption in PIM-1 at 35 °C, at pure and mixed-gas conditions. (a) Pure gas and ternary mixtures. (b) Pure gas and binary mixtures. The stars represent pure-gas uptake from integral expansions, empty triangles were obtained in a differential experiment. Lines represent NELF model predictions.

Ogieglo et al. [18] studied the sorption of water/n-hexane mixtures in PIM-1 and reported a dependency of the final result on the exposure sequence. They interpreted the results in terms of a dual mode picture of sorption and attributed the dependence on the exposure order to the strong chemical dissimilarity between the two components (measured by their difference in Hildebrand solubility parameter). They argue that the first gas to occupy the membrane preferentially fills the microvoids associated to sorption in the Langmuir mode. When the second component is loaded in the system, it tends to avoid the first one, for which it does not have affinity, and, therefore, the second component can only be sorbed to a lesser extent, according to Henry's mode, in the denser portions of the material. The opposite happens if the order is reversed, leading to final different amounts of each gas sorbed in the membrane. However, the difference in the solubility parameters of CO_2 (19.1 $MPa^{1/2}$ [39]) and C_2H_6 (15.5 $MPa^{1/2}$ [39]) is not as high as the difference between water (48 $MPa^{1/2}$ [18]) and n-hexane (14.9 $MPa^{1/2}$ [18]). In their formulation, neither the Dual Mode Sorption model nor the NELF model can take into account directly the different results obtained by switching the loading order of the penetrants.

In the present case, it is hypothesized that the observed higher-than-expected ethane solubility, and the inaccuracy of the NELF model are linked to hysteresis phenomena. At step *n+1* the partial pressure of the gas(es) equilibrated at step *n* will be lower compared to the previous step. It is commonly observed in the case of swelling gases [40] that when the pressure is decreased from a higher to a lower value, the sorbed concentration is higher than the corresponding value measured when the sample was not previously exposed to higher pressure of the gas. In the future, additional tests will be performed to investigate this hypothesis, by quantifying the hysteresis associated to sorption and desorption of each gas and the effect of changing the loading order.

5.6.2 Multicomponent Solubility-Selectivity

In **Figure 5.10** a comparison of the multicomponent solubility-selectivity for the binary and ternary mixtures tested is provided. In **Figure 5.11** the solubility-selectivity of each gas is reported separately, together with NELF model predictions. Filled symbols and solid lines represent ternary mixtures, empty symbols and dash-dot lines represent binary mixtures.

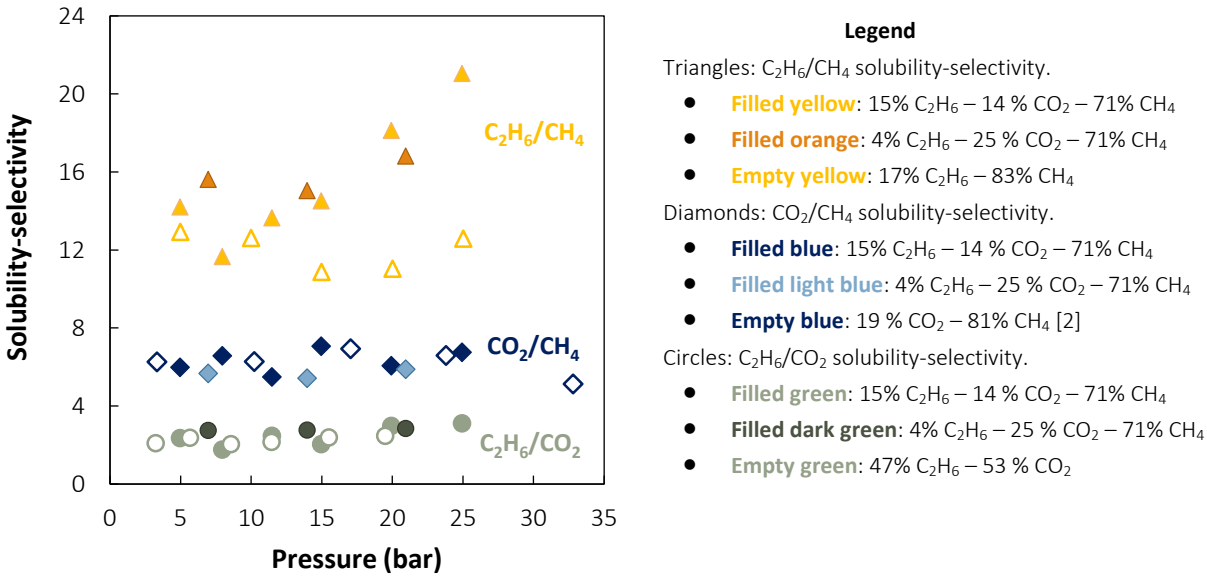

Figure 5.10. Multicomponent solubility-selectivity in PIM-1 at 35 °C. Indications of gas-couples and mixture compositions are reported in the legend. Data for the binary CO_2/CH_4 mixture are taken from [2].

Concerning the **CO_2/CH_4** case, the solubility-selectivity is nearly unaffected by the presence of C_2H_6. This was unexpected prior to the tests. However, in the analysis of the sorption isotherms it was shown that C_2H_6 affects the sorption of the two gases to a similar extent, in such a way that the solubility-selectivity in not markedly affected by its presence. However, by causing a reduction in solubility, it potentially lowers CO_2 permeability (unless a change in diffusivity compensates this effect), therefore having a detrimental effect on the performance of the membrane.

The predictions of the NELF model for this case show an almost pressure-independent trend. The calculated solubility-selectivity increases at increasing CO_2 fraction in the mixture, both in the binary and the ternary cases, as expected. For the binary case, this is a direct result of the exclusion power of CO_2 over CH_4, that increases as the concentration of CO_2 increases. In the ternary case, CH_4 fraction was kept constant, while C_2H_6 decreased and CO_2 increased between the two tests. In the test performed at lower content of C_2H_6, CO_2 was less affected by competitive effects exerted by C_2H_6, meaning that it could be sorbed to a higher level into the membrane. At the same time, CH_4 sorption showed only a modest variation, leading to an increase in the solubility-selectivity (light blue solid line higher than the dark blue one in **Figure 5.11 (a)**).

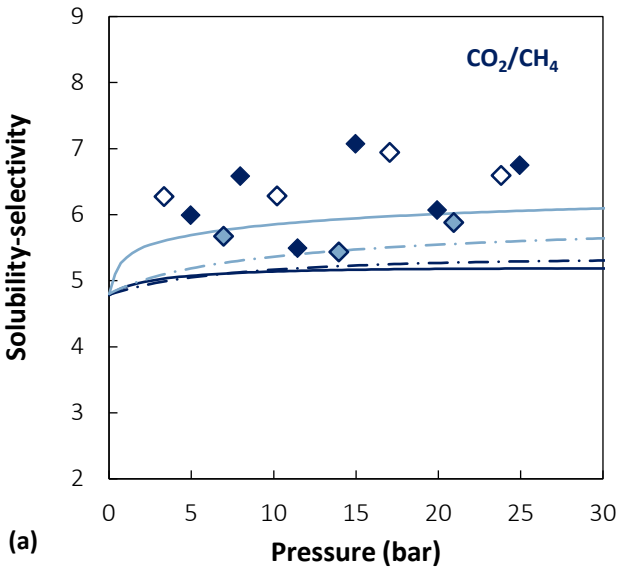

Legend: CO_2/CH_4 solubility-selectivity.

- **Filled blue symbols & solid line**
  15% C_2H_6 – 14 % CO_2 – 71% CH_4
- **Filled light blue symbols & solid line**
  4% C_2H_6 – 25 % CO_2 – 71% CH_4
- **Empty blue symbols & dash-dot line**
  19 % CO_2 – 81% CH_4 [2]
- **Light blue dash-dot line**
  26 % CO_2 – 74% CH_4

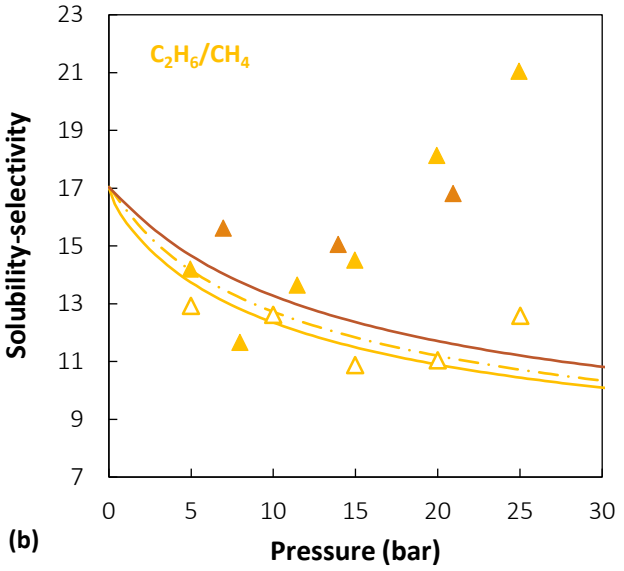

Legend: C_2H_6/CH_4 solubility-selectivity.

- **Filled yellow symbols & solid line**
  15% C_2H_6 – 14 % CO_2 – 71% CH_4
- **Filled orange symbols & solid line**
  4% C_2H_6 – 25 % CO_2 – 71% CH_4
- **Empty yellow line & dash.dot line**
  17% C_2H_6 – 83% CH_4

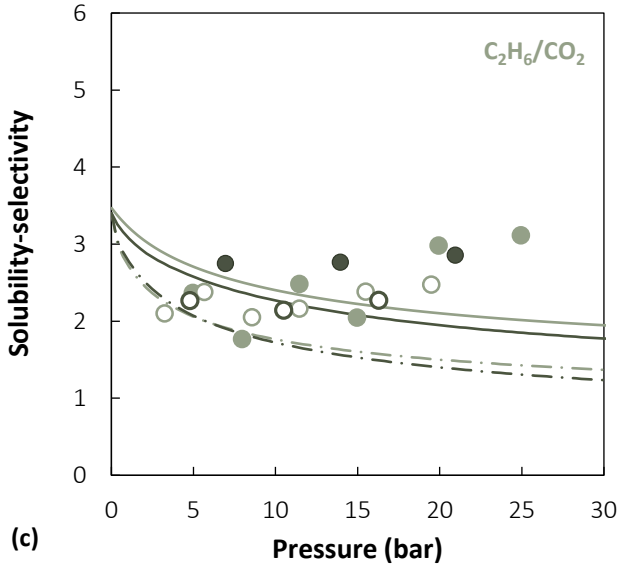

Legend: C_2H_6/CH_4 solubility-selectivity.

- **Filled green symbols & solid line**
  15% C_2H_6 – 14 % CO_2 – 71% CH_4
- **Filled dark green symbols & solid line**
  4% C_2H_6 – 25 % CO_2 – 71% CH_4
- **Empty green symbols & dash-dot line**
  47% C_2H_6 – 53 % CO_2
- **Empty dark green symbols & dash-dot line**
  15% C_2H_6 – 85 % CO_2

Figure 5.11. Experimental data and NELF model predictions of multicomponent solubility-selectivity in PIM-1 at 35 °C. Indications of gas-couples and mixture compositions are reported in the legend. Data for the binary CO_2/CH_4 mixture are taken from [2].

Comparing the **C_2H_6/CH_4** solubility-selectivity at constant relative amount of C_2H_6 and CH_4 in the binary mixture and in the two ternary mixtures, it can be seen that, in the presence of CO_2, the selectivity is higher, especially at higher pressure. This results from the fact that the presence of CO_2 leaves C_2H_6 sorption unchanged, while it enhances the exclusion of CH_4 from the membrane. The NELF model is unable to capture this feature, underestimating C_2H_6 concentration, therefore the calculations underestimate the solubility-selectivity for the ternary mixture at high pressure.

The values obtained for **C_2H_6/CO_2** solubility-selectivity in the case of a binary mixture or in the presence of CH_4 show little variation. Indeed, binary tests with C_2H_6/CH_4 and CO_2/CH_4 mixtures have shown that the presence of CH_4 has little effect on the solubility of both gases, therefore the C_2H_6/CO_2 solubility-selectivity is barely affected by its presence in the ternary mixtures. The NELF model predicts a weak increase in the selectivity at increasing C_2H_6 concentration in the binary mixture, consistently with the fact that, for this gas couple, C_2H_6 is the one less affected by competitive effects, therefore its exclusion effect over CO_2 is increased at increased molar fraction in the gas phase. The trend is decreasing with total pressure and, for both compositions considered, there is a slight increase in the selectivity in the presence of a third component, likely because C_2H_6 is less affected by CH_4 compared to CO_2, even though the effect is weak.

5.6.3 Dual Mode Sorption Model

Figure 5.12 shows the prediction of the DMS model for the sorbed concentrations of CO_2, CH_4, and C_2H_6 in PIM-1 at 35 °C. The calculation is performed using the-gas polymer parameters reported in **Table 5.4** and the DMS model expression for sorbed concentration reported in **Chapter 2**.

The results for the ternary sorption tests performed at compositions of 15% C_2H_6 – 14% CO_2 – 71% CH_4 and 4% C_2H_6 – 25% CO_2 – 71% CH_4 are shown. In general, a good prediction was yielded by the model, in particular in the case of CO_2, for which the multicomponent result is very accurate. CH_4 sorption is overestimated compared to the experimental data, yielding a lower accuracy than the NELF model. For C_2H_6 the DMS model significantly underestimates the uptake at multicomponent conditions, as previously seen also for the NELF model.

On the whole, the prediction of the solubility-selectivity shows a weakly decreasing trend with increasing pressure for all gas pairs and an almost negligible effect of mixture composition. The quantitative accuracy is found to be higher at lower pressure, for all gas pairs, but especially in the case of C_2H_6/CH_4. Even though the NELF model yielded more accurate results, the DMS model results for the ternary mixtures were satisfactory.

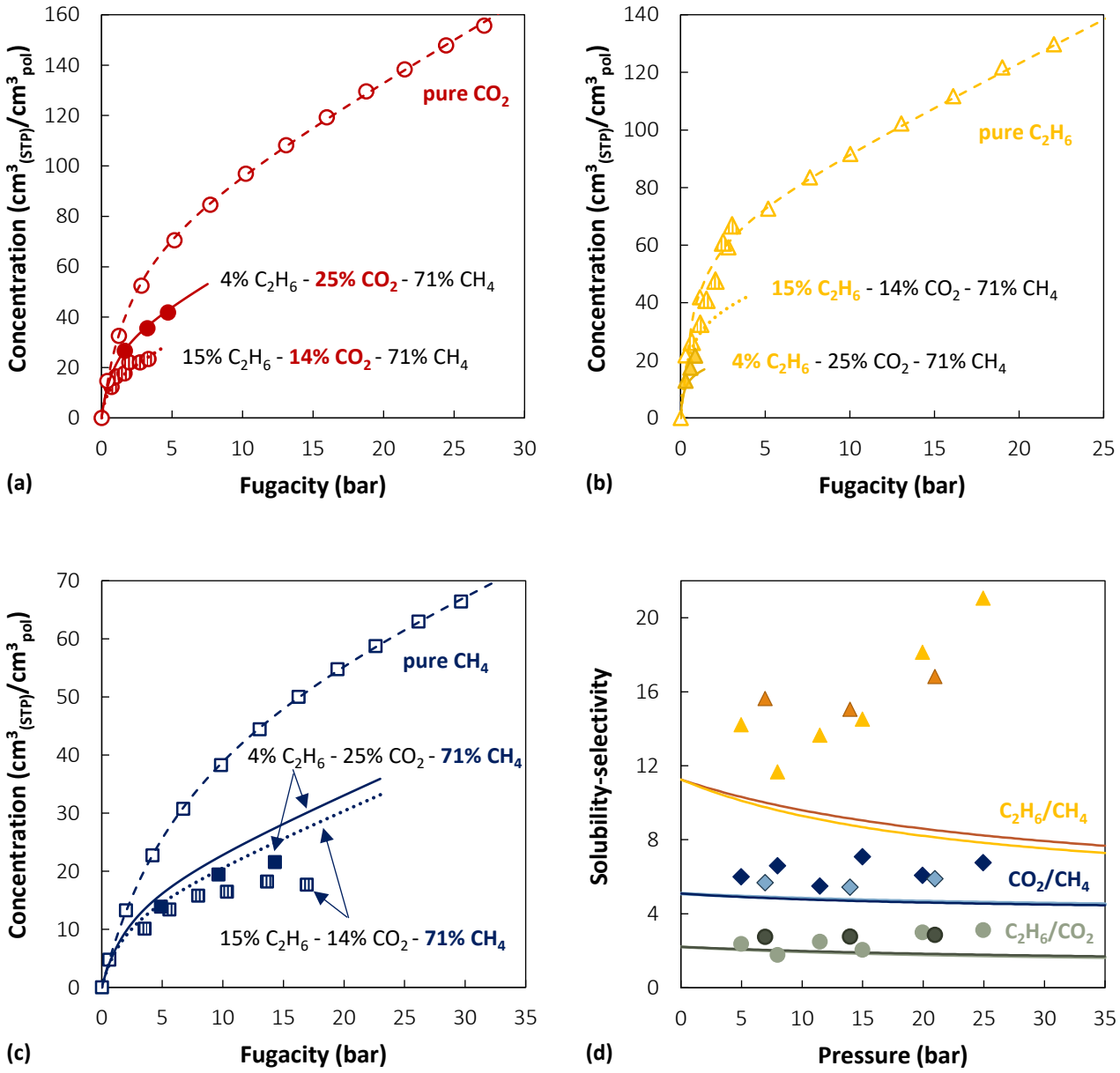

Figure 5.12. Dual Mode Sorption model predictions of sorption isotherms and solubility selectivity of ternary mixtures of $C_2H_6/CO_2/CH_4$ in PIM-1 at 35°C.

5.7 Conclusions

In this chapter, a new measurement protocol for the study of sorption of ternary gas mixtures has been developed and described. The method constitutes a generalization of previous works on binary mixtures to mixtures with an arbitrary number of components. Mixed-gas sorption is determined using a pressure-decay apparatus in which the gases are sequentially loaded into the systems. The loading pressures required to obtain the desired composition in the mixture at equilibrium with sample are estimated by solving molar balances in conjunction with phase equilibria calculated with the NELF model.

This technique was applied to measure mixed-gas sorption of C_2H_6/ CO_2/CH_4 mixtures in PIM-1. In addition, also the characterization of sorption of binary mixtures of C_2H_6/CO_2 and C_2H_6/CH_4 has been performed. Competitive sorption effects, previously seen for the sorption of CO_2/CH_4 mixtures in glassy polymers, have been found also for these gas couples. In the case of C_2H_6/CH_4, a similar behavior to the C_2H_6/CH_4 case was obtained. This was expected, considering that the difference in condensability between CO_2 and CH_4 is the same as between C_2H_6 and CH_4. Nonetheless, it was found that C_2H_6 has a stronger exclusion power over CH_4, compared to CO_2 at the same composition.

Unexpectedly, strong competition was found for the C_2H_6/CO_2 mixture. The two gases show very similar pure-gas uptake, however, when they are exposed to the polymer simultaneously, CO_2 suffers from severe exclusion from the membrane. This is a negative effect for the CO_2/CH_4 separation at hand. Even though it was found that the effect of the presence of C_2H_6 on the CO_2/CH_4 selectivity is not pronounced, a drop in the solubility could be directly reflected in a decrease in the permeability as well, unless other effects concur to determine a proportionally larger increase in diffusivity. The enhancement of CH_4 diffusivity at multicomponent conditions, due to swelling of the membrane caused by CO_2, is likely responsible for the increase in CH_4 permeability in the case of mixed CO_2/CH_4 permeation. This is not expected to happen to the same extent to CO_2 in the presence of C_2H_6, because the difference in the tendency to swell the membrane between CO_2 and C_2H_6 is much smaller than the difference between CO_2 and CH_4.

From sorption tests using ternary mixtures, sorption isotherms of the single gases at constant composition of the gas phase in equilibrium were obtained. The results are consistent with the corresponding binary tests and allowed making considerations on the effect of a third component on the solubility-selectivity of each gas pair.

Because of the time limitations intrinsic to this technique, the variability of the mixed-gas sorption results obtained from different samples was not investigated. It is expected not to be greater than the variability present in pure-gas sorption tests, which was commented upon in **Section 5.2.1**. It would be interesting to verify this assumption, and also whether the NELF model would be able to reflect the experimental behavior by taking into account the different density of different samples, as it was demonstrated in the case of pure gases [41]. On the other hand, the repeatability of the results of two subsequent tests performed on the same sample using the same loading pressures was verified in the present work three times: the final equilibrium concentrations were superimposed, and very high repeatability was found.

The use of a model to predict mixed-gas sorption constitutes an important part of the experimental protocol and the NELF model was found to be a suitable choice, since the final mixture compositions obtained were always less than 2% apart from the target values. In this particular case, also the DMS model would have yielded a good estimate of the loading pressures, since it was verified that it was able to represent mixed-gas data with a comparable accuracy to the NELF model. However, the lack of robustness of this model when it is used predictively, discussed in **Chapter 4**, should be borne in mind.

The NELF model was unable to account for the strong competition among CO_2 and C_2H_6. For all other cases the prediction was consistently very accurate, and further investigation will be devoted to uncovering the reason of this discrepancy. In general, good estimates of solubility and solubility-selectivity were obtained with the model. Therefore, the NELF model is a valid tool for predictive evaluations also in more complex cases and it can be reliably used to evaluate the effects of mixture composition, to reduce the number of experiments performed. Each point of a mixed-gas sorption isotherm requires between seven to ten days to be measured, and a whole isotherm needs several weeks to be obtained, whereas NELF calculations are computationally inexpensive and immediate.

The lowest concentration at which the equipment was tested was 5% C_2H_6. At these conditions consistent and reproducible results were obtained. Ethane is a highly sorbing gas, even at low concentration, therefore, in the future, tests at lower concentrations could be performed to identify the limits of the technique. The low concentrations range is of interest in order to be able to evaluate the effect of impurities on the main separation of interest. Additional tests to bring the laboratory characterization closer to actual operating conditions could be performed by loading more than three gases to the system, since the protocol developed can be applied in principle to an arbitrary number of components in the mixture. Further developments of the protocol would concern the ideation of loading schemes to overcome the limitations in the case of loading pressures exceeding 500 psia. The investigation of the possibility to load more gases simultaneously would be desirable, especially if the number of components in the mixtures is increased beyond three, in order to lower the equilibration times required and perform multicomponent tests in a more practical way, but still obtaining results at constant composition of the gas phase in equilibrium with the sample. Finally, to complete the fundamental analysis of multicomponent effects, it would be interesting to couple these findings with multicomponent permeability or diffusivity measurements, to identify the relevant phenomena related to third component effects, responsible for the final performance of the materials.

5.8 Attribution

This work was carried out in collaboration with Francesco M. Benedetti and Antonella Noto. In particular, Francesco M. Benedetti took part in designing the experiment and setting-up of the apparatus. Volumes calibrations, GC calibrations, membrane casting and density measurement were performed by Francesco M. Benedetti. Gas sorption measurements were performed in collaboration with both Francesco M. Benedetti and Antonella Noto.

References

1. Vopička, O.; De Angelis, M.G.; Sarti, G.C. Mixed gas sorption in glassy polymeric membranes: I. CO_2 /CH_4 and n-C_4/CH_4 mixtures sorption in poly(1-trimethylsilyl-1-propyne) (PTMSP). *J. Memb. Sci.* 2014, *449*, 97–108, doi:10.1016/j.memsci.2013.06.065.
2. Vopička, O.; De Angelis, M.G.; Du, N.; Li, N.; Guiver, M.D.; Sarti, G.C. Mixed gas sorption in glassy polymeric membranes: II. CO_2/CH_4 mixtures in a polymer of intrinsic microporosity (PIM-1). *J. Memb. Sci.* 2014, *459*, 264–276, doi:10.1016/j.memsci.2014.02.003.
3. Kamaruddin, H.D.; Koros, W.J. Some observations about the application of Fick's first law for membrane separation of multicomponent mixtures. *J. Memb. Sci.* 1997, *135*, 147–159, doi:10.1016/S0376-7388(97)00142-7.
4. Ricci, E.; Benedetti, F.M.; Dose, M.E.; De Angelis, M.G.; Freeman, B.D.; Paul, D.R. Experimental Characterization and Modelling of Mixed Gas Sorption of CO_2/CH_4 in HAB-6FDA Polyimide and its Thermally Rearranged Derivative. *J. Memb. Sci.* 2019, Prep.
5. Benedetti, F.M.; Ricci, E.; De Angelis, M.G.; Carta, M.; McKeown, N.B. Sorption of CO_2/CH_4 and their mixtures in PIM-EA-TB. *In preparation*
6. Gemeda, A.E.; De Angelis, M.G.; Du, N.; Li, N.; Guiver, M.D.; Sarti, G.C. Mixed gas sorption in glassy polymeric membranes. III. CO2/CH4 mixtures in a polymer of intrinsic microporosity (PIM-1): Effect of temperature. *J. Memb. Sci.* 2017, *524*, 746–757, doi:10.1016/j.memsci.2016.11.053.
7. Gemeda, A.E. Polymeric Gas Separation Membranes: CO_2/CH_4 Mixed Gas Sorption in Glassy Polymers, University of Bologna, 2015.
8. Ricci, E.; Gemeda, A.E.; Du, N.; Li, N.; De Angelis, M.G.; Guiver, M.D.; Sarti, G.C. Sorption of CO_2/CH_4 mixtures in TZ-PIM, PIM-1 and PTMSP: Experimental data and NELF-model analysis of competitive sorption and selectivity in mixed gases. *J. Memb. Sci.* 2019, *585*, 136–149, doi:10.1016/j.memsci.2019.05.026.
9. Genduso, G.; Ghanem, B.S.; Pinnau, I. Experimental Mixed-Gas Permeability, Sorption and Diffusion of CO_2-CH_4 Mixtures in 6FDA-mPDA Polyimide Membrane: Unveiling the Effect of Competitive Sorption on Permeability Selectivity. *Membranes (Basel).* 2019, *9*, 10, doi:10.3390/membranes9010010.
10. Genduso, G.; Litwiller, E.; Ma, X.; Zampini, S.; Pinnau, I. Mixed-gas sorption in polymers via a new barometric test system: sorption and diffusion of CO_2-CH_4 mixtures in polydimethylsiloxane (PDMS). *J. Memb. Sci.* 2019, *577*, 195–204, doi:10.1016/j.memsci.2019.01.046.
11. Genduso, G.; Wang, Y.; Ghanem, B.S.; Pinnau, I. Permeation, sorption, and diffusion of CO_2-CH_4 mixtures in polymers of intrinsic microporosity: The effect of intrachain rigidity on plasticization resistance. *J. Memb. Sci.* 2019, *584*, 100–109, doi:10.1016/j.memsci.2019.05.014.
12. Walker, D.R.B.; Koros, W.J. Transport characterization of a polypyrrolone for gas separations. *J. Memb. Sci.* 1991, *55*, 99–117, doi:10.1016/S0376-7388(00)82329-7.
13. Story, B.J.; Koros, W.J. Sorption of CO_2/CH_4 mixtures in poly (phenylene oxide) and a carboxylated derivative. *J. Appl. Polym. Sci.* 1991, *42*, 2613–2626.
14. David, O.C.; Gorri, D.; Urtiaga, A.; Ortiz, I. Mixed gas separation study for the hydrogen recovery from H_2/CO/N_2/CO_2 post combustion mixtures using a Matrimid membrane. *J. Memb. Sci.* 2011, *378*, 359–368, doi:10.1016/j.memsci.2011.05.029.
15. Woo, K.T.; Dong, G.; Lee, J.; Kim, J.S.; Do, Y.S.; Lee, W.H.; Lee, H.S.; Lee, Y.M. Ternary mixed-gas separation for flue gas CO_2 capture using high performance thermally rearranged (TR) hollow fiber membranes. *J. Memb. Sci.* 2016, *510*, 472–480, doi:10.1016/j.memsci.2016.03.033.
16. Ghadimi, A.; Sadrzadeh, M.; Shahidi, K.; Mohammadi, T. Ternary gas permeation through a synthesized PDMS membrane: Experimental and modelling. *J. Memb. Sci.* 2009, *344*, 225–236, doi:10.1016/j.memsci.2009.08.001.

17. Cersosimo, M.; Brunetti, A.; Drioli, E.; Fiorino, F.; Dong, G.; Woo, K.T.; Lee, J.; Lee, Y.M.; Barbieri, G. Separation of CO_2 from humidified ternary gas mixtures using thermally rearranged polymeric membranes. *J. Memb. Sci.* 2015, *492*, 257–262, doi:10.1016/j.memsci.2015.05.072.

18. Ogieglo, W.; Furchner, A.; Ghanem, B.; Ma, X.; Pinnau, I.; Wessling, M. Mixed-Penetrant Sorption in Ultrathin Films of Polymer of Intrinsic Microporosity PIM-1. *J. Phys. Chem. B* 2017, *121*, 10190–10197, doi:10.1021/acs.jpcb.7b10061.

19. Sanders, E.S.; Koros, W.J.; Hopfenberg, H.B.; Stannett, V.T. Mixed gas sorption in glassy polymers: Equipment design considerations and preliminary results. *J. Memb. Sci.* 1983, *13*, 161–174, doi:10.1016/S0376-7388(00)80159-3.

20. Peng, D.; Robinson, D.B. A New Two-Constant Equation of State. *Ind. Eng. Chem. Fundam.* 1976, *15*, 59–64, doi:10.1021/i160057a011.

21. Sandler, S.I. *Chemical, Biochemical, and Engineering Thermodynamics*; 5th Editio.; John Wiley & Sons: Hoboken, NJ, USA, 2017;

22. Dung, E.J.; Bombom, L.S.; Agusomu, T.D. The effects of gas flaring on crops in the Niger Delta, Nigeria. *GeoJournal* 2008, *73*, 297–305, doi:10.1007/s10708-008-9207-z.

23. Green, D.W.; Southard, M.Z. *Perry's Chimical Engineers' Handbook*; Ninth Edit.; McGraw-Hill Education, 2019;

24. Tiwari, R.R.; Jin, J.; Freeman, B.D.; Paul, D.R. Physical aging, CO_2 sorption and plasticization in thin films of polymer with intrinsic microporosity (PIM-1). *J. Memb. Sci.* 2017, *537*, 362–371, doi:10.1016/j.memsci.2017.04.069.

25. Bernardo, P.; Bazzarelli, F.; Tasselli, F.; Clarizia, G.; Mason, C.R.; Maynard-Atem, L.; Budd, P.M.; Lanč, M.; Pilnáček, K.; Vopička, O.; Friess, K.; Fritsch, D.; Yampolskii, Y.P.; Shantarovich, V.; Jansen, J.C. Effect of physical aging on the gas transport and sorption in PIM-1 membranes. *Polym. (United Kingdom)* 2017, *113*, 283–294, doi:10.1016/j.polymer.2016.10.040.

26. Pilnáček, K.; Vopička, O.; Lanč, M.; Dendisová, M.; Zgažar, M.; Budd, P.M.; Carta, M.; Malpass-Evans, R.; McKeown, N.B.; Friess, K. Aging of polymers of intrinsic microporosity tracked by methanol vapour permeation. *J. Memb. Sci.* 2016, *520*, 895–906, doi:10.1016/j.memsci.2016.08.054.

27. Low, Z.X.; Budd, P.M.; McKeown, N.B.; Patterson, D.A. Gas Permeation Properties, Physical Aging, and Its Mitigation in High Free Volume Glassy Polymers. *Chem. Rev.* 2018, *118*, 5871–5911, doi:10.1021/acs.chemrev.7b00629.

28. Salinas, O.; Ma, X.; Litwiller, E.; Pinnau, I. Ethylene / ethane permeation , diffusion and gas sorption properties of carbon molecular sieve membranes derived from the prototype ladder polymer of intrinsic microporosity (PIM-1). *J. Memb. Sci.* 2016, *504*, 133–140, doi:10.1016/j.memsci.2015.12.052.

29. Doghieri, F.; Sarti, G.C. Nonequilibrium Lattice Fluids: A Predictive Model for the Solubility in Glassy Polymers. *Macromolecules* 1996, *29*, 7885–7896, doi:10.1021/ma951366c.

30. Matteucci, S.; Yampolskii, Y.; Freeman, B.D.; Pinnau, I. Transport of Gases and Vapor in Glassy and Rubbery Polymers. In *Materials Science of Membranes for Gas and Vapor Separation*; Yampolskii, Y., Pinnau, I., Freeman, B.D., Eds.; John Wiley & Sons, Ltd, 2006.

31. Roberts, D.L.; Abraham, I.C.; Blum, Y.; Way, J.D. Gas Separation With Glass Membranes. *Rep. DOE/MC/25204–3133* 1992, doi:10.1017/CBO9781107415324.004.

32. Sakurovs, R.; Day, S.; Weir, S. Relationships between the sorption behaviour of methane, carbon dioxide, nitrogen and ethane on coals. *Fuel* 2012, *97*, 725–729, doi:10.1016/j.fuel.2012.03.014.

33. Minelli, M.; Friess, K.; Vopička, O.; De Angelis, M.G. Modelling gas and vapor sorption in a polymer of intrinsic microporosity (PIM-1). *Fluid Phase Equilib.* 2013, *347*, 35–44, doi:10.1016/j.fluid.2013.03.003.

34. De Angelis, M.G.; Merkel, T.C.; Bondar, V.I.; Freeman, B.D.; Doghieri, F.; Sarti, G.C. Gas sorption and

dilation in poly(2,2-bistrifluoromethyl-4,5-difluoro-1,3-dioxole-co-tetrafluoroethylene): Comparison of experimental data with predictions of the nonequilibrium lactice fluid model. *Macromolecules* 2002, *35*, 1276–1288, doi:10.1021/ma0106090.

35. Doghieri, F.; Sarti, G.C. Predicting the low pressure solubility of gases and vapors in glassy polymers by the NELF model. *J. Memb. Sci.* 1998, *147*, 73–86, doi:10.1016/S0376-7388(98)00123-9.
36. Minelli, M.; De Angelis, M.G.; Baschetti, M.G.; Doghieri, F.; Sarti, G.C.; Ribeiro, C.P.; Freeman, B.D. Equation of State Modelling of the Solubility of CO2/C2H6 Mixtures in Cross-Linked Poly(ethylene oxide). *Ind. Eng. Chem. Res.* 2015, *54*, 1142–1152, doi:10.1021/ie5038215.
37. Sanchez, I.C.; Lacombe, R.H. Theory of liquid–liquid and liquid–vapour equilibria. *Nature* 1974, *252*, 381–383, doi:10.1038/252381a0.
38. Sanchez, I.C.; Lacombe, R.H. Statistical Thermodynamics of Polymer Solutions. *Macomolecules* 1978, *11*, 1145–1156.
39. Marcus, Y. Solubility parameters of permanent gases. *J. Chem.* 2016, *2016*, doi:10.1155/2016/4701919.
40. Jordan, S.M.; Koros, W.J.; Beasley, J.K. Characterization of CO_2-induced conditioning of polycarbonate films using penetrants with different solubilities. *J. Memb. Sci.* 1989, *43*, 103–120, doi:10.1016/S0376-7388(00)82356-X.
41. Carla, V.; Wang, K.; Hussain, Y.; Efimenko, K.; Genzer, J.; Grant, C.; Sarti, G.C.; Carbonell, R.G.; Doghieri, F. Nonequilibrium Model for Sorption and Swelling of Bulk Glassy Polymer Films with Supercritical Carbon Dioxide. 2005, 10299–10313, doi:10.1021/ma0506684.

Chapter 6

Molecular Simulations of Atactic Polystyrene (PS) and PS/CO_2 Systems

6.1 Introduction

Supercritical CO_2 has found many applications in the fabrication and processing of polymers, to selectively control and manipulate their physical properties by changing temperature and pressure, taking advantage of the fact that its critical point allows operating at mild conditions (304.2 K and 7.4 MPa [1]). Among several applications, supercritical CO_2 is used as a reaction solvent and as an extraction medium, especially in the food and pharmaceutical industries, owing to its non-toxic nature. It is also applied in the impregnation of polymers to introduce dyes, antibacterial or antioxidant substances, or additives in general into the matrix. Moreover, it is employed in fractionation, foaming, blending, particle formation and injection molding [2], usually exploiting the swelling and plasticization of the polymer resulting from the inclusion of high amounts of CO_2 into the matrix. Indeed, the addition of compressed CO_2 to a condensed phase is responsible for substantial changes in the physical properties of interest during processing, such as viscosity, permeability, interfacial tension, and glass transition temperature. A detailed understanding of the effects of CO_2 on polymers properties is therefore of great interest in a wide range of sectors.

Atactic polystyrene (aPS), whose repeating unit is displayed in **Figure 6.1**, is one of the most common plastic materials, ubiquitously used in manufacturing and packaging. For this reason, a rich characterization of its properties has been performed over the years, including its gas transport properties and the effect of CO_2 on its thermodynamic, structural and mechanical properties, both in the glassy and the melt state.

Chiou et al. [3] analyzed the suppression of the glass transition temperature of polymers exposed to increasing pressure of CO_2 by using Differential Scanning Calorimetry (DSC), finding a decrease from a value of 100 °C to a value of 78 °C for a sample of aPS equilibrated with 20 atm of CO_2. Wissinger and Paulaitis [4] performed creep compliance tests for aPS as a function of time in the presence of CO_2 at a constant temperature and pressure. They measured the glass transition temperature and assessed also the swelling effect associated: for a CO_2 pressure of 60 bar a T_g as low as 35 °C was observed and a percent volume dilation of 7.4% compared to the density at T_g in the absence of CO_2. Wang et al. [5] studied the effects of the temperature of exposure as well as that of pressure of CO_2 (since both conditions influence the amount of gas dissolved) on the Young modulus and the glass transition temperature of the polymer. They found that a maximum depression of T_g is attained at around 20 MPa for different temperatures of exposure and that the decrease in T_g is higher for samples exposed to CO_2 at lower temperatures, where the solubility is higher. At higher pressures T_g starts to increase again due to the prevailing of hydrostatic effects, which lead to a densification of the material and an increase of the glass transition temperature, over plasticization.

Sorption and diffusion of CO_2 in glassy aPS were measured by several authors under different conditions. Toi and Paul studied the effect of molecular weight of aPS on carbon dioxide sorption isotherms in the glassy state [6] in the range 35–55 °C and 3600–850000 g/mol, finding that the extent of sorption decreased with increasing temperature but increased as the molecular weight increased. Carfagna [7] studied CO_2 solubility in oriented and unoriented atactic glassy polystyrene films, between 27-100 °C and 0-30 atm, discovering that orientation does not change the dual sorption nature of the process, but it

decreases the level of solubility because of the increase in polymer density due to orientation. Wissinger and Paulaitis [8] measured CO_2 sorption and swelling between 35–65 °C and 0–100 atm, identifying, for each temperature, the onset of the devitrification induced by gas sorption. Aubert [9] used a gravimetric technique instead of a manometric one to measure gas sorption obtaining consistent results. In addition, CO_2 sorption in aPS blended with other polymers has been characterized. Conforti et al. [10] used sorption and dilation data of CO_2 in aPS and poly(2,6-dimethyl-1,4-phenylene oxide) (PPO) to parametrize the glassy polymer lattice sorption model (GPLSM) [11,12], in order to calculate the enthalpy of mixing for the two polymers. Kato et al. [13] studied CO_2 solubility in aPS blends with polycarbonate at 25 °C, while Zhang et al. [14] studied CO_2 sorption and induced swelling in block copolymers containing styrene at 35 °C and up to 100 bar, modelling the system with the Lattice Fluid equation of state (EoS). Shieh and Liu [15] evaluated the interaction of CO_2 and aPS and poly(methyl methacrylate) (PMMA) by examining the sorption isotherms and the desorption time variation of characteristic infrared absorption bands. They found that the carbonyl groups in PMMA endowed this material with higher affinity to CO_2 with respect to aPS. More recently, Pantoula et al. [16,17] characterized the aPS-CO_2 system in terms of gas sorption and swelling in the range 35–132 °C and up to 45 MPa. They also applied the Non-Random Hydrogen-Bonding (NRHB) model [18,19] to represent the behavior of the system in this wide range of conditions.

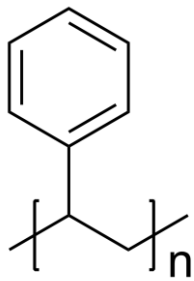

Figure 6.1. Repeating unit of Polystyrene

Fewer studies were devoted to the characterization of aPS-CO_2 system in the melt state. Newitt and Wheale [20] in 1948 reported a few values of CO_2 solubility and diffusivity in aPS melt at high temperature and pressure. Hilic et al. [21] performed the simultaneous measurement of the sorption and associated swelling effects for nitrogen and carbon dioxide in polystyrene from 65 °C to 130 °C and up to 45 MPa. Areerat et al. [22] extended the range of available data by studying CO_2 sorption in polystyrene with a gravimetric technique in the range 150–200°C up to 12 MPa. Moreover, they determined CO_2 diffusion coefficients from the analysis of sorption kinetics and modelled the system using the Sanchez-Lacombe EoS. Sato et al. [23–25] worked extensively on the aPS-CO_2 systems, obtaining sorption isotherms as well as diffusion coefficients in the melt state up to 200 °C and 20 MPa, using both manometric and gravimetric techniques. More recently, Perez-Blanco et al. [26] determined CO_2 solubility and diffusivity in aPS, both in the glassy and the melt state, from 30 to 200 °C and up to 8.5 MPa, finding good agreement with previous works.

Concerning molecular modelling, aPS is one of the benchmark systems for methodological development, and there is a wide body of works devoted to reproducing the properties of the pure polymer [27–32], nanocomposite aPS-filler systems [33–36], polymer blends [37], and also gas-polymer systems, using Molecular Dynamics (MD), Monte Carlo (MC) simulations, or a combination of both. An overview of simulation works on CO_2 solubility and diffusivity in aPS, both in the glassy and in the melt state, is given in **Table 6.1**. Cuthbert et al. [38] used an all-atom representation to study system size effects on the calculated excess chemical potential of gases in amorphous polystyrene glass at 300 K. Their results showed that small system sizes are, on average, unable to form cavities of sufficient size to accommodate larger

gases, such as CO_2, resulting in insufficient sampling with the Widom's test particle insertion method [39]. They found that, for the case of CO_2 in atactic polystyrene, at least a single chain of 364 units (box side length 40 Å) is required to obtain a reasonable value of the excess chemical potential. Kucukpinar et al. [40] used the Transition State Approach [41] instead, in the degrees of freedom of a spherical penetrant representation, allowing only an elastic motion for the polymer matrix. Under these approximations, they determined diffusion coefficients that, in the case of CO_2 in aPS at 300 K, were one order of magnitude lower than the experimental values, whereas solubility values were in significantly better agreement: higher by a factor ranging between 1.5–2.8. Eslami et al. [42] used the Grand Equilibrium Molecular Dynamics method to evaluate infinite dilution solubility coefficients up to 500 K and sorption isotherms up to high pressure at 298 and 373 K, in good agreement with experimental measurements. Mozaffari et al. [43] combined infinite dilution coefficients and diffusivities in the zero pressure limit, evaluated through the mean squared displacement of gas molecules during MD trajectories, to obtain estimates of the permeability coefficients of several light gases in aPS, including CO_2, in the range 300–500 K. Spyriouni et al. [44] calculated CO_2 sorption isotherms up to high pressure both in the glassy and in the low temperature melt state by means of an iterative procedure comprising *N_1N_2PT* MD simulations, Direct Particle Deletion (DPD) tests for the calculations of gas fugacity inside the matrix, coupled to EoS modelling with the PC-SAFT EoS to find the corresponding pressure of the system at a given concentration and fugacity. Their results were in very good agreement with experimental measurements both in terms of sorption and polymer swelling.

Table 6.1. Molecular modelling studies on aPS-CO_2 system properties. AA = all atoms. UA = united atoms. CG = coarse-grained.

Reference	Temperature	System size	Representation	Properties studied
Cuthbert et al. [38]	300 K	Singles chain 40 –364 units	AA	Infinite dilution solubility coefficient in the glassy state
Kucukpinar et al. [40]	300 K	Single Chain 80 units	AA	Infinite dilution solubility and diffusion coefficient in the glassy state
Eslami et al. [42]	298– 500 K	Single chain 200 units	AA	Infinite dilution solubility in the glassy and melt state and sorption isotherms in the glassy state
Mozaffari et al. [43]	300 – 500 K	Single Chain 200 units	AA	Diffusivity and permeability coefficients in the zero-pressure limit
Spyriouni et al. [44]	308 – 405 K	3 Chains 150 units	CG / UA	Sorption isotherms of CO_2 up to 300 bar

Most of these reports are limited to the calculation at a single temperature, in the zero-pressure limit, or for monodisperse systems at a single molecular weight (M_w). The work presented in this chapter focuses on a comprehensive study of temperature (T), gas concentration (c_{CO2}) or, correspondingly, pressure (P), and polymer molecular weight effects on the system properties in the melt state. Sorption isotherms have been evaluated up to high concentrations, using an iterative scheme similar to the one presented in reference [44], as described in **Section 6.2.5**. Diffusion coefficients have been extracted from the mean squared

displacement of gas molecules during long MD runs and, moreover, the volumetric properties, local structural features and local dynamics of the system have been evaluated as a function of T, P, and M_w.

The increase in computational power has made it possible to achieve longer simulation times and bigger system sizes, however, in order to tackle the study of polymeric systems whose M_w resembles the ones used in real applications, brute force approaches are still insufficient, and the use of multiscale strategies is necessary to achieve the equilibration of high M_w polymeric chains. In the case of polystyrene, commercial grades can go as up as 200000 g/mol, even though there is also market for aPS with M_w < 10000 g/mol, which is used as plasticizer, in paper coating and in pressure-sensitive tapes fabrication [27]. In this work, low M_w systems are generated and equilibrated directly at the atomistic level, while for higher M_w systems a different strategy is applied. Instead of MD equilibration, MC simulations at the coarse grained level were performed to this aim, because they offer the possibility of designing moves that permit a more effective sampling of the configuration space of polymer melts. For instance, a class of connectivity-altering MC algorithms [45,46] involving elementary moves that operate on single chains or pairs of chains has been demonstrated to be very advantageous in equilibrating long polymeric chains at all length scales. However, the direct application of connectivity-altering moves to systems possessing bulky side chain groups, such as the phenyl ring in aPS, leads to very low acceptance rates, thus nullifying the potential advantage in their use. This issue can be circumvented by resorting to coarse-grained (CG) models, which involve fewer degrees of freedom for the representation of the material. The application of connectivity altering MC moves to this simpler geometry leads to the expected benefits, enabling the full equilibration of the system. Several coarse-graining schemes have been devised for aPS. The one adopted for the generation of high M_w aPS chains studied in this work is the one proposed by Milano and Müller-Plathe [27]. Their model preserves information on the stereochemical configuration of the chain and they applied it to study structural and dynamic properties of aPS chains of 36000 g/mol. The same model was later employed to study aPS of molar mass up to 420000 g/mol [33] and specifically aPS-CO_2 properties up to 16000 g/mol [44]. Further details about the initial configuration generation and equilibration of the systems are given in **Section 6.2.2**.

The results have been compared also to equations of state (EoS) predictions using the Sanchez-Lacombe Equation of state (SL EoS) [47]. Analysis of previously reported parameter sets for aPS revealed their inadequacy in representing the properties of the material in the low M_w range. Therefore, a molecular weight dependent parametrization was performed (**Section 6.2.6**). The resulting parameter set was employed in the calculation of sorption equilibria and volumetric properties of the system, using a CO_2-PS binary interaction parameter determined from the best fit of experimental sorption data.

6.2 Methodology

In this work, monodisperse melts of atactic polystyrene of different molecular weights (M_w) were studied, consisting of (a) 5 chains of 300 repeating units (~31000 g/mol), (b) 30 chains of 50 repeating units (~5200 g/mol) and (c) 75 chains of 20 repeating units (~2100 g/mol). The simulation box side length was approximately 65 Å and the number of atoms in each system around 24000. **Table 6.2** summarizes the specifics of each pure polymer system. The system was simulated in full atomistic detail during all equilibration and production runs, with the exception of the case of high M_w polystyrene, for which a coarse-grained representation was adopted at the equilibration stage, followed by reverse-mapping to the atomistic level for further equilibration and production runs as detailed in **Section 6.2.2**. All simulations were performed with the LAMMPS package [48].

MD simulations were performed partly at the ARIS infrastructure of the GRNET (Greek National Infrastructure for Research and Technology) and partly at the MARCONI cluster of CINECA (Italian Interuniversity Consortium of Automated Computing). On ARIS Intel Xeon E5-2680v2 processors were used and optimal parallel scaling was achieved using 3 nodes consisting of 20 cores each. On MARCONI, Intel Xeon Phi 7250 (Knights Landing) processors were used, with optimal parallel scaling using 2 nodes consisting of 68 cores each.

Table 6.2. Number of atoms and molecular weight of the systems studied

System	Molecular weight (g/mol)	Number of atoms
75 chains x 20 repeating units	2099	24375
30 chains x 50 repeating units	5223	24150
5 chains x 300 repeating units	31261	24025

6.2.1 Force Field

Potential energy parameters for an all-atoms (AA) representation of PS from the work of Müller-Plathe [49] were adopted, in conjunction with harmonic constants for bond stretching from the work of Ndoro et al. [34], while the EPM2 model was chosen for CO_2 [50]. Any deviation from the referenced works is justified in **Section 6.2.3** ("Preliminary tests"). **Table 6.3**, **Table 6.4**, **Table 6.5** and

Table 6.6 summarize the functional forms and the values of the parameters of the potential energy contributions included in the polystyrene force field, while **Table 6.7** reports those used for CO_2. For the phenyl groups of polystyrene, the parameters are derived from ab initio calculations of benzene [51], where partial charges were used to reproduce the electric quadrupole moment of the molecule. Similarly, small partial charges are applied on all the carbon atoms of the polystyrene rings, with the exception of the

carbon bonded to the backbone. A charge of opposite sign is present on the aromatic hydrogen atoms. Parameters for the backbone atoms of polystyrene were first introduced in the simulation of aliphatic polymers [52] and do not include partial charges. This model has been used in the study of atactic as well as syndiotactic polystyrene [53].

Lorentz-Berthelot mixing rules were applied for nonbonded interaction between unlike atoms of the polymer:

$$\sigma_{ij} = \frac{\sigma_{ii} + \sigma_{jj}}{2} \qquad \text{Eq. (6.1)}$$

$$\varepsilon_{ij} = \sqrt{\varepsilon_{ii}\varepsilon_{jj}} \qquad \text{Eq. (6.2)}$$

A geometric mean combining rule was adopted for C_{CO2}–O_{CO2} nonbonded interactions, both for ε and σ [50]. For interactions between CO_2 and polystyrene atoms, Lorentz-Berthelot mixing rules were applied. Nonbonded interactions were excluded between first and second neighbors. A cutoff of 12 Å was used and a pairwise neighbor list of 14 Å of radius was updated every 5 time steps. Long-range Van der Waals interactions were treated with tail corrections and long range electrostatics were computed with a particle-particle particle-mesh (pppm) solver [54] with a relative error in forces evaluation of 10^{-6}.

Table 6.3. Force field parameters for non-bonded interactions of all-atom polystyrene [49].

Nonbonded Interactions	$U_{NB}(r_{ij}) = 4\varepsilon\left[\left(\frac{\sigma}{r_{ij}}\right)^{12} - \left(\frac{\sigma}{r_{ij}}\right)^{6}\right] + \frac{q_i q_j}{4\pi\epsilon_0 r_{ij}}$		
	$\varepsilon\ (kcal/mol)$	σ (Å)	$q_i\ (e)$
C_{AL}	0.0841	3.207	0
H_{AL}	0.0760	2.318	0
C_{AR}	0.0703	3.55	– 0.115
H_{AR}	0.0301	2.42	+ 0.115

Table 6.4. Force field parameters for bond stretching of all-atom polystyrene [34].

Bond Stretching	$U_l(r_{ij}) = K_l(r_{ij} - r_0)^2$	
	$K_l\left(\frac{kcal}{mol}\right)$	r_0 (Å)
C_{AL} – C_{AL}	310.4	1.53
C_{AR} – C_{AR}	469.7	1.39
C_{AL} – C_{AR}	317.5	1.51
C_{AL} – H_{AL}	239.0	1.09
C_{AR} – H_{AR}	239.0	1.08

Table 6.5. Force field parameters for angle vibrations of all-atom polystyrene [49].

Angle Vibration	$U(\phi_i) = K_\phi(\phi_i - \phi_0)^2$	
	$K_\phi\left(\frac{kcal}{mol\ rad^2}\right)$	$\phi_0\ (deg)$
$H_{AL} - C_{AL} - H_{AL}$	36.616	109.45
$C_{AL} - C_{AL} - H_{AL}$	43.846	109.45
$C_{AL} - C_{AL} - C_{AL}$	57.636	109.45
$C_{AR} - C_{AL} - H_{AL}$	43.846	109.45
$C_{AL} - C_{AL} - C_{AR}$	57.636	109.45
$C_{AL} - C_{AR} - C_{AR}$	45.005	120
$C_{AR} - C_{AR} - C_{AR}$	45.005	120
$C_{AR} - C_{AR} - H_{AR}$	50.048	120

Table 6.6. Force field parameters for dihedral and improper angles of all-atom polystyrene [49].

Backbone dihedral	$U(\varphi_i) = K_\varphi(1 + \cos(3\varphi_i)^2)$	
	$K_\varphi\left(\frac{kcal}{mol}\right)$	
$C_{AL} - C_{AL} - C_{AL} - C_{AL}$	1.434	
$C_{AL} - C_{AL} - C_{AL} - H_{AL}$ (terminal methyl only)	1.434	
Ring Dihedral	$U(\vartheta_i) = K_\vartheta(\vartheta_i - \vartheta_0)^2$	
	$K_\vartheta\left(\frac{kcal}{mol\ rad^2}\right)$	$\vartheta_0\ (deg)$
$C_{AR} - C_{AR} - C_{AR} - C_{AR}$	20.005	0
Impropers	$U(\theta_i) = K_\theta(\theta_i - \theta_0)^2$	
	$K_\theta\left(\frac{kcal}{mol\ rad^2}\right)$	$\theta_0\ (deg)$
$C^{II}_{AR} - C^{III}_{AR} - C^{I}_{AR} - H^{(on\ II)}_{AR}$	20.005	0
$C^{II}_{AR} - C^{III}_{AR} - C^{I}_{AR} - C^{(on\ II)}_{AL}$	20.005	0

Table 6.7. EPM2 force field parameters for CO_2 [50]

Nonbonded Interactions	$U_{NB}(r_{ij}) = 4\varepsilon\left[\left(\frac{\sigma}{r_{ij}}\right)^{12} - \left(\frac{\sigma}{r_{ij}}\right)^{6}\right] + \frac{q_i q_j}{4\pi\epsilon_0 r_{ij}}$		
	$\varepsilon\ (kcal/mol)$	σ (Å)	$q\ (e)$
C_{CO2}	0.0559	2.757	+ 0.6512
O_{CO2}	0.1600	3.033	–0.3256
Bond Stretching	$U_l(r_{ij}) = K_l(r_{ij} - r_0)^2$		
	$K_l\left(\frac{kcal}{mol}\right)$	r_0 (Å)	
$C_{CO2} - O_{CO2}$	1000	1.149	
Angle Vibration	$U(\phi) = K_\phi(1 - \cos\phi)$		
	$K_\phi\left(\frac{kcal}{mol\ rad^2}\right)$		
$O_{CO2} - C_{CO2} - O_{CO2}$	147.706		

6.2.2 Initial Configurations

The highest molecular weight initial configurations (300 repeating units) were generated by Dr. Georgios Vogiatzis, according to the coarse-grained equilibration and reverse-mapping strategy described in [30,33,44]. The coarse-grained representation adopted, specifically developed for the study of vinyl polymers [27], groups all atoms of a repeating unit into one super-atom, mapping the polymer to a linear chain. Depending on the configuration of two subsequent methylene backbone carbons, a sequence of meso and racemo dyads can be univocally defined and used to keep track of the stereochemistry of the chain. The coarse-grained model parameters were derived from an all-atom potential using the Iterative Boltzman Inversion (IBI) method.

The system is equilibrated at the coarse-grained level, through a Monte Carlo simulation, making use of connectivity altering moves [45,46], which have been shown to yield a very efficient sampling of configuration space and true equilibration of long-chain systems at all length scales. Following equilibration, the system is back-mapped to the target all-atom representation for final equilibration at the atomistic level and production runs. This multiscale strategy has proven to be very effective in equilibrating polystyrene melts up to 4000 repeating units [30].

The intermediate and lower M_w systems were generated using the Rotational Isomeric State (RIS) model [55] as modified by Theodorou and Suter [56] and directly equilibrated at the atomistic level, as detailed in **Section 6.2.4**.

6.2.3 Preliminary Tests

Preliminary tests were conducted on small systems of two molecular weights (1 chain of 300 units and 15 chains of 75 units), to evaluate the best molecular representation and interaction potential for the subsequent analysis at a larger scale. Both pure polymer systems as well as gas-polymer systems, containing 20 to 80 CO_2 molecules were simulated at this stage. All simulations were performed with the LAMMPS package [48], therefore all the algorithms referenced in the following refer to their LAMMPS implementation.

The model adopted for the representation of polystyrene is that of Müller-Plathe [49]. In his work, all polystyrene bonds lengths were constrained using the SHAKE algorithm [57], however, the LAMMPS implementation of the SHAKE algorithm allows only to constrain the C-H bonds, not also the C-C ones at the same time. At first, the fluctuations of the remaining bond length were kept as low as possible by using high values for the bond harmonic potential constant k_b. This representation proved effective in reproducing the density of the pure-polymer systems. However, it was abandoned in favor of a flexible representation [34] following the introduction of CO_2 to the system. CO_2 is represented using the EPM2 force-field by Harris and Yung [50]. To achieve good energy conservation when CO_2 was added to the system, a 0.5 fs timestep was necessary. In consideration of the long simulation times required by the subsequent analysis of the dynamical properties of the system, the possibility to benefit from the use of the multi-step reversible

reference system propagation algorithm (r-RESPA) [58] to reduce the computational time was tested. Unfortunately, if the SHAKE and the r-RESPA algorithms are used simultaneously in LAMMPS, time reversibility is lost [59]. Therefore, the constrained representation of polystyrene bonds was substituted with a flexible one [34,60]. In this way a twofold gain in computational time was obtained, owing to the use of the r-RESPA algorithm.

In the EPM2 representation of CO_2 a harmonic potential of the form $E(\phi) = \frac{K}{2}(\phi - \phi_0)$ is used for the angle vibrations. However, as Müller-Plathe noted [52], a singularity arises when using such harmonic potential when the angle ϕ becomes 180° and the equilibrium value ϕ_0 is also 180°, which is the case with CO_2. To bypass this issue, it is possible to adopt a rigid geometric representation of CO_2, however, this led to poor energy conservation and unphysically high diffusion rates in conjunction with r-RESPA.

To implement a flexible angle representation and overcome the singularity at $\phi = \pi$, Müller-Plathe suggested [52] to locally approximate $\phi - \phi_0$ with $\sin(\phi)$ around $\phi_0 = \pi$, taking advantage of the linearity of the sine function around π. In this way the angle potential becomes $E(\phi) = K(1 + \cos\phi)$, with the same numerical constant *K* used in the harmonic potential. The average value of CO_2 angle in this representation is 175 ± 3°, therefore the use of this approximation is warranted, and it was adopted in all simulations. The fluctuations of the bond length of CO_2 were kept as low as possible by using a harmonic potential with a high value for the constant k_b. It was verified that in this way the bond length of CO_2 deviated less than 0.01% from its equilibrium value of 1.1490 Å.

6.2.4 Simulation Details

The system was simulated in periodic boundary conditions using the rRESPA multi-timescale integrator [58], with 2 levels: at the innermost level a time step of 0.5 fs was employed to compute all bonded and short-range nonbonded interactions, while long-range electrostatic interactions were computed every 1 fs. For temperature and pressure control the Nose-Hoover thermostat and barostat were used [61] with a damping parameter of 100 fs for temperature relaxation and 1000 fs for pressure relaxation.

The three different molecular weight systems were generated at 500 K. At first, energy minimization was performed, using the conjugated gradient method for 5000 steps, in order to remove close contacts between atoms originated during the system generation or the back-mapping procedure. Afterwards, to obtain initial configurations at different temperatures (450 K and 550 K), the system was heated or cooled to the target temperature by applying a temperature ramp of 5 K/ns. The systems were then equilibrated at each temperature with 5 ns *NVT* runs followed by a 20 ns *NPT* run and a second 20 ns *NVT* run. Afterwards, the systems were simulated for 50 to 100 ns in the *NVE* ensemble, depending on the relaxation times of the local dynamics of the system: at lower temperature, lower CO_2 concentration and high molecular weight longer times are required to observe decorrelation of the system from its initial state. During the *NVE* runs, the system's pressure and temperature were monitored in order to ensure that they corresponded to the desired values. In this ensemble, the absence of barostatting or thermostatting allows to study the dynamics of the system without any external influence.

The nine individual equilibrated pure polymer configurations (three M_w systems at three different temperature each) were subsequently loaded with CO_2, at three different concentrations for each temperature, therefore the total number of gas-polymer systems is 27. Each gas-polymer system underwent a similar sequence of equilibration steps: energy minimization, 5 ns *NVT* run followed by a series of 20 ns N_1N_2PT to compute the equilibrium pressure corresponding to each value of concentration chosen. This is accomplished with an iterative procedure described in the following paragraph. Once this step was completed, the system was further equilibrated for 20 ns in the *NVT* ensemble and finally 50-100 ns production runs were performed.

6.2.5 Sorption Isotherms Calculation

The concentration values used to load the polystyrene models with gas molecules are reported in **Table 6.8**. They were chosen from the analysis of experimental data of CO_2 sorption isotherms at different temperatures [25] and extrapolating the behavior at higher temperatures of interest using the Sanchez-Lacombe Equation of State [47]. Since equilibrium gas concentration and equilibrium pressure are not thermodynamically independent, an iterative scheme was applied to attain consistency between them, by performing a series of N_1N_2PT runs and Widom's particle insertion tests.

Table 6.8. CO_2 concentration at each temperature and molecular weight.

Concentration (g_{CO2}/g_{pol})	T = 450 K	T = 500 K	T = 550 K
Low	$7.00 \cdot 10^{-3}$	$5.70 \cdot 10^{-3}$	$5.00 \cdot 10^{-3}$
Intermediate	$3.65 \cdot 10^{-2}$	$2.82 \cdot 10^{-2}$	$2.40 \cdot 10^{-2}$
High	$6.87 \cdot 10^{-2}$	$5.05 \cdot 10^{-2}$	$4.08 \cdot 10^{-2}$

The iterative scheme implemented consists of the following steps [44]. At first, a 20 ns N_1N_2PT run is performed using a guess value for the target pressure. The initial guess values were chosen as the equilibrium pressures calculated with the Sanchez-Lacombe Equation of State corresponding to each concentration value. Afterwards, Widom test particle insertions [39] are performed to compute the excess chemical potential of CO_2 ($\mu_{CO_2}^{ex}$) in the system with the following relation, in the *NPT* ensemble [62]:

$$\exp\left(-\frac{\mu_{CO_2}^{ex}}{RT}\right) = \frac{\langle V \exp\{-\beta[\Delta u_{inter}]\}\rangle}{\langle V\rangle} \qquad \text{Eq. (6.3)}$$

where $\beta = 1/k_BT$, k_B is the Boltzmann constant, T is the temperature, and Δu_{inter} is the change to the intermolecular energy of the system brought by the insertion of the additional molecule (*i.e.* the potential energy of interaction between the test molecule and the other molecules of the system). The last half of the well equilibrated part of the trajectory is used (10 ns), which corresponds to 2000 frames. In each frame, 1000 insertions are performed, corresponding to $2 \cdot 10^6$ insertions in total. Position and orientation of the molecule to be inserted were chosen at random from a pure CO_2 trajectory, sampling the

configuration space of the pure gas at the same temperature. The total number of insertions was chosen to ensure that the exponential of the excess chemical potential reached convergence. CO_2 fugacity in the gas-polymer system was obtained from the chemical potential as follows [63]:

$$f_{CO_2} = N_{CO_2} k_B T \langle 1/V \rangle \exp(\beta \mu_{CO_2}^{ex}) \qquad \text{Eq. (6.4)}$$

N_2 is the number of CO_2 molecules in the polymer matrix, $\langle 1/V \rangle$ is the average inverse volume of the system under *N₁N₂PT* conditions, k_B is the Boltzmann constant, $\beta = 1/k_B T$, and T is the temperature of the simulation. The phase equilibrium condition implies that $f_{CO_2}^{gas} = f_{CO_2}^{pol} = f_{CO_2}$. Therefore, the total pressure corresponding to the CO_2 fugacity was calculated using the Peng-Robinson Equation of State [64]. This new value of the pressure was used to perform a new 20 ns *N₁N₂PT* run. This was repeated until the target pressure of the MD run and the value calculated during post-processing converged. Convergence was reached after three iterations at maximum.

By performing Widom insertions on pure polymer configurations, the excess chemical potential at infinite dilution is obtained, from which the Henry's law constant can be calculated, using the mass fraction based relation reported below:

$$H_{CO_2} = \frac{\rho RT}{M_{CO_2}} \lim_{x_i \to 0} \left[\exp\left(-\frac{\mu_{CO_2}^{ex}}{RT} \right) \right] \qquad \text{Eq. (6.5)}$$

Where ρ is the mass density of the pure polymer system and M_{CO_2} is the molar mass of CO_2.

6.2.6 Sanchez-Lacombe EoS Parameters regression

Equations of state parameters for pure polymers are usually obtained from the best fit of *PVT* data sets. In order to perform an analysis of the M_w effects on various properties with the Sanchez-Lacombe EoS, the ability of existing parameter sets to account for the difference in *PVT* properties at different M_w was tested, using the experimental measurements of Zoller and Walsh [65] as target. Three different parameter sets were tested [22,23,66], and they are reported in **Table 6.9**, but they were able to represent correctly only the properties of high M_w polystyrene and failed to account for the M_w effect on *PVT* properties.

Table 6.9. Sanchez-Lacombe EoS parameter sets for high M_w polystyrene.

T^* (K)	P^* (MPa)	$\rho^*(g/cm^3)$	Ref.
739.9	387	1.108	[23]
750	360	1.099	[66]
744.4	392.9	1.1047	[22]

For this reason, new parameter sets valid also for the low M_w range were determined from the best fit of the data reported by Zoller and Walsh [65]. Only data above the glass transition were included in the fitting procedure, as equation of state model do not apply to the nonequilibrium state of glassy polymers.

A good fit could be obtained at all conditions, especially at lower pressures. The maximum deviation between experimental data and EoS result was 1.1 % at 110000 g/mol, 1% at 34500 g/mol and 9000 g/mol, and 2.5% at 910 g/mol. The average deviation was 0.4% in all cases. The comparison between experimental data and EoS results is shown in **Figure 6.2** and the parameters obtained for each case are reported in **Table 6.10**.

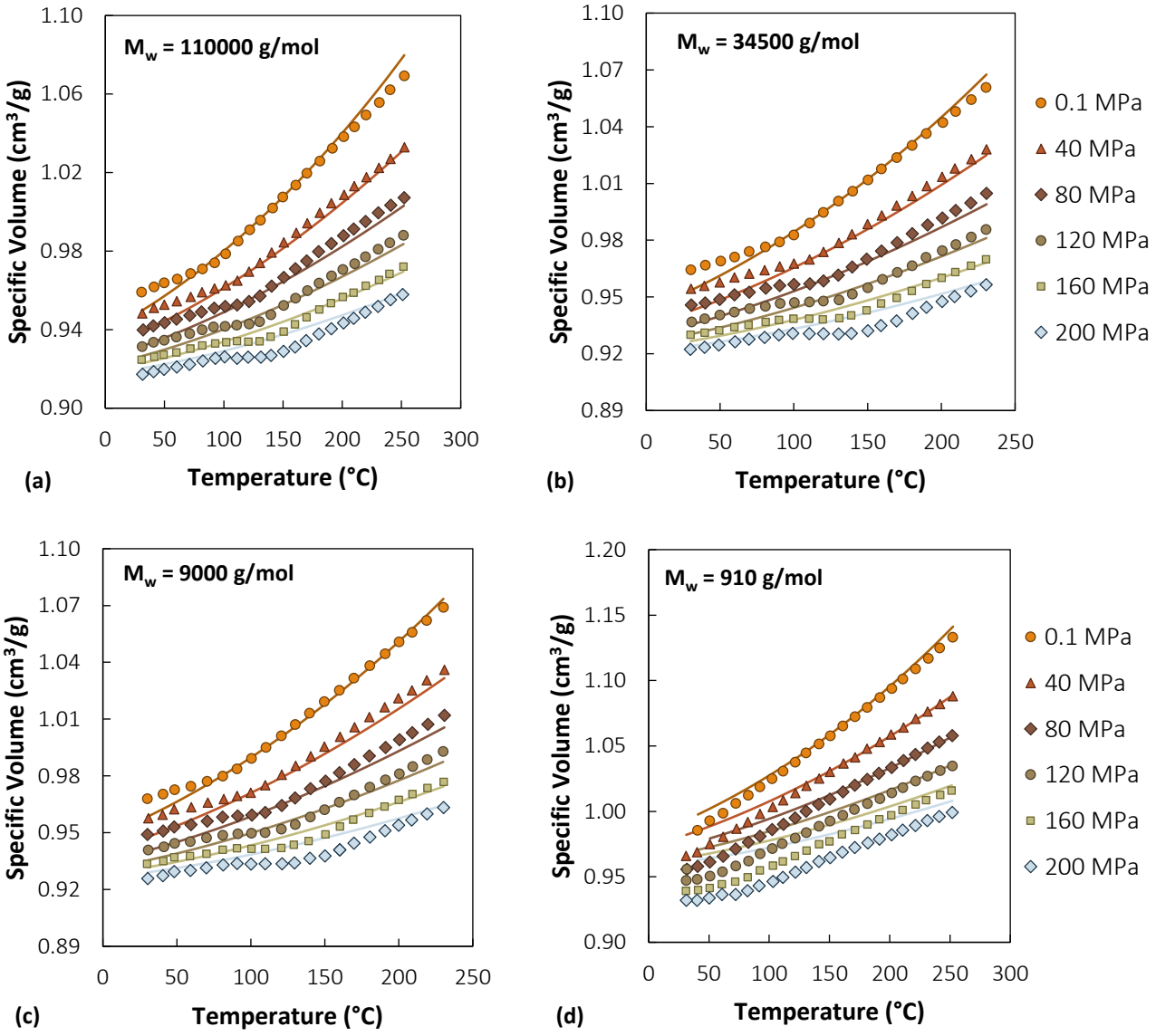

Figure 6.2. PVT curves for aPS at different M_w together with SL EoS results calculated using the parameters reported in **Table 6.10**.

Table 6.10. Sanchez-Lacombe EoS parameter sets for polystyrene at different M_w obtained from the best fit of data from [65]. 95% confidence intervals were estimated using a MC method. [67].

$M_w\ (g/mol)$	$T^*\ (K)$	$P^*\ (MPa)$	$\rho^*(g/cm^3)$
110000	750.0 ± 10	366 ± 26	1.096 ± 0.005
34500	749.5 ± 8	370 ± 24	1.094 ± 0.004
9000	748.5 ± 9	378 ± 27	1.088 ± 0.004
910	737.0 ± 10	400 ± 30	1.050 ± 0.006

The M_w dependence of the parameters is shown in **Figure 6.3**. The results for T^* and ρ^* were interpolated using Eq. (6.6), while for p^* Eq. (6.7) was used.

$$f(x) = \frac{abx}{1+bx} \qquad \text{Eq. (6.6)}$$

$$f(x) = \frac{a}{x^b} + c \qquad \text{Eq. (6.7)}$$

The values for the best fit constants are: a = 750 ± 10 and b = 0.063 ± 0.020 for T^*, a = 470 ± 35, b = 0.36 ± 0.04 and c = 360 ± 20 for p^*, a = 1.099 ± 0.003 and b = 0.023 ± 0.002 for ρ^*. T^* is expressed in K, p^* in MPa, ρ^* in g/cm^3 and M_w in g/mol. In the high M_w limit, these relations yield the parameter set from reference [66]. Using these relations, the parameters corresponding to the M_w of the simulated systems were obtained and they are reported in **Table 6.11**.

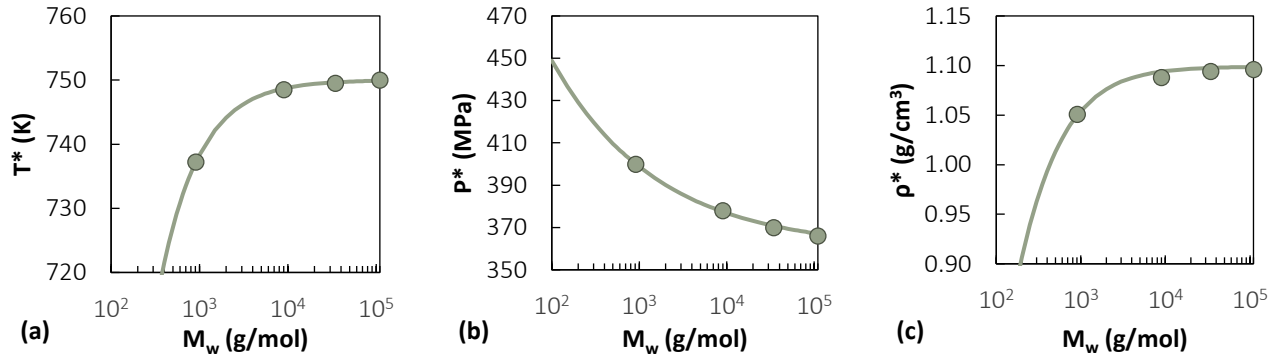

Figure 6.3. M_w dependence of Sanchez-Lacombe EoS parameters for aPS. The lines represent interpolations obtained with Eq. (6.6) for (a) T^* and (c) ρ^* and Eq. (6.7) for P^* (b).

Table 6.11. Sanchez-Lacombe EoS parameter sets corresponding to the M_w of the aPS systems simulated in this work and CO_2 parameter set from the literature. 95% confidence intervals were estimated using a MC method [67].

$M_w\ (g/mol)$	$T^*\ (K)$	$P^*\ (MPa)$	$\rho^*(g/cm^3)$
2100	744 ± 10	390 ± 29	1.077 ± 0.004
5200	748 ± 10	381 ± 27	1.090 ± 0.002
31000	750 ± 10	371 ± 24	1.098 ± 0.003
CO_2 [68]	300	630	1.515

Furthermore, in order to calculate the properties of aPS-CO_2 systems, the value for the binary interaction parameter k_{ij} must be determined. Since this parameter is usually temperature dependent, its value as well as its temperature dependence were determined by the best fit of the sorption isotherms reported by Sato et al. [23] in the temperature range 373 – 453 K. This data set was selected because the sorption isotherm at 453 K showed the best agreement with the simulated data, as it will be shown in **Figure 6.44**. For CO_2 the SL parameter set reported in **Table 6.11** was used. The binary interaction parameter is assumed to be independent of M_w and concentration. The following linear relation was obtained for the CO_2-aPS binary interaction parameter in the range 373 – 453 K:

$$k_{ij} = -3.90 \cdot 10^{-4}\, T + 1.35 \cdot 10^{-1} \qquad \text{Eq. (6.8)}$$

This was extrapolated to the temperatures of interest, therefore, a value of $k_{ij} = -0.041$ was used at 450 K, $k_{ij} = -0.060$ at 500 K, $k_{ij} = -0.080$ at 550 K.

This temperature dependence, however, led to a deviation from the expected Arrhenius behavior of the solubility as a function of temperature in the high-temperature range, as it can be seen in **Figure 6.43**. The expected trend could be obtained by extrapolating the values of k_{ij} using a quadratic temperature dependence instead of a linear one:

$$k_{ij} = 1.69 \cdot 10^{-4}\, T^2 - 1.84 \cdot 10^{-3}\, T + 4.44 \cdot 10^{-1} \qquad \text{Eq. (6.9)}$$

In this way, a value of $k_{ij} = -0.041$ was used at 450 K, $k_{ij} = -0.052$ at 500 K, $k_{ij} = -0.055$ at 550 K. Further implications of this choice are discussed in each section.

6.3 Thermodynamic Properties and Chain Conformations

6.3.1 Density

The ability to predict the volumetric properties is an important prerequisite of the model for a reliable prediction of sorption and diffusion.

Average density values were computed for each pure polymer system from the second half of the *NPT* trajectory, over 10 ns. The results are compared in **Figure 6.4** against experimental data at different molecular weights from different studies and in **Figure 6.6** against molecular simulation results.

Zoller reported volumetric properties of aPS [65] as a function of temperature and pressure (*PVT* data) at several molecular weights. The curve at atmospheric pressure for each M_w is reported in **Figure 6.4**. The results for the highest M_w (110000 g/mol) are in good agreement with the high M_w *PVT* measurements reported by Ougizawa [69] (100000 g/mol). Comparison with an even higher M_w curve reported by Quach et al. [70] (279000 g/mol) suggests that a stronger M_w dependence should be expected in the low M_w range, whereas in the high M_w limit an asymptotic behavior is found.

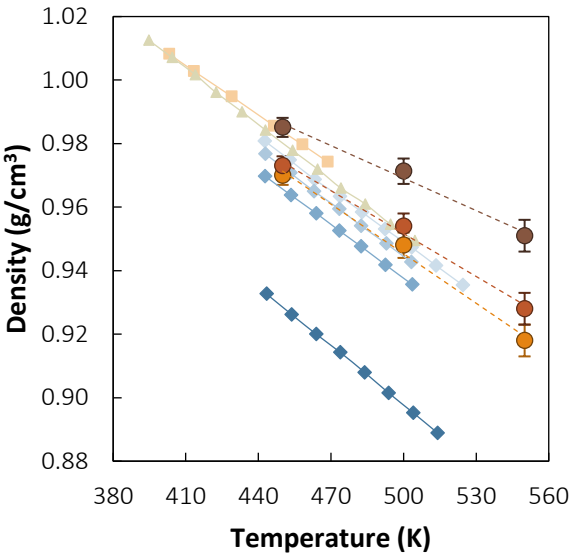

Figure 6.4. Comparison between density of the simulated atactic polystyrene systems and experimental values at different molecular weights. Simulations are represented with circles: brown represents **31000 g/mol**, red is **5200 g/mol**, orange is **2100 g/mol**. Three experimental sets are included for comparison: values from [70] are reported in yellow squares and are at **279000 g/mol**, values from [69] are reported in green triangles and are at **100000 g/mol**, values from [65] are reported in blue diamonds and are at **910 g/mol**, **9000 g/mol**, **34500 g/mol**, **110000 g/mol**.

For the simulated systems the expected trends are observed, with lower density at higher temperature and lower M_w. However, systems with systematically slightly higher density compared to the experimental ones were obtained. For example, between our results at 31000 g/mol and the curve at 34500 g/mol reported by Zoller [65] there is a 2% deviation at 450 K and 3% at 500 K. Nevertheless, it appears that the M_w

dependence of the density is not well captured by the simulated data set, as the difference between the results at 2100 g/mol and 5200 g/mol would be expected to be larger than the difference between the 5200 g/mol curve and the results at 31000 g/mol. Fox and Flory [71] found a linear relationship between specific volume and inverse M_w for polystyrene melts. In the present case, the linear trend is reasonably followed, considering that only three points are available for evaluation, as it can be observed in **Figure 6.5**. By comparing the experimental curve at 490 K and the simulated data at 500 K, it can be seen that the slope of the line interpolating the simulation results is similar to the experimental one, although the absolute values of the simulated volumes are lower. The closer agreement is found with the system of 5200 g/mol, whereas the lower M_w and the higher M_w are even more dense.

Similar results in terms of density were obtained by different authors in molecular modelling studies of polystyrene, both with all atoms (AA) or united atoms (UA) representations, as it can be seen by comparing the data reported in **Figure 6.6**. In most of the cases, low M_w curves display values closer to the experimental ones at much higher M_w. A possible explanation for this density overestimation could be that, in the force field adopted, the nonbonded interactions are optimized to reproduce the density of a high M_w material in simulations of moderately long chains. Peculiarly, the results obtained by Ndoro et al. [34] at 2100 g/mol (light blue diamonds in **Figure 6.6**), are systematically 2% higher than the results obtained here at the same M_w using the same model. The only difference between the two systems is the size: the present system contains 75 chains, the one by Ndoro et al. 200 chains. The preliminary tests carried out here on smaller systems had evidenced a possible system size effect for the density: a 1% increase in density was obtained for the low M_w system and a 2% for the high M_w system when the system size was increased by a factor 5. A discussion of the temperature dependence of the curves is reported in **Section 6.3.3**.

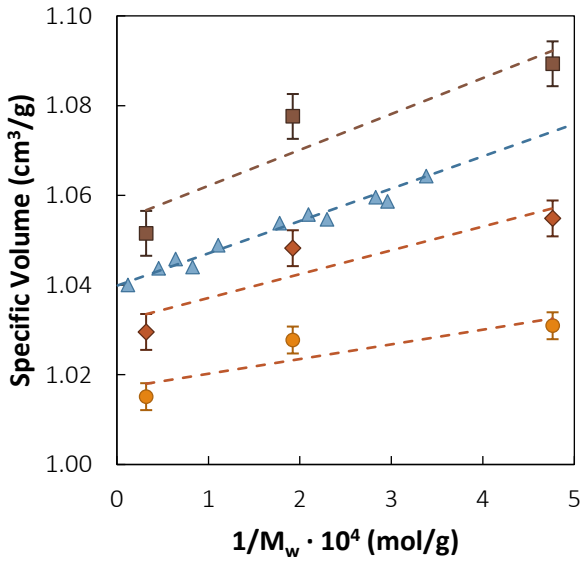

Figure 6.5. Specific volume of aPS as a function of inverse molecular weight. Orange circles are data at 450 K, red diamonds at 500 K, brown squares at 550 K. The results of Fox et al. [71] at 490 K are included for comparison.

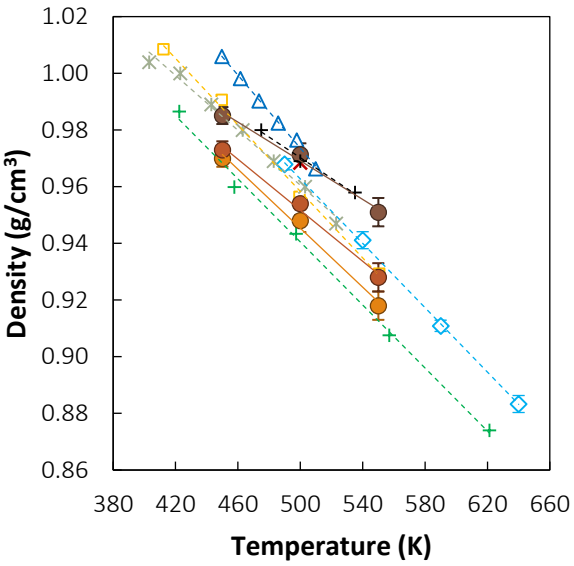

Figure 6.6. Comparison between bulk atactic polystyrene density obtained in different simulation works. The results of this work are represented with circles: brown is **31000 g/mol**, red is **5200 g/mol**, orange is **2100 g/mol**. Dark blue triangles are results for an AA representation of **21000 g/mol** from [42], light orange squares are results for a UA representation of **8300 g/mol** from [72], light green asterisks are results for an AA representation of **1000 g/mol** from [73], the red cross is a result for a UA representation of **10500-105000 g/mol** from [30], light blue diamonds are results for an AA representation of **2100 g/mol** from [34], dark green pluses are results for a UA representation of **8300 g/mol** from [74], black pluses are results for a AA representation of **2200 g/mol** from [31]

In **Figure 6.7**, the density of the systems as a function of CO_2 content is reported. These values are computed as the average over the second half of the last iteration of N_1N_2PT trajectories, when the pressure had converged to its equilibrium values. A linear trend is followed, as observed also experimentally in the case of sorption of light gases in rubbery polymers [75,76]. The slope of the linear trend is very similar across temperatures and M_w, signifying that systems at different temperatures and M_w, but exposed to the same CO_2 concentration dilate to a similar extent. This is even more apparent in calculated swelling curves, reported in **Figure 6.8**. No experimental measurements for the dilation of aPS as a function of CO_2 concentration at these temperatures were retrieved in the literature, therefore the results were compared with the predictions of the SL EoS. The comparison of the swelling obtained from the simulated systems and calculated with the SL EoS is reported in **Figure 6.11**.

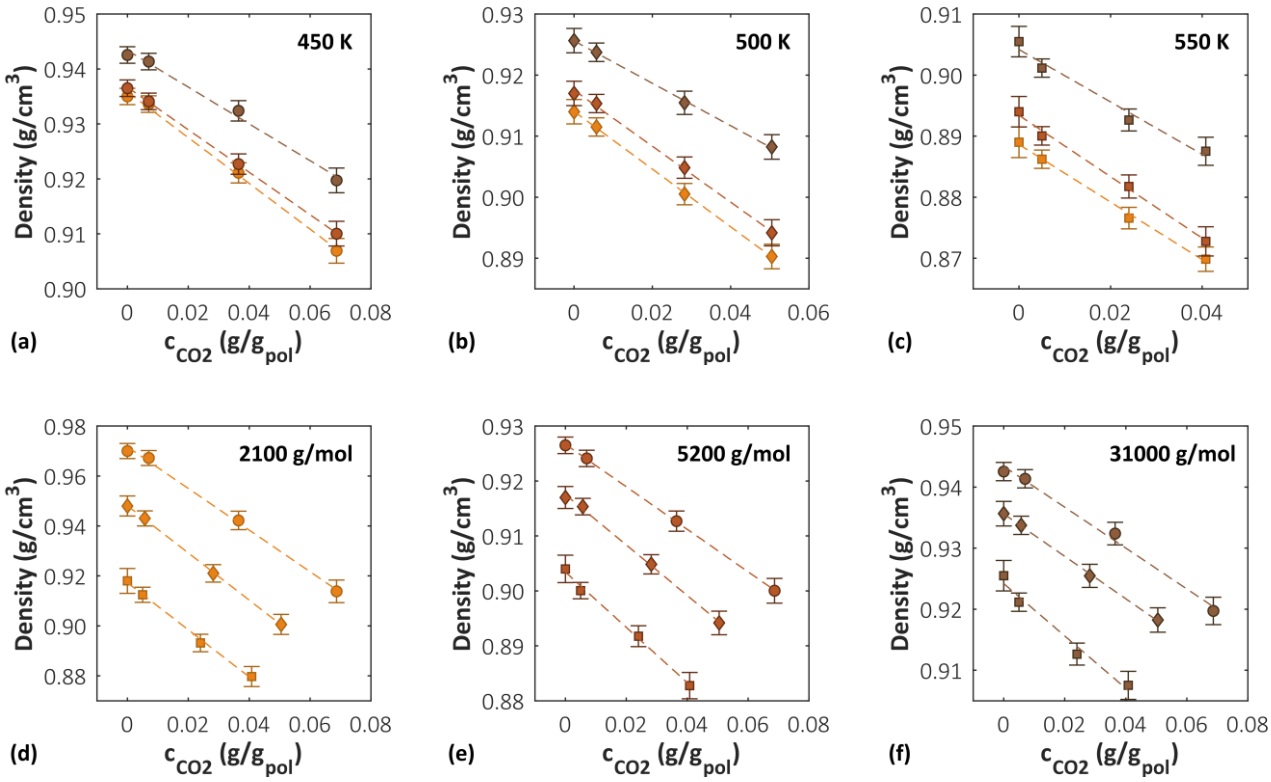

Figure 6.7. Density of atactic polystyrene as a function of CO_2 concentration. Plots (a), (b) and (c) show the effect of molecular weight at fixed temperature, plots (e), (f) and (g) show the effect of temperature at fixed molecular weight. Circles represent data at 450 K, diamonds at 500 K, squares at 550 K. Molecular weight of 2100 g/mol is depicted in **orange**, 5200 g/mol in **red** and 31000 g/mol in **brown**.

6.3.2 Swelling

The percent volume dilation of the polymer was calculated and is reported in **Figure 6.8**. It increases as pressure increases, as reported experimentally [77], with a linear trend in the pressure range investigated. Accounting also for the size of the error bar, it appears that at a fixed M_w, the polymer shows similar swelling in the whole temperature range inspected. Experimental measurements of CO_2-induced swelling in aPS in the melt state were performed by Pantoula et al. [17] at 405 K on a sample of 230000 g/mol M_w, using a magnetic suspension balance. In **Figure 6.9** their results are compared with the values simulated at 450 K for the three M_w inspected in this work. Considering the limited temperature dependence of the simulated results, only the effects of M_w is relevant. Even though the experimental sample had a M_w two orders of magnitude higher than the low and intermediated M_w systems simulated, the swelling is very similar, while the higher M_w simulated displays swelling up to 30% lower than the experimental value at high pressure. Therefore, parallel to a slight overestimate of the pure polymer density, the simulated systems display lower swelling than it would be expected for their M_w.

Royer et al. [77] reported the swelling induced by CO_2 in molted Poly(dimethylsiloxane) (PDMS) at 30, 50 and 70 °C, finding that swelling would increase from 30 to 50 °C, but decrease at 70 °C, with a certain degree of superposition of the curves, especially below 200 atm, similarly to observations from the

simulations of polystyrene. Royer et al. observed a different slope of the curves of swelling *vs*. pressure at different temperatures, while in the present case at fixed M_w systems at different temperature have the same slope. It must be noted, though, that the data by Royer et al. [77] is closer to the critical temperature of CO_2. At fixed temperature, the higher stiffness of the high M_w aPS chains makes them less susceptible to CO_2-induced dilation and the system exhibits lower swelling compared to the other systems, especially at higher temperature. Royer et al. [77] reported also an analysis of M_w effects on polymer swelling induced by CO_2 in PDMS from 95 to 284 kg/mol. They found little effect of M_w on swelling, however, they investigated samples with M_w higher than the entanglement M_w and advise that the M_w dependence could be more marked at lower M_w.

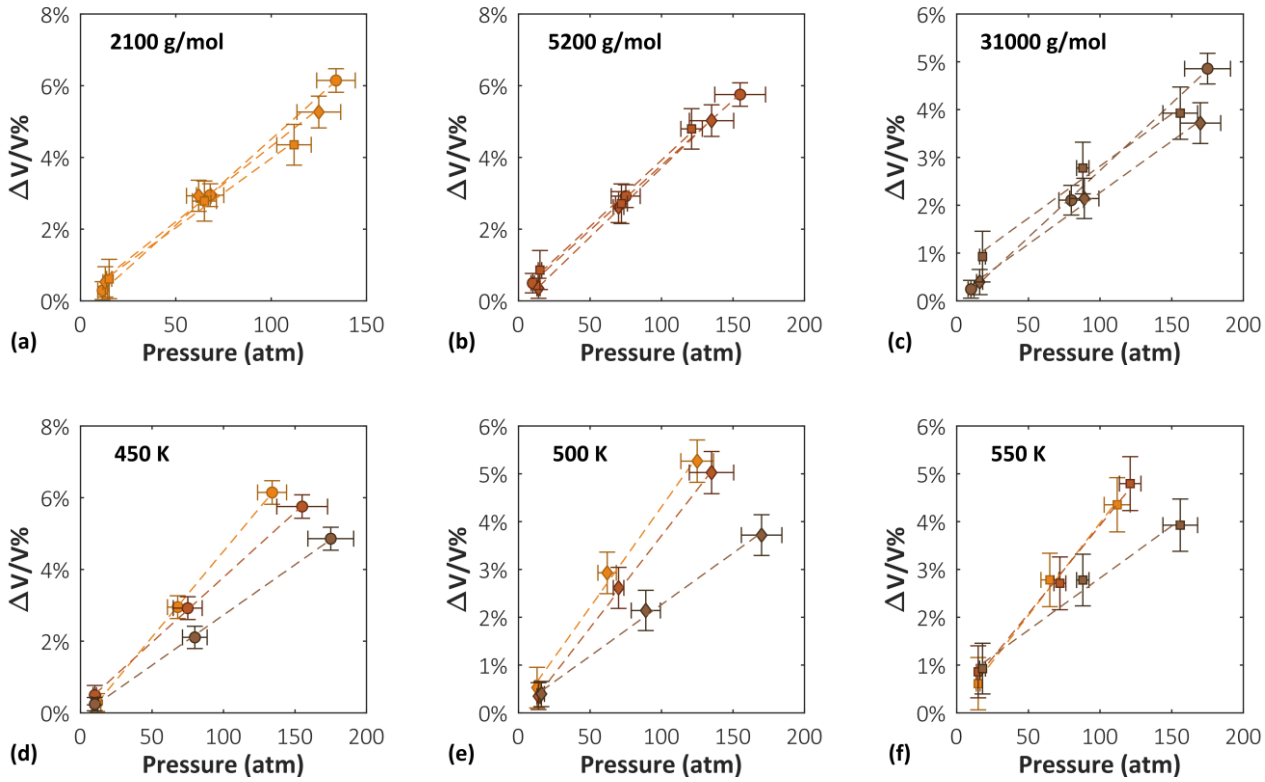

Figure 6.8. Relative polymer volume dilation as a consequence of CO_2 sorption at different temperatures and polymer molecular weight. Plots (a), (b) and (c) show the effect of temperature at fixed molecular weight, plots (e), (f) and (g) show the effect of molecular weight at fixed temperature. Circles represent data at 450 K, diamonds at 500 K, squares at 550 K. Molecular weight of 2100 g/mol is depicted in **orange**, 5200 g/mol in **red** and 31000 g/mol in **brown**.

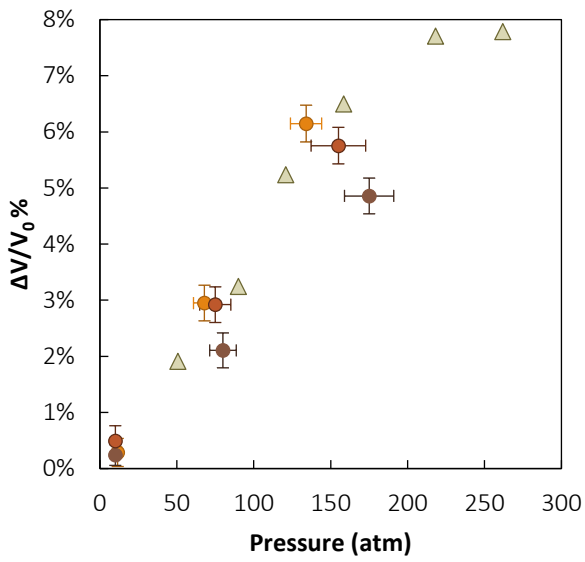

Figure 6.9. Comparison between swelling of the simulated systems at 450 K (M_w of 2100 g/mol is depicted in **orange**, 5200 g/mol in **red** and 31000 g/mol in **brown**) and the experimental measurements of Pantoula et al. [17] at 405 K (green triangles).

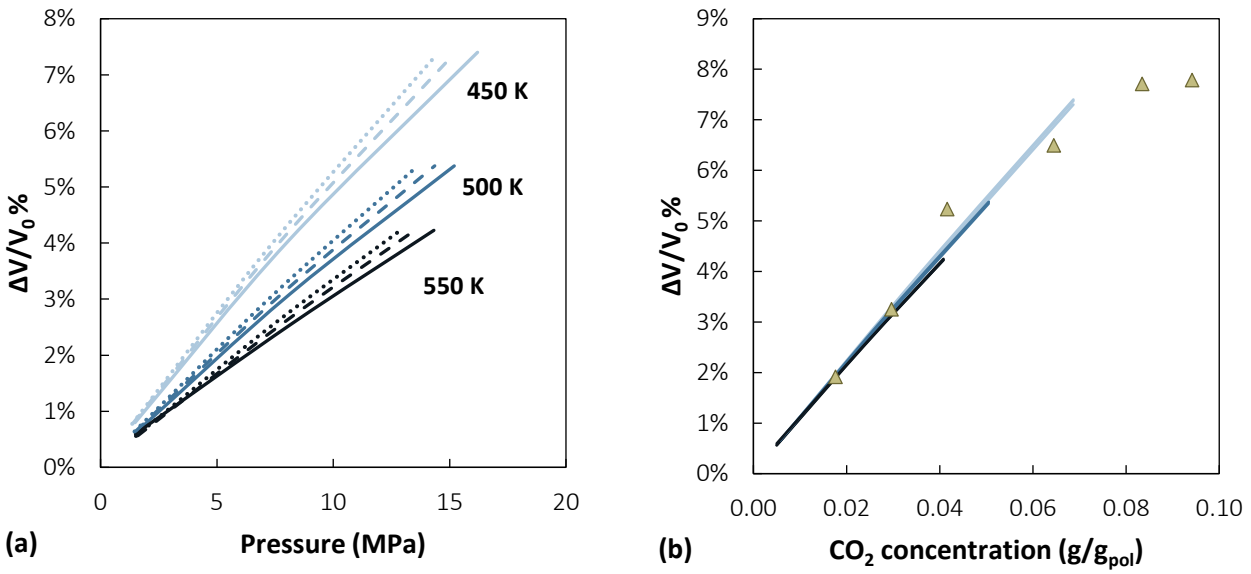

Figure 6.10. SL Equation of State prediction of CO_2 induced swelling in aPS plotted against pressure (a) and concentration (b). **Light blue** represents data at 450 K, **blue** at 500 K, **dark blue** at 550 K. In the left plot solid lines represent data at 31000 g/mol, dashed lines at 5200 g/mol, dotted lines at 2100 g/mol. In the right plot curves for different M_w are collapsed onto one another. The experimental measurements of Pantoula et al. [17] at 405 K are represented in (b) as green triangles.

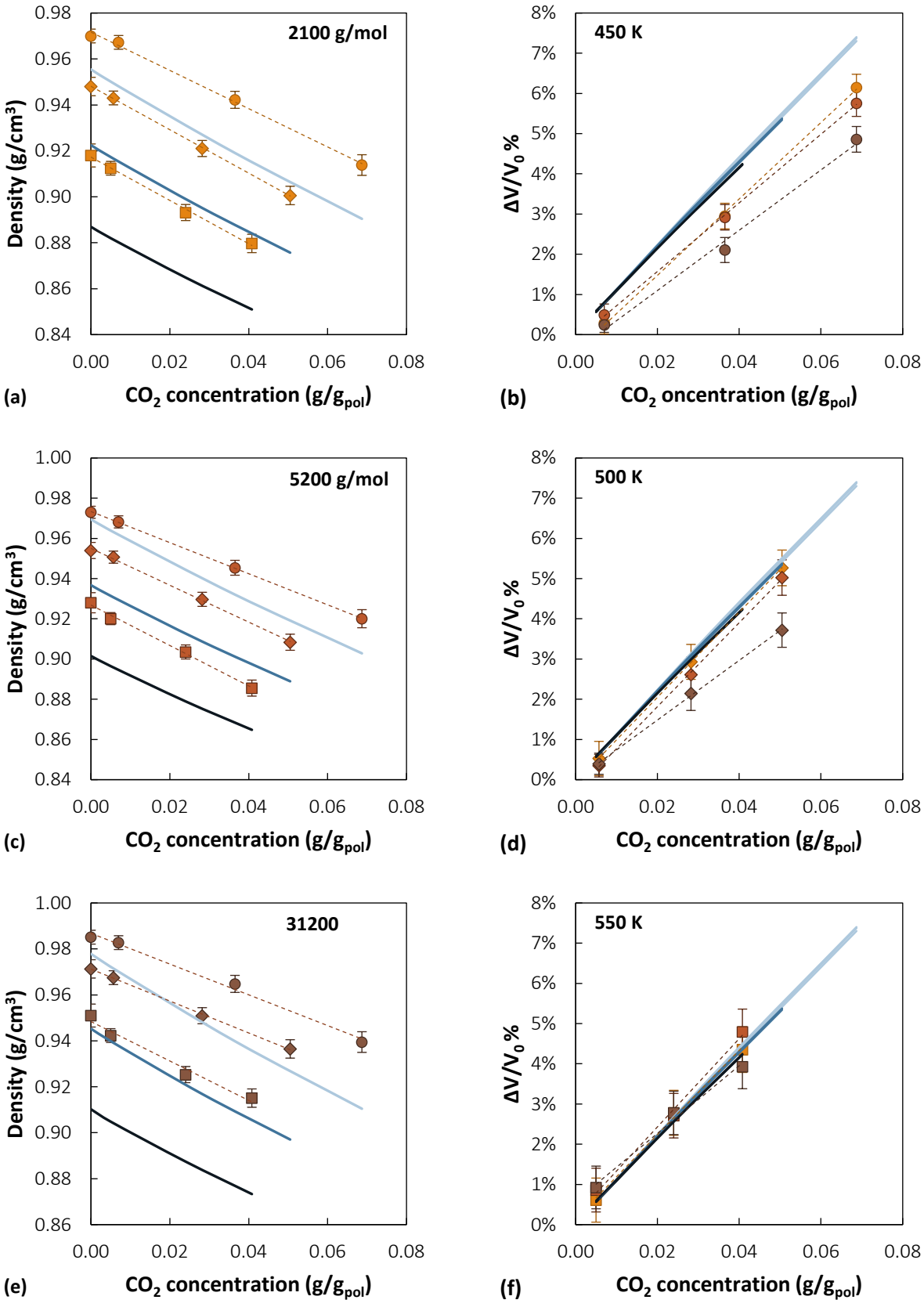

Figure 6.11. Comparison of simulation and EoS calculations of polymer density and relative volume dilation of atactic polystyrene as a function of CO_2 concentration. Circles represent data at 450 K, diamonds at 500 K, squares at 550 K. Molecular weight of 2100 g/mol is depicted in **orange**, 5200 g/mol in **red** and 31000 g/mol in **brown**. Solid lines are the results obtained with the SL EoS: **light blue** at 450 K, **blue** at 500 K and **dark blue** at 550 K.

The polymer density values calculated with the SL EoS are reported in **Figure 6.11 (a), (c)** and **(e)**, as a function of CO_2 concentration and they are compared with the values obtained in the simulations. The equation of state was parametrized on pressure-volume-temperature experimental data, therefore it closely reproduces the density of the pure polymer at different molecular weights. As already noted, simulations tend to overestimate the polymer density, with deviations being al all cases less than 3.5%. The highest difference between EoS and simulation results is observed at 550 K, with an average deviation of 3.4% with respect to the simulated value (1.7% at 450 K and 2.7% at 500 K). Density values calculated with the k_{ij} values extrapolated using a linear temperature dependence differed less than 1% from those obtained using the k_{ij} values calculated with **Eq. (6.9)**. The latter results are those shown in **Figure 6.11.** While the absolute density values show larger deviations at higher temperatures, the slope of the dilation curves tends to be higher in the molecular simulations, especially at lower temperatures and higher M_w. The same consideration can be drawn by observing percent volume change curves. Equation of state predictions indicate that the M_w dependence as well as the T dependence of percent volume swelling are negligible when comparing data at the same sorbed concentration (**Figure 6.10 (b)**). Remarkably, the experimental data by Pantoula et al. [17] also falls onto this mastercurve. Plotting the simulated values at constant concentration does not eliminate the differences, as it can be seen in **Figure 6.11 (b), (d)** and **(f)**. At the highest temperature data at all M_w falls into the mastercurve, while at 500 K the highest M_w curve deviates from the others. At 450 K all systems exhibit lower swelling compared to the EoS predictions.

6.3.3 Isothermal Compressibility and Thermal Expansion Coefficients

The isothermal compressibility k_t was calculated from the volume (V) fluctuations during the *NPT* runs using the following relationship:

$$k_t = \frac{1}{k_b T} \frac{\langle V^2 \rangle - \langle V \rangle^2}{\langle V \rangle} \qquad \text{Eq. (6.10)}$$

The results are reported in **Figure 6.12** and, even though there is some scattering, a decreasing trend with increasing M_w and decreasing temperature can be observed. Error bars were calculated with the block averaging method and they are smaller than the size of the symbols. The results compare well with the experimental values, reported to be $5.30 \cdot 10^{-10} – 1.13 \cdot 10^{-9}$ Pa^{-1} in the temperature range 373-593 K [78]. The agreement is significantly higher compared to the result of $2.50 \cdot 10^{-8}$ obtained by Spyriouni et al. [30] using a CG representation which is very close to the one adopted in the equilibration of high M_w chain here. In their work, they identified as the source of this discrepancy the poor transferability of CG intermolecular interactions to high pressures, that failing to reflect the true compressibility of the material. In this work, the CG representation has been employed only in the equilibration stage, while all production runs were performed using an AA representation and force field, which does not seem to suffer from the same limitation.

The temperature dependence of the density was assessed by calculating the thermal expansion coefficients at atmospheric pressure for the pure polymer systems using **Eq. (3.2)**. The results are reported in **Table**

6.12 and compared to the values calculated for all the experimental and simulated data sets reported in **Figure 6.4** and **Figure 6.6**.

$$k_p = -\frac{1}{V}\frac{\partial V}{\partial T}\bigg|_p \qquad \text{Eq. (6.11)}$$

The temperature dependence of the simulated systems is weaker compared to the experimental data, but in the same order of magnitude. In fact, the thermal expansion coefficient for the higher M_w simulated is a factor 2 lower than the experimental ones. The data at different M_w from Zoller et al. [65] indicate an increasing trend with decreasing M_w, which is observed also for the systems simulated in this work.

Table 6.12. Thermal expansion coefficient of polystyrene at atmospheric pressure calculated with **Eq. (3.2)**.

Experimental	M_w (g/mol)	k_p (K^{-1})
Quach, Simha [70]	279000	$5.23 \cdot 10^{-4}$
Ougizawa et al. [69]	100000	$5.91 \cdot 10^{-4}$
Zoller, Walsh [65]	110000	$5.74 \cdot 10^{-4}$
Zoller, Walsh [65]	34500	$5.87 \cdot 10^{-4}$
Zoller, Walsh [65]	9000	$5.89 \cdot 10^{-4}$
Zoller, Walsh [65]	910	$6.81 \cdot 10^{-4}$
Simulated	**M_w (g/mol)**	**k_p (K^{-1})**
Eslami, Müller-Plathe [42]	21000	$6.53 \cdot 10^{-4}$
Han, Boyd [72]	8300	$6.07 \cdot 10^{-4}$
Lyulin, Michels [74]	8300	$6.03 \cdot 10^{-4}$
Ndoro et al. [35]	2100	$6.14 \cdot 10^{-4}$
Fritz et al. [73]	1000	$4.96 \cdot 10^{-4}$
This work	31000	$3.53 \cdot 10^{-4}$
	5200	$4.74 \cdot 10^{-4}$
	2100	$5.52 \cdot 10^{-4}$

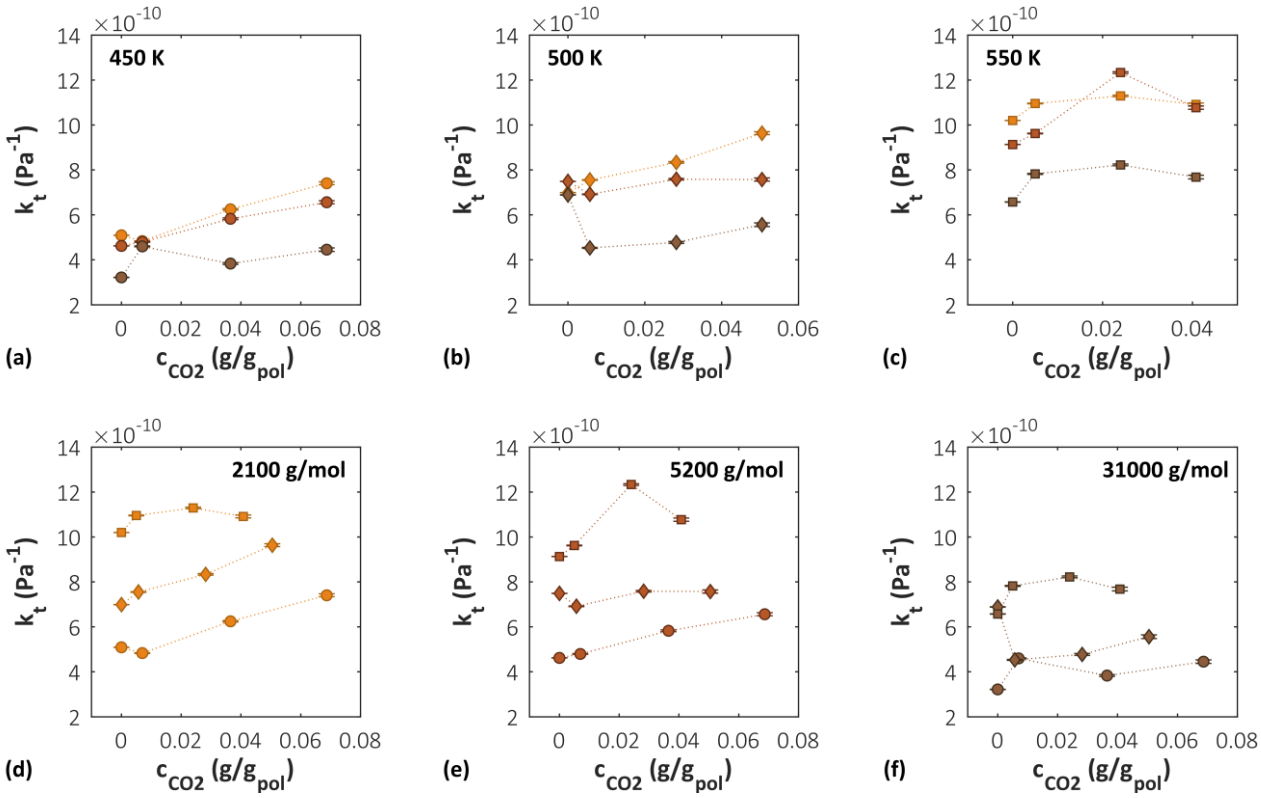

Figure 6.12. Isothermal compressibility as a function of CO_2 concentration, calculated using **Eq. (6.10)**. Plots (a), (b) and (c) show the effect of molecular weight at fixed temperature, plots (e), (f) and (g) show the effect of temperature at fixed molecular weight. Circles represent data at 450 K, diamonds at 500 K, squares at 550 K. Molecular weight of 2100 g/mol is depicted in **orange**, 5200 g/mol in **red** and 31000 g/mol in **brown**.

6.3.4 Chain Dimensions

The analysis of long-range conformational features of chains provides good indicators to assess whether full equilibration of the system at all length scales was achieved. The radius of gyration and Flory's characteristic ratio were determined to evaluate the average chain dimensions and their trends with *T*, M_w and gas concentration. An analysis of subchain dimensions provided insight on the level of equilibration of the systems.

6.3.4.1 Radius of Gyration

Values for the root mean squared radius of gyration $\langle R_g^2 \rangle^{1/2}$ were obtained for all the systems using **Eq. (6.12)** and are reported in **Figure 6.13** as a function of CO_2 content.

$$\langle R_g^2 \rangle^{1/2} = \sqrt{\frac{1}{m_{tot}} \sum_{i=1}^{N} m_i (r_i - r_{com})^2} \qquad \text{Eq. (6.12)}$$

In the previous relation r_{com} is the position of the center of mass of a chain, r_i the position of atom i of mass m_i along the same chain and m_{tot} is the total mass of the chain. Error bars in the plots represent the standard deviation of the mean value.

The results obtained for the system of M_w 2100 g/mol are in very good agreement with the value of 9.86 ± 0.06 Å obtained with the same all atom model and at the same M_w by Ndoro at al. [34]. As it can be seen in **Figure 6.13**, the values obtained are independent of temperature. This is in agreement with the experimental measurements reported by Boothroyd et al. [79] for the radius of gyration of polystyrene melts in the temperature range 393–513 K.

Despite having a swelling effect on the system (see **Section 6.3.1**), increasing CO_2 concentration does not appear to affect significantly the average radius of gyration of the chains or their distribution at any M_w. By looking at individual chains, the addition of the CO_2 molecules in the high M_w system resulted in a very modest but systematic increase in the radius of gyration of all chains, between 1% and 1.5% with respect to the corresponding values in the absence of CO_2. In the lower M_w systems, that are endowed with higher mobility and can rearrange their conformation more easily, individual chains displayed either an increase or a decrease in their radius of gyration by increasing CO_2 concentration and, on average, these variations canceled out. The observed volumetric dilation despite the invariance of the average chain dimensions could explained by an average increase in the distance between the chains upon increasing CO_2 concentration, as suggested also by the analysis of radial distribution functions presented in **Section 6.4.1.1**.

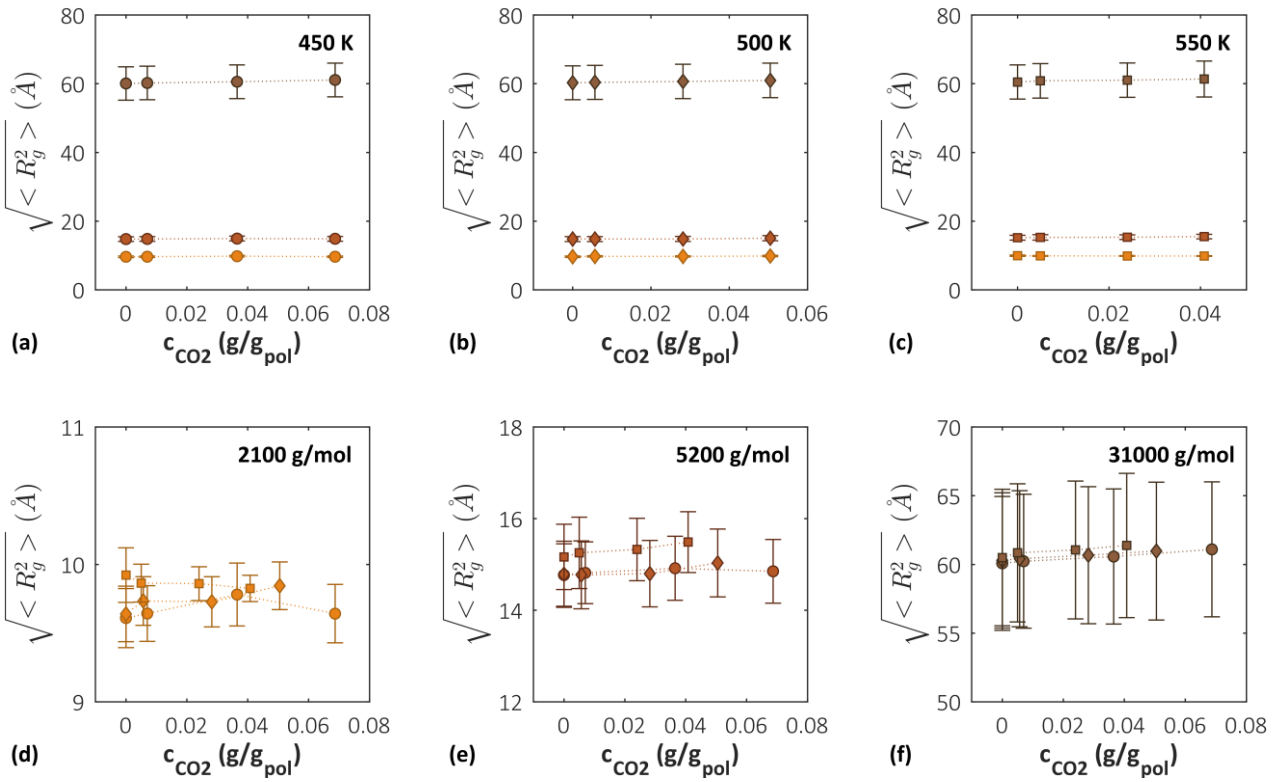

Figure 6.13. Radius of gyration of the polymer chains as a function of CO_2 concentration. Plots (a), (b) and (c) show the effect of molecular weight at fixed temperature, plots (e), (f) and (g) show the effect of temperature at fixed molecular weight. Circles represent data at 450 K, diamonds at 500 K, squares at 550 K. Molecular weight of 2100 g/mol is depicted in **orange**, 5200 g/mol in **red** and 31000 g/mol in **brown**.

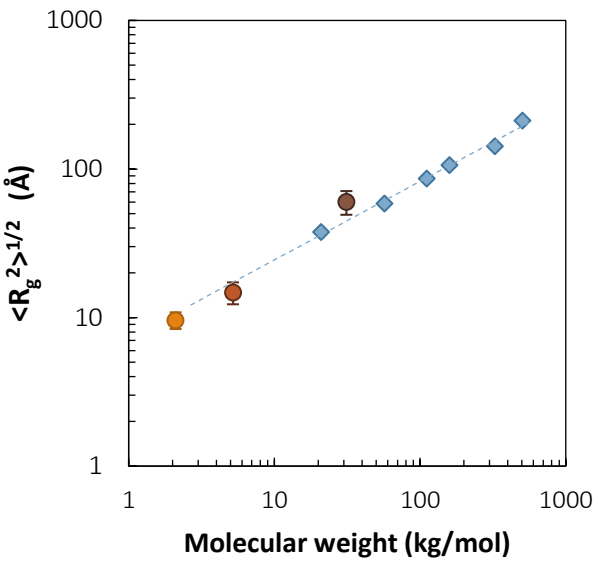

Figure 6.14. Comparison between the root mean squared radius of gyration of the polymer chains at 500 K and the experimental data of reference [80] obtained from neutron scattering experiments (blue diamonds). Circles represent the simulated values: molecular weight of 2100 g/mol is depicted in **orange**, 5200 g/mol in **red** and 31000 g/mol in **brown**.

The M_w dependence of $\langle R_g^2 \rangle^{1/2}$ is evaluated in **Figure 6.14** by comparing the simulated results at 450 K with values determined by neutron scattering for monodisperse aPS ranging from 21000 to 1100000 g/mol at 393 K [80]. The experimental data set does not cover the low M_w range investigated here. However, extrapolation of the trend to lower M_w would indicate a very good agreement for the radius of gyration of the simulated systems at low and intermediate M_w. The higher M_w chains display, on average, a higher radius of gyration than expected. This fact, combined also with the results for subchain dimensions presented in the next section, could be a signal of insufficient equilibration for this system. However, considering that the multiscale equilibration scheme adopted was able to reproduce the radius of gyration of aPS chains in a wide range of M_w [27,30,33] and the fact that the system used here contains only 5 chains, the discrepancy could also be ascribed to poor statistics.

6.3.4.2 Subchain Dimensions and Characteristic Ratio

As a criterion of equilibration of the chain conformations, it is possible to analyze subchain dimensions, by computing the average squared distance between the extremes of a chain segment consisting of n_u repeating units ($R^2(n_u)$) divided by n_u: $\langle R^2(n_u) \rangle / n_u$. This quantity is of interest because it has been shown [81] that, for well equilibrated chains, it increases monotonically with n_u until it reaches a plateau. Very similar trends were obtained at all temperatures in this analysis, therefore only the results at 500 K are reported in **Figure 6.15**. As it can be observed in **Figure 6.15 (a)**, the intermediate M_w reaches a plateau of 24.5 Å^2 for n_u greater than 20, which is an indication that the system is sufficiently equilibrated at all chain lengths. In the same figure, it is also shown that a very similar behavior is displayed by the low M_w system. **Figure 6.15 (b)** shows the results obtained for the high M_w system. A plateau is reached at

intermediate subchain lengths, but for higher values of n_u the trend is broken, and the ratio shows a significant increase, which signifies that on average elongated configurations are assumed by the chains, compared to unperturbed ones. This could be ascribed either to insufficient equilibration of the high M_w system or to poor statistic of this system compared to the other two (5 chains instead of 30 or 75).

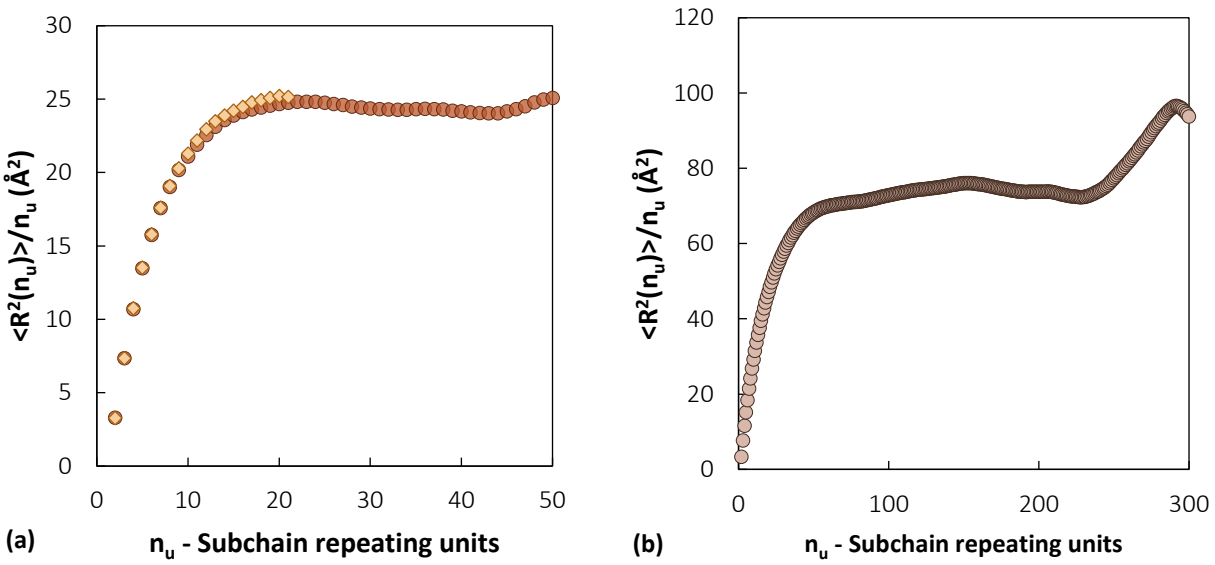

Figure 6.15. Average squared end-to-end distance of subchains consisting of n_u repeating units for (a) the systems having a M_w of 5200 g/mol (50 repeating units – orange) and 2100 g/mol (20 repeating units – yellow) and (b) the system having a M_w of 31000 g/mol (300 repeating units).

From the mean square end-to-end distances $\langle R^2 \rangle$ of the chains, Flory's characteristic ratio C_N can be determined for a chain having N_{BB} backbone bonds of average length l_{BB}:

$$C_N = \frac{\langle R^2 \rangle}{N_{BB} l_{BB}^2} \qquad \text{Eq. (6.13)}$$

The calculated values at 500 K are reported in **Figure 6.16**, alongside the results obtained by previous works employing a multiscale equilibration strategy very similar to the one used for the high M_w system in this work. It is expected that, for high M_w, C_N should reach a plateau (C_∞), whose experimental value is in the range 8.7 – 9.6 between 393 K and 513 K [79]. However, the value calculated for the highest M_w system here is almost double and characterized by a very large error bar. The error bar is obtained as the standard deviation of the average value for the characteristic ratio of individual chains. Such a high error bar is again a symptom of poor statistics in this system. On the contrary, the two systems at lower M_w follow the same trend as the referenced works [27,30], which is an indication that, even though they were equilibrated directly with MD runs, equilibrated chain conformations were achieved.

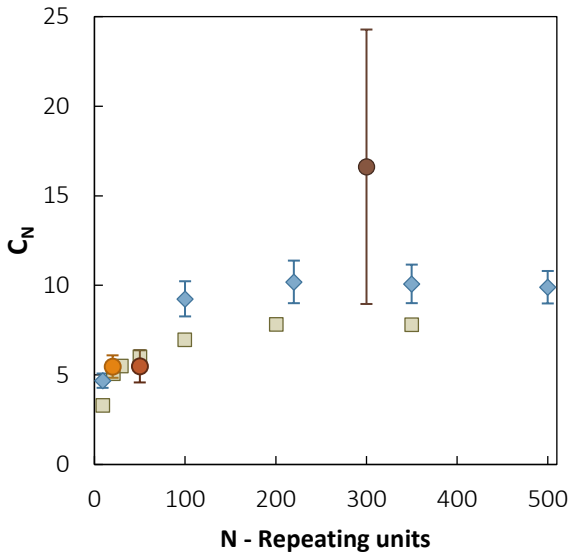

Figure 6.16. Flory's characteristic ratio of aPS chains as a function of chain length (M_w). Circles represent the simulated values in this work: molecular weight of 2100 g/mol is depicted in **orange**, 5200 g/mol in **red** and 31000 g/mol in **brown**. Green squares are the results reported in ref. [27], blue diamonds are the results reported in ref. [30]. All data are at 500 K.

6.4 Local Structure

6.4.1 Radial Distribution Functions

The radial distribution function (RDF) $g(r)_{i-j}$ expresses the probability of finding a particle of type j located on the surface of a sphere of radius r centered on a particle of type i. Radial distribution functions provide a quantitative description of molecular packing and they can be readily obtained for different pairs of atoms in simulated systems [61]. Information from pair distribution functions can be related to x-ray, neutron or electron diffraction experiments by a Fourier transform.

6.4.1.1 RDF of Polystyrene

A number of studies were devoted to the analysis of molecular packing in polystyrene: Wecker et al. [82] observed that samples of atactic polystyrene with different thermal histories yielded very similar x-ray scattering patterns, while Burge et al. [83] performed measurements on isotactic polystyrene samples, which provided insight into its tertiary structure. The temperature dependence of the radial difference distribution function was analyzed in the range 293 to 455 K [84] and that of the structure factor [85] from 298 K to 523 K. Londono et al. [86] reported the radial distribution function of polystyrene, excluding the contributions coming from first and second bonded neighbors. This is directly compared with the simulation results for aPS in **Figure 6.17 (b)**, finding very good agreement between the two, confirming that the adopted model is capable of representing the local structure of the polymer closely.

Experimental measurements including also the short range contributions showed peaks at 1.4 – 1.5, 2.5, 5, 6, and 10 Å [82,84] in the radial difference distribution function of aPS. The first peak is intramolecular and

stems out from correlations between next neighbors, both on the chain and on the ring. These two contributions are separated in the radial distribution functions calculated for the simulated systems (**Figure 6.17**): the peak at 1.39 Å represents the distance between carbon atoms on the ring, while the lower peak at ~1.5 Å includes the contributions coming from neighboring backbone carbons (bond length 1.53 Å) and from the ring carbon bonded to the backbone (bond length 1.51 Å). The second peak is also attributed to intramolecular correlations, in this case of second neighbors in the backbone and the ring. These two contributions are fused in the simulation results, however, it is possible to attribute the shoulder in the right side of the peak to the correlations originating from the backbone, as it can be seen in **Figure 6.18** where the contributions from ring and backbone carbons have been calculated separately. Additionally, in the radial distribution functions of the simulated systems, another peak can be recognized at 2.8 Å, which represents the correlations associated to carbons located on opposite sides of a phenyl ring. Another peak is located at 3.8 Å, and it can be associated to third neighbors on the backbone. Additionally, a small feature is present at 3.2 Å, and it is associated to backbone carbons correlations. Peaks at ~5 Å were interpreted by different authors as containing both interchain contributions and intramolecular correlations [82], possibly deriving from phenyl interactions in sequences of monomers with different tacticity [84]. At higher distances, peaks located around 6 Å and 10 Å were interpreted as originating predominantly from interchain contributions. A magnification of this region of the radial distribution functions of the simulated system reported in (**Figure 6.17 (b)**) shows weak features located at these distances as well. By computing the correlations of ring and backbone carbon atoms separately and comparing the result with the overall radial distribution function of carbon atoms (**Figure 6.18**), it appears that the features at distances of 5 – 6 Å are indeed originated prominently by ring positions, whereas around 10 Å the backbone correlations are stronger, as suggested by several authors [82,84].

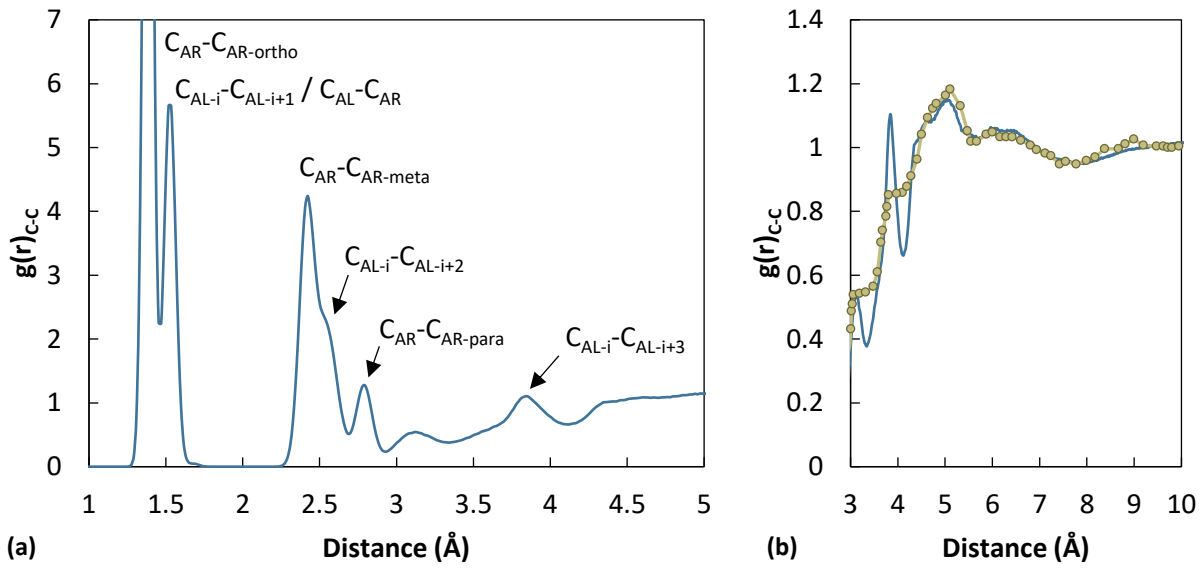

Figure 6.17. Radial distribution function of pairs of carbon atoms. The solid lines represent the simulated system of M_w 2100 g/mol at 500 K. Green circles are the experimental measurements of Londono et al. [86] at 323 K for a sample with M_w 794 g/mol.

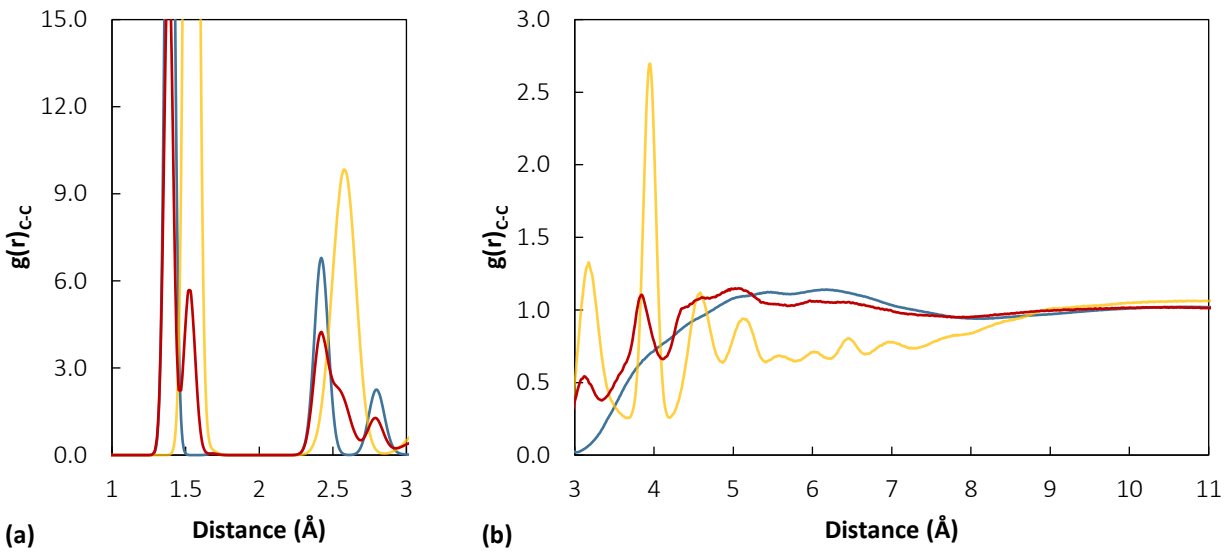

Figure 6.18. Radial distribution function of pairs of carbon atoms (2100 g/mol, 450 K). **Red** lines represent the overall correlations of carbon atoms, **yellow** lines the correlations of backbone carbons, the **blue** ones the correlations of ring atoms.

Concerning the temperature dependence of the C-C radial distribution function, the trend reported in reference [84] shows that the peaks at 1.4 and 2.5 Å remain at the same distance, but become more intense at higher temperature, which is not expected, because usually a temperature increase is associated with a less defined structure, therefore lower peaks. In their work, the peaks at 5 and 6 Å display a small shift towards higher distances at increasing temperature, which is another indication of their intermolecular origin. Moreover, the peak at around 10 Å showed the same trend. In the simulation results (**Figure 6.19**) the first two peaks, associated with first and second neighbors, become slightly less intense and broader as the temperature increases, as expected. The peaks at higher distance also decrease in intensity as the temperature increases and, especially in the case of the feature at 10 Å, a slight shift towards higher distances is observed. The temperature dependence of the peaks is shown in **Figure 6.19** for the low M_w system. The same trend was observed at all molecular weights.

An analysis of the temperature dependence of the ring and backbone correlations, displayed in **Figure 6.20** shows that the stronger effect is displayed in the case of the backbone correlations at around 10 Å, while in the distance 5 – 6 Å also an effect on the phenyl correlations is present. This will be seen also in the analysis of the temperature dependence of the peaks in the x-ray structure factor and the characteristic temperature dependence of its first peak for polystyrene.

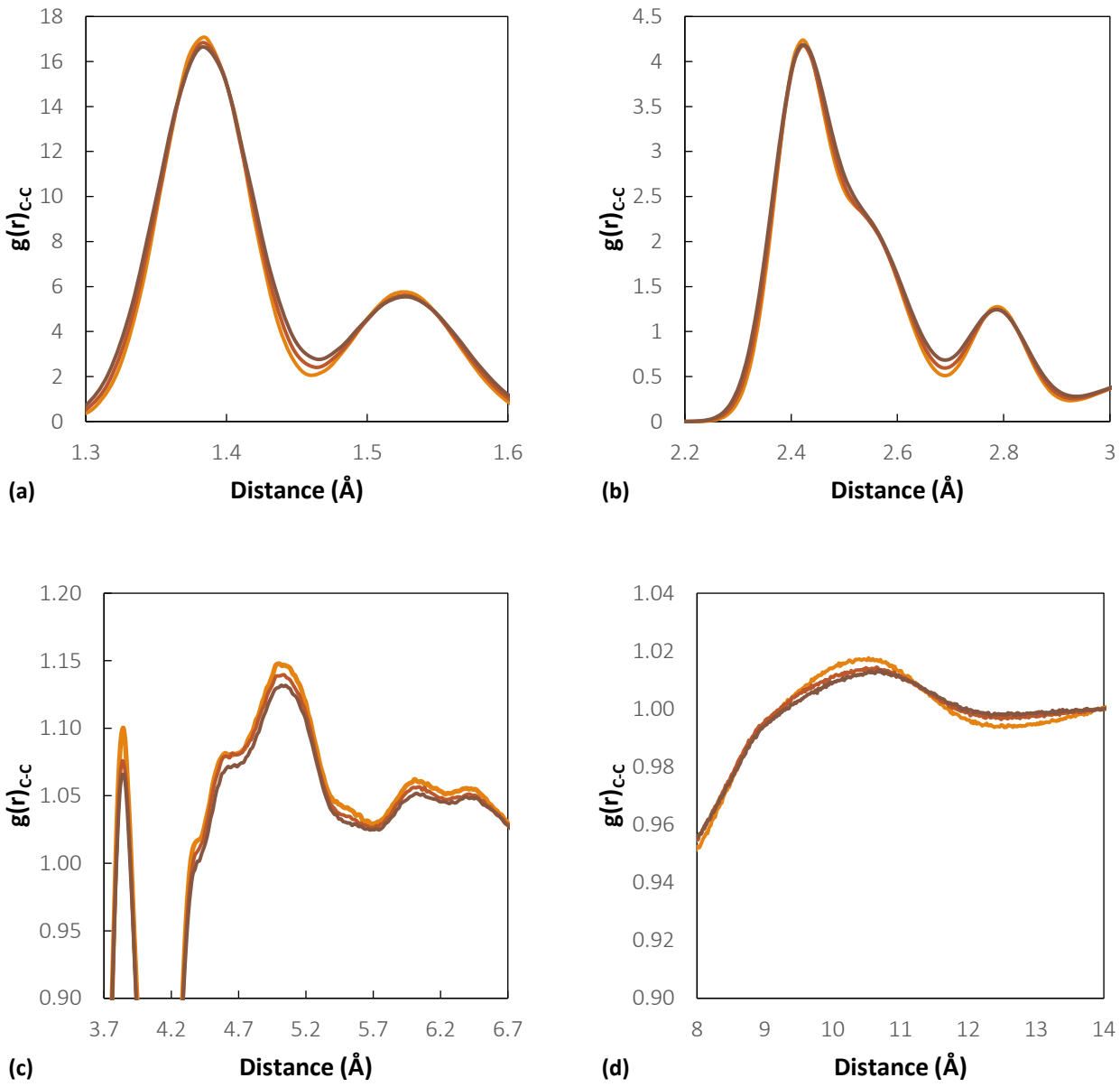

Figure 6.19. Effect of temperature on the peaks of the radial distribution function of pairs of carbon atoms. System: pure polymer of M_w 2100 g/mol, **orange** represents 450 K, **red** 500 K, **brown**, 550 K. (a) Represent the short-range peaks corresponding to bonded atoms and (b) the correlations originated from second neighbors. (c) and (d) show a magnification of the features of the g(r) at higher distances, where also intermolecular correlations are present.

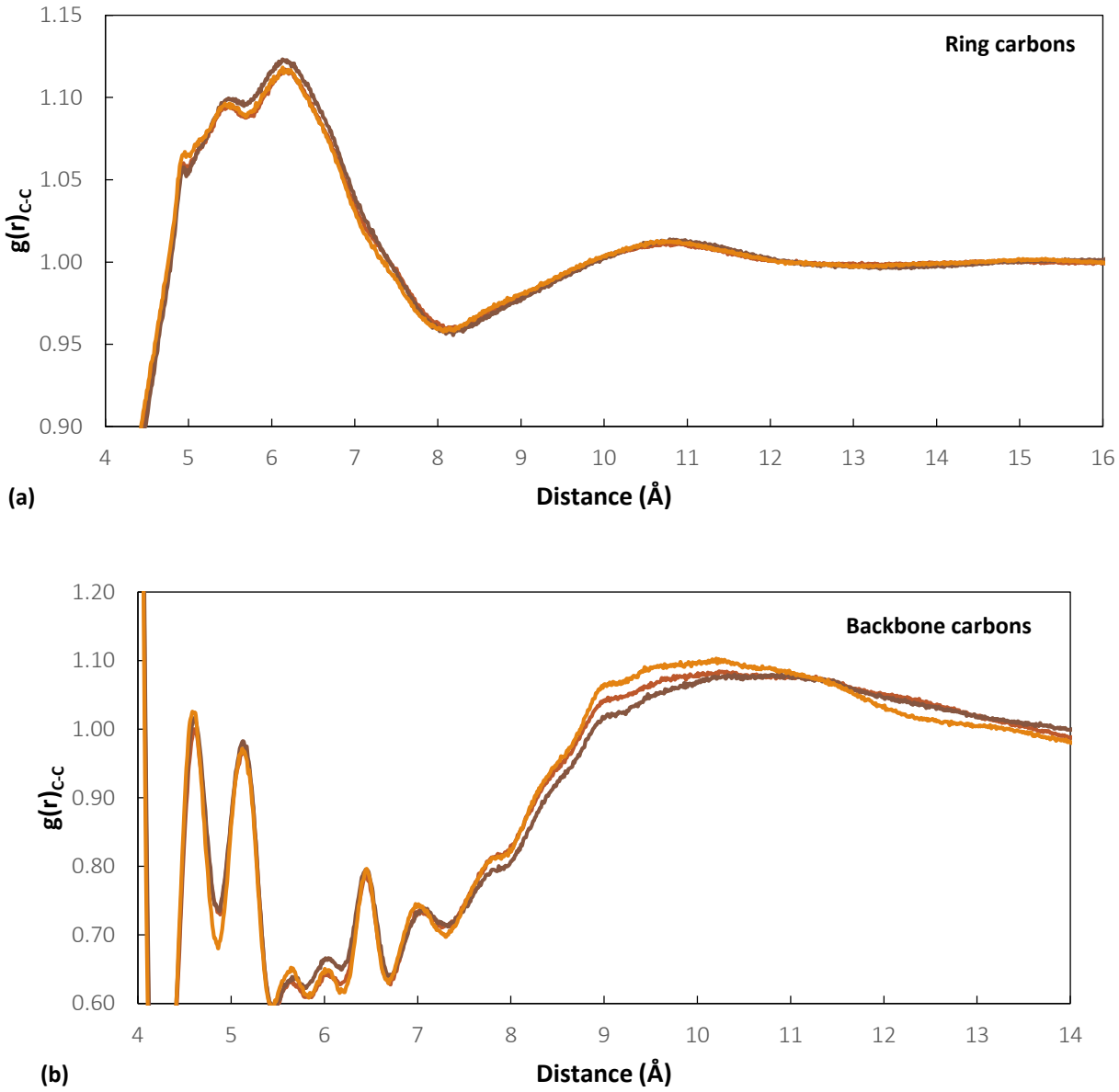

Figure 6.20. Effect of temperature on the peaks of the radial distribution function of pairs of carbon atoms. (a) Carbons on the phenyl rings. (b) Carbons on the backbone. System: pure polymer of M_w 2100 g/mol, **orange** represents 450 K, **red** 500 K, **brown**, 550 K.

Schubach measured the RDF of aPS samples of M_w of 165, 225 and 300 kg/mol [84] and did not find any appreciable dependency on the M_w of the chain in this range. In the simulation results, the effect on the height of the peaks was indeed minimal and not monotonous, while the effect on the correlations at higher distances is shown in **Figure 6.21**. The system at the highest M_w shows some qualitative differences in the relative height of the two small peaks around 6 Å and in the shape of the curve in the region 7 – 10 Å. The latter discrepancy is probably also related to the different trend observed for the high M_w system in the calculated structure factors and their M_w dependence, shown in **Figure 6.31**.

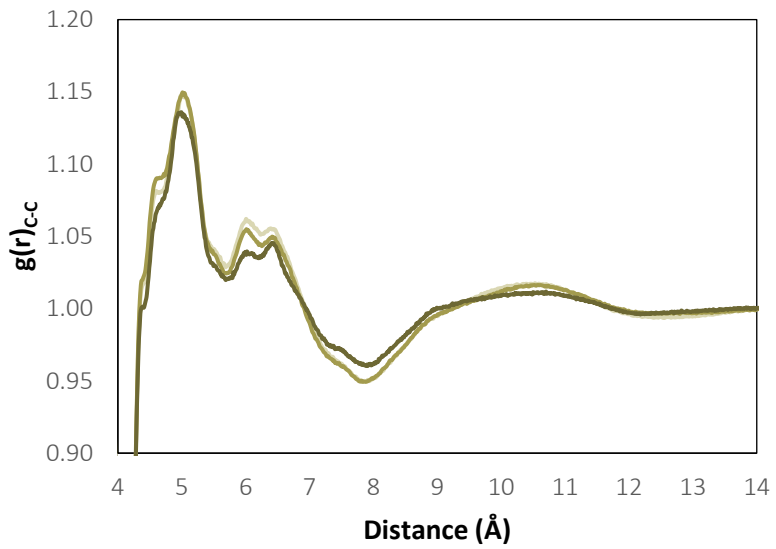

Figure 6.21. Effect of M_w on the radial distribution function of pairs of carbon atoms. Pure polymer at 450 K. Darker shades of green indicate higher M_w.

The effect of CO_2 concentration on the radial distribution function of carbon atoms in aPS is shown in **Figure 6.22**. There does not seem to be here a clear effect on the intermolecular feature at 10 Å. However, a slight effect is present in the intermolecular features at 5 and 6 Å. As it will be seen in the next paragraph, CO_2 presence has a strong effect on x-ray scattering pattern features associated with intermolecular correlations. Therefore, the apparent lack of clear trends in the corresponding peaks in the radial distribution function was surprising. An analysis of the contributions originating from backbone and ring carbon correlations separately, however, showed that indeed a clear effect is visible for the backbone carbon correlations upon increase of CO_2 concentration, as it can be seen in **Figure 6.23**. The features located around 5-6 Å show an increase in intensity as CO_2 concentration increases, while the broad peak located around 10 Å displays a decrease in intensity and shifts towards higher distances as CO_2 concentration increases. Comparing this result with the effect of CO_2 on the radius of gyration, it can be concluded that CO_2 affects interchain packing more significantly than the average chain dimensions. No effect is detected in the corresponding radial distribution function for the carbon atoms of the rings, even at a close resolution.

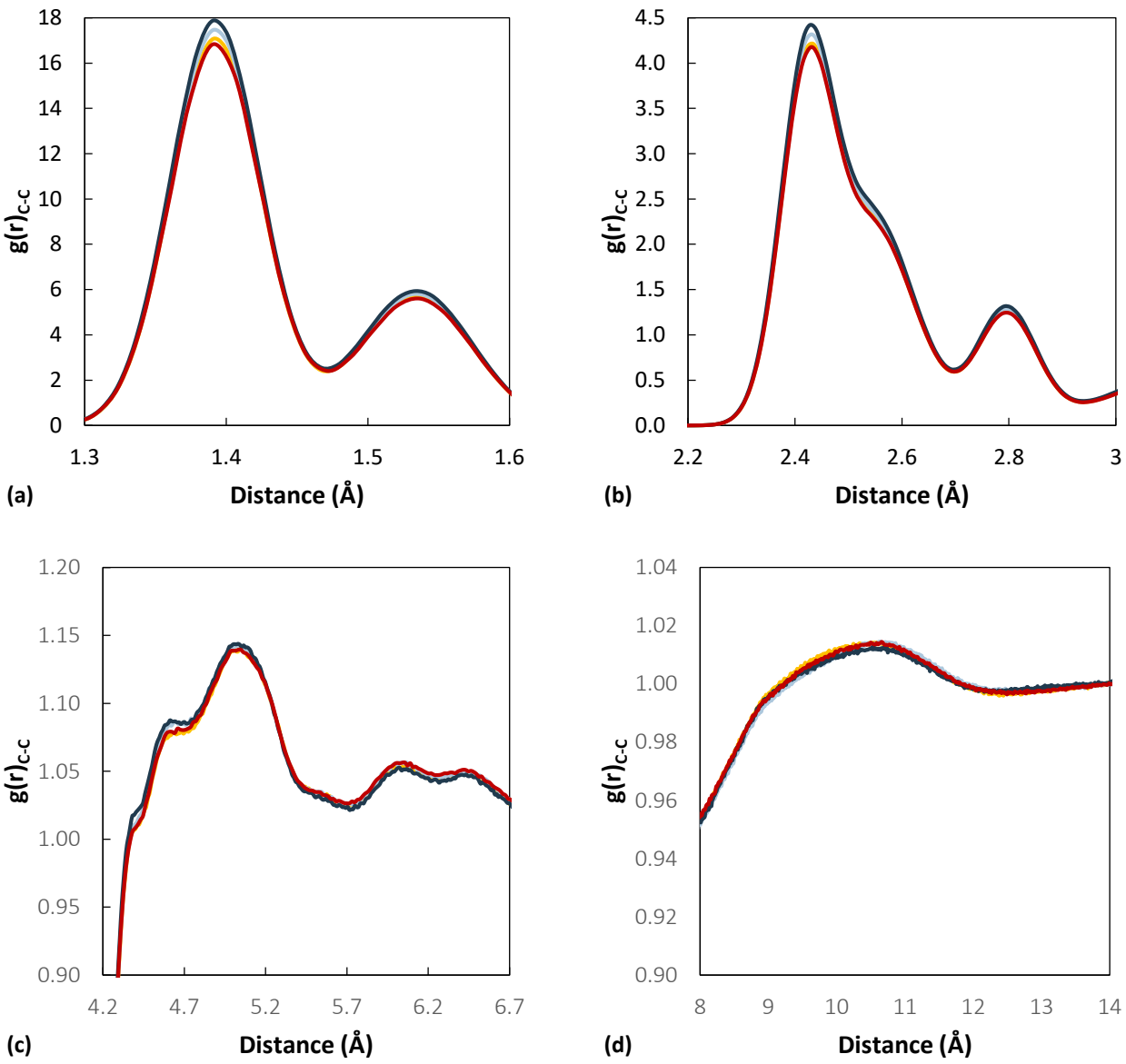

Figure 6.22. Effect of CO_2 concentration on the peaks of the radial distribution function of pairs of carbon atoms. System: M_w 2100 g/mol at 500 K. **Red** represent results for the pure polymer, **yellow** $5.70 \cdot 10^{-3}$ g_{CO2}/g_{pol}, **light blue** $2.82 \cdot 10^{-2}$ g_{CO2}/g_{pol}, **blue** $5.05 \cdot 10^{-2}$ g_{CO2}/g_{pol}.

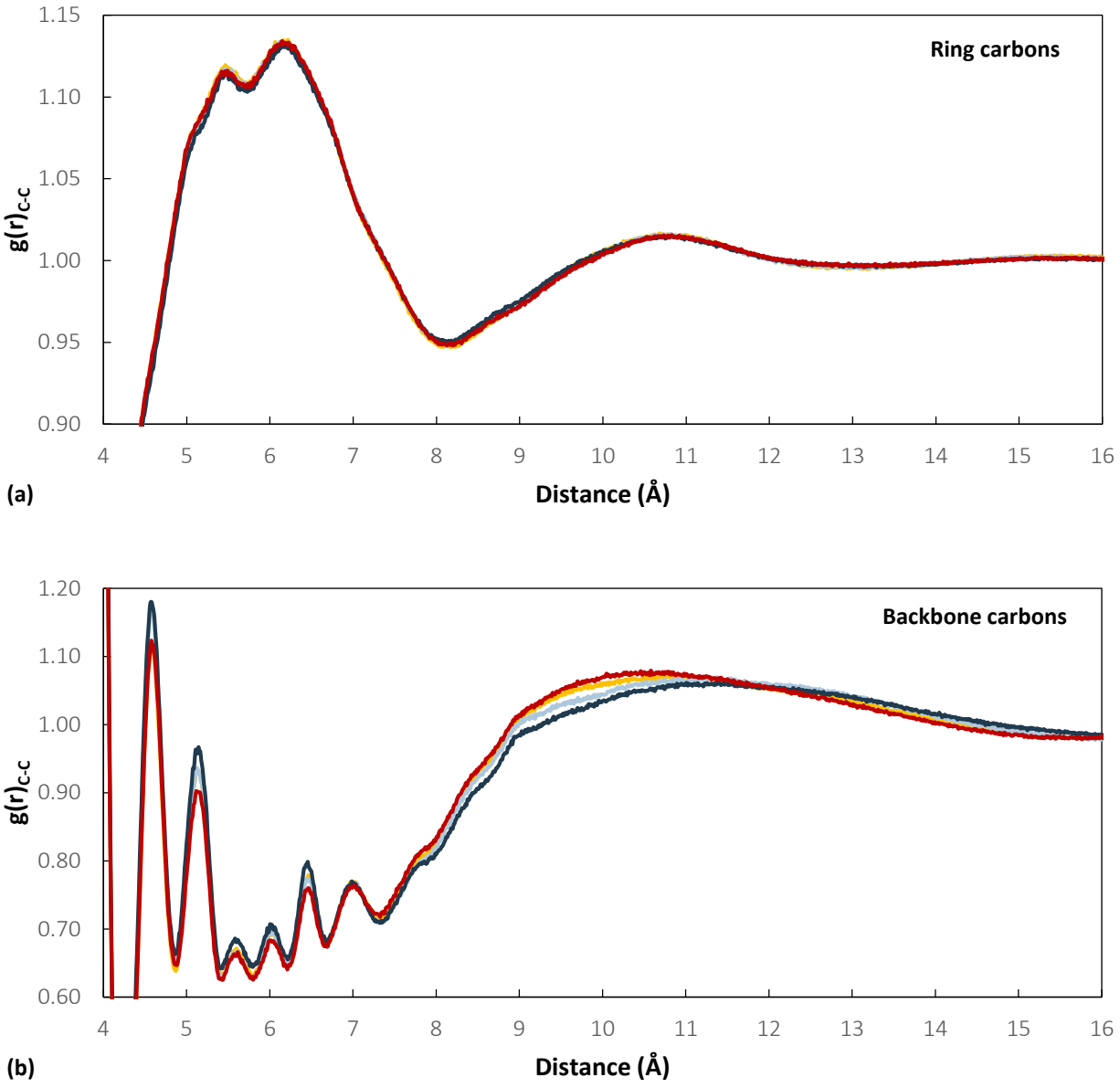

Figure 6.23. Effect of CO_2 concentration on the peaks of the radial distribution function of pairs of carbon atoms. (a) Carbons on the phenyl rings. (b) Carbons on the backbone. System: M_w 2100 g/mol at 500 K. **Red** represent results for the pure polymer, **yellow** 5.70 · 10^{-3} g_{CO2}/g_{pol}, **light blue** 2.82 · 10^{-2} g_{CO2}/g_{pol}, **blue** 5.05 · 10^{-2} g_{CO2}/g_{pol}.

6.4.1.2 CO_2-Polystyrene RDF

Radial distribution functions of CO_2 atoms with polystyrene were evaluated as a function of concentration, temperature and molecular weight of the polymer. Some representative cases are reported in the following figures. **Figure 6.24** shows the correlations of carbon dioxide with atoms on the ring and the backbone respectively. In every case, CO_2 oxygen is closer than CO_2 carbon to the polymer, reasonably. Furthermore, CO_2 is closer to the hydrogens of the polymer, both on the ring and on the backbone, as expected. Finally, CO_2 is located closer to the rings than to the backbone. This could be due to the fact that the bulky rings

block access to the backbone to CO_2, but it could be also a consequence of stronger interactions between CO_2 and the ring, due to electrostatic forces.

With increasing temperature, the height of the peaks systematically decreases, especially in the features at lower distance, as it can be observed in **Figure 6.25**. On the other hand, increasing CO_2 concentration does not have a discernible systematic effect (**Figure 6.26**). Generally, in the higher M_w systems, peaks tended to be slightly higher and broader, but this was not a systematic trend. It should be mentioned that the results at the lowest concentration are endowed with worse statistics than the other cases, therefore the curves are less smooth, and it becomes difficult to establish trends in some cases.

In **Figure 6.27** the correlations between CO_2 atoms are shown. The peaks corresponding to C-O bond length and O-C-O distance can be recognized at 1.15 Å and 2.3 Å. Subsequent peaks at 3 Å and 3.8 Å indicate the presence of other CO_2 molecules, which do not move isolated inside the polymer, even at low concentration. The position of the peaks was invariant with concentration and temperature, but their height decreased at higher temperature.

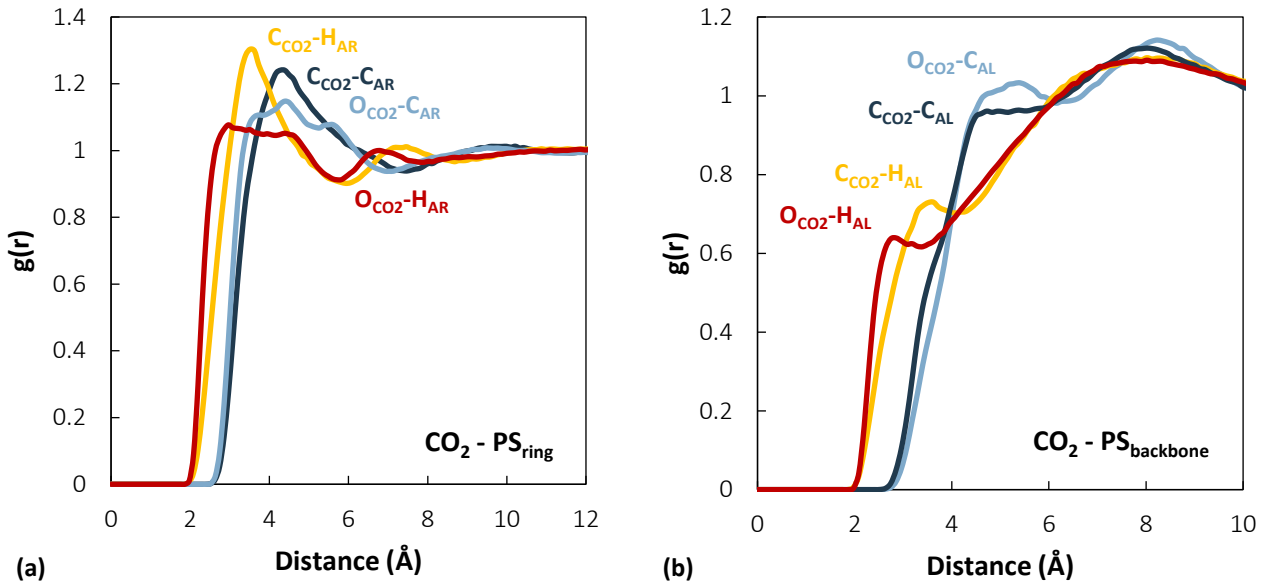

Figure 6.24. Radial distribution functions of pairs of CO_2-PS atoms in the 2100 g/mol system at 450 K and highest CO_2 concentration.

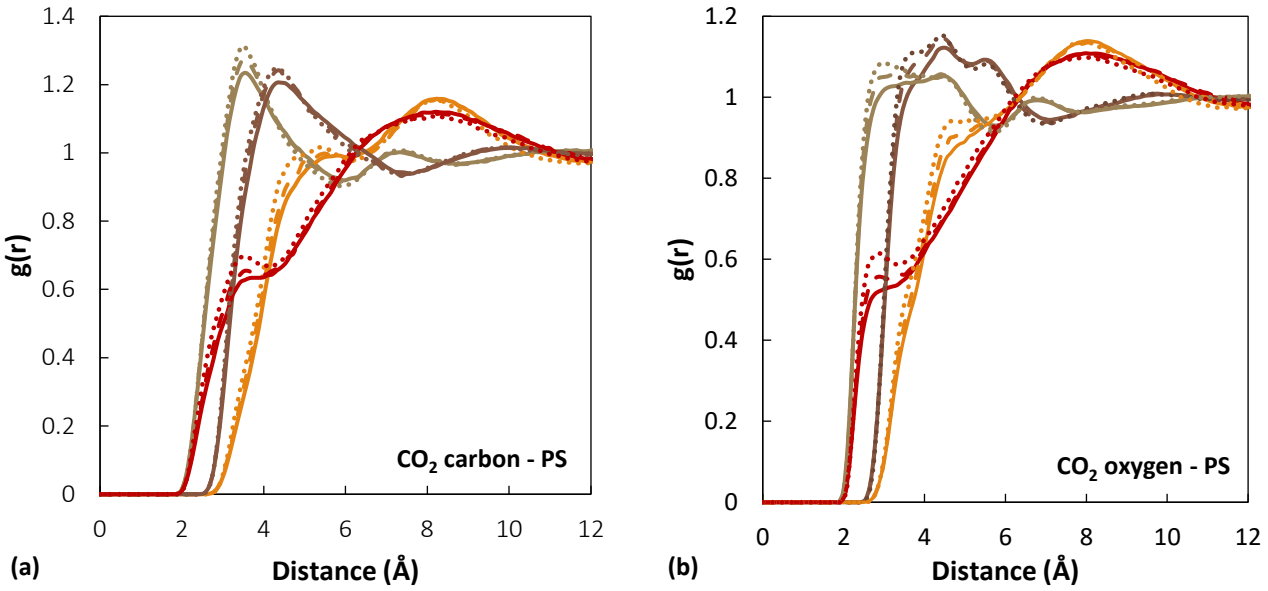

Figure 6.25. Radial distribution functions of pairs of CO_2-PS atoms as a function of **temperature** in the 5200 g/mol system at highest CO_2 concentration. The radial distribution functions of carbon atoms of the CO_2 molecule are reported in figure (a), oxygen in figure (b). **Brown** lines represent correlations with aromatic carbons, **green** with aromatic hydrogens, **orange** with aliphatic carbons, **red** with aliphatic hydrogens. Solid lines are data at 450 K, dashed lines 500 K, dotted lines 550 K.

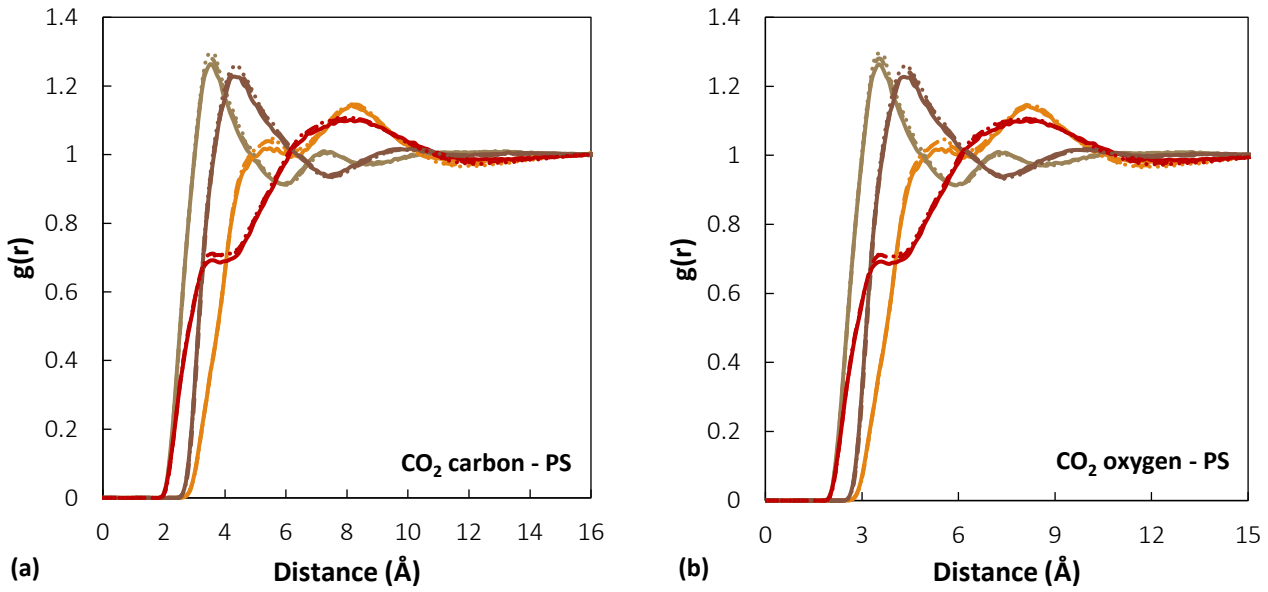

Figure 6.26. Radial distribution functions of pairs of CO_2-PS atoms as a function of **CO_2 concentration**, 2100 g/mol system at 500 K. The radial distribution functions of carbon atoms of the CO_2 molecule are reported in figure (a), oxygen in figure (b). **Brown** lines represent correlations with aromatic carbons, **green** with aromatic hydrogens, **orange** with aliphatic carbons, **red** with aliphatic hydrogens. Solid lines are data at low CO_2 concentration, dashed lines low CO_2 concentration, dotted lines high CO_2 concentration.

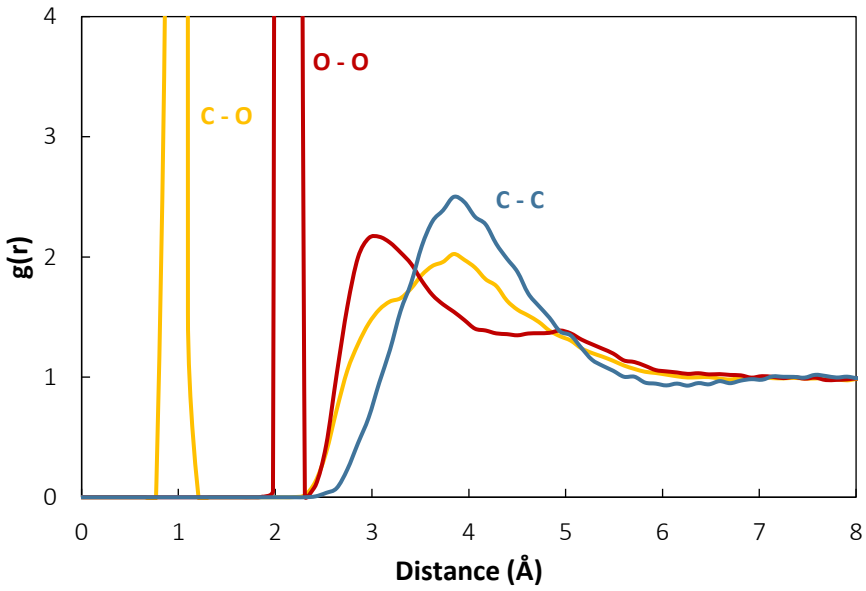

Figure 6.27. Radial distribution functions of pairs of CO_2-CO_2 atoms in the 2100 g/mol system at 450 K and highest CO_2 concentration.

6.4.2 X-ray Scattering Patterns

The structural investigation of materials is routinely carried out with X-Ray scattering measurements, also in the case of polymers [87]. For amorphous materials, the diffracted intensity $I(q)$ depends only on the modulus of the wavevector q. Alternatively, comparisons can be carried out also in terms of the static structure factor $S(q)$. For a simulated system, $S(q)$ can be calculated from the knowledge of the radial distribution functions $g(r)$ and atomic from factors $f(q)$ [88,89]. For the case of polystyrene, where only two atom types are present, the static structure factor is obtained with Errore. L'origine riferimento non è stata trovata..

$$I(q) \propto S(q) + \sum_i f_i^2(q) \qquad \text{Eq. (6.14)}$$

$$S(q) = \rho \int_0^\infty [y_C^2 f_C(q)^2 (g_{C-C}(r) - 1) + 2y_C y_H f_C(q) f_H(q)(g_{C-H}(r) - 1) + y_H^2 f_H(q)^2 (g_{H-H}(r) - 1)] \frac{\sin(qr)}{qr} 4\pi r^2 dr \qquad \text{Eq. (6.15)}$$

Features at low q values reflect intermolecular correlations in the bulk, whereas peaks at higher q values are originated by intramolecular correlations, therefore features at higher distance in the radial distribution functions affect the low q portion of the structure factor and vice-versa.

Polystyrene exhibits a special characteristic, that is generally not present in non-crystalline polymers: its wide-angle X-ray scattering (WAXS) pattern shows a diffuse halo at q = 0.75 A^{-1} which, on the contrary, is absent from the scattering pattern of the monomer. Tests carried out on mechanically extended samples supported the hypothesis that this peak is associated with spatial correlations between chains [85].

Experimentally, the most intense peak is located at 1.4 $Å^{-1}$, and other peaks, in addition to the one at 0.75 $Å^{-1}$, are found at 3.1, 5.6, 9 and 10 $Å^{-1}$ [85]. The comparison between experimental structure factor at 293 K [85] and the simulated one at 450 K (the lowest temperature available in the present study for comparison) shows that the positions of the peaks are well predicted. Also the fact that the highest peak at 1.4 $Å^{-1}$ is slightly shifted to the lower q values is consistent with the temperature dependence of this feature, as it will be shown later. A scattering intensity curve was available at a higher temperature (523 K) [85] and it was compared with the simulation results at 550 K, finding remarkable agreement (**Figure 6.28**).

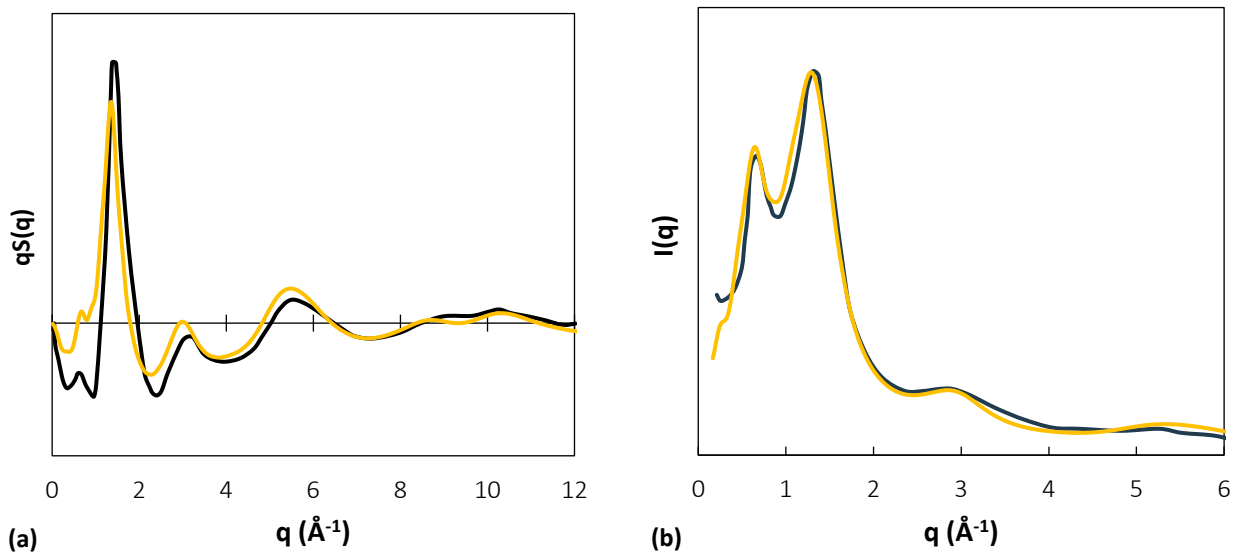

Figure 6.28. (a) q-weighted structure factor of aPS. The blue line is an experimental curve at 293 K [85], the orange one the simulation result for the system of 2100 g/mol at 450 K. (b) X-Ray scattering intensity of aPS. The blue line is an experimental curve at 523 K [85], the orange one the simulation result for the system of 2100 g/mol at 550 K.

For many non-crystalline polymers, the peak at the lowest angle in the scattering curve is the most intense and it represents interchain correlations. It is usually found at the same position in scattering patterns of the corresponding monomer. However, in the case of polystyrene this is true for the second peak encountered in the scattering pattern, while the first one is very weak in intensity and it is not found in the scattering pattern of the monomer.

Moreover, it displays an unusual temperature dependence: unlike the peak at 1.4 $Å^{-1}$, which slightly decreases in intensity and shifts towards smaller angles as temperature increases, the peak at 0.75 $Å^{-1}$ increases significantly in intensity with increasing temperature. Further peaks are little affected by temperature. A decrease in peak intensity with increasing temperature is usually a result of both an increase in thermal disorder and a reduction in electron density due to thermal expansion. The fact that there is no significant effect of temperature on peaks shapes or widths is an indication that the polymer expands without any general structural reorganization [85].

These effects are displayed also in the simulated systems, as it can be seen in **Figure 6.29**. From the analysis of the corresponding radial distribution functions, the temperature dependence of the first peak is attributed mainly to backbone correlations, as the correlation functions of the rings does not display a temperature dependence at higher distances. Also, the fact that this peak is not observed in the case of the monomer is an indication that it could be originated by backbone correlations, which are absent in the case of the monomer. In the range 5-7 Å of the radial distribution functions, the dominant contribution is related to ring correlations and they show indeed a weak temperature dependence, that is assumed to originate the second peak and its temperature trend.

This interpretation is confirmed also by an analysis of the inter- and intramolecular components of the structure factors of polystyrene obtained from MD trajectories [90]. The authors calculated partial structure factor isolating the contributions originated from ring and backbone correlations. Their study showed that the peak at 1.4 $Å^{-1}$ arises primarily from phenyl-phenyl correlations, both intra- and intermolecular. While the intermolecular contribution showed a tendency to shift to lower angles with increasing temperature, the intramolecular part was nearly insensitive to temperature, resulting in a weak temperature dependence of this peak. Moreover, the peak at 0.75 $Å^{-1}$ could be ascribed primarily to intermolecular correlations of backbone atoms, which showed the expected decrease in intensity and shifting to lower q with increasing temperature. The superposition of the shift to lower angles of intermolecular phenyl-phenyl and phenyl-backbone gives rise to the anomalous increase in temperature of this peak.

Interestingly, an increase in CO_2 concentration has the same effect on the intensity and position of the first two peaks of the x-ray scattering patter of aPS as an increase in temperature (**Figure 6.30**). However, as it was observed in the analysis of radial distribution functions, an increase in concentration affects only backbone-backbone correlations with a decrease in intensity and shift to higher distances. This is reflected by the shift to lower angles of the 0.75 $Å^{-1}$ peak at increasing concentration. In this case, though, its increase in intensity cannot not be ascribed to a superposition of effects related to ring correlations, as these correlations were unaffected by the increase in CO_2 concentration. It could be informative to evaluate phenyl-backbone correlations to assess their concentration dependence and also isolate the inter- and intramolecular contributions of the correlations, to interpret the concentration dependence of this low q feature of the structure factor.

Finally, the effect of M_w on the structure factor is displayed in **Figure 6.31**. The peak at 1.4 $Å^{-1}$ shows a decrease in intensity at increasing M_w, while the peak at 0.76 Å does not display a monotonous temperature dependence. The reason for this is not completely clear, however, it can be related to the M_w trend of the radial distribution function in the range 7 – 10 Å.

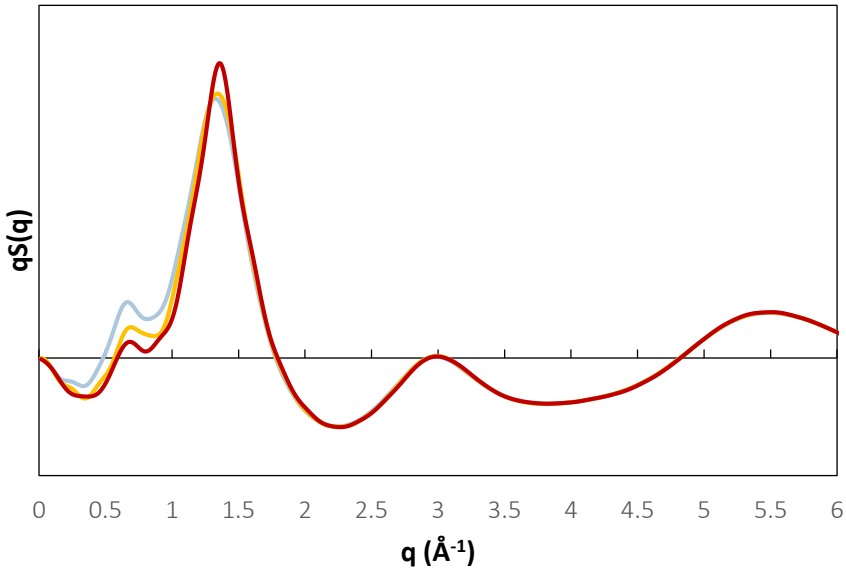

Figure 6.29. q-weighted structure factor of aPS. System: pure polymer M_w 2100 g/mol. **Red** represent results at 450 K, **yellow** at 500 K, **light blue** at 550 K.

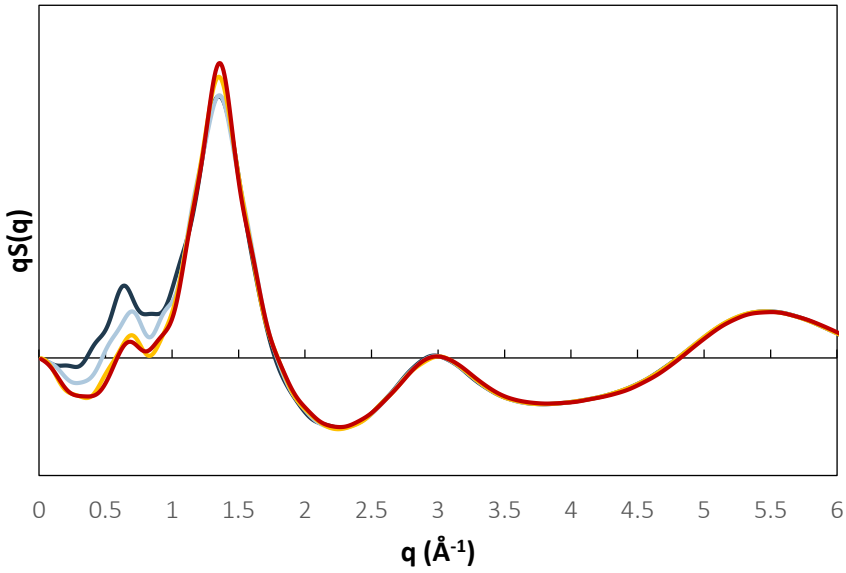

Figure 6.30. q-weighted structure factor of aPS. System: Mw 2100 g/mol at 450 K. **Red** represent results for the pure polymer, **yellow** $5.70 \cdot 10^{-3}$ g_{CO2}/g_{pol}, **light blue** $2.82 \cdot 10^{-2}$ g_{CO2}/g_{pol}, **blue** $5.05 \cdot 10^{-2}$ g_{CO2}/g_{pol}.

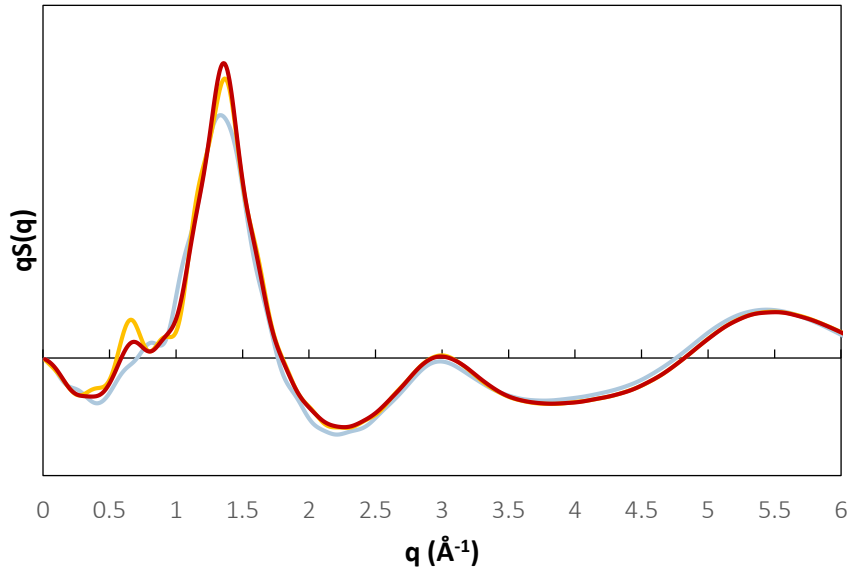

Figure 6.31. q-weighted structure factor of aPS. Effect of M_w 450 K, pure polymer. **Red** represent results for 2100 g/mol, **yellow** 5200 g/mol, **light blue** 31000 g/mol.

6.5 Local Dynamics

In amorphous polymers, motions with a wide range of characteristic times take place. The fastest motions are those of bond and angle vibrations, which occur in the timescale of femtoseconds, and are not influenced by the overall packing of the system, but only by the very localized neighboring interactions. The reorientation of pendant groups or bonds (local segmental dynamics) has characteristic times in the order of tens of picoseconds to nanoseconds, exhibits a strong temperature dependence, and it is very sensitive to packing density. The longer relaxation phenomena are those related to the long-range conformational rearrangements, reorientation of the end-to-end vector and self-diffusion of the chains. Segmental motions are relevant for the diffusion of small penetrants in the matrix because they affect the thermal fluctuations of accessible volume regions through which the gas diffuses.

6.5.1 Segmental Dynamics

The MD trajectories at constant energy were analyzed to extract information about the local dynamics and the effect of temperature, M_w and gas concentration of the motion of various polymer segments. In the case of polystyrene, the vectors characterizing the orientation of the phenyl ring and the orientation of the C–H bonds are of interest, since they can be compared directly to dielectric spectroscopy (DS) results and NMR measurements. The orientational decorrelation with time is analyzed considering ensemble-averaged Legendre polynomials of order k ($P_k(t)$) of $\langle \hat{v}|_{t_0} \cdot \hat{v}|_{t_0+\Delta t} \rangle$, the inner product of a unit vector $\hat{v}$ along itself at times t_0 and $t = t_0 + \Delta t$.

To compare the simulation results with DS measurement, the vector that begins from the backbone carbon connected to the phenyl ring and ends at the center of mass of the ring ($\mathrm{C}-\mathrm{com}_{\mathrm{Ring}}$ vector) is considered, since the dipole moments of the monomer are approximately directed along this vector. The first Legendre polynomial of $\langle \mathrm{C}-\mathrm{com}_{\mathrm{Ring}}\big|_{t_0} \cdot \mathrm{C}-\mathrm{com}_{\mathrm{Ring}}\big|_{t_0+\Delta t}\rangle$ is considered:

$$P_1(t) = \langle \cos\theta(t) \rangle \qquad \text{Eq. (6.16)}$$

Here $\theta(t)$ is the angle by which the vector has rotated in a time t relative to its original position at the time origin t_0. The average over all $\mathrm{C}-\mathrm{com}_{\mathrm{Ring}}$ vectors and across multiple time origins is considered. DS measurements include both self- and cross-correlations of the dipole vectors, unlike this analysis, which considers only self-correlations. However, it was shown that the correlations of neighboring dipole moments contributes minimally to the segmental relaxation [91,92].

To compare the simulation results with NMR data, the orientational autocorrelation function of $\mathrm{C}-\mathrm{H}$ bonds is analyzed. Spin−lattice relaxation of ^{2}H nuclei is dominated by electric quadrupole coupling and the spin relaxation time can be directly related to the reorientation of the $\mathrm{C}-\mathrm{H}$ bonds. In this case, to extract this information from the simulations, the second order Legendre polynomial of $\langle \mathrm{C}-\mathrm{H}|_{t0} \cdot \mathrm{C}-\mathrm{H}|_{t0+\Delta t}\rangle$ is to be computed as a measure of the polymer segmental dynamics:

$$P_2(t) = \frac{3}{2}\langle \cos^2\theta(t) \rangle - \frac{1}{2} \qquad \text{Eq. (6.17)}$$

Here $\theta(t)$ is the angle by which the vector has rotated in a time t relative to its original position at the time origin t_0. The average over all $\mathrm{C}-\mathrm{H}$ bonds, both on the phenyl ring and on the backbone, is performed across multiple time origins.

The long-time decay of the orientational autocorrelation function is well represented by a modified Kohlrausch–William–Watts (mKWW) equation [93–95].

$$P_k(t) = \alpha_{lib} \exp\left(-\frac{1}{\tau_{lib}}\right) + (1-\alpha_{lib}) \exp\left[-\left(\frac{1}{\tau_{seg}}\right)^{\beta_{KWW}}\right] \qquad \text{Eq. (6.18)}$$

This function consists of two parts. The first term is associated to a fast exponential decay having amplitude α_{lib}. This represents the fast librations of torsion angles around skeletal bonds and the bond stretching and bond angle bending vibrations of skeletal and pendant bonds near their equilibrium values, which have a characteristic time τ_{lib}. The second term is the decay associated to cooperative torsional transitions in the polymer and is represented by a stretched exponential, where τ_{seg} is the characteristic correlation time and β_{KWW} the stretching exponent. By integrating this curve, the segmental relaxation time τ_c (characteristic correlation time of segmental motion) can be calculated, using the following equation.

$$\tau_c = \int_0^\infty P_k(t)dt = \alpha_{lib}\tau_{lib} + (1-\alpha_{lib})\frac{\Gamma(1/\beta_{KWW})}{\beta_{KWW}}\tau_{seg} \qquad \text{Eq. (6.19)}$$

It is useful to resort to the above fitting procedure for the calculation of the relaxation time, since in several cases the orientational autocorrelation function does not decay to zero within the limits of the simulation.

As a consequence, a degree of uncertainty is inevitably introduced when extrapolating the behavior to longer times with the mKWW function.

Simulated configurations were recorded at intervals of 5 ps along the trajectory, therefore no points below this value are present to characterize the decay of the fast librations at very short times, which is the physical meaning of the parameter τ_{lib}. He et al. [31] suggested the use of a fixed value of 1 ps for τ_{lib} during this fitting procedure. Here τ_{lib} was optimized together with the other parameters, finding values between 1 and 2 ps in all cases for the $\mathrm{C}-\mathrm{H}$ bonds and 0.4 ps for $\mathrm{C}-\mathrm{com}_{\mathrm{Ring}}$ vectors, which are very close to the suggested one. Indeed, larger values would lead the fast librations to decay at longer times than 5 ps, which is not observed in the simulated curves. Using smaller values, on the other hand, would not affect the calculated decorrelation times, which are mostly sensitive to the long-time tail. Therefore, the obtained values are deemed appropriate.

In **Figure 6.32**, **Figure 6.34** and **Figure 6.33** some representative decorrelation functions calculated from the simulated trajectories are shown, to highlight the effect of *T*, M_w and CO_2 concentration on the segmental dynamics. **Figure 6.32** shows the $P_2(t)$ of the $\mathrm{C}-\mathrm{H}$ bonds for the pure polymer system of 5200 g/mol. Different colors represent different temperatures. In **Figure 6.33** the effect of M_w at fixed temperature (500 K) is shown for the pure polymer systems, but analogous trends were obtained also in the presence of CO_2. In **Figure 6.34** the effect of CO_2 concentration on the extracted $P_2(t)$ and on the calculated relaxation times is shown. **Table 6.13** summarizes the parameters obtained by fitting the mKWW function to the orientational autocorrelation of $\mathrm{C}-\mathrm{com}_{\mathrm{R}}$ vectors, while **Table 6.14** contains the parameters obtained for the $\mathrm{C}-\mathrm{H}$ bonds.

The temperature dependence of the reorientational decorrelation followed an Arrhenius behavior at all cases considered, as it can be observed in **Figure 6.36**, where the logarithm of the relaxation times is plotted against the inverse temperature and a linear trend is followed, both for the $\mathrm{C}-\mathrm{H}$ bonds and the $\mathrm{C}-\mathrm{com}_{\mathrm{Ring}}$ vector. Concerning the M_w dependence, it can be seen qualitatively in **Figure 6.33** that an increase in molecular weight of the polymer causes the segmental dynamics to become slower. Experimentally, it was observed that in the high M_w range this dependence asymptotically vanishes. However, in the M_w range of the simulated systems, an effect of M_w on the local dynamics was experimentally documented [31] as well.

Increasing CO_2 concentration systematically enhances the local dynamics. Systems with higher CO_2 concentration are less dense and this promotes the mobility of the polymer. At the same time, a higher gas concentration corresponds to a higher pressure, which would act in the opposite way, slowing down the polymer dynamics. However, this effect is overcome by the higher mobility induced by the presence of the penetrant, resulting in lower decorrelations times at higher concentration. To compare the relative strength of this effect in the different systems, the relative decrease in the decorrelation times as a function of CO_2 concentration with respect to the value of the pure polymer was calculated. This is reported in **Figure 6.34 (d).** The effect is more pronounced in the case of the lower M_w system.

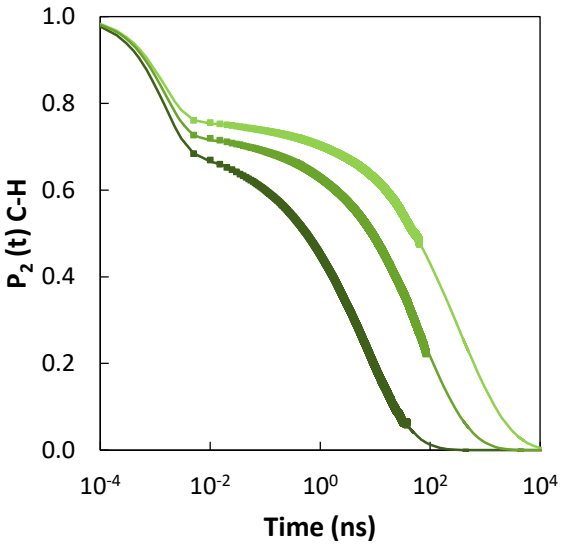

Figure 6.32. Effect of temperature on the orientational autocorrelation of the C – H bonds of pure aPS. As a representative case the 5200 g/mol aPS system is represented. Symbols represent simulation results at 450 K (light green), 500 K (green) and 550 K (dark green). Solid lines show extrapolation at lower and higher times with a mKWW function.

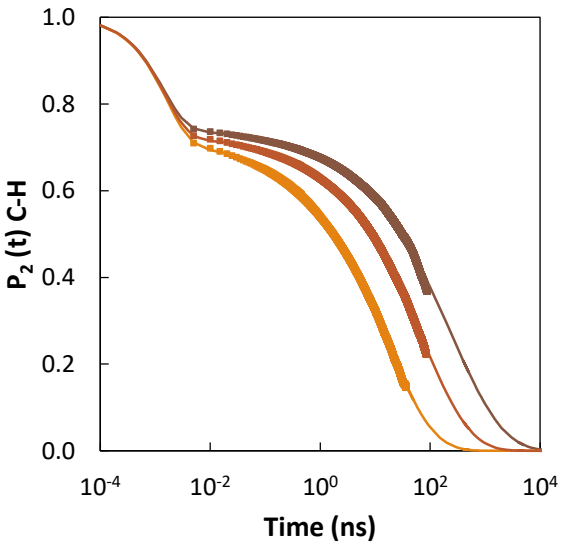

Figure 6.33. Effect of M_w on the orientational autocorrelation of the C – H bonds of pure aPS. The symbols represent simulated data at 500 K. Molecular weight of 2100 g/mol is depicted in **orange**, 5200 g/mol in **red** and 31000 g/mol in **brown** Solid lines show extrapolation at lower and higher times with a mKWW function.

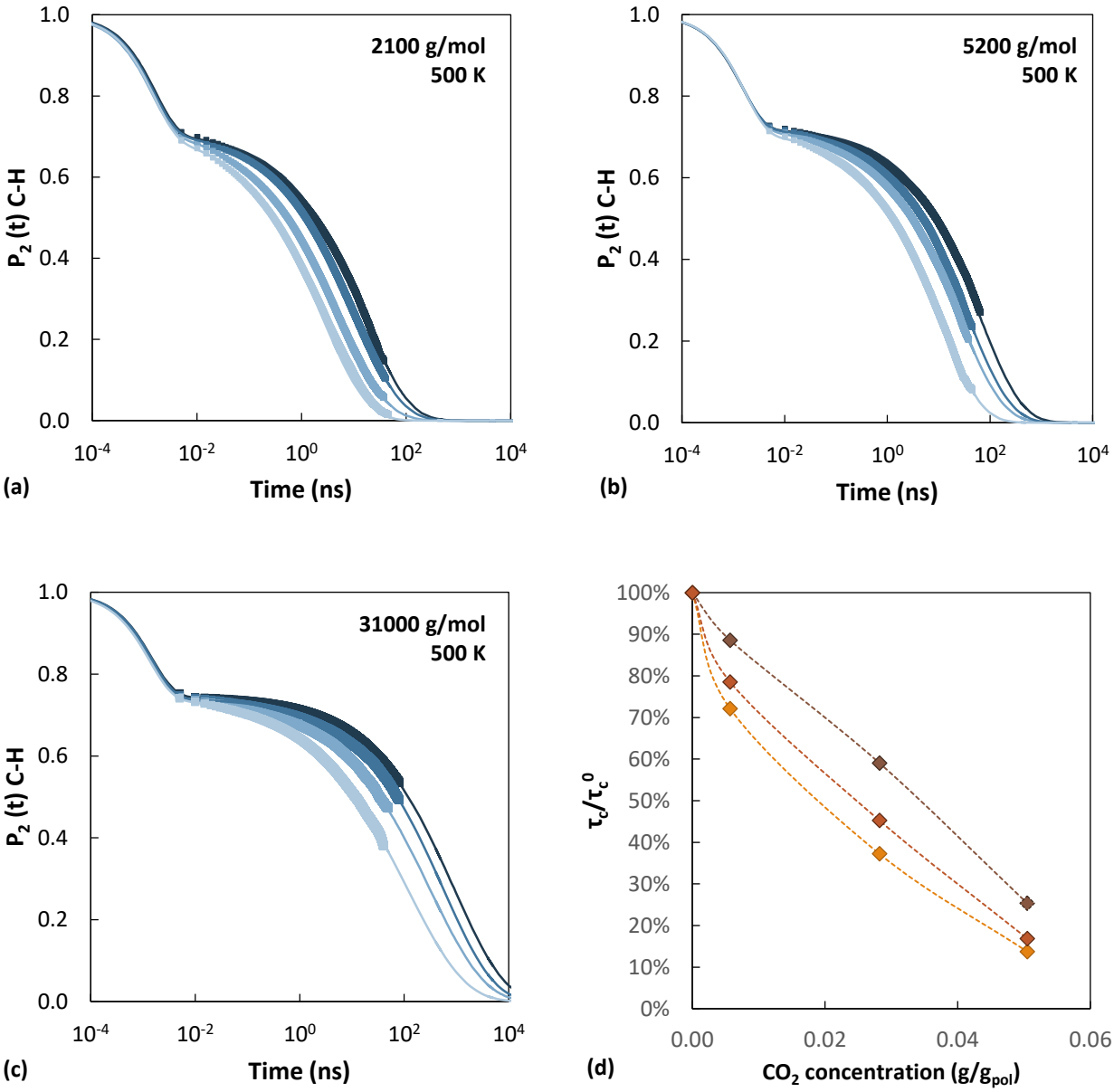

Figure 6.34. Effect of CO_2 concentration on the orientational autocorrelation of the C – H bonds of pure aPS. The symbols represent simulated data at M_w (a) 2100 g/mol (b) 5200 g/mol and (c) 31000 g/mol at 500 K. Lighter colors indicate higher gas concentration. Solid lines show extrapolation at lower and higher times with a mKWW function. In (d) the relative decrease in the decorrelation times as a function of CO_2 concentration with respect to the value of the pure polymer is reported.

Table 6.13. Best fit parameters of the mKWW equation used to represent the $P_1(t)$ of the orientational autocorrelation function of the $\mathrm{C}-\mathrm{com}_{\mathrm{Ring}}$ vectors.

M_w	$T\ (K)$	c_{CO_2} (g/g_{pol})	α_{lib}	τ_{seg} (ns)	β_{KWW}	τ_{lib} (ps)	τ_c (ns)
2100 g/mol	450	0	0.04	304.92	0.65	0.40	400.99
		0.007	0.05	303.44	0.72	0.36	356.09
		0.037	0.04	114.52	0.58	0.43	172.97
		0.069	0.04	67.66	0.54	0.38	112.97
	500	0	0.05	46.32	0.58	0.44	69.34
		0.006	0.04	39.38	0.54	0.60	66.22
		0.028	0.04	14.79	0.53	0.46	25.35
		0.050	0.05	8.80	0.57	0.45	13.54
	550	0	0.04	3.65	0.57	0.43	5.70
		0.005	0.03	3.21	0.52	0.35	5.72
		0.024	0.03	2.10	0.56	0.35	3.38
		0.041	0.04	1.55	0.57	0.35	2.39
5200 g/mol	450	0	0.03	795.30	0.60	0.35	1162.19
		0.007	0.04	757.81	0.62	0.35	1052.34
		0.037	0.03	501.48	0.57	0.35	781.79
		0.069	0.04	258.64	0.53	0.35	447.54
	500	0	0.04	170.50	0.60	0.35	247.52
		0.006	0.04	115.07	0.55	0.35	189.99
		0.028	0.04	68.56	0.57	0.35	106.96
		0.050	0.04	29.02	0.59	0.35	42.81
	550	0	0.05	17.43	0.58	0.35	26.23
		0.005	0.05	14.37	0.54	0.35	24.10
		0.024	0.04	9.38	0.53	0.35	16.50
		0.041	0.04	4.64	0.56	0.35	7.38
31000 g/mol	450	0	0.03	12479.47	0.58	0.41	19092.56
		0.007	0.03	10985.94	0.59	0.36	16273.36
		0.037	0.03	6015.50	0.52	0.35	10883.53
		0.069	0.03	1886.27	0.50	0.35	3698.80
	500	0	0.04	917.56	0.51	0.35	1714.97
		0.006	0.04	1753.90	0.54	0.35	2964.46
		0.028	0.04	1066.86	0.49	0.35	2157.88
		0.050	0.04	345.97	0.49	0.35	688.75
	550	0	0.05	168.73	0.57	0.41	263.14
		0.005	0.05	147.67	0.56	0.35	232.53
		0.024	0.04	85.97	0.45	0.35	207.29
		0.041	0.04	75.43	0.48	0.35	159.67

Table 6.14. Best fit parameters of the mKWW equation used to represent the $P_2(t)$ of the orientational autocorrelation function of the $\mathrm{C-H}$ bonds.

M_w	$T\ (K)$	c_{CO_2} (g/g_{pol})	α_{lib}	τ_{seg} (ns)	β_{KWW}	τ_{lib} (ps)	τ_c (ns)
2100 g/mol	450	0	0.26	130.42	0.50	1.63	183.99
		0.007	0.25	140.15	0.55	1.48	177.51
		0.037	0.26	38.44	0.50	1.62	57.66
		0.069	0.26	23.46	0.44	1.57	44.87
	500	0.000	0.29	15.53	0.51	1.61	21.62
		0.006	0.28	10.11	0.48	1.50	15.59
		0.028	0.28	4.66	0.46	1.36	8.05
		0.050	0.29	2.06	0.50	1.50	2.97
	550	0	0.30	1.09	0.48	1.28	1.66
		0.005	0.29	0.95	0.46	1.17	1.56
		0.024	0.29	0.62	0.49	1.21	0.92
		0.041	0.29	0.41	0.48	1.23	0.63
5200 g/mol	450	0	0.24	337.32	0.47	1.42	580.33
		0.007	0.24	296.22	0.48	1.48	477.92
		0.037	0.25	164.95	0.47	1.49	280.02
		0.069	0.25	82.00	0.45	1.60	150.58
	500	0	0.28	57.92	0.53	1.50	76.42
		0.006	0.28	40.33	0.49	1.50	60.02
		0.028	0.28	24.08	0.50	1.58	34.60
		0.050	0.29	9.95	0.53	1.67	12.89
	550	0	0.30	5.90	0.49	1.47	8.53
		0.005	0.30	5.03	0.47	1.43	7.78
		0.024	0.29	2.90	0.46	1.34	4.87
		0.041	0.28	1.37	0.45	1.16	2.40
31000 g/mol	450	0	0.23	3664.22	0.50	1.22	5721.04
		0.007	0.23	2850.16	0.48	1.24	4664.78
		0.037	0.23	1550.49	0.44	1.38	3211.86
		0.069	0.23	882.57	0.37	1.43	2732.46
	500	0.000	0.25	659.23	0.46	1.50	1163.00
		0.006	0.26	569.23	0.45	1.50	1030.03
		0.028	0.26	314.26	0.42	1.39	687.03
		0.050	0.25	115.37	0.40	1.34	294.64
	550	0	0.28	66.05	0.46	1.00	111.12
		0.005	0.29	54.44	0.45	1.30	96.69
		0.024	0.26	27.23	0.36	1.07	93.13
		0.041	0.27	22.15	0.35	1.10	78.79

By analyzing the values of the parameters extracted from fitting the orientational decorrelation function, trends in good agreement with experimental evidence were observed. In the case of the $\mathrm{C-H}$ bonds, the weighted average of backbone and phenyl bonds is considered. However, a separate analysis of the two contributions showed that bonds on the ring are endowed with faster dynamics than those on the

backbone, as it was evidenced also experimentally [31], with relaxation times 1.5 – 3 times higher, which is consistent also with the results obtained in other simulation works [96].

Both in the reorientation of phenyl rings and $\mathrm{C-H}$ bonds, the values of α_{lib} obtained are fairly independent of concentration and M_w, while they display a weak decreasing trend with decreasing temperature. The same trend with temperature was obtained also by Vogiatzis et al. [33], who simulated the local dynamics of aPS melts, both pure and in the presence of fullerene nanoparticles, using a united-atom representation. In the case of the phenyl rings, very similar values, ranging from 0.03 to 0.05 were obtained for α_{lib}, while for the $\mathrm{C-H}$ bond, the values obtained here are three times higher than those calculated by Vogiatzis et al. [33]. Comparing with the fitting parameters retrieved on the experimental curves measured by He et al. [31], it can be seen that similar values to the ones of the present work are obtained for α_{lib} (on average 0.22 in their work for a 2200 g/mol sample at different temperatures) and also for β (0.45) concerning the relaxation of $\mathrm{C-H}$ bonds. On the contrary, the values of τ_{seg} are orders of magnitude higher than the experimental ones. Values of 0.5 – 0.6 for the stretching exponent in the $\mathrm{C-com_{Ring}}$ vectors are consistent with those determined from Dielectric Spectroscopy measurements [96]. In the case of β there is no apparent dependence on concentration, T or M_w. The little variation of α_{lib} and β with temperature is a consequence of the invariance of the shape of the decorrelation curve with T. Low values of the stretching exponent, below unity, are indicative of a high degree of cooperativity in the reorientational motion in the melt [97], and indeed the values obtained for all cases are of the order of 0.5 – 0.6. τ_{seg} displays a clear exponential trend with concentration for both vectors analyzed at all temperatures and M_w, as it can be seen in **Figure 6.35** for the case of the $\mathrm{C-H}$ bonds.

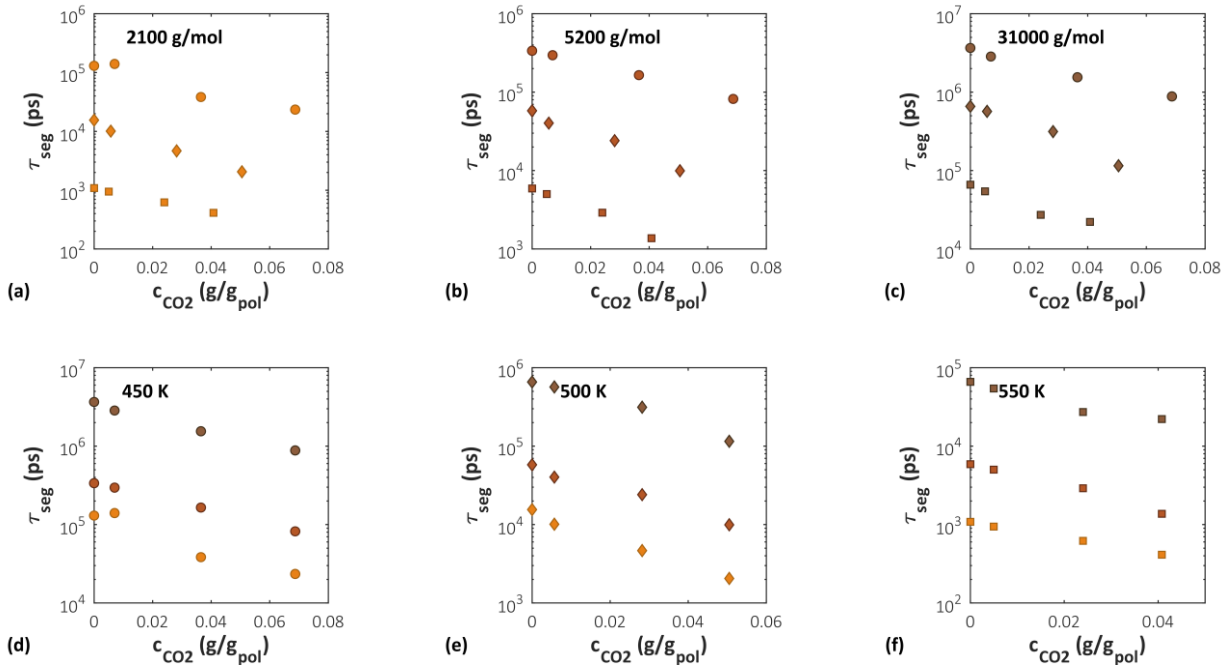

Figure 6.35. Parameter τ_{seg} of mKWW function fitted to the C-H bonds of aPS as a function of CO_2 concentration at different temperatures and molecular weights. Circles represent data at 450 K, diamonds at 500 K, squares at 550 K. Molecular weight of 2100 g/mol is depicted in **orange**, 5200 g/mol in **red** and 31000 g/mol in **brown**.

The temperature and molecular weight dependence of the relaxation times were compared with the experimental measurements performed by He et al. [31] and with the simulation results of Vogiatzis et al. [33], which are in close agreement with experimental results and therefore were considered a reliable extrapolation to higher temperatures, where experimental data were not available. The result of the comparison is shown in **Figure 6.36**. As already seen in the case of the fitting parameter τ_{seg}, also the decorrelations times obtained are orders of magnitude higher than expected. The temperature trend, however, is better captured. To make a closer comparison, in **Figure 6.37** the experimental results were arbitrarily shifted in order to superimpose the curve at 2100 g/mol with the simulation results at the same M_w. It can be noted that the three simulation sets display a similar temperature dependence, however, compared to the experimental data, the temperature dependence for the low molecular weights simulated is captured better than in the high M_w case. The relaxation times show an exponential decrease with increasing CO_2 concentration at all temperatures and M_w, as it can be seen in **Figure 6.38**.

A possible explanation of the slower dynamics exhibited in the simulation is that the adopted force field does not reproduce correctly the conformational energy barriers of aPS. However, the relative weight of the energy barriers for various bonds are represented correctly, yielding the following ordering concerning the rapidness of orientational decorrelation, from slower to faster: backbone $\mathrm{C}-\mathrm{C}$ bond, phenyl ring orientation, backbone $\mathrm{C}-\mathrm{H}$ bond, phenyl $\mathrm{C}-\mathrm{C}$ bond, average $\mathrm{C}-\mathrm{H}$ bonds, $\mathrm{C}-\mathrm{H}$ bonds on the ring. The same ordering was obtained also in other simulation works [96] and also confirmed experimentally for the vectors that could be probed. Another effect related to the slower dynamics observed in the simulations could be the higher density compared to the experimental values for the corresponding molecular weight. However, pure PS systems with comparable density, that were simulated using a different interaction potential, yielded more realistic relaxation times [31].

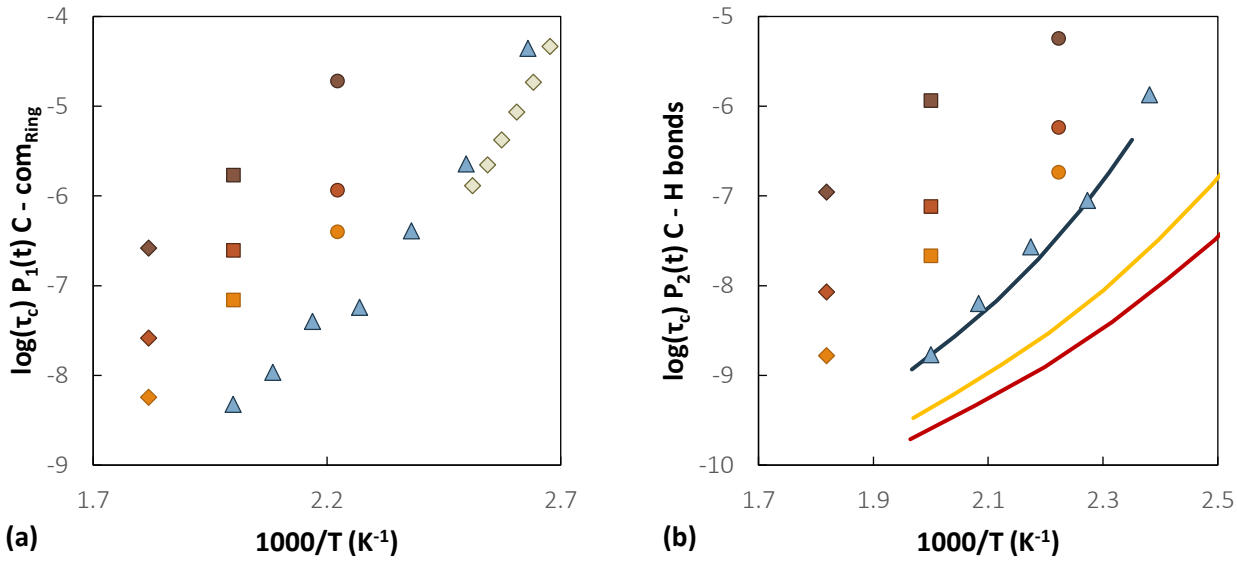

Figure 6.36. Relaxation times of (a) $\mathrm{C}-\mathrm{com}_{\mathrm{Ring}}$ vectors and (b) $\mathrm{C}-\mathrm{H}$ bonds. Circles represent data at 450 K, diamonds at 500 K, squares at 550 K. The molecular weight of 2100 g/mol is depicted in **orange**, 5200 g/mol in **red** and 31000 g/mol in **brown**. In (a) **Green** diamonds represent experimental data from [98]. In (b) Lines are NMR measurements [31]: **blue** correspond to a sample of 10900 g/mol, **yellow** to 2100 g/mol, **red** to 1600 g/mol. In both (a) and (b) blue triangles are simulation results from [33].

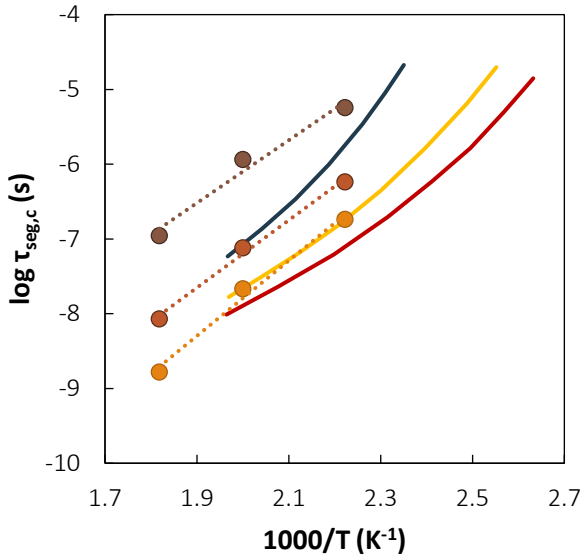

Figure 6.37. Relaxation times for pure aPS as a function of temperatures. Simulations are represented with circles: brown represents **31000 g/mol**, red is **5200 g/mol**, orange is **2100 g/mol**. Lines are NMR measurements [31], arbitrarily shifted to compare the temperature dependence. **Blue** correspond to a sample of 10900 g/mol, **yellow** 2100 g/mol, **red** 1600 g/mol.

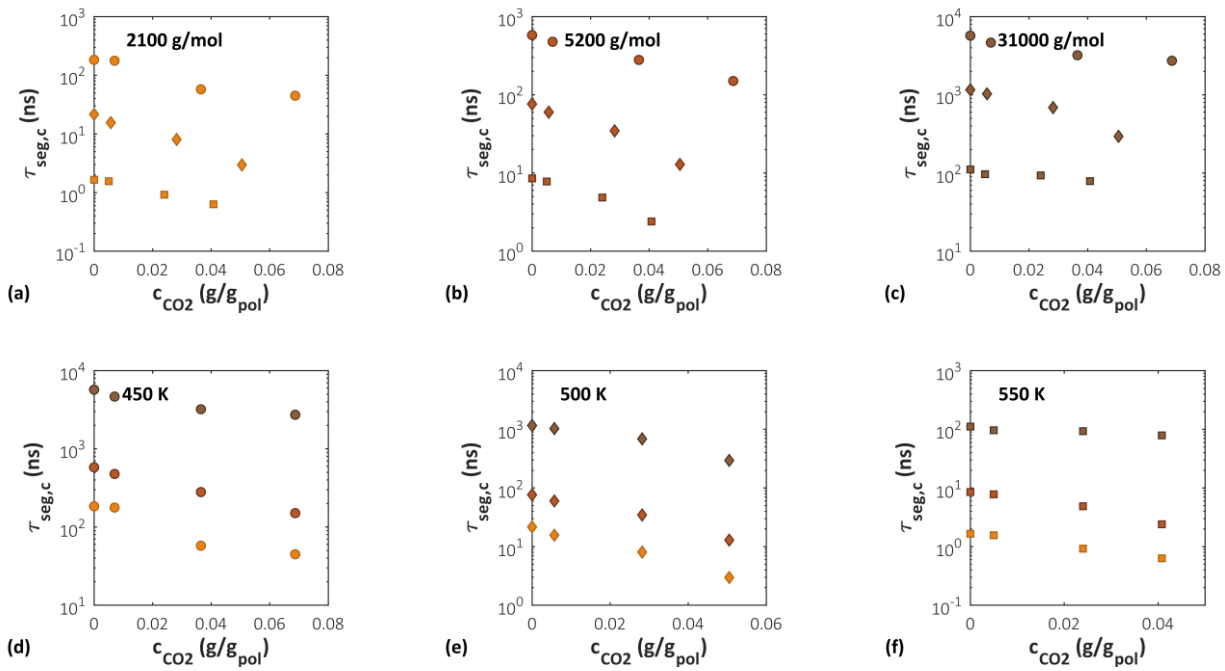

Figure 6.38. Relaxation times of the C-H bonds of aPS as a function of CO_2 concentration at different temperatures and molecular weights. Circles represent data at 450 K, diamonds at 500 K, squares at 550 K. Molecular weight of 2100 g/mol is depicted in **orange**, 5200 g/mol in **red** and 31000 g/mol in **brown**.

6.5.2 End-to-end Vector

The decorrelation of the end-to-end vector was evaluated, as a measure of chain dynamics. The results are shown in **Figure 6.39**. As it can be seen, the dynamics at the chain level is strongly dependent on the molecular weight. The higher M_w case does not show a significant decorrelation, even in 100 ns of simulation. This is an indication of the fact that the long time scales involved in the high M_w systems, even in the melt state, may not be properly sampled by MD. The effect of CO_2 concentration on the dynamics of the polymer is not only a local effect, but it affects also the overall mobility of the chain. Also in this case, the relative higher mobility induced by CO_2 is more pronounced for the low M_w system, as it can be observed in **Figure 6.39 (d)**, where the orientational decorrelation functions of the three systems at the highest CO_2 concentrations have been normalized using the corresponding pure polymer curve. This can be a consequence of the different swelling experienced by the different systems at the same value of CO_2 concentration: the low M_w systems was swollen more and its chain dynamics results enhanced to a greater extent.

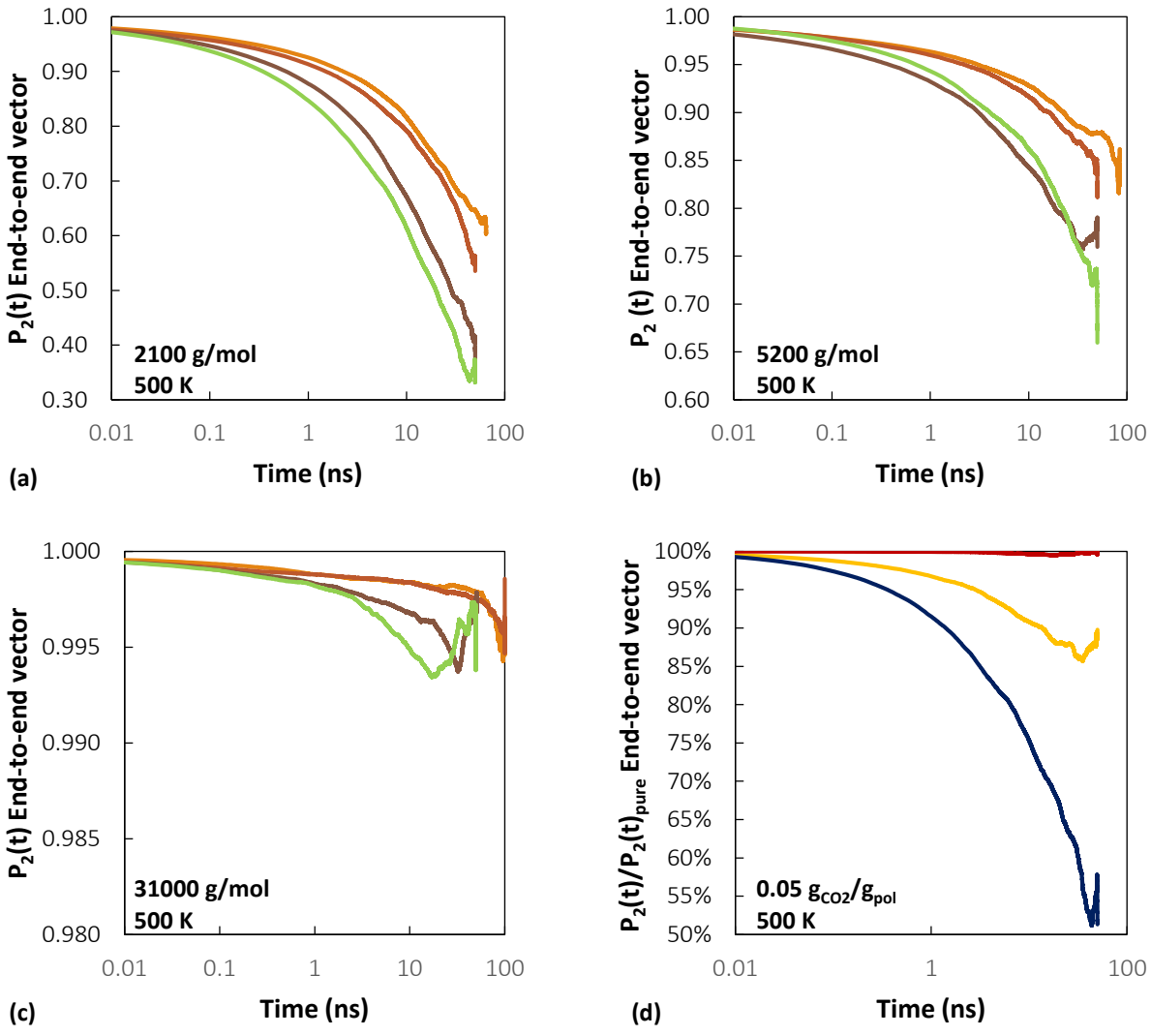

Figure 6.39. Effect of CO_2 concentration on end-to-end vector reorientation at 500 K and at different molecular weights. **Orange** represent results for the pure polymer, **red** 5.70 · 10^{-3} g_{CO2}/g_{pol}, **brown** 2.82 · 10^{-2} g_{CO2}/g_{pol}, **green** 5.05 · 10^{-2} g_{CO2}/g_{pol}. In subplot (d) **blue** represents the 2100 g/mol system, **yellow** represents the 5200 g/mol system, **red** represents the 31000 g/mol system.

6.5.3 Dynamics of Different Chain Segments

The plasticizing effect of CO_2 was probed at different positions along the chain, in order to assess if it affected more pronouncedly the chain towards the ends compared to the center, and how this effect is displayed at different molecular weights. As a test case, the second order Legendre polynomial of the C–H bond on the rings (C_{ar} – H_{ar}) was considered at 500 K. The chains were split in 10 subsections from the chain ends up to the center and the orientational decorrelation of the bonds belonging to each subsection was evaluated as a function of CO_2 concentration. **Table 6.15** reports how the repeating units in chains of different M_w were divided. Within a subsection, the bonds belonging to different repeating units displayed relaxation times less than 10% apart. $P_2(t)$ functions were fit with the mKWW function and thus extrapolated to longer times than those simulated. From the integral of the mKWW relaxation times were calculated. The results are reported in **Table 6.16**. In **Figure 6.40 (a)**, **(c)** and **(e)**, the orientational decorrelation of the C_{ar} – H_{ar} bonds in the chain ends (first repeating unit displayed in green, second repeating unit displayed in orange) and in the central portion of the chain (displayed in blue) is shown as a function of increasing CO_2 concentration. **Figure 6.40 (b)**, **(d)** and **(f)** show the relaxation times in all the ten subsections as a function of increasing CO_2 concentration for the different M_w of the polymer chains.

Table 6.15. Scheme of the subdivision of the chains and assignment of repeating unit to different subsections.

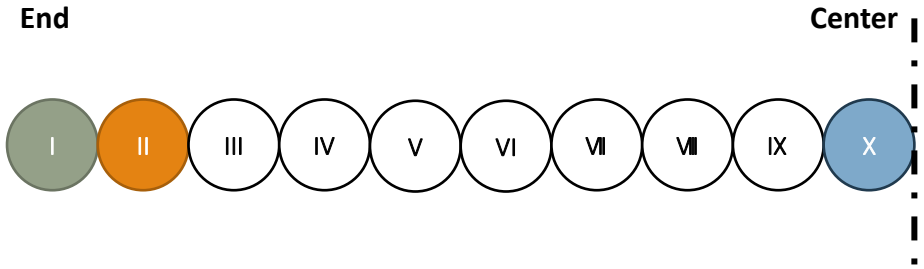

	Repeating units included in each subsection									
M_w	**I**	**II**	**III**	**IV**	**V**	**VI**	**VII**	**VIII**	**IX**	**X**
2100 g/mol	1	2	3	4	5	6	7	8	9	10
5200 g/mol	1	2	3-4	5-7	8-10	11-13	14-16	17-19	20-22	23-25
31000 g/mol	1	2	3-10	11-30	31-50	51-70	71-90	91-110	111-130	131-150

Chain-end effects are generally concentrated only to the three terminal subunits considered, with the rest of the chain behaving similarly. Indeed, the first and second repeating units display significantly higher mobility at all M_w, whereas towards the center of the chain the relaxation times tend to a plateau value. The same trend is observed at all M_w. Increasing CO_2 concentration in the system does not seem to affect the scope of chain end effects. The presence of the gas leads to a systematic acceleration of the dynamics, to a comparable extent in all subunits considered, not limitedly to the chain ends. This can be immediately

visualized in **Figure 6.41 (b)**, **(d)**, **(f)**. In the figure, the relative difference of the relaxation times between the pure polymer and the different gas-polymer cases are plotted for all subunits. It can be seen that, even though in some of the cases the chain ends experience a slightly higher acceleration compared to central sections of the chain, the effect is limited, especially in the cases of higher CO_2 concentration, and not systematic. It should be noted that the results for the higher CO_2 concentration are endowed with higher accuracy, because the higher mobility results in a greater decorrelation during the time of the simulation, reducing the uncertainty in the fitting procedure and in the relaxation times calculated.

Table 6.16. Relaxation times of C_{ar} – H_{ar} bond located in different chain segments.

	Subsection	**I**	**II**	**III**	**IV**	**V**	**VI**	**VII**	**VIII**	**IX**	**X**
M_w (g/mol)	**c_{CO2} (g_{CO2}/g_{pol})**	**Relaxation time (ns)**									
2100	0	3.0	7.0	10.9	13.7	14.5	18.2	20.6	20.3	20.9	22.9
	0.006	1.5	4.1	6.9	10.3	11.9	14.0	14.7	13.9	16.1	16.2
	0.028	0.9	2.4	4.0	5.0	6.4	7.4	8.6	9.0	9.3	9.4
	0.050	0.4	1.2	2.0	2.4	2.9	3.6	3.7	3.8	3.8	4.1
5200	0	12.7	30.0	57.3	71.9	72.1	73.6	74.7	86.0	86.2	86.7
	0.006	4.8	11.2	20.3	30.6	33.2	35.1	36.8	47.1	50.6	59.2
	0.028	2.6	7.0	13.3	18.1	24.7	26.6	31.4	33.8	33.0	34.8
	0.050	1.1	3.2	8.3	14.5	14.8	14.9	13.1	15.3	14.2	15.9
31000	0	38.4	300.1	885	948	959	1068	1112	1083	1191	1230
	0.006	11.4	284.3	876.3	889.5	827.0	878.7	908.8	915.0	909.7	933.2
	0.028	9.5	183.2	513.1	646.2	598.1	630.4	668.6	661.8	618.1	678.3
	0.050	3.1	50.9	189.9	219.3	200.3	201.3	229.7	234.6	261.0	263.2

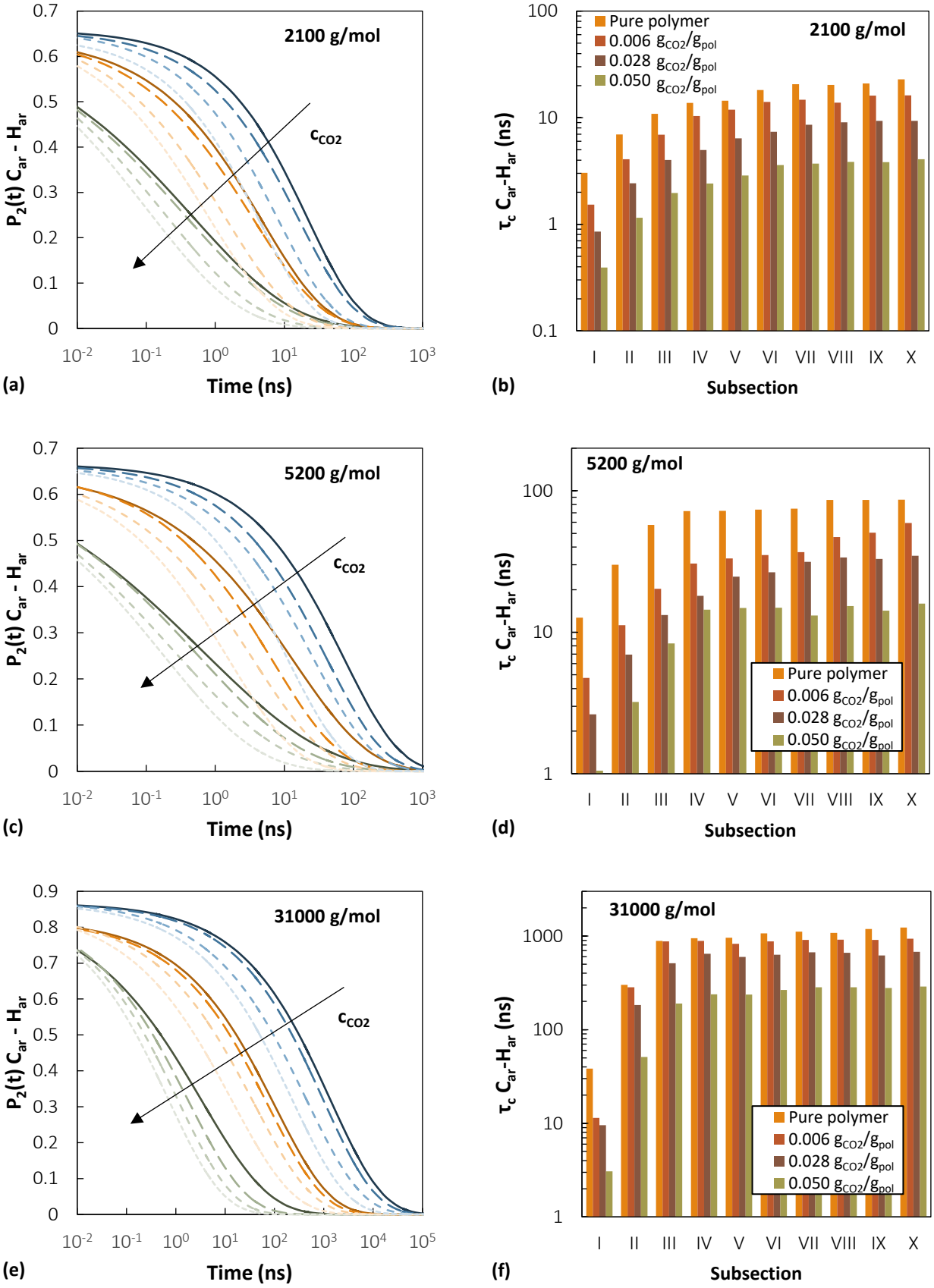

Figure 6.40. Effect of CO_2 concentration on the reorientational decorrelation of C_{ar} – H_{ar} bonds in different chain subsections, for the three different polymer M_w at 500 K. **Table 6.15** reports how the repeating units in chain of different M_w were divided. In plots (a), (c), (e) green represents the chain end, orange the second repeating unit starting from the chain end, and blue is the central section of the chain. Lighter shades and shorter dashes represent higher CO_2 concentration.

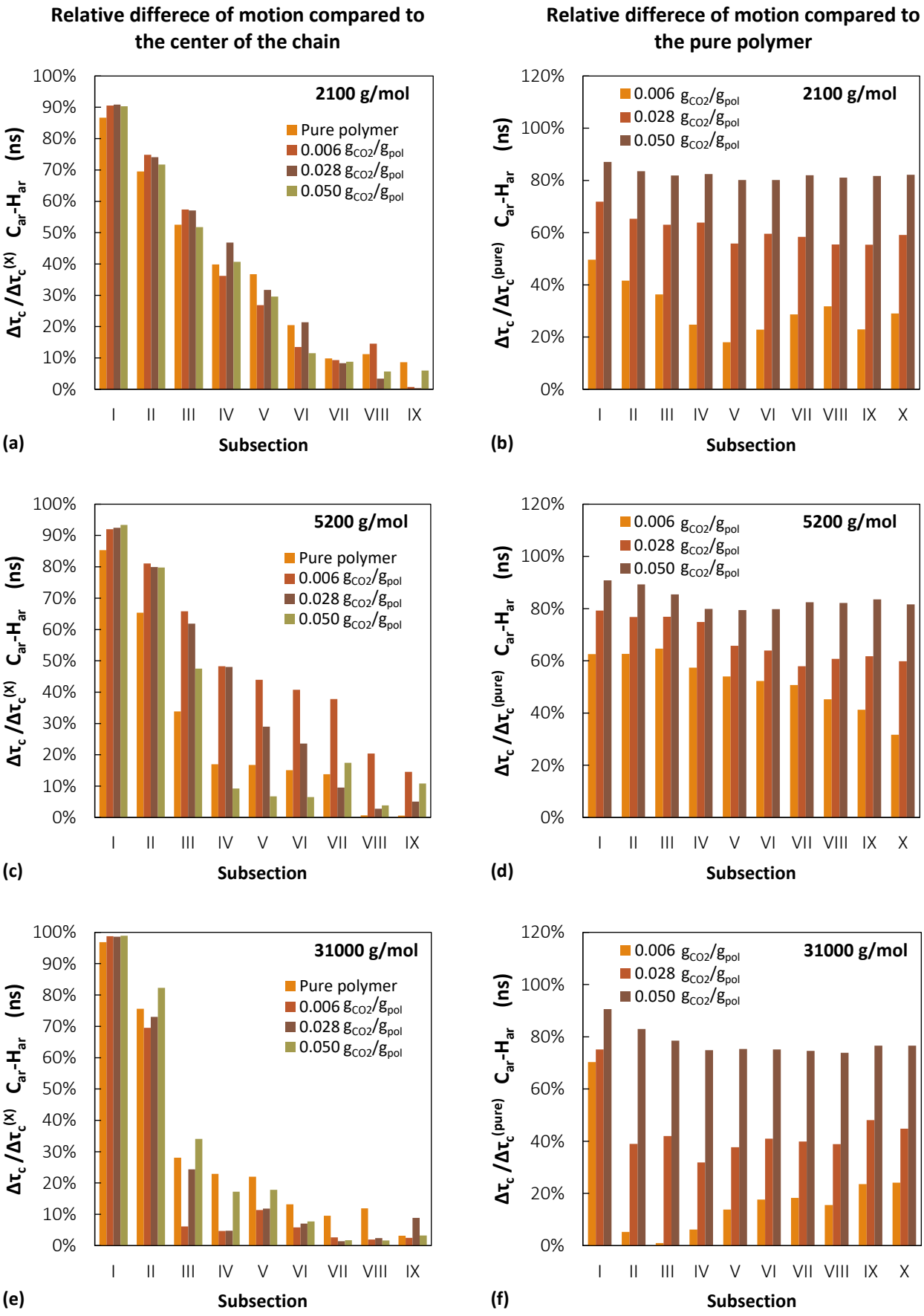

Figure 6.41. Relative difference between the relaxation times of different chain subsections and the center of the chain (a,b,e) or the corresponding subunit in the pure polymer case (b,d,f).

6.6 Solubility

6.6.1 Henry's Law Constant

Widom's test particle insertion test was performed on the pure polymer systems and the calculated values for the excess chemical potential were used to evaluate the Henry's law constant with **Eq. (6.5)**. In **Figure 6.42**, they are compared against experimental values reported by Durill et al. [99] and Sato et al. [25] (previous results from Sato et al. [23] are in very good agreement with the measurements in their subsequent work, therefore, only one data set is included in the plot). In addition, results obtained with the Sanchez-Lacombe EoS are shown. They were calculated using the following expression of the model for the infinite dilution solubility coefficient for a two components system, S^0. Based on the definition given in **Eq. (6.5)**, this corresponds to the inverse of the Henry's law constants obtained in the simulations.

$$\ln S^0 = \ln\left(\frac{T_{STP}}{p_{STP}T}\right) + r_i^0\left\{\left[1+\left(\frac{v_1^*}{v_2^*}-1\right)\frac{\rho_1^*}{\rho_1^0}\right]\ln\left(1-\frac{\rho_1^0}{\rho_1^*}\right)+\left(\frac{v_1^*}{v_2^*}-1\right)+\frac{\rho_1^0}{\rho_1^*}\frac{T_1^*}{T}\frac{2}{p_1^*}(1-k_{12})\sqrt{p_1^*p_2^*}\right\} \qquad \text{Eq. (6.20)}$$

All symbols pertaining to the Sanchez-Lacombe EoS are defined in **Chapter 2**. From the comparison of the different data sets, it emerges that, in the temperature range where both experiments and simulations were performed, the simulated values are approximately a factor 2 higher than the results by Sato et al. [25]. The deviation is a result of an underestimate of the excess chemical potential. At 500 K, a value of $\mu_{CO_2}^{ex}$ = 3.8 kJ/mol was obtained for the low M_w system, 3.4 kJ/mol for the intermediate M_w and 3.1 kJ/mol for the high M_w system. These values are about 3 – 4 times lower than the value of 11.77 kJ/mol reported by Eslami et al. for CO_2 sorption in polystyrene at the same temperature. The results obtained with the SL equation of state, using the k_{ij} values calculated with **Eq. (6.9)** show a significantly weaker M_w dependence compared to the simulation results.

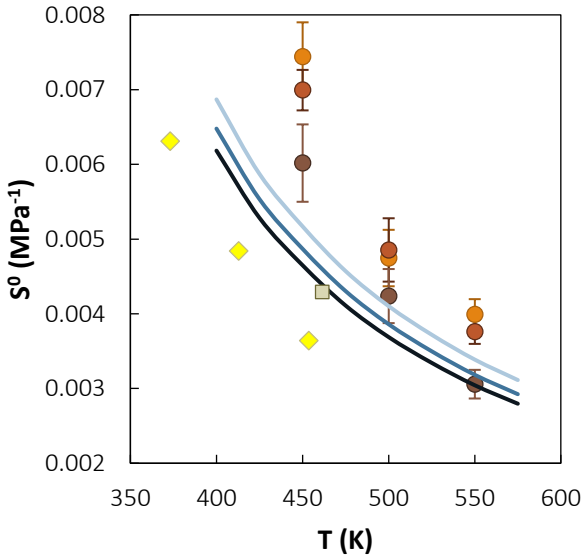

Figure 6.42. Calculated infinite dilution solubility coefficients for CO_2 solubility in atactic polystyrene in the infinite dilution regime, compared to experimental values of Durrill et al. [99] (green square) and Sato et al. [25] (yellow diamonds). Circles represent the simulated values of the inverse of the henry's law constants defined in **Eq. (6.5)**: molecular weight of 2100 g/mol is depicted in **orange**, 5200 g/mol in **red** and 31000 g/mol in **brown**. Values calculated with the SL EoS are shown with solid lines: **light blue** at 2100 g/mol, **blue** at 3200 g/mol and **dark blue** at 31200 g/mol.

6.6.2 Enthalpy of Sorption

From the slope of an Arrhenius plot of $\ln(S^0)\ vs.\ 1/T$ it is possible to evaluate the enthalpy of sorption. The result obtained for the experimental data of Sato et al. [25] is 9.6 kJ/mol. For the simulated systems a linear trend is obtained for $\ln(S^0)\ vs.\ 1/T$ in the case of the high M_w system, for which a value of 13.9 kJ/mol was obtained. Simulated data at 2100 g/mol and 5200 g/mol are more scattered, but by linear interpolation values of 13 kJ/mol and 12.8 kJ/mol were obtained respectively for the enthalpy of sorption of the low and intermediate M_w. The values calculated with the Sanchez-Lacombe EoS using k_{ij} with a linear temperature dependence deviate from the linear trend at high temperature, whereas, if the k_{ij} values calculated with **Eq. (6.9)** are used, the trend is linear in the whole temperature range. This finding would suggest that the extrapolation of the values of k_{ij} to higher temperatures using a linear relation might be inaccurate, and therefore it was abandoned. A value of 8.6 kJ/mol is obtained for the enthalpy of sorption at all molecular weights, which is in good agreement with the experimental value. Even though both the simulations and the SL EoS overestimate the value of the solubility coefficients in the zero-pressure limit, the EoS captures the temperature dependence slightly more accurately. Nonetheless, it must be noticed that simulations are characterized by a higher predictive power with respect to an Equation of State. Firstly, because they are not obtained through the use of empirical adjustable parameters. Secondly, the strength of a molecular approach is that the same model and molecular representation allow to predict not only macroscopic thermodynamic quantities like density, swelling, sorption, as in the case of the EoS, but also dynamic quantities, like the diffusivity, reported hereafter, and structural features like the X-ray structure factor and RDFs.

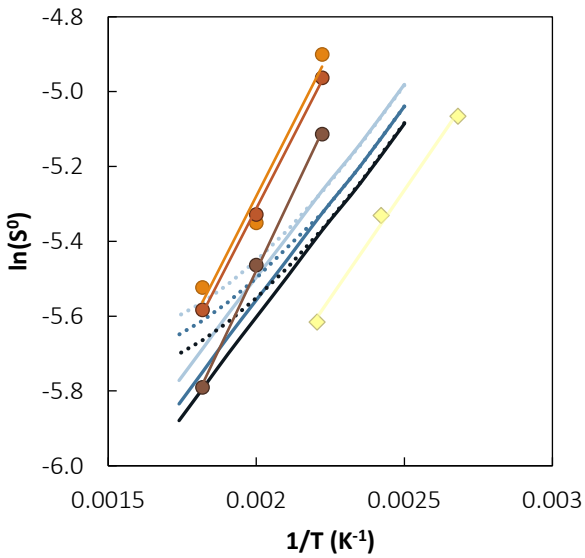

Figure 6.43. Arrhenius plot for the infinite dilution solubility coefficient for the evaluation of the enthalpy of sorption. Circles represent the simulated values of the inverse of the henry's law constant defined in **Eq. (6.5)**: molecular weight of 2100 g/mol is depicted in **orange**, 5200 g/mol in **red** and 31000 g/mol in **brown**. Values calculated with the SL EoS are shown with lines: **light blue** at 2100 g/mol, **blue** at 3200 g/mol and **dark blue** at 31200 g/mol. Solid lines re obtained with k_{ij} values calculated using **Eq. (6.9)**, dotted lines with k_{ij} values calculated using **Eq. (6.8)**. Yellow diamonds are the experimental data of Sato et al. [25].

6.6.3 CO_2 Sorption Isotherms

Using the iterative procedure described in **Section 6.2.5**, the equilibrium pressures corresponding to the value of CO_2 concentration in each system were determined. The results are reported in **Figure 6.44**. A consistent set of results was obtained, with solubility values decreasing with increasing temperature and M_w. The trend of all sorption isotherms is rather linear, as expected for sorption of light gases in rubbery polymers [76]. The error bars in **Figure 6.44** were obtained with the block average method.

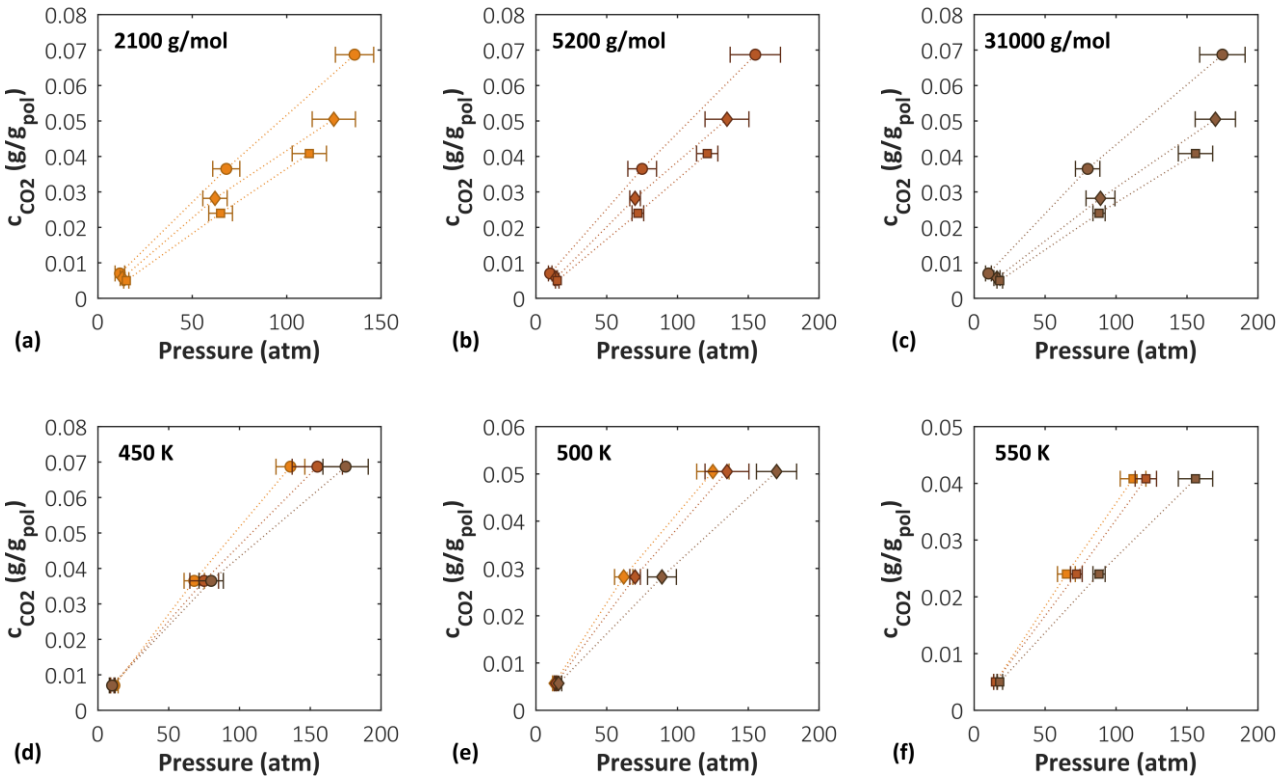

Figure 6.44. Simulated CO_2 sorption isotherms in atactic polystyrene at different temperatures and polymer molecular weight. Plots (a), (b) and (c) show the effect of temperature at fixed molecular weight, plots (e), (f) and (g) show the effect of molecular weight at fixed temperature. Circles represent data at 450 K, diamonds at 500 K, squares at 550 K. Molecular weight of 2100 g/mol is depicted in **orange**, 5200 g/mol in **red** and 31000 g/mol in **brown**.

In **Figure 6.45**, the simulated data at the highest M_w at 450 K and 500 K are compared with experimental values of Sato et al. [25] at 423 K and 473 K (blue squares). The experimental sample had a M_w of 330000 g/mol. Green circles are data from [23] for a sample of M_w of 187000 g/mol at 453 K. As it can be seen, the simulated curves overlap with experimental data at a temperature lower by 27 °C, indicating that the simulations overestimate the solubility. However, by taking into account also the variability in experimental data, apparent in the comparison between the green and blue curves in **Figure 6.45**, the simulation predictions can be considered very satisfactory.

Toi and Paul [6] evaluated the effect of M_w in the sorption isotherms for CO_2 in glassy polystyrene at different molecular weights ranging from 3600 to 850000 g/mol. Contrarily to what was found in this work

for the melt state, in the glassy state the extent of sorption increased as the molecular weight increased, due to the higher fraction of excess free volume present in high M_w systems compared to low M_w ones. In the glass, this effect outweighs the increase in free volume associated with a higher number of chain ends, leading to the observed trend. In the melt state, the unrelaxed excess free volume is not present and the increasing solubility with decreasing M_w is associated to a higher number of chain ends, that are responsible for a lower density of the matrix.

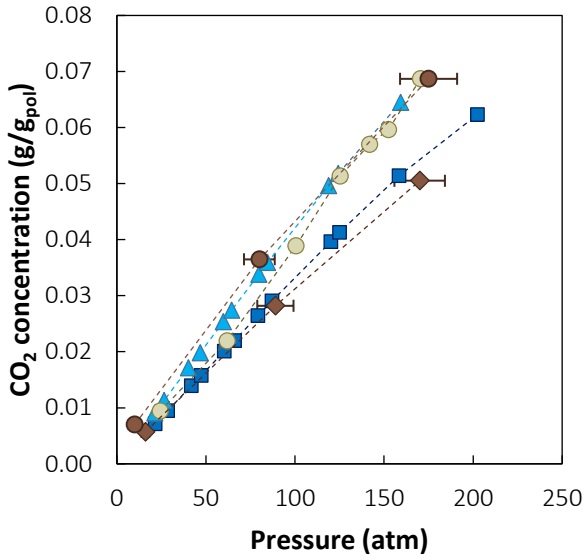

Figure 6.45. Comparison between the sorption isotherms simulated at the highest molecular weight (31000 g/mol) at 450 K (brown circles) and 500 K (brown diamonds) and the experimental data of Sato et al. [25] at 423 K (blue triangles) and 473 K (blue squares). Green circles are data measured by the same group at 453 K [23].

In **Figure 6.46** the simulation results are compared with the predictions of the Sanchez Lacombe EoS. The EoS results would suggest a lower M_w dependence at high pressure, especially at 500 K and 550 K compared to the simulated results. At higher pressure the difference between the density predicted by the simulations and calculated with the equation of state is higher. However, the high M_w system generally displays lower solubility compared to the EoS results, consistently with the fact that the simulations predict higher density of the system. However, the low and intermediate M_w system, display comparable or even higher solubility, despite the fact that they are also denser.

The EoS results are quite sensitive to the values of k_{ij} used. In **Figure 6.46 (d)** the results obtained using the k_{ij} values calculated with **Eq. (6.8)** (linear temperature dependence) at 550 K are shown. A 15% difference is caused by the change of k_{ij} from the value –0.080 to –0.055 at all three molecular weights.

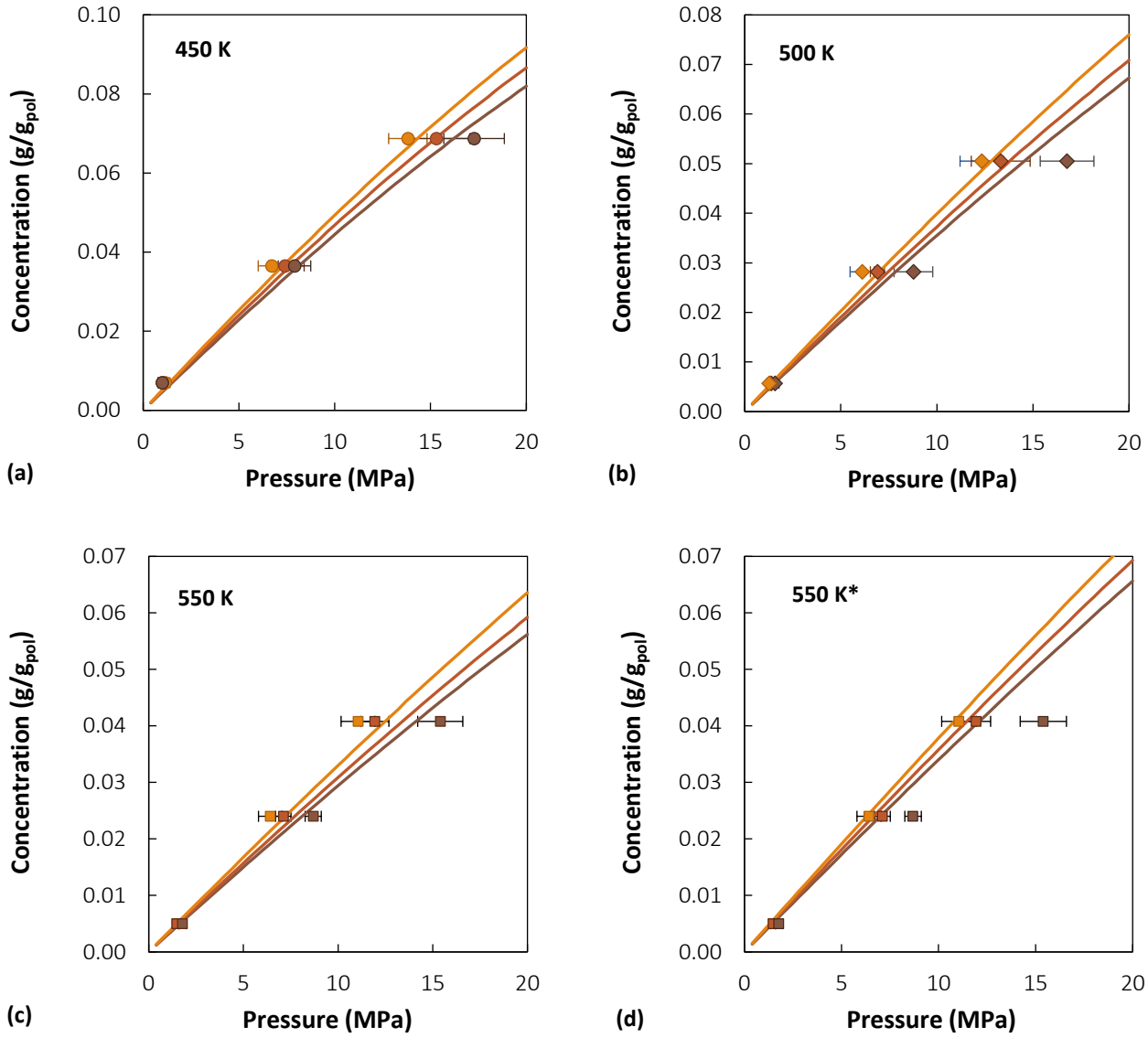

Figure 6.46. Comparison between simulated sorption isotherms and the results obtained with the Sanchez-Lacombe EoS (solid lines). Circles represent simulated data at 450 K, diamonds at 500 K, squares at 550 K. Molecular weight of 2100 g/mol is depicted in **orange**, 5200 g/mol in **red** and 31000 g/mol in **brown**. *Figure (d) shows the results obtained using the k_{ij} values calculated using **Eq. (6.8)**.

6.7 Diffusivity

The mean squared displacement (MSD) of CO_2 molecules during the NVE trajectories was evaluated, averaging over multiple time origins:

$$MSD = \langle (R_i(t) - R_i(0))^2 \rangle \qquad \text{Eq. (6.21)}$$

$R_i(t)$ is the position of the center of mass of a CO_2 molecule at time t and $R_i(0)$ was its position at the initial time. MSD is related to the diffusion coefficient through the Einstein relation:

$$D_i = \lim_{t \to \infty} \frac{\langle (R_i(t) - R_i(0))^2 \rangle}{2dt} \qquad \text{Eq. (6.22)}$$

In the previous relation d is the dimensionality of the system, 3 in the present case. The logarithm of MSD was plotted against the logarithm of time, to identify the Einstein diffusion regime region, characterized of a slope equal to 1 of $\log(MSD)$ *vs.* $\log(t)$ (**Figure 6.47 (b)**): the slope of MSD vs. t in this region is equal to $6D_i$ for diffusion in three dimensions. It was verified that diffusion is isotropic, with components on the three axial directions of similar value similar and approximately 1/3 of magnitude of the overall displacement r^2, while the cross components are oscillating around zero, as it can be seen in **Figure 6.47 (b)** for the case of 0.07 g_{CO2}/g_{pol} in the 2100 g/mol polymeric system at 500 K.

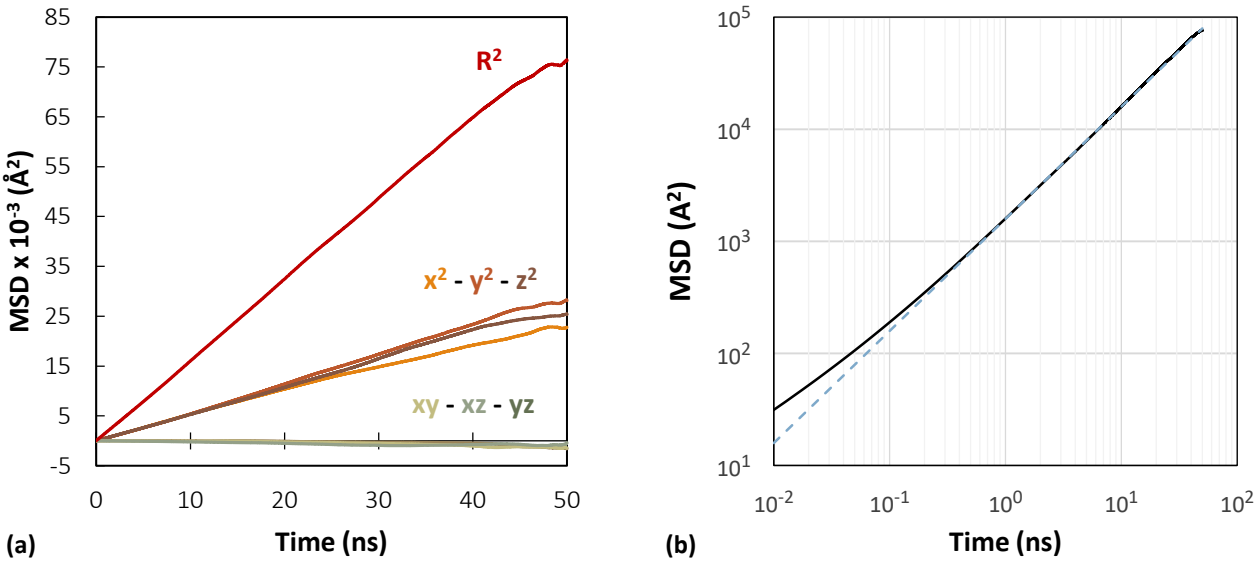

Figure 6.47. Mean square displacement of CO_2 molecules in the case of 0.07 g_{CO2}/g_{pol} in the 2100 g/mol polymeric system at 500 K. (a) Comparison of displacement in the axial directions ($x^2 - y^2 - z^2$), cross components ($xy - xz - yz$), and overall displacement (R^2). (b) Visualization of the Einstein regime region of the simulation (the dotted line corresponds to a slope equal to unity).

Self-diffusivities are a good approximation of binary diffusivities in case of infinitely diluted system. Since in the present study higher concentration values were considered, binary diffusion coefficients were calculated from the values of the self-diffusivities of CO_2 [97]:

$$D_i \simeq \left(\frac{\partial \ln f_i}{\partial \ln c_i}\right)_{T,P} D_{i,self} \qquad \text{Eq. (6.23)}$$

In the previous relation it is assumed that the polymer diffusivity is negligible in comparison to that of the gas. At the lower and intermediate temperatures, the Fickian diffusion regime was not reached by the polymer during the simulation, therefore the calculation of polymer diffusivities is not warranted. On the other hand, such evaluation was possible at the highest temperature, and it was indeed verified that the polymer diffusivities were 3, 4 and 6 orders of magnitude lower than those of the gas for the cases of M_w 2100 g/mol, 5200 g/mol and 31200 g/mol respectively. Since the sorption isotherms have a linear shape, the correction introduced by the thermodynamic factor in **Eq. (6.23)** is small: it is lower than 10% in all cases, except at 450 K, where it is 18% for the 5200 g/mol case and 24% in the 31200 g/mol case.

Figure 6.48 shows the calculated binary diffusion coefficients as a function of gas concentration, at different temperatures and molecular weights. An exponential trend with concentration is found at all conditions with comparable slopes in the systems of different M_w at the same temperature. Diffusivity consistently increases with increasing temperature and decreasing M_w.

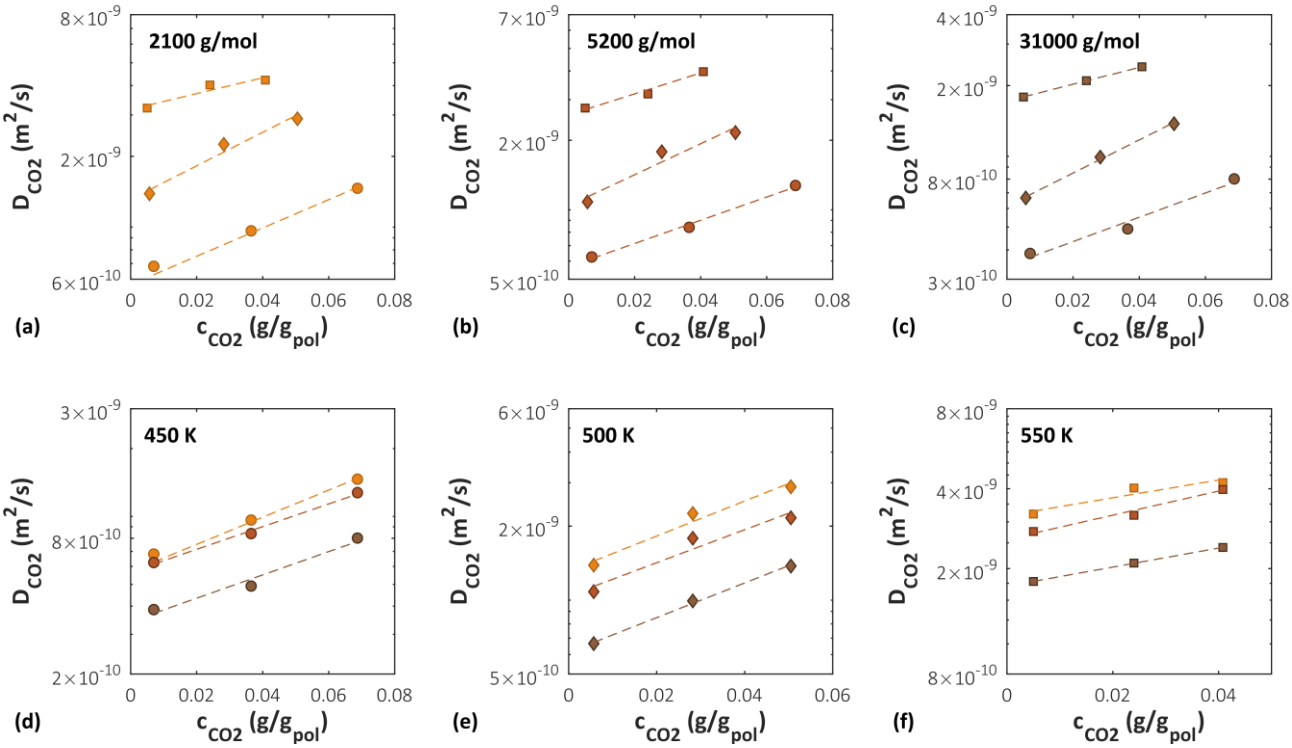

Figure 6.48. CO_2 diffusion coefficients in atactic polystyrene as a function of concentration, at different temperatures and polymer molecular weight. Plots (a), (b) and (c) show the effect of temperature at fixed molecular weight, plots (e), (f) and (g) show the effect of molecular weight at fixed temperature. Circles represent data at 450 K, diamonds at 500 K, squares at 550 K. Molecular weight of 2100 g/mol is depicted in **orange**, 5200 g/mol in **red** and 31000 g/mol in **brown**.

Figure 6.49 shows the comparison with experimental data. The three data sets used for comparison are for high M_w PS samples at two different temperatures, 423 K and 473 K in [22] and [25] and 438 K and 473 K in [26]. Therefore, there is approximately the same temperature difference between the two series and the simulated data presented for the case 450 K and 500 K for all M_w. Indeed, the difference between data at two temperatures is consistent between simulations and experiments. Simulation results are in the same order of magnitude of the experimental data, located in between the different sets: they are lower than the diffusivity values determined by Areerat et al. [22] (blue symbols in **Figure 6.49**), but comparable to those of Sato et al. [100]. The comparison is also satisfactory with older data measured by Newitt at al. [20] (grey crosses in the Figure). Taking into account also the considerable scattering of the experimental data at the same temperature, the agreement of the simulated results is satisfactory.

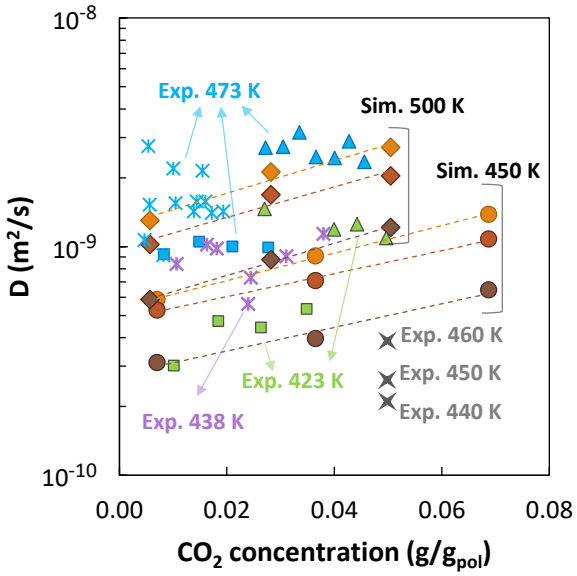

Figure 6.49. Comparison between experimental and simulated CO_2 diffusion coefficients in atactic polystyrene as a function of concentration, at different temperatures and polymer molecular weight. Circles represent simulated data at 450 K, diamonds at 500 K. Molecular weight of 2100 g/mol is depicted in **orange**, 5200 g/mol in **red** and 31000 g/mol in **brown**. Squares are data from ref.[25] (blue 473 K green, M_w of 330000 g/mol), triangles from ref.[22] (blue, M_w of 250000 g/mol) and circles from ref.[26] (M_w of 168000 g/mol). Blue represents data at 473 K, green at 423 K, purple at 438 K. Grey crosses are data from Newitt et al. [20].

6.8 Conclusions

Molecular simulation is a powerful tool to investigate the thermodynamic structural, dynamical and transport properties of dense amorphous polymers. In this study, molecular simulations were applied to the study of a polymeric system containing a plasticizing agent. Fully atomistic configurations of atactic polystyrene were generated and equilibrated up to high molecular weights, through a multiscale equilibration procedure for the case of the systems at the highest molecular weight. A systematic analysis of temperature, molecular weight and gas concentration effects on several properties of the system was presented and the calculated properties were compared against available experimental data and the Sanchez-Lacombe EoS, which was purposely re-parametrized to capture the molecular wight dependence of the macroscopic properties more accurately. The density of the system was slightly overestimated in the simulations at all M_w, however, the temperature dependence and chain dimension were in good agreement with experimental measurements. The local structural characteristics of the simulated systems were found to be in very close agreement with the experimental results and the contributions of different segments of the chain to the structural features provided a detailed interpretation of their origin. In the case of gas-polymer systems, it was found that CO_2 affects interchain packing more significantly than the average chain dimensions.

The interaction potential resulted in slower segmental dynamics, compared to experiments, but consistent and meaningful trends with respect to the variables considered were calculated. The local dynamics of the matrix is faster at higher gas concentration, which is a manifestation of the plasticization effect induced by the presence of CO_2 and the more mobile system at lower M_w is affected to a greater extent. The plasticizing effect of CO_2 is of comparable strength along the whole chain, and not limited to the chain ends.

The agreement between diffusion coefficients obtained from the mean squared displacement of CO_2 molecules and experimental results was good, also in terms of temperature and concentration dependence. Therefore, the ability to give a close representation of the structure was sufficient to obtain a reliable estimate of gas diffusivity, even though characteristic times of the polymer dynamics were overestimated.

The iterative scheme adopted for the calculation of solubility allowed the prediction of sorption isotherms up to high pressures, difficult to reach experimentally, with rapid convergence. Moreover, it enabled the study of the penetrant induced swelling as a function of concentration.

A wealth of detailed information on the microscopic characteristics and on the macroscopic behaviour of a system can be extracted by the implementation of molecular modelling methods. The application of these methods to gas-polymer properties prediction and the elucidation of the underlying molecular mechanisms is very appealing for the design of efficient membrane separations and barrier materials for packaging, as well as in supercritical CO_2 processes.

References

1. Green, D.W.; Southard, M.Z. *Perry's Chimical Engineers' Handbook*; Ninth Edit.; McGraw-Hill Education, 2019;

2. Tomasko, D.L.; Li, H.; Liu, D.; Han, X.; Wingert, M.J.; Lee, L.J.; Koelling, K.W. A Review of CO_2 Applications in the Processing of Polymers. *Ind. Eng. Chem. Res.* 2003, *42*, 6431–6456, doi:10.1021/ie030199z.

3. Chiou, J.S.; Barlow, J.W.; Paul, D.R. Plasticization of glassy polymers by CO_2. *J. Appl. Polym. Sci.* 1985, *30*, 2633–2642, doi:10.1002/app.1985.070300626.

4. Wissinger, R.G.; Paulaitis, M.E. Glass transitions in polymer/CO_2 mixtures at elevated pressures. *J. Polym. Sci. Part B Polym. Phys.* 1991, *29*, 631–633, doi:10.1002/polb.1991.090290513.

5. Wang, W.-C. V.; Kramer, E.J.; Sachse, W.H. Effects of high-pressure CO_2 on the glass transition temperature and mechanical properties of polystyrene. *J. Polym. Sci. Polym. Phys. Ed.* 1982, *20*, 1371–1384, doi:10.1002/pol.1982.180200804.

6. Toi, K.; Paul, D.R. Effect of polystyrene molecular weight on the carbon dioxide sorption isotherm. *Macromolecules* 1982, *15*, 1104–1107, doi:10.1021/ma00232a028.

7. Carfagna, C.; Nicodemo, L.; Nicolais, L.; Campanile, G. CO_2 sorption in uniaxially drawn atactic polystyrene. *J. Polym. Sci. Part B Polym. Phys.* 1986, *24*, 1805–1812, doi:10.1002/polb.1986.090240815.

8. Wissinger, R.G.; Paulaitis, M.E. Swelling and sorption in polymer–CO_2 mixtures at elevated pressures. *J. Polym. Sci. Part B Polym. Phys.* 1987, *25*, 2497–2510, doi:10.1002/polb.1987.090251206.

9. Aubert, J.H. Solubility of carbon dioxide in polymers by the quartz crystal microbalance technique. *J. Supercrit. Fluids* 1998, *11*, 163–172, doi:10.1016/S0896-8446(97)00033-8.

10. Conforti, R.M.; Barbari, T. a; Pozo de Fernandes, M.E. Enthalpy of Mixing for a Glassy Polymer Blend from CO_2 Sorption and Dilation Measurements. *Macromolecules* 1996, *29*, 6629–6633, doi:10.1021/ma951838n.

11. Conforti, R.M.; Barbari, T.A.; Vimalchand, P.; Donohue, M.D. A Lattice-Based Activity Coefficient Model for Gas Sorption in Glassy Polymers. *Macromolecules* 1991, *24*, 3388–3394, doi:10.1021/ma00011a054.

12. Barbari, T.A.; Conforti, R.M. The effect of lattice compressibility on the thermodynamics of gas sorption in polymers. *J. Polym. Sci. Part B Polym. Phys.* 1992, *30*, 1261–1271.

13. Kato, S.; Tsujita, Y.; Yoshimizu, H.; Kinoshita, T.; Higgins, J.S. Characterization and CO_2 sorption behaviour of polystyrene/polycarbonate blend system. *Polymer (Guildf).* 1997, *38*, 2807–2811.

14. Zhang, Y.; Gangwani, K.K.; Lemert, R.M. Sorption and swelling of block copolymers in the presence of supercritical fluid carbon dioxide. *J. Supercrit. Fluids* 1997, *11*, 115–134, doi:10.1016/S0896-8446(97)00031-4.

15. Shieh, Y.T.; Liu, K.H. The effect of carbonyl group on sorption of CO_2 in glassy polymers. *J. Supercrit. Fluids* 2003, *25*, 261–268, doi:10.1016/S0896-8446(02)00145-6.

16. Pantoula, M.; Panayiotou, C. Sorption and swelling in glassy polymer/carbon dioxide systems. Part I-Sorption. *J. Supercrit. Fluids* 2006, *37*, 254–262, doi:10.1016/j.supflu.2006.03.010.

17. Pantoula, M.; von Schnitzler, J.; Eggers, R.; Panayiotou, C. Sorption and swelling in glassy polymer/carbon dioxide systems: Part II—Swelling. *J. Supercrit. Fluids* 2007, *39*, 426–434, doi:10.1016/j.supflu.2006.03.010.

18. Panayiotou, C.; Pantoula, M.; Stefanis, E.; Tsivintzelis, I.; Economou, I.G. Nonrandom hydrogen-bonding model of fluids and their Mixtures. 1. Pure fluids. *Ind. Eng. Chem. Res.* 2004, *43*, 6592–6606.

19. Panayiotou, C.; Tsivintzelis, I.; Economou, I.G. Nonrandom hydrogen-bonding model of fluids and their mixtures. 2. Multicomponent mixtures. *Ind. Eng. Chem. Res.* 2007, *46*, 2628–2636, doi:10.1021/ie0612919.

20. Newitt, D.M.; Wheale, K.E. Solution and Diffusion of Gases in Polystyrene at High Pressures. *J. Chem. Soc.* 1948,

1541–1549.

21. Hilic, S.; Boyer, S.A.E.; Pàdua, A.A.H.; Grolier, J.P.E. Simultaneous measurement of the solubility of nitrogen and carbon dioxide in polystyrene and of the associated polymer swelling. *J. Polym. Sci. Part B Polym. Phys.* 2001, *39*, 2063–2070, doi:10.1002/polb.1181.

22. Areerat, S.; Funami, E.; Hayata, Y.; Nakagawa, D.; Ohshima, M. Measurement and prediction of diffusion coefficients of supercritical CO_2 in molten polymers. *Polym. Eng. Sci.* 2004, *44*, 1915–1924.

23. Sato, Y.; Yurugi, M.; Fujiwara, K.; Takishima, S.; Masuoka, H. Solubilities of carbon dioxide and nitrogen in polystyrene under high temperature and pressure. *Fluid Phase Equilib.* 1996, *125*, 129–138.

24. Sato, Y.; Fujiwara, K.; Takikawa, T.; Sumarno; Takishima, S.; Masuoka, H. Solubilities and diffusion coefficients of carbon dioxide and nitrogen in polypropylene, high-density polyethylene, and polystyrene under high pressures and temperatures. *Fluid Phase Equilib.* 1999, *162*, 261–276, doi:10.1016/S0378-3812(99)00217-4.

25. Sato, Y.; Takikawa, T.; Takishima, S.; Masuoka, H. Solubilities and diffusion coefficients of carbon dioxide in poly(vinyl acetate) and polystyrene. *J. Supercrit. Fluids* 2001, *19*, 187–198.

26. Perez-Blanco, M.; Hammonds, J.R.; Danner, R.P. Measurement of the Solubility and Diffusivity of Blowing Agents in Polystyrene. *J. Appl. Polym. Sci.* 2009, *116*, 2359–2365, doi:10.1002/app.

27. Milano, G.; Müller-Plathe, F. Mapping atomistic simulations to mesoscopic models: A systematic coarse-graining procedure for vinyl polymer chains. *J. Phys. Chem. B* 2005, *109*, 18609–18619, doi:10.1021/jp0523571.

28. Harmandaris, V.A.; Adhikari, N.P.; Van Der Vegt, N.F.A.; Kremer, K. Hierarchical modeling of polystyrene: From atomistic to coarse-grained simulations. *Macromolecules* 2006, *39*, 6708–6719, doi:10.1021/ma0606399.

29. Harmandaris, V.A.; Kremer, K. Dynamics of polystyrene melts through hierarchical multiscale simulations. *Macromolecules* 2009, *42*, 791–802, doi:10.1021/ma8018624.

30. Spyriouni, T.; Tzoumanekas, C.; Theodorou, D.; Müller-Plathe, F.; Milano, G. Coarse-grained and reverse-mapped united-atom simulations of long-chain atactic polystyrene melts: Structure, thermodynamic properties, chain conformation, and entanglements. *Macromolecules* 2007, *40*, 3876–3885, doi:10.1021/ma0700983.

31. He, Y.Y.; Lutz, T.R.; Ediger, M.D.; Ayyagari, C.; Bedrov, D.; Smith, G.D. NMR experiments and molecular dynamics simulations of the segmental dynamics of polystyrene. *Macromolecules* 2004, *37*, 5032–5039.

32. Lyulin, A. V.; Balabaev, N.K.; Michels, M.A.J. Correlated Segmental Dynamics in Amorphous Atactic Polystyrene: A Molecular Dynamics Simulation Study. *Macromolecules* 2002, *35*, 9595–9604, doi:10.1063/1.1580808.

33. Vogiatzis, G.G.; Theodorou, D.N. Local segmental dynamics and stresses in polystyrene-C60 mixtures. *Macromolecules* 2014, *47*, 387–404, doi:10.1021/ma402214r.

34. Ndoro, T.V.M.; Voyiatzis, E.; Ghanbari, A.; Theodorou, D.N.; Michael, C.B.; Florian, M. Interface of Grafted and Ungrafted Silica Nanoparticles with a Polystyrene Matrix : Atomistic Molecular Dynamics Simulations. *Macromolecules* 2011, *44*, 2316–2327, doi:10.1021/ma102833u.

35. Ndoro, T.V.M.; Boehm, M.C.; Müller-Plathe, F. Interface and Interphase Dynamics of Polystyrene Chains near Grafted and Ungrafted Silica Nanoparticles. 2012, 171–179, doi:10.1021/ma2020613.

36. Mathioudakis, I.G.; Vogiatzis, G.G.; Tzoumanekas, C.; Theodorou, D.N. Multiscale simulations of PS–SiO2 nanocomposites: from melt to glassy state. *Soft Matter* 2016, *12*, 7585–7605, doi:10.1039/C6SM01536K.

37. Zoller, P.; Hoehn, H.H. Pressure-Volume-Temperature Properties of Blends of Poly (2,6-dimethyl-1,4-phenylene Ether) with Polystyrene. *J Polym Sci B Polym Phys* 1982, *20*, 1385–1397.

38. Cuthbert, T.; Wagner, N.; Paulaitis, M. Molecular simulation of glassy polystyrene: size effects on gas solubilities. *Macromolecules* 1997, *30*, 3058–3065.

39. Widom, B. Some Topics in the Theory of Fluids. *J. Chem. Phys.* 1963, *39*, 2808–2812, doi:10.1121/1.418538.

40. Kucukpinar, E.; Doruker, P. Molecular simulations of small gas diffusion and solubility in copolymers of styrene. *Polymer (Guildf).* 2003, *44*, 3607–3620, doi:10.1016/S0032-3861(03)00166-6.

41. Gusev, A.A.; Arizzi, S.; Suter, U.W.; Moll, D.J. Dynamics of light gases in rigid matrices of dense polymers. *J. Chem. Phys.* 1993, *99*, 2221–2227, doi:10.1063/1.465283.

42. Eslami, H.; Muller-Plathe, F. Molecular dynamics simulation of sorption of gases in polystyrene. *Macromolecules* 2007, *40*, 6413–6421, doi:10.1021/ma070697+.

43. Mozaffari, F.; Eslami, H.; Moghadasi, J. Molecular dynamics simulation of diffusion and permeation of gases in polystyrene. *Polymer (Guildf).* 2010, *51*, 300–307, doi:10.1016/j.polymer.2009.10.072.

44. Spyriouni, T.; Boulougouris, G.C.; Theodorou, D.N. Prediction of sorption of CO_2 in glassy atactic polystyrene at elevated pressures through a new computational scheme. *Macromolecules* 2009, *42*, 1759–1769, doi:10.1021/ma8015294.

45. Karayiannis, N.C.; Giannousaki, A.E.; Mavrantzas, V.G.; Theodorou, D.N. Atomistic Monte Carlo simulation of strictly monodisperse long polyethylene melts through a generalized chain bridging algorithm. *J. Chem. Phys.* 2002, *117*, 5465–5479, doi:10.1063/1.1499480.

46. Karayiannis, N.C.; Mavrantzas, V.G.; Theodorou, D.N. A Novel Monte Carlo Scheme for the Rapid Equilibration of Atomistic Model Polymer Systems of Precisely Defined Molecular Architecture. *Phys. Rev. Lett.* 2002, *88*, 4.

47. Sanchez, I.C.; Lacombe, R.H. Statistical Thermodynamics of Polymer Solutions. *Macomolecules* 1978, *11*, 1145–1156.

48. Plimpton, S. Fast Parallel Algorithms for Short–Range Molecular Dynamics. *J. Comput. Phys.* 1995, *117*, 1–19.

49. Müller-Plathe, F. Local Structure and Dynamics in Solvent-Swollen Polymers. *Macromolecules* 1996, *29*, 4782–4791, doi:10.1021/ma9518767.

50. Harris, J.G.; Yung, K.H. Carbon Dioxide's Liquid-Vapor Coexistence Curve And Critical Properties as Predicted by a Simple Molecular Model. *J. Phys. Chem.* 1995, *99*, 12021–12024, doi:10.1021/j100031a034.

51. Jorgensen, W.L.; Severance, D.L. Aromatic-Aromatic Interactions: Free Energy Profiles for the Benzene Dimer in Water, Chloroform, and Liquid Benzene. *J. Am. Chem. Soc.* 1990, *112*, 4768–4774, doi:10.1021/ja00168a022.

52. Müller-Plathe, F. Unexpected Diffusion Behavior of Gas Molecules in Crystalline Poly(4-Methyl-1-Pentene). *J. Chem. Phys.* 1995, *103*, 4346–4351, doi:10.1063/1.470673.

53. Milano, G.; Guerra, G.; Mu, F.; Muller-Plathe, F. Anisotropic Diffusion of Small Penetrants in the δ Crystalline Phase of Syndiotactic Polystyrene : A Molecular Dynamics Simulation Study. *Chem. Mater.* 2002, 2977–2982.

54. Hockney, R.W.; Eastwood, J.W. *Computer Simulation Using Particles*; CRC Press: Boca Raton, 1988;

55. Flory, P.J. *Statistical mechanics of chain molecules*; Interscience: New York, 1969;

56. Theodorou, D.N.; Suter, U.W. Detailed Molecular Structure of a Vinyl Polymer Glass. *Macromolecules* 1985, *18*, 1467–1478, doi:10.1021/ma00149a018.

57. Ryckaer, J.-P.; Ciccotti, G.; Berendsen, H.J.C. Numerical integration of the cartesian equations of motion of a system with constraints: molecular dynamics of n-alkanes. *J. Comput. Phys.* 1977, *23*, 327–341.

58. Tuckerman, M.; Berne, B.J.; Martyna, G.J. Reversible multiple time scale molecular dynamics. *J. Chem. Phys.* 1992, *97*, 1990–2001, doi:10.1063/1.463137.

59. https://lammps.sandia.gov/doc/run_style.html.

60. Algaer, E.A.; Alaghemandi, M.; Böhm, M.C.; Müller-Plathe, F. Anisotropy of the thermal conductivity of stretched amorphous polystyrene in supercritical carbon dioxide studied by reverse nonequilibrium molecular dynamics simulations. *J. Phys. Chem. B* 2009, *113*, 14596–14603, doi:10.1021/jp906447a.

61. Frenkel, D.; Smit, B. *Understanding Molecular Simulation: From Algorithms to Applications*; Elsevier, Ed.; 2001;

62. Shing, K.S.; Chung, S.T. Computer simulation methods for the calculation of solubility in supercritical extraction systems. *J. Phys. Chem.* 1987, *91*, 1674–1681, doi:10.1021/j100290a077.

63. Theodorou, D.N. Principles of Molecular Simulation of Gas Transport in Polymers. In *Materials Science of Membranes for Gas and Vapor Separation*; John Wiley & Sons: Hoboken, NJ, USA, 2006 ISBN 047085345X.

64. Peng, D.; Robinson, D.B. A New Two-Constant Equation of State. *Ind. Eng. Chem. Fundam.* 1976, *15*, 59–64.

65. Zoller, P.; Walsh, D. *Standard Pressure–Volume–Temperature Data for Polymers*; Technomic- Lancaster, 1995;

66. Doghieri, F.; Sarti, G.C. Predicting the low pressure solubility of gases and vapors in glassy polymers by the NELF model. *J. Memb. Sci.* 1998, *147*, 73–86, doi:10.1016/S0376-7388(98)00123-9.

67. Bevington, P.R.; Robinson, D.K. *Data Reduction and Error Analysis for the Physical Sciences, 3rd edn.*; McGraw-Hill: Boston, MA, USA, 2003; ISBN 0072472278.

68. Doghieri, F.; Sarti, G.C. Nonequilibrium Lattice Fluids: A Predictive Model for the Solubility in Glassy Polymers. *Macromolecules* 1996, *29*, 7885–7896, doi:10.1021/ma951366c.

69. Ougizawa, T.; Dee, G.T.; Walsh, D.J. PVT properties and equations of state of polystyrene : molecular weight dependence of the characteristic parameters in equation-of-state theories. *Polymer.* 1988, *30*, 1675–1679.

70. Quach, A.; Simha, R. Pressure-volume-temperature properties and transitions of amorphous polymers; polystyrene and poly(orthomethylstyrene). *J. Appl. Phys.* 1971, *42*, 4592–4606, doi:10.1063/1.1659828.

71. Fox, T.G.; Flory, P.J. The glass temperature and related properties of polystyrene. Influence of molecular weight. *J. Polym. Sci.* 1954, *14*, 315–319, doi:10.1002/pol.1954.120147514.

72. Han, J.; Boyd, R.H. Molecular packing and small-penetrant diffusion in polystyrene: a molecular dynamics simulation study. *Polymer (Guildf).* 1996, *37*, 1797–1804, doi:10.1016/0032-3861(96)87295-8.

73. Fritz, D.; Harmandaris, V.A.; Kremer, K.; Van Der Vegt, N.F.A. Coarse-grained polymer melts based on isolated atomistic chains: Simulation of polystyrene of different tacticities. *Macromolecules* 2009, *42*, 7579–7588,

74. Lyulin, A. V.; Michels, M.A.J. Molecular dynamics simulation of bulk atactic polystyrene in the vicinity of Tg. *Macromolecules* 2002, *35*, 1463–1472, doi:10.1021/ma011318u.

75. Raharjo, R.D.; Freeman, B.D.; Sanders, E.S. Pure and mixed gas CH_4 and n-C_4H_{10} sorption and dilation in poly (dimethylsiloxane). *J. Memb. Sci.* 2007, *292*, 45–61, doi:10.1016/j.memsci.2007.01.012.

76. Matteucci, S.; Yampolskii, Y.; Freeman, B.D.; Pinnau, I. Transport of Gases and Vapor in Glassy and Rubbery Polymers. In *Materials Science of Membranes for Gas and Vapor Separation*; Yampolskii, Y., Pinnau, I., Freeman, B.D., Eds.; John Wiley & Sons, Ltd, 2006.

77. Royer, J.R.; DeSimone, J.M.; Khan, S.A. Carbon dioxide-induced swelling of poly(dimethylsiloxane). *Macromolecules* 1999, *32*, 8965–8973, doi:10.1021/ma9904518.

78. Brandrup, J.; Immergut, E.H.; Grulke, E.A.; Abe, A.; Bloch, D.R. *Polymer Handbook*; Wiley: New York, 1999;

79. Boothroyd, A.T.; Road, P. Temperature coefficients for the chain dimensions of polystyrene and polymethylmethacrylate. *J. Chem. Phys* 1993, *99*.

80. Cotton, J.P.; Farnoux, B.; Jannink, G.; Decker, D.; Benoit, H.; Picot, C.; Higgins, J.; Ober, R.; des Cloizeaux, J. Conformation of Polymer Chain in the Bulk. *Macromolecules* 1974, *7*, 863–872, doi:10.1021/ma60042a033.

81. Auhl, R.; Everaers, R.; Grest, G.S.; Kremer, K.; Plimpton, S.J. Equilibration of long chain polymer melts in computer simulations. *J. Chem. Phys.* 2003, *119*, 12718–12728, doi:10.1063/1.1628670.

82. Wecker, S.M.; Davidson, T.; Cohen, J.B. A structural study of glassy polystyrene. *J. Mater. Sci.* 1972, *7*, 1249–

1259.

83. Burge, R.E.; Adams, R.; Balyuzi, H.H.M.; Burge, R.E. The structure of amorphous polystyrene by X-ray scattering and simple conformational analysis. *J. Mater. Sci.* 1978, *13*, 391–401, doi:10.1007/BF00647784.

84. Schubach, H.R.; Nagy, E.; Heise, B. Short range order of amorphous polymers derived by WAXS. *COLLOID Polym. Sci. KOLLOID-ZEITSCHRIFT* 1981, *5*, 553–554, doi:10.1016/j.jemermed.2014.06.025.

85. Mitchell, G.R.; Windle, A.H. Structure of polystyrene glasses. *Polymer (Guildf).* 1984, *25*, 906–920.

86. Londono, J.D.; Habenschuss, A.; Curro, J.G.; Rajasekaran, J.J. Short-range order in some polymer melts from x-ray diffraction. *J. Polym. Sci. Part B Polym. Phys.* 1996, *34*, 3055–3061, doi:10.1002/(SICI)1099-0488(199612)34:17<3055::AID-POLB17>3.0.CO;2-6.

87. An Approach to the Solution of Structure Problems of Organic Chain Polymers. *Bjornhaug, A. Ellefsen, O. Tonnesen, B.A.* 1954, *XII*, 621–632.

88. https://ia600406.us.archive.org/19/items/InternationalTablesForX-rayCrystallographyVol3/MacgillavryRieckEds-internationalTablesForX-rayCrystallographyVol3.pdf.

89. http://lampx.tugraz.at/~hadley/ss1/crystaldiffraction/atomicformfactors/formfactors.php.

90. Ayyagari, C.; Bedrov, D.; Smith, G.D. Structure of Atactic Polystyrene: A Molecular Dynamics Simulation Study. *Macromolecules* 2000, *33*, 6194–6199, doi:10.1021/ma0003553.

91. Smith, G.D.; Yoon, D.Y.; Wade, C.G.; O'Leary, D.; Chen, A.; Jaffe, R.L. Dynamics of poly(oxyethylene) melts: Comparison of 13 C nuclear magnetic resonance spin-lattice relaxation and dielectric relaxation as determined from simulations and experiments . *J. Chem. Phys.* 1997, *106*, 3798–3805, doi:10.1063/1.473433.

92. Doxastakis, M.; Theodorou, D.N.; Fytas, G.; Kremer, F.; Faller, R.; Müller-Plathe, F.; Hadjichristidis, N. Chain and local dynamics of polyisoprene as probed by experiments and computer simulations. *J. Chem. Phys.* 2003, *119*, 6883–6894, doi:10.1063/1.1603720.

93. Kohlrausch, R. Theorie des elektrischen Rückstandes in der Leidener Flasche. *Ann. der Phys. und Chemie* 1854, *167*, 179–214, doi:10.1002/andp.18541670203.

94. Williams, G.; Watts, D.C. Non-symmetrical dielectric relaxation behaviour arising from a simple empirical decay function. *Trans. Faraday Soc.* 1970, *66*, 80, doi:10.1039/tf9706600080.

95. Logotheti, G.E.; Theodorou, D.N. Segmental and chain dynamics of isotactic polypropylene melts. *Macromolecules* 2007, *40*, 2235–2245, doi:10.1021/ma062234u.

96. Harmandaris, V.A.; Floudas, G.; Kremer, K. Temperature and pressure dependence of polystyrene dynamics through molecular dynamics simulations and experiments. *Macromolecules* 2011, *44*, 393–402.

97. Theodorou, D.N. Molecular Simulations of Sorption and Diffusion in Amorphous Polymers. In *Diffusion in Polymers*; Neogi, P., Ed.; Marcel Dekker: New York, Basel, Honk Kong, 1996; pp. 67–142.

98. Pschorn, U.; Roessler, E.; Sillescu, H.; Kaufmann, S.; Schaefer, D.; Spiess, H.W. Local and Cooperative Motions at the Glass Transition of Polystyrene: Information from One- and Two-Dimentional NMR as Compared with Other Techniques. *Macomolecules* 1991, *24*, 398–402, doi:10.1021/ma00002a009.

99. Durrill, P.L.; Griskey, R.G. Diffusion and solution of gases in thermally softened or molten polymers: Part I. Development of technique and determination of data. *AIChE J.* 1966, *12*, 1147–1151.

100. Sato, Y.; Takikawa, T.; Sorakubo, A.; Takishima, S.; Masuoka, H.; Imaizumi, M. Solubility and Diffusion Coefficient of Carbon Dioxide in Biodegradable Polymers. *Ind. Eng. Chem. Res.* 2000, *39*, 4813–4819.

Chapter 7

Conclusions

The transport of gases and vapors in dense polymeric materials is a process of great importance in several industrial applications, including membrane separations. This phenomenon is described through the solution-diffusion mechanism and two distinct contributions concur into the determination of the final permeability of membrane materials, namely solubility and diffusivity. The independent analysis of each of these contributions helps shedding light on the fundamental aspects of the process, to provide guidelines for the future design of better performing materials.

This dissertation focused primarily on the solubility contribution to permeability, analyzing materials for gas separation membranes, with emphasis on the CO_2/CH_4 separation. In particular, suitable modelling approaches have been identified and validated for the prediction of solubility and solubility-selectivity at multicomponent conditions of several different polymer families: cellulose acetates, polystyrene, polyimides, thermally rearranged (TR) polymers and polymers of intrinsic microporosity (PIMs).

The majority of current industrial standards and prospective new candidates as membrane materials are glassy polymers. These are nonequilibrium structures, whose properties depend, besides chemical makeup, also on the complex interplay between thermal history and fabrication conditions. Different strategies were employed to overcome the specific limitations encountered in the modelling of gas sorption in several representative case studies.

Gas solubility in cellulose diacetate (CDA) and triacetate (CTA), widely employed industrially, yet still poorly understood materials, was evaluated in the framework of the Non-Equilibrium Thermodynamics for Glassy Polymers approach, broadening the available characterization in order to be able to describe their properties in a wide range of temperatures, both with equilibrium and nonequilibrium thermodynamic models. The effect of the crystallinity of the materials was accounted for during the retrieval of the model

parameters and in modelling gas sorption. The comparison of the modelling results with experimental data yielded encouraging indications concerning the transferability of the parameters obtained.

It is a well-known issue that the estimate of material performance based on pure-gas data is often unreliable, and this prevents the adoption of many potentially advantageous materials as membranes in the industry. To overcome this impasse and take steps towards a more realistic assessment of the properties of membrane materials, it is necessary to evaluate the separation performance at multicomponent conditions and in a range of operating parameters relevant for the target applications already at the laboratory scale. This problem was address both from the experimental and the modelling point of view. Multicomponent tests are significantly more delicate and time consuming than pure-gas ones. Therefore, the modelling of sorption at multicomponent conditions using predictive tools, requiring at most pure-gas sorption data to be parametrized, is of great interest. To use these tools confidently, their validation is required. Two models were tested to this aim, the Non-Equilibrium Lattice Fluid (NELF) model, and the Dual Mode Sorption (DMS) model. The results have been systematically compared against several experimentally available data sets for CO_2/CH_4 sorption at mixed-gas conditions in PTMSP, PIM-1, TZ-PIM, PIM-EA-TB, HAB-6FDA and TR450. The accuracy of the models in representing the non-idealities that arise during mixed-gas sorption was assessed, and the strengths and weaknesses of each model were highlighted. The reduction in solubility due to competition, when a second gas is present in the mixture, was correctly captured by both models, as well as the temperature and concentration trends expected. In general, the NELF model showed a higher quantitative accuracy, consistency of the results, and robustness with respect to a perturbation of the input parameters. On the other hand, the multicomponent Dual Mode Sorption model is of more immediate use, but it yielded on average predictions of lower accuracy. Moreover, a sensitivity analysis revealed a severe lack of robustness with respect to a small perturbation of its input data.

The use of the NELF model to predict solubility and solubility-selectivity at the desired conditions of temperature and composition allowed the coupling of the results with mixed-gas permeation measurements, to gather indirect information on diffusivity trends at mixed-gas conditions, for a more detailed assessment of the relevant phenomena during mixed-gas permeation. In particular, a combined analysis of multicomponent permeation data from the literature and sorption data, either measured or modelled with the NELF model, revealed, as a general trend, that the selectivity at multicomponent conditions becomes controlled by solubility differences, owing to the simultaneous effects of competitive sorption, which enhances solubility-selectivity, and swelling, which lowers the diffusivity-selectivity.

As anticipated, the problem of providing a more realistic picture of membrane performance was addressed also from the experimental point of view, by generalizing a protocol for the measurement of gas sorption of mixtures of an arbitrary number of components using a pressure decay apparatus. $C_2H_6/CO_2/CH_4$ mixtures in PIM-1 were used as a test case. In addition, also the characterization of sorption of binary mixtures of C_2H_6/CO_2 and C_2H_6/CH_4 has been performed. From the ternary mixture sorption tests, sorption isotherms of each gas at constant equilibrium composition of the gas phase were obtained. The results revealed interesting features, in terms of competition and its effect on the solubility-selectivity, and paved the way

for an analysis of the effects of pollutants and third components on solubility, which is of interest for several applications, besides the CO_2/CH_4 separation. The NELF model was used both in the estimate of the loading pressures necessary to perform the experiment, and to predict the results, finding remarkably good agreement with the experimental data for different mixtures and compositions investigated. Unexpected behavior for the C_2H_6/CO_2 mixture was recorded, which will be further investigated. Performing evaluations of multicomponent sorption with a modelling tool that requires only pure-gas data to be parametrized, constitute a powerful tool to gain relevant additional information directly, taking advantage of experimental characterization already widely available in the literature or with reduced effort, related only to the measurement of pure-gas sorption.

It is clear, however, that the NELF model is not completely predictive, because it requires preliminary knowledge of data for the pure-components and the single gas-polymer mixture to be employed. In fact, pressure-volume-temperature measurements on cellulose acetates and pure-gas sorption measurements of CO_2, CH_4 and C_2H_6 were performed in the context of this dissertation precisely to this aim.

Molecular simulations, on the other hand, allow a truly predictive study of material properties. They were applied in this dissertation to the study of the polystyrene-CO_2 system, in order to assess the possibility to correctly account for polymer molecular weight, temperature and gas concentration effects on material properties. It was found that a very accurate description of the structural properties and their dependencies on the variables considered could be obtained, whereas the local dynamics was orders of magnitude slower than expected. Nonetheless, even for the local dynamics, meaningful trends with respect to the relevant variables were obtained. Solubility and diffusivity, as well as swelling and plasticization effects, were evaluated up to high pressure, difficult to reach experimentally, displaying satisfactory agreement with experimental measurements and consistent trends with respect to all the variables considered. The greatest advantage of these techniques is the possibility to make an in-depth analysis of the molecular origin of the macroscopic features uncovered an provide an interpretation of the results, that can guide design of future materials.

Future work concerning the topics of this dissertation could address the need to expand the still limited database of mixed-gas sorption data and modelling. In particular, it would be interesting to test other relevant gas couples for membrane separations where condensable components are present. These gas couples are expected to display relevant nonidealities in multicomponent sorption: CO_2/N_2, H_2/CO_2, for CO_2 capture from power plants and industrial exhaust gases and in syngas production, C_3H_6/N_2, C_2H_4/N_2, C_2H_4/Ar, C_{3+}/CH_4, for vapor recovery and olefin/paraffin separations that are currently preformed with very energy intensive distillation processes. It would be interesting also to probe the presence and relevance of these effects in other important membrane separations such as O_2/N_2, or in the case when one hardly soluble and one not very soluble gas are present: H_2/N_2, H_2/CH_4, H_2/CO for hydrogen recovery, and He/CH_4 for natural gas treatment. In addition, multicomponent sorption effects could be probed in other families of materials, such as perfluorinated polymers, innovative microporous polymers, or Mixed Matrix Membranes, to gather a broader picture of mixed-gas sorption effects in different systems and draw

structure-properties correlations. Moreover, tests and modelling analysis of sorption of more complex mixtures, with third or additional components will provide a more realistic assessment of the material performance and insight on the phenomena at play at the fundamental level.

Concerning the use of molecular modelling tools, the extremely high computational effort required by atomistic approaches, combined to the system-specificity of several methods, remains a drawback in their application to the study of the gas separation properties of high molecular weight polymers. At present, in the case of the complex chemical structures of interest in gas separation applications, only low molecular weight chains can be fully equilibrated with the computational resources available. Even in the case of low molecular weight chains in full atomistic detail, their equilibration is often accomplished by means of heuristic algorithms, in the lack of efficient mesoscale models for a fast and theoretically sound sampling of the configuration space. Significant research effort is currently being devoted to the development of suitable mesoscale models for the representation of the gas separation properties of glassy polymers of complex chemical makeup by means of molecular models with reduced computer time. When simulations catch up with chemistry, it will enable a true computation assisted materials development for a rational design of membranes.

Acknowledgements

Any experience in life is defined by the people that share the road with us and that we cross path with, and a Ph.D. is no exception. All notable encounters in life will expand our minds and expand our hearts, leaving us with more passion for discovery, more thirst for knowledge, more openness to experiences and more appetite for life. It is with immense gratitude that I reflect upon my experience as a Ph.D. student, and realize it contained so many of such encounters.

Heartfelt thanks to my supervisor, prof. Maria Grazia De Angelis, for the possibility to embark on this journey and her support during these years. Her guidance, trust and her encouragement to explore new directions gave me freedom and confidence to indulge all my curiosities and expand my scientific horizons. It is with immense gratitude that I acknowledge all the opportunities to collaborate and the support to connect with the research community that she provided, which were invaluable for my personal as well as my professional growth.

I am grateful to prof. Doros Theodorou, for welcoming me to spend many months of my graduate studies in his group at the National Technical University of Athens, and for the many enlightening conversations, from which every time I learn so much. My deepest thank to Dr. Niki Vergadou, of the National Center for Scientific Research Demokritos, for her warm hospitality and generosity, her passion for sharing knowledge, the tireless help in and out of the lab and her closeness, that made my stay in Greece a truly life-defining time. Ευχαριστώ πολύ to all the amazing friends I made over there. Thanks to the people at the Co.M.S.E. lab at NTUA, Akis, Stefanos, Spyros, Aris, Orestis, to the people at NCSR Demokritos, Kostas, Manolis, Loukas, Vasilis, Elias, and to my friends from Mechanical Engineering, James, Danae, Morteza, Iannis, Christos, Katerina. Thanks for all the great times, all the laughter, the food, the music, the history and culture you shared with me. You all went above and beyond to make me feel welcome and a part of the

family. Special thanks to Flavio, Kostas, Chiara & Chiara, Vasilis and Christianna, companions of many Hellenic adventures. Good luck to all of you for a bright and prosperous future.

Warmest thanks go to my lab mates in Bologna, Riccardo Rea, Davide Venturi, Francesco Maluta, Matilde De Pascale, Riccardo Casadei, Luca Olivieri, Eleonora Lalli, which I can be so fortunate to call my friends. We are confronted daily with the fact that alone we can accomplish so little, but the certainty to be able to count on one another, your enthusiasm and generosity, made coming to the lab a pleasure every day and pushing through the bad times so much easier. Even though we are already scattered all around the world, I know it is a seed that we all carry with us. I wish to thank Francesco Benedetti in particular, for it was a rare gift to be able to share so much in such little time, inside of the lab and outside.

To my lifelong friends Francesca “Tullia” Mariano Narni, Giorgia Zagni, Riccardo Sighinolfi, I owe you for your continuing friendship and support throughout all the ups and downs of these years, for always being there to cheer me up and having wise words to share. A warm thank goes to Andrea Ghermandi, that shared a long part of this journey, and of life, with me. Many thanks also my friends and band mates Federico Salvarani, Greta Salvalai, Federico Bedostri and Tommaso Marchesini. Music has always been my relief valve, and I am so proud of what we create under the name Atertrip. Kudos to you for providing creative solutions to my times of existential crisis (“less polymers, more polyrhythmics!”).

And finally, the most important thank to my family, my mother, father and sister. Here words would never do justice to my feelings, and I can only say I am beyond grateful to you for always believing in me, even when I was doubting myself. I would not stand here today if it were not for all your never-ending support, encouragement and love.